














THE 62ND ICFA ADVANCED BEAM DYNAMICS WORKSHOP ON HIGH LUMINOSITY CIRCULAR e^+e^- COLLIDERS (eeFACT2018)

24-27 Sep 2018

Goals of the eeFACT2018 workshop

- ✓ Reviewing and documenting the state of the art in e^+e^- factory design
- ✓ Reviewing and drawing lessons from SuperKEKB phase 2 commissioning
- ✓ Catalyzing further contributions to the SuperKEKB, FCC, CEPC & tau-charm design efforts
- ✓ Fostering synergies and new collaborations across communities, in particular with the low-emittance light sources and between continents
- ✓ Jointly developing novel solutions to outstanding problems

Committee Members

-  **Rob Appleby**
The University of Manchester
-  **Ralph Assmann**
Deutsches Elektronen-Synchrotron (DESY)
-  **Marica Enrica Biagini**
National Institute for Nuclear Physics (INFN), Italy
-  **Alain Blondel**
CERN
-  **Manuela Boscolo**
National Institute for Nuclear Physics (INFN), Italy
-  **Alex Chao**
Stanford University (Retired)
-  **Weiren Chou**
Institute of High Energy Physics (IHEP), Chinese Academy of Sciences
-  **Andrew Cohen (co-chair)**
The Hong Kong University of Science and Technology
-  **Yoshihiro Funakoshi (co-chair)**
High Energy Accelerator Research Organization (KEK)
-  **Jie Gao**
Institute of High Energy Physics (IHEP), Chinese Academy of Sciences
-  **Patrick Janot**
CERN
-  **Haruyo Koiso**
High Energy Accelerator Research Organization (KEK)
-  **Eugene Levichev**
Budker Institute of Nuclear Physics (BINP)

Workshop Organizers

-  **Andrew Cohen (Local Committee Chair)**
HKUST
-  **Yoshihiro Funakoshi**
High Energy Accelerator Research Organization (KEK)
-  **Qing Qin**
Institute of High Energy Physics (IHEP), Chinese Academy of Sciences
-  **Frank Zimmermann**
CERN
-  **Peter McIntosh**
Science and Technology Facilities Council, UK
-  **Katsunobu Oide**
High Energy Accelerator Research Organization (KEK)
-  **Yukiyoshi Onishi**
High Energy Accelerator Research Organization (KEK)
-  **Qing Qin (co-chair)**
Institute of High Energy Physics (IHEP), Chinese Academy of Sciences
-  **Peter Ratoff**
The Cockcroft Institute of Accelerator Science and Technology
-  **Bob Rimmer**
Thomas Jefferson National Accelerator Facility
-  **John Seeman**
SLAC National Accelerator Laboratory
-  **Chuanxiang Tang**
Tsinghua University
-  **Jorg Wenninger**
CERN
-  **Ferdinand Willeke**
Brookhaven National Laboratory
-  **Chenghui Yu**
Institute of High Energy Physics (IHEP), Chinese Academy of Sciences
-  **Frank Zimmermann (co-chair)**
CERN



Enquiries:

+852 2358 5061 eefact2018@ust.hk <http://eefact2018.ust.hk>



eeFACT2018

The 62nd ICFA Advanced Beam Dynamics Workshop on High Luminosity Circular e+e—Colliders
24-27 Sep 2018 HKUST Jockey Club Institute for Advanced Study, HK

ics

HKUST JOCKEY CLUB
INSTITUTE FOR ADVANCED STUDY

THE HONG KONG
UNIVERSITY OF SCIENCE
AND TECHNOLOGY



Institute of High Energy Physics
Chinese Academy of Sciences



Committees

Workshop organisers:

Andrew Cohen (Local Committee Chair), HKUST
Yoshihiro Funakoshi, KEK
Qing Qin, IHEP
Frank Zimmermann, CERN

Committee Members:

Rob Appleby, the University of Manchester
Ralph Assmann, DESY
Marica Enrica Biagini, INFN
Alain Blondel, CERN
Manuela Boscolo, INFN
Alex Chao, Stanford University (Retired)
Weiren Chou, IHEP
Andrew Cohen (co-chair), HKUST
Yoshihiro Funakoshi (co-chair), KEK
Jie Gao, IHEP
Patrick Janot, CERN
Haruyo Koiso, KEK
Eugene Levichev, BINP
Peter McIntosh, Science and Technology Facilities Council, UK
Katsunobu Oide, KEK
Yukiyoshi Onishi, KEK
Qing Qin (co-chair), IHEP
Peter Ratoff, The Cockcroft Institute of Accelerator Science and Technology
Bob Rimmer, TJNAF
John Seeman, SLAC
Chuanxiang Tang, Tsinghua University
Jorg Wenninger, CERN
Ferdinand Willeke, BNL
Chenghui Yu, IHEP
Frank Zimmermann (co-chair), CERN

Editorial Board:

Yingying Li, HKUST
Lu Li, IMP
Volker RW Schaa, GSI

Contents

Preface

Foreword	iii
Committees	iv
Contents	v

Papers

MOXAA02 – Highlights from SuperKEKB Commissioning	1
MOXBA01 – Challenges for Circular e^+e^- Colliders	7
MOYAA01 – Several Topics on Beam Dynamics in FCC-ee	18
MOYAA02 – Status of DAΦNE: from KLOE-2 to SIDDHARTA-2 Experiment with Crab-Waist	23
MOYAA05 – The Status of CEPC	30
MOYBA01 – Round Colliding Beams at Vepp-2000 with Extreme Tuneshifts	34
MOYBA04 – Report from ARIES Muon Collider Workshop in Padua	41
TUOAB01 – Dynamic Aperture Limitation Due to the Synchrotron Radiation from Quadrupole Magnets in very High Energy Colliders	46
TUOAB02 – Low-emittance Tuning for Circular Colliders	57
TUOAB04 – Optics Corrections including IP Local Coupling at SuperKEKB	63
TUOBB01 – Optics Aberration at IP and Beam-beam Effects	66
TUOBB02 – Off-momentum Optics at SuperKEKB	71
TUOBB03 – Progress of Preliminary Work for the Accelerators of a 2-7GeV Super Tau Charm Facility at China	76
TUOBB04 – Different Optics within Large Energy Region at BEPCII	79
TUYAA01 – High Currents Effects in DAΦNE	82
TUYAA03 – Impedances and Collective Effects for JLEIC	90
TUYAA04 – Study to Mitigate Electron Cloud Effect in SuperKEKB	95
TUYBA01 – Benchmarking of Simulations of Coherent Beam-beam Instability	103
TUYBA02 – Beam-beam Effects at High Energy e^+e^- Colliders	106
TUYBA03 – Beam-beam Blowup in the Presence of x-y Coupling Sources for FCC-ee	112
TUYBA04 – Some Issues on Beam-beam Interaction at CEPC	116
TUPAB01 – KEKB Injection Developments	121
TUPAB02 – Low Emittance Beam Transport for e^-/e^+ LINAC	126
TUPAB03 – Overall Injection Strategy for FCC-ee	131
TUPAB04 – Overall Design of the CEPC Injector LINAC	139
TUPAB05 – An On-axis Injection Design for CEPC	143
TUPAB06 – Design and Beam Dynamics of the CEPC Booster	146
TUPAB07 – Commissioning of Positron Damping Ring and the Beam Transport for SuperKEKB	152
TUPBB03 – Performance of the FCC-ee Polarimeter	157
TUPBB04 – Resonant Depolarization at Z and W at FCC-ee	165
TUPBB05 – Beam Instrumentation at SuperKEKB	169
TUPBB06 – Fast Luminosity Monitoring for the SuperKEKB Collider (LumiBelle2 Project)	173
WEXAA01 – High Precision Experiments in the J/psi, Psi(2S) and Tau Sector	179
WEXAA02 – Polarization Issues at CEPC	182
WEXAA04 – Ideas for Longitudinal Polarization at the Z/W/H/top Factory	190
WEXBA01 – IR Design for High Luminosity and Low Backgrounds	194
WEXBA02 – Machine Detector Interface for the e^+e^- Future Circular Collider	201
WEXBA03 – Beam Blowup due to Lattice Coupling/Dispersion with/without Beam-beam	207
WEXBA04 – Early Commissioning of the Luminosity Dither System for SuperKEKB	212
WEXBA05 – Machine Detector Interface for CEPC	217
WEXBA06 – Beam Background at SuperKEKB During Phase 2 Operation	221
WEOAB01 – Commissioning Status of SuperKEKB Vacuum System	226
WEOAB04 – Single Bunch Instabilities and NEG Coating for FCC-ee	234
WEOBB02 – CEPC Superconducting Magnets	241
WEOBB05 – CEPC Collider and Booster Magnets	247
WEYAA02 – Large Scale Superconducting RF Production	251
WEYAA03 – SRF System for KEKB and SuperKEKB	256
WEPAB02 – CEPC Civil Engineering Design	264

WEPAB03 – FCC-ee Operation Model, Availability & Performance	269
WEPAB04 – KEKB/SuperKEKB Cryogenics Operation	276
WEPAB05 – Conceptional design of CEPC Cryogenic system	282
WEPBB01 – Operation of SuperKEKB in Phase 2	286
THXBA01 – Summary on Accelerator Infrastructures and Commissioning	290
Appendices	293
List of Authors	293
Institutes List	297

HIGHLIGHTS FROM SuperKEKB PHASE 2 COMMISSIONING

Y. Ohnishi*, KEK, 1-1 OHO, Tsukuba, Ibaraki 305-0801, Japan

on behalf of the SuperKEKB Commissioning Group and the Belle II Commissioning Group

Abstract

SuperKEKB is an electron-positron asymmetric-energy collider to search new physics phenomena appeared in B-meson decays. In order to accomplish this purpose, 40 times the luminosity as high as the KEKB collider is demanded. The strategy is that the vertical beta function at the IP is squeezed down to 1/20 and the beam currents double those of KEKB while keeping the same beam-beam parameter. The vertical beta function at the interaction point(IP) will be much smaller than the bunch length, however, the hour-glass effect which degrades the luminosity will be reduced by adopting a novel “nano-beam” scheme. First of all, the Phase 2 commissioning was focused on the verification of nano-beam scheme. Secondary, beam related background at the Belle II detector was also studied for the preparation of the pixel vertex detector installed before the Phase 3 operation. The preliminary results and accomplishments of the commissioning in Phase 2 will be reported in this article.

INTRODUCTION

SuperKEKB is an electron-positron collider [1] and the Belle II detector [2] built to explore new phenomena in particle physics. The physics program of the next B-factory delivering ultra high statistics is almost independent of, and complementary to, the high energy experiments at the LHC. The target luminosity is $8 \times 10^{35} \text{ cm}^{-2}\text{s}^{-1}$, which is 40 times the performance of the predecessor, KEKB [3], which has been operated for 11 years until 2010. The strategy for the luminosity upgrade is a nano-beam scheme. The nano-beam scheme was first proposed by P. Raimondi in Italy [4]. The collision of low emittance beams under a large crossing angle allows squeezing the beta functions at the IP much smaller than the bunch length. Consequently, extremely higher luminosity can be expected with only twice the beam current of KEKB.

The SuperKEKB operation is divided by 3 stages, Phase 1, Phase 2, and Phase 3. The upgrade work was started after the shutdown of KEKB, and it took 6 years to make the Phase 1 commissioning ready. The final focus system(QCS) [5] and Belle II detector were not installed in Phase 1 [6]. The subjects were vacuum scrubbing for new vacuum system replaced with ante-chambers, low emittance tuning for new arc lattice to realize low emittance, and beam background study prepare for the installation of Belle II detector before Phase 2. The final focus system and Belle II detector were installed during a long shutdown between Phase 1 and Phase 2. Prior to the main ring operation, the commissioning of the positron damping ring [7] started on 8th February 2018 almost in 2 years after the Phase 1 commissioning. The

Phase 2 commissioning started on 19th March 2018. The commissioning in Phase 2 was finished on 17th July 2018 and the duration was about 4 months in total. The common machine parameters during Phase 2 are shown in Table 1.

The Phase 3 operation will start in the early 2019, which is a full-scale collider experiment after installation of the pixel vertex detector(PXD) to Belle II.

Table 1: Machine Parameters related to the RF system in Phase 2. The intra-beam scattering and other collective effects are not included.

	LER	HER	Unit
Beam Energy	4	7	GeV
Circumference	3016.3		m
Harmonic no.	5120		
Total RF voltage	8.4	12.8	MV
α_p	2.88×10^{-4}	4.50×10^{-4}	
σ_z	4.8	5.4	mm
σ_δ	7.53×10^{-4}	6.3×10^{-4}	
U_0	1.76	2.43	MV
ν_s	-0.0220	-0.0258	

TARGET OF THE PHASE 2 COMMISSIONING

The overlap region for the narrow colliding beams with a large crossing angle can be small along the beam axis which implies a head-on collision of effective beams having the very short bunch length. A picture of the effective beams is a projection of the real beams to the x -axis which is an isovolumetric deformation. The effective beam is considered in the nano-beam scheme which is written by

$$\sigma_{z,eff} = \frac{\sigma_x^*}{\phi_x} \quad (1)$$

$$\sigma_{x,eff}^* = \sigma_z \phi_x, \quad (2)$$

where σ_x^* is the horizontal beam size at the IP, σ_z is the bunch length, and ϕ_x is the half crossing angle. Then, the luminosity and beam-beam parameters are calculated by using the effective beam. In order to avoid an hourglass effect, the following condition is necessary.

$$\beta_y^* \geq \sigma_{z,eff} = \frac{\sigma_z}{\Phi}, \quad (3)$$

where the Piwinski angle is defined by

$$\Phi = \frac{\sigma_{x,eff}^*}{\sigma_x^*}. \quad (4)$$

* yukiyooshi.ohnishi@kek.jp

The Piwinski angle is larger than 10 in the nano-beam scheme while that of the conventional collision scheme is smaller than 1. Therefore, β_y^* can be squeezed down to 300 μm with assuming $\sigma_z = 6$ mm and $\Phi = 20$. The arc cell and the interaction region are designed to realize the low emittance and large Piwinski angle in the nano-beam scheme. Another point of view of the overlap region is distributions of primary vertex positions. In the case of nano-beam scheme, the vertex distribution along the z -axis is constrained in the small region, for example $\sigma_{vertex} = 550$ μm in Phase 2 in contrast with $\sigma_{vertex} = 4.5$ mm in the conventional scheme such as KEKB which are measured by the vertex detectors.

The luminosity in the nano-beam scheme is written by

$$L = \frac{N_- N_+ n_b f_0}{4\pi\sigma_{x,eff}^* \sqrt{\varepsilon_y \beta_y^*}} \approx \frac{\gamma_{\pm}}{2er_e} \frac{I_{\pm} \xi_{y\pm}}{\beta_y^*}, \quad (5)$$

where the vertical beam-beam parameter is

$$\xi_{y\pm} = \frac{r_e N_{\mp}}{2\pi\gamma_{\pm}\sigma_{x,eff}^*} \sqrt{\frac{\beta_y^*}{\varepsilon_y}}. \quad (6)$$

In Eqs. 5 and 6, $\varepsilon_{y-} = \varepsilon_{y+}$ and $\beta_{y-}^* = \beta_{y+}^*$ are assumed, n_b is the number of bunches, N_{\pm} is the number of particles in a bunch, f_0 is the revolution frequency. When the β_y^* is squeezed, the ξ_y becomes small proportional to $\sqrt{\beta_y^*}$, however, the luminosity increases proportional to $1/\sqrt{\beta_y^*}$. If we can make ε_y small similar to the ratio of the beta squeezing, the luminosity is proportional to $1/\beta_y^*$ with keeping the same ξ_y .

The targets in the Phase 2 commissioning are

1. Verification of the nano-beam scheme. Confirm the luminosity increases even though β_y^* becomes smaller than σ_z . The beam-beam parameter is $\xi_y > 0.03$. The luminosity is $L = 10^{34} \text{ cm}^{-2}\text{s}^{-1}$ at 1 [A] in LER.
2. Understanding and reduction of Belle II beam related backgrounds.
3. Establishment of the injection system [8].

ACHIEVEMENTS IN THE PHASE 2 COMMISSIONING

The commissioning of the HER and LER was started with the large beta functions at the IP, which is called “detuned optics”, in order to capture beams. The beta functions at the IP were $\beta_x^* = 400$ mm and $\beta_y^* = 81$ mm in the HER, $\beta_x^* = 384$ mm and $\beta_y^* = 48.6$ mm in the LER. After beams were stored first, calibrations of the QCS response, beam-based alignments, and vacuum scrubbing were performed.

The beta functions at the IP were squeezed down to 200 mm for β_x^* and 8 mm for β_y^* for each ring in the middle of April 2018. Then, the beta functions at the IP were squeezed down to 3 mm for β_y^* gradually. The history of beta squeezing is shown in Fig. 1. The smallest β_y^* is 1.5 mm in the HER and 2 mm in the LER, which were tests to squeeze

β_y^* and the global optics correction was applied although those were not used for the luminosity run. This value is the smallest β_y^* in the world.

The maximum beam current is 860 mA in the LER and 800 mA in the HER during Phase 2, respectively. The history of beam currents and luminosity in the Phase 2 commissioning is shown in Fig. 2.

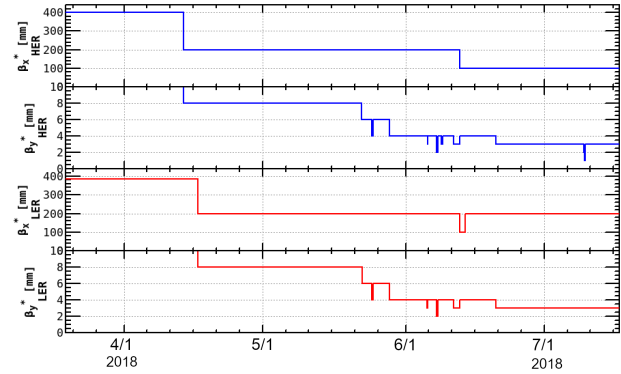


Figure 1: History of the beta squeezing at the IP.

Luminosity Performance

Figure 3 shows the specific luminosity as a function of β_y^* . The specific luminosity is defined by

$$\begin{aligned} L_{sp} &= \frac{L}{n_b I_{b+} I_{b-}} = \frac{1}{4\pi\sigma_z \phi_x e^2 f_0 \bar{\sigma}_y^*} \\ &= \frac{1.25 \times 10^{25}}{\bar{\sigma}_y^*} [\text{cm}^{-2}\text{s}^{-1}/\text{mA}^2], \end{aligned} \quad (7)$$

where $I_{b\pm}$ is the bunch current and

$$\bar{\sigma}_y^* = \frac{\sqrt{\sigma_{y-}^{*2} + \sigma_{y+}^{*2}}}{\sqrt{2}} = \frac{\Sigma_y^*}{\sqrt{2}}. \quad (8)$$

When β_y^* was squeezed from 6 mm to both 4 mm and 3 mm which were smaller than the bunch length, the specific luminosity was not improved in the early luminosity tuning. The global optics correction has been successfully working [9]. The vertical dispersions and XY couplings were corrected by using skew quadrupole coils wound in the sextupole magnets. The beta functions and horizontal dispersions were corrected by adjustment of the quadrupole field gradient and horizontal local bump orbit at the sextupole pairs. The typical result of global optics correction is shown in Table 2. We suspected that there is machine error locally in the vicinity of the IP such as a waist shift, local XY coupling at the IP, and so on [10]. The machine error due to the QCS can affect the vertical beam size at the IP as following:

$$\begin{aligned} \sigma_y^{*2} &= \mu^2 \varepsilon_y \left(\beta_y^* + \frac{\Delta s^2}{\beta_y^*} \right) + (\eta_y^* \sigma_\delta)^2 \\ &\quad + \frac{(r_2 + r_4 \Delta s)^2}{\beta_x^*} + \beta_x^* (r_1 + r_3 \Delta s)^2, \end{aligned} \quad (9)$$

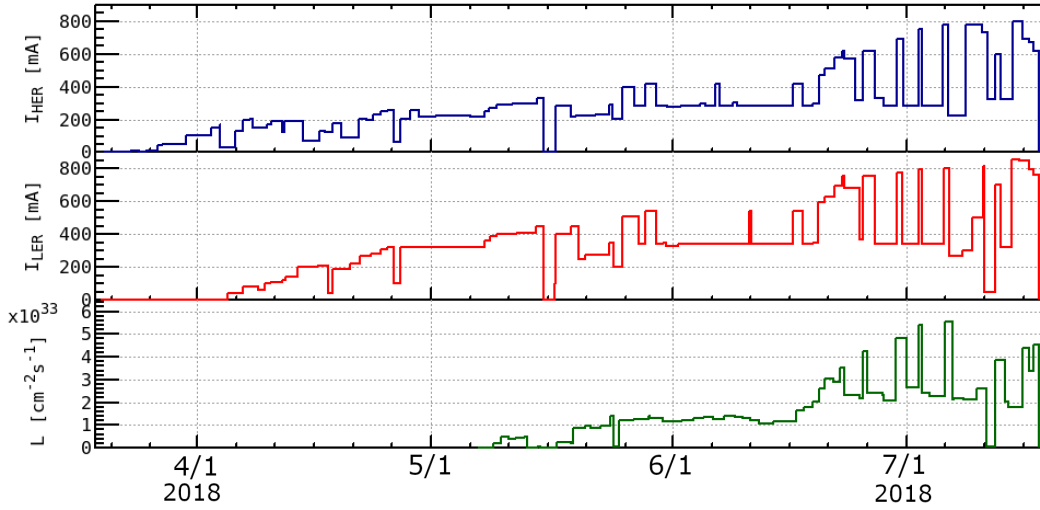


Figure 2: History of beam currents and luminosity in the Phase 2 commissioning.

where r_{1-4} are the XY coupling parameters, $\mu^2 = 1 - (r_1 r_4 - r_2 r_3)$, Δs is the waist shift. The physical coordinate system of a particle, (x, p_x, y, p_y) , is written by

$$\begin{pmatrix} x \\ p_x \\ y \\ p_y \end{pmatrix} = \begin{pmatrix} \mu & 0 & r_4 & -r_2 \\ 0 & \mu & -r_3 & r_1 \\ -r_1 & -r_2 & \mu & 0 \\ -r_3 & -r_4 & 0 & \mu \end{pmatrix} \begin{pmatrix} u \\ p_u \\ v \\ p_v \end{pmatrix}, \quad (10)$$

where (u, p_u, v, p_v) is the decoupled coordinate system.

The specific luminosity was improved by correction of r_2 which is one of the XY couplings with QCS skew quadrupole correctors and the waist position with adjustment of the QCS quadrupole coils. Thus, it is found that the specific luminosity is consistent with the behavior of $1/\beta_y^*$ even though β_y^* is squeezed smaller than the bunch length.

Table 2: The typical result of global optics correction. The value is rms for those at all BPMs in the ring. The ε_y is the projected vertical emittance measured by the X-ray beam size monitor.

Item	LER	HER	Unit
$\text{rms}(\Delta\beta_x/\beta_x)$	2	3	%
$\text{rms}(\Delta\beta_y/\beta_y)$	4	3	%
$\text{rms}(\Delta y/\Delta x)$	0.014	0.008	
$\text{rms}(\Delta\eta_x)$	10	9	mm
$\text{rms}(\Delta\eta_y)$	4	3	mm
ε_y	23	9	pm
$\varepsilon_y/\varepsilon_x$	1.35	0.20	%

The machine parameters in Phase 2 and comparisons with the final parameters in Phase 3 are shown in Table 3. The beam operations are classified according as “High bunch current”, “Reference”, and “High current”. In the high bunch current, the luminosity can be predicted to be $9 \times 10^{33} \text{ cm}^{-2} \text{ s}^{-1}$ if the number of bunches increases 4 times large with keeping the bunch currents. The specific luminosity

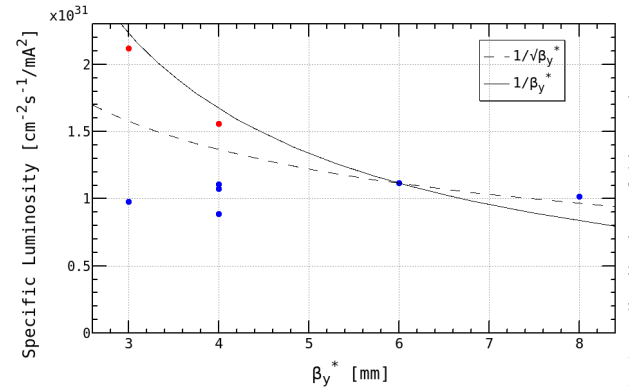


Figure 3: Specific luminosity as a function of β_y^* . Red plots indicate the specific luminosity after the correction of XY couplings at the IP and the waist with QC1s.

as a function of bunch current product for the reference and high bunch current is shown in Fig. 4. If the lower bunch current product is focused, the specific luminosity is $4 \times 10^{31} \text{ cm}^{-2} \text{ s}^{-1} / \text{mA}^2$ which corresponds to $\bar{\sigma}_y^* = 300 \text{ nm}$ ($\varepsilon_y = 30 \text{ pm}$). The vertical beam size at the IP is consistent with the estimation from projected emittance, $\varepsilon_y = 23 \text{ pm}$, which measured by the X-ray beam size monitor in the LER. However, the beam blowup was observed in the higher bunch current product. The beam-beam simulations(weak-strong) suggest some indications that XY couplings, chromatic XY couplings, and skew sextupole components at the IP affect the beam-beam blowup. This issue is under study and will be investigated in Phase 3.

Figure 5 shows the beam-beam parameters correspond to the specific luminosity as shown in Fig. 4. Here, the beam-beam parameter is defined by

$$\xi_{y\pm} = \frac{r_e N_{\mp} \beta_y^*}{2\pi \gamma_{\pm} \sigma_z \phi_x \bar{\sigma}_y^*}, \quad (11)$$

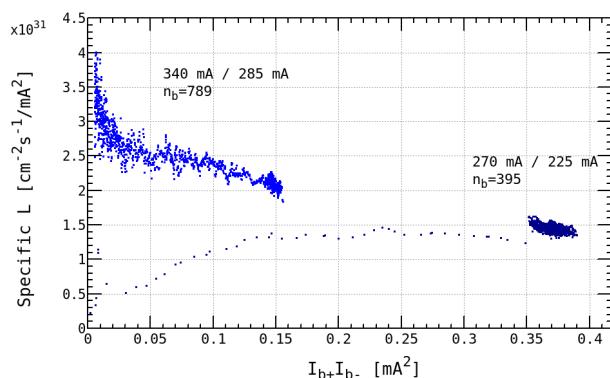


Figure 4: Specific luminosity as a function of bunch current product.

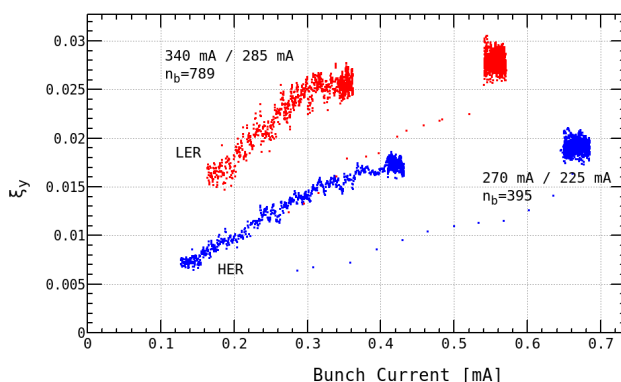


Figure 5: Beam-beam parameter as a function of bunch current product.

Figure 7 shows the specific luminosity as a function of bunch current product multiplied by number of bunches. It is found that the specific luminosity for the reference is improving day by day. The total luminosity contours are also plotted in this figure. The green plots corresponds to the high bunch current can be extrapolated to almost $L = 10^{34} \text{ cm}^{-2} \text{ s}^{-1}$ by multiplying factor 4 as explained previously. The extrapolated beam current becomes 1060 mA with keeping the bunch current in the LER.

Since the beta squeezing was the first priority in Phase 2, it was focused for two months. The beam currents increased

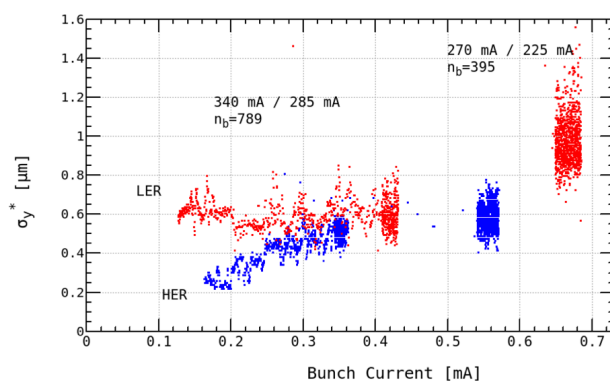


Figure 6: Vertical beam size at the IP as a function of bunch current. The beam size is measured by the X-ray beam size monitor.

for about last one month. The peak luminosity of $5.55 \times 10^{33} \text{ cm}^{-2} \text{ s}^{-1}$ was achieved during the high current operation. However, the vertical emittance in the LER was increased by vertical dispersions artificially made according to dispersion knob to increase Touscheck lifetime as much as possible. Note that the peak luminosity is not optimized since the vertical beam size is large in the LER as shown in Table 3.

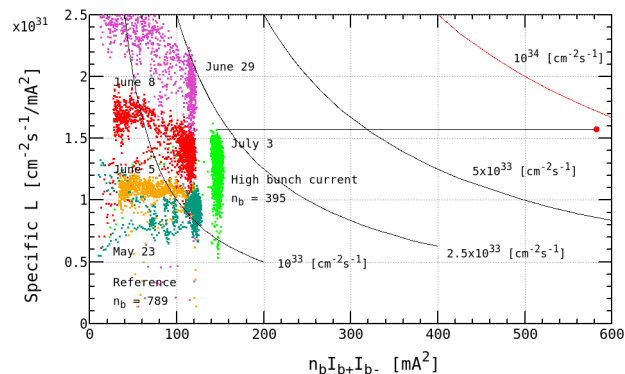


Figure 7: Specific luminosity as a function of bunch current product multiplied by number of bunches. Red point indicates the luminosity extrapolated from the high bunch current by multiplying factor of 4.

Electron Cloud

The electron cloud effect (ECE) [11] was observed in Phase 1 although the ante-chambers and TiN coating were adopted in the LER. Therefore, additional solenoid-like permanent magnets have been installed for the beam pipes as much as possible before the Phase 2 commissioning since the electron cloud are produced and formed in the drift space. Those magnetic field is several ten gausses. Figure 8 shows the vertical beam size as a function of bunch current divided by the rf bucket spacing. The vertical beam size was measured by the X-ray beam size monitor in the LER. The beam blowup due to ECE was not observed up to 0.4 mA as $I/n_b/n_{sp}$. The threshold is much improved more than twice

Table 3: Machine Parameters in Phase 2. The parameters in Phase 3 is the final design of SuperKEKB. The σ_y^* is estimated from the vertical beam size at the light-source point measured by the X-ray beam size monitor. The $\bar{\sigma}_y^* = \Sigma_y^*/\sqrt{2}$ is obtained from the luminosity. Intra-beam scattering is considered in the horizontal emittance.

	Phase 2						Phase 3		Unit
	High bunch current		Reference		High current		Final		
	LER	HER	LER	HER	LER	HER	LER	HER	
I at L_{peak}	265	217	327	279	788	778	3600	2600	mA
n_b	395		789		1576		2500		
I/n_b	0.670	0.549	0.414	0.353	0.500	0.494	1.44	1.04	mA
ε_x	1.8	4.6	1.7	4.6	1.7	4.6	3.2	4.6	nm
β_x^*	200	100	200	100	200	100	32	25	mm
β_y^*	3	3	3	3	3	3	0.27	0.3	mm
σ_z					6				mm
$2\phi_x$					83				mmrad
Φ	13.1	11.6	13.5	11.6	13.5	11.6	24.6	23.2	
ν_x	44.562	45.542	44.558	45.541	44.561	45.545	44.53	45.53	
ν_y	46.617	43.609	46.615	43.610	46.614	43.612	46.57	43.57	
σ_y^*	883	652	692	486	1285	528	48	62	nm
$\bar{\sigma}_y^*$	797		552		879		55		nm
ξ_y	0.030	0.021	0.0277	0.0186	0.0244	0.0141	0.088	0.081	
L_{sp}	1.57×10^{31}		2.27×10^{31}		1.43×10^{31}		2.14×10^{32}		$\text{cm}^{-2}\text{s}^{-1}/mA^2$
L	2.29×10^{33}		2.62×10^{33}		5.55×10^{33}		8×10^{35}		$\text{cm}^{-2}\text{s}^{-1}$

0.2 mA which is the threshold observed in Phase 1. The mode of coupled bunch instability changes and the growth rate is reduced after the installation of additional permanent magnets.

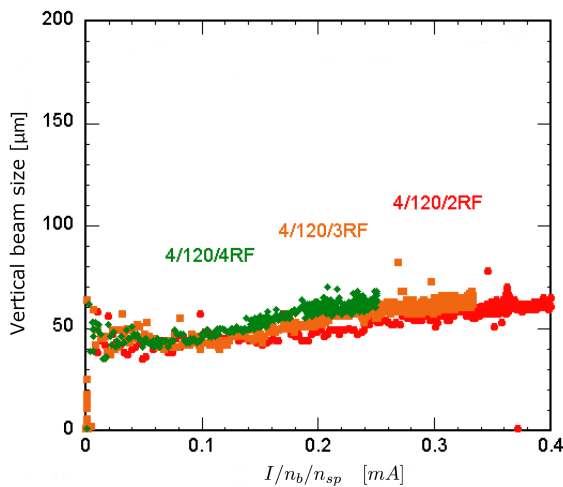


Figure 8: Vertical beam size measured by X-ray beam size monitor as a function of bunch current divided by rf bucket spacing. There are 3 fill patterns which are indicated by (number of trains)/ n_b/n_{sp} .

ISSUES IN PHASE 2

QCS Quench

We had 24 times QCS quenches during the Phase 2 commissioning in total. Half of them occurred before the middle of April since the movable masks were almost fully open. Beam loss of injection beams caused the most of QCS quenches before optics corrections after the beta squeezing. The horizontal oscillation of the injected beam due to injection error is transformed to the vertical oscillation because the XY coupling is very large before optics corrections. Then, the beam hits the QCS because the vertical physical aperture in the QCS is smallest in the ring. We decided to adjust the movable collimators not only to reduce the Belle II background but also to avoid QCS quenches. Several QCS quenches occurred until the end of May although the collimators were optimized, however, human error in the operation or troubles of the injection kickers caused them. Another cure is the fast abort system with the diamond sensor has been adopted since the end of May. No QCS quench occurred for a month since then. Several QCS quenches occurred from the end of June to July again when the beam currents increased larger than 500 mA and β_y^* was 3 mm. There were incidents that a head of the movable collimator was damaged with the QCS quench simultaneously. The cases of QCS quench are categorized into during injection and during beam storage. About 8000 particles hitting the superconducting coil causes a QCS quench when a simple calculation is considered with an assumption of all energy lost. However, more particles should be necessary because of an energy spread of the lost particles in the real machine.

The movable collimators and the fast abort system could avoid QCS quenches for the injection beams. The both devices could avoid most of the QCS quenches for the storage beams, there were still a few events not understood.

Damage of Movable Collimator Head

The vertical collimator [12] which is based on the design for PEP-II at SLAC has been installed for each ring. We had a damage of the head in the vertical collimator for the LER and HER, respectively. We observed sudden pressure rise in the vicinity of the movable collimator accompanied by a beam abort and QCS quench. The injection background became very high and there was no way to reduce backgrounds by optimizing the collimator aperture after this incident. Thus, a gutter and spine on the collimator head were found, which were made by hitting the beams. The reason of incident is unclear because beam instabilities and a large orbit drift were not observed. There is a possibility of a dust trapping. In order to cure the injection background due to the spine, the collimator was moved by a few mm in the horizontal direction. Further investigation of the incident is necessary in Phase 3.

CONCLUSIONS

We have performed the Phase 2 commissioning since 19th March until 17th July in 2018. The beam currents are stored up to 860 mA in the LER and 800 mA in the HER, respectively. We changed the machine parameters from the non-collision optics to the collision optics which is completely different lattice. The beta functions at the IP were adopted to be 200 mm in the horizontal and 8 mm in the vertical plane for the initial collision tuning. Then, we observed the first hadronic event on 26th April 2018. The vertical beta function at the IP was successfully squeezed from 8 mm down to 3 mm. The luminosity has increased even though β_y^* is smaller than the bunch length.

We have experienced the issues such as QCS quenches and damages of collimator head. We do not understand completely all of them and there are still unclear for some of the incidents.

We confirmed the nano-beam scheme in the Phase 2 commissioning and determined to move on Phase 3.

ACKNOWLEDGMENT

The authors wish to thank all of the Beast II groups and also the collaborators from overseas. Many thanks go to the KEKB review committee for always encouraging us and suggesting plenty of recommendations for many years.

REFERENCES

- [1] Y. Ohnishi *et al.*, "Accelerator design at SuperKEKB", *Prog. Theor. Exp. Phys.*, vol. 2013, no. 3, p. 03A011, Mar. 2013, <https://doi.org/10.1093/ptep/pts083>
- [2] Belle II Technical Design Report, <http://arXiv.org/abs/1011.0352>
- [3] T. Abe *et al.*, "Achievements of KEKB", *Prog. Theor. Exp. Phys.*, vol. 2013, no. 3, p. 03A001, Mar. 2013, <https://doi.org/10.1093/ptep/pts102>
- [4] "SuperB Conceptual Design Report", INFN/AE-07/2, SLAC-R-856, LAL 07-15, March 2007.
- [5] N. Ohuchi *et al.*, presented at *IPAC'18*, Vancouver, BC, Canada, May 2018, paper TUZGBE2, pp. 1215–1219.
- [6] Y. Funakoshi *et al.*, in *Proc. IPAC'16*, Busan, Korea May 2016, paper TUOBA01, pp. 1019–1021.
- [7] M. Kikuchi *et al.*, in *Proc. IPAC'10*, Kyoto, Japan, May 2010, paper TUPEB054, pp. 1641–1643.
- [8] M. Satoh *et al.*, in *Proc. IPAC'16*, Busan, Korea May 2016, paper THPOY027, pp. 4152–4154.
- [9] A. Morita *et al.*, presented at *eeFACT2018*, Hong Kong, China, September 2018, paper TUOAB04, this conference.
- [10] K. Ohmi *et al.*, presented at *eeFACT2018*, Hong Kong, China, September 2018, paper TUBOBB01, this conference.
- [11] Y. Suetsugu *et al.*, presented at *eeFACT2018*, Hong Kong, China, September 2018, paper TUYAA04, this conference.
- [12] K. Shibata *et al.*, presented at *eeFACT2018*, Hong Kong, China, September 2018, paper WEOAB01, this conference.

CHALLENGES FOR CIRCULAR e^+e^- COLLIDERS*

Frank Zimmermann[†], CERN, Geneva, Switzerland

Abstract

This paper sketches the glorious past and the tantalizing future of circular e^+e^- colliders, highlighting some of the key issues.

HISTORY

Circular e^+e^- Colliders can look back at a 50-year success story, illustrated in Fig. 1. The collider with the highest energy so far was LEP/LEP2. LEP had a circumference of about 27 km, and was in operation from 1989 to 2000. During this time it delivered an integrated luminosity of 1000 pb^{-1} . LEP2 reached a maximum c.m. energy of 209 GeV, a maximum synchrotron radiation power of 23 MW, and a critical photon energy close to 1 MeV. A further important step forward was made by the two B factories, PEP-II and KEKB; see Fig. 2. They established collider operation at very high beam current (well above 1 Ampere per beam), world record luminosities, and top-up injection as a routine mode of operation. Another machine, DAΦNE, demonstrated the merits of crab-waist collisions, with a small β_y^* and large vertical beam-beam tune shift (Fig. 3).

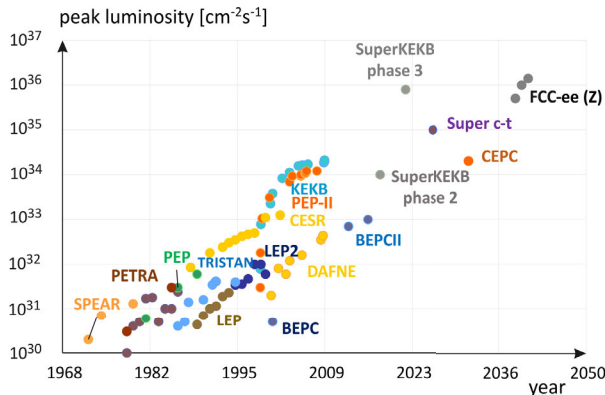


Figure 1: Peak luminosity of circular e^+e^- colliders as a function of year — for past, operating, and proposed facilities including the Future Circular Collider (Historical data courtesy of Y. Funakoshi).

NEXT STEPS

The next big step will be the SuperKEKB (Fig. 4), whose beam commissioning started in 2016. SuperKEKB will operate with a “nanobeam collision scheme” (similar to the crab waist, but without any crab-waist sextupoles). It features a design beam lifetime of no more than 5 minutes, and a vertical IP beta function β_y^* of only 0.3 mm.

* This work was supported by the European Commission under the HORIZON 2020 project ARIES no. 730871.

[†] frank.zimmermann@cern.ch

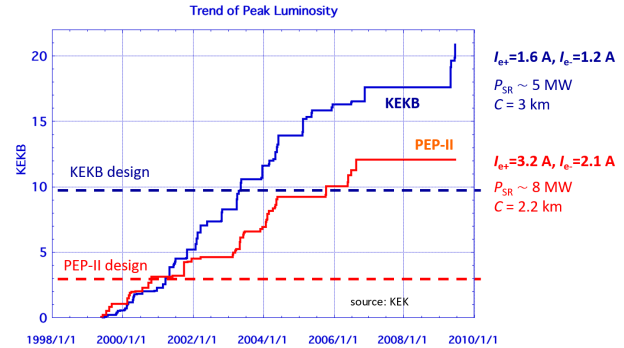


Figure 2: Peak luminosity of PEP-II and KEKB as a function of year along with the design luminosity, and a few key parameters.

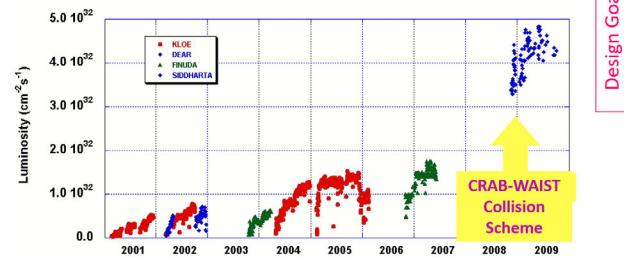


Figure 3: DAΦNE peak luminosity versus time, and the step increase in 2008/9 thanks to the introduction of crab-waist collisions (P. Raimondi, M. Zobov).

The proposed future highest-energy highest-luminosity e^+e^- colliders build on past successes and lessons. LEP has pushed high-energy beam operation and experienced synchrotron-radiation effects like those expected for FCC-ee $t\bar{t}$ running. The B-factories KEKB and PEP-II have operated with high beam currents, as needed for the FCC-ee Z pole operation. They have also established the top-up injection mode. DAΦNE has demonstrated the crab waist collision scheme. The Super B factory SuperKEKB will explore the operation with extremely low β_y^* . The SLC, KEKB and SuperKEKB have demonstrated the positron source operation at high intensity. Finally, HERA, LEP, and RHIC have delivered important lessons on spin gymnastics, spin-orbit matching and operating storage rings with polarized beams.

The next machines are combining all the recently established concepts, as indicated in Fig. 5. Figure 6 compares the resulting tantalizing performance reach of FCC-ee with other proposed future colliders.

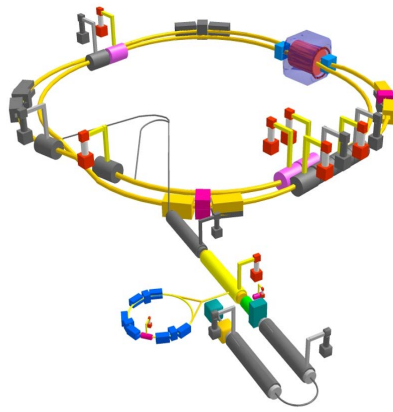


Figure 4: Schematic of SuperKEKB (K. Oide et al.).

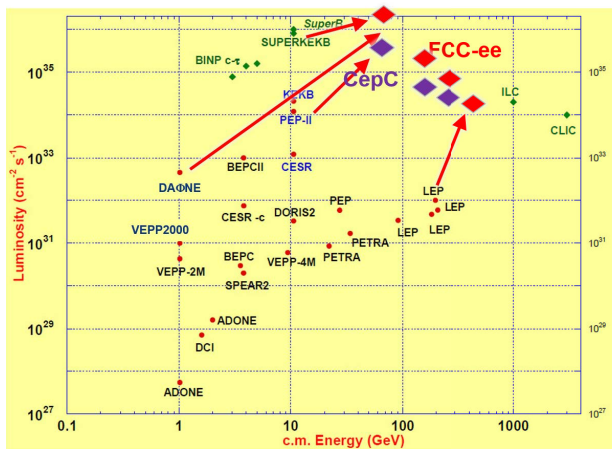


Figure 5: Past, present and future collider landscape: combining recent, novel ingredients yields extremely high luminosity at high energies (Marica Biagini).

FEASIBILITY AND OPTIMIZATION

Already in the mid 1970's it was observed that "an e^+e^- storage ring in the range of a few hundred GeV in the centre of mass can be built with present technology." [and] "...would seem to be ... most useful project on the horizon." [1]. In the same reference [1] it was shown that 365 GeV c.m. energy corresponds to a cost-optimized circumference of about 100 km, thereby validating the much more recent FCC-ee design choice.

Table 1 shows that the FCC-ee machine faces quite different requirements in its various modes of operation. For example, on the Z pole FCC-ee is an Ampere-class storage ring, like PEP-II, KEKB and DAΦNE, with a high beam current, but a low RF voltage, of order 0.1 GV. For the $t\bar{t}$ mode, the beam current is only a few mA, as for the former LEP2, while an RF voltage above 10 GV is required. In both cases a total of 100 MW RF power must be constantly supplied to the two circulating beams.

Three sets of RF cavities are proposed to cover all operation modes for the FCC-ee collider rings and booster. (1) For

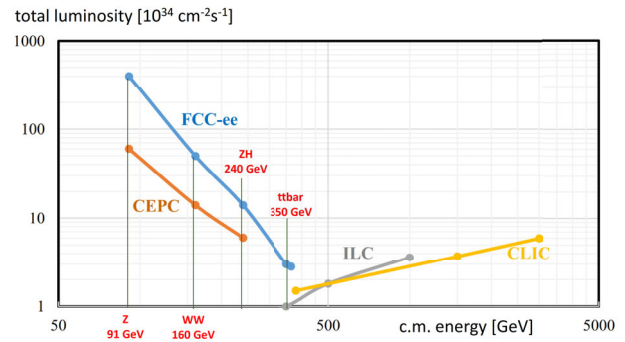


Figure 6: Total luminosity forecast for four proposed future e^+e^- colliders as a function of c.m. energy.

the high intensity operation (Z, FCC-hh) 400 MHz mono-cell cavities (4 per cryomodule) based on Nb/Cu thin-film technology at 4.5 K are proposed; (2) for higher energy (W, H, $t\bar{t}$) 400 MHz four-cell cavities (4 per cryomodule) again based on Nb/Cu technology at 4.5 K, and (3), finally for the $t\bar{t}$ machine a complement of 800 MHz five-cell cavities (again 4 per cryomodule) based on bulk Nb at 2 K. The installation sequence (Fig. 7) is comparable to the one of LEP, where about 30 cryomodules were installed per shutdown.

Table 1: RF voltage, number of bunches, and beam current for the four modes of FCC-ee operation

mode	RF voltage [GV]	# bunches	current [mA]
Z	0.1	16640	1390
W	0.44	2000	147
ZH	2.0	393	29
$t\bar{t}$	10.9	48	5.4

HIGH BEAM CURRENT

High current, short bunches, and a large ring can give rise to higher-order-mode (HOM) losses and single-bunch instabilities. HOM heat loads can easily destroy beamline elements, as is illustrated in Fig. 8 with photographs from PEP-II [3]. The HOM power is given by [3]

$$P_{\text{HOM}} = t_{\text{bs}} k_{\parallel} I_b^2, \quad (1)$$

where I_b denotes the beam current, t_{bs} the bunch spacing, k_{\parallel} the loss factor, and I_b the total beam current. HOM mitigation calls for shielded, damped, suitably designed beamline components. The HOMs in the RF cavities restrict the possible bunch spacings [4]. As a design criterion, the total HOM energy loss should stay much smaller than the energy loss from synchrotron radiation.

Novel thin NEG coatings can simultaneously ensure: acceptable vacuum conditions (good pumping properties), suppression of electron cloud build up (low secondary emission yield), and a longitudinal single-bunch impedance below the threshold of the microwave instability [5]; see Fig. 9. Figure

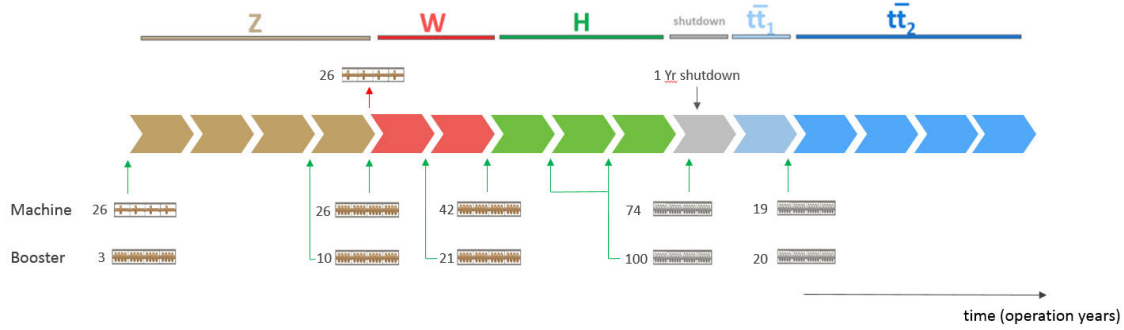


Figure 7: FCC-ee operation time line. The bottom part indicates the number of cryomodules to be installed in the collider and booster, respectively, during the various shutdown periods (O. Brunner); also see [2].

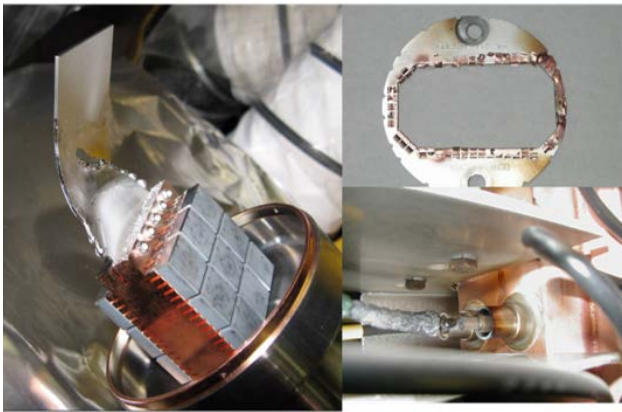


Figure 8: Photos of PEP-II spoiler, RF shield and beam-position monitor damaged by HOM heating.

10 shows, for the example of CEPC [6], that the resistive-wall contribution indeed dominates the total longitudinal short-range wake field.

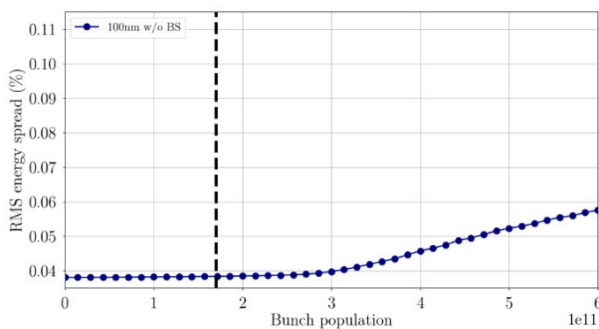


Figure 9: FCC-ee microwave instability threshold with 100 nm NEG coating on top of a copper chamber.

Resistive-wall and cavity resonances can also drive multi-bunch instabilities. For FCC-ee and CEPC the fundamental cavity mode impedance is important. The optimum cavity detuning is (minus) four revolution harmonics for FCC-ee and (minus) 6 revolution harmonics for CEPC. As a result for FCC-ee the most unstable multi-bunch mode corresponds to $m = -4$; see Fig. 11. The effective cavity impedance

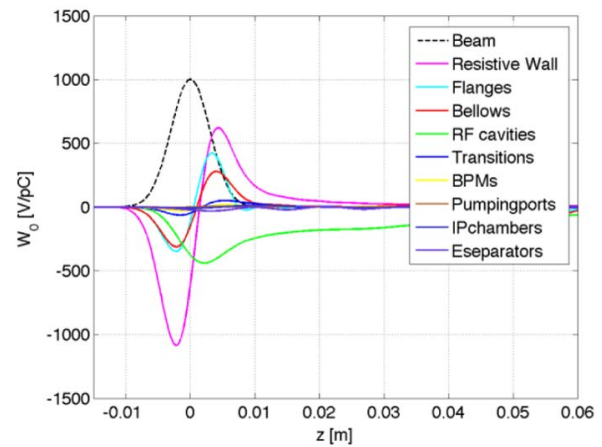


Figure 10: CEPC longitudinal partial single-bunch wake field due to various components and the total wake field [6] (N. Wang).

can be drastically reduced by strong RF feedback, as is illustrated in Fig. 12. Figure 13 demonstrates that using such feedback all coupled-bunch growth rates become weaker than the radiation damping rate.

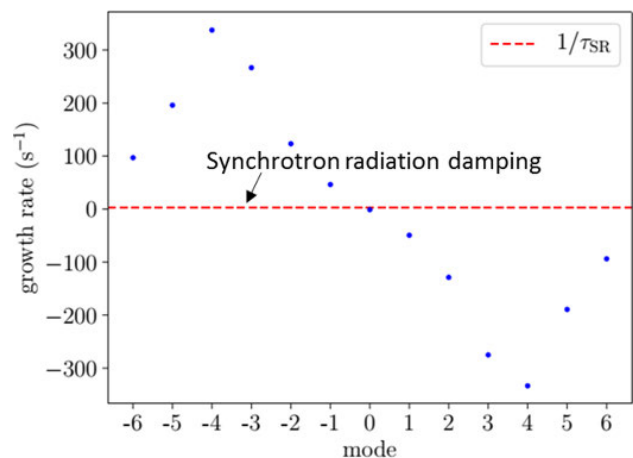


Figure 11: Longitudinal coupled-bunch growth rates without RF feedback, compared with the radiation damping rate [7].

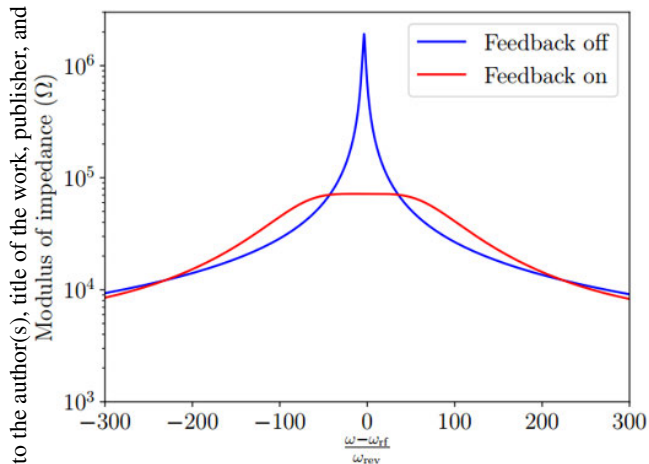


Figure 12: Cavity impedance without and with strong RF feedback [7].

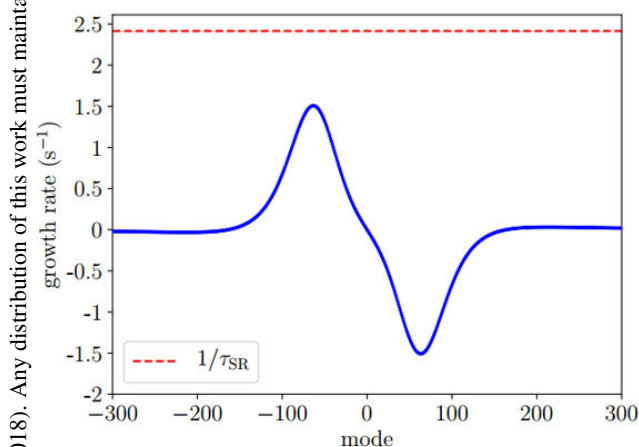


Figure 13: Longitudinal coupled-bunch growth rates with strong RF feedback, compared with the radiation damping rate [7].

Obtaining a high beam current in the positron ring requires a thorough suppression of electron-cloud formation everywhere around the ring. The countermeasures adopted for SuperKEKB [8] include (1) beam pipe with antechamber [Fig. 14 (right)], (2) rough surfaces at the primary photon impact region inside the antechamber, (3) low-SEY [TiN] coatings for 90% of the beam pipes [Fig. 14 (right)], (4) grooves inside the bending magnets [see Fig. 14 (left)], (5) clearing electrodes in the wiggler chambers, (6) solenoidal fields of about 50 G in all drift spaces, plus, finally, (7) beam conditioning. This suite of countermeasures has proven highly successful. So far at SuperKEKB no blow up of the vertical beam size has been observed for the nominal bunch spacing of two 500-MHz RF buckets (i.e. 4 ns) up to bunch currents exceeding 60% of the design value; see Fig. 15.

Yet another challenge arising from the high beam current is machine protection. Several collimators of SuperKEKB were damaged due to beam impact, already in the commissioning phase 2 [13]. The collimators of future machines should be robust enough, and be positioned sufficiently pre-

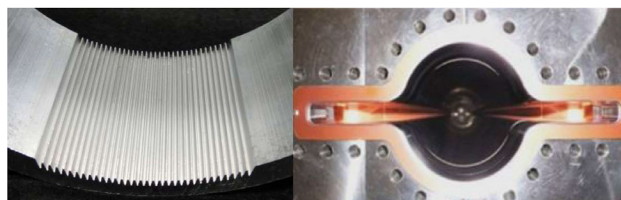


Figure 14: Anti-electron-cloud measures at SuperKEKB: grooves in bending magnets (left), and TiN coated beam pipe with antechamber (right) [8].

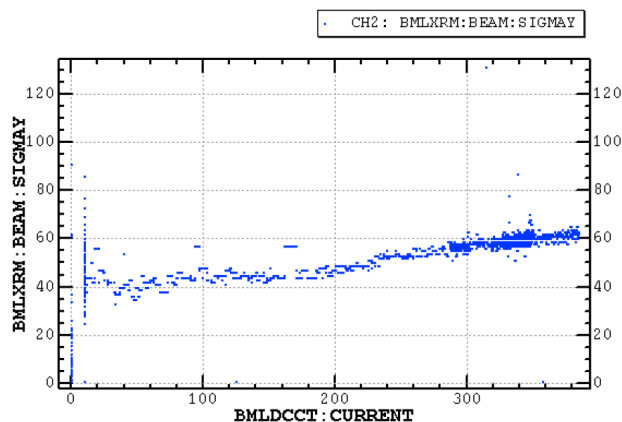


Figure 15: Vertical beam size in the SuperKEKB positron ring as a function of total beam current for a filling pattern consisting of 4 trains with 120 bunches each, and the nominal 2 bucket (4 ns) spacing (Y. Suetsugu, H. Fukuma, July 2018). No clear blow up is seen up to bunch currents of 0.8 mA (to be compared with a design value of 1.4 mA), which shows that the electron cloud density stays below the threshold of the electron-cloud induce fast head-tail instability [9, 10]. The monotonic increase of the beam at higher beam currents could either be instrumental or be caused by other effects (e.g. intrabeam scattering [11], incoherent effects of electron cloud [12], etc.).

cise, to withstand any unavoidable beam impact, or, otherwise, the beam must be aborted by interlock systems before any damage can occur.

HIGH ENERGY

One challenge related to the high beam energy is the photon energy spectrum of the synchrotron radiation. While the radiation at the Z pole (beam energy of 45.6 GeV) is easily shielded, this is no longer the case when operating as a Higgs factory or at the $t\bar{t}$ threshold (Fig. 16). Upon impact on common accelerator materials, photons of energies around 1 MeV can produce neutrons, and activate or damage accelerator components. For FCC-ee a local lead shielding mounted around dedicated discrete photon stops is foreseen; see Fig. 17.

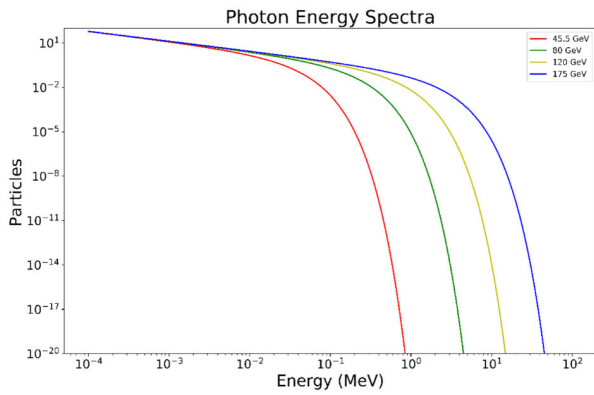


Figure 16: Synchrotron-radiation energy spectra for four different beam energies in a 100 km ring [6].

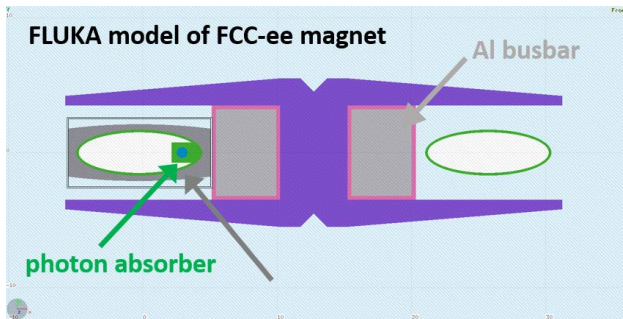


Figure 17: FLUKA model of an FCC-ee dipole magnet with lead shield integrated around the photon absorber (F. Cerutti, I. Besana).

SHORT BEAM LIFETIME

The short design beam lifetime of all future colliders, together with the high beam current, determines the particle rates for top-up operation to be provided by the injector complex. Filling the machine from zero after a failure might demand ever higher rates, depending on the filling time to be achieved. In case of the FCC-ee, this filling time is less than 20 minutes for all modes of operation.

Figure 18 shows the FCC-ee injector complex, which meets all the requirements [14, 15]. It comprises an SLC/SuperKEKB-like 6 GeV linac accelerating 1 or 2 e^+ or e^- bunches with a repetition rate of 100 or 200 Hz. The same linac is also used to accelerator other electrons for positron production at 4.46 GeV. After acceleration through the remaining part of the linac, the emittances of the positron beam are reduced in a damping ring operating at 1.54 GeV. Both electron and positron bunches at 6 GeV (end of the linac) are injected into a Pre-Booster Ring (which could be either a refurbished SPS or a new ring) and then accelerated to 20 GeV. The injection into the main top-up booster occurs at 20 GeV with an interleaved filling of e^+ and e^- for either full filling from zero or for continuous top-up.

The CEPC injector complex features a higher-energy 10 GeV linac and injects beam from the end of this linac directly into the main booster, without passing through any

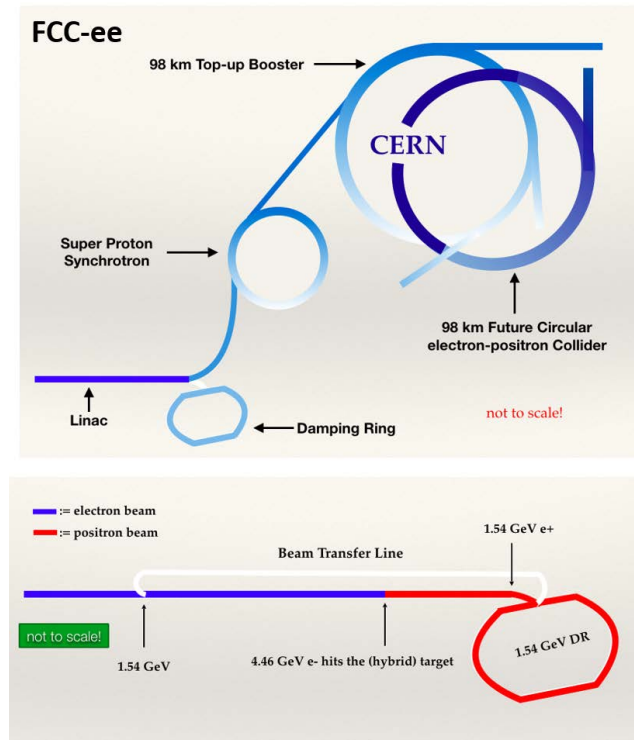


Figure 18: FCC-ee injector complex [14, 15] (S. Ogur, K. Oide, Y. Papaphilippou, O. Etisken, et al.).

The positron source is one crucial element of the injector complexes. Table 2 compares the positron production rates required for CEPC and FCC-ee with two existing (or past) sources, namely the world record SLC source (production with a 30 GeV electron beam) and the SuperKEB source.

Table 2: Positron production rates and two existing (or past) and two proposed e^+e^- colliders (I. Chaikovska, R. Chehab, P. Martyshkin, K. Oide, L. Rinolfi, Y. Papaphilippou).

coll.	CEPC	SuperKEKB	SLC	FCC-ee
$e^+/\text{sec.}$	10^{12}	2.5×10^{12}	6×10^{12}	10^{13}

EMITTANCE

Figure 19 illustrates that for a ring as large as the FCC-ee it should be rather straightforward to obtain the target horizontal emittance, even using a conventional FODO optics. Reaching the target vertical emittance will be more challenging. Residual coupling, spurious vertical dispersion, intrabeam scattering, electron-cloud effects, beam-ion instabilities and beam-beam related blow up will also contribute to the vertical emittance.

In particular, the beam-beam collisions can increase the vertical emittance, as is illustrated in Fig. 20. The blow up

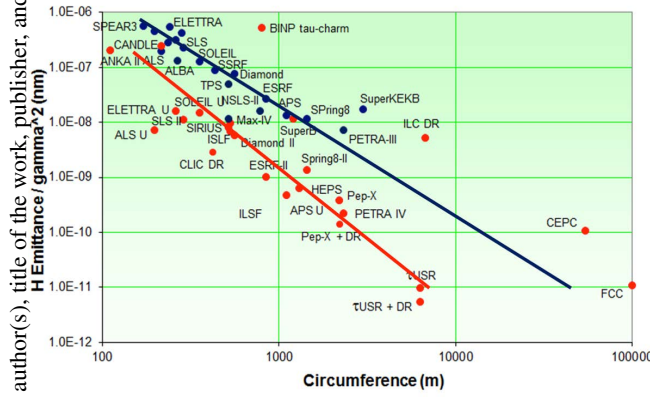


Figure 19: Emittance normalized to beam energy vs. circumference for storage rings in operation (blue dots) and under construction or being planned (red dots). The ongoing generational change is indicated by the transition from the blue line to the red line (R. Bartolini, 2016).

depends on the type of residual errors and on the working point in the tune diagram [16]. Figure 21 compiles demonstrated past and expected future emittance ratios $\varepsilon_y/\varepsilon_x$ as a function of the actual or design beam-beam tune shift, at several e^+e^- colliders.

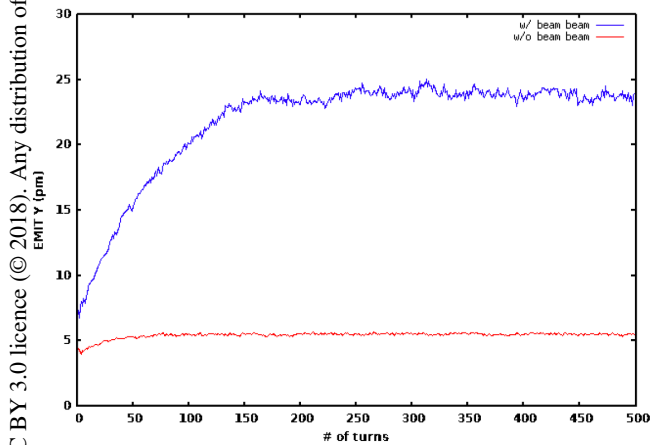


Figure 20: Example simulation of FCC-ee vertical emittance with and without collision, as a function of turn number, for one random seed (D. El Khechen, 2018).

A coherent synchro-betatron (x - z) beam-beam instability [18, 19] and 3D flip-flop effect with beamstrahlung [20] further complicate the choice of operating point, as is shown by Fig. 22.

INTERACTION POINT BETA FUNCTION

Figure 23 shows the historical evolution of the vertical interaction-point (IP) beta function at e^+e^- colliders. A barrier around 1 cm had been recognized by Talman, e.g. [21]. The linear collider SLC and also KEKB achieved lower values. The next great step forward will be made by SuperKEKB, with a design value of $\beta_y^* \approx 0.3$ mm, even lower than what is planned for FCC-ee or CEPC.

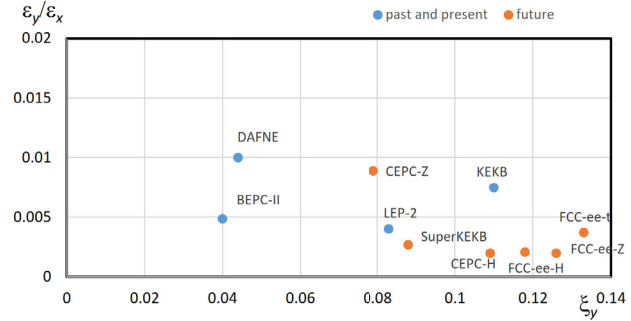


Figure 21: Vertical-to-horizontal emittance ratios achieved in various past e^+e^- colliders (blue) along with target values for future machines (orange) as a function of beam-beam parameter (per IP); past values were extracted from Ref. [17].

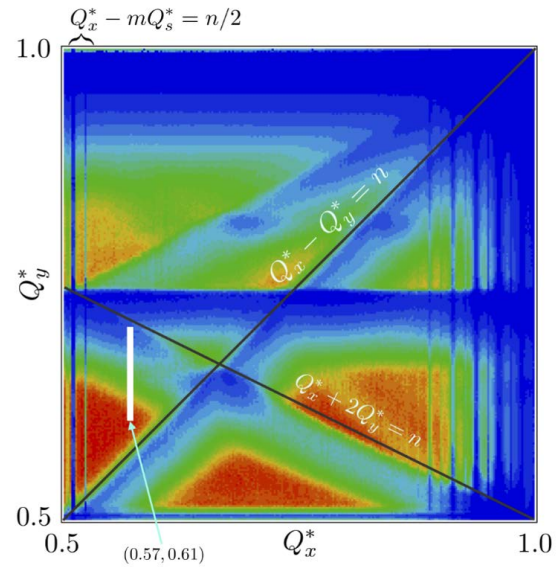


Figure 22: FCC-ee luminosity at the Z as a function of betatron tunes. The colour scale from zero (blue) to $2.3 \times 10^{36} \text{ cm}^{-2} \text{ s}^{-1}$ (red). The white narrow rectangle above (0.57, 0.61) shows the footprint due to the beam-beam interaction. A few synchrotron-betatron resonance lines $Q_x^* - mQ_y^* = n/2$ [20].

For the FCC-ee the small beta function is accomplished with the help of a special final-focus optics, shown in Fig. 24, which complies with a multitude of constraints. This optics is asymmetric to suppress synchrotron radiation emitted towards the IP. even for $\bar{t}\bar{t}$ running, the critical photon energy in the dipole magnets stays below 100 keV over the last 450 m upstream of the IP. A total of only four sextupoles (a—d), used for the local vertical chromaticity correction and for generating the crab waist, are optimized at each working point. One purpose of the sextupoles a and d is to cancel the geometric aberrations generated by the vertical-chromaticity sextupoles b and c. However, decreasing the strength of these compensating sextupoles produces the “crab waist” at the collision point. A common arc lattice is employed for all energies, with 60 degree phase advance per cell for the

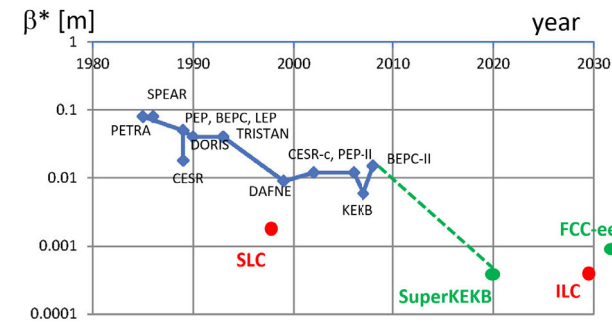


Figure 23: Vertical IP beta function for various e^+e^- colliders as a function of year.

Z and W running, and a more strongly focusing 90 degree for the ZH and $t\bar{t}$ operation, so as to maximize stability and luminosity.

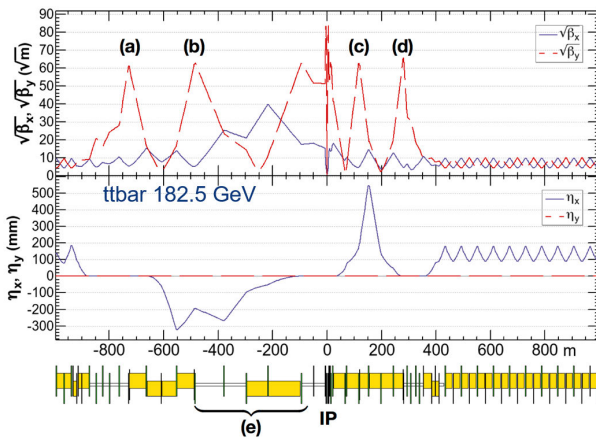


Figure 24: FCC-ee final-focus optics [22] (K. Oide). The yellow boxes indicate dipole magnets. Four sextupoles (a—d), used for the local vertical chromaticity correction and for generating the crab waist, are optimized for each working point. Common arc lattice for all energies, 60 deg for Z, W and 90 deg for ZH, $t\bar{t}$ for maximum stability and luminosity

A high-quality final-focus optics is essential for obtaining an adequate dynamic aperture. An example from the CEPC design is shown in Fig. 25. The dynamic aperture can be optimized by empirically adjusting the strength of hundreds of individual sextupole pairs in the collider arcs. Efforts are ongoing to improve the dynamic aperture by particle-swarm optimization (PSO) and by training a neural network. Figure 26 illustrates the PSO process for the FCC-ee.

TOP-UP INJECTION PROCESS

The top-up injection process is essential for achieving the targeted luminosity performance. For FCC-ee, fairly “conventional” injection schemes are being considered, such as using either conventional injection or multipole-kicker schemes both on-energy and off-energy [24]. At each injection, only a few per cent of the nominal bunch charge will be transferred from the booster to the collider [24]. For

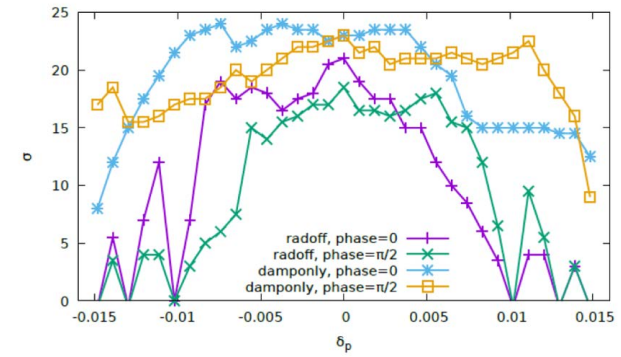


Figure 25: Off-momentum dynamic aperture for CEPC, determined by particle tracking with and without radiation damping [6].

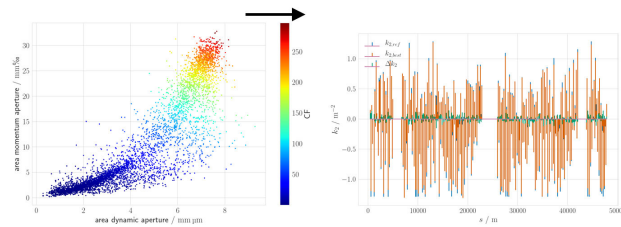


Figure 26: Particle-swarm optimization leading to enlarged momentum acceptance and transverse dynamic aperture (left), while also minimizing the strengths of the arc sextupoles (right) (T. Tydecks) [23].

CEPC a novel “swap-out” injection process is proposed, where individual bunches are first extracted from the collider ring, in order to then be merged, in the top-up booster, with lower-intensity top-up bunches, and the replenished bunches are finally sent back from the booster to the collider. This swap-out scheme is illustrated in Fig. 27

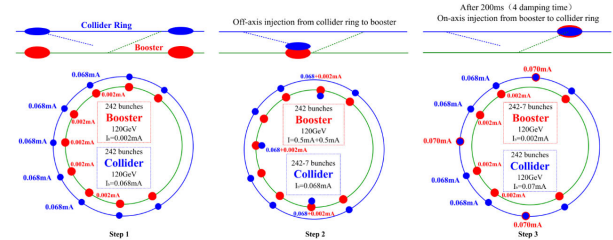


Figure 27: Swap-out injection process proposed for CEPC. [6].

SPOT SIZE

At the CERN Intersecting Storage Rings (ISR), the IP beam size was of the order of 1 mm. The rms beam sizes at the LHC are about 10 μm . The vertical beam size at the SLAC Linear Collider (SLC) amounted to about 1 mm. Linear collider test facilities, like the SLAC FFTB and the KEK ATF-2, have achieved, at least occasionally, spot sizes between 50 and 100 nm. Similar spot sizes are also required

for the circular colliders SuperKEKB, FCC-ee and CEPC. Future linear colliders like ILC and CLIC require spot sizes of a few nm. Table 3 presents an overview.

Table 3: RMS (vertical) spot size at various colliders and test facilities; shown in regular font are achieved values; shown in italics are design values or expected values.

collider/test facility	σ_y^* [nm]
LEP2	3500
KEKB	940
SLC	700
ATF-2, FFTB	55 (35), 70 (50)
CEPC	60
SuperKEKB	50
FCC-ee	40

Obtaining and maintaining the design spot size is a challenge. Succeeding in this endeavour requires regular IP aberration tuning. Figure 28 shows the increase in specific luminosity during one month of SuperKEKB phase 2 commissioning. Top-up injection and operation at constant beam current provide for rather stable conditions, which facilitate the IP tuning. Figure 29 recalls the final increase in the luminosity of the former KEBK, which was achieved by tuning skew sextupoles located in the arcs of both collider rings so as to minimize the chromatic coupling at the collision point.

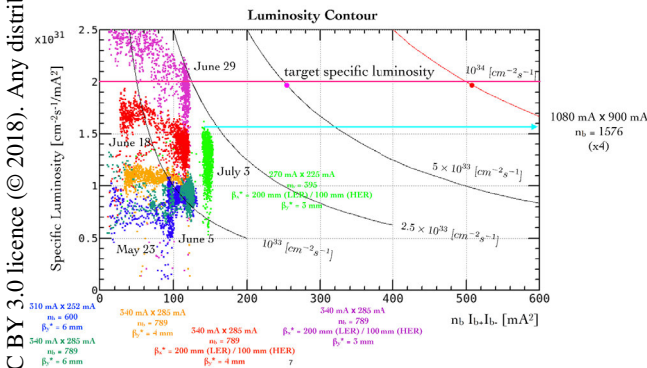


Figure 28: Improvements in SuperKEKB specific luminosity versus number of bunches and bunch current product during SuperKEKB commissioning phase 2 [13] (Y. Funakoshi).

IR QUADRUPOLES AND BEAM LOSS

The interaction region (IR) of the double-ring lowest-beta colliders contain complicated superconducting magnet systems, including corrector packages which cancel the field errors arising due to the magnets of the adjacent beam line. Figure 30 presents the intricate layout of the superconducting magnet system for SuperKEKB. Figure 31 shows a photo of the assembled superconducting magnets.

SuperKEKB experienced several quenches of the final superconducting quadrupoles in both rings) due to particle losses. It is estimated that the local loss of a few 10^3 electrons or positrons at 7 (4) GeV can quench the final quadrupole

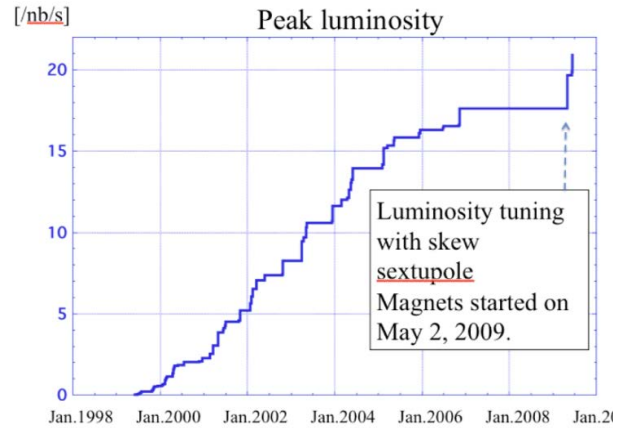


Figure 29: Peak luminosity trend since the KEBK commissioning. The peak luminosity went up significantly by tuning 20 and 8 skew sextupole magnets in the KEBK HER and LER, respectively [25] (M. Masuzawa).

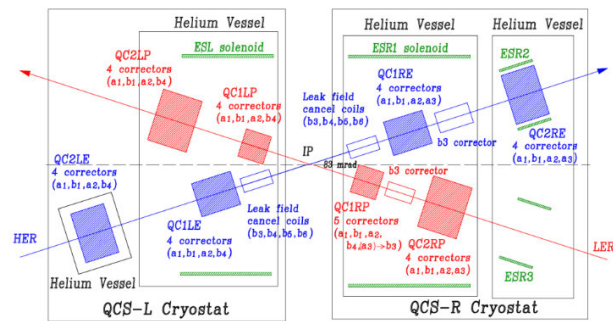


Figure 30: Layout of superconducting magnets in the SuperKEKB interaction region [26] (N. Ohuchi).

QCS [27]. The recovery time after a quench is 2–3 hours; see Fig. 32.

Simulations for CEPC in Fig. 33 indicate that the rate of particles lost due to unavoidable radiative Bhabha scattering immediately downstream of the collision point could already be close to the quench limit of the final quadrupole, if the quench level is similar to the one at SuperKEKB.

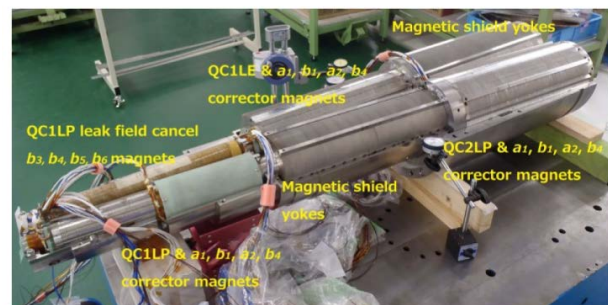


Figure 31: Assembled superconducting magnets in the front helium vessel of the "QCSL" cryostat [26] (N. Ohuchi).

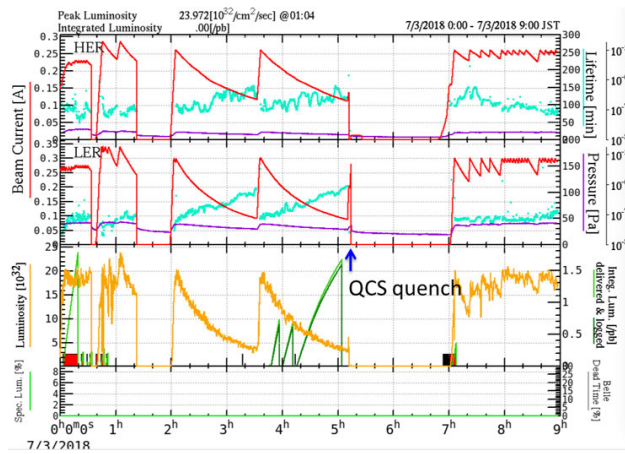


Figure 32: Two hours of downtime caused by a final-quadrupole quench at SuperKEKB during commissioning phase 2 (Y. Funakoshi).

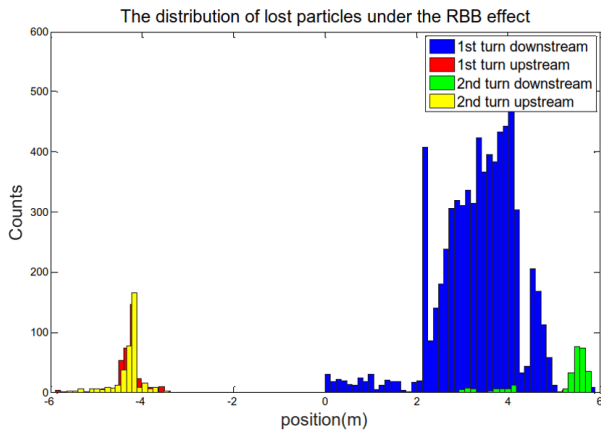


Figure 33: Simulated particles lost near the CEPC IP (at position 0) due to radiative Bhabha scattering, for a total of 200,000 radiative Bhabha scattering events (S. Bai) [6].

The quench limit might be significantly improved by a novel canted-cosine theta (CCT) quadrupole, which is being developed and prototyped for FCC-ee [28]; see Fig. 34. Other main advantages of the CCT quadrupole are as follows: excellent field quality (<1 unit); no need for b_3 correctors; no additional space required for any other correctors; excellent local field quality even at the edges; excellent cross-talk compensation between the two beam apertures; and cost-effective production (no pre-stress, simple winding, light construction). Magnet design and mechanical design are complete. Responses to manufacturing call were already received. The next project milestones are coil winding, impregnation, field measurement (at warm or cold), and quench training plus ultimate current studies.

POLARIZATION

A few percent of vertical polarization enables a precise energy calibration, at the 10^{-6} level, using the method of resonant depolarization [29]. Figure 35 shows that, for FCC-

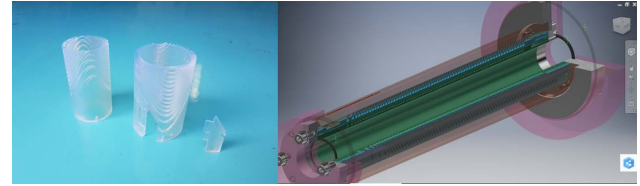


Figure 34: The FCC-ee final-focus canted cosine theta quadrupole project (M. Koratzinos) [28].

ee, a high level of equilibrium polarization is expected at the Z pole without any particular effort, and that dedicated spin-orbit matching will help achieve the required polarization level at the WW threshold.

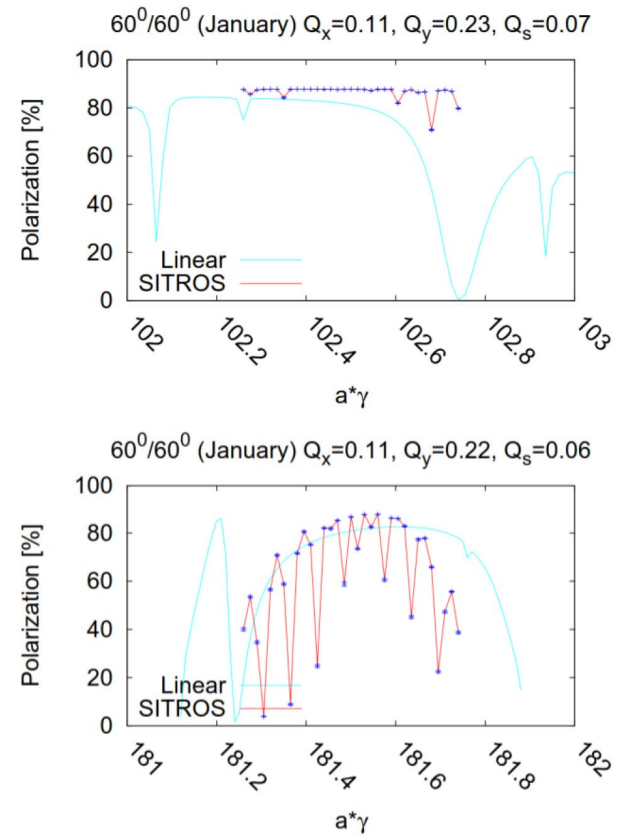


Figure 35: Polarization on the Z pole after closed-orbit correction only (top) and at the WW threshold after correcting the closed orbit, minimizing the spin-orbit coupling, correcting the betatron coupling and aligning the \vec{n}_0 axis (bottom) [30] (E. Gianfelice-Wendt). A linear polarization calculation (SLIM [31]) and the results of nonlinear spin tracking (SITROS [32]) are compared.

“GREEN” ACCELERATOR

The future colliders should be extremely energy efficient. This is achieved, for example, by the development of highly efficient RF power sources [33] and low-power twin aperture magnets [34] (Fig. 36). Such technological improvements

lead to the total FCC-ee electric power budgets compiled in Table 4 (also see [35]).

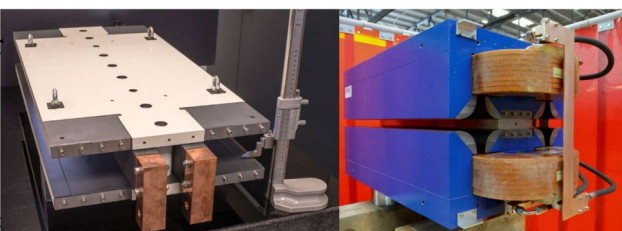


Figure 36: Photos of low-power twin-aperture dipole and quadrupole prototype magnets [34].

KEY ROLE AND OUTLOOK

A final challenge for machines like FCC-ee and CEPC is to serve as a key stepping stone towards the next hadron collider (Fig. 37). Indeed, FCC-ee/CEPC will provide (1) a 100 km tunnel, (2) the technical infrastructure (general services, cryogenics, cooling + ventilation, RF system, etc.); (3) the time (15–20 years) needed to develop and build 1000's of efficient high-field magnets, (4) additional physics motivations and a clear target energy for the subsequent pp collider.

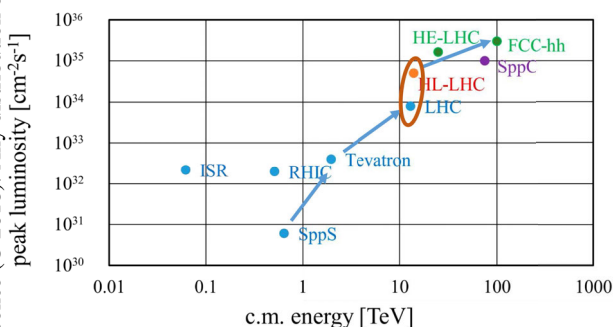


Figure 37: Past, present and proposed hadron colliders.

REFERENCES

- [1] B. Richter, "Very High Energy Electron-Positron Colliding Beams for the Study of Weak Interactions," *Nucl. Instr. Methods* 136 (1976) 47–60.
- [2] A. Apollonio *et al.*, "FCC-ee Operation Model, Availability, and Performance," Proc. eeFACT2018, Hong Kong (2018)
- [3] A. Novokhatski, "Coherent Wave Excitation in a High Current Storage Ring," presented at eeFACT2016, Cockcroft Institute, Daresbury, 23–27 October 2016.
- [4] I. Karpov, R. Calaga, and E. Shaposhnikova, "High order mode power loss evaluation in future circular electron-positron collider cavities," *Phys. Rev. Accel. Beams* 21, 071001 (2018).
- [5] E. Belli *et al.*, "Beam dynamics effects of electron cloud and impedance with coated beam chamber in the Future Circular e^+e^- Collider and characterization of TiZrV thin films," submitted to PRAB (2018).
- [6] The CEPC Study Group, "CEPC Conceptual Design Report," arXiv:1809.00285 (2018).
- [7] R. Calaga, I. Karpov, S. Gorgi Zadeh, "RF system for FCC-ee," presentation at eeFACT2018, Hong Kong (2018).
- [8] Y. Suetsugu, "Electron Cloud Effect (ECE) Mitigation Studies in SuperKEKB," Proc. eeFACT2018, Hong Kong (2018)
- [9] K. Ohmi, F. Zimmermann, "Head-tail instability caused by electron cloud in positron storage rings," *Phys. Rev. Lett.* 85 (2000) 3821–3824
- [10] K. Ohmi, F. Zimmermann, E.A. Perevedentsev, "Wake-field and fast head-tail instability caused by an electron cloud," *Phys. Rev. E* 65 (2001) 016502
- [11] K.L.F. Bane, H. Hayano, K. Kubo, T. Naito, T. Okugi, J. Urakawa, "Intrabeam scattering analysis of measurements at KEK's Accelerator Test Facility damping ring," *Phys. Rev. ST Accel. Beams* 5 (2002) 084403
- [12] E. Benedetto, G. Franchetti, F. Zimmermann, "Incoherent effects of electron cloud in proton storage rings," *Phys. Rev. Lett.* 97 (2006) 034801
- [13] Y. Ohnishi, "Highlights from SuperKEKB Phase 2 Commissioning," presentation at eeFACT2018, Hong Kong (2018).
- [14] S. Ogur *et al.*, "Overall Injection Strategy for FCC-ee" presentation at eeFACT2018, Hong Kong (2018).
- [15] S. Ogur *et al.*, "Preliminary design of FCC-ee pre-injector complex," *Journal of Physics: Conference Series*, Volume 874, conference 1 (2017).
- [16] D. El Khechen *et al.*, "Beam-beam Blowup in the Presence of xy Coupling Sources at FCC-ee," Proc. eeFACT2018, Hong Kong (2018)
- [17] K.A. Olive *et al.* (Particle Data Group), *Chin. Phys. C*, 38, 090001 (2014) section 30.
- [18] Coherent Beam-Beam Instability in Collisions with a Large Crossing Angle K. Ohmi, N. Kuroo, K. Oide, D. Zhou, and F. Zimmermann, *Phys. Rev. Lett.* 119, 134801 (2017).
- [19] N. Kuroo, K. Ohmi, K. Oide, D. Zhou, and F. Zimmermann, "Cross-wake force and correlated head-tail instability in beam-beam collisions with a large crossing angle," *Phys. Rev. Accel. Beams* 21, 031002 (2018).
- [20] D. Shatilov, "IP Beam Parameter Optimization for FCC-ee," *FCC Week 2018*, Amsterdam, 9–13 April 2018 (2018).
- [21] R. Talman, "Scaling Behaviour of Circular Colliders Dominated by Synchrotron Radiation," arXiv:1504.01627 (2015).
- [22] K. Oide *et al.*, "Design of beam optics for the future circular collider e^+e^- collider rings," *Phys. Rev. Accel. Beams* 19, 111005 (2016).
- [23] T. Tydecks, "First results of dynamic aperture optimisation using PSO," *78th FCC-ee Optics Design Meeting*, 7 September 2018 (2018).
- [24] M. Aiba, B. Goddard, K. Oide, Y. Papaphilppou, A. Saa Hernandez, D. Schwartz, S. White, F. Zimmermann, "Top-up injection schemes for future circular lepton collider," *Nucl. Instr. Methods A*, vol. 880 (2018) 98–106; <https://doi.org/10.1016/j.nima.2017.10.075>
- [25] M. Masuzawa *et al.*, "Installation of Skew Sextupole Magnets at KEKB," *Proc. IPAC10 Kyoto* (2010) 1533.

Table 4: Target values for average power per subsystem in different operation modes of FCC-ee, compared with the average power of LEP2 (computed, for each system, as total energy consumed in the year 2000 [36] divided by 200 days).

lepton collider	Z	W	ZH	$t\bar{t}$	LEP2
beam energy [GeV]	45.6	80	120	182.5	104
total RF power [MW]	163	163	145	145	42
collider cryogenics [MW]	1	9	14	46	18
collider magnets [MW]	4	12	26	60	16
booster RF & cryogenics [MW]	3	4	6	8	N/A
booster magnets [MW]	0	1	2	5	N/A
pre-injector complex [MW]	10	10	10	10	10
physics detectors (2) [MW]	8	8	8	8	9
data center [MW]	4	4	4	4	N/A
cooling & ventilation [MW]	30	31	31	37	16
general services [MW]	36	36	36	36	9
total electrical power [MW]	259	278	282	359	~120

- [26] N. Ohuchi, “Final-focus Superconducting Magnets for SuperKEKB,” *Proc. IPAC’18 Vancouver* (2018) 1215.
- [27] Y. Ohnishi, “Report on SuperKEKB Phase 2 Commissioning,” *Proc. IPAC’18 Vancouver* (2018) 1.
- [28] M. Koratzinos, G.A. Kirby, J. V. Nugteren, A.R. Dudarev, “A Method for Greatly Reduced Edge Effects and Crosstalk in CCT Magnets,” *IEEE Transactions on Applied Superconductivity*, vol. 28, no. 3 (2018).
- [29] E. Gianfelice-Wendt, “Investigation of beam self-polarization in the future e^+e^- circular collider,” *Phys. Rev. Accel. Beams* 19, 101005 (2016).
- [30] E. Gianfelice-Wendt, private communication (2018).
- [31] A.W. Chao, “Evaluation of Radiative Spin Polarization in an Electron Storage Ring,” *Nucl. Instr. Meth.* 180 (1981) 29.
- [32] J. Kewisch, “Simulation of Electron Spin Depolarisation with the computer Code SITROS,” *DESY* 83-032 (1983). IM
- [33] Andrey Yu. Baikov, Chiara Marrelli, and Igor Syratychev, “Toward High-Power Klystrons With RF Power Conversion Efficiency on the Order of 90%,” *IEEE Transactions on Electron Devices*, VOL. 62, NO. 10, OCTOBER 2015 (2015).
- [34] A. Milanese, “Efficient twin aperture magnets for the future circular e^+e^- collider,” *Phys. Rev. Accel. Beams* 19, 112401 (2016).
- [35] F. Zimmermann *et al.*, “Electrical Power Budget for FCC-ee,” *Proc. IPAC’16, Busan* (2016) p. 3828
- [36] “Énergie Électrique, Rapport Mensuel Décembre 2000, Bilan Année 2000”, *CERN internal report* (2000).

SEVERAL TOPICS ON BEAM DYNAMICS IN FCC-ee*

K. Oide[†], KEK, Tsukuba, Japan

D. Shatilov, BINP SB RAS, Novosibirsk, Russia

S. Aumon, T. K. Charles, D. El Khechen, T. Tydecks, CERN, Geneva, Switzerland

Abstract

The FCC-ee is a double-ring e^+e^- collider to be installed in a common tunnel of ~ 100 km circumference, as a potential first step before the FCC-hh hadron collider. Several studies on the beam dynamics at FCC-ee: low emittance tuning, dynamic aperture, beam blowup with/without beam beam, are introduced in the paper.

INTRODUCTION

The beam energy of FCC-ee covers at least from the Z-pole (45.6 GeV) to $t\bar{t}$ (182.5 GeV). The design luminosity is the highest ever at each energy, under the constraint that the synchrotron radiation (SR) power is less than 100 MW for the total of two beams. The design is based on existing technologies verified in e^+e^- colliders in the world, including VEPP-IV, LEP, PEP-II, KEKB, DAΦNE, BEPC II, SuperKEKB. The main characteristics of the optics design [1] have been double ring, with ~ 100 km circumference, two interaction points (IPs) per ring, horizontal crossing angle of 30 mrad at the IP, and the crab-waist scheme with local chromaticity correction system. A so-called "tapering" of the magnets is applied, which scales all fields of magnets with the local beam energy determined by the SR. An asymmetric layout near the interaction region suppresses the critical energy of SR incoming to the detector at the IP below 100 keV. Sufficient transverse/longitudinal dynamic apertures (DAs) have been obtained to assure adequate beam lifetime with beamstrahlung and top-up injection. Table 1 lists the basic parameters of FCC-ee. For the estimation of the running plan at each energy, luminosities less than numbers in this table by 10–20% are used at each energy to have a margin for operation.

LOW EMITTANCE TUNING WITH DYNAMIC APERTURE

Due to the low emittance budget and the small β^* at the interaction point, the FCC-ee is a challenging accelerator to correct when misalignments are introduced in the simulations. These errors produce a large vertical dispersion (several hundred meters without any correction applied) and coupling, which compromise the target emittances, in particular at high energy. Several correction methods and algorithms were developed in order to preserve the emittances as close as possible to their design values.

Horizontal correctors were installed at every focusing quadrupole and vertical correctors at every defocusing quadrupole. Beam Position Monitors (BPM) were placed at each quadrupole, including at the doublet of the IPs. Skew quadrupole correctors with a trim quadrupole are placed at the sextupoles to correct the beta-beat and rematch the horizontal dispersion. Special skew quadrupoles were installed in the interaction region to compensate the tilt of the doublet quadrupoles at the IPs. The effect of the tilt of dipoles and field errors will be included in the next phase of the study. The vertical dispersion distortion was corrected with orbit correctors via the dispersion free steering method [2] first and with skew quadrupoles with the help of response matrices. The linear coupling was corrected by adjusting the linear coupling resonance driving term parameters, as tested at the ESRF [3]. Trim quadrupoles were used to rematch the phase advances between the BPMs, again using response matrices. Satisfactory results for the misalignment tolerance were found when the magnets were misaligned as defined in Table 2.

1000 seeds were tested with the correction algorithm using the input misalignments listed in Table 2 and 70% of them converged, as shown in Fig. 1, with the following results for the emittances:

$$\epsilon_y = 0.10 \pm 0.013 \text{ pm}$$

$$\epsilon_x = 1.52 \pm 0.01 \text{ nm}$$

$$\epsilon_y/\epsilon_x = 0.0065\%$$

More studies are going on with less number of orbit correctors using trim windings on the arc sextupoles, with more machine errors including the roll of dipoles, misalignments taking the scheme of girders into account, and BPM errors [4].

The resulting dynamic aperture (DA) at $t\bar{t}$ has been evaluated as shown in Fig. 2. The average of them are just on the design DA. The variation is within the margin for the plan of the integrated luminosity.

DYNAMIC AND MOMENTUM APERTURE OPTIMIZATION USING PSO

Applying particle swarm optimization (PSO) in accelerator physics to improve machine parameters is a worthwhile method to cope with the increasingly large number of degrees of freedom to optimize. With an existing machine it is possible to optimize the sextupole setting by improving dynamic aperture through lifetime optimization using PSO [5].

* Work supported by the European Commission under Capacities 7th Framework Programme project EuCARD-2, grant agreement 312453, and under the Horizon 2020 Programme project CREMLIN, grant agreement 654166.

[†] katsunobu.oide@cern.ch

Table 1: Machine parameters of the FCC-ee for different beam energies

		Z	WW	ZH	tt	
Circumference	[km]	97.756				
Bending radius	[km]	10.760				
Free length to IP ℓ^*	[m]	2.2				
Solenoid field at IP	[T]	2.0				
Full crossing angle at IP	[mrad]	30				
SR power / beam	[MW]	50				
Beam energy	[GeV]	45.6	80	120	175	182.5
Beam current	[mA]	1390	147	29	6.4	5.4
Bunches / beam		16640	2000	328	59	48
Average bunch spacing	[ns]	19.6	163	994	2763 ^a	3396 ^a
Bunch population	[10 ¹¹]	1.7	1.5	1.8	2.2	2.3
Horizontal emittance ε_x	[nm]	0.27	0.84	0.63	1.34	1.46
Vertical emittance ε_y	[pm]	1.0	1.7	1.3	2.7	2.9
Arc cell phase advances	[deg]	60/60			90/90	
Momentum compaction α_p	[10 ⁻⁶]	14.8			7.3	
Arc sextupole families		208			292	
Horizontal β_x^*	[m]	0.15	0.2	0.3	1.0	
Vertical β_y^*	[mm]	0.8	1.0	1.0	1.6	
Horizontal size at IP σ_x^*	[μ m]	6.4	13.0	13.7	36.7	38.2
Vertical size at IP σ_y^*	[nm]	28	41	36	66	68
Energy spread (SR/BS) σ_δ	[%]	0.038/0.132	0.066/0.131	0.099/0.165	0.144/0.186	0.150/0.192
Bunch length (SR/BS) σ_z	[mm]	3.5/12.1	3.0/6.0	3.15/5.3	2.01/2.62	1.97/2.54
Piwiński angle (SR/BS)		8.2/28.5	3.5/7.0	3.4/5.8	0.8/1.1	0.8/1.0
Length of interaction area L_i	[mm]	0.42	0.85	0.90	1.8	1.8
Hourglass factor R_{HG}						
Crab sextupole strength	[%]	97	87	80	40	40
Energy loss / turn	[GeV]	0.036	0.34	1.72	7.8	9.2
RF frequency	[MHz]	400			400 / 800	
RF voltage	[GV]	0.1	0.75	2.0	4.0 / 5.4	4.0 / 6.9
Synchrotron tune Q_s		0.0250	0.0506	0.0358	0.0818	0.0872
Long. damping time	[turns]	1273	236	70.3	23.1	20.4
RF acceptance	[%]	1.9	3.5	2.3	3.36	3.36
Energy acceptance (DA)	[%]	± 1.3	± 1.3	± 1.7	-2.8 +2.4	
Polarisation time t_p	[min]	15000	900	120	18.0	14.6
Luminosity / IP	[10 ³⁴ /cm ² s]	230	28	8.5	1.8	1.55
Horizontal tune Q_x		269.139	269.124	389.129	389.108	
Vertical tune Q_y		269.219	269.199	389.199	389.175	
Beam-beam ξ_x/ξ_y		0.004/0.133	0.010/0.113	0.016/0.118	0.097/0.128	0.099/0.126
Allowable e ⁺ e ⁻ charge asymmetry	[%]	± 5	± 3			
Lifetime by rad. Bhabha	[min]	68	59	38	40	39
Actual lifetime by BS	[min]	> 200	> 200	18	24	18

^a A half ring is filled with the common rf scheme

Table 2: Tolerances for misalignments and roll for arc quadrupoles, sextupoles, and the IP quadrupoles." This could be changed to "Misalignment errors introduced to the lattice before correction applied. Misalignments and roll angles applied randomly with a probability governed by a Gaussian distribution (truncated at 2.5 σ) with the a standard derivation values as stated.

Magnet type	σ_x μ m	σ_y μ m	θ μ rad
Arc quadrupoles	100	100	100
Sextupoles	100	100	0
IP quadrupoles	50	50	50

A particle swarm optimizer is a kind of genetic algorithm with both cognitive and social components, originally influenced by bird flocking behavior [6]. PSO can be employed to improve dynamic and momentum aperture of FCC with its high number of degrees of freedom.

In the case of FCC-ee, the number of degrees of freedom may be reduced by keeping the proposed $-I$ transform between sextupole pairs, and additionally maintaining periodicity of the machine after each half-turn. Doing so, there are 294 degrees of freedom left. This number is clearly out of range for brute force scanning and genetic algorithms like PSO are better equipped to handle the optimization.

The optimizer improves the objective function(s) over time by iteratively adjusting position and speed of the candidate solutions (particles) in search space:

$$\vec{x}_{n+1} = \vec{x}_n + \vec{v}_{n+1}, \quad (1)$$

$$\vec{v}_{n+1} = \omega \vec{v}_n + c_r r_1 (\vec{x}_{p\text{-best}} - \vec{x}_n) + c_s r_2 (\vec{x}_{g\text{-best}} - \vec{x}_n). \quad (2)$$

Here, \vec{x} is the position in search space, which in this scenario would be a vector containing the individual sextupole strengths, \vec{v} is the velocity (change of position per generation) of the individual particle in search space. Additionally,

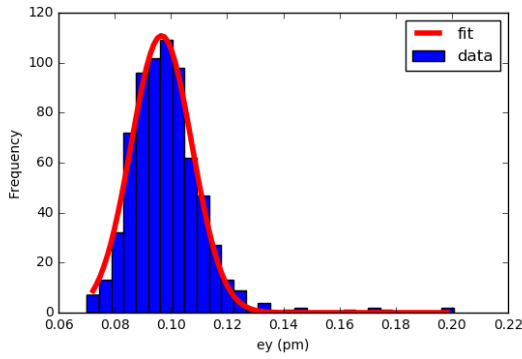


Figure 1: Statistical distribution of the vertical emittance for 700 different seeds resulting from the input misalignments given in Table 2. Initially 1000 seeds were tested and 70% of them converged.

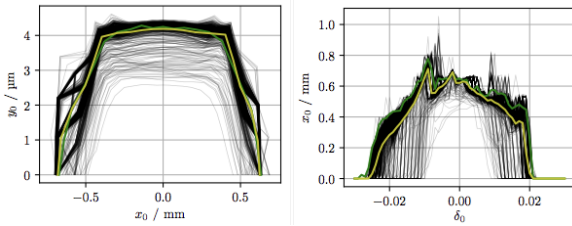


Figure 2: Variation of the dynamic aperture with the misalignment after correction for converged samples, transverse (left) and momentum (right). Evaluated at \bar{t} with tapering by MADX/PTC.

there is $\vec{x}_{p\text{-best}}$, which is the position where the individual particle has best performed in its history, and $\vec{x}_{g\text{-best}}$, which is the global best position known so far. The velocity for the next generation \vec{v}_{n+1} therefore depends on

- the initial velocity \vec{v}_n , weighted by factor ω , describing the rigidity of movement,
- the individual particles personal best solution $\vec{x}_{p\text{-best}}$, weighted by cognitive factor c_c ,
- the global best solution $\vec{x}_{g\text{-best}}$, weighted by social factor c_s .

Based on tracking dynamic and momentum aperture for different candidate solutions, candidates are assigned a score (value function in Fig. 3) which makes them more or less successful in their impact on the population. With the way the value function is set, the algorithm may be steered towards favoring one objective over another (e. g. favoring area of momentum aperture over area of dynamic aperture).

The particles are initialized with the sum of a vector containing the reference sextupole setting and a random vector, with maximum change in k_2 per sextupole of 0.01 m^{-2} .

The solution presented here is found in the 17th generation. It yields an improvement of the area of momentum aperture of 18.0 % compared to the reference lattice, as shown in Fig. 4.

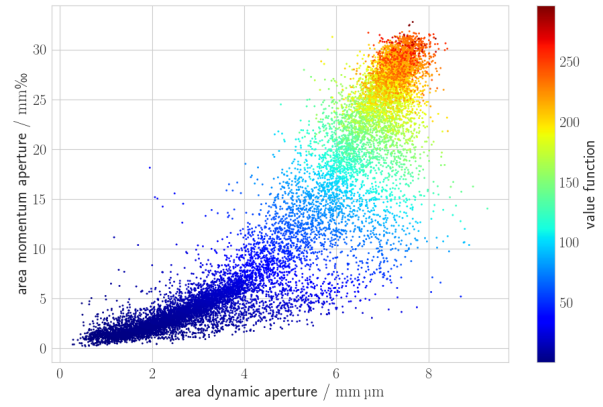


Figure 3: Value function as a function of area of momentum aperture and area of dynamic aperture for all solutions of the PSO algorithm.

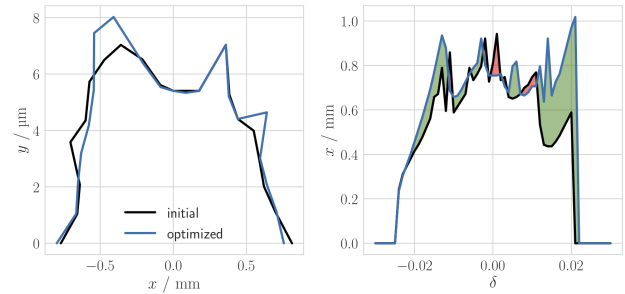


Figure 4: Dynamic aperture (left) and momentum aperture (right) for reference lattice (black) and optimized lattice (blue). The area of dynamic aperture is improved by 3.1 % while the area of momentum aperture is increased by 18.0 %.

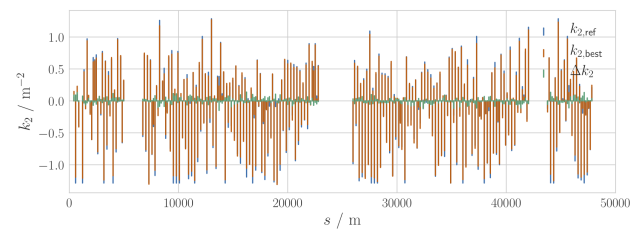


Figure 5: Change in sextupole strengths (green) between optimized solution (red) and reference solution (blue) for one half ring.

In Fig. 5, the change of k_2 between the optimized solution and the reference solution is presented. Although at first glance the solution appears to be as arbitrary as the reference setting, when looking closely at the peak sextupole strengths a difference can be observed: the peak sextupole strengths appear to have been reduced by the optimizer compared to the reference setting.

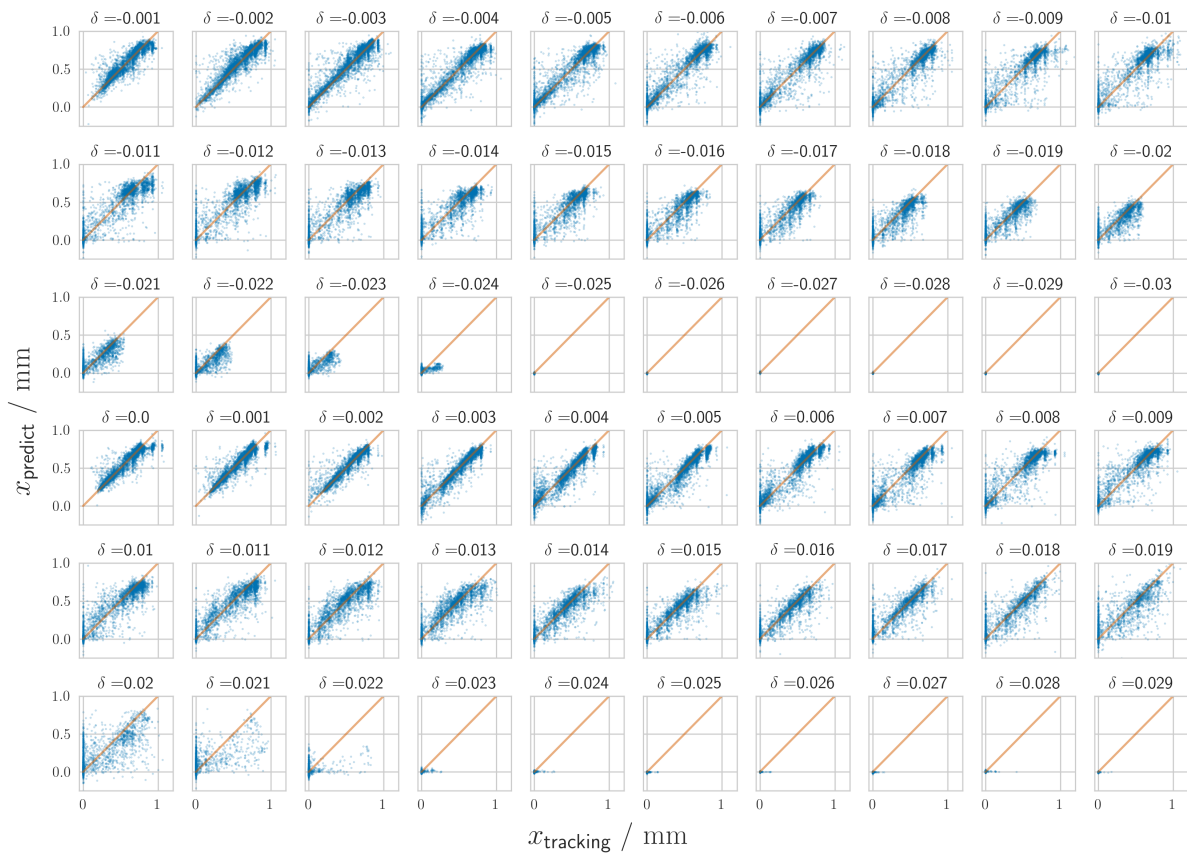


Figure 6: Aperture predictions for different energy deviations of trained model together with true values from particle tracking determined for a test data set (which has been withheld from training).

Prospects of Employing Machine Learning Concepts for PSO

As a side effect of the optimization, a large number of sextupole settings has been investigated regarding dynamic / momentum aperture (comp. Fig. 3). These settings can be used to train an artificial neural network (NN) to predict resulting momentum aperture for different sextupole settings. With this model, the optimization process can be significantly accelerated since time consuming particle tracking can be avoided.

As a proof of principle, a NN containing an input layer, three hidden layers, and an output layer has been tested. As input, the NN takes the 298 sextupole strengths (including final focus). The hidden layers all accept 300 input values and produce 300 output values. The output layer is the 61 horizontal apertures for different energy deviations ranging from -3% to 3% in steps of 1% . First results indicate reasonably good agreement with the predictions by the trained model and the actual data for a test data set, withheld from training (comp. Fig. 6).

However, for large energy deviations, the trained model fails to reproduce tracked apertures. Since the training data set contains only small apertures for large energy deviations, the model will assume that any combination of sextupole

strengths must lead to small apertures for large energy deviations.

Nevertheless, the trained model itself can be used in a PSO algorithm, performing the formerly time consuming step of determining the aperture in a matter of milliseconds. Doing so, the model can be used to enhance aperture for energy deviations in a range where the training data set found considerable aperture already. By testing promising candidates through tracking, the training data set (and the model) may be continuously enhanced with respect to large energy deviation apertures.

Thus, a shortcut in optimizing dynamic aperture can be provided. Furthermore, it is possible to evaluate different objective functions, e. g. favoring particular shapes of aperture, based on the trained model. In addition, analysis of the trained model might provide insight into which sextupoles have less impact on dynamic aperture compared to others, in order to mainly use those for chromaticity correction.

In a future application, machine learning can be used to optimize the repopulating step in PSO. By intervening in the evolution process through selecting high potential candidates whilst maintaining diversity, the optimization process can be significantly enhanced as has been shown in the light source community [7].

UNEXPECTED BEAM BLOWUP

A blowup of vertical emittance has been observed in particle tracking simulations with beam-beam and lattice misalignments [8]. Its was somewhat unexpected, since estimation without lattice errors did not predict such a blowup unless a residual vertical dispersion at the interaction point (IP) is larger than a certain amount. Table 3 shows the such a criteria on the residual dispersion at the IP. The beam-beam

Table 3: Tolerances for residual dispersions at the IP for each energy of FCC-ee, obtained by quasi strong-weak model without lattice. The tolerance $\Delta\eta_y^*$ corresponds to 5% increase of vertical beam size σ_y^* at the IP with beamstrahlung.

Beam energy [GeV]	45.6	80	120	175
Design σ_y^* [nm]	28	41	35	66
Energy spread ^a [%]	0.13	0.13	0.165	0.185
$\Delta\eta_y^*$ [μm]	1	5	4	6

^a with beamstrahlung

simulations were done by SAD [9] with BBWS weak-strong model implemented within it [10]. Even beam-beam simulations with lattice without misalignments did not show such blowup [11].

Figure 7 shown an example of such a blowup for two seeds of random numbers of misalignments of arc sextupoles. Note that the residual dispersion at the IP for seed 3 is smaller than the previous criteria given in Table 3, while giving even larger blowup than another seed 19, which has larger dispersions at the IP.

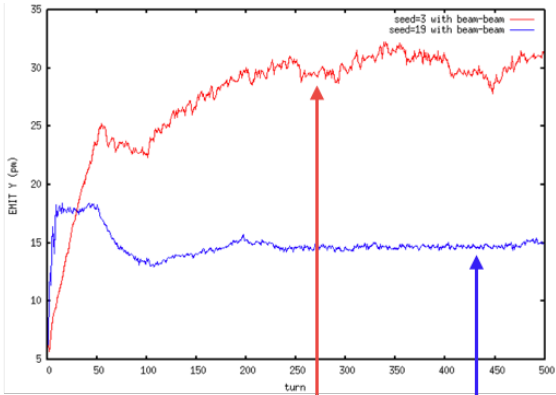
Later it was found that such a blowup happens only by lattice coupling/dispersion without beam-beam. Then it was shown that this is a effect called “anomalous emittance” as described in Ref. [12], caused by synchro-beta resonance with the lattice chromaticity in the x - y coupling and dispersion. Such a phenomenon can be described by a Vlasov model in the synchrotron phase space. See a detailed description in Ref. [13]. This kind of blowup is intrinsic to a lattice with chromatic dispersions and x - y coupling. Mitigations are possible by a low emittance tuning toward well below the design emittance ratio combined with a better choice of operating tunes.

ACKNOWLEDGEMENT

The authors thank M. Benedikt, A. Blondel, M. Boscolo, E. Levichev, K. Ohmi, D. Zhou, F. Zimmermann, and the entire FCC-ee Collaboration Tefor encouraging the research, useful discussions, and suggestions.

REFERENCES

[1] K. Oide, *et al.*, *Phys. Rev. Accel. Beams* 19 (2016) no.11, 111005.
[2] R. Assmann, P. Raimondi, G. Roy and J. Wenninger, “Emittance optimization with dispersion free steering at LEP”, *Phys. Rev. ST Accel. Beam*, 3,p. 121001(2000).



Coupling (%)	0.2	0.2
RMS of sext. Offset (°)	11	15
Seed	3	19
η_y @ (IP.1, IP.2) (°)	(-5.3, 4.24)	(-8.9,8)
$\eta_{py} \times \beta_y^*$ @ (IP.1, IP.2) (°)	(6.8, 1.04)	(35.4,23)
R2 parameter	(1.8x10 ⁻³ ,1.8x10 ⁻³)	(-5.1x10 ⁻⁵ , -1.8x10 ⁻⁴)

Figure 7: Blowup of vertical emittance measured at he IP by a particle tracking with beam-beam, beamstrahlung, and lattice. The arc sextupoles are vertically misaligned randomly to produce the vertical emittance of the design ratio $\varepsilon_y/\varepsilon_x = 0.2\%$. Two examples for different seeds are shown, corresponding residual vertical dispersions at the IP in the table.

[3] A. Franchi *et al.*, “Vertical emittance reduction and preservation in electron storage rings via resonance driving terms correction”, *Phys. Rev. ST Accel. Beam*, 14, p. 034002(2015).
[4] T. K. Charles, presented at eeFACT2018, Hong Kong, Sep 2018, paper TUOAB02, this conference.
[5] Li, Yongjun and Cheng, Weixing and Yu, Li Hua and Rainer, Robert, “Genetic algorithm enhanced by machine learning in dynamic aperture optimization”, *PRAB* 21,p.054601(2018).
[6] R. Eberhart and J. Kennedy, “A new optimizer using particle swarm theory”, *MHS’95. Proc of the Sixth International Symposium on Micro Machine and Human Science*, pp.39–43(1995).
[7] Li, Yongjun and Cheng, Weixing and Yu, Li Hua and Rainer, Robert, “Genetic algorithm enhanced by machine learning in dynamic aperture optimization”, *Phys. Rev. Accel. Beams*, 21, 5, p. 11 (2018).
[8] D. El Khechen, presented at eeFACT2018, Hong Kong, Sep 2018, paper TUYBA03, in this conference.
[9] <http://acc-physics.kek.jp/SAD/index.html>, <https://github.com/KatsOide/SAD>
[10] K. Ohmi, *et al.*, “BEAM-BEAM SIMULATION STUDY FOR CEPC”, THPRI003, *IPAC’14* (2014).
[11] D. Zhou, presented at FCC Week 2016, 11–15 April 2016, Rome, Italy(2016).
[12] K. Oide and H. Koiso, “Anomalous equilibrium emittance due to chromaticity in electron storage rings”, *Phys.Rev. E49* pp. 4474-4479(1994).
[13] K. Oide, presented at eeFACT2018, Hong Kong, Sep 2018, paper WEXBA03, in this conference.

STATUS OF DAΦNE: FROM KLOE-2 TO SIDDHARTA-2, EXPERIMENTS WITH CRAB-WAIST

C. Milardi[†], D. Alesini, S. Bini, O. R. Blanco-García, M. Boscolo, B. Buonomo, S. Cantarella, S. Caschera, A. De Santis, G. Delle Monache, C. Di Giulio, G. Di Pirro, A. Drago, A. D'Uffizi, L. G. Foggetta, A. Gallo, R. Gargana, A. Ghigo, S. Guiducci, S. Incremona, F. Iungo, C. Ligi, M. Maestri, A. Michelotti, L. Pellegrino, R. Ricci, U. Rotundo, L. Sabbatini, C. Sanelli, G. Sensolini, A. Stecchi, A. Stella, A. Vannozzi, M. Zobov, LNF-INFN, Frascati, Italy
J. Chavanne, G. Le Bec, P. Raimondi, ESRF, Grenoble, France
G. Castorina, INFN-Roma1, Roma, Italy

Abstract

DAΦNE, the Italian lepton collider, is running since more than a decade thanks to a radical revision of the approach used to deal with the beam-beam interaction: the *Crab-Waist* Collision Scheme. In this context, the collider has recently completed a long term activity program aimed at providing an unprecedented sample of data to the KLOE-2 detector, a large experimental apparatus including a high intensity axial field strongly perturbing ring optics and beam dynamics. The KLOE-2 run has been undertaken with the twofold intent of collecting data for rare decay and flavor physics studies, and testing the effectiveness of the new collision scheme in presence of a strongly perturbing experimental apparatus. The performances of the collider are reviewed and the limiting factors discussed along with the preparatory phase activities planned to secure a new collider run to the SIDDHARTA-2 experiment.

INTRODUCTION

The DAΦNE [1] accelerator complex consists of a double ring lepton collider working at the c.m. energy of the Φ -resonance (1.02 GeV) and an injection system. The collider includes two independent rings, each 97 m long. The two rings share an interaction region (IR), where the detector taking data, one at the time, is installed. Beam injection is performed on energy, also in topping-up mode during collisions as well, by a system including an S-band LINAC, 180 m long transfer lines and an accumulator damping ring. DAΦNE became operational in 2001, and it still is an attractive collider to perform relevant experiments aimed at understanding flavour physics. This has been possible thanks to a continuous effort finalized at increasing the collider performances, which culminated in 2009 with the realization of a new approach to the beam-beam interaction: the *Crab-Waist* (CW) Collision Scheme. The new approach to collisions is based on large Piwinski angle (ψ) and CW compensation of the beam-beam induced instabilities [2, 3, 4]. It was, implemented during the run dedicated to a tabletop experiment, SIDDHARTA, and allowed to increase the instantaneous luminosity by a factor three, paving the way to a new run dedicated to a revised KLOE detector: KLOE-2 [5], that, in view of a higher luminosity, extended its

physics search programs. In fact, the upgraded KLOE-2 setup includes calorimeter devices close to the IR, as well as a cylindrical GEM detector, the Inner Tracker (IT) installed at a distance of 15 cm from the Interaction Point (IP). However, a long-term run finalized to deliver a large statistical sample of data can only be planned if all the collider subsystems perform in a highly reliable way. For this reason, in the first six months of 2013, before starting the data-delivery phase, the DAΦNE infrastructure underwent a general consolidation program [6]; exploiting the long planned shutdown foreseen to install the new detector layers. Still some activities were not completed at that time, due to delays in the spare parts procurement, thus they have been finalized during the data taking, profiting from the seasonal shutdowns.

The DAΦNE collider parameters are listed in Table 1.

Table 1: DAΦNE Beam Parameters

	DAΦNE native (2000÷2006)	DAΦNE CW Since 2007
Energy (MeV)	510	
β_y^* (cm)	1.8	0.85
β_x^* (cm)	160	23
σ_x^* (μ m)	760	250
σ_y^* (μ m) at low current	5.4	3.1
σ_z (cm)	2.5	1.5
Bunch spacing (ns)	2.7	
Damping times τ_E, τ_x (ms)	17.8/36.0	
Cros. angle $\theta_{\text{cross}}/2$ (mrad)	12.5	25
Piwinski angle ψ (mrad)	0.6	1.5
ϵ (mm mrad)	0.34	0.28
RF frequency [MHz]	368.26	368.667
Harmonic number	120	

Presently DAFNE, after having successfully completed the KLOE-2 run [7], is facing the preparatory phase propaedeutical to a new operation period aimed at delivering data to the SIDDHARTA-2 detector [8], an upgraded version of the old one. The new experimental apparatus aims at performing the first kaonic deuterium measurement by improving its measurement resolution which, in turn, requires to considerably reduce the signal background ratio increasing, at the same time, the signal rate. The

[†] catia.milardi@lnf.infn.it

smoother injections, and stable and reproducible luminosity trends.

In general, it is worth reminding that machine studies and developments have been limited to very few aspects in favour of the experiment's data taking.

BEAM DYNAMICS ISSUES

The maximum e^- current accumulated during operations has been $I^- \sim 1.7$ A, stored in 98 consecutive bunches. However, at regime in collision, only currents in the range $1.4 \div 1.5$ A have been injected. The quality of the e^- beam depended heavily on the mitigation of the effect induced by the ions of the residual vacuum, such effect is counteracted by leaving a suitable empty gap in the batch. The width of such gap is a compromise between opposite requirements posed by e^- beam dynamics and high luminosity. It depends greatly on the vacuum condition which improve with the stored beam dose. In fact, the best results in terms of luminosity have been achieved, by the second half of the run, through collisions of 106 consecutive bunches.

Concerning the e^+ current, it is strongly dominated by the *e-cloud* effects [11] which are mitigated by using solenoidal winding around the beam pipe, clearing electrodes (ECEs), and feedback systems. ECEs were installed during the shutdown for the KLOE detector roll-in. At that time 4 and 8 devices were inserted inside wiggler and dipole vacuum chambers respectively, in order to mitigate the *e-cloud* formation. DAΦNE has been the first collider to operate with, and thanks to the ECEs. They have been fundamental, especially at the beginning of the operations when the vacuum level in the ring was not optimal yet. At that stage, a careful tuning of each stripline polarization voltage has been done in order to avoid sudden variation in the e^+ beam orbit. Then, progressively during the data taking, several ECEs had to be switched off due to faulty behaviour. The KLOE-2 run finished with only 2 ECEs fully operative, but, at that point, the benefits coming from the scrubbing process helped in keeping the *e-cloud* instabilities under control, as confirmed by comparing the pressure rise in the arcs of the e^+ ring for the two periods with 80% and only 2 ECE working properly. A conclusive explanation of the process leading the largest part of the ECEs to exhibit a faulty behaviour, after having worked for some time, is under way since it requires to extract and analyse in detail the striplines concerned. During the whole KLOE-2 run the maximum current stored in the e^+ beam has been of the order of $I^+ \sim 1.2$ A, although, at regime in collision, a current $I^+ > 0.95$ has been rarely injected; a value somewhat lower than the one achieved during the previous DAΦNE's run periods.

Beam currents were affected by longitudinal quadrupole oscillations. This instability has been controlled by a special technique [12] implemented at DAΦNE in the synchrotron (dipole) feedback system. This is done by detuning the Quadrature Phase Shift Keying (QPSK) modulation in the feedback back end for damping both dipole and quadrupole beam motions. Also the environmental RF and DC noise coming from pickups, and leading to undesirable vertical beam size growth, was minimized by installing a

low noise front end, designed in collaboration with SuperKEK Team, for the vertical feedback.

In general beam dynamics has been affected by the several new components installed on the two rings during the preparatory phase for the KLOE-2 run [13, 14]. In fact the new kicker developed for the transverse horizontal positron feedback has also been used for the horizontal electron feedback, and as beam dumper. This adds a new kicker per ring in the opposite section with respect to the IR. The IP vacuum chamber has been replaced with a new section having a slightly different mechanical design. The rectangular vacuum chambers of the collimators close to the IP, the most effective ones, have been replaced with some chambers of reduced volume in order to increase the blade insertion length. The four wigglers installed in each ring have been modified in order to reduce the higher order multipoles of the magnetic field [15], and removing a purpose built sextupole component, which was efficiently used to implement a smooth and distributed chromaticity control.

LUMINOSITY PERFORMANCES

Luminosity in DAΦNE is evaluated by using different approaches. A fast γ monitor measures the photons emitted at small angle (~ 1 mrad) in the e^+e^- inelastic scattering, by means of two detectors aligned along the direction of each beam from the IP. They are used for relative luminosity measurements only, during collision optimization. The absolute luminosity measurement is provided by the experimental detector. Another dedicated tool based on the direct signals of CCALT, one of the new KLOE-2 layers, provides bunch by bunch luminosity measurements [16].

The data taking for the KLOE-2 detector has been organized in four runs, as shown in Fig. 1. For each run milestones have been agreed upon, in order to grant to the experiment a total integrated delivered luminosity of the order of 6 fb^{-1} , after 40 months of operations.

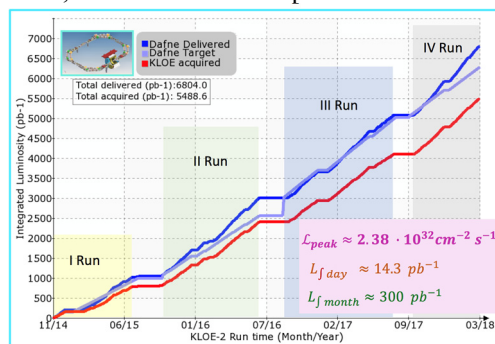


Figure 1: KLOE-2 data taking summary.

Trends in integrated luminosity show how the agreed milestones have been achieved for each data taking period, and often even exceeded. By the end of operations, the DAΦNE collider has been able to provide a total integrated luminosity of the order of $L_{\text{del}} \sim 6.8 \text{ fb}^{-1}$, of which $L_{\text{jacq}} \sim 5.5 \text{ fb}^{-1}$ has been stored on disk by the experiment.

The maximum instantaneous luminosity measured has been $L_{\text{peak}} \sim 2.38 \cdot 10^{32} \text{ cm}^{-2} \text{ s}^{-1}$ which is the highest luminosity ever measured by KLOE. Such a result could, without

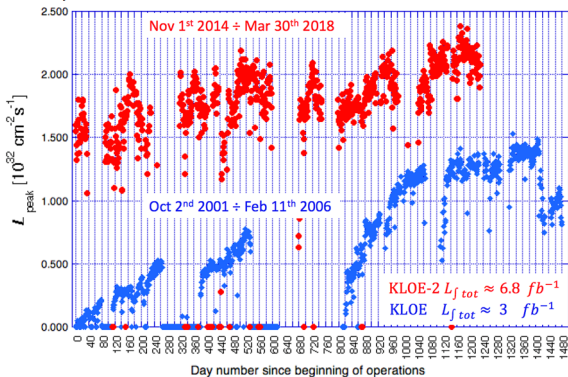


Figure 2: Instantaneous luminosity trend.

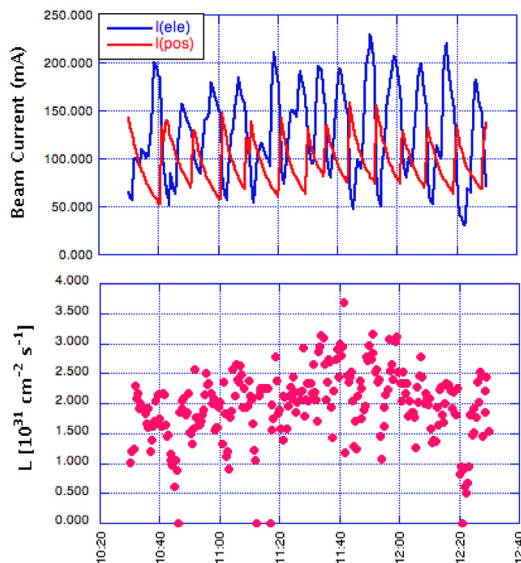


Figure 3: Ten bunches collisions.

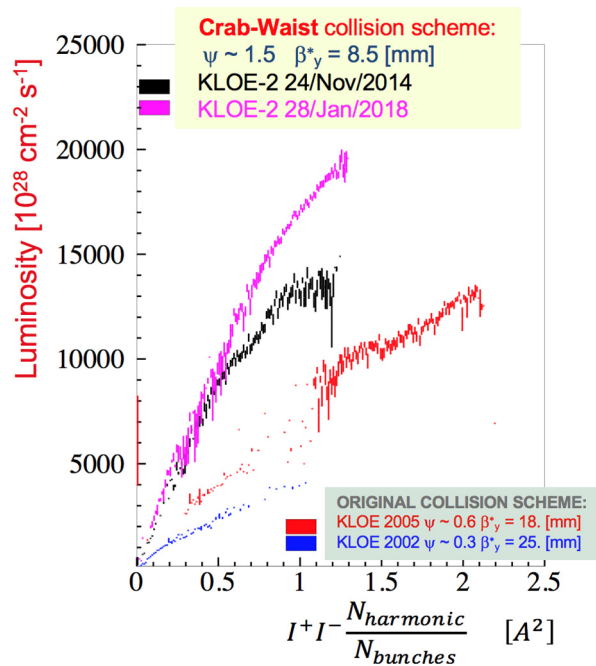


Figure 4: Luminosity as a function of the beam currents product normalized per number of interacting bunches, before (blue and red curves) and after (black and pink curves) implementing the *CW* Collision Scheme.

Already in 2005 increasing the Piwinski angle and the beam focusing at the IP allowed a consistent improvement in terms of luminosity, see red plot in Fig. 4. Then, after implementing a new IR based on *CW*, such luminosity gain became remarkable, mainly at low currents, even before any extensive collider optimization, see the black plot in Fig. 4. Eventually, after a comprehensive machine tuning, luminosity growth extended up to high currents, without showing any sign of saturation, see pink plot in Fig. 4.

As far as the integrated luminosity is concerned, the *CW* collisions at DAΦNE have been able to more than double the integrated delivered luminosity, in fact 3 fb^{-1} only had been delivered with the nominal collision scheme, in almost the same period of previous operations. Remarkable performances have been achieved also in terms of delivered daily and monthly integrated luminosities, which have been of the order of $L_{\text{day}} \sim 14.3 \text{ pb}^{-1}$ and $L_{\text{month}} \sim 300 \text{ pb}^{-1}$ respectively. It is worth noticing that the best delivered monthly luminosity has been obtained in 26 days of activity only, see Fig. 5. Furthermore, the maximum daily integrated luminosity is comparable with the highest ever achieved at DAΦNE, $L_{\text{day}} \sim 15 \text{ pb}^{-1}$, occasionally measured [18] during the test of the *CW* collision scheme with the SIDDHARTA experiment. Last, but not least, the aforementioned record luminosities have been achieved despite maximum currents in collision were somewhat lower than the ones used during the past DAΦNE runs. Such current reduction can be estimated to be of the order of 30% and 20% for the electron and the positron beam respectively.

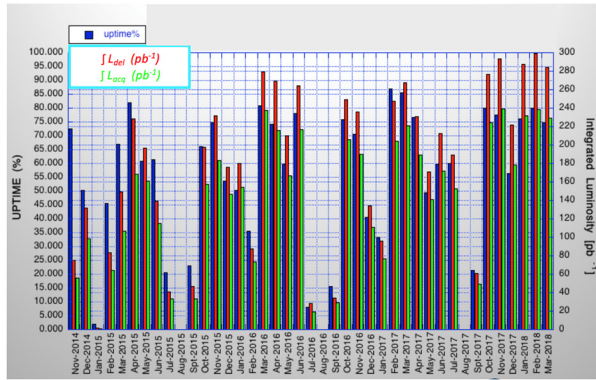


Figure 5: Month by month performances.

SIDDHARTA-2 PREPARATORY PHASE

Interaction Region

Several well founded considerations led us to install the SIDDHARTA-2 apparatus in place of KLOE-2 one that, as a consequence, must be moved back into its hangar.

Regardless, the IR hosting the SIDDHARTA-2 detector is based on the *CW* Collision Scheme too, it is deeply different from the one used to deliver data to the KLOE-2 experiment. The only components that could be reused were the Permanent Magnet Quadrupoles, PMQs, of the low- β which, however, should be extracted from the inner side of the apparatus requiring considerable time and manpower. The decision to build new PMQs gave us a useful opportunity to speed up the installation procedure and to improve design aspects of the low- β quadrupoles as well.

Low- β Quadrupoles

The low- β insertion of the SIDDHARTA-2 IR requires six magnets: two defocusing quadrupoles, PMQDs, common for the two beams, and four focusing magnets, PMQFs, one for each branch of the IR.

The new PMQs, shown in Fig. 6, have been designed in collaboration with the ESRF magnet group with the intent to improve: good field region, gradient uniformity, aperture, and mechanical assembly. The last aspect has special relevance for the PMQFs which are installed very close to each other, see Fig. 7. Bore radius is one of the main issues in order to provide a proper stay clear aperture for the beams and reduce background on the detector. A larger horizontal aperture is very relevant mainly for the PMQDs, in which colliding beams trajectories passes of axis.

The new PMQs are Halbach type magnets made of SmCo₂:17, some of their more relevant parameters are shown in Table 2 along with the corresponding beam pipe apertures.

PMQDs consist of 2 rings of permanent magnet wedges, as in Fig. 6, the inner blocks are arranged according a fixed elliptical symmetry, while the outermost ones are disposed with circular symmetry and can be moved radially to shim the gradient strength and its inhomogeneities.

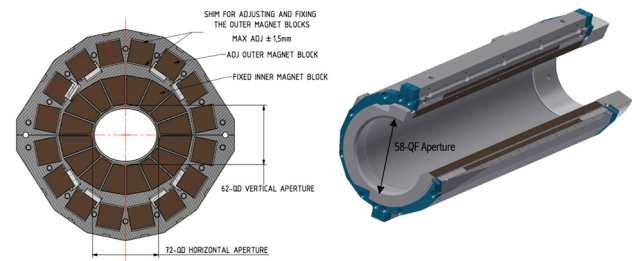


Figure 6: PMQD mechanical cross section (left), and PMQF 3-quarter section (right).

PMQFs are based on 2 concentric cylinders of PM wedges having different lengths, see Fig. 6, also in this configuration the PM blocks of the outer cylinder can be moved radially for shimming purpose.

Table 2: PMQ and Beam Pipe Parameters

	PMQD	PMQF
Beam Pipe Aperture H-V (mm)	57	54
at IP (I row) and at Y (II row) side	69 - 55	
Inner Apert. With Case H-V (mm)	72 - 62	58
Outer Diameter H-V (mm)	238 - 220	95.6
Mech. Length Inner-Outer (mm)	220	168 - 240
Nominal Gradient (T/m)	29.2	12.6
Integrated Gradient (T)	6.7	3.0
Good Field Region (mm)	±20	±20
Integrated Field Quality dB/B	5.00E-4	5.00E-4
Magnet Assembly	2 halves	2 halves

Aluminium casing has been designed relying on a comprehensive analysis of the magnetic forces among the different PM wedges, and paying attention to installation requirements as well. The new PMQD vacuum chamber has a tapered design allowing to match the elliptical quadrupole aperture, on the side of the Y-shape beam pipe, and the IR circular one at the entrance of the common vacuum chamber, as shown in Fig. 7.

IR Vacuum Chamber

The vacuum chamber of the low- β section have been designed in order to fit with the new quadrupole apertures, paying great attention to the impedance budget of the new structure.

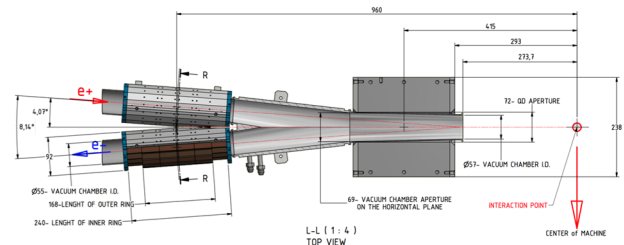


Figure 7: Half IR mechanical assembly, top view.

In a collider composed of two separate rings having a common IR it is unavoidable to create electromagnetic Higher Order Modes (HOM) in the area where the vacuum beam pipes of the two rings merge in the common beam pipe (Y-shape chamber) [19, 20].

The numerical simulations with HFSS [21] have revealed the existence of two HOMs trapped in the Y-chamber of the new SIDDHARTA-2 IR at frequencies of 1.863 MHz and 2.299 MHz respectively. These modes are rather weak to create any dangerous multi-bunch instability that can be always controlled by the powerful feedback systems of DAΦNE. However, despite these are the TE-like modes, there are non-negligible longitudinal fields along the beam trajectory contributing into the longitudinal beam coupling impedance. Since the mode frequencies are rather close to the beam power spectrum lines there is a high probability of power loss enhancement in multi-bunch operations. For example, the first mode frequency is very close to the 5th harmonic of the RF frequency at 1.843 MHz. In the worst scenario of the full coupling of the spectrum line with the mode frequency the released power is estimated to be of the order of 0.5 kW. In order to avoid excessive overheating of the Y-chamber, and a resulting vacuum pressure rise in the vicinity of IR, it has been decided to apply cooling pipes on the top of the chamber. The simulations with ANSYS [22] have confirmed that the chamber temperature is kept under control in that case. Moreover, the temperature variation can also help in shifting the mode frequency with respect to the spectrum line thus providing another safety knob.

Luminosity Measurements

In order to ensure fast absolute luminosity measurement, the IR will be equipped with several independent diagnostic tools.

The main luminosity measurement will rely on the small angle Crystal CALorimeters with Time measurement, CCALT [23], that was part of the KLOE-2 detector, in order to measure the Bhabha scattering events at small angle. The CCALT consists of two identical crystal calorimeters installed in front of each PMQD. This detector has been efficiently used, during the KLOE-2 run, to implement an absolute instantaneous luminosity measurement with an accuracy of the order of $5 \div 10\%$ depending on repetition rate and threshold settings [16].

The CCALT luminosity measurement has been successfully cross-checked with the more accurate one provided by KLOE-2 apparatus. Moreover the diagnostics time resolution has proven to be suitable to implement bunch by bunch luminosity measurement.

The two High Energy Tagger (HET) [24] stations, also inherited from the KLOE-2 apparatus, will be used to detect Bhabha scattering at very low angle. The HET plastic scintillators allow to measure the arrival time and the distance from the nominal trajectory of the scattered particles. The two HET stations can measure the instantaneous luminosity independently using single-arm event rate determination with a good accuracy of the order of 5%. A third diagnostics based on gamma bremsstrahlung proportional counter will be installed as well. This detector, thanks to the very high rates, can be efficiently used as real time tool during machine luminosity optimization. However, it cannot provide a reliable absolute luminosity measurement since it is heavily affected by beam losses due to interaction

with the residual gas, Touschek effect, and low angle scattered particles generated along the IR.

Subsystems Revamping

In view of the SIDDHARTA-2 physics run many other subsystems and machine components are going to be revamped [25].

Mechanical structures supporting and giving access to the IR must be reviewed in order to be compliant with the new experimental apparatus and with the present safety standards. Several vacuum components will be replaced. New sputter ion pumps will substitute for faulty devices and for the NEG ones previously installed in the IR.

A general checkup of more than 500 power supplies has been already completed. Each power supply has been tested in all its components with special attention to the cooling units and to the DCCT calibration.

The capacitor banks of the power supplies powering the two pulsed dipoles, the more sophisticated magnets of the Transfer Lines, have been replaced with new components.

Each capacitor bank is composed by 50 capacitors and the total capacity amount is about 7 mF.

The Power Supplies, PSs, of the correctors (short and long type) both in the positrons and in the electrons rings are going to be substituted with new equipment. The new PSs have accuracy and resolution improved by more than a factor 10 with respect to the old devices. This last aspect is of extreme importance in order to guarantee reproducible and stable beam trajectory during operations.

The two dump kickers, one in each ring, previously installed in the section opposite to the IR are going to be replaced by a straight beam pipe in the e^- ring, and by a new feedback kicker in the e^+ one in order to implement an additional horizontal feedback system. The latter is intended for doubling the total power available for the horizontal feedback in order to keep under control the *e-cloud* induced instability. In fact the *e-cloud* detrimental effects are expected to be more harmful due to the new Al vacuum chambers installed in the IR, and to the dramatic reduction of the properly working ECEs.

CONCLUSION

DAΦNE has just concluded the run for the KLOE-2 experiment achieving unprecedented results in terms of luminosity. This has been possible thanks to an effective integration of the *Crab-Waist* Collision Scheme with the high field detector solenoid.

The *Crab-Waist* Collision Scheme has proven to be a viable approach to increase luminosity in circular colliders even in presence of an experimental apparatus strongly perturbing beam dynamics. Definitely good news for all the new machines and projects around the world that have adopted *Crab-Waist* as their main design concept.

A comprehensive work program has been defined, and is under way to prepare the run for the SIDDHARTA-2 experiment at DAΦNE. Several aspects of the collider and many subsystems have been upgraded in order to grant the highest performances in terms of luminosity and the lowest background contamination on the acquired data.

The run for SIDDHARTA-2 will be the very last physics run of DAΦNE as a collider; thereafter the accelerator complex will most likely be converted to a test facility.

ACKNOWLEDGEMENT

The Author wishes to thank all members of the DAΦNE Operation Team. With their competence and commitment, they have been giving substantial contributions to the activities on DAΦNE, both in terms of KLOE-2 data taking, and SIDDHARTA-2 preparatory phase.

REFERENCES

- [1] G. Vignola *et al.*, "Status report on DAΦNE", *Frascati Phys. Ser.*, Vol. 4, pp. 19-30, Oct. 1996.
- [2] P. Raimondi, D. Shatilov and M. Zobov, "Beam-beam issues for colliding schemes with large Piwinski angle and crabbed waist", *e-Print: physics/0702033*, LNF-07-003-IR, 2007.
- [3] P. Raimondi, D. Shatilov and M. Zobov, "Suppression of beam-beam resonances in crab waist collisions", in *Proc. 11th European Particle Accelerator Conference (EPAC 2008)*, pp. 2620-2622, 2008.
- [4] M. Zobov *et al.*, "Test of crab-waist collisions at DAΦNE Φ-factory", *Phys. Rev. Lett.*, Vol. 104, p. 174801, 2010.
- [5] G. Amelino-Camelia *et al.*, "Physics with the KLOE- 2 experiment at the upgraded DAΦNE", *Eur. Phys. J.*, Vol. C68, pp. 619-681, Mar. 2010.
- [6] C. Milardi *et al.*, "DAΦNE general consolidation and upgrade", in *Proc. 5th International Particle Accelerator Conference (IPAC 2014)*, pp. 3760-3762, 2014.
- [7] C. Milardi *et al.*, "A Review of DAΦNE Performances during the KLOE-2 Run", in *Proc. 9th International Particle Accelerator Conference (IPAC 2018)*, pp. 1883-1885, 2018.
- [8] SIDDHARTA-2 Collaboration, *Technical Report*, May 2016.
- [9] D. Shatilov, "Beam-beam simulations at large amplitudes and lifetime determination", *Part. Accel.*, Vol. 52, pp. 65-93, 1996.
- [10] M. Zobov *et al.*, "Simulation of crab waist collisions in DAΦNE with KLOE-2 interaction region", *IEEE Trans. Nucl. Sci.*, Vol. 63, no. 2, pp. 818-822, 2016.
- [11] D. Alesini *et al.*, "DAΦNE operation with electron cloud clearing electrodes", *Phys. Rev. Lett.*, Vol. 110, p. 124801, 2013.
- [12] A. Drago *et al.*, "Longitudinal quadrupole instability and control in the Frascati DAΦNE electron ring", *Phys. Rev. ST Accel. Beams*, Vol. 6, p. 052801, 2003.
- [13] C. Milardi *et al.*, "DAΦNE developments for the KLOE-2 experimental run", in *Proc. 1st Int. Particle Accelerator Conf. (IPAC'10)*, pp. 1527-1529.
- [14] C. Milardi *et al.*, "DAΦNE tune-up for the KLOE-2 experiment", in *Proc. 2nd Int. Particle Accelerator Conf. (IPAC'11)*, pp. 3687-3689.
- [15] S. Bettoni *et al.*, "Multipoles Minimization in the DAFNE Wigglers", in *Proc. 1st Int. Particle Accelerator Conf. (IPAC'10)*, pp. 4665-4667.
- [16] A. De Santis *et al.*, "DAΦNE luminosity monitor", in *Proc. 9th International Particle Accelerator Conference (IPAC 2018)*, pp. 338-340, 2018.
- [17] C. Milardi, M. Preger, P. Raimondi and F. Sgamma, "High luminosity interaction region design for collisions inside high field detector solenoid", *JINST*, Vol. 7, p.T03002, 2012.
- [18] C. Milardi *et al.*, "Experience with DAΦNE upgrade including crab waist", in *Proc. 23rd Particle Accelerator Conf. (PAC'09)*, pp. 80-84.
- [19] D. Brandt *et al.*, "On trapped modes in the LHC recombination chambers: numerical and experimental results", *Nucl. Instrum. Meth.*, Vol. A517, pp. 19-27, 2004.
- [20] A. Novokhatskii *et al.*, "Unavoidable trapped mode in the interaction region of colliding beams", *Phys. Rev. Accel. Beams*, Vol. 20, no. 11, p. 111005, 2017.
- [21] HFSS, "ANSYS, Inc." Ver 19.0 (2018).
- [22] Workbench, "ANSYS, Inc" Ver. 19.0 (2018).
- [23] F. Happacher, M. Martini, S. Miscetti and I. Sarra, "Tile and crystal calorimeter for KLOE-2 experiment", *Nucl. Phys. Proc. Suppl.*, 197:215–218, 2009.
- [24] D Babusci *et al.*, "The KLOE-2 High Energy Tagger detector", *NIM A718*, pp. 577, 2013.
- [25] C. Milardi *et al.*, "Preparation activity for the SIDDHARTA-2 run at DAΦNE", in *Proc. 9th International Particle Accelerator Conference (IPAC 2018)*, pp. 334-337, 2018.

STATUS OF CIRCULAR ELECTRON-POSITRON COLLIDER

C. H. Yu^{†, 1}, Y. Zhang¹, Y. W. Wang, D. Wang, N. Wang, S. Bai, X. H. Cui, C. Meng, Y. S. Zhu, H. P. Geng, D. H. Ji, Y. Y. Wei, Y. D. Liu, J. Y. Zhai, D. J. Gong, H. J. Zheng, Q. Qin, J. Gao, T. J. Bian
Key Laboratory of Particle Acceleration Physics and Technology,
Institute of High Energy Physics, Chinese Academy of Sciences, Beijing 100049, China
¹also at University of Chinese Academy of Sciences, Beijing 100049, China

Abstract

Circular electron-positron collider (CEPC) is a dedicated project proposed by China to research the Higgs boson. The collider ring provides e^+e^- collision at two interaction points (IP). The luminosity for the Higgs mode at the beam energy of 120GeV is $3\times10^{34}\text{ cm}^{-2}\text{s}^{-1}$ at each IP while the synchrotron radiation (SR) power per beam is 30MW. Furthermore, CEPC is compatible with W and Z experiments, for which the beam energies are 80 GeV and 45.5 GeV respectively. The luminosity at the Z mode is higher than $1.7\times10^{35}\text{ cm}^{-2}\text{s}^{-1}$ per IP. Top-up operation is available during the data taking of high energy physics. The status of CEPC will be introduced in detail in this paper.

MACHINE LAYOUT

CEPC [1] which aims at researching Higgs boson is a double ring scheme optimized at the beam energy of 120 GeV. Super proton-proton collider (SPPC) will be the next project after the operation of CEPC in the future. The circumference of CEPC is 100km while matching the geometry of SPPC as much as possible. The circumference is determined by the requirements of SPPC so that the SPPC bending magnets can be designed and manufactured. The arc regions of the SPPC collider ring, the CEPC collider ring and the CEPC booster ring are in the same tunnel. The cross section of the tunnel in the arc region is shown in Fig. 1.

The interaction region of SPPC is located in the same long straight sections where the CEPC RF cavities are placed. The collimation region of SPPC with length of about 4km is located in the interaction region of CEPC. Due to the special collision orbit at the IP and the very large size of detector, bypass geometry or independent tunnel for SPPC and CEPC in the two regions is needed. The layout design of CEPC in the RF region and interaction region follows the space constraints. However, it still will be potential space conflict in the two regions during the geometry optimization of SPPC in the future. Since the operation of CEPC will be much earlier than SPPC. So SPPC and CEPC are arranged in the outside and inside respectively. SPPC team can optimize SPPC geometry with relatively lower magnetic field of bending magnet especially in the bypass region. The design of CEPC can keep fixed during the modification of SPPC. The booster ring of CEPC shown in Fig. 1 is located above collider ring with the distance of 2.4 m. The distance is sufficient to avoid the magnetic interference between the collider ring and the booster ring.

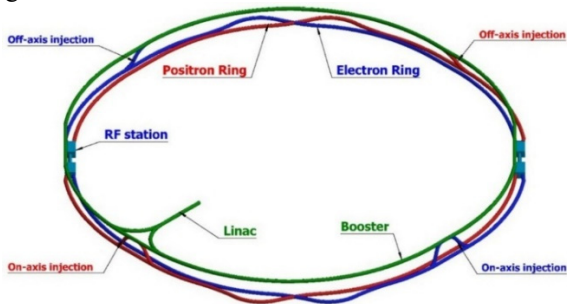


Figure 2: The layout of CEPC

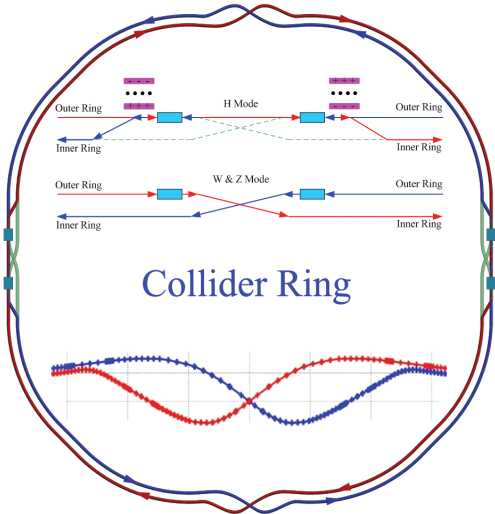


Figure 3: The layout of CEPC collider ring.

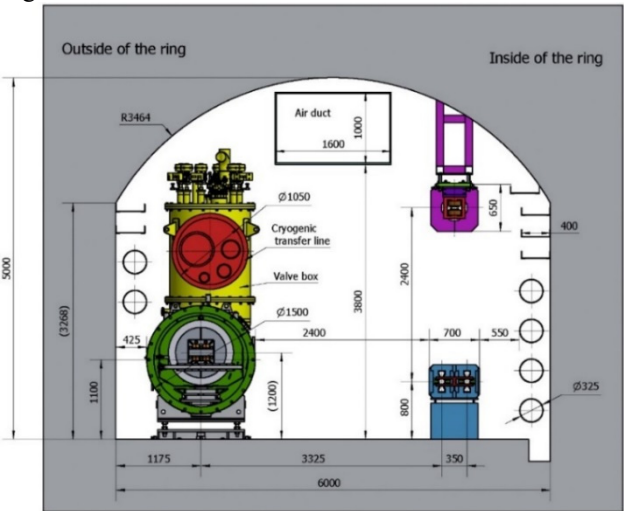


Figure 1: The cross section of the tunnel in the arc region.

[†] yuch@ihep.ac.cn

The layout of CEPC including Linac, transfer lines, booster ring and collider ring is shown in Fig. 2. The Linac is located at ground level with length of 1200 m. The Booster is underground at a depth of approximately 100 m. The Linac and Booster are connected by two transfer lines for e^+ and e^- respectively. These lines have a slope of 1:10. There are 8 straight sections in the collider ring. They are 2 interaction regions, 2 RF regions and 4 injection regions. Among them, two off-axis injection regions are the function regions for the operation of Higgs, W and Z. The two on-axis injection regions are used only during operation in the Higgs mode.

Figure 3 shows the layout of CEPC collider ring. The design of collider ring is optimized at Higgs mode with 650 MHz two cell RF cavities. There are two dedicated surveys in the RF region for the Higgs, W and Z modes. During the operation of Higgs mode all the RF cavities are shared by both e^+ and e^- beams using combining magnets [2][3] near the RF cavities. Each beam is filled in half ring so that all e^+ and e^- bunches can pass the RF cavities in turn. This filling scheme in Higgs mode with half the ring won't reduce the luminosity because the required bunch number is relatively small and the bunch spacing is quite large. For the W and Z modes the surveys of e^+ and e^- rings in the RF region are designed independently by turning off the combined magnets so that all bunches can be filled along the whole e^+ and e^- rings. The beam current during the operation of W and Z modes is made as much as possible to improve the luminosity. W and Z modes use the same RF cavities which are used in Higgs mode to save cost. Half number of the cavities are distributed in e^+ and e^- rings respectively for the W and Z modes. The machine parameters for the Z mode do not increase the budget which is based on operation as a Higgs factory.

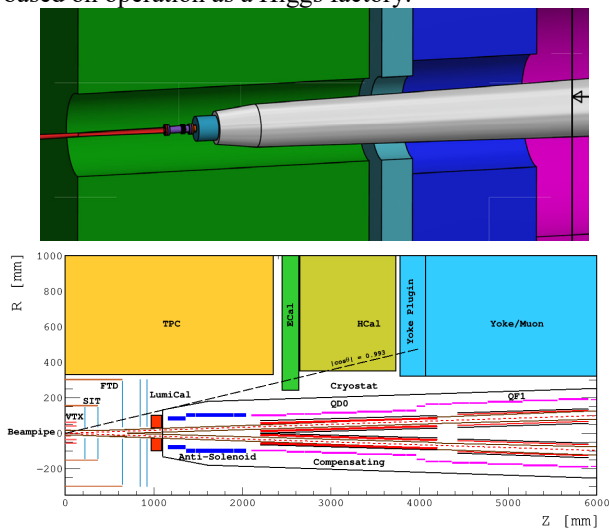


Figure 4: The central part of the interaction region.

The central part of the interaction region is shown in Fig. 4. There is a Be pipe of length 14 cm and inner diameter 28 mm. The final focusing magnet is 2.2 m away from the IP. The horizontal crossing angle at the IP is 33 mrad to allow enough space for the superconducting quadrupole

coils in a two-in-one type with space for a room temperature vacuum chamber. The accelerator components inside the detector are distributed within a conical space with an opening angle of 13.6° . The luminosity calorimeter is located 0.95~1.11 m away from the IP and has inner radius 28.5mm and outer radius 100 mm.

Twin-aperture dipoles and quadrupoles [4] are in the arc region. The distance between the two beams is 0.35 m. The magnets in the other regions and all the sextupoles are independently powered for flexibility of the optics.

MAIN PARAMETERS OF COLLIDER

The beam stay clear region is defined as $\pm (18 \sigma_x + 3 \text{ mm})$ and $\pm (22 \sigma_y + 3 \text{ mm})$ in the horizontal and vertical directions respectively. Coupling is 1%. The synchrotron radiation (SR) power per beam is limited to 30 MW. The high-energy physics goals of CEPC are to provide e^+e^- collisions at a beam energy of 120 GeV and attain a luminosity of $3 \times 10^{34} \text{ cm}^{-2}\text{s}^{-1}$ at each IP for operation in the Higgs mode. Furthermore, the CEPC should be able to run at 80 GeV and 45.5 GeV for experiments running in the W and Z modes respectively. The luminosity in Z mode is $1.7 \times 10^{35} \text{ cm}^{-2}\text{s}^{-1}$ per IP, and in W mode $1 \times 10^{35} \text{ cm}^{-2}\text{s}^{-1}$ per IP.

Main parameters of CEPC collider ring is shown in Table 1. The detector solenoid is 3 T with a length of 7.6 m as the baseline design. There are 22 anti-solenoid sections with different inner diameters within the final doublet region at each side of the IP to compensate for the effects on the beam of the strong detector solenoid [5]. For the Higgs mode, with the constraint of 30 MW, the design luminosity per IP is $3 \times 10^{34} \text{ cm}^{-2}\text{s}^{-1}$ with 242 bunches and beam current of 17.4 mA. The horizontal and vertical β functions at the IP are 0.36 m and 1.5 mm respectively. Operation is in top-up mode. The energy acceptance in Higgs mode is 1.35%. The beam lifetime with the beam-beam effect is greater than 26 minutes.

The Collider lattice in W mode is the same as in the Higgs mode. The design luminosity per IP is $1 \times 10^{35} \text{ cm}^{-2}\text{s}^{-1}$ with 1524 bunches and beam current of 87.9 mA, again with the constraint of 30 MW beam power.

For the Z mode, the horizontal and vertical β functions at the IP are 0.2 m and 1.5 mm respectively to avoid the strong coherent beam-beam instability [6] with the detector solenoid at 3T. The design luminosity per IP is $1.7 \times 10^{35} \text{ cm}^{-2}\text{s}^{-1}$ with 12000 bunches and beam current of 461 mA. During operation in the Z mode the synchrotron radiation power of each beam can only reach 16.5 MW due to the limitation of HOM heating in the RF cavities and the electron cloud instability in the positron ring. The coupling in Z mode is 2.2% which is much larger than expected because the strong fringe field of solenoids leads to a serious coupling growth of both beams. If the detector solenoid could be 2 T, the coupling can be controlled and the vertical β function at the IP can be reduced from 1.5 mm to 1.0mm so that the luminosity in Z mode per IP can reach $3.2 \times 10^{35} \text{ cm}^{-2}\text{s}^{-1}$.

Table 1: Main Parameters of CEPC Collider Ring

	Higgs	W	Z (3T)	Z (2T)
Number of IPs	2			
Beam energy (GeV)	120	80	45.5	
Circumference (km)	100			
Synchrotron radiation loss/turn (GeV)	1.73	0.34	0.036	
Crossing angle at IP (mrad)	16.5×2			
Piwinski angle	3.48	7.0	23.8	
Particles /bunch N_e (10^{10})	15.0	12.0	8.0	
Bunch number	242	1524	12000 (10% gap)	
Bunch spacing (ns)	680	210	25	
Beam current (mA)	17.4	87.9	461.0	
Synch. radiation power (MW)	30	30	16.5	
Bending radius (km)	10.7			
Momentum compaction (10^{-5})	1.11			
β function at IP β_x^*/β_y^* (m)	0.36/0.0015	0.36/0.0015	0.2/0.0015	0.2/0.001
Emittance x/y (nm)	1.21/0.0024	0.54/0.0016	0.18/0.004	0.18/0.0016
Beam size at IP σ_x/σ_y (μm)	20.9/0.06	13.9/0.049	6.0/0.078	6.0/0.04
Beam-beam parameters ξ_x/ξ_y	0.018/0.109	0.013/0.123	0.004/0.06	0.004/0.079
RF voltage V_{RF} (GV)	2.17	0.47	0.10	
RF frequency f_{RF} (MHz)	650			
Harmonic number	216816			
Natural bunch length σ_z (mm)	2.72	2.98	2.42	
Bunch length σ_z (mm)	4.4	5.9	8.5	
Damping time $\tau_x/\tau_y/\tau_E$ (ms)	46.5/46.5/23.5	156.4/156.4/74.5	849.5/849.5/425.0	
Natural Chromaticity	-468/-1161	-468/-1161	-491/-1161	-513/-1594
Betatron tune ν_x/ν_y	363.10 / 365.22			
Synchrotron tune ν_s	0.065	0.040	0.028	
HOM power/cavity (2 cell) (kw)	0.46	0.75	1.94	
Natural energy spread (%)	0.100	0.066	0.038	
Energy spread (%)	0.134	0.098	0.080	
Energy acceptance requirement (%)	1.35	0.90	0.49	
Energy acceptance by RF (%)	2.06	1.47	1.70	
Photon number due to beamstrahlung	0.082	0.050	0.023	
Beamstrahlung /quantum lifetime (min)	80/80	>400		
Lifetime (hour)	0.43	1.4	4.6	2.5
F (hour glass)	0.89	0.94	0.99	
Luminosity/IP ($10^{34} \text{ cm}^{-2}\text{s}^{-1}$)	3	10	17	32

THE DESIGN OF INJECTION

The beam stay clear region for the Booster is defined as $\pm (4 \sigma + 5 \text{ mm})$ in both horizontal and vertical directions with a round beam and emittance of 120 nm. This provides sufficient beam lifetime and transfer efficiency during in-

jection and energy ramping. The diameter of the inner aperture of the vacuum chamber is chosen to be 55 mm from considerations of impedance.

The Booster uses 1.3 GHz 9-cell superconducting RF cavities. At the injection energy of 10 GeV from the Linac, the threshold of the single bunch current is 25.7 μA and the

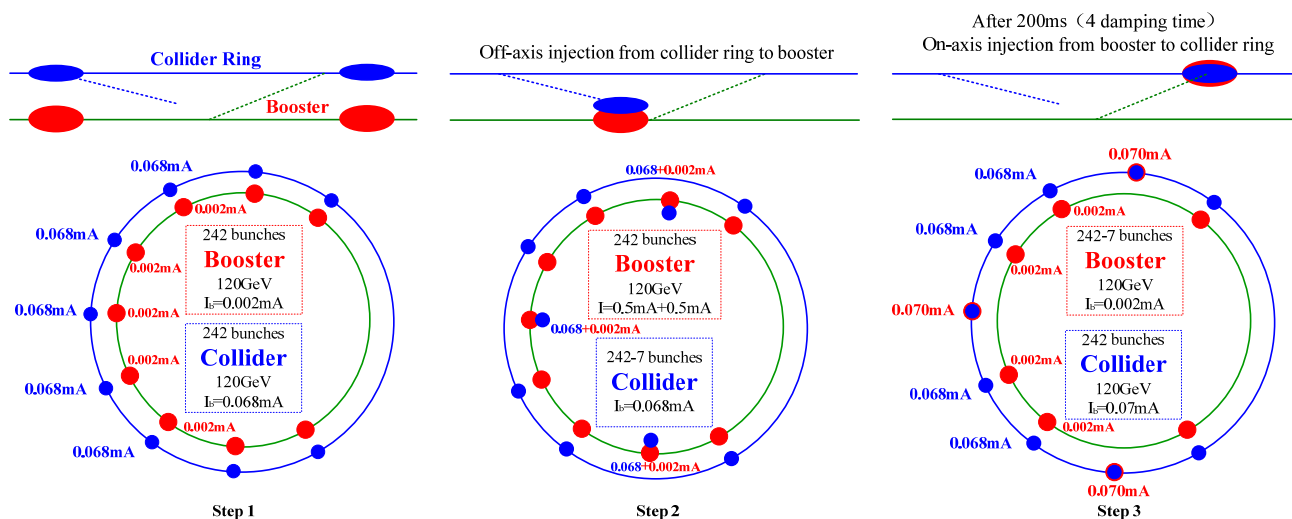


Figure 5: On-axis injection scheme only for Higgs operation.

threshold of beam current limited by RF power is 1.0 mA. The on-axis injection scheme is shown in Fig. 5. The Linac bunches are injected into the Booster by horizontal on-axis injection at an energy of 10 GeV. At the extraction energies when operating in W and Z modes the circulating bunches of the Booster will be injected into the Collider by horizontal off-axis injection. However, in order to keep a sufficient margin in dynamic aperture, especially with machine errors included, at the extraction energy during Higgs mode operation a special on-axis injection scheme is used, which can significantly relax the requirements on dynamic aperture compared with conventional off-axis injection schemes. First, several circulating bunches from the Collider are extracted to the Booster while the energy is 120 GeV and the beam current limited to 1 mA. The Booster circulating bunches are then merged with the injected bunches from the Collider after 4 damping times. Then, the merged bunches in the Booster are injected back into the Collider by vertical on-axis injection. This procedure will be repeated several times so that all the circulating bunches in the Booster can be accumulated into the Collider. The simulation result indicates that the collision of the stored bunches and the injected bunches is stable. The beam loading effect in the Booster RF system with the same bunch density as the Collider during the on-axis injection procedure in Higgs mode is weak. The maximum cavity voltage drop is 0.48% and the maximum phase shift is 0.63 degree. The peak HOM power per RF cavity is 62 W which is acceptable for the Booster RF system. The dynamic aperture in the Booster is sufficient for vertical off-axis injection from the Collider. The injection duration of both beams during top-up operation are 35.4 s, 45.8 s and 275.2 s for Higgs, W mode and Z mode respectively. The injection intervals with current decay of 3% are 47 s, 153 s and 504 s for Higgs, W mode and Z mode based on beam lifetime. The injection duration from an empty ring are 0.17 h, 0.25 h and 2.2 h for Higgs, W mode and Z mode respectively.

The requirements for sufficient injection efficiency are electron and positron bunch charge of 1.5 nC and repetition rate of 100 Hz. The total beam transfer efficiency from

transfer line to the injection point of the Collider is greater than 90% with beam emittance of 120 nm and energy spread of 0.2% at the exit of the Linac. The transfer efficiency can be made much higher with a damping ring of energy 1.1 GeV while the beam emittance of Linac can be reduced to 40 nm. The Linac beam energy is 10 GeV so that magnetic field of Booster dipoles could be 30 Gauss at the injection energy. This is the minimum at which a good quality magnetic field can be obtained.

CONCLUSION

The status of CEPC is introduced in detail in this paper. The design of accelerator physics can meet the luminosity requirements at Higgs, W and Z. The finalization of the beam parameters and the specifications of special magnets have been finished. The hardware devices are all reasonable. The optimization to reduce machine cost and improve the beam performance is always under studying.

REFERENCES

- [1] The CEPC Study Group, "CEPC conceptual design report", Vol. I-Accelerator, IHEP-CEPC-DR-2018-01, August 2018.
- [2] M. Benedikt, K. Oide, F. Zimmermann, *et al.*, Status and Challenges for FCC-ee, e-Print: arXiv:1508.03363, a combination of two articles published in the *ICFA Beam Dynamics Newsletter*, September 2015.
- [3] The BEPCII Study Group, "Design Report of BEPCII", Accelerator Part, 2003.
- [4] A. Milanese, "Efficient Twin Aperture Magnets for the Future Circular e^+e^- Collider", *Phys. Rev. Accel. Beams* 19, 112401 (2016).
- [5] C. H. Yu, Y. Z. Wu, Z. S. Yin, *et al.*, Interaction region design and realization for the Beijing Electron Positron Collider, *Nuclear Instruments and Methods in Physics Research A*, Vol. 608 (2009) 234–237.
- [6] K. Ohmi, N. Kuroo, K. Oide, *et al.*, Coherent Beam-Beam instability in collisions with a large crossing angle, *Physical review letters*, vol. 119, 134801 (2017).

ROUND COLLIDING BEAMS AT VEPP-2000 WITH EXTREME TUNESHIFTS

D. Shwartz[†], V. Anashin, O. Belikov, D. Berkaev, K. Gorchakov, A. Kasaev, A. Kirpotin, I. Koop¹, A. Krasnov, G. Kurkin, A. Lysenko, S. Motygin, E. Perevedentsev¹, V. Prosvetov, D. Rabusov, Yu. Rogovsky¹, A. Semenov, A. Senchenko¹, D. Shatilov, P. Shatunov, Yu. Shatunov¹, O. Shubina, M. Timoshenko, I. Zemlyansky, Yu. Zharinov

Budker Institute of Nuclear Physics, Novosibirsk, 630090, Russia
¹also at Novosibirsk State University, Novosibirsk, 630090, Russia

Abstract

VEPP-2000 is the only electron-positron collider operating with round beams that results in enhancement of beam-beam limit. VEPP-2000 with SND and CMD-3 detectors carried out two successful data-taking runs after new BINP injection complex was commissioned. The 2016/2017 run was dedicated to high energy range (640-1000 MeV per beam) while the 2017/2018 run was focused at 275-600 MeV/beam energies. With sufficient positron production rate and upgraded full-energy booster the collider luminosity was limited by beam-beam effects, namely flip-flop effect. Thorough machine tuning together with new ideas introduced to suppress flip-flop allowed to achieve high beam-beam tunes and bunch-by-bunch luminosity values at specific beam energies. The achieved luminosity increased 2-5 times in a whole energy range in comparison to phase-1 operation (2010-2013).

ROUND COLLIDING BEAMS

The VEPP-2000 collider [1-3] exploits the round beam concept (RBC) [4] firstly proposed for the Novosibirsk Phi-factory project [5]. This approach, in addition to the straightforward geometrical gain factor in luminosity should yield the beam-beam limit enhancement. An axial symmetry of the disruptive nonlinear counter-beam force together with the X - Y symmetry of the transfer matrix between the two IPs provide an additional integral of motion, namely, the longitudinal component of angular momentum $M_z = x'y - xy'$. Although the particles' dynamics remain strongly nonlinear due to beam-beam interaction, it becomes effectively one-dimensional. The reduction of degrees of freedom thins out the resonance grid and suppress the diffusion rate resulting finally in a beam-beam limit enhancement [6].

Thus, there are several demands upon the storage ring lattice suitable for the RBC:

1. Head-on collisions (zero crossing angle).
2. Small and equal β functions at IP ($\beta_x^* = \beta_y^*$).
3. Equal beam emittances ($\varepsilon_x = \varepsilon_y$).
4. Equal fractional parts of betatron tunes ($\nu_x = \nu_y$).

The first three requirements provide the axial symmetry of collisions while requirements (2) and (4) are needed for X - Y symmetry preservation between the IPs.

VEPP-2000 OVERVIEW

VEPP-2000 is a small 24 m perimeter single-ring collider operating in one-by-one bunch regime in the energy range below 1 GeV per beam. Its layout is presented in Fig. 1-2. Collider itself hosts two particle detectors [7, 8], Spherical Neutral Detector (SND) and Cryogenic Magnetic Detector (CMD-3), placed into dispersion-free low-beta straights. The final focusing (FF) is realized using superconducting 13 T solenoids. The main design collider parameters are listed in Table 1.

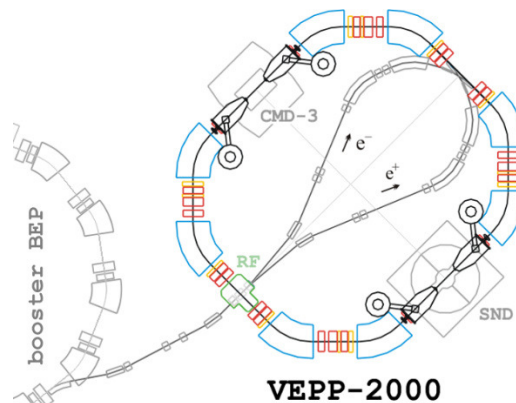


Figure 1: VEPP-2000 storage ring layout.

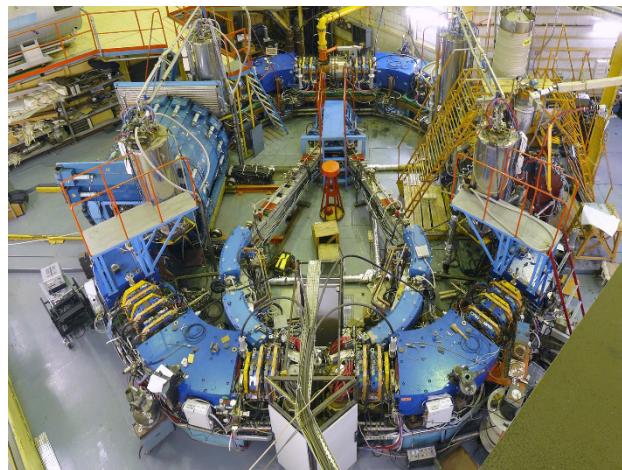


Figure 2: VEPP-2000 collider photo.

[†] d.b.shwartz@inp.nsk.su

Table 1: VEPP-2000 Design Parameters (at $E = 1$ GeV)

Parameter	Value
Circumference, C	24.39 m
Energy range, E	150–1000 MeV
Number of bunches	1×1
Number of particles per bunch, N	1×10^{11}
Betatron functions at IP, $\beta_{x,y}^*$	8.5 cm
Betatron tunes, $\nu_{x,y}$	4.1, 2.1
Beam emittance, $\epsilon_{x,y}$	1.4×10^{-7} m rad
Beam–beam parameters, $\xi_{x,z}$	0.1
Luminosity, L	1×10^{32} cm $^{-2}$ s $^{-1}$

Injection Chain Upgrade

During commissioning and first operation phase in 2010-2013 VEPP-2000 used old positron production and injection chain that restricted available positron beam intensity and limited the luminosity at energy range above 500 MeV. Since 2016 VEPP-2000 is linked to the new BINP injection complex (IC) [9, 10] via long transfer channel. In addition, the booster BEP was upgraded in order to increase top energy up to 1 GeV and perform top-up injection [11].

Circular Modes

The RBC at VEPP-2000 was implemented by placing two pairs of superconducting focusing solenoids into two interaction regions (IR) symmetrically with respect to collision points. There are several combinations of solenoid polarities that satisfy the round beams' requirements: “normal round” ($++ \text{ ---}$), “Möbius” ($++ \text{ +-}$) and “double Möbius” ($++ \text{ ++}$) options rotate the betatron oscillation plane by $\pm 90^\circ$ and give alternating horizontal orientation of the normal betatron modes outside the solenoid insertions.

Two “flat” combinations ($+- \text{ +-}$ or $+- \text{ +-}$) also satisfy the RBC approach if the betatron tunes lie on the coupling resonance $\nu_x - \nu_y = 2$ to provide equal emittances via residual X-Y coupling.

Unfortunately, options with mode rotations suffer from serious limitation of the dynamic aperture (DA). Thus hereafter we will suppose conventional “flat” mode ($+- \text{ +-}$) with equal emittance due to tunes chosen at the main coupling resonance.

Short Solenoids

Each of four solenoid knobs in fact consists of several coils [12]. The small very forward coil is used to compensate the longitudinal field of CMD-3 detector. The main coil is split in longitudinal direction into two parts powered in series with middle point brought out to room-temperature commutation deck for quench control. At the beam energy range below 600 MeV it is possible to use only forward parts of main coils that helps effectively to move final focusing closer to IP.

All the solenoids configuration changes (“flat” to “möbius”, “long” to “short”) unfortunately results in strong closed orbit distortion and needs solenoids beam-based re-alignment.

Machine Tuning

VEPP-2000 operates in a wide energy range with strong saturation of magnetic elements at the top energy. In contrast, at low energies the fixed 1.3 T longitudinal field of CMD-3 detector significantly disturbs the focusing. Thus while energy scanning to achieve high machine performance of great importance is the machine tuning at each energy level. The lattice functions correction including X-Y coupling is made at VEPP-2000 using Orbit Response Matrix (ORM) analysis [13].

The ORM is used also to determine and correct closed orbit at quadrupoles by varying their strength, thus using them as additional BPMs. The similar technique is used for final beam-based alignment of solenoids.

Very important it turned out to minimize the dipole correctors' currents, done with help of ORM as well. The reason is poor quality of the steering coils being embedded in quadrupoles due to lack of space.

FLIP-FLOP EFFECT

The final beam-beam limit at VEPP-2000 corresponds to the onset of a flip-flop effect [14]: the self-consistent situation when one of the beam size is blown-up while another beam size remains almost unperturbed. The simple linear model of flip-flop was discussed earlier [15], with a very high threshold intensity. Observed in VEPP-2000 behavior is most likely caused by an interplay of beam-beam interaction and nonlinear lattice resonances.

In Fig. 3 images from the online control TV camera are presented for the cases of regular beams (a), blown-up electron beam (b) or positron beam (c). The corresponding coherent oscillations spectra are shown on the right. One can see in the spectra of a slightly kicked bunch that the shifted tune (π -mode) sticks to the 1/5 resonance in the case of a flip-flop.

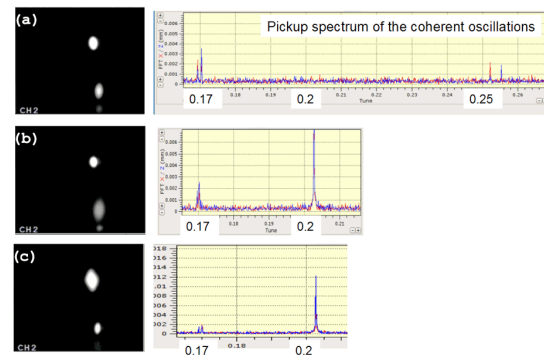


Figure 3: Coherent beam-beam oscillations spectra.

The flip-flop threshold is sensitive to several tuning knobs, in particularly to X-Y coupling and beta-functions misbalance at IP. In addition, the influence of bunch length on the threshold was observed.

BUNCH LENGTHENING

While studying the dependence of beam-beam effects on bunch length at relatively low energy of 392.5 MeV it was found that the RF voltage decrease from 30 kV to 17 kV gives a significant benefit in beams intensity and luminosity threshold.

This enhancement with lower voltage comes from the bunch lengthening. In our particular case, this lengthening is the result of several effects. In addition to regular growth of radiative bunch length with voltage two collective effects take place: potential well distortion and microwave instability. The latter one is observed at low energies with a low RF voltage above a certain bunch intensity [16, 17]. In Fig. 4 the measured by dissector bunch length dependence on beam current is presented for two levels of RF voltage. In Fig. 5 the extracted from transverse horizontal beam size measurements energy spread as a function of intensity is shown. Red points correspond to microwave instability above the threshold.

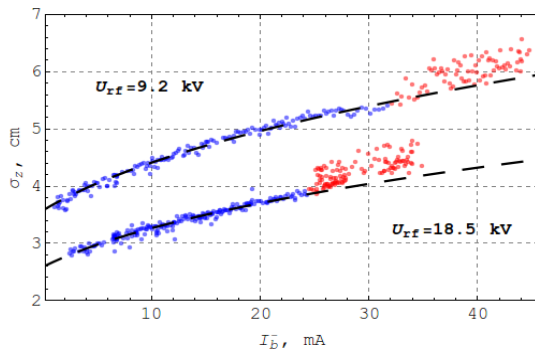


Figure 4: Bunch length as a function of beam current @ E = 480 MeV.

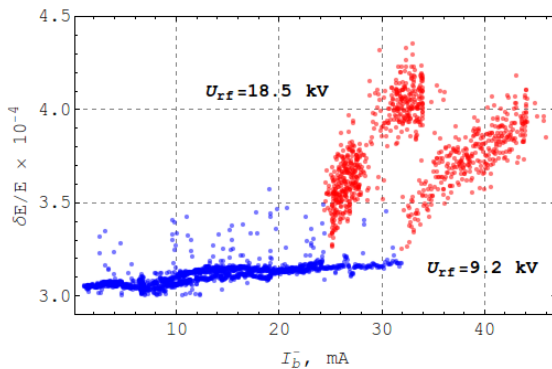


Figure 5: Beam energy spread as a function of beam current @ E = 480 MeV.

The analysis of logged data was done at the energy of 392.5 MeV where enough data was stored for short (a) and long (b) bunch cases. Only "strong-strong" data was selected, i.e. the beam currents difference does not exceed 10%. In Fig. 6 the measured vertical sizes of electron (σ_{4MILy}) and positron (σ_{1MIRy}) beams as a function of beam currents geometric average are shown.

One can see that in both cases the flip-flop develops (unequal positron and electron beam sizes) for beams intensity higher than 15 mA that corresponds to $\xi_{nom} \sim 0.1$. But the

longer bunch tends to mitigate this effect for higher intensities.

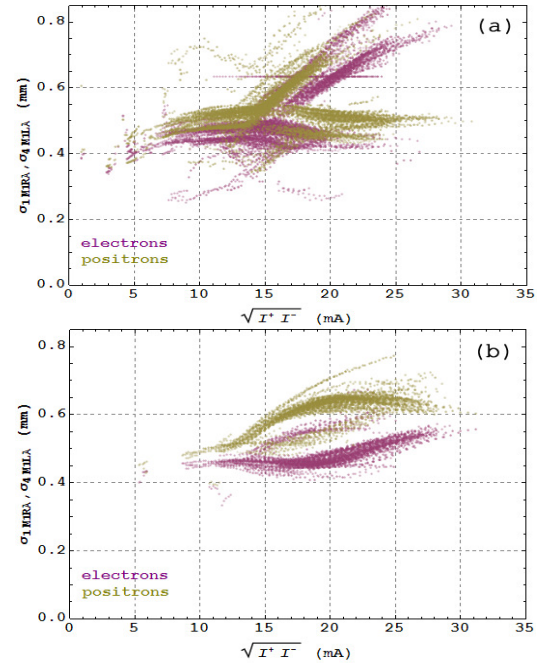


Figure 6: Beam sizes vs. beam current.

BEAM SHAKING

While taking data at low energy range where the radiative emittance is small but significant beta-squeeze is not allowed due to the DA shrinking thus leaving mechanical aperture not fully used the natural desire appeared to increase the emittance. It allows to increase the beam current with fixed particles density, i.e. with fixed at the threshold beam-beam parameter, and to increase luminosity linearly to beam intensity.

Due to very tight components arrangement there is no room to install the wiggler for emittance excitation as it was done at VEPP-2M [18]. The idea was proposed to kick the beam weakly (in comparison to beam size) and frequently (in comparison to damping time). In the presence of strong nonlinear forces of colliding beam after the single kick the excited coherent oscillation decoheres very quickly thus increasing effective beam emittance. This method was probably firstly proposed and tested in 1960-s at VEP-1 collider [19].

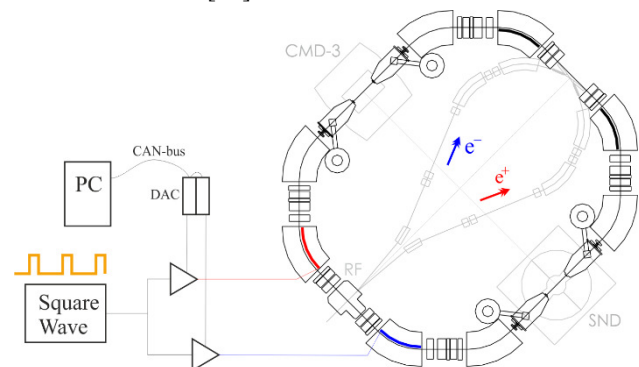


Figure 7: The scheme of beam shaking.

During complex upgrade in order to obtain injection at top energy two additional kicker plates were installed inside dipoles opposite to injection region (see Fig. 7). At low energy the plates are not in use. The square wave generator was used to produce pulses of ~ 300 ns duration. Separated and amplified independently in two channels by software controlled amplifiers pulses are applied to the plates in a running wave manner to affect only on one beam per channel. In fact, in routine operation inevitably both beams are affected via beam-beam interaction.

The typical pulses parameters are the following: pulse duration ~ 300 ns (3-4 turns), repetition rate $(50 \mu\text{s})^{-1}$, pulse amplitude 50-100 V (depends on beam energy).

The example of beam behavior observed by pickup at 360 MeV with shaker switched on is presented in Fig. 8. Here the opposite beam is absent, kicks excite horizontal oscillations (red). One can see the fast swap to vertical oscillations (blue) due to operating at coupling resonance and relatively fast decoherence due to machine nonlinearities.

The spectrum becomes line spectrum due to presence of several kicks periodically exciting oscillations during the period of Fourier analysis.

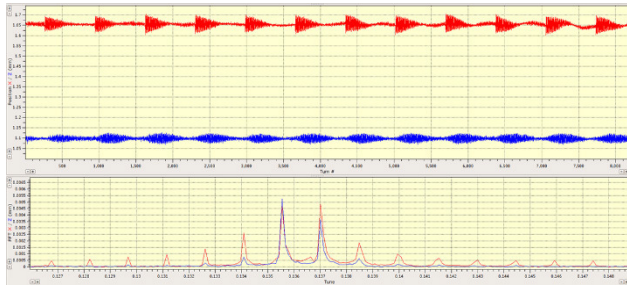


Figure 8: The signal of the single beam shaking at pickup and its Fourier spectrum.

Next Fig. 9 shows the pickup signal fragment of 274 MeV beam being shaken in the collision regime. The single kick excites oscillation with $\sim 30 \mu\text{m}$ amplitude which decoheres during ~ 50 turns. At this energy the beam size is equal to $250 \mu\text{m}$ while the damping time 130 ms corresponds to 1.6×10^6 turns.

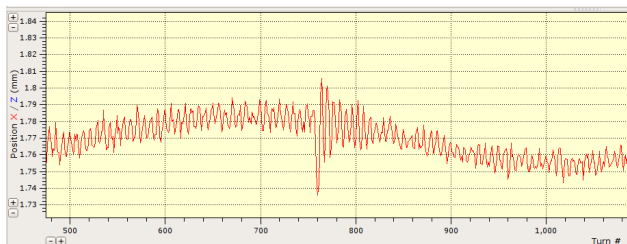


Figure 9: The signal of the single beam shaking at pickup and its Fourier spectrum. The slow oscillation corresponds to synchrotron motion.

The beam shaking experimentally results in beams emittance growth. This growth depends on the controllable shaker parameters (pulse amplitude, pulse duration, repetition rate). The properly increased emittance prevents the flip-flop development during injection cycle: the "strong" beam can't shrink to unperturbed size when "weak" beam

oscillates with large amplitudes. In addition the beam lifetime is improved due to Touschek scattering is suppressed with increased emittance.

LUMINOSITY AND BEAM-BEAM PARAMETER

As a result of beam shaking technique implementation the beams intensities and luminosity at low energy range increased significantly. In Fig. 10 the luminosity is presented achieved in 2013 and in 2018 at the same given energy of 391-391 MeV.

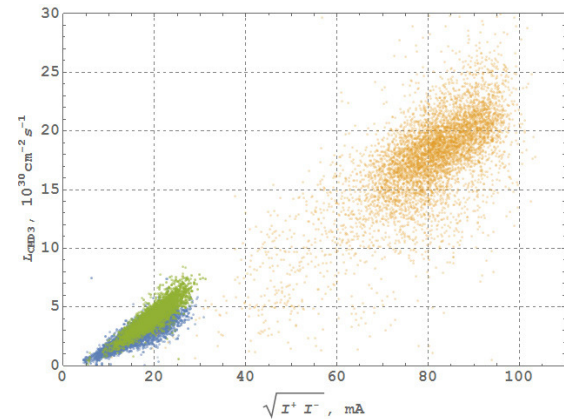


Figure 10: The CMD-3 recorded luminosity as a function of beam currents. Blue and green dots correspond to machine performance in 2013 with short and long bunch correspondingly. Yellow dots corresponds to 2018.

The luminosity increased linearly with the current growth in spite of the naïve expectation of quadratic dependence from the expression for round beam:

$$L = \frac{N^+ N^-}{4\pi\sigma^{*2}} f_0, \quad (1)$$

that is an evidence of beam size growth driven by beam-beam interaction.

For the measured luminosity and beams intensities we can extract from (1) the real beam size which indeed shows the linear growth with intensity (see Fig. 11).

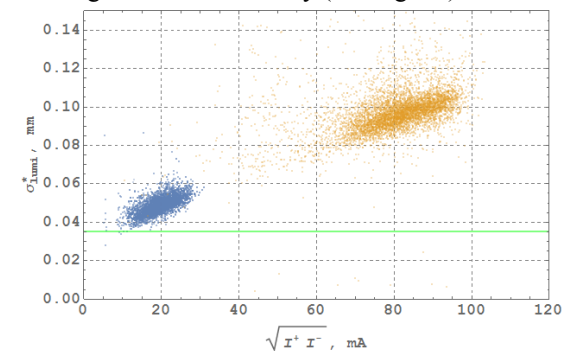


Figure 11: Beam size at IP extracted from CMD-3 luminosity. Blue and yellow dots corresponds to 2013 and 2018 data. Green line show the design beam size value.

With beam size extracted from luminosity measurements we can define the "achieved" beam-beam parameter as:

$$\xi_{\text{lumi}} = \frac{N^- r_e \beta_{\text{nom}}^*}{4\pi\gamma\sigma_{\text{lumi}}^*}, \quad (2)$$

where the beta function is nominal design value at IP. In addition we can define "nominal ξ " in a similar way:

$$\xi_{\text{nom}} = \frac{N^- r_e \beta_{\text{nom}}^*}{4\pi\gamma\sigma_{\text{nom}}^*}, \quad (3)$$

where beam size is unperturbed. Due to strong emittance and beam size growth ξ_{nom} has nothing to do with real beam-beam tuneshifts being just a beam intensity normalized to clean out the dependence on energy.

We can now express directly the luminosity via beam-beam parameter:

$$L = \frac{N_f \gamma \xi_{\text{lumi}}}{r_e \beta_{\text{nom}}^*}. \quad (4)$$

Finally, the achieved beam-beam parameter extracted from luminosity at 391-392 MeV is presented in Fig. 12. It saturates strongly and doesn't exceed 0.08.

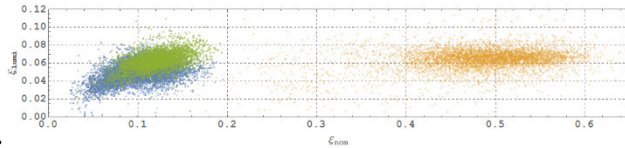


Figure 12: Beam-beam parameter extracted from CMD-3 luminosity. Notation is the same as in Fig. 11.

COHERENT MODES

The cross-check for the acting beam-beam parameter value can be done through the analysis of the coherent beam oscillation spectrum. Usually we excite eigen modes with tiny kick, but with constant beam shaking modes tunes are always visible in pickup signal spectra. In Fig. 13 the example of coherent spectrum and spectrogram at beam energy of 360 MeV are shown. Left peak corresponds to so called σ -mode with unperturbed betatron tune 0.135 while the right peak indicate the π -mode with shifted tune to 0.345. The total tuneshift is $\Delta\nu = 0.21$.



Figure 13: Beam-beam modes spectrum @ 360 MeV.

With given incoherent beam-beam parameter ξ_{inc} , i.e. parameter that is seen by the single particle interacting with opposite "strong" beam, the coherent beam-beam parameter will be

$$\xi_{\text{coh}} = 2 \cdot \frac{1}{2} \cdot Y \cdot \xi_{\text{inc}}, \quad (5)$$

where factor 2 shows that the distance between two beams centroids is twice larger than coordinate shift in π -eigen mode; factor $\frac{1}{2}$ ("Hirata's one half") appears due to the proper averaging over Gaussian distribution in the model of two rigid Gaussian beams [20]; Yokoya factor Y is responsible for transverse distribution deformation during the oscillation excitation [21].

We assume that $Y = 1$ since the oscillations with very small amplitude ($\sim 5 \mu\text{m} = 0.1 \sigma^*$) were excited by a fast kick and the spectrum was investigated for only 8000 turns that is much shorter than damping time. During this short time beam distribution is not deformed by an oscillating counter beam. This assumption was studied thoroughly at VEPP-2M [22]. First simulations by *Lifetrac* code [23] in quasi-strong-strong regime also do not show significant deviation of Y-factor from unity.

Finally, with the given modes' tunes calculated ξ per one IP is equal to:

$$\xi = \frac{\cos(\pi\nu_\sigma) - \cos(\pi\nu_\pi)}{2\pi \sin(\pi\nu_\sigma)} \approx 0.17, \quad (6)$$

that is twice higher than beam-beam parameter defined from luminosity measurements. This discrepancy is not yet understood. However, the coherent tuneshift is routinely used for the machine fine tuning including beamshaker amplitude and completely correlates with luminosity maximization.

DATA COLLECTION

The 2016/17 run was the first data taking VEPP-2000 run with new injector [24-27]. It was dedicated to energy range from 640 MeV to 1003.5 MeV per beam. The design top energy was exceeded in order to achieve the mass of $D^0(2007)$. The run 2017/18 was dedicated to the data collection at low beam energies: 274 – 600 MeV. Fig. 14 presents the online status web-page during regular operation at 395.5 MeV energy in May 2018.

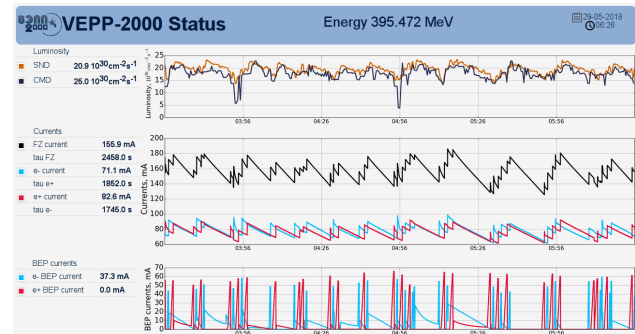


Figure 14: VEPP-2000 operation @ 395 MeV.

The achieved luminosity in comparison to 2010-2013 performance is shown in Fig. 15. In the middle energy range the achieved luminosity is well above all expectations. At the same time at top energy luminosity is lower than design value in a factor of two.

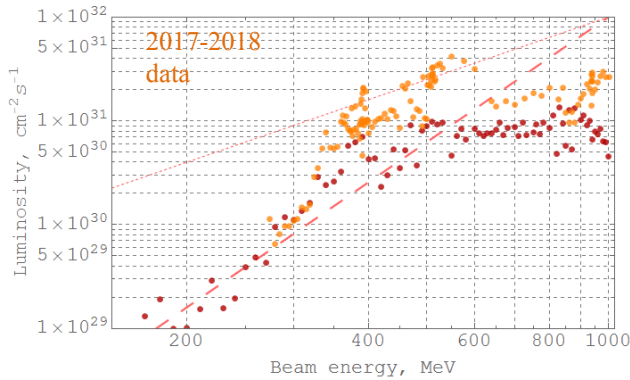


Figure 15: CMD-3 recorded in 2010-2013 (crimson) and in 2017-2018 (orange) luminosity averaged over 10% of best runs. Pink lines show scaling laws with fixed and variable β^* .

The next figure presents the integrated luminosity as compared for several operating years. One should beware of direct comparison of integrals due to luminosity dependence on energy. 2012/13 and 2017/18 runs were spent for data taking below 500 MeV while the others were dedicated to higher energies.

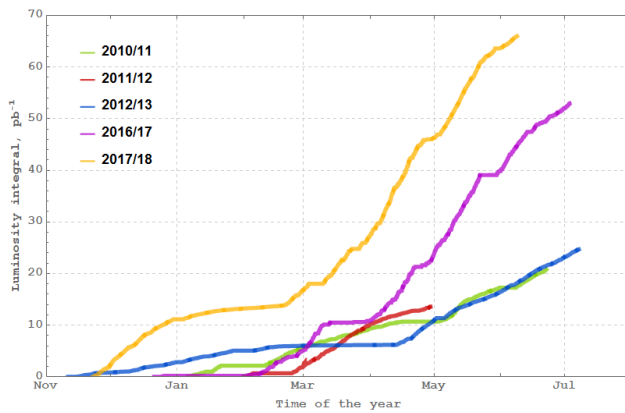


Figure 16: CMD-3 recorded luminosity integral.

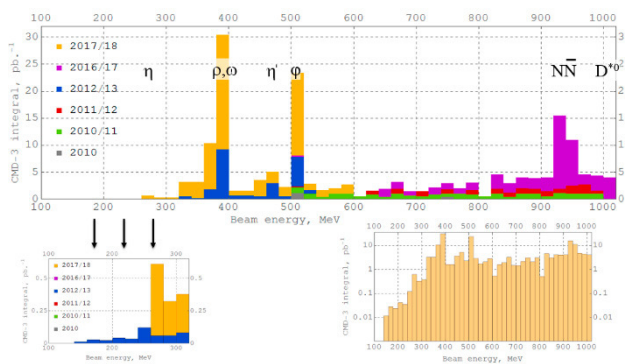


Figure 17: CMD-3 recorded luminosity integral.

The distribution of luminosity integral over energy is presented in Fig. 17. Although all the energy range is already covered mainly integral sticks to several points of interest such as different light mesons masses and threshold of nucleon-antinucleon production [28-30].

STREAK CAMERA

Recently the streak camera was installed at VEPP-2000 at one of the SR output (e^- direction) in parallel to regular CCD-camera [31]. The first studies were carried out at the energy of 392.5 MeV, with beamshaker switched off. While observing the single electron circulating beam with intensity above beam-beam threshold the positron bunch with the same intensity was injected. The latter's lifetime is very short, several milliseconds, due to beam-beam interaction. The single-turn snapshots of electron beam vertical-to-longitudinal distribution were made by streak camera at the chosen turn number after injection. In Fig. 18 the bunch profile is presented at 40th and 80th turn. Unfortunately significantly longer delays were not available with current hardware.

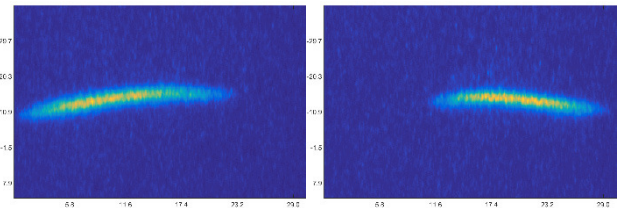


Figure 18: Streak camera e^- bunch profiles. Vertical/horizontal axis corresponds to vertical/longitudinal coordinate, both in arbitrary units.

It is clearly seen that bunch acquires a vertical tilt and this tilt oscillates very fast if compared to synchrotron motion. The synchrotron tune during this study was $\nu_s = 0.002$ thus equivalent to 500 turns. The tilt should exist not exclusively in vertical plane since the colliding beams are round, i.e. X-Y-symmetric, but streak camera was not able to observe horizontal coordinate.

For inverse situation when electron bunch is injected to the storage ring with circulating positron bunch the disruption is even worse. Distribution can be split into two parts as presented in Fig. 19.

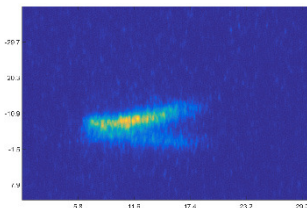


Figure 19: Injected e^- bunch in the presence of circulating intensive e^+ bunch.

These first observations in addition to mentioned above influence of bunch length on beam-beam threshold indicates the importance of longitudinal motion on beam-beam effects. We plan to continue studies with streak-camera.

CONCLUSION

Round beams give a serious luminosity benefit. VEPP-2000 with new BINP injector and upgraded booster started data taking in all energy range of 200–1000 MeV with a luminosity increased in a factor of 2-5. Novel technique ("beamshaking") for effective emittance control allow to suppress flip-flop effect and increase beams intensity at middle energies. Strong discrepancy between coherent and incoherent beam-beam parameter ξ is observed: problem to be solved. First studies with streak-camera have shown fast oscillating longitudinal bunch tilts. Upcoming new run will be devoted to energy range above 500 MeV with intent to achieve the target luminosity at top energy.

ACKNOWLEDGEMENT

We are grateful to A.M. Batrakov, D.B. Burenkov, I.N. Churkin, P.V. Logachev, M.I. Nepomnyashchikh, A.L. Romanov, V.S. Seleznev, A.N. Skrinsky, Yu.M. Velikanov, V.D. Yudin for continuous support.

This work is partially supported by Russian Science Foundation under project N 14-50-00080.

REFERENCES

- [1] Yu.M. Shatunov *et al.*, "Project of a New Electron-Positron Collider VEPP-2000", in *Proc. EPAC'00*, Vienna, Austria, 2000, pp. 439-441.
- [2] D. E. Berkaev *et al.*, "The VEPP-2000 electron-positron collider: First experiments", *J. Exp. Theor. Phys.*, Vol.113, no.2, p.213 (2011)
- [3] D. Shwartz *et al.*, "Implementation of Round Colliding Beams Concept at VEPP-2000", in *Proc. eeFACT'16*, Daresbury, UK (2016), p. 32.
- [4] V.V. Danilov *et al.*, "The Concept of Round Colliding Beams", in *Proc. EPAC'96*, Sitges, Spain, 1996, pp. 1149-1151.
- [5] L.M. Barkov *et al.*, "Phi-Factory Project in Novosibirsk", in *Proc. 14th HEACC'89*, Tsukuba, Japan, 1989, p. 1385.
- [6] K. Ohmi, K. Oide and E.A. Perevedentsev, "The beam-beam limit and the degree of freedom", in *Proc. EPAC'06*, Edinburgh, Scotland, 2006, pp.616-618.
- [7] T.V. Dimova *et al.*, "Recent Results on $e^+e^- \rightarrow$ hadrons Cross Sections from SND and CMD-3 Detectors at VEPP-2000 collider", *Nucl. Part. Phys. Proc.*, vol. 273-275, pp. 1991-1996, 2016.
- [8] A.A. Korol *et al.*, "Measurement of the hadronic cross sections with the CMD-3 and SND detectors at the VEPP-2000 collider", *EPJ Web of Conferences*, 182, 02068 (2017).
- [9] D. Berkaev *et al.*, "VEPP-5 Injection Complex: Two Colliders Operation Experience", in *Proc. IPAC'17*, Copenhagen, Denmark, pp. 2982-2984.
- [10] Yu. Maltseva *et al.*, "VEPP-5 Injection Complex: New Possibilities for BINP Electron-Positron Colliders", in *Proc. IPAC'18*, Vancouver, Canada, pp. 371-373.
- [11] D. Shwartz *et al.*, "Booster of Electrons and Positrons (BEP) Upgrade to 1 GeV", in *Proc. IPAC'14*, Dresden, Germany, pp. 102-104.
- [12] P.Yu. Shatunov *et al.*, "Magnet Structure of the VEPP-2000 Electron-positron Collider", in *Proc. EPAC'06*, Edinburgh, Scotland, 2006, pp. 628-630.
- [13] A.L. Romanov *et al.*, "Round Beam Lattice Correction using Response Matrix at VEPP-2000", in *Proc. IPAC'10*, Kyoto, Japan, 2010, pp. 4542-4544.
- [14] D. Shwartz *et al.*, "Recent Beam-Beam Effects at VEPP-2000 and VEPP-4M", in *Proc. ICFA Mini-Workshop on Beam-Beam Effects in Hadron Colliders (BB2013)*, Geneva, Switzerland, 2013, CERN-2014-004, pp. 43-49.
- [15] A.V. Otboev and E.A. Perevedentsev, "On self-consistent β -functions of colliding bunches", in *Proc. PAC'1999*, New York, USA, 1999, pp. 1524-1526.
- [16] Yu.A. Rogovsky *et al.*, "Status and Perspectives of the VEPP-2000 Complex", in *Proc. RuPAC'14*, Obninsk, Russia, 2014, pp. 6-10.
- [17] Yu.A. Rogovsky *et al.*, "Current Dependence of Bunch Dimensions in VEPP-2000 Collider", in *Proc. RuPAC'18*, Protvino, Russia, 2018, THCEMH04.
- [18] P.M. Ivanov *et al.*, "Luminosity and the Beam-Beam Effects on the Electron-Positron Storage Ring VEPP-2M with Superconducting Wiggler Magnet", in *Proc. 3rd Advanced ICFA Beam Dynamics Workshop on Beam-Beam Effects in Circular Colliders*, Novosibirsk, USSR, 1989, pp. 26-33.
- [19] G.M. Tumaikin, private communication.
- [20] K. Hirata, "Coherent Betatron Oscillation Modes Due to Beam-Beam Interaction", *Nucl. Instrum. Methods Phys. Res. A* 269, 1988, pp. 1-22.
- [21] K. Yokoya, H. Koiso, "Tune Shift of Coherent Beam-Beam Oscillations", *Particle Accelerators*, 1990, Vol.27, pp. 181-186.
- [22] P.M. Ivanov *et al.*, "Experimental Studies of Beam-Beam Effects at VEPP-2M", in *Proc. Workshop on Beam-Beam Effects in Circular Colliders*, Fermilab, USA, 2001, p. 36.
- [23] D. Shatilov, *Part. Accel.*, vol. 52, p. 65, 1996.
- [24] D. Berkaev *et al.*, "Commissioning of Upgraded VEPP-2000 Injection Chain", in *Proc. IPAC'16*, Busan, Korea, pp. 3811-3813.
- [25] D. Shwartz *et al.*, "Recommissioning and Perspectives of VEPP-2000 e^+e^- Collider", *PoS ICHEP2016* (2016), p.054.
- [26] P. Shatunov *et al.*, "High Luminosity at VEPP-2000 Collider With New Injector", in *Proc. IPAC'17*, Copenhagen, Denmark, pp. 2989-2991.
- [27] Yu. M. Shatunov *et al.*, "Commissioning of the Electron-Positron Collider VEPP-2000 after the Upgrade", *Phys. Part. Nucl. Lett.* (2018) 15, pp. 310-314.
- [28] R.R. Akhmetshin *et al.*, "Hadronic cross sections with the CMD-3 detector at the VEPP-2000", *Nucl. Part. Phys. Proc.*, 294-296 (2018) pp. 170-176.
- [29] E.A. Kozyrev *et al.*, "Study of the process $e^+e^- \rightarrow K^+K^-$ in the center-of-mass energy range 1010–1060 MeV with the CMD-3 detector", *Phys. Lett. B*, 779 (2018) pp. 64-71.
- [30] A.A. Korol *et al.*, "Recent Results from the SND Detector", *Phys. Part. Nucl.*, 49 (2018) pp. 730-734.
- [31] M. Timoshenko *et al.*, "Development of longitudinal beam profile diagnostics for beam-beam effects study at VEPP-2000", in *Proc. IBIC'18*, Shanghai, China, paper WEPA18.

REPORT FROM ARIES MUON COLLIDER WORKSHOP IN PADUA*

Marco Zanetti, INFN and University of Padua, Italy
Frank Zimmermann[†], CERN, Geneva, Switzerland

Abstract

Several novel concepts could help the muon collider become a reality. These concepts include parametric ionization cooling, low-emittance muon production by positron annihilation (LEMMA scheme), production of low-emittance muon or positron beams using the Gamma Factory concept, and strategies to upgrade large accelerator complexes, like the LHC or the FCC, into a highest-energy muon collider. The muon collider workshop organized by ARIES APEC at Padua in July 2018 gathered the international community in order to review the recent progress and to formulate a common R&D strategy. Several important conclusions and recommendations were drawn.

INTRODUCTION

On 2–3 July 2018 a Muon Collider workshop at the University of Padua attracted 78 experts from Europe and the US, as illustrated in Figs. 1 and 2. This exciting and forward-looking workshop was the second event organized in the frame of the EU co-funded ARIES Work Package 6.6 (WP6.6), after the Photon Beams workshop in 2017 [1].



Figure 1: Some participants of the ARIES WP6 workshop on Muon Colliders, Padua, 2-3 July 2018.

More specifically, the muon collider workshop was organized by ARIES WP6.6 coordinators Marco Zanetti (INFN Padova) and Frank Zimmermann (CERN), together with the newly established European Muon Collider Study Group, chaired by Nadia Pastrone (INFN Torino). ARIES is an integrating activity co-funded by the European Commission in the HORIZON 2020 Research and Innovation programme under grant agreement no 730871. Work Package 6 “Accelerator Performance and Concepts” (APeC) contains a Task 6.6, which looks at far-future concepts.

* This work was supported by the European Commission under the HORIZON 2020 project ARIES no. 730871.

[†] frank.zimmermann@cern.ch



Figure 2: Snapshots from the ARIES WP6 workshop on Muon Colliders, including Alex Bogacz, Carlo Rubbia, Rolland Johnson, Mark Palmer, Manuela Boscolo, Marco Zanetti, Pantaleo Raimondi, and Jean-Pierre Delahaye.

ADVANCED PROTON-DRIVEN SCHEMES

Setting the stage, Carlo Rubbia, from CERN and INFN, the recipient of the 1984 Nobel Prize for Physics and a life-long Member of the Senate of the Italian Republic, called for an initial experiment to demonstrate muon cooling and the particular merits of parametric ionization cooling [2]; see Fig. 3. He pointed out that the first muon facility would comprise a ring at the scale of the PS, and hinted at the ESS as being the ideal place for a muon-beam facility in Europe.



Figure 3: Recognizing the muon collider as a project of reasonable cost and of reasonably fast construction, Nobel laureate Carlo Rubbia admonished the audience to focus on scientific work instead of PowerPoint studies.



Figure 4: BNL's Mark Palmer recommended construction of NuSTORM and pursuit of an advanced-cooling demonstration.

under the names “muon photocathode”, “Gamma Factory,” and “LEMMA”.

Camilla Curatolo, from INFN Padua discussed a “muon photocathode” [8, 9], which could be realized in hadron-photon collisions using a free electron laser (FEL). To study such a scheme she developed a dedicated event generator. For an FCC-based example, the normalized emittance would be less than 1 micron. The proton-gamma luminosity could be $10^{38}/\text{cm}^2/\text{s}$. Muon accumulation and muon polarization are to be considered.

Witek Krasny, from LPNHE Paris and CERN, introduced the “Gamma Factory,” where partially-stripped heavy ion (PSI) beams at high energy are collided with laser or FEL pulses [10, 11]. The basic idea underlying the Gamma factory is to replace the electron beam, traditionally used for laser Compton backscattering light sources, by a PSI beam, as is illustrated in Fig. 5. The PSI beam allows for a resonant interaction with much higher cross section and with significantly higher photon energies than an electron-based Compton source. A Gamma Factory could allow for the production of huge rates of polarized muons or positrons. For example, an FCC-based Gamma Factory could provide more than 10^{17} positrons per second. A successful proof-of-principle experiment at the LHC in summer 2018 has demonstrated an excellent lifetime of the partially stripped heavy-ion beams at top energy, which represents an important milestone towards the realization of a first Gamma Factory; see Fig. 6. Witek Krasny highlighted three specific scenarios for producing polarized leptons using the Gamma Factory concept, and the associated ongoing SPS experiments. A breakthrough scheme with Pb^{+79} ions will avoid the double excitation of electrons into the continuum.

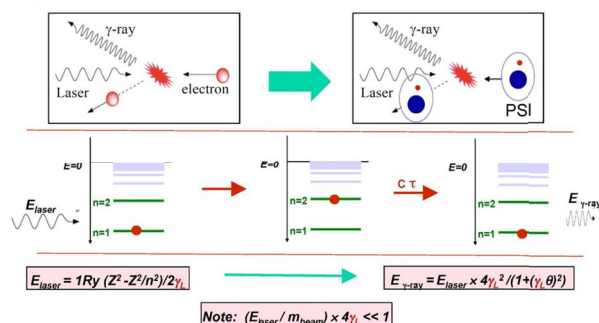


Figure 5: Concept of the “Gamma Factory” where Lorentz-boosted laser photons collide, and interact resonantly, with a PSI beam circulating in the LHC or FCC-hh. The resonant laser-PSI interaction excites atomic (ionic) transitions. The photons emitted when excited ions, nearly instantly, decay back into their ground state are once again Lorentz boosted, yielding photon energies of up to a few hundred MeV.

Manuela Boscolo from INFN Frascati presented the Low EMittance Muon Accelerator (LEMMA) scheme, which she had first proposed together with Pantaleo Raimondi (ESRF) and Mario Antonelli (INFN) [12, 13]. At LEMMA, positrons

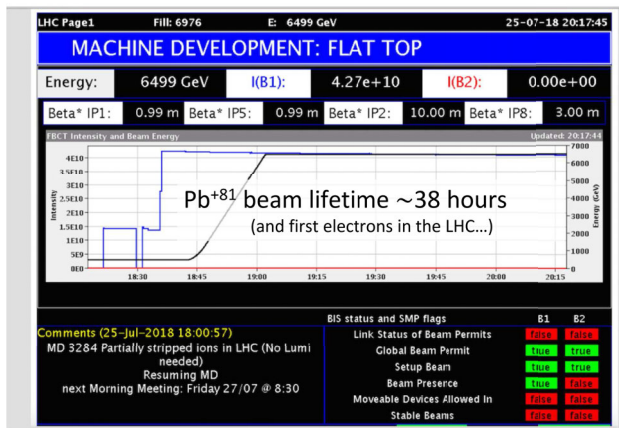


Figure 6: Gamma Factory proof-of-principle experiment at the LHC in July 2018. A Pb^{+81} beam was injected and accelerated to top energy, where the beam lifetime, limited by stripping off the residual gas, was about 38 hours. This experiment also saw the first electrons in the LHC. Dima Budker from the University of Mainz (the son of the inventor of the muon collider) called this experiment “one of the main scientific advances in the whole of physics this year”.

of about 45 GeV energy, circulating in a storage ring, annihilate with electrons at rest in a thin internal target, which results in muon production just above threshold, and, hence, with a low transverse emittance. The LEMMA scheme and the classical proton-driven muon production scheme with ionization cooling are compared in Fig. 7.

from US-MAP (2015) to LEMMA scheme (2017)

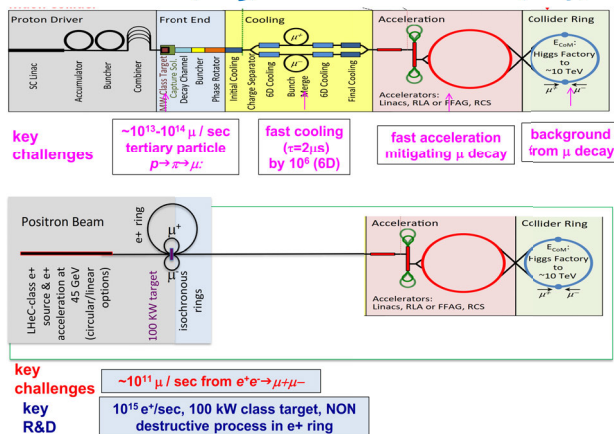


Figure 7: Comparison of US-MAP scheme for a muon collider, based on proton driver and ionization cooling, and the novel LEMMA scheme based on a positron storage ring with e^+e^- annihilation on a thin internal target (M. Boscolo, P. Raimondi, et al.). Key challenges for the two alternative approaches are also indicated.

The LEMMA positron beam loses several tens of MW energy passing through the target, made e.g. from beryllium, carbon, or hydrogen. About 200 kW of this power is deposited inside the target. Target survival is an open question.

Liquid targets or rotating targets are among the options proposed. The workshop participants agreed on the need for experimental target tests. Oscar Blanco from INFN-LNF reported on the LEMMA muon accumulator ring. He pointed out that the muon beam emittance is limited by multiple scattering in the annihilation target. Citing Daniel Schulte of CERN, he also showed that for a 3 mm Be target the minimum normalized emittance is 600 nm, significantly larger than the 40 nm emittance previously assumed. Simone Liuzzo of ESRF explained that, for LEMMA, more than 120 MW of synchrotron radiation are emitted in a 6.2 km positron ring. For a 27 km ring the synchrotron-radiation power drops below 30 MW. Frank Zimmermann of CERN pointed out that this power would become even lower if the 100 km FCC-ee ring is employed. Serendipitously, the latter ring, thanks to its Z-pole running mode, already offers the right beam energy for low-emittance muon production through annihilation. Intriguingly, Francesco Collamati, from INFN Roma, showed that the abundant bremsstrahlung photons which are equally emitted from the target can be used to generate more positrons, leading to a self-amplification of the positron beam, which could solve the challenge of generating positrons at the rate required for LEMMA. Susanna Guiducci from INFN-LNF reviewed the state of the art in positron sources, which would be an integral part of LEMMA.

MUON ACCELERATION

Daniel Schulte of CERN discussed the potential use for muon-collider R&D of an experimental programme using electron beams from the CERN SPS, with a CLIC-like injector [14]. He underlined that plasma acceleration is a perfect match for muons, which typically are of low intensity and fairly large emittance. He argued that “if it is not suitable here, plasma acceleration probably cannot be used for any other type of collider”.

Scott Berg of BNL and Alex Bogacz from JLAB discussed more conventional options for muon acceleration [15–17], including the FFA accelerator prototype CBETA [18] under construction at Cornell (see also the recent first ever experimental demonstration of muon radiofrequency acceleration at J-PARC [19]).

HIGH-ENERGY MUON COLLIDERS

In an exceptional remote presentation of this workshop, David Neuffer of FNAL, presented the fascinating option of a 14 TeV muon collider in LHC tunnel, which could be a cost-effective approach for reaching the ten-TeV scale in lepton collisions [20]. The proposal is illustrated in Fig. 8. Upon request, he also detailed the three fundamental laws of beam physics.

Daniel Kaplan of IIT reviewed limits from neutrino radiation [21]. Concerning the next steps, he recalled that “you don’t get tenure by saving government money”.

Frank Zimmermann, of CERN, sketched a possible upgrade of the FCC lepton and hadron-collider complex to a high-energy muon collider, using a combination of Gamma

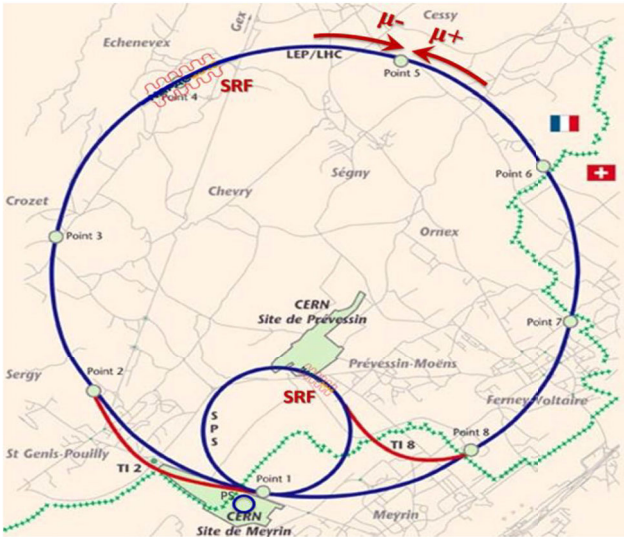


Figure 8: A 14 TeV muon collider in the LHC tunnel, based on short high-field magnets operating at a constant field of 16 T, and pulsed ± 3.8 T SC magnets and an SRF system providing more than 10 GV accelerating voltage (D. Neuffer and V. Shiltsev).

Factory and LEMMA concepts [22,23] – Fig. 9. He showed that for various reasons and in view of the scaling laws – which call for a ring of large circumference and with high magnetic field – the FCC appears to be the ideal basis for constructing a future 100 TeV muon collider.

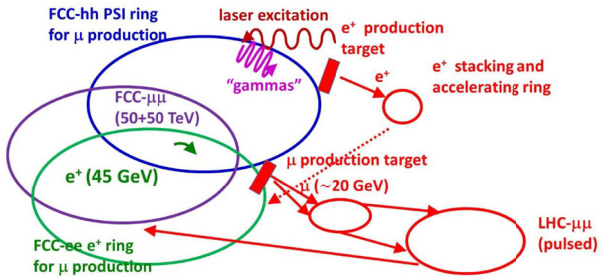


Figure 9: A 100 TeV muon collider, “FCC- $\mu\mu$ ”, in one of the FCC-hh rings, with e^+ production from a Gamma Factory using partially stripped ion beams circulating in the other FCC-hh ring, and with LEMMA type muon production from a positron beam stored in one of the 45 GeV FCC-ee rings; this concept would enable an FCC physics program extending over more than 100 years (Frank Zimmermann).

CERN’s Jean-Pierre Delahaye compared the performance of several proposed future lepton colliders, introducing two figures of merit, the luminosity per construction cost and the luminosity per electrical power. This was an exciting update to an earlier similar study [24]. He showed that, with regard to both figures-of-merit, the FCC-ee was the best of all options, while the values of the muon collider extended all across the figure-of-merit plane from the worst (muon Higgs factory) to among the best (multi-TeV muon collider) – see Fig. 10.

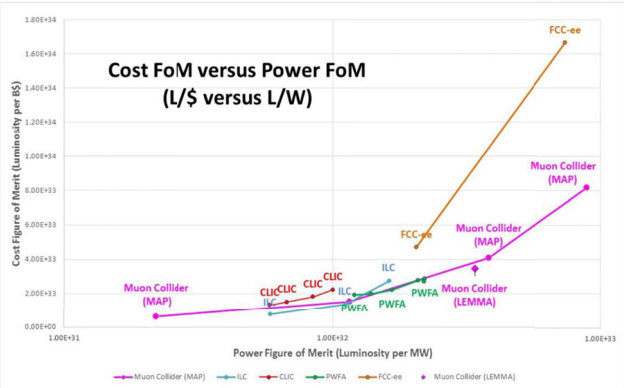


Figure 10: Cost-figure-of-merit versus power-figure-of-merit for future lepton colliders (Jean-Pierre Delahaye).

Alain Blondel from the University of Geneva pointed out that luminosity measurement techniques for muon colliders still need to be worked out. Mario Greco from Roma Tre emphasized the importance of QED radiative effects for a precision study of the Higgs pole line shape and the signal-to-background ratio, both at a Higgs-factory muon collider and at the FCC-ee.

CONCLUSIONS

At the workshop, a general consensus was reached that the steps forward should include: (1) the design and implementation of a 6D cooling experiment; (2) LEMMA target tests; (3) the Gamma Factory development; (4) the establishment of particle-physics programme based on high-intensity, high-energy muon beam, e.g. NuSTORM.

At the end of the workshop, Nadia Pastrone, from INFN Torino, the coordinator of the European muon collider study group, drew some enthusiastic conclusions and discussed the muon-collider input to the 2019/20 European Strategy Update.

More details and all presentations can be found on the indico web site of the Muon Collider workshop [25].

ACKNOWLEDGEMENT

We thank G. Arduini and M. Giovannozzi for a careful reading of the manuscript.

REFERENCES

- [1] *ARIES Photon Beams workshop*, Padua, 27–28 November 2018, <https://indico.cern.ch/event/668097/>
- [2] Ya.S. Derbenev, V.S. Morozov, A. Afanasev, K.B. Beard, R. Johnson, B. Erdelyi, J.A. Maloney, “Parametric-resonance Ionization Cooling of Muon Beams,” arXiv:1205.3476 (2012).
- [3] J.-P. Delahaye *et al.*, “Enabling Intensity and Energy Frontier Science with a Muon Accelerator Facility in the U.S.: A White Paper Submitted to the 2013 U.S. Community Summer Study of the Division of Particles and Fields of the American Physical Society,” *FERMILAB-CONF-13-307-APC*, and arXiv:1308.0494 (2013).

- [4] P. Kyberd *et al.*, “nuSTORM: Neutrinos from STORED Muons,” arXiv:1206.0294 (2012).
- [5] V. Blackmore, “MICE and NuSTORM,” *Nuclear and Particle Physics Proceedings*, Vol. 265–266 (2015) 205–207.
- [6] J.-P. Delahaye, “The NuMAX Long Baseline Neutrino Factory Concept,” arXiv:1803.07431 (2018).
- [7] T.A. Mohayai, “First Demonstration of Ionization Cooling in MICE,” *Proc. IPAC’18*, Vancouver (2018) 5035; arXiv:1806.01807.
- [8] L. Serafini, C. Curatolo, V. Petrillo, “Low emittance pion beams generation from bright photons and relativistic protons,” arXiv:1507.06626 (2015).
- [9] C. Curatolo, “High brilliance photon pulses interacting with relativistic electron and proton beams,” PhD thesis, U. Milano (2016).
- [10] M.W. Krasny, “The Gamma Factory proposal for CERN,” arXiv:1511.07794 (2015).
- [11] M.W. Krasny, R. Alemany *et al.*, “The CERN Gamma Factory Initiative: An Ultra-High Intensity Gamma Source,” *Proc. IPAC’18*, Vancouver (2018) 1780.
- [12] M. Antonelli, M. Boscolo, R. Di Nardo, P. Raimondi, “Novel proposal for a low emittance muon beam using positron beam on target,” *Nuclear Instr. Meth. A*, vol. 807 (2016) 101–107.
- [13] M. Boscolo, M. Antonelli, O.R. Blanco-García, S. Guiducci, S. Liuzzo, P. Raimondi, and F. Collamati, “Low emittance muon accelerator studies with production from positrons on target,” *Phys. Rev. Accel. Beams* 21, 061005 (2018).
- [14] T. Åkesson, Y. Dutheil, L. Evans, A. Grudiev, Y. Papaphilipou, S. Stapnes, “A primary electron beam facility at CERN,” arXiv:1805.12379 (2018).
- [15] J.S. Berg *et al.*, “FFAGs for Muon Acceleration,” *Proc. PAC 2003* (2003) 3413.
- [16] J.S. Berg, H. Witte, “Pulsed Synchrotrons for very rapid Acceleration,” in *Proc. AAC 2014*, San Jose, *AIP Conference Proceedings* 1777, 100002 (2016).
- [17] S.A. Bogacz, “Muon Acceleration Concepts for NuMAX: ‘Dual-use’ Linac and ‘Dogbone’ RLA,” *Journal of Instrumentation*, vol. 13 (2018).
- [18] D. Trbojevic *et al.*, “CBETA – Cornell University Brookhaven National Laboratory Electron Energy Recovery Test Accelerator,” *Proc. IPAC’17*, Copenhagen (2017) 1285–1289.
- [19] *CERN Courier*, 9 July 2018; <https://cerncourier.com/muons-accelerated-in-japan>
- [20] V. Shiltsev, D. Neuffer, “On the Feasibility of a Pulsed 14 TeV C.M.E. Muon Collider in the LHC tunnel,” *Proc. IPAC’18*, Vancouver (2018) 296–299
- [21] N. Mokhov, A. Van Ginneken, “Neutrino Radiation at Muon Colliders and Storage Rings,” *J. Nucl. Sci. Tech.* 37 (2000) 172
- [22] F. Zimmermann, “Future Colliders for Particle Physics – ‘Big and Small’ ” *Proc. EAAC’17*, La Biodola, published in *Nucl. Instr. Meth. A*, DOI 10.1016/j.nima.2018.01.034, and arXiv:1801.03170 (2018).
- [23] F. Zimmermann, “LHC- and FCC-Based Muon Colliders,” *Proc. IPAC’18*, Vancouver (2018) 273–276.
- [24] J.-P. Delahaye *et al.*, “A Staged Muon Accelerator Facility For Neutrino and Collider Physics,” *Proc. IPAC’14*, Dresden, arXiv:1502.01647 (2014).
- [25] *ARIES Muon Collider workshop*, Padua, 2–3 July 2018, web site <https://indico.cern.ch/event/719240>.

reduces the dynamic aperture. This is due to the induced synchrotron motion through the radiation loss”.

We crosschecked the simulation made by Oide using MAD-X PTC [11] and the homemade software TracKing [12] including SR from quadrupoles and found good agreement between all three codes. Nevertheless, detailed consideration has shown different nature of the particle loss in horizontal and vertical planes. Radiation from quadrupoles at large horizontal amplitude indeed greatly shifts the synchronous phase, induces large synchrotron oscillation, excites strong synchro-betatron resonances and, finally, moves the horizontal tune toward the integer resonance (due to the nonlinear chromatic and geometrical aberrations) according to the mechanism described by Jowett and Oide. However, in the vertical plane the picture of the particle loss was quite different. The energy loss from radiation in quadrupoles for the vertical plane is substantially smaller than for the horizontal plane and does not provide large displacement of the synchronous phase and synchrotron oscillation. Instead, we found that increase of the vertical betatron oscillation amplitude modifies the vertical damping until, at some threshold, the damping changes to rising and the particle gets lost.

This new effect is a parametric resonance in oscillations with friction; radiation from quadrupoles modulates the particle energy at the double betatron frequency; therefore, quadrupole focusing strength also varies at the doubled betatron frequency creating the resonant condition. However, due to friction, resonance develops only if oscillation amplitude is larger than a certain value. The remarkable property of this resonance is that it occurs at any betatron tune (not exactly at half-integer) and hence can be labeled as “self-inducing parametric resonance”.

We will derive particle equations of motion in presence of the radiation from quadrupoles, consider particle loss for both transverse planes and compare results with computer simulation.

PARAMETERS VALUES AND OBSERVATIONS FROM TRACKING

For the FCC-ee lattice “FCCee_z_202_nosol_13.seq” at 45 GeV Figs. 2 and 3 show dynamic aperture obtained by MADX PTC [11] tracking with synchrotron radiation from all magnetic elements and without. Figure 4 compares dynamic aperture with synchrotron radiation from dipoles only and dynamic aperture with radiation from dipoles and quadrupoles obtained by homemade software (TracKing [12]). The observation point is interaction point (IP).

Inclusion of synchrotron radiation in quadrupoles into tracking software decreases dynamic aperture

- in vertical direction from $R_y = 142\sigma_y$ to $R_y = 57\sigma_y$,
- in horizontal direction from $R_x = 109\sigma_x$ to $R_x = 65\sigma_x$.

FCC-ee lattice has two IPs and Table 1 gives the relevant parameters.

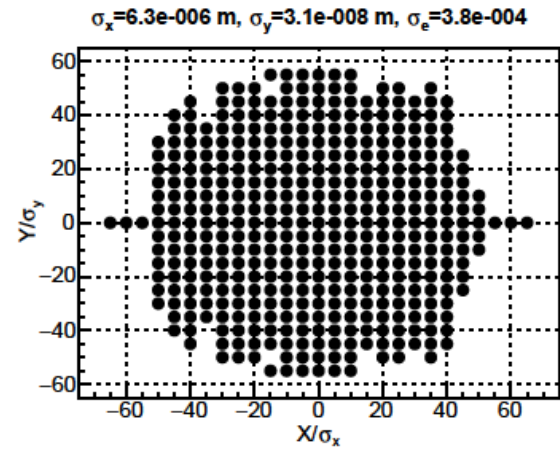


Figure 2: Dynamic aperture with synchrotron radiation from all magnetic elements, tracking by MADX PTC.

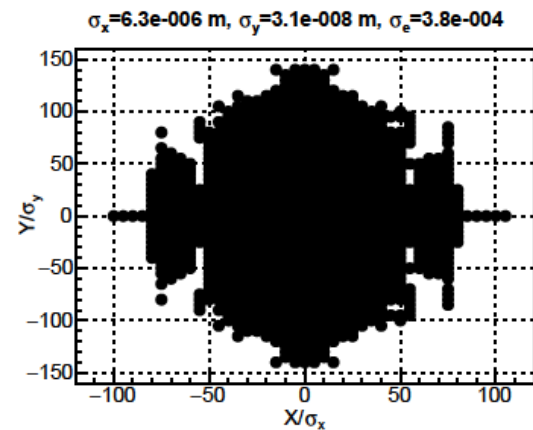


Figure 3: Dynamic aperture without synchrotron radiation from all magnetic elements, tracking by MADX PTC.

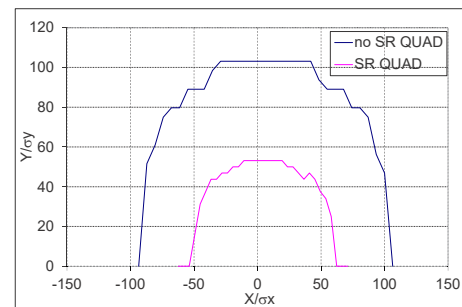


Figure 4: Dynamic aperture with synchrotron radiation from quadrupoles (blue) and without (magenta), tracking by homemade software.

Table 2 lists total synchrotron radiation energy loss from different type of magnets. For particles with vertical amplitude energy loss from final focus (FF) quadrupoles dominates the loss from the arc quadrupoles. For particles

Table 1: FCC-ee lattice parameters

E_0 [Gev]	45.6
tunes: $\nu_x/\nu_y/\nu_s$	269.14/267.22/0.0413
damping times: $\tau_x/\tau_y/\tau_\sigma$ [turns]	2600/2600/1300
IP: β_x/β_y [m]	0.15/0.001
$\varepsilon_x/\varepsilon_y$ [m]	$2.7 \times 10^{-10}/9.6 \times 10^{-13}$
IP: σ_x/σ_y [m]	$6.3 \times 10^{-6}/3.1 \times 10^{-8}$
σ_δ	3.8×10^{-4}

with horizontal amplitude energy losses in FF and the quadrupoles are comparable.

Table 2: Total energy loss from dipoles, final focus quadrupoles QFF, focusing and defocusing arc quadrupoles QF and QD

Type	N	$U(50\sigma_x)$, MeV	$U(50\sigma_y)$, MeV
Dipoles	2900	35.96	
QFF	4	12	2
QF	1470	4.1	3.7×10^{-3}
QD	1468	1.5	1.5×10^{-2}

Averaged over betatron phases radiation from quadrupoles is

$$U_q = \frac{C_\gamma}{2\pi} E_0^4 \oint \sum_i K_i^2 (x^2 + y^2) ds \quad (1)$$

$$= E_0 \Gamma \Pi [\langle K_1^2 \beta_x \rangle J_x + \langle K_1^2 \beta_y \rangle J_y],$$

where $\Gamma = \frac{C_\gamma}{2\pi} \frac{E_0^4}{p_0 c}$ is radiation related factor, Π is circumference, and the corresponding lattice integrals are

$$\langle K_1^2 \beta_x \rangle = 4 \times 10^{-3} \text{ m}^{-3},$$

$$\langle K_1^2 \beta_y \rangle = 1.4 \times 10^{-1} \text{ m}^{-3}.$$

For understanding the reasons of particle loss we studied with tracking particle trajectories in vicinity of dynamic aperture border. Figure 5 shows phase and time trajectories of the first unstable particle with initial vertical coordinate $y = 58\sigma_y$ and remaining five coordinates are zero. In the longitudinal plane $\{PT, T\}$ synchrotron oscillations excited by additional power loss are damped to zero and suddenly something forces particle to walk away.

Figure 6 shows the change of envelope evolution for particles with initial vertical coordinate around the dynamic aperture boundary $y = \{50; 52; 55; 57.5; 58; 58.5\} \times \sigma_y$, horizontal coordinates are zero, longitudinal are chosen with respect to the new synchronous point.

Figures 7 and 8 show phase and time trajectories of the first unstable particle with initial vertical coordinate $x = 67.1\sigma_x$ and remaining five zero. There is no damping and walking away in the longitudinal plane $\{PT, T\}$ as in case of vertical initial conditions Fig. 5. On Fig. 8 notice the bottom left plot showing phase advance per turn with respect to turn number; the particle action starts to grow after phase advance per turn reaches an integer.

EQUATIONS OF MOTION

We start from Hamiltonian

$$H(x, \sigma, y, p_x, p_\sigma, p_y; s) = 1 + p_\sigma + K_0 x + K_0^2 \frac{x^2}{2} + K_1 \frac{x^2 - y^2}{2} + K_2 \frac{x^3 - 3xy^2}{6} - (1 + K_0 x) \sqrt{(1 + p_\sigma)^2 - p_x^2 - p_y^2} + \left(-\frac{eV_0}{p_0 c} \right) \frac{\lambda_{RF}}{2\pi} \cos \left(\phi_s + \frac{2\pi\sigma}{\lambda_{RF}} \right) \delta(s - s_0), \quad (2)$$

where c is the speed of light, p_0 and E_0 are the reference momentum and energy, e is the electron charge, $B\rho = -e/p_0 c$ is the rigidity, $K_0 = B_y(0)/B\rho$ is the reference orbit curvature, $K_1 = (dB_y/dx)/B\rho$ is the normalized quadrupole gradient, $K_2 = (d^2 B_y/dx^2)/B\rho$ is the normalized sextupole strength, $p_\sigma = \Delta E/p_0 c$ is the longitudinal momentum, $p_{x,y} = P_{x,y}/p_0$ are the normalized transverse momenta, V_0, λ_{RF} are the RF cavity voltage amplitude and wave length, s is the azimuth along the orbit, $\sigma = s - ct$ is the longitudinal coordinate conjugate to the longitudinal momentum p_σ , s_0 is the position of point like RF cavity, ϕ_s is the phase of RF field.

Radiation power with assumption of negligible electron mass ($\beta = v/c = 1, E = pc$) is

$$\mathcal{P} = c \frac{C_\gamma}{2\pi} e^2 E^2 B^2 = c \frac{C_\gamma}{2\pi} E_0^4 \left(1 + 2p_\sigma \right) (K_0^2 + 2K_0 K_1 x + K_1^2 (x^2 + y^2)) = c \frac{C_\gamma}{2\pi} E_0^4 \left(K_0^2 (1 + 2p_\sigma) + 2K_0 K_1 x + K_1^2 (x^2 + y^2) \right), \quad (3)$$

where $B^2 = (B_y + x dB_y/dx)^2 + y^2 (dB_y/dx)^2$ and we dropped terms with p_σ^2 and $4K_0 K_1 x p_\sigma, 2K_1^2 p_\sigma (x^2 + y^2)$.

The next step is to expand Hamiltonian Eq. (2) up to third order in all variables, neglect the term $K_0 x (p_x^2 + p_y^2)/2$ due to its smallness, and obtain equations of motion where radiation is included by hand with the term describing the change of momenta,

$$x' = p_x - p_x p_\sigma \quad (4)$$

$$p_x' = K_0 p_\sigma - x(K_0^2 + K_1) - K_2 \frac{x^2 - y^2}{2} - \Gamma p_x [K_0^2 (1 + 2p_\sigma) + x(2K_0 K_1 + K_0^3) + K_1^2 (x^2 + y^2)] \quad (5)$$

$$y' = p_y - p_y p_\sigma \quad (6)$$

$$p_y' = y K_1 + K_2 x y - \Gamma p_y [K_0^2 (1 + 2p_\sigma) + x(2K_0 K_1 + K_0^3) + K_1^2 (x^2 + y^2)] \quad (7)$$

$$\sigma' = -K_0 x - \frac{p_x^2}{2} - \frac{p_y^2}{2} \quad (8)$$

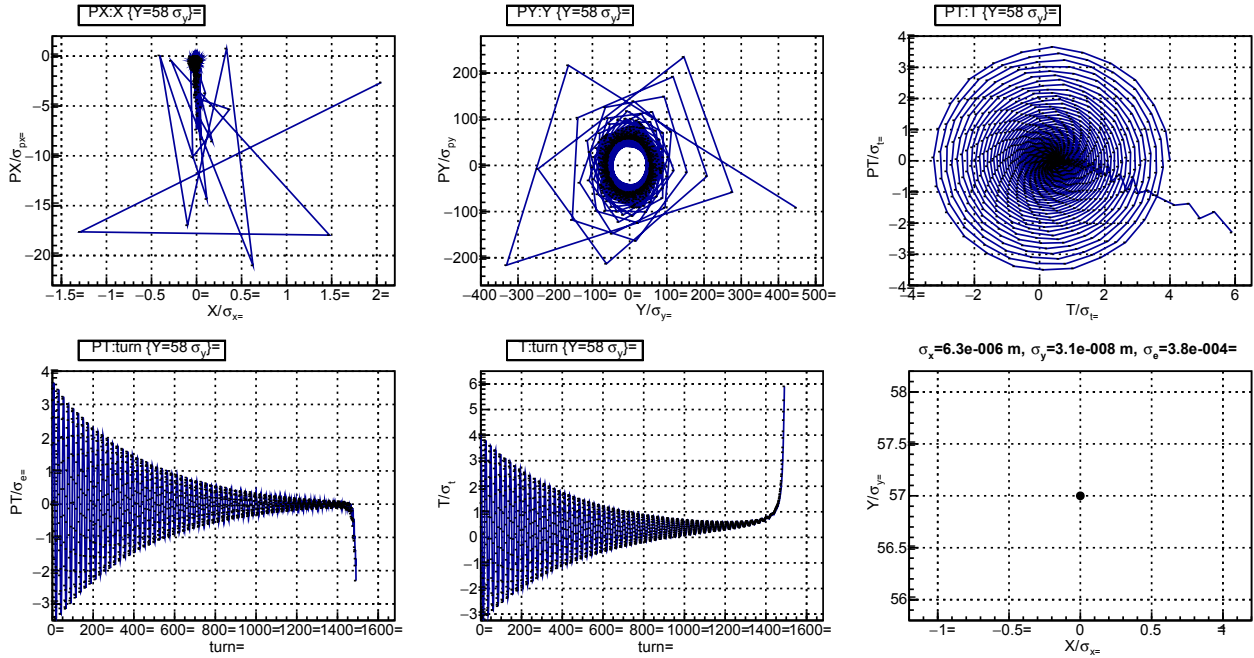


Figure 5: Phase and time trajectories of the first unstable particle with initial conditions $\{x = 0, y = 58\sigma_y, p_x = 0, p_y = 0, \sigma = 0, p_\sigma = 0\}$.

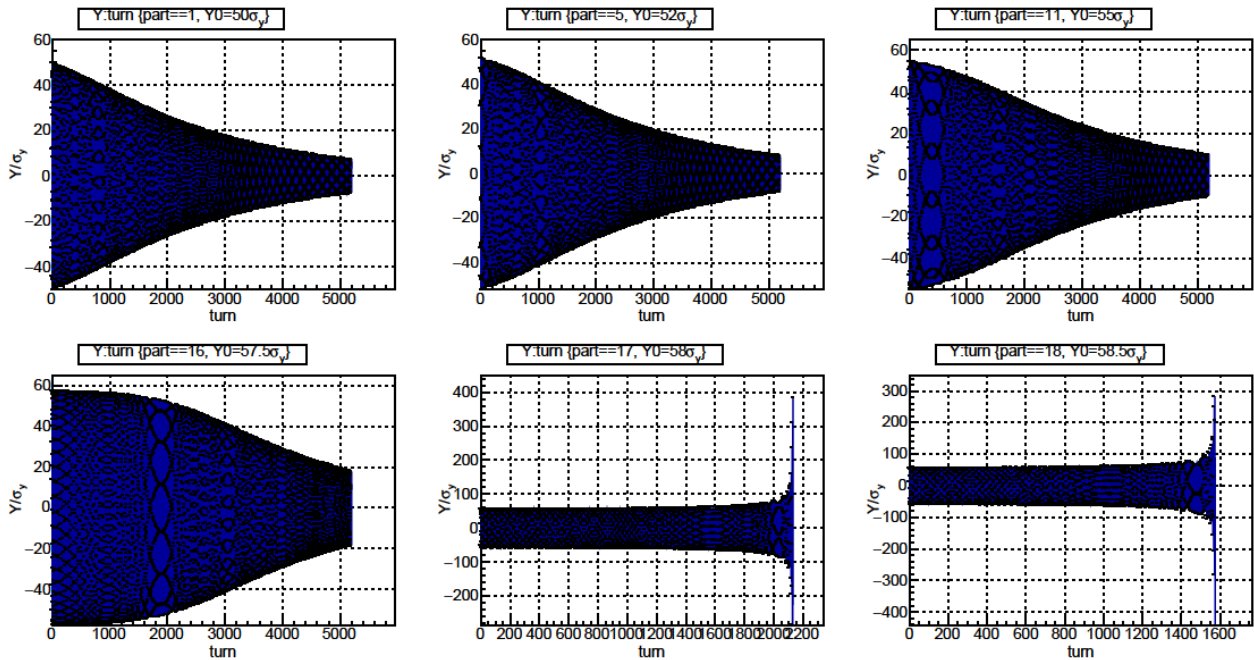


Figure 6: Time evolution of vertical oscillations for particles with initial vertical coordinate $y = \{50; 52; 55; 57.5; 58; 58.5\} \times \sigma_y$, horizontal coordinates are zero, longitudinal are adjusted for synchronous point.

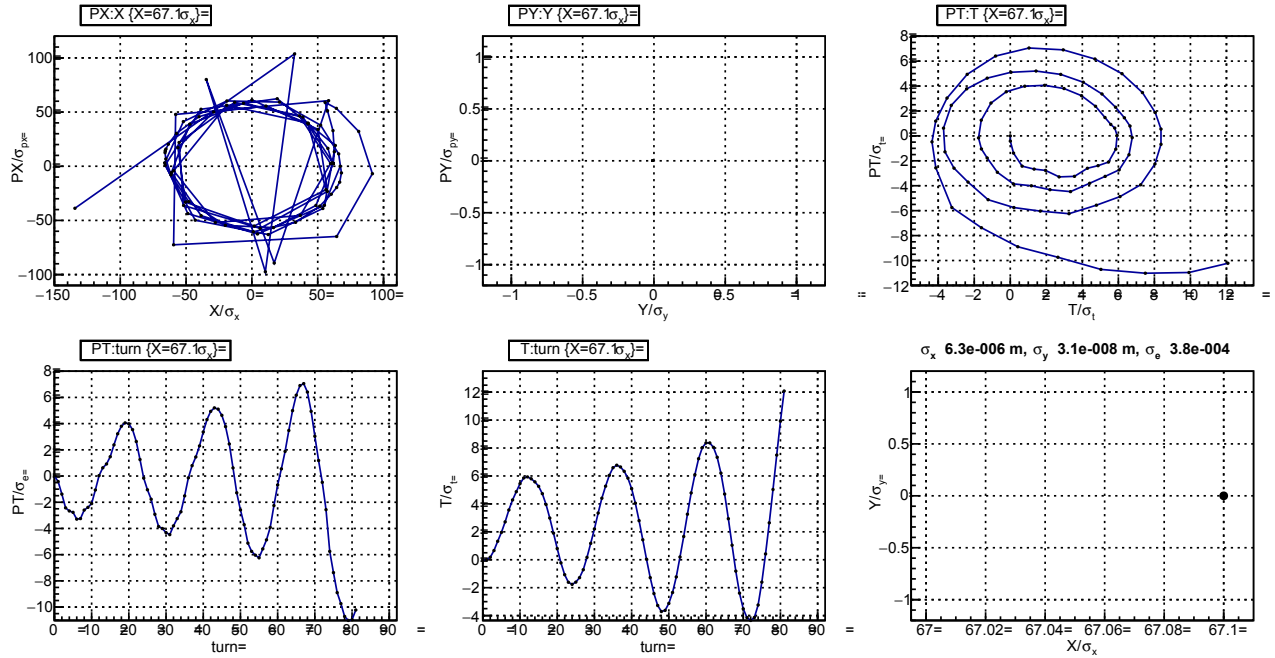


Figure 7: Phase and time trajectories of the first unstable particle with initial conditions $\{x = 67.1\sigma_x, y = 0, p_x = 0, p_y = 0, \sigma = 0, p_\sigma = 0\}$.

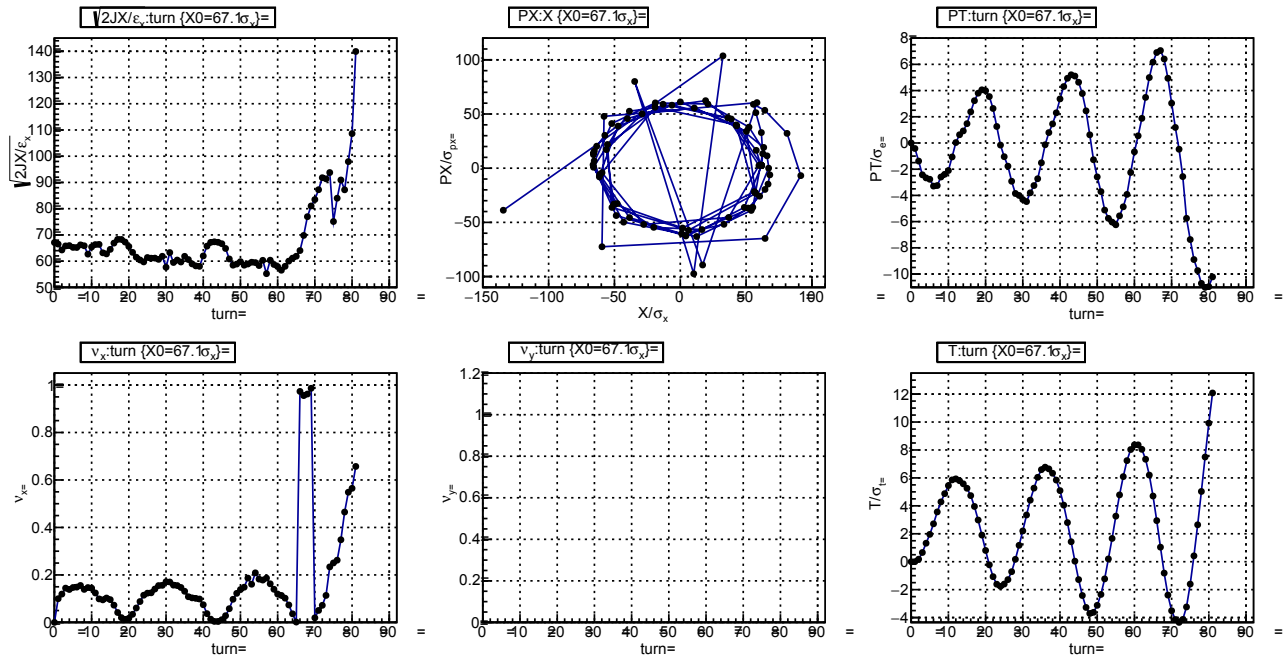


Figure 8: Square root of action and phase advance of the first unstable particle with initial conditions $\{x = 67.1\sigma_x, y = 0, p_x = 0, p_y = 0, \sigma = 0, p_\sigma = 0\}$.

$$p'_\sigma = \left(-\frac{eV_0}{p_0c} \right) \left(\sin \phi_s + \frac{2\pi\sigma}{\lambda_{RF}} \cos \phi_s \right) \delta(s - s_0) - \Gamma \left[K_0^2(1 + 2p_\sigma) + x(2K_0K_1 + K_0^3) + K_1^2(x^2 + y^2) \right], \quad (9)$$

where $\Gamma = \frac{C_\gamma}{2\pi} \frac{E_0^4}{p_0c}$, and we expanded RF related $\cos(\dots)$ to first order of σ .

SOLUTION OF LONGITUDINAL EQUATIONS OF MOTION

At first, we will solve longitudinal equations of motion Eqs. (8) and (9) considering motion in the vertical plane and neglecting motion in the horizontal plane. Due to the fact that longitudinal motion is much slower than transverse (synchrotron oscillation frequency is lower than betatron), we consider vertical oscillation amplitude independent of time and solve decoupled equations. Splitting horizontal motion into betatron part and dispersion part $x = x_\beta + \eta p_\sigma$, $p_x = p_{x\beta} + \xi p_\sigma$, neglecting betatron motion $x_\beta = 0$, $p_{x\beta} = 0$ yields equations

$$\sigma' = -K_0\eta p_\sigma - \xi^2 \frac{p_\sigma^2}{2} - \frac{p_z^2}{2} \quad (10)$$

$$p'_\sigma = \left(-\frac{eV_0}{p_0c} \right) \left(\sin \phi_s + \frac{2\pi\sigma}{\lambda_{RF}} \cos \phi_s \right) \delta(s - s_0) - \Gamma \left[K_0^2 + p_\sigma(2K_0^2 + 2K_0K_1\eta + K_0^3\eta) + K_1^2(\eta^2 p_\sigma^2 + y^2) \right]. \quad (11)$$

Averaging of the obtained equations over the revolution period (as usually done for synchrotron motion) introduces familiar quantities: momentum compaction

$$\alpha = \langle K_0\eta \rangle = \frac{1}{\Pi} \oint K_0\eta ds, \quad (12)$$

the relative energy loss from dipoles per turn

$$\frac{1}{\Pi} \frac{U_0}{p_0c} = \Gamma \langle K_0^2 \rangle, \quad (13)$$

wave vector of synchrotron oscillations

$$k_s^2 = \frac{\alpha}{\Pi} \left(-\frac{eV_0}{p_0c} \right) \sum \frac{\pi}{\lambda_{RF}} \cos \phi_s = \left(\frac{\nu_s}{R} \right)^2, \quad (14)$$

longitudinal damping decrement

$$\begin{aligned} 2\alpha_\sigma[m^{-1}] &= \Gamma \langle (2K_0^2 + 2K_0K_1\eta + K_0^3\eta) \rangle \\ &= \frac{U_0}{\Pi p_0c} \left(2 + \frac{\oint \sum K_0K_1\eta + K_0^3\eta ds}{\oint \sum ds} \right) \\ &= \frac{U_0}{\Pi p_0c} \left(2 + \frac{I_4}{I_2} \right), \end{aligned} \quad (15)$$

where $\Pi = 2\pi R$ is the ring circumference, R is the average radius, angular brackets denote averaging over circumference $\langle \dots \rangle = \oint \sum \dots ds / \Pi$, ν_s is the synchrotron oscillations tune,

the RF field phase is chosen according to $(-eV_0) \sin \phi_s = U_0$, I_4 and I_2 are the synchrotron integrals [13].

The factors $\langle \xi^2 \rangle$ and $\langle K_1^2 \eta^2 \rangle$ are small, and multiplication by p_σ^2 makes them even smaller; therefore, we neglect them.

In order to deal with the terms y^2 and p_y^2 , we use the principal solution of the vertical motion equation [14]

$$y = A_y f_y + A_y^* f_y^* \quad (16)$$

$$p_y = A_y f_y' + A_y^* f_y^{*'},$$

where constant amplitude A_y depends on initial conditions, f_y is Floquet function with following properties

$$f_y = \sqrt{\beta_y} e^{i\psi_y}, \quad (17)$$

$$\psi_y(s) = \int_0^s \frac{d\tau}{\beta_y(\tau)}, \quad (18)$$

$$f_y f_y^{*'} - f_y' f_y^* = -2i, \quad (19)$$

$$f_y' = \frac{1}{\sqrt{\beta_y}} \left(\frac{\beta_y'}{2} + i \right) e^{i\psi_y}, \quad (20)$$

$$f_y' f_y^{*'} = \frac{1}{\beta_y} \left[\left(\frac{\beta_y'}{2} \right)^2 + 1 \right] = \gamma_y, \quad (21)$$

$$f_y'^2 = \frac{1}{\beta_y} \left[\left(\frac{\beta_y'}{2} \right)^2 - 1 + i\beta_y' \right] e^{i2\psi_y}, \quad (22)$$

where i is imaginary unit, β_y is beta function, ψ_y is betatron phase advance. Hence,

$$y^2 = (A_y f_y + A_y^* f_y^*)^2 = J_y \beta_y + A_y^2 f_y^2 + A_y^{*2} f_y^{*2}, \quad (23)$$

$$p_y^2 = (A_y f_y' + A_y^* f_y^{*'})^2 = J_y \gamma_y + A_y^2 f_y'^2 + A_y^{*2} f_y^{*2},$$

where action relates to amplitudes as $J_y = 2A_y A_y^*$, Twiss parameter gamma is $\gamma_y = (1 + \alpha_y^2)/\beta_y$, $\alpha_y = -\beta_y'/2$ and the subscript prime ' denotes d/ds .

In order to use Krylov-Bogolyubov averaging method we expand p_y^2 and $\Gamma K_1^2 y^2$ into Fourier series:

$$\begin{aligned} \Gamma K_1^2 y^2 &= \Gamma K_1^2 \beta_y J_y + \Gamma A_y^2 e^{i2k_y s} \sum_{n=-\infty}^{\infty} F_{y,n} e^{in \frac{s}{R}} \\ &\quad + \Gamma A_y^{*2} e^{-i2k_y s} \sum_{n=-\infty}^{\infty} F_{y,n}^* e^{-in \frac{s}{R}}, \end{aligned} \quad (24)$$

$$\begin{aligned} p_y^2 &= J_y \gamma_y + A_y^2 e^{i2k_y s} \sum_{n=-\infty}^{\infty} P_{y,n} e^{in \frac{s}{R}} \\ &\quad + A_y^{*2} e^{-i2k_y s} \sum_{n=-\infty}^{\infty} P_{y,n}^* e^{-in \frac{s}{R}}, \end{aligned} \quad (25)$$

where $k_y = 2\pi\nu_y/\Pi = \nu_y/R$ is a wave vector of vertical betatron oscillations with tune ν_y ,

$$\begin{aligned} F_{y,n} &= \frac{1}{\Pi} \int_0^{\Pi} K_1^2(s) f_y^2(s) e^{-i2k_y s - in \frac{s}{R}} ds \\ &= \frac{1}{\Pi} \int_0^{\Pi} K_1^2(s) \beta_y(s) e^{i(2\psi_y(s) - 2\nu_y \frac{s}{R} - n \frac{s}{R})} ds, \end{aligned} \quad (26)$$

$$P_{y,n} = \frac{1}{\Pi} \int_0^{2\pi} f_y'^2(s) e^{-i2k_y s - i n \frac{s}{R}} ds$$

$$= \frac{1}{\Pi} \int_0^{2\pi} \frac{1}{\beta_y(s)} \left(\frac{\beta_y'(s)}{2} \right)^2 - 1 + i\beta_y'(s) \times \quad (27)$$

$$\times e^{i(2\psi_y(s) - 2\nu_y \frac{s}{R} - n \frac{s}{R})} ds.$$

Applying averaging method and keeping only slowly oscillating terms (Jowett omitted these terms in [15]) yields equations of motion

$$\sigma' = -\alpha p_\sigma - J_y \frac{\langle \gamma_y \rangle}{2}$$

$$- \frac{A_y^2}{2} P_{y,n} e^{i \frac{s}{R} (2\nu_y + n)} \quad (28)$$

$$- \frac{A_y^{*2}}{2} P_{y,n}^* e^{-i \frac{s}{R} (2\nu_y + n)},$$

$$p_\sigma' = \frac{k_s^2}{\alpha} \sigma - 2\alpha_\sigma p_\sigma - \Gamma \langle K_1^2 \beta_y \rangle J_y$$

$$- \Gamma A_y^2 F_{y,n} e^{i \frac{s}{R} (2\nu_y + n)} \quad (29)$$

$$- \Gamma A_y^{*2} F_{y,n}^* e^{-i \frac{s}{R} (2\nu_y + n)},$$

where $n = -[2\nu_y]$ is the negative integer part of the double betatron tune and is the only slow oscillating harmonic.

Synchronous Phase

Equating the right parts of the Eqs. (28) and (29) to zero and eliminating the oscillating terms results in synchronous longitudinal point

$$\sigma = -\frac{\alpha_\sigma}{k_s^2} \langle \gamma_y \rangle \sum_y + \frac{\alpha}{k_s^2} \Gamma \langle K_1^2 \beta_y \rangle J_y \quad (30)$$

$$p_\sigma = -\frac{1}{2\alpha} \langle \gamma_y \rangle J_y, \quad (31)$$

where the term with Γ corresponds to additional energy loss from radiation in quadrupoles, the other terms come from lengthening of particle trajectory. Jowett obtained similar equations in [6] and [16].

Particle with not adjusted initial conditions will develop synchrotron oscillations with respect to the new synchronous point. Using the longitudinal invariant

$$\sigma^2 + \frac{\alpha^2}{k_s^2} p_\sigma^2 = const \quad (32)$$

yields maximum energy deviation

$$p_{\sigma,max} = J_y \sqrt{-\frac{\alpha_\sigma \langle \gamma_y \rangle}{k_s \alpha} + \frac{\Gamma \langle K_1^2 \beta_y \rangle \sum_y}{k_s} + \frac{\langle \gamma_y \rangle^2}{4\alpha^2}} \quad (33)$$

Solution without Oscillating Terms

Solution of Eqs. (28) and (29) without oscillating terms is known and consist of the constant term describing the shift of synchronous energy, and two terms describing damping

synchrotron oscillations (only for p_σ)

$$p_\sigma = -\frac{\langle \gamma_y \rangle}{2\alpha} \sum_y + B_1 e^{-\alpha_\sigma s} \cos \left(s \sqrt{k_s^2 - \alpha_\sigma^2} \right)$$

$$+ B_2 e^{-\alpha_\sigma s} \sin \left(s \sqrt{k_s^2 - \alpha_\sigma^2} \right) \sum \quad (34)$$

Particular Solution

Introducing $\mathfrak{x}_y = (2\nu_y + n)/R$ and transforming the system of first order differential Eqs. (28) and (29) into the the second order equation gives

$$p_\sigma'' + k_s^2 p_\sigma + 2\alpha_\sigma p_\sigma' =$$

$$- A_y^2 \left(\sum_s^2 P_{y,n} + i\Gamma \mathfrak{x}_y F_{y,n} \right) \sum \mathfrak{x}_y s \quad (35)$$

$$- A_y^{*2} \left(\sum_s^2 P_{y,n}^* - i\Gamma \mathfrak{x}_y F_{y,n}^* \right) \sum \mathfrak{x}_y s.$$

Particular solution of Eq. (35) is

$$p_\sigma = -\frac{A_y^2 \left(\sum_s^2 P_{y,n} + i\Gamma \mathfrak{x}_y F_{y,n} \right)}{k_s^2 - \mathfrak{x}_y^2 + i2\mathfrak{x}_y \alpha_\sigma} e^{i\mathfrak{x}_y s}$$

$$- \frac{A_y^{*2} \left(\sum_s^2 P_{y,n}^* - i\Gamma \mathfrak{x}_y F_{y,n}^* \right)}{k_s^2 - \mathfrak{x}_y^2 - i2\mathfrak{x}_y \alpha_\sigma} e^{-i\mathfrak{x}_y s}. \quad (36)$$

Since

$$\mathfrak{x}_y \gg k_s \gg \alpha_\sigma, \quad (37)$$

$$\Gamma \mathfrak{x}_y |F_{y,n}| \gg \frac{k_s^2}{2\alpha} |P_{y,n}| \quad (38)$$

we can rewrite solution as

$$p_\sigma \approx iA_y^2 \frac{\Gamma F_{y,n}}{\mathfrak{x}_y} e^{i\mathfrak{x}_y s} - iA_y^{*2} \frac{\Gamma F_{y,n}^*}{\mathfrak{x}_y} e^{-i\mathfrak{x}_y s}. \quad (39)$$

Putting it in the form comfortable for the future use we have

$$p_\sigma = c_n A_y^2 e^{i\mathfrak{x}_y s} + c_n^* A_y^{*2} e^{-i\mathfrak{x}_y s}$$

$$= |c_n| J_y \cos(\mathfrak{x}_y s + \chi_0) \sum \quad (40)$$

where

$$c_n = -\frac{\left(\frac{k_s^2}{2\alpha} P_{y,n} + i\Gamma \mathfrak{x}_y F_{y,n} \right)}{k_s^2 - \mathfrak{x}_y^2 + i2\mathfrak{x}_y \alpha_\sigma} \approx i \frac{\Gamma F_{y,n}}{\mathfrak{x}_y} \quad (41)$$

and the phase $\chi_0 = \arg(c_n A_y^2)$ depends on transverse initial conditions. The appearance of phase χ_0 is ambiguous, because in the averaging over the revolution period we lose all the information regarding particle initial transverse phase. Therefore, we will choose χ_0 in order to simplify further calculations.

SOLUTION OF VERTICAL EQUATIONS OF MOTION

With the same assumptions as in the previous paragraph Eqs. (6) and (7) are

$$y' = p_y - p_y p_\sigma, \quad (42)$$

$$p_y' = K_1 y + K_2 \eta p_\sigma y - \Gamma p_y [K_0^2 + p_\sigma D + K_1^2 y^2], \quad (43)$$

where $D = 2K_0^2 + 2K_0 K_1 \eta + K_0^3 \eta$ and for machines with separate functions magnets is negligible, we neglected the small term $\Gamma p_y K_1^2 \eta^2 p_\sigma^2$. We may apply Krylov-Bogolyubov averaging method directly to Eq. (42), Eq. (43), but it is more illustrative to apply it to y'' equation. During derivation of y'' equation we neglect the terms containing p_σ' , because it either oscillates with synchrotron tune or with double fractional part of betatron frequency, and after derivation will receive a small factor. The desired equation is

$$y'' - (K_1 - (K_1 - K_2 \eta) p_\sigma) y + \Gamma (K_0^2 + K_1^2 y^2) y' = 0. \quad (44)$$

This is an equation of parametric oscillator; the second term depends on p_σ which contains terms oscillating at fractional double betatron frequency Eq. (40). It is also a Van der Pol oscillator (nonlinear friction, the the third term). Jowett obtained Van der Pol equation for nonlinear wiggler (combined quadrupole and sextupole) in [16].

Substituting expression for p_σ , we neglect the constant shift and damped synchrotron oscillations Eq. (34), and keep only particular solution Eq. (40) oscillating on fractional part of double betatron frequency, i.e. we consider only parametric resonance. Substituting principal solution for y Eq. (16), averaging and keeping only slowly oscillating terms yields equation for amplitude evolution

$$\begin{aligned} (-2i)A_y' &= A_y \langle \Gamma K_0^2 (-\alpha_y + i) \rangle \\ &+ A_y^2 A_y^* |c_n| \langle (K_1 - K_2 \eta) \beta_y e^{i(-2\psi_y + \alpha_{y,s} + \chi_0)} \rangle \\ &- 3A_y^2 A_y^* \langle \Gamma K_1^2 \beta_y \alpha_y \rangle \sum i A_y^2 A_y^* \langle \Gamma K_1^2 \beta_y \rangle. \end{aligned} \quad (45)$$

The terms $\langle \Gamma K_1^2 \beta_y \alpha_y \rangle$ and $\langle \Gamma K_1^2 \beta_y \rangle$ are small and we neglect them, obtaining

$$\begin{aligned} A_y' &= -\frac{1}{2} \langle \Gamma K_0^2 (1 + i\alpha_y) \rangle A_y \\ &+ \frac{i}{2} |c_n| \langle (K_1 - K_2 \eta) \beta_y e^{i(-2\psi_y + \alpha_{y,s} + \chi_0)} \rangle A_y^2 A_y^* \\ &= -B_1 A_y + iB_2 A_y^2 A_y^*. \end{aligned} \quad (46)$$

The real part of the obtained equation describes evolution of the A_y (e.g. damping), the imaginary part describes the change of the betatron tune. In order to solve Eq. (46) we introduce coefficients

$$B_1 = \frac{1}{2} \langle \Gamma K_0^2 (1 + i\alpha_y) \rangle \quad (47)$$

$$B_2 = \frac{1}{2} |c_n| \langle (K_1 - K_2 \eta) \beta_y e^{i(-2\psi_y + \alpha_{y,s} + \chi_0)} \rangle \quad (48)$$

where phase χ_0 appeared from Eq. (40) and is undefined. Multiplying Eq. (46) by A_y^* and adding a complex conjugate of the equation yields

$$(A_y A_y^*)' = -2\text{Re}(B_1) A_y A_y^* - 2\text{Im}(B_2) (A_y A_y^*)^2 \quad (49)$$

or

$$J_y' = -2\text{Re}(B_1) J_y \mp \text{Im}(B_2) J_y^2, \quad (50)$$

where $J_y = 2A_y A_y^*$, $\text{Re}()$ and $\text{Im}()$ stand for real and imaginary parts. The first term describes damping of the action with vertical damping coefficient $2\text{Re}(B_1) = \langle \Gamma K_0^2 \rangle$, the second term if negative increases damping, if positive than counteracts damping. The sign of the second terms depends on the sign of the phase χ_0 , which appeared from solving averaged over revolution period longitudinal equations of motion Eqs. (35) and (40). Since longitudinal motion is slow than it can not depend on the phase of the transverse motion; whatever the phase was initially, it will change with time. Therefore, originally damping oscillations will change into rising oscillations (parametric resonance). Equation (50) solution is

$$J_y(s) = \frac{J_{y,0} e^{-2\text{Re}(B_1)s}}{1 \pm J_{y,0} \frac{\text{Im}(B_2)}{2\text{Re}(B_1)} (1 - e^{-2\text{Re}(B_1)s})}. \quad (51)$$

With appropriate sign before the second term, Eq. (50) permits existence of the boundary initial actions $J_{y,\text{lim}}$: lower initial actions will provide negative J_y' i.e. damping, larger will provide positive J_y' i.e. rising or unstable motion. This limiting action is the boarder of dynamic aperture and is

$$J_{y,\text{lim}} = \frac{2\text{Re}(B_1)}{\pm \text{Im}(B_2)}. \quad (52)$$

Existence of initial amplitudes with stable motion at parametric resonance is due to friction (radiation damping).

Parametric resonance In order to prove the choice of χ_0 we will solve Eq. (46) differently. Distinguishing modulus and argument of amplitude $A_y = a_y e^{i\varphi_y}$, $B_1 = |B_1| e^{i\varphi_1}$, $B_2 = |B_2| e^{i\varphi_2 + i\chi_0}$ and substituting in Eq. (46) results in two equations

$$a_y' = -a_y |B_1| \cos(\varphi_1) - a_y^3 |B_2| \sin(-2\varphi_y + \varphi_2 + \chi_0) \quad (53)$$

$$\varphi_y' = -|B_1| \sin(\varphi_1) + a_y^2 |B_2| \cos(-2\varphi_y + \varphi_2 + \chi_0) \quad (54)$$

where $|B_1| \sin(\varphi_1) = \text{Im}(B_1) = \frac{1}{2} \langle \Gamma K_0^2 \alpha_y \rangle \approx 0$ is small and describes the change of vertical betatron tune because of damping; this is equivalent to $\varphi_1 = 0$. The second term in Eq. (54) describes tune dependence on amplitude. Equations (53) and (54) have complex topology in $\{a_y, \varphi_y\}$ space, which has two stable points $\varphi_y = \varphi_2 + \chi_0 \pm \pi/4$ providing

$\varphi'_y = 0$. At this points the modulus of amplitude is

$$a_y(s) = \frac{a_{y,0}e^{-|B_1|s}}{1 + a_{y,0}^2 \frac{|B_2|}{|B_1|} \sin(-2\varphi_y + \varphi_2 + \chi_0) (1 - e^{-|B_1|s})}$$

$$= \frac{a_{y,0}e^{-|B_1|s}}{1 \pm a_{y,0}^2 \frac{|B_2|}{|B_1|} (1 - e^{-|B_1|s})} . \quad (55)$$

The amplitude has two solutions: rising and damping. This is typical for parametric resonance and damping solution always changes into rising.

LONGITUDINAL AND HORIZONTAL MOTION

Horizontal (Eqs. (4-5)) and longitudinal (Eqs. (8-9)) equations of motion with $y = 0$ and $p_y = 0$ are similar to longitudinal and vertical Eqs. (6-7) with $x_\beta = 0$ $p_{x\beta} = 0$. The unique for horizontal motion term $-K_0 x_\beta$ in Eq. (8) will produce a synchro-betatron resonance at $\nu_x \pm \nu_s = \text{integer}$. This resonance plays an important role, but out of scope of our work. Table 3 shows that the shift of synchronous point and amplitude of synchrotron oscillations, if initial longitudinal coordinates are not adjusted to the new synchronous point, are significantly larger for horizontal oscillations than for vertical at the boundary of dynamic aperture. Observation of

Table 3: Synchronous point and amplitude of synchrotron oscillations for different transverse initial conditions

$\{X_0, Y_0\}$	$\{67\sigma_x, 0\}$	$\{0, 58\sigma_y\}$
$p_{\sigma, \max}/\sigma_\delta$	4	0.26
$p_{\sigma, \text{syn}}/\sigma_\delta$	-2.5	-0.026
$\sigma_{\text{syn}}/\sigma_\delta$	3.05	0.29

phase advance per turn (bottom left) on Fig. 8 suggests that particle is lost when phase advance reaches an integer (turn 65) and it happens when $p_\sigma = 7\sigma_\delta$. Using the detuning coefficient and its chromaticity with initial conditions yields

Table 4: Tune shift contribution from detuning and detuning chromaticity

$\frac{\partial \nu_x}{\partial J_x}$	-5×10^4
$\frac{\partial^2 \nu_x}{\partial J_x \partial \delta}$	-6.8×10^7
J_x	$67^2 \varepsilon_x / 2$
p_σ	$7\sigma_\delta$
$\Delta \nu_x = \frac{\partial \nu_x}{\partial J_x} J_x$	-0.03
$\Delta \nu_x = \frac{\partial^2 \nu_x}{\partial J_x \partial \delta} J_x p_\sigma$	-0.11
$\nu_x(J_x = 0, p_\sigma = 0)$	0.14

COMPARISON WITH TRACKING AND NUMERICAL ESTIMATIONS

For given vertical tune harmonic number is $n = -534$, $\mathfrak{x}_y = 2.8 \times 10^{-5} \text{ m}^{-1}$, $k_s = 2.6 \times 10^{-6} \text{ m}^{-1}$. The harmonics Eqs. (26), (27) and (41) are

$$F_{y,n} = (-0.14, 3 \times 10^{-5}) \text{ m}^{-3} \quad F_{y,n} = 0.14 \text{ m}^{-3}$$

$$P_{y,n} = (-0.13, 0.0006) \text{ m}^{-1} \quad P_{y,n} = 0.13 \text{ m}^{-1}$$

$$c_n = (-42.11, -6474.19) \text{ m}^{-1} \quad |c_n| = 6474.33 \text{ m}^{-1} .$$

The numbers prove the inequality Eq. (38)

$$\Gamma \mathfrak{x}_y F_{y,n} = 5.13 \times 10^{-6}$$

$$\frac{k_s^2}{2\alpha} P_{y,n} = 3.22 \times 10^{-8} .$$

Coefficients Eqs. (47) and (48) are

$$B_1 = (4.03 \times 10^{-9}, -2.76 \times 10^{-10}) \text{ m}^{-1}$$

$$|B_1| = 4.04 \times 10^{-9} \text{ m}^{-1}$$

$$B_2 = (10.35, 6.43) \text{ m}^{-2}$$

$$|B_2| = 12.18 \text{ m}^{-2} .$$

The border of dynamic aperture Eq. (52) is

$$R_y = \overline{2J_{y, \text{lim}} \beta_y} = 51.2\sigma_y , \quad (56)$$

which corresponds well to the tracking result $R_y = 57\sigma_y$.

Resemblance of longitudinal phase trajectories on Figs. 5 and 9 proves our approach in solving longitudinal Eqs. (28) and (29). Figure 9 presents numerical solution of the longitudinal Eqs. (28) and (29) with vertical action in the form Eq. (51) corresponding to initial condition $y = 58\sigma_y$.

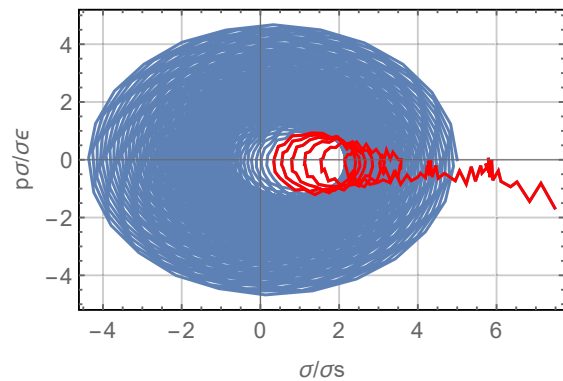


Figure 9: Longitudinal phase trajectories from numerical solution of Eqs. (28) and (29) with vertical action in the form Eq. (51) corresponding to initial condition $y = 58\sigma_y$. The last 200 turns are shown in red. Compare with top right plot of Figure 5.

Figure 10 and Fig. 11 compare results of tracking and calculations of longitudinal coordinate evolution (synchronous phase) when initial longitudinal conditions were adjusted

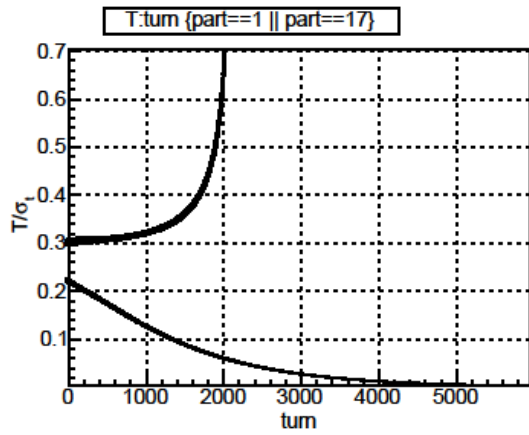


Figure 10: Evolution of longitudinal coordinate from tracking corresponding to initial conditions $y = 50\sigma_y$ and $y = 58\sigma_y$ and adjusted longitudinal initial conditions Eqs.(30) and (31).

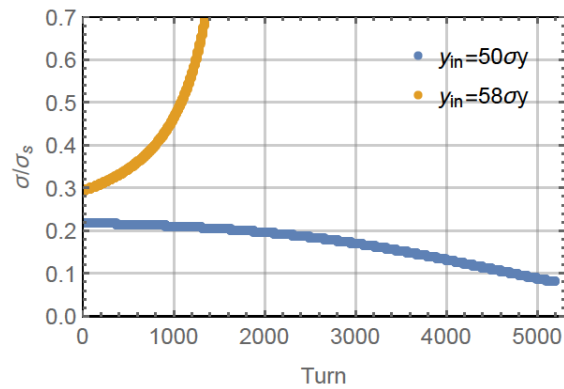


Figure 11: Evolution of longitudinal coordinate from calculations by Eqs. (30) and (31) corresponding to initial conditions $y = 50\sigma_y$ and $y = 58\sigma_y$.

according to Eqs. (31) and (30) in order to eliminate synchrotron oscillations, for two particles with $y = 50\sigma_y$ and $y = 58\sigma_y$.

Figure 12 and Fig. 13 show spectra of vertical and longitudinal motion, proving existence of fractional part of double betatron frequency in longitudinal motion. The double frequency harmonic amplitude according to Eq. (40) is $p_\sigma = 3.6 \times 10^{-2}\sigma_\delta$, which closely corresponds to the value on Fig. 13

Figure 14 and Fig. 15 compare vertical action evolution from tracking and calculation with Eq. (51). The boundary of stable motion is $57.5\sigma_y$ from tracking and $51\sigma_y$ from calculations by Eq. (52).

CONCLUSION

In horizontal plane, additional energy loss due to radiation in quadrupoles, shifts synchronous point and develops large synchrotron oscillations. Horizontal betatron tune dependence on amplitude and chromaticity of this detuning shift the tune toward the integer resonance resulting in particle

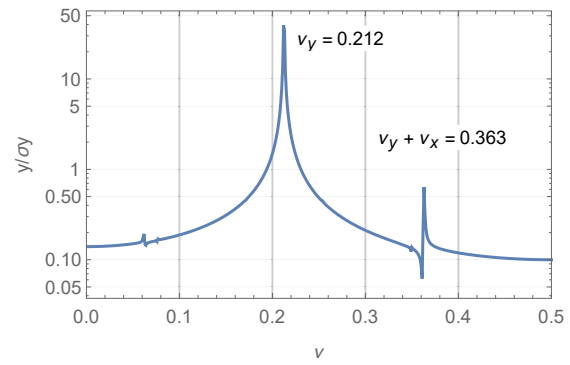


Figure 12: Spectrum of vertical motion tracking corresponding to initial condition $y = 58\sigma_y$, and adjusted longitudinal initial conditions Eqs. (30) and (31).

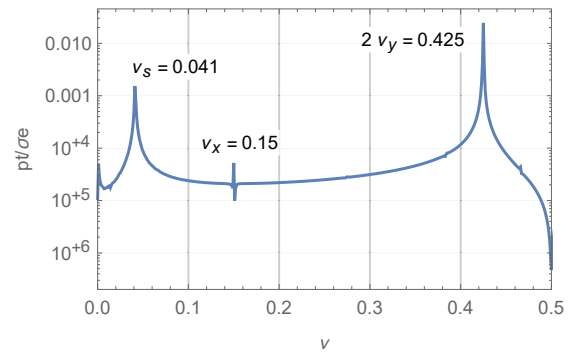


Figure 13: Spectrum of longitudinal motion tracking corresponding to initial condition $y = 58\sigma_y$, and adjusted longitudinal initial conditions Eqs. (30) and (31).

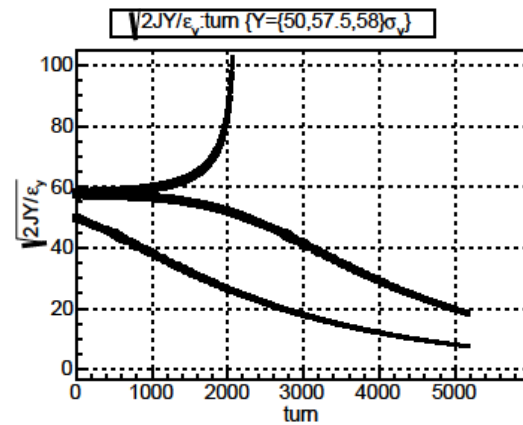


Figure 14: Evolution of normalized square root of vertical action from tracking corresponding to initial conditions $y = 50\sigma_y$, $y = 57.5\sigma_y$, $y = 58\sigma_y$, and adjusted longitudinal initial conditions in Eqs. (30) and (31).

loss. This is similar to Radiative Beta-Synchrotron Coupling (RBSC) proposed by Jowett [6].

Dynamic aperture reduction in the vertical plane with inclusion of synchrotron radiation in quadrupoles in FCC-ee is due to parametric resonance. Radiation from quadrupoles modulates the particle energy at the double betatron fre-

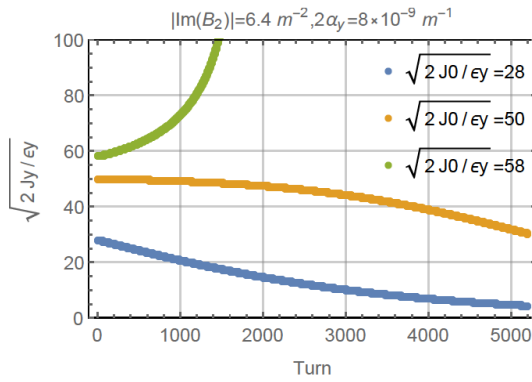


Figure 15: Evolution of normalized square root of vertical action from tracking corresponding to initial conditions $y = 28\sigma_y$, $y = 50\sigma_y$, $y = 58\sigma_y$.

quency; therefore, quadrupole focusing strength also varies at the doubled betatron frequency creating the resonant condition. However, due to friction, resonance develops only if oscillation amplitude is larger than a certain value. The remarkable property of this resonance is that it occurs at any betatron tune (not exactly at half-integer) and hence can be labeled as “self-inducing parametric resonance”. Our calculations give the border of dynamic aperture $R_y = 51.2\sigma_y$, which corresponds well to the tracking result $R_y = 57\sigma_y$.

REFERENCES

- [1] FCC site: <http://cern.ch/fcc>
- [2] CEPC site: <http://cepc.ihep.ac.cn/>
- [3] Augustin, J.E. and Dikansky, N. and Derbenev, Ya. and Rees, J. and Richter, Burton and others, “Limitations on performance of e^+e^- storage rings and linear colliding beam systems at high energy”, *eConf, C781015*, 1978, pp. 87-105.
- [4] Telnov, V. I., “Restriction on the energy and luminosity of e^+e^- storage rings due to beamstrahlung”, *Phys. Rev. Lett.*, 110(11), 2013, pp.114801-114806,
- [5] A. Bogomyagkov, E. Levichev, and D. Shatilov, “Beam-beam effects investigation and parameters optimization for a circular e^+e^- collider TLEP to study the Higgs boson”, *Phys. Rev. ST Accel. Beams* 17, (2014) 041004.
- [6] Jowett, J., “Dynamic aperture for LEP: Physics and calculations”, *Proceedings: LEP Performance Workshop*, 4th, Chamonix, France, Jan, 17-21, 1994, pp. 47-71.
- [7] Barbarin, F. and Iselin, F. C. and Jowett, J. M., “Particle dynamics in LEP at very high-energy”, *4th European Particle Accelerator Conference (EPAC 94) London*, England, June 27-July 1, 1994, pp. 193-195.
- [8] Jowett, John M., “Beam dynamics at LEP”, *CERN-SL-98-029-AP*, 1998., pp. 15-38.
- [9] SAD site: <http://acc-physics.kek.jp/SAD/index.html>
- [10] Oide, K. and others, “Design of beam optics for the Future Circular Collider e^+e^- -collider rings”, *Phys. Rev. Accel. Beams*, 19(11):111005, 2016 [Addendum: *Phys. Rev. Accel. Beams* 20, no.4, 049901(2017)].
- [11] MADX site: <http://madx.web.cern.ch/madx/>.
- [12] S. Glukhov and others, “6D Tracking with Compute Unified Device Architecture (CUDA) technology”, WEP34, *Proceedings of ICAP2015*, Shanghai, China, 2015, pp. 115-117.
- [13] Helm, Richard H. and Lee, Martin J. and Morton, P. L. and Sands, M., “Evaluation of synchrotron radiation integrals”, *Proceedings, 1973 Particle Accelerator Conference*, Accelerator Engineering and Technology: San Francisco, California, March 5-7, 1973, *IEEE Trans. Nucl. Sci.*, 20, 1973, pp. 900-901.
- [14] Courant, E. D. and Snyder, H. S., “Theory of the alternating gradient synchrotron”, *Annals Phys.*, 3, 1958, pp. 1-48 [Annals Phys.281,360(2000)].
- [15] Jowett, John M., “Introductory statistical mechanics for electron storage rings”, *AIP Conf. Proc.*, 153, 1987, pp. 864-970.
- [16] Jowett, John M., “Electron dynamics with radiation and non-linear wigglers”, *CERN Accel.School* 1985:0570, 1986.

LOW-EMITTANCE TUNING FOR CIRCULAR COLLIDERS

T.K. Charles^{*12}, S. Aumon³, B. Holzer¹, K. Oide¹⁴, T. Tydecks¹, F. Zimmermann¹,

¹ European Organization for Nuclear Research (CERN), Geneva, Switzerland

² School of Physics, University of Melbourne, 3010, Victoria, Australia

³ ADAM SA (Applications of Detector and Accelerators to Medicine), Geneva, Switzerland

⁴ KEK, Oho, Tsukuba, Ibaraki 305-0801, Japan

Abstract

The 100 km FCC-ee e^+e^- circular collider requires luminosities in the order of $10^{35} \text{ cm}^{-2} \text{ s}^{-1}$ and very low emittances of 0.27 nm-rad for the horizontal plane and 1 pm-rad in the vertical. In order to reach these requirements, extreme focusing of the beam is needed in the interaction regions, leading to a vertical beta function of 0.8 mm at the IP. These challenges make the FCC-ee design particularly susceptible to misalignment and field errors. This paper describes the tolerance of the machine to magnet alignment errors and the effectiveness of optics and orbit correction methods that were implemented in order to bring the vertical dispersion to acceptable values, which in turn limits the vertical emittance. Thousands of misalignment and error seeds were introduced in MADX simulations and a comprehensive correction strategy, which includes macros based upon Dispersion Free Steering (DFS), linear coupling correction based on Resonant Driving Terms (RDTs) and response matrices, was implemented. The results are summarized in this paper.

INTRODUCTION

Electron-positron circular colliders profit from small vertical beam size due to vertical emittances close to the quantum excitation. The light source community has propelled the drive for smaller and smaller vertical emittances [1,2]. Many of the lessons learned can be applied to circular electron-positron colliders in their strive for higher luminosity.

The Future Circular Collider (FCC) will have four energies of operation ranging from the Z-pole (45.6 GeV=beam) to the $t\bar{t}$ production threshold (182.5 GeV=beam) [3]. A summary of the key parameters can be found in Table 1 and in the upcoming Conceptual Design Report (CRD).

In order to produce a high luminosity, extreme focusing is required at the interaction regions. With this comes challenging optics parameters. For the Z resonance, a vertical β^* of 0.8 mm, and a vertical emittance of 1 pm-rad is required, for a luminosity of $230 \times 10^{34} \text{ cm}^{-2} \text{ s}^{-1}$. Within the final focusing region, the maximum values of the beta functions $\beta_{x,\text{max}} = 1587.97 \text{ m}$ and $\beta_{y,\text{max}} = 6971.55 \text{ m}$ (see Fig. 1).

These large beta values, and the strong sextupoles required for chromaticity correction, make the machine extremely sensitive to magnet misalignments and field errors.

The two main sources of vertical emittance growth are coupling between the transverse planes and residual vertical dispersion. The betatron coupling poses a large threat due

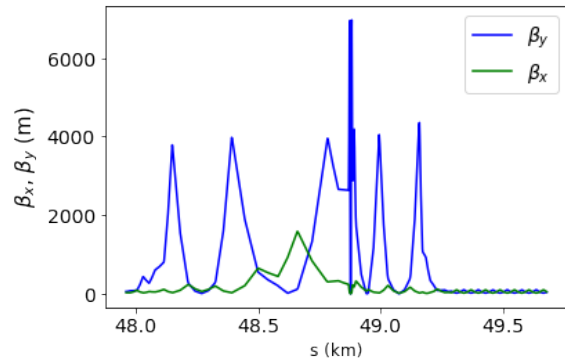


Figure 1: Beta functions near one of the IPs for the 182.5 GeV lattice. The maximum values of the beta functions $\beta_{x,\text{max}} = 1587.97 \text{ m}$ and $\beta_{y,\text{max}} = 6971.55 \text{ m}$.

Table 1: Baseline beam parameters of the four operational energies for FCCee [3].

Parameters	Z	W	H	$t\bar{t}$
Beam Energy [GeV]	45.6	80	120	182.5
ϵ_x [nm-rad]	0.27	0.28	0.63	1.45
ϵ_y [pm-rad]	1	1	1.3	2.7
Beam current [mA]	1390	147	29	5.4
\mathcal{L} [$10^{34} \text{ cm}^{-2} \text{ s}^{-1}$]	230	32	8	1.5

to the small emittance ratio (or coupling ratio) of $\epsilon_y/\epsilon_x = 0.27 \%$ (for the Z energy). The vertical dispersion grows the vertical emittance in accordance with the equilibrium emittance equation,

$$\epsilon_y = \left(\frac{dp}{p} \right)^2 (\gamma D_y^2 + 2\alpha D_y D'_y + \beta D_y'^2) \quad (1)$$

where D_y is the vertical dispersion, D'_y is the derivative of the dispersion with respect to s , dp/p is the momentum spread, and γ , α and β are the usual Twiss parameters.

Generally the smaller the value of the beta function at the IP, β_y^* , the larger the chromaticity, and the stronger the chromaticity correction required [4]. The sextupole magnets employed for this chromaticity correction introduce nonlinearities in the ring, which can lead to difficulties in performing the correction schemes that are outlined in the next section. This is because the correction techniques are inherently linear. If the beam is directed off-axis through the sextupole magnets, the effect to the beam seeing a skew quadrupole field, unaccounted for in the correction schemes.

* tessa.charles@cern.ch

Initial Assessment of Errors

Small misalignment errors were introduced and the resulting effect of vertical dispersion and the vertical orbit were measured. These results, which are summarized in Table 2, indicate that arc quadrupole vertical misalignment has the largest influence on the vertical dispersion. Introducing an error of only $2 \mu\text{m}$ randomly Gaussian distributed around the ring, will increase the maximum vertical dispersion to 326.71 mm .

Figure 2 shows the distribution of the vertical dispersions for 100 difference seeds, resulting from quadrupole vertical misalignments of $2 \mu\text{m}$ and then sextupole vertical misalignments of $10 \mu\text{m}$.

Vertical quadrupole misalignments result in vertical closed orbit distortion which can generate vertical emittance growth from vertical dispersion, as well as vertical emittance growth from betatron coupling coming from vertical beam misalignment in the sextupoles.

Table 2: Increase (from zero) of the vertical closed orbit and vertical dispersion due to small misalignments and roll angles of individual magnetic elements, to indicate the severity of the errors introduced by various magnets.

Error type	y_{max} (mm)	$D_{y,\text{rms}}$ (mm)
quad arc ($\Delta y = 2 \mu\text{m}$)	8.809	326.71
quad arc ($\Delta x = 10 \mu\text{m}$)	0.0	0.0
quad arc ($\Delta \phi = 10 \mu\text{rad}$)	0.0	2.677
sextupoles ($\Delta y = 10 \mu\text{m}$)	0.0245	57.13
sextupoles ($\Delta x = 10 \mu\text{m}$)	0.0	0.0
sextupoles ($\Delta \phi = 10 \mu\text{rad}$)	0.0	0.004

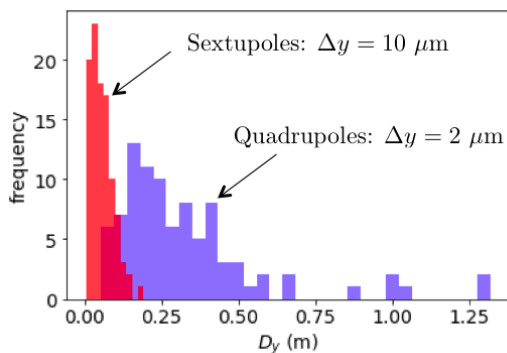


Figure 2: Distribution of vertical dispersion introduced from small sextupole and quadrupole misalignment of $\Delta y = 2 \mu\text{m}$ for the quadrupoles and $\Delta y = 10 \mu\text{m}$ for the sextupoles.

CORRECTION METHODS

Reducing the x - y coupling and residual vertical dispersion over the ring are key to minimizing the vertical emittance and reaching high luminosity. The correction methods implemented (in addition to orbit correction) to achieve this

are Dispersion Free Steering (DFS), coupling correction and beta-beat correction.

The following subsections briefly outline the main components of the correction techniques used.

Table 3 summarizes the magnet misalignment and roll errors used in the simulations presented in the following sections. The values quoted in Table 3 are the standard derivation of the error applied through a Gaussian distribution with a random seed.

Corrector magnets and Beam Position Monitors (BPMs) are installed at every quadrupole magnet, tallying 1598 in the horizontal plane and 1596 in the vertical plane, around the 100 km ring. One skew quadrupole and one trim quadrupole are installed at every sextupole magnet for dispersion free steering and beta beat correction.

Dispersion Free Steering

DFS aims to correct the orbit and dispersion simultaneously, and in doing so effectively overcomes the sensitivity to BPM offsets. The method, which was used at LEP [5], is based upon response matrices relating the orbit, y and dispersion, D_y to the corrector kick, θ ;

$$\begin{pmatrix} (1-\alpha)\vec{y} \\ \alpha\vec{D}_y \end{pmatrix} + \begin{pmatrix} (1-\alpha)\mathbf{A} \\ \alpha\mathbf{B} \end{pmatrix} \vec{\theta}$$

where \mathbf{A} and \mathbf{B} are the responses matrices of the orbit and the dispersion due to a corrector kick, and α is a weight factor, which can shift the emphases to or from correcting the vertical orbit or the vertical dispersion. A singular value decomposition (SVD) of the responses matrices can be written as,

$$\mathbf{A} = \mathbf{U}\mathbf{W}\mathbf{V}^T \quad (2)$$

where the columns of \mathbf{U} are the eigenvectors of $\mathbf{A}\mathbf{A}^T$, and \mathbf{V} are the eigenvectors of $\mathbf{A}^T\mathbf{A}$ and \mathbf{W} is a diagonal matrix of singular values, w_i . The tolerance or cutoff, can be applied with the SVD-method to optimize the efficiency of the calculation. More singular values moves the emphasis to more local correction but more noise, while less singular values will put the emphasis onto more global correction [6].

DFS efficiently reduces the vertical dispersion and the orbit, even in cases where the maximum weight ($\alpha = 1$) is applied on the dispersion. This is convenient for machines very sensitive to BPM reading errors.

The scale of the vertical dispersion before correction is extremely large. The Root Mean Square (RMS) value before correction is 261.1 m . After applying a series of correction methods which includes orbit correction and coupling correction and DFS, the final RMS vertical dispersion at full sextupole strength, is 1.02 mm .

Coupling

Coupling introduced by sextupole misalignment and rolled quadrupoles, can be counteracted through skew quadrupoles installed at every sextupole magnet.

Coupling between the horizontal and vertical planes need to be limited to below 0.1 %, not only in order to ensure the equilibrium vertical emittance is small, but also in order to reduced beam-beam blow up thought to be enlarged when the coupling ratio is greater than 0.1 % [7–9].

The coupling effect can be quantified through two coupling Resonant Driving Terms (RDTs) f_{1001} and f_{1010} . The analytical form of these two terms are:

$$f_{1010}^{1001} = \frac{\sum_w J_e \sqrt{\beta_x^w \beta_y^w} e^{i(\Delta\phi_{w,x} \pm \Delta\phi_{w,y})}}{4(1 - e^{2\pi i i(Q_u \pm Q_v)})} \quad (3)$$

where J is the vector of the skew strength, β_x^w and β_y^w are the horizontal and vertical beta functions at the location of the skew strength, and $\Delta\phi_{w,x}$ and $\Delta\phi_{w,y}$ are the phase advances between the observation point and the skew component in the x and y plane respectively.

A response matrix, \mathbf{M} of the RDTs can be written to measure the response of the RDTs to a skew quadrupole field, $\vec{\mathbf{J}}$. The system, which can be inverted via SVD, is [10]:

$$\begin{pmatrix} f_{1001} \\ f_{1010} \end{pmatrix}_{meas} = -\mathbf{M} \vec{\mathbf{J}}$$

where f_{1001} and f_{1010} are the complex coupling RDTs computed at the BPM locations.

Beta-beta Correction

Beta-beating introduced by offset sextupole magnets and quadrupole field errors, can compromise the value of β^* and reduce the achievable luminosity.

Trim quadrupole fields installed at the sextupole magnets can be used to counteract beta-beating. A response matrix method is used in two stages. Firstly, a response matrix calculated the response of the change in phase advance between the sextupoles where the trim quadrupoles are installed [11]. And in a second response matrix a beta-beating response matrix is measured and the correction applied with a weighted SVD [12].

It has been previously shown [13] that correction of the phase advance is as effective as correcting the actual beta function, and therefore the phase-beating between consecutive BPMs can be used.

For n trim quadrupoles which can exercise a small field strength k_1 , the weighted SVD can be applied through adding weighting factors f to each measurement of the beta-beat.

$$\begin{pmatrix} f_1 \left(\frac{\beta_1 - \beta_{y0}}{\beta_{y0}} \right) \\ f_2 \left(\frac{\beta_2 - \beta_{y0}}{\beta_{y0}} \right) \\ \dots \\ f_m \left(\frac{\beta_m - \beta_{y0}}{\beta_{y0}} \right) \end{pmatrix}_{meas} = \begin{pmatrix} f_1 (R_{11}, R_{12}, R_{13}, \dots, R_{1n}) \\ f_2 (R_{21}, R_{22}, R_{23}, \dots, R_{2n}) \\ \dots \\ f_m (R_{m1}, R_{m2}, R_{m3}, \dots, R_{mn}) \end{pmatrix} * \begin{pmatrix} k_1 \\ k_2 \\ \dots \\ k_n \end{pmatrix}$$

where β_{y0} is the ideal beta function at the given BPM, $R_{i,j}$ are elements in the response matrix.

The weighted SVD can provide additional emphasis on the quadrupoles where large values of the beta function are expected. In our case, a weighting factor of 10 was applied to the quadrupoles where the design value of the β_y was above 3000 m, and for every other quadrupole, the weight factor was unity. By doing this, we can ensure more accurate beta-beat correction at the location of the IP.

Figure 3 shows the iterative application of the weighted SVD approach showing a gradual reduction in the β -beat at the IPs.

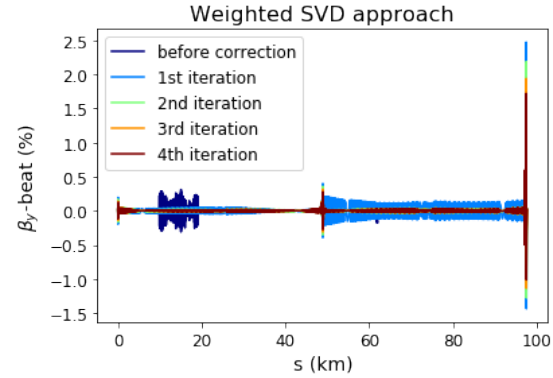


Figure 3: Weighted SVD approach, using a beta-beat response matrix and a weighted of 10 applied to the IP quadrupoles. Note $s = 49$ km and $s = 100$ km correspond to the two IPs.

CORRECTION STRATEGY

In order to minimize the equilibrium vertical emittance, a correction strategy was implemented that utilizes a number of correction schemes. Importantly the sextupole strengths are initial set to zero. This is because the initial magnet misalignment, tilts and field errors are likely to direct the beam off centre through the sextupole magnets, which has the same effect as a skew quadrupole would in its place. This results in a vertical displacement of the closed orbit with respect to the sextupole's magnetic center, and can generate vertical emittance growth through the introduction of vertical dispersion. Therefore the correction strategy begins with turning the sextupoles off. After an initial closed orbit correction, coupling correction, and beta-beat correction, the sextupole strengths are changed to 10 % of the design strength, and further orbit and optics corrections are applied and rematching of the tune. Looping through the correction strategy, increasing the sextupole strength 10 % each time, reduces the likelihood of not being able to find the closed orbit, or the risk of running into the integer or half-integer resonance. The final stage of the correction scheme includes further coupling correction to lower the vertical emittance.

All of the corrections methods were applied without RF activated and energy loss from synchrotron radiation not included. This approach allows for faster computation time and is considered valid for a fully tapered machine [14]. In the final stage of the simulations, synchrotron radiation

Table 3: Misalignment errors introduced into the lattice before correction applied.

	σ_x (μm)	σ_y (μm)	σ_θ (μrad)
arc quadrupoles	100	100	100
IP quadrupoles	0	0	0
sextupoles	100	100	0

is turned on to compute the emittance. The emittance is calculated using the EMIT command in MADX, which is based upon the Chao formalism for equilibrium emittance calculation [15].

The following correction strategy was implemented:

1. Introduce BPMs and corrector magnets at every quadrupole, and introduce skew and trim quadrupoles at every sextupole. Misalignment and roll errors are then applied to magnets around the ring, distributed via a Gaussian distribution truncated at 2.5 sigma. Several simulations with different random seeds were used.
2. Sextupoles were turned off, and an orbit correction performed with MICADO in MADX [16].
3. Coupling correction is performed, followed by rematch-ing of the tune, followed by beat-beat correction.
4. DFS (D_y correction) is performed followed by coupling correction (which is needed due to the change in the corrector strengths brought about by DFS). These two correction techniques are one after another.
5. Sextupoles are then set to 10% of their design strength.
 - (a) orbit corrections
 - (b) coupling correction
 - (c) tune matching
 - (d) beta beat correction
 - (e) coupling + dispersion correction
 - (f) increase sextupole strengths by 10% , and repeat Step 5 until 100% of design sextupole strength is reached.
6. Final correction of coupling and beat-beat correction can be applied in the final step.

CORRECTED LATTICE

After applying the correction scheme outlined in the previous section, the final emittances can be reduced to an acceptable level. Figure 4 shows the vertical dispersion before and after the correction strategy has been applied. Figure 5 shows the distribution of horizontal and vertical emittances for 500 random seeds. The mean vertical of the emittance is 0.093 pm-rad, and the horizontal emittance is 1.520 nm-rad. The ratio of the emittance (or the coupling ratio), $\epsilon_y/\epsilon_x = 0.006\%$.

Including the IP quadrupoles increase the level of difficulty in performing the correction. However a large number of seeds still converge - 700 out of 1000 seeds. For the errors

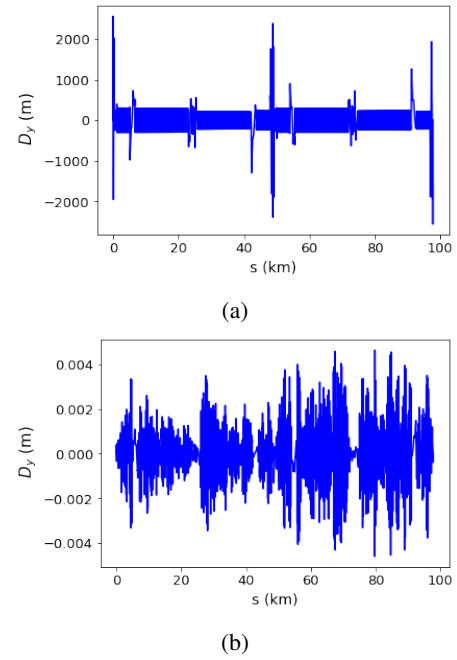


Figure 4: (a) Vertical dispersion after errors (Table 3) are introduced. Before correction the RMS vertical dispersion is 261.1 m. (b) After all correction methods applied, including DFS. The final RMS vertical dispersion is 1.02 mm.

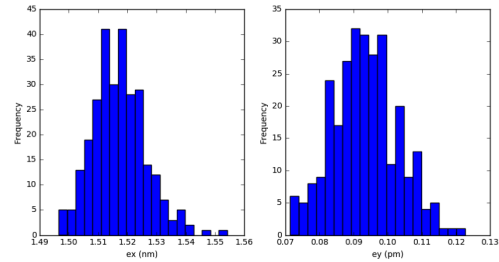


Figure 5: Distribution of vertical and horizontal emittances for the corrected lattices from many random seeds. The errors that were introduced are summarised in Table 3.

summarised in Table 4, the distribution of horizontal and vertical emittances are shown in Fig. 6.

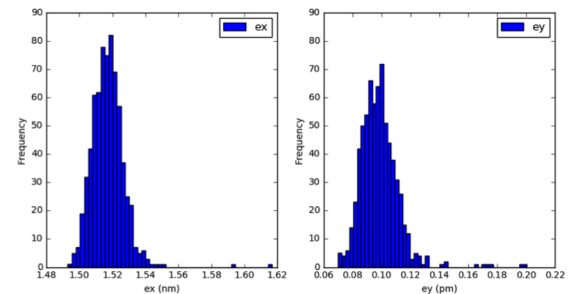


Figure 6: Distribution of vertical and horizontal emittances for the corrected lattices from many random seeds. The errors that were introduced are summarised in Table 4.

Table 4: Misalignment errors introduced into the lattice before correction applied.

	σ_x (μm)	σ_y (μm)	σ_θ (μrad)
arc quadrupoles	100	100	100
IP quadrupoles	50	50	50
sextupoles	100	100	100

Table 5: Misalignment errors introduced into the lattice before correction applied.

	σ_x (μm)	σ_y (μm)	σ_θ (μrad)
arc quadrupoles	100	100	100
IP quadrupoles	100	100	100
sextupoles	100	100	

Finally, Fig 7 shows the resulting emittances when the tolerance of the misalignment of the IP quadrupoles is extended out to 100 μm . For this scenario 369 out of 1000 seeds converged, however the seeds that did successfully converge reached similar emittance values as to those shown in Fig. 5 and Fig. 6. Further study is underway to improve the correction strategy to increase the number of successful seeds. The mean vertical emittance in Fig. 7 is 0.11 pm-rad, and the horizontal emittance is 1.52 nm-rad. The ratio of the emittance (or the coupling ratio), $\epsilon_y/\epsilon_x = 0.007\%$.

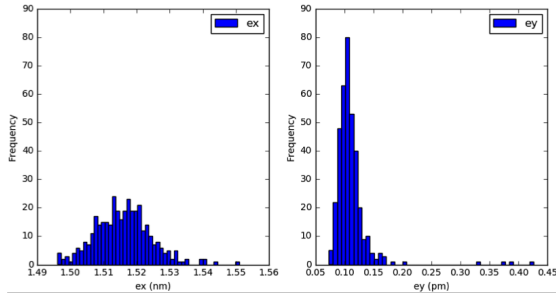


Figure 7: Distribution of vertical and horizontal emittances for the corrected lattices from many random seeds. The errors that were introduced are summarised in Table 5.

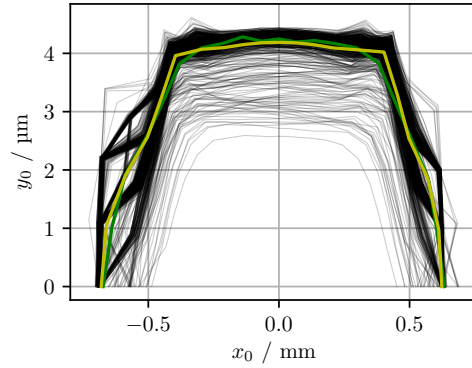
DYNAMIC APERTURE

Continuous top-up injection is mandatory for FCC-ee in order to guarantee high luminosity. Injection into a fully squeezed machine optics is therefore required. The effects of magnet misalignments on dynamic and momentum aperture were tested by means of particle tracking in MAD-X-PTC. The misalignments used in this scenario are listed in Tab. 6.

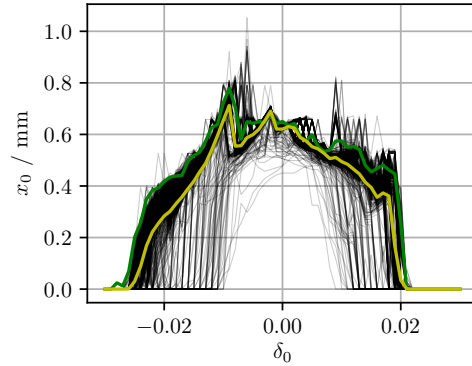
Out of 1000 seeds started for correction, 700 converged and returned with corrected optics which were then used to study the resulting apertures. In Fig. 8, the resulting dynamic and momentum apertures for the corrected machines are presented taking only radiation damping into account, whereas Fig. 9 shows the case including radiation damping and quantum excitation.

Table 6: Misalignment errors used for studying dynamic and momentum aperture.

	σ_x (μm)	σ_y (μm)	σ_θ (μrad)
arc quadrupoles	100	100	100
IP quadrupoles	50	50	50
sextupoles	100	100	



(a) Dynamic aperture



(b) Momentum aperture

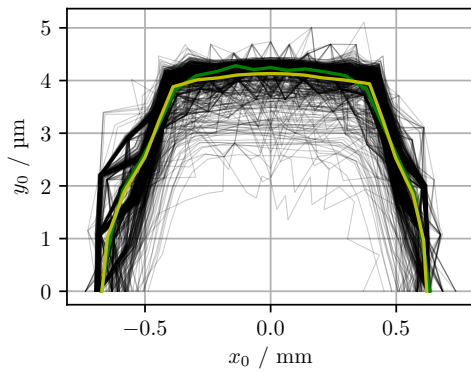
Figure 8: Dynamic and momentum aperture for misaligned machine (grey), average of misaligned machines (yellow), and reference without errors (green). Simulation including radiation damping only.

Using the mean horizontal emittance of 1.52 nm rad for all seeds, and the value of horizontal aperture in Fig. 8a, the resulting aperture in multiples of horizontal beam size is approximately 16 σ_x , sufficient for injection and beam storage.

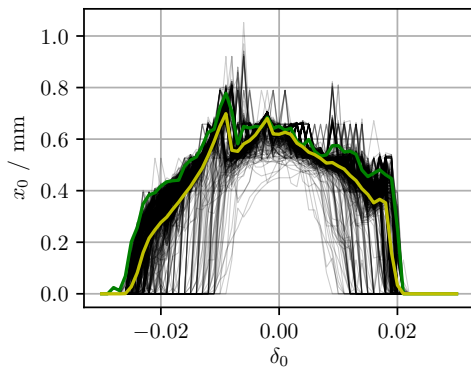
The resulting apertures show that with the set up automated correction scheme, it is possible to achieve sufficient dynamic and momentum aperture to accommodate injection and to stably store beam for most seeds.

CONCLUSION

FCC-ee present unique challenges when it comes to emittance tuning. The small values of the vertical emittance (1



(a) Dynamic aperture



(b) Momentum aperture

Figure 9: Dynamic and momentum aperture for misaligned machine (grey), average of misaligned machines (yellow), and reference without errors (green). Simulation including radiation damping and quantum excitation.

pm-rad) and the low coupling ratio ($>0.1\%$) makes the FCC-ee design particularly susceptible to misalignment and field errors. This paper outlines the correction strategy approach, which includes orbit corrections, Dispersion Free Steering, linear coupling correction based on Resonant Driving Terms and beta-beat correction using response matrices. For misalignments of $100\mu\text{m}$ in x and y and a roll angle error of $100\mu\text{rad}$, the final vertical emittance achieved is 0.11 pm-rad , and a coupling ratio of $\epsilon_y/\epsilon_x = 0.007\%$.

REFERENCES

- [1] M. Aiba, M. Böge, N. Milas, and A. Streun, "Ultra low vertical emittance at SLS through systematic and random optimization," *Nucl. Instruments Methods Phys. Res. Sect. A Accel. Spectrometers, Detect. Assoc. Equip.*, **694**, pp. 133–139, 2012.
- [2] R. Dowd, M. Boland, G. Leblanc, and Y. R. E. Tan, "Achievement of ultralow emittance coupling in the Australian Syn-

chrotron storage ring," *Phys. Rev. ST AB*, **14**, 012804, 2011.

- [3] K. Oide, et al, "Design of beam optics for the future circular collider e^+e^- collider rings," *Phys. Rev. AB*, **19**, 111005, 2016.
- [4] K. Oide "Electron-Positron Circular Colliders," *Reviews of Accelerator Science and Technology Volume 7: Colliders*, World Scientific, ISBN: 978-981-4651-48-6 2015.
- [5] R. W. Assmann, P. Raimondi, G. Roy, and J. Wenninger, "Emittance optimization with dispersion free steering at LEP," *Phys. Rev. ST AB*, **3**, 121001, 2000.
- [6] S. Aumon, B. Holzer, K. Katsunobu A. Doblhammer, B. Haerer, "Tolerance Studies and Dispersion Free Steering for Extreme Low Emittance in the FCC-ee Project," *Proc. of IPAC2016, Busan, Korea*, **3**, THPOR001, 2016.
- [7] K. Oide, D. Shatilov, S. Aumon, T. Charles, D. El Khechen, and T. Tydecks, "Several topics on Beam Dynamics in FCC-ee," *eeFACT 2018, Hong Kong*, These Proc., 2018.
- [8] K. Oide "Optics Choices for High Luminosity IR Including Crab Waist Scheme," *eeFACT 2018, Hong Kong*, These Proc., 2018.
- [9] D. El Khechen, K. Oide, F. Zimmerman "Beam Losses Due to Beam-beam and Beamstrahlung under Lattice Nonlinearity", *eeFACT 2018, Hong Kong*, These Proc., 2018. These Proc., 2018.
- [10] A. Franchi, L. Farvacque, J. Chavanne, F. Ewald, B. Nash, K. Scheidt, and R. Tomás, "Vertical emittance reduction and preservation in electron storage rings via resonance driving terms correction," *Phys. Rev. ST AB*, **14**, no. 3, pp. 1–19, 2011.
- [11] S. Aumon, B. Holzer, and K. Oide, "Vertical Dispersion And Betatron Coupling Correction For FCC-ee," *Proc. of IPAC2017, Copenhagen, Denmark*, MOPIK097, 2017.
- [12] C. Liu, R. Hulsart, A. Marusic, R. Michnoff, M. Minty, V. Pitisyn, and N. York, "Weighted SVD algorithm for Closed-Orbit Correction and 10 Hz Feedback in RHIC," *Proc. IPAC2012, New Orleans, Louisiana, USA*, WEP0084, pp. 2906–2908, 2012.
- [13] R. Tomás, O. Brüning, R. Calaga, S. Fartoukh, A. Franchi, M. Giovannozzi, Y. Papaphilippou, S. Peggs, and F. Zimmermann, "Procedures and Accuracy Estimates for Beta-Beat Correction in the LHC," *Proc. EPAC06*, pp. 2023–2025, 2006.
- [14] S. Aumon, B. Holzer, K. Oide, A. D. Technische, U. Wien, B. H. Kit, and B. Haerer, "Coupling and Dispersion correction for the Tolerance Study in FCC-ee," *Proc. eeFACT2016, Daresbury, UK*, pp. 151–156, 2016.
- [15] A. Chao, "Evaluation of Beam Distribution Parameters in an Electron Storage Ring," *J.Appl.Phys.*, **50**, 595, pp. SLAC-PUB-2143, 1979.
- [16] "Methodical Accelerator Design Manual," <http://madx.web.cern.ch>.

OPTICS CORRECTIONS INCLUDING IP LOCAL COUPLING AT SuperKEKB*

A. Morita[†], H. Koiso, Y. Onishi, H. Sugimoto, K. Ohmi, D. Zhou,
KEK, 1-1 Oho, Tsukuba, Ibaraki 305-0801, Japan

Abstract

SuperKEKB is an asymmetric energy electron-positron collider designed by using a novel collision scheme. The beam collision test was performed during the phase-2 commissioning. In the phase-2 commissioning, global optics corrections worked fine except for local coupling at the interaction point(IP). IP local coupling was adjusted by IP tuning knobs to maximize luminosity. After IP local coupling adjustment, the specific luminosity improvement by squeezing the vertical beta function at IP down to half of the bunch length was confirmed.

INTRODUCTION

The SuperKEKB accelerator [1] is an asymmetric energy electron-positron collider which is designed to achieve a luminosity of $8 \times 10^{35} \text{cm}^{-2}\text{s}^{-1}$ by using the “nano-beam” collision scheme. Its main rings are constructed by 7 GeV electron high energy ring (HER) and 4 GeV positron log energy ring (LER). The SuperKEKB accelerator commissioning is divided into 3 phases. At this moment, the second phase so called “phase-2 commissioning” has been completed and we are preparing the phase-3 commissioning.

The phase-1 commissioning [2] without the final focus system was performed from February 1, 2016 to June 28, 2016 for establishing the low emittance beam operation. After the phase-1 commissioning both the final focus system and the Belle II detector were installed. The phase-2 commissioning [3] was performed from March 19, 2018 to July 17, 2018 to verify “nano-beam” collision.

In the following sections, the global optics correction performed as a part of beam commissioning and the IP local coupling issue are reported.

GLOBAL OPTICS CORRECTION

Both optical function measurement and correction algorithm for the phase-2 beam operation are same as the phase-1 commissioning [4]. The optical function measurement of the SuperKEKB standard operation is based on the closed orbit response measurement by using the multi-turn beam position monitors(BPMs). In the optics correction, the correction parameter is calculated from both the linear model response and the measured optical function error by using the singular value decomposition (SVD). The global optics correction sequence for the beam operation contains XY-coupling correction, physical dispersion correction and beta correction.

* Work supported by JSPS KAKENHI Grant Number 17K05475.

[†] akio.morita@kek.jp

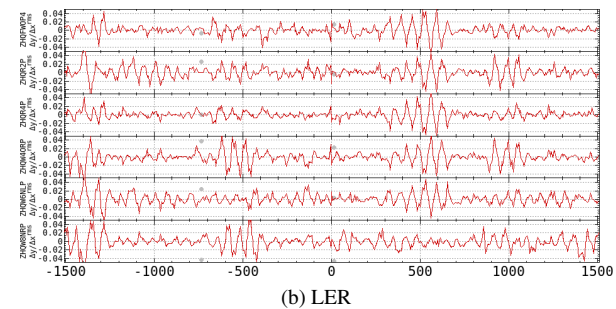
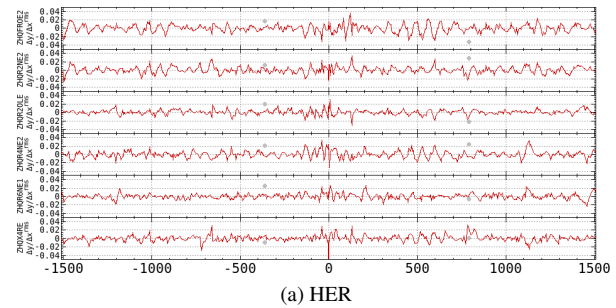


Figure 1: XY-Coupling measurement. Horizontal axis shows the distance from the IP in m units. Each graph columns show the discrepancy between model prediction and measurement of vertical leakage orbit of single horizontal steering kick shown in column label.

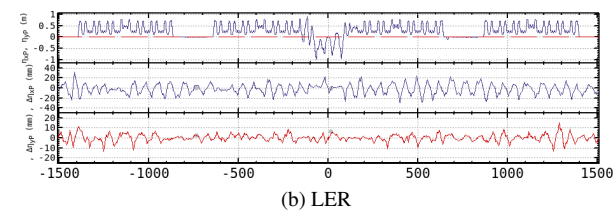
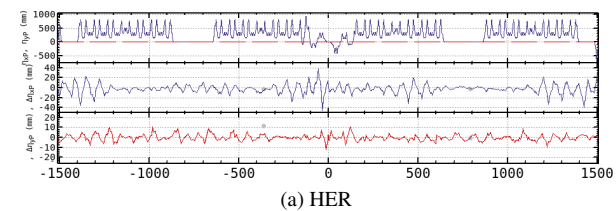


Figure 2: Physical dispersion measurement. From the top of the graph columns, graph columns correspond with model dispersion, horizontal dispersion error and vertical dispersion error, respectively.

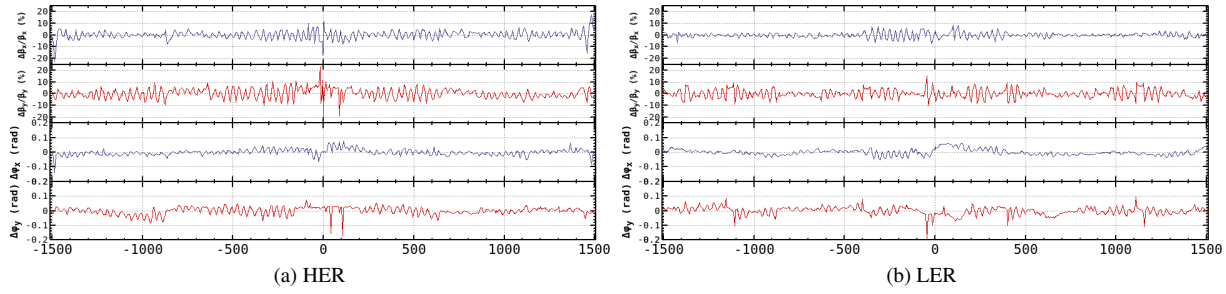


Figure 3: Beta function measurement. From the top of the graph columns, graph columns correspond with relative horizontal beta function error, horizontal betatron phase error, relative vertical beta function error and vertical betatron phase error, respectively.

The global optics corrections work fine enough for the phase-2 optics. Figures 1, 2 and 3 show the normalized vertical orbit leakage of the horizontal single steering kick response (XY-coupling error), the physical dispersion error and the relative beta-function error, respectively. These optics errors were measured on $\beta_y^* = 3$ mm collision optics after global correction at the end of phase-2 commissioning. The residual errors are summarized in Table 1, where Δy^{rms}

Table 1: Results of Optics Corrections; XY-Coupling, Physical Dispersion, and Beta Function

Item	LER	HER	Unit
XY-coupling: $\Delta y^{rms} / \Delta x^{rms}$	1.4	0.8	%
Hor. dispersion: $\Delta \eta_x^{rms} / \Delta x^{rms}$	10.6	9.8	mm
Ver. dispersion: $\Delta \eta_y^{rms} / \Delta y^{rms}$	3.7	3.1	mm
Hor. β function: $(\Delta \beta_x / \beta_x)^{rms}$	2.2	3.6	%
Ver. β function: $(\Delta \beta_y / \beta_y)^{rms}$	3.8	4.5	%
Hor. tune: $\Delta \nu_x$	3.6	-0.8	10^{-4}
Ver. tune: $\Delta \nu_y$	-0.05	-4.8	10^{-4}

and Δx^{rms} are rms error amplitude of the vertical leakage orbit and rms amplitude of the horizontal single steering kick perturbation, respectively. These residual errors are almost same as the phase-1 achievements shown in the previous eeFACT paper [5] except for the LER XY-coupling error residual. The LER XY-coupling error shown in Fig. 1b is not localized around the IP which is shown at the center of the figure. The vertical alignment error due to the SuperKEKB tunnel subsidence and the permanent magnet device installed to suppress the electron cloud effect are suspected as the XY-coupling error source. In order to achieve ultra low emittance, further XY-coupling correction study is required in the phase-3 commissioning.

IP LOCAL COUPLING

At β_y^* squeezing from 6 mm to 4 mm, the specific luminosity improvement corresponding with β_y^* squeezing was not observed. The vertical beam size measurement by using X-ray beam size monitor at the end of the arc section and global XY-coupling & dispersion measurement results sug-

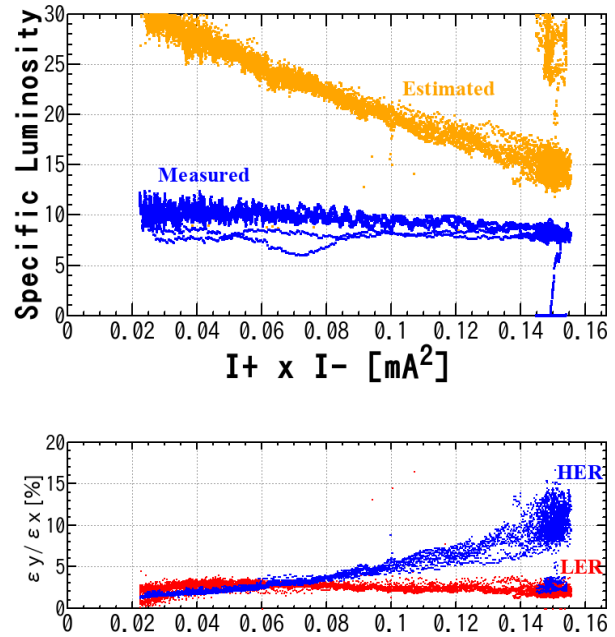


Figure 4: Specific luminosity before IP local coupling adjustment. Horizontal axis show a bunch current product. Vertical axes show the specific luminosity for upper graph and the normalized vertical emittance(square of vertical beam size) measured by X-ray beam size monitors, respectively. Blue and yellow points in the upper graph correspond with the measured specific luminosity and the specific luminosity estimated from the beam size, respectively. Red and blue points in the lower graph correspond with the LER beam and the HER beam, respectively.

gest that the vertical emittance of the single beam operation is not degraded by β_y^* squeezing.

Figure 4 shows the bunch current product dependency of the specific luminosity measured on such $\beta_y^* = 4$ mm collision operation with decaying beam current. In Fig. 4, the LER vertical beam size is almost kept against bunch current decay, however, the HER vertical beam size shrinks by a half corresponding with bunch current product decaying from 0.15 mA^2 to 0.03 mA^2 . On the other hand, the bunch current product dependency of the measured specific

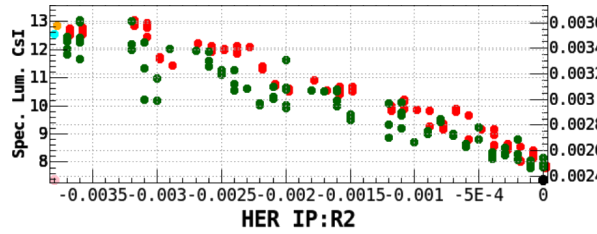


Figure 5: HER R2* parameter scan result. Horizontal axis shows R2 parameter at the IP in m units. Vertical axis shows the measured luminosity.

luminosity is small compared with the prediction from the analytic formula. Furthermore, the vertical beam size at the IP estimated from the beam-beam scan measurement at low bunch current operation by scanning vertical collision orbit offset is about $1.25 \mu\text{m}$ under the assumption that the IP vertical beam sizes of the colliding beams are equal to each other, however, the typical vertical beam sizes measured by using X-ray beam size monitor at the decayed low current beam condition are $0.5 \mu\text{m}$ for HER and $0.4 \mu\text{m}$ for LER, respectively. These results suggest the geometrical beam mismatch at the IP.

In order to find the source of such geometrical beam mismatch, the vertical beam waist scan, the IP coupling parameter scans ($R1^*$, $R2^*$, $R3^*$, $R4^*$) and the IP vertical dispersion scans (η_y^* , $\eta_{y'}^*$) were performed, where $R1$, $R2$, $R3$ and $R4$ parameters are described by using the x-y-coupling parameter definition of the accelerator code SAD [6]. From such IP parameter scans, a large HER $R2^*$ error shown in Fig. 5 is found. At this moment, $R2^*$ parameter scan range is limited within almost 3.8 mm by the maximum excitation current of skew quadrupole corrector winding on chromaticity corrector sextupole magnet pair, however, this scan range is not enough to find the luminosity peak. In order to search correct $R2^*$ parameter, the old IP tuning knob based on the vertical local bump around sextupole magnet pair, which is used in the KEKB B-factory tuning [7], is temporarily reintroduced to extend $R2^*$ parameter scan range. The total amount of $R2^*$ adjustments at the luminosity peak of $R2^*$ scans is about 6 mm.

Finally, this big $R2^*$ error is adjusted by using the skew quadrupole corrector of the vertical final focus quadrupole magnets (QC1 magnets). Figure 6 shows the specific luminosity trend after these IP local coupling adjustments. In Fig. 6, the vertical beam size blowup is reduced and the IP vertical beam size estimated by the beam-beam scan measurement becomes almost half and the measured specific luminosity approaches to the predicted performance by inverse square root of β_y^* .

SUMMARY

The global optics correction works fine enough for the phase-2 optics, however, IP local coupling must be suppressed for obtaining good luminosity performance. The global XY-coupling & dispersion measurement by using

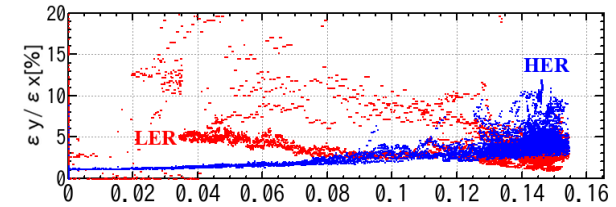
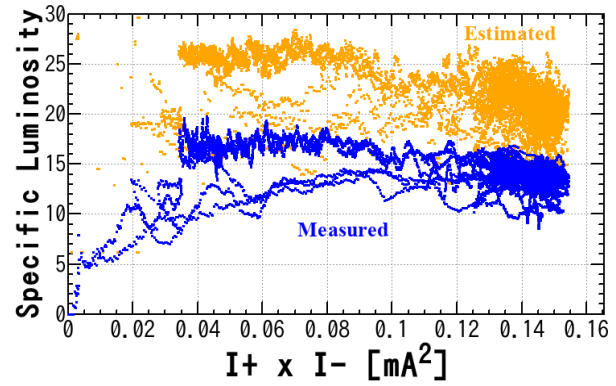


Figure 6: Specific luminosity after IP local coupling adjustment. Notations are same as Fig. 4.

BPMs installed around quadrupole magnets can not detect IP local coupling. In order to suppress IP local coupling, we have to adjust IP coupling/dispersion tuning knobs to maximize the measured specific luminosity. After IP local coupling adjustment, we confirm the specific luminosity improvement by squeezing β_y^* down to 3 mm which is about half of the bunch length.

REFERENCES

- [1] Y. Ohnishi *et al.*, “Accelerator design at SuperKEKB”, *Prog. Theor. Exp. Phys.* 2013 03A011 (2013), Doi:10.1093/ptep/pts083.
- [2] Y. Funakoshi *et al.*, “Beam Commissioning of SuperKEKB”, *Proc. of IPAC2016*, Busan, Korea, May 2016, TU0BA01, p. 1019 (2016), Doi:10.18429/JACoW-IPAC2016-TU0BA01.
- [3] Y. Ohnishi, “Report on SuperKEKB Phase 2 Commissioning”, *Proc. of IPAC2018*, Vancouver, BC, Canada, April 2018, MOXGB1, p. 1 (2018), Doi:10.18429/JACoW-IPAC2018-MOXGB1.
- [4] Y. Ohnishi *et al.*, “Optics Measurements and Corrections at the Early Commissioning of SuperKEKB”, *Proc. of IPAC2016*, Busan, Korea, May 2016, THPOR007, p. 3782 (2016), Doi:10.18429/JACoW-IPAC2016-THPOR007.
- [5] Y. Ohnishi *et al.*, “Optics Correction and Low Emittance Tuning at the Phase 1 Commissioning of SuperKEKB”, *Proc. of eeFACT2016*, Daresbury, UK, October 2016, TUT3BH2, p. 143 (2016), Doi:10.18429/JACoW-eeFACT2016-TUT3BH2.
- [6] x-y-coupling parameter definition of SAD, <http://acc-physics.kek.jp/SAD/SADHelp.html#L539>
- [7] T. Abe *et al.*, “Commissioning of KEKB”, *Prog. Theor. Exp. Phys.* 2013 03A010 (2013), Doi:10.1093/ptep/pts101.

OPTICS ABERRATION AT IP AND BEAM-BEAM EFFECTS

K. Ohmi*, K. Hirose, Y. Funakoshi, H. Koiso, A. Morita, Y. Ohnishi, D. Zhou,
KEK/Soken-dai, Tsukuba, Japan

Abstract

Collision in SuperKEKB phase II commissioning has started in April 2018. Luminosity was lower than the geometrical value even in very low bunch current at the early stage. Linear x-y coupling at IP caused by skew of QCS was conjectured as error source. x-y coupling correction using skew corrector of QCS resulted in luminosity recover of 2 times. After the QCS skew correction, luminosity is still limited at relatively low bunch current. Nonlinear x-y coupling at IP is conjectured as a source of the luminosity limitation in the next stage. We discuss effects of linear and nonlinear x-y coupling at IP on the beam-beam performance.

INTRODUCTION

SuperKEKB is asymmetric e^+e^- collider, which consists of low and high energy rings (LER & HER) with the energies $E = 4$ and 7 GeV, respectively. The target luminosity is $L = 8 \times 10^{35} \text{ cm}^{-2}\text{s}^{-1}$ at beam current $I_{+,tot} = 3.6$ A and $I_{-,tot} = 2.6$ A with the number of bunches $N_b = 2,500$. Two beams collide with half crossing angle $\theta_c = 41.5$ mrad. Beta function at Interaction Point (IP) is squeezed to $\beta_x^* \sim 30$ mm and $\beta_y^* \sim 0.3$ mm. Piwinski angle is $\theta_c \sigma_z / \sigma_x$ is very large ~ 20 ; so-called, nano-beam/ superbunch/ large Piwinski angle collision is adopted. Phase-I commissioning in 2016 was focused to start the operation of the two storage ring (LER and HER) without collision. In Phase-II commissioning started from March 2018, beam-beam collision and luminosity tuning were main subjects. β^* was squeezed step-by-step during the commissioning. Table 1 summarizes the parameters. The beam-beam tune shift $\Delta\nu_{x,y}$ in Phase-II is calculated by the emittance without collision. Beam-beam parameter $\xi_y \sim \Delta\nu_y$ estimated by the achieved luminosity is lower than the value; lower value is $\xi_{L,-} = 2r_e\beta_y^*L/(N_- \gamma_{rep}) \sim 0.02$ due to a vertical emittance increase mainly in e^+ beam at beam-beam collision..

Optics aberrations at the interaction point have affected the beam-beam performance since KEKB operation. The operation had been continued while scanning the IP optics parameters for most of the time in day-by-day. Correction of the aberrations should be also very important for SuperKEKB. We discuss correction of linear aberration done in Phase-II and nonlinear aberrations toward future commissioning, Phase-III.

LINEAR COUPLING CORRECTION AT IP IN PHASE-II OPERATION

Specific luminosity, which is bunch luminosity normalized by bunch current product, is used as a measure for

Table 1: Parameters for SuperKEKB

parameter	design		Phase-II	
	LER	HER	LER	HER
$N_{\pm}(10^{10})$	9	6.5	4.8	4.0
$\varepsilon_{x/y} \text{ (nm/pm)}$	3.2/8.64	4.6/13	2.1/21	4.6/30
$\beta_{x/y}^* \text{ (mm)}$	32/0.27	25/0.3	200/3	100/3
ν_z	0.0247	0.028	0.022	0.026
$\Delta\nu_x$	0.0028	0.0012	0.0073	0.0025
$\Delta\nu_y$	0.088	0.081	0.075	0.077
ξ_L	0.088	0.081	0.03	0.02
$\sigma_z \theta_c / \sigma_x$	24.7	19.4	12.1	11.6

the beam-beam performance. When the beam particles distribute Gaussian in the transverse plane, the specific luminosity is represented only by the rms beam size,

$$L_{sp} = \frac{L}{I_+ I_-} = \frac{1}{2\pi\sigma_{xc}\sigma_{yc}e^2 f_0}, \quad (1)$$

where the beam size is square mean of e^{\pm} beams, $\sigma_{yc} = \sqrt{\sigma_{y+}^2 + \sigma_{y-}^2}$. For collision with a large crossing angle $\theta_c \sigma_z / \sigma_x \gg 1$, the horizontal beam size is effectively projection of the bunch length into horizontal plane: i.e., $\sigma_{x,eff} = \theta_c \sigma_z$, where θ_c is the half crossing angle. σ_{xc} is square mean of the effective horizontal size of the two beams. The specific luminosity is characterized by the vertical beam size and bunch length. We expect that the specific luminosity is given by the vertical beam size determined by the vertical emittance ε_y and β_y^* , when beam-beam effect is negligible. By increasing beam current, the beam-beam effect dominates. Vertical beam size blow-up due to the beam-beam interaction results decrease of the specific luminosity.

Figure 1 presents the specific luminosity as function of beam current product at early stage of squeezing beta to $\beta_y = 4$ mm (June 10, 2018). Vertical beam size is measured by X-ray monitor for both beams. As the beta function at the monitor is well-calibrated, the beam size corresponds to the vertical emittance. The beam sizes written in the figure are calculated by the measured vertical emittance $\sigma_y^* = \sqrt{\varepsilon_y \beta_y^*}$ in each (total) current, where the number of bunches are 788. The specific luminosity calculated by Eq. (1) using the beam size is plotted by red stars. The specific luminosity disagrees at low current. This result means the beam size at IP is deviate from $\sqrt{\beta_y^* \varepsilon_y}$ geometrically. The discrepancy of the specific luminosity is small at high bunch current. Electron beam is enlarged strongly at high current. Peak luminosity was $L_{peak} = 1.2 \times 10^{33} \text{ cm}^{-2}\text{s}^{-1}$ for 285mA(e^-)x340mA(e^+) at $N_b = 788$.

There are several possibility for the disagreement of the specific luminosity. Beam collision offset is scanned in

* ohmi@post.kek.jp

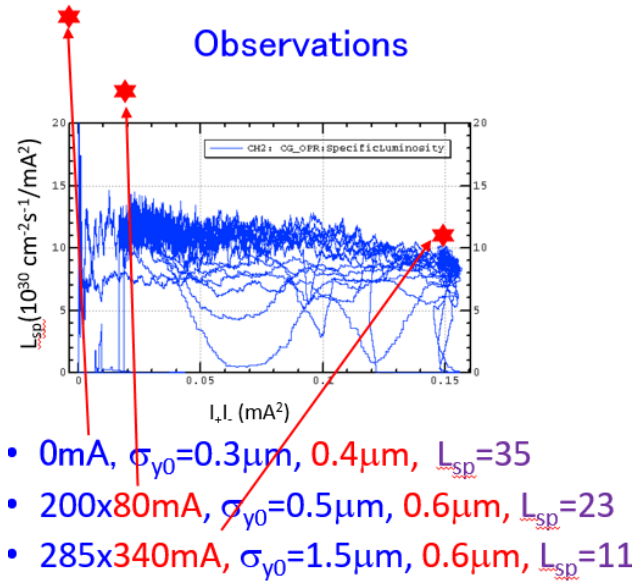


Figure 1: Specific luminosity as function of current product just after squeezing $\beta^*=(200,4)$ mm.

x, y, z directions. β^* is checked by measurement at β at both side of final quadrupole magnets. Waist of β^* are scanned. Remained possibilities can come from local x - y coupling and vertical dispersion at IP.

x - y coupling is parameterized by R matrix for the 4×4 revolution matrix at IP.

$$M = RM_{2 \times 2}R^{-1} \quad (2)$$

where $M_{2 \times 2}$ is block diagonalized matrix, which is represented by β^*, α^* and ν in x and y plane. R matrix is represented by 4 parameters as

$$R = \begin{pmatrix} R_0 & 0 & R_4 & -R_2 \\ 0 & R_0 & -R_3 & R_1 \\ -R_1 & -R_2 & R_0 & 0 \\ -R_3 & -R_4 & 0 & R_0 \end{pmatrix} \quad (3)$$

where $R_0 = \sqrt{1 - R_1 R_4 + R_2 R_3}$.

R_1 characterizes rotation of beam in real x - y space, while R_2 characterizes rotation in x - p_y space. Figure 2 presents schematic view of collision at IP, where LER (positron) is ideal and HER (electron) has errors. Whether the rotation of the real space or the rotation of the momentum space, the beam size projected to y plane contributes to the luminosity.

The projected vertical beam size at IP in the presence of x - y coupling and vertical dispersion is expressed by

$$\sigma_y^2 = \varepsilon_y \beta_y + \varepsilon_x \beta_x \left(\frac{R_2^2}{\beta_x^2} + R_1^2 \right) + (\eta_y \sigma_\delta)^2. \quad (4)$$

Correction of R_2

The specific luminosity at zero current was half of the prediction from the measured emittance as shown in Fig. 1.

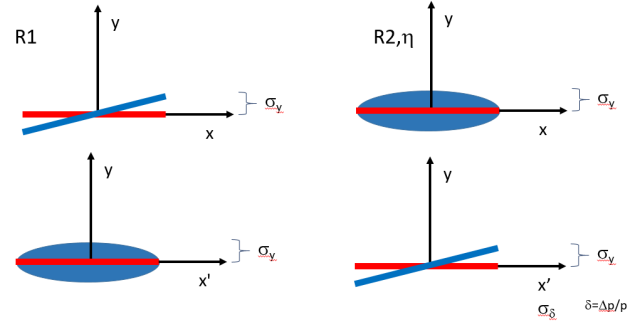


Figure 2: Phase space distribution of beam at IP in the presence of R_1, R_2, η_y . Red and blue depict distributions of positron and electron beam.

Electron beam was weak at high current: that is, errors seemed to exist in HER optics. It was conjectured that σ_y of electron beam was about 3 times larger than the nominal value $\sqrt{\varepsilon_y \beta_y^*}$ at zero current. Corresponding errors are estimated to be

$$R_1 = \pm 30 \sim 60 \text{ mrad} \quad R_2 = \pm 3 \sim 6 \text{ mm} \quad \eta_y = \pm 1.5 \text{ mm}.$$

R parameters were changed by closed bump in arc sextupole magnets. Figure 3 presents luminosity, beam life time, vertical beam size for changing R_2 . Luminosity increased, while life time and vertical beam size decreased for decreasing to $R_2 = -3.9$ mm. Optimum R_2 seemed to be further negative value. Increasing the bump height to change R_2 gives a side effect in vertical emittance increase due to induced vertical dispersion. We stopped to change R_2 to further negative direction at the first step.

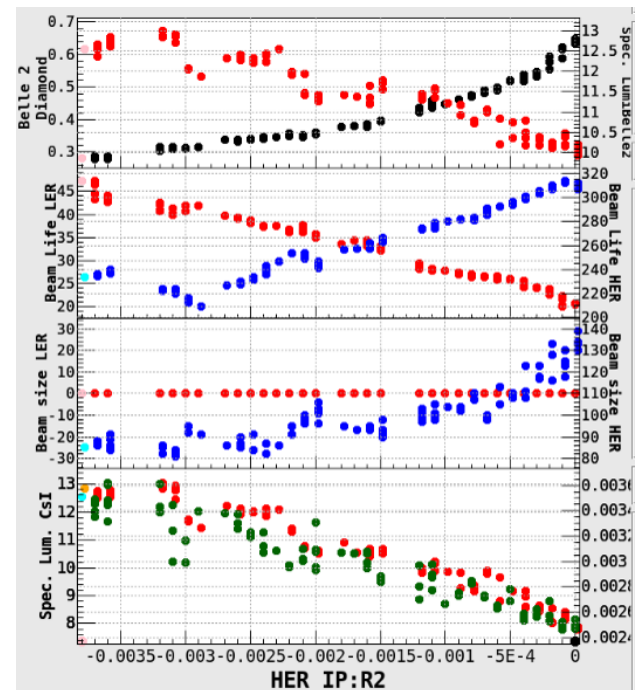


Figure 3: Luminosity, life time and beam size for r_2 scan.

The linear transformation for R_2 is equivalent to

$$RM_{2 \times 2} R^{-1} = e^{-R_2 p_x p_y} M_{2 \times 2} e^{R_2 p_x p_y} \quad (5)$$

The source of R_2 seems to be skew of the final quadrupole magnets, QC1 or QC2. QC1 defocusing magnets are located at 0.6-1.9 m from IP. QC2 focusing magnets are located at 1.9-3.4 m from IP. Betatron phase difference between QC's and IP is about $\pi/2$ in both of $x-y$ plane as shown in Figure 4. Skew of QC magnets give a transformation with generating function of $H = ap_x p_y$. When both side of quadrupole magnets have rotation with the same angle but opposite direction, $a = \pm R_2$ ($\beta^* \beta(QC) \sim 1$), induced x-y coupling is confined in IR region and is invisible outside of IR. Transfer for H is $\bar{x} = x \pm R_2 p_y$, and $\bar{y} = y \pm R_2 p_x$, agree with the transfer matrix R in Eq. (3).

We do not change strength of IR magnets for squeezing β^* . R_2 induced by the rotation of QC is kept for squeezing β^* , because transfer from IP to QC's does not change. This means that the contribution to the beam size of R_2 in Eq. (4) is enhanced for squeezing β^* : that is, squeezing β^* results larger beam size at IP depending on R_2 .

The correction of R_2 done by sextupole bump was replaced by exciting skew corrector in QC1. The skew corrector induces a small leak of R_3 component outside of IR, which was corrected by skew winding of sextupoles in arc. The side effect of the vertical emittance increase was eliminated.

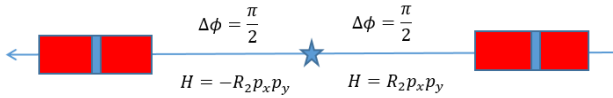


Figure 4: Transformation for R_2 .

We repeat to find optimum R_2 using sextupole bump and to correct the R_2 using skew corrector of QC1. R_2 was changed -7 mm in total. Figure 5 presents specific luminosity after the correction of R_2 . Peak luminosity was $L_{peak} = 2.5 \times 10^{33} \text{ cm}^{-2} \text{ s}^{-1}$ for the same condition in Fig. 1, $285 \text{ mA}(e^-) \times 340 \text{ mA}(e^+)$ at $N_b = 788$. The luminosity gain is due to recovering the geometrical loss and relax a beam dynamical effect of R_2 at high current. Beam size blow-up in e^+ beam became stronger than that in e^- beam after the R_2 correction.

Measurement of x-y Coupling

x-y coupling is measured by turn-by-turn monitors. Beam is kicked by injection error, then the positions of the monitors is recorded. Horizontal betatron motion with v_x is excited, and leaks in the vertical direction due to x-y coupling. There are 4 turn-by-turn monitors in IR section. Nearest monitors at IP (MQC1L-R) are placed inside of QC1. Using the left and right side of monitors, 4 dimensional phase space trajectory for the horizontal betatron motion at IP is solved. Figure 6 presents FFT signal given by the monitors. Top two plots show FFT amplitude of x, y position at Left and Right monitors. The signal with v_x was seen in vertical of R

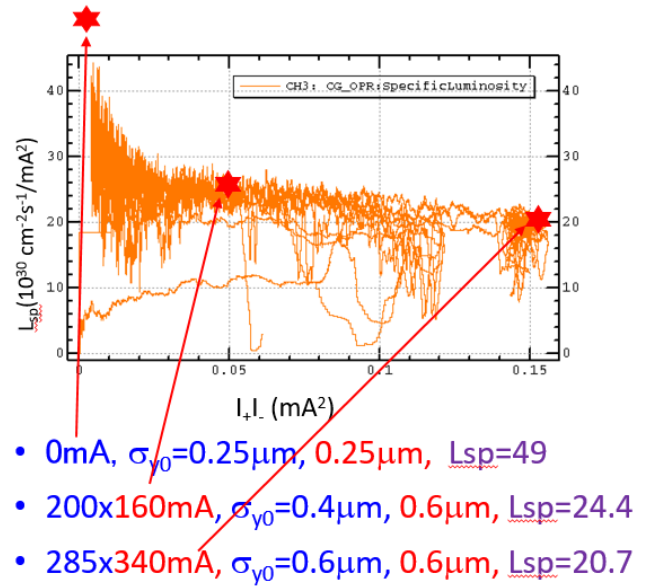


Figure 5: Specific luminosity as function of current product after r_2 correction.

and L monitors. Bottom two plots show FFT amplitude of x, y position and their slope $p = p_x = x', q = p_y = y'$ at IP. Roughly speaking, y_{IP} is evaluated by summation of y at left and right monitor, $y_L + y_R$, while q_{IP} is by difference of them, $y_L - y_R$. Clear signal for horizontal betatron motion was seen in q_{IP} , but was not in y_{IP} . R_1 and R_2 are evaluated by y_{IP} signal, while R_3 and R_4 are by q_{IP} signal. This result means that measurement of R_1 and R_2 is difficult compare with that of R_3 and R_4 .

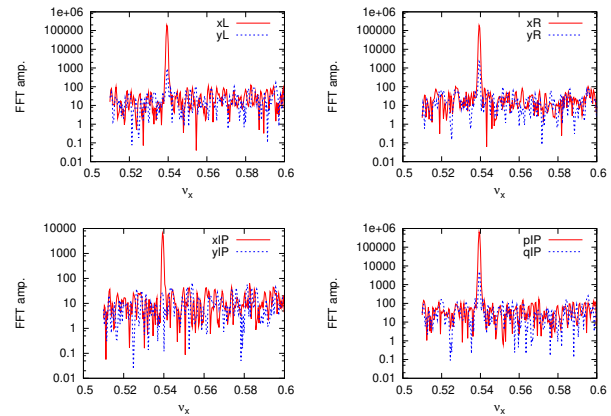


Figure 6: FFT amplitude for x and y signal of MQC1 monitors.

Figure 7 presents measured R_3 and R_4 . Top two plot are given for HER and bottom plots are for LER. The measurement was performed for changing RF frequency (± 200 Hz) also to evaluate their chromatic effect. The revolution frequency is $f_0 = 99.4$ kHz for $C = 3016$ m. The energy deviation is $\delta = \pm 0.2$ %.

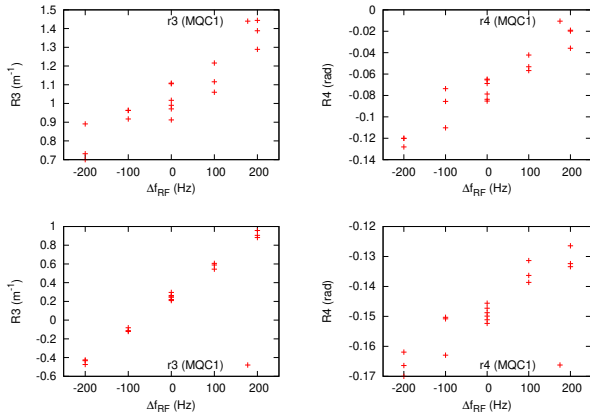


Figure 7: Measured R_3 and R_4 as function of RF frequency shift. Top two plot are given for HER and bottom plots are for LER.

The coupling parameters R_3 and R_4 and their chromatic components are obtained by fitting the measurement,

$$\begin{aligned} \text{HER:} \quad R_3 &= 1.0 - 137\delta & R_4 &= -0.073 - 23.3\delta \\ \text{LER:} \quad R_3 &= 0.24 - 338\delta & R_4 &= -0.15 - 8.9\delta. \end{aligned}$$

TOWARD PHASE-III

Linear x-y coupling and vertical dispersion have been controlled well in the final stage of Phase II. The beam size at IP agreed with $\beta_y^* \epsilon_y$ at collision with low bunch current $\sim 0.01\text{mA}$ very well. However we still have luminosity degradation at high bunch current. Increase of the vertical emittance measured by X ray monitor well explains the luminosity degradation: that is, vertical emittance growth is caused by the beam-beam interaction. Emittance growth is not serious for beam-beam simulation without errors at IP, where the bunch current is still 50-60% of the design.

In experiments, e^+ beam has enlarged vertically at the end of Phase-II. We perform weak-strong simulation [1], in which e^+ beam is tracked in the fixed e^- beam force. In experiment, specific luminosity at the bunch current ($0.68 \times 0.57 = 0.39\text{mA}^2$) was around $L_{sp} = 15 \times 10^{30} \text{ cm}^{-2} \text{ s}^{-1} \text{ mA}^{-2}$. The simulations were performed with applying IP errors to realized the degraded specific luminosity.

Figure 8 present the specific luminosity as function of bunch current product with/without linear x-y coupling. The specific luminosity without error is 29×10^{30} at the highest current 0.39 mA^2 . Applied coupling parameters are written in the figure. R_1 and R_2 are possible errors in reality. We actually corrected R_2 with -7 mm . R_3 and R_4 which are measured by turn-by-turn monitor, are far smaller than the values $R_3 = 50 \text{ m}^{-1}$ and $R_4 = 2$. Errors of linear coupling parameters are not possible source of the luminosity behavior in Fig. 5.

Nonlinear coupling is possibility to explain the specific luminosity behavior. Assuming errors induced by QCS magnets, the nonlinearities are expressed by p_y at IP. Betatron phase difference deviate from $\pi/2$ in horizontal. Though p_x

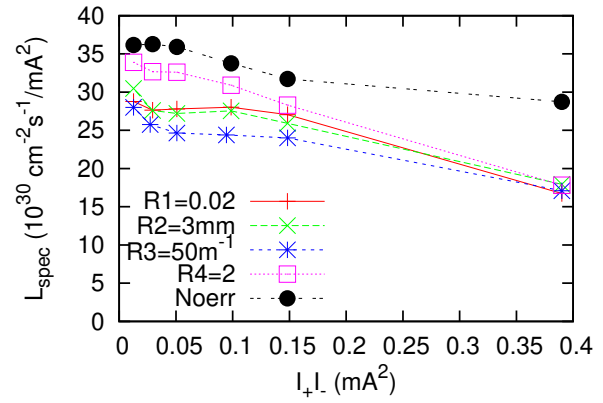


Figure 8: Specific luminosity as function of current product for linear aberrations obtained by weak-strong simulation.

terms are dominant, x terms should be taken into account. Figure 9 presents specific luminosity for considering 3-rd order terms; The transformation at IP are given by generating function,

$$H = c_1 p_x p_y^2 + c_2 p_x^2 p_y + c_3 p_y^3 + c_4 x^2 p_y. \quad (6)$$

The specific luminosity for $p_x^2 p_y$ component agrees with the measurement of Fig. 5, The coefficient is $c_2 = 8 \text{ m}$. The coefficient had evaluated in the design stage [2,3] was 0.07 m : that is, 100 times larger. The nonlinearity was induced at skew sextupole component of QC magnets and octupoles component of edge and body of their magnets in the presence of a vertical closed orbit.

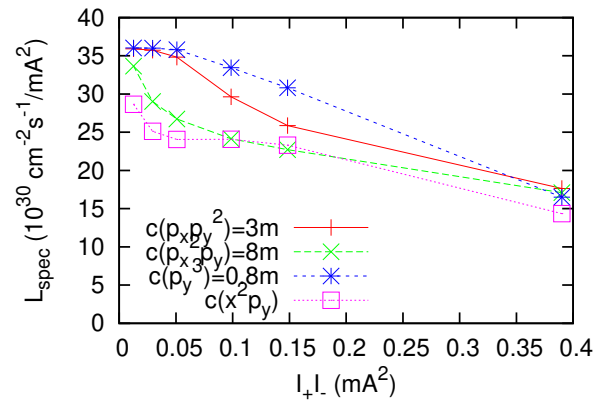


Figure 9: Specific luminosity as function of current product for nonlinear aberrations obtained by weak-strong simulation.

Another possibility is chromatic coupling. Figure 10 presents specific luminosity for chromatic coupling [4, 5]. The chromatic coupling for R_3 and R_4 are measured as shown in Fig. 7. The values $R'_3 = 35,000$ and $R'_4 = 1500$ are 100 times larger than the measurement. The behavior of the specific luminosity is different from the measurement in

Fig. 5. For R'_1 and R'_2 , the behaviors agree with the measurement. Measurement of R'_1 and R'_2 was difficult and has not performed yet.

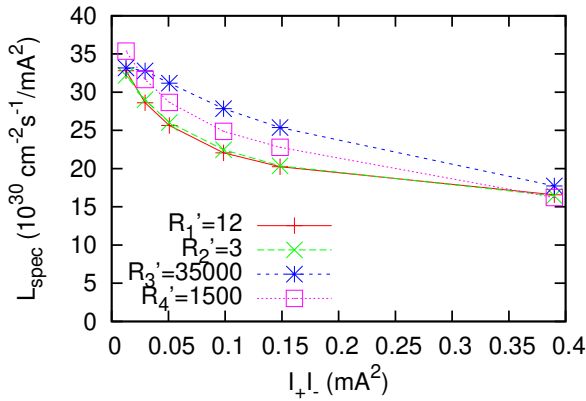


Figure 10: Specific luminosity as function of current product for chromatic coupling aberrations obtained by weak-strong simulation.

SUMMARY

SuperKEKB is squeezing β^* step-by-step in the commissioning of Phase II. Luminosity increase proportional to β_y^* is not trivial at all. Expected luminosity is only achieved, when the optics aberration at IP are perfectly corrected. QC magnet as error source and corrector is key component. Errors induced at QC magnets are enhanced for squeezing β^* . Correction of nonlinear aberration is next target in Phase-III commissioning.

The target specific luminosity in the design is $L_{sp} = 220 \times 10^{30} \text{ cm}^{-2} \text{ s}^{-1} \text{ mA}^{-2}$ at $I_+ I_- = 1.5 \text{ mA}^2$.

REFERENCES

- [1] K. Ohmi et al., *Phys. Rev. ST-AB* 7, 104401 (2004).
- [2] D. Zhou et al., in *Proc. IPAC'15*, paper WEYB3.
- [3] K. Hirose et al., in *Proc. IPAC'18*, paper THPAK099.
- [4] D. Zhou et al., *Phys. Rev. ST-AB* 13, 021001 (2010).
- [5] Y. Ohnishi et al., *Phys. Rev. ST-AB* 12, 091002 (2009).

OFF-MOMENTUM OPTICS AT SuperKEKB

Y. Ohnishi*, H. Koiso, A. Morita, K. Ohmi, H. Sugimoto, KEK, OHO 1-1, Tsukuba, Japan
K. Oide, CERN, Geneva, Switzerland

Abstract

The nano-beam scheme can squeeze the vertical beta function at the IP much smaller than the bunch length. It implies that the large chromaticity is generated in the vicinity of the final focus quadrupole magnets and the strong sextupoles, for instance the local chromaticity corrections, are adopted to correct the chromaticity. While understanding of the off-momentum optics is important to optimize the dynamic aperture to make Touschek lifetime long and to reduce the luminosity degradation due to chromatic behaviors. In general, there is a discrepancy between measurements of chromaticity and those obtained from the optics model. The chromatic phase-advance is introduced to measure the off-momentum optics and correct by adjustments of sextupole magnets.

INTRODUCTION

SuperKEKB is an electron-positron double-ring collider [1] and the Belle II detector [2] built to explore new physics in the collider experiment. The physics program of the recent B-factory delivering extremely high statistics is almost independent of and complementary to the high energy experiments at the LHC. The target luminosity is $8 \times 10^{35} \text{ cm}^{-2} \text{ s}^{-1}$, which is 40 times the performance of KEKB [3] that has been operated for 11 years until 2010. The strategy for the luminosity upgrade is a nano-beam scheme. The collision of low emittance beams under a large crossing angle allows squeezing the beta functions at the IP to value much smaller than the bunch length. Consequently, extremely higher luminosity can be expected with only twice the beam current of KEKB.

The small beta functions at the IP implies that a large chromaticity is generated in the vicinity of the final focus magnets (QC1 and QC2). The natural chromaticity calculated from the lattice model in Phase 2 is shown in Table 1. Because the chromaticity generated from QC1 and QC2 is very large, we adopt local chromaticity corrections for both x and y directions. The local chromaticity correction and the arc lattice utilize non-interleaved sextupole correction scheme. Two identical sextupole magnets are connected by $-I'$ transfer matrix. A nonlinear kick from either of two sextupole magnets can be compensated by another sextupole magnets for on-momentum particles in this scheme. Therefore, a large dynamic aperture can be expected. The number of sextupole families is 54 for each ring. The field strength of the sextupole magnet is optimized to maximized the dynamic aperture or Touschek lifetime as well as adjustments of the linear chromaticity.

Figure 1 shows comparisons between typical measured chromaticity and that calculated from the model lattice. The

Table 1: Typical parameters such as the beta functions and chromaticity in Phase 2

	LER	HER	Unit
Beam Energy	4	7	GeV
β_x^*	200	100	mm
β_y^*	3	3	mm
β_x at QC2L	62.2	235.2	
β_x at QC2R	62.1	288.0	
β_y at QC1L	255.6	578.0	
β_y at QC1R	254.7	581.6	
ξ_{x0}	-69	-97	
ξ_{y0}	-146	-168	
ξ_x (QC2)	-8	-25	
ξ_y (QC1)	-67	-100	
ν_x	44.558	45.541	
ν_y	46.615	43.610	
α_p	2.88×10^{-4}	4.50×10^{-4}	

optical functions are calculated by using SAD [4] for the model lattice. There are discrepancies between the measured value and the model by $\Delta\xi_x = 1 \sim 1.5$ and $\Delta\xi_y = 2.5 \sim 3.3$ in the LER, $\Delta\xi_x = 0.5 \sim 0.7$ and $\Delta\xi_y = 3 \sim 3.3$ in the HER, which corresponds to $1 \sim 2$ % deviation.

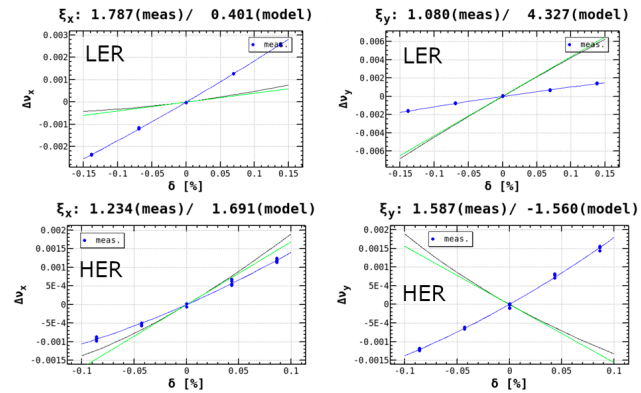


Figure 1: Chromaticity in the LER and HER, respectively. The blue plots indicate measured tune shift and black line for the model calculation. The green line show a derivative of the model tune shift at the on-momentum.

First of all, as the motivation of this article, why there is discrepancy between model and measurement? We can change the chromaticity as a relative value by using model calculations. However, the absolute value is unclear even though optics corrections have been done and worked well for corrections of beta functions and dispersions. Secondary, the off-momentum optics is necessary to understand well to

* yukiyoishi.ohnishi@kek.jp

optimize dynamic aperture. The low emittance lattice and low beta at the IP reduce dynamic aperture and Touschek lifetime becomes an issue for both linac injector capability although a top-up injection and detector backgrounds.

MEASUREMENT AND CORRECTION OF CHROMATIC PHASE ADVANCE

The beta function and phase advance are measured by close orbit distortions induced by dipole corrector magnets [5]. The close orbit is written by

$$\Delta x_i^j = \frac{\Delta \theta_j}{2 \sin(\pi \nu)} \sqrt{\beta_i \beta_j} \cos(|\psi_i - \psi_j| - \pi \nu) \quad (1)$$

$$= A_j \{C_j(C_i \cos \pi \nu + a_{ij} S_i \sin \pi \nu) \quad (2)$$

$$+ S_j(S_i \cos \pi \nu - a_{ij} C_i \sin \pi \nu)\}, \quad (3)$$

where

$$A_j = \frac{\Delta \theta_j}{2 \sin \pi \nu} \quad (4)$$

$$C_{i,j} = \sqrt{\beta_{i,j}} \cos \psi_{i,j} \quad (5)$$

$$S_{i,j} = \sqrt{\beta_{i,j}} \sin \psi_{i,j} \quad (6)$$

$$a_{ij} = \text{sign}(\psi_i - \psi_j). \quad (7)$$

The fitting parameters are A_j , $C_{i,j}$, and $S_{i,j}$, for i th BPM from 1 to N and j th dipole corrector from 1 to M . These equations can be solved by a least-square fitting with a minimization of

$$X^2 = \sum_{i,j}^{N,M} (\Delta x_i^j - \Delta x_{i,meas.}^j)^2 \quad (8)$$

$$\sum_{i=1}^N \frac{1}{\beta_i} = \sum_{i=1}^N \frac{1}{\beta_{i,design}}, \quad (9)$$

when $N \times M > 2(M + N)$ is satisfied, the number of BPMs is about 450 for each ring and six different kinds of dipole correctors are used to induce closed orbit distortions.

The chromatic phase-advance in the horizontal and the vertical direction are expressed as

$$\chi_i(w) = \frac{1}{2\pi} \frac{\partial \Delta \psi_{w,i}}{\partial \delta}, \quad (10)$$

where

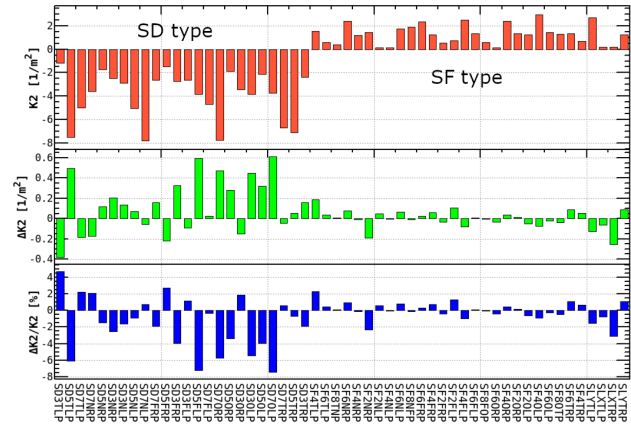
$$\Delta \psi_{w,i} = \psi_{w,i} - \psi_{w,i-1}, \quad (11)$$

and w stands for x or y . The number of locations is about 450 for each ring which corresponds to the neighboring BPMs. In order to correct the chromatic phase-advance, the field gradient of the sextupole magnets, ΔK_2 , are obtained

by solving these equations:

$$\begin{pmatrix} \chi_{1,m}(x) - \chi_{1,d}(x) \\ \vdots \\ \chi_{N,m}(x) - \chi_{N,d}(x) \\ \chi_{1,m}(y) - \chi_{1,d}(y) \\ \vdots \\ \chi_{N,m}(y) - \chi_{N,d}(y) \\ \xi_{x,m} - \xi_{x,d} \\ \xi_{y,m} - \xi_{y,d} \end{pmatrix} = M_{resp} \begin{pmatrix} \Delta K_{2,1}/K_{2,1} \\ \Delta K_{2,2}/K_{2,2} \\ \vdots \\ \Delta K_{2,M}/K_{2,M} \end{pmatrix}, \quad (12)$$

where m indicates the measurements, d indicates the model calculation, M_{resp} is a response matrix calculated by the model lattice, N is the number of BPMs, and M is the number of families of the sextupole magnets, M is 54. These equations are solved by using a singular value decomposition (SVD). The phase advance for each momentum deviations are measured with the frequency shift between -250 Hz and +250 Hz for 5 different momentum deviations. The rf frequency is 509 MHz, then the momentum deviation is calculated with the momentum compaction, α_p , which is shown in Table 1. The corrections for the sextupole families in the LER are shown in Fig. 2. The field gradient, K_2 , which corresponds to the rated current for the defocusing sextupole(SD) is -8.2 1/m² and 5.0 1/m² for the focusing sextupole(SF). The amount of the sextupole correction is within 7 % of the rated current.



The chromaticity before and after the correction is shown in Fig. 5. The comparison of chromaticity before and after the correction is shown in Table 2. The chromaticity in the model lattice is also corrected to the measurement by the correction of chromatic phase-advance.

Table 2: Chromaticity before and after correction in the LER

	Meas.	Model before	Model after
ξ_x	1.97	1.04	2.01
ξ_y	-2.15	2.62	-1.66

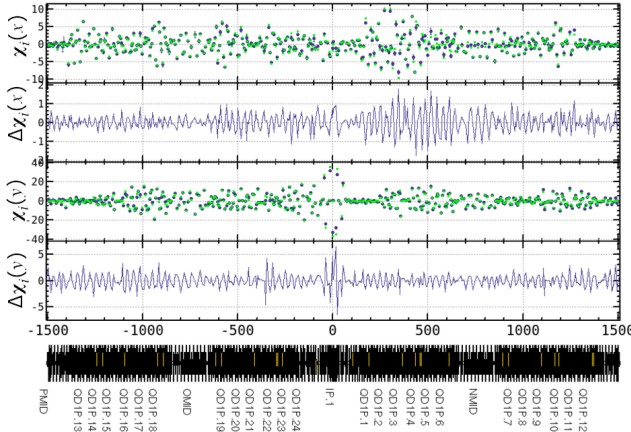


Figure 3: Chromatic phase-advance before correction in the LER.

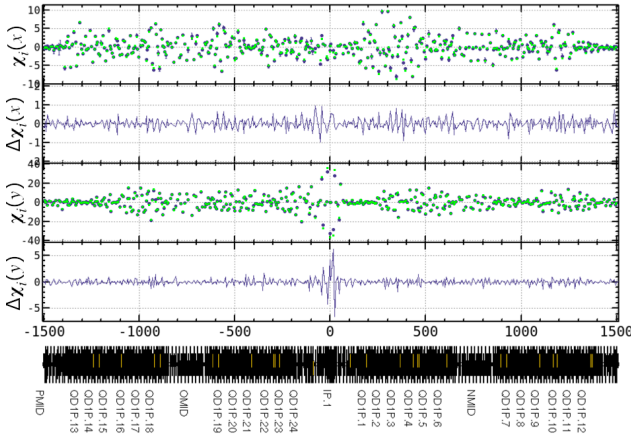


Figure 4: Chromatic phase-advance after correction in the LER.

MEASUREMENT OF CHROMATIC XY COUPLING

The interaction region is very complicated at SuperKEKB because of the final focus magnets inside the solenoid field generated by Belle II detector and anti-solenoid to compensate the detector solenoid field of 1.5 T as much as possible.

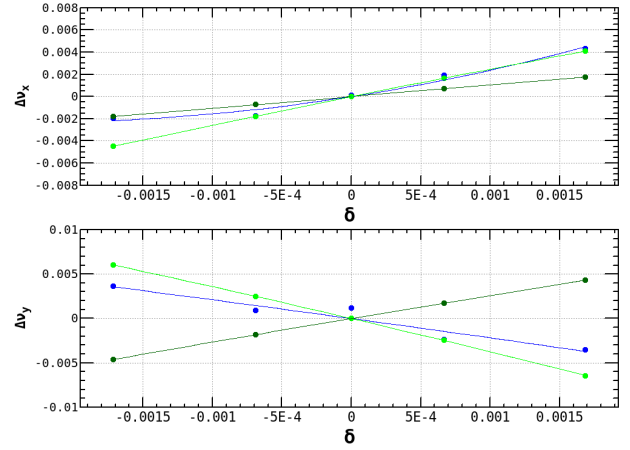


Figure 5: Chromaticity in the LER. The blue plots indicate measured values. The dark green plots indicate before correction and the green plots indicate after correction.

Furthermore, the final focus magnet has a slant angle against the solenoid axis by the half of crossing angle and the position of the magnet is shifted on the xy plane for each QC1s and QC2s. Although the XY couplings at the IP is zero in the model lattice, chromatic XY couplings are finite values which can be corrected by using skew sextupole magnets in principle.

The relationship between a physical coordinate and decoupled coordinate system of a particle is written by

$$\begin{pmatrix} x \\ p_x \\ y \\ p_y \end{pmatrix} = \begin{pmatrix} \mu & 0 & r_4 & -r_2 \\ 0 & \mu & -r_3 & r_1 \\ -r_1 & -r_2 & \mu & 0 \\ -r_3 & -r_4 & 0 & \mu \end{pmatrix} \begin{pmatrix} u \\ p_u \\ v \\ p_v \end{pmatrix}, \quad (13)$$

where (x, p_x, y, p_y) is the physical coordinate system, (u, p_u, v, p_v) is the decoupled coordinate system, $r_1 \sim r_4$ are the XY coupling parameters, and $\mu^2 + (r_1 r_3 - r_2 r_4) = 1$. The XY coupling parameter is defined at each point along the beam orbit. When only one mode is excited, the phase space of the beam accompanied with a betatron oscillation in the physical coordinate can be obtained by $v = 0$ and $p_v = 0$ for the H-mode, on the other hand $u = 0$ and $p_u = 0$ for the V-mode, respectively. In the case of H-mode, the XY coupling parameters are derived by

$$\begin{pmatrix} r_1 & r_3 \\ r_2 & r_4 \end{pmatrix} = -\mu \Sigma^{-1} \begin{pmatrix} \langle xy \rangle & \langle xp_y \rangle \\ \langle p_x y \rangle & \langle p_x p_y \rangle \end{pmatrix}, \quad (14)$$

where

$$\Sigma = \begin{pmatrix} \langle x^2 \rangle & \langle xp_x \rangle \\ \langle xp_x \rangle & \langle p_x^2 \rangle \end{pmatrix}. \quad (15)$$

The beam orbit for the betatron oscillation can be measured by Turn-by-Turn BPMs (TbT BPMs) [6]. Here, the betatron oscillation in the horizontal plane is induced by an injection kicker. The beam centroid position on two orthogonal coordinates is estimated by two TbT BPMs, which are located

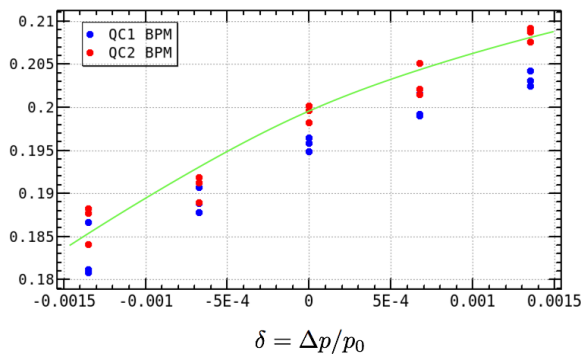


Figure 6: Chromatic horizontal beta function at the IP in the LER. The blue plots indicates the values obtained from QC1 and the red plots from QC2.

When the phase space of x and p_x is considered, the horizontal beta function at the IP can be obtained. Figure 6 shows the horizontal beta function at the IP as a function of the momentum deviation in the LER, namely the chromatic beta function. The chromatic beta function at the IP is $(\partial\beta_x^*/\partial\delta)/\beta_x^* = 50$ in the figure.

The chromatic XY coupling parameters at the IP measured by TbT BPMs in the LER are shown in Fig. 7. The absolute value of XY coupling, r_4^* , is different between QC1 and QC2 BPM but $r_1^* \sim r_3^*$ are consistent with each other. The chromatic XY couplings obtained from QC1 and QC2 BPMs are almost same results.

SUMMARY

The analysis of off-momentum optics has been performed. Understanding of the off-momentum optics is necessary not only to optimize a dynamic aperture but also to improve

luminosity performance [7]. Measurements of the chromatic phase-advance and the correction by using adjustment of field gradient for the sextupole magnets are presented. The correction of the sextupole magnets is less than 7 % of the rated current. Consequently, the chromatic phase-advance and chromaticity can be corrected on the model lattice. There is a residual between measurements and the model for the chromatic phase-advance in the vicinity of the final focus magnets. This behavior causes there is sextupole error field in the final focus magnets which has sextupole corrector coils.

The chromatic XY couplings at the IP are also measured by using TbT BPMs. In order to reconstruct the phase space, two TbT BPMs are utilized with assuming the transfer matrix of the model lattice. The r_3^* and r_4^* can be measured, however, r_1^* and r_2^* are difficult to measure absolute values due to an accuracy of the BPM resolution. The leakage amplitude of the beam position in the vertical plane from the horizontal oscillation is very small since the phase advance between the QC1 BPM and the IP is almost $\pi/2$. The relative change for the momentum deviation can be observed. The chromatic XY couplings at the IP is almost flat except for r_3^* and $r_3'^*$ is measured to be -470 in the LER.

ACKNOWLEDGMENT

This work was supported by JSPS KAKENHI Grant Number 17K05475.

REFERENCES

- [1] Y. Ohnishi *et al.*, "Accelerator design at SuperKEKB", *Prog. Theor. Exp. Phys.*, vol. 2013, no. 3, p. 03A011, Mar. 2013, <https://doi.org/10.1093/ptep/pts083>
- [2] Belle II Technical Design Report, <http://arXiv.org/abs/1011.0352>
- [3] T. Abe *et al.*, "Achievements of KEKB", *Prog. Theor. Exp. Phys.*, vol. 2013, no. 3, p. 03A001, Mar. 2013, <https://doi.org/10.1093/ptep/pts102>
- [4] *Strategic Accelerator Design*, <http://acc-physics.kek.jp/SAD>
- [5] A. Morita *et al.*, presented at eeFACT2018, Hong Kong, China, September 2018, paper TUOAB04, this conference.
- [6] Y. Ohnishi *et al.*, "Measurement of chromatic X-Y coupling", *Phys. Rev. ST-AB*, **12**, 091002 (2009).
- [7] K. Ohmi *et al.*, presented at eeFACT2018, Hong Kong, China, September 2018, paper TUOBB01, this conference.

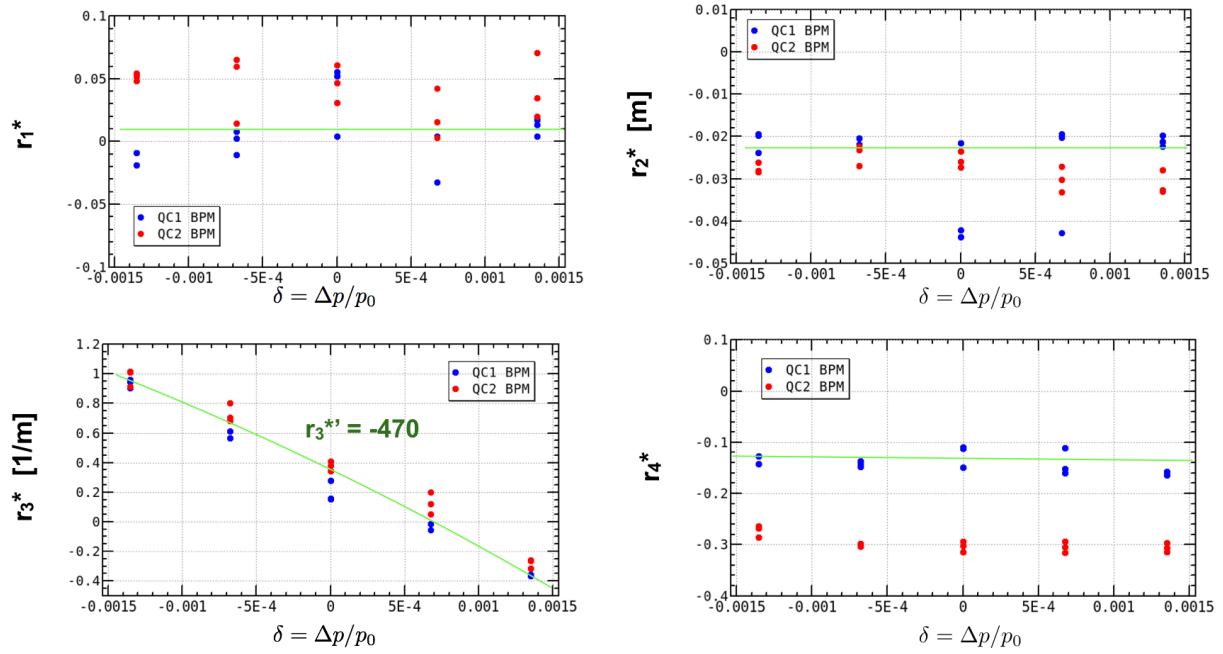


Figure 7: Chromatic XY coupling at the IP in the LER. The blue plots indicates the values obtained from QC1 and the red plots from QC2.

PROGRESS OF PRELIMINARY WORK FOR THE ACCELERATORS OF A 2-7 GeV SUPER TAU CHARM FACILITY AT CHINA *

Q. Luo[†], D. Xu, National Synchrotron Radiation Laboratory,
University of Science and Technology of China, 230029 Hefei, China

Abstract

As the most successful tau-charm factory of the world, BEPC II will celebrate its 10th birthday this year and will finish its historical mission in the next decade. Because of its very important role in high energy physics study, BEPC II will certainly need a successor, a new tau-charm collider. This paper discusses the feasibility of a greenfield next generation tau-charm collider named HIEPA. The luminosity of this successor is about 5×10³⁴ cm⁻²s⁻¹ pilot and 1×10³⁵cm⁻²s⁻¹ nominal, with the electron beam longitudinally polarized at the IP. The general scheme of the accelerators and the beam parameters are shown. Several key technologies such as beam polarization and beam emittance diagnostics are also discussed.

INTRODUCTIONS

The most successful tau-charm factory of the world in operation is Beijing Electron Positron Collider II (BEPC II), which reached a luminosity of higher than 1×10³³cm⁻²s⁻¹ in the year 2016. We believe that the unique collider in China would finish its historical mission in the next decade, maybe around the year 2022 or later. Although many scientists show strong interests in the very ambitious Higgs factory proposal known as CEPC-SPPC in China, it is clear that the Higgs factory will be a long-term plan that will cost a price of several orders higher than a tau charm factory and a period of study and construction of more than 20 years, and require global cooperation. As a transitional choice, a new tau charm collider facility was proposed by high energy physicists in the Collaborative Innovation Center for Particles and Interactions (CICPI, China) [1] to replace BEPC II after its retirement and before the construction of CEPC. The new tau-charm collider was named High Intensity Electron Positron Accelerator (HIEPA) due to its very high luminosity and current. It will be a next generation electron-positron collider operating in the range of center-of-mass energies from 2 to 7 GeV utilize polarized electron beam in collision. The pilot luminosity will be 5×10³⁴ cm⁻²s⁻¹ and the nominal luminosity will be 1×10³⁵cm⁻²s⁻¹.

The construction of a new 2-7 GeV tau-charm factory will help to maintain China's leading advantage at tau-charm area. In addition, many common technologies which are useful for both CEPC-SPPC and tau charm factory will be developed and a strong team of scientists will be trained. At last, a tau-charm factory would be a good backup plan if the CEPC-SPPC construction cannot begin on time as

planned. We expect the new tau charm facility to be an important part of Hefei Comprehensive National Science Center. This paper discussed not only the feasibility of the next tau-charm factory, but also several related key technologies needed to be developed in the future 5~10 years. The accelerator division of the National Synchrotron Radiation Laboratory of China now organizes the preliminary study of STCF accelerators.

BEAM PARAMETERS AND LATTICE DESIGN OF THE ACCELERATOR

Last year we reported two possible routes that might lead to a successor of BEPC II [2]. Now IHEP is planning to upgrade the luminosity of the BEPC II to 2-3 times higher. This paper will only introduce the plan of a greenfield tau-charm collider.

Table 1: Main Parameters for Accelerators, Pilot

Parameters	Value
Peak Luminosity	5×10 ³⁴ cm ⁻² s ⁻¹
Beam Energy	2GeV, 1-3.5GeV tunable
Circumference	324.3m
Current	1.5 A
Beam Emittance ε _x /ε _y	2.4/0.03 nm·rad
β _x [*] /β _y [*]	66.5/0.55 mm
Crossing Angle	60 mrad
Hourglass factor H	0.8
ξ _y	0.06

Table 2: Main Parameters for Accelerators, Nominal

Parameters	Value
Peak Luminosity	1×10 ³⁵ cm ⁻² s ⁻¹
Beam Energy	2GeV, 1-3.5GeV tunable
Circumference	324.3m
Current	2 A
Polarization	>85% (e-)
Beam Emittance ε _x /ε _y	5/0.05 nm·rad
β _x [*] /β _y [*]	67/0.6 mm
Crossing Angle	60 mrad
Hourglass factor H	0.8
ξ _y	0.08

As shown in Table 1 and 2, the whole construction of the collider will be divided to two stages: the pilot and the nominal. During the pilot stage, the peak luminosity will achieve 5×10³⁴cm⁻²s⁻¹. During the nominal stage, the peak

* Work supported by National Natural Science Foundation of China U1832169 and the Fundamental Research Funds for the Central Universities, Grant No WK2310000046

[†] Email address: luoqing@ustc.edu.cn

luminosity will achieve $10^{35} \text{ cm}^{-2}\text{s}^{-1}$ and an electron beam with 85% longitudinal polarization will also be deployed and replace the non-polarized electron beam. The new facility will be a dual-ring collider with symmetric and flat beams and one interaction region. Full energy injection linac is used, so there will be no boosters for injection beams, but a small damping ring for positron beam is still indispensable. The 3.5 GeV full energy linac can also be a good platform for FEL applications, positron annihilation spectroscopy, and γ rays and nuclear physics study. To avoid the luminosity loss due to hourglass effect, considering the collective effects, the sensible way is use large Piwinski angle collision and crabbed waist scheme, the ξ_y can approach 0.1 while the limit to bunch length can be avoided [3].

The general goal of the pilot stage is to finish the frame of the collider, check the whole design of accelerator physics and technologies, and reserve theoretical and physical room for electron beam polarization. The goal of the nominal stage is to suppress the β function at the interaction point, increase the beam current and the ξ_y , and use Siberian snakes to realize the longitudinally polarized electron beam at the IP, while the negative electron affinity photocathode guns will be used as polarized electron sources.

LATTICE DESIGN PROGRESS

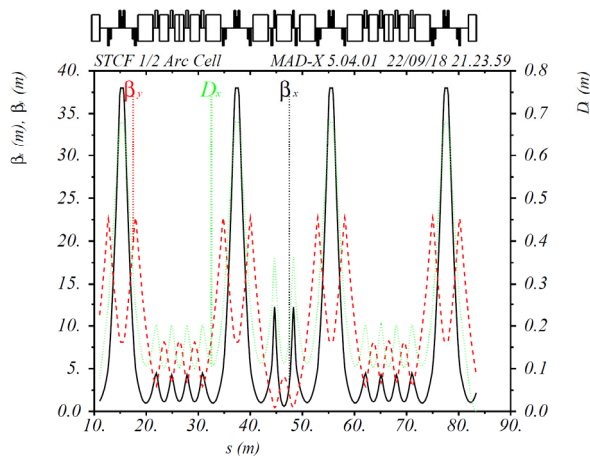


Figure 1: MBA-based arc.

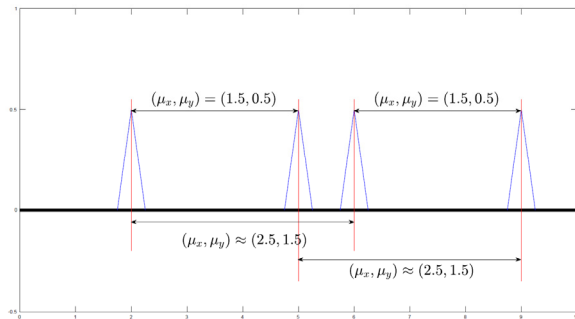


Figure 2: Double nonlinear cancellation.

Figures 1 and 2 show the arc part of the lattice design. Here we modified the design of INFN [3]. We can see that

there will be one more combined bending magnet, 2QDs and 2QFs, the phase advance will satisfy more nonlinear cancellation. Therefore, it may achieve better dynamic aperture and emittance.

POLARIZED POSITRON BEAM

A long-term plan is to utilize polarized positron in the new collider. The polarized positrons come from circular polarized gamma rays bombarding amorphous targets. Among the three main methods, use circular-polarized gamma rays from helical undulators can achieve the highest yield, but need giant linacs and thus will be extremely expensive. Compton backscattering or direct bombardment method are cheaper, but in China, there is no practical facility yet. On the other hand, polarized positron annihilation spectroscopy plays a unique role in solid state physics and material science, but the traditional positron sources based on radioisotope have achieved their performance bottleneck. The research and development of high performance polarized positron source based on accelerators is then imperative.

The feasibility of a Compton backscattering gamma ray source and polarized positron source based on 3.5 GeV linac will be discussed. As shown in Fig. 3, an ERL loop can also be induced in the facility.

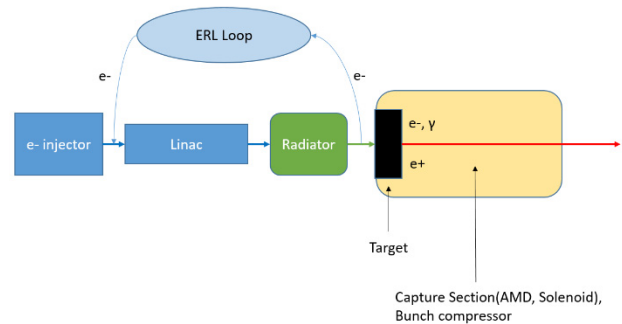


Figure 3: Polarized gamma rays from Compton backscattering.

On the other hand, a plasma wakefield accelerator cell can be used as a super energy and brightness booster for linacs [4]. As shown in Fig. 4, If a plasma cell of Cascaded HTR PWFA is used as a booster for HIEPA 3.5GeV linac, a helical undulator can be installed and generate circular-polarized gamma rays.



Figure 4: Polarized gamma rays from helical undulators.

ULTRA-LOW EMITTANCE MEASUREMENT

As known, the emittance of a next generation storage ring will be very small, especially for vertical emittance with low coupling. Due to the requirements of on-line measurement, using the SR to obtain the bunch size is an optimal choice. Since the bunch size is very small, the

spatial resolution should be of the order of 100pm. Therefore, traditional methods in the third generation light sources are not appropriate. Compared to the imaging method, the interference method can measure smaller beam size with better resolution and more reasonable performance price ratio. If work with synchrotron radiation of shorter wavelength, interference method may achieve a resolution of better than 100pm.

To measure the beam emittance and profile precisely, we will design an X-ray interferometer for future HIEPA vertical emittance measurement and give the requirements of the components of the interferometer. We will also use rotating wave-front division method to reconstruct the beam profile. The related study will introduce an international advanced beam diagnostic approach and may lead to a satisfactory answer to the question about how to measure the ultra-low emittance and very small beam size precisely for the diffraction limit storage rings.

FUTURE PLAN AND HEFEI COMPREHENSIVE NATIONAL SCIENCE CENTER

The University of Science and Technology of China has decided to support the HIEPA proposal using First Class Discipline Construction funds from Ministry of Education of China. The first instalment is 10 million RMB. Our next move is to apply for financial and human resource support from Chinese Academy of Sciences.

Meanwhile, a comprehensive national science center is now under construction in Hefei. The local authority has already reserved space for HIEPA, just in the district of national labs and big science facilities (Red area in Fig. 5).

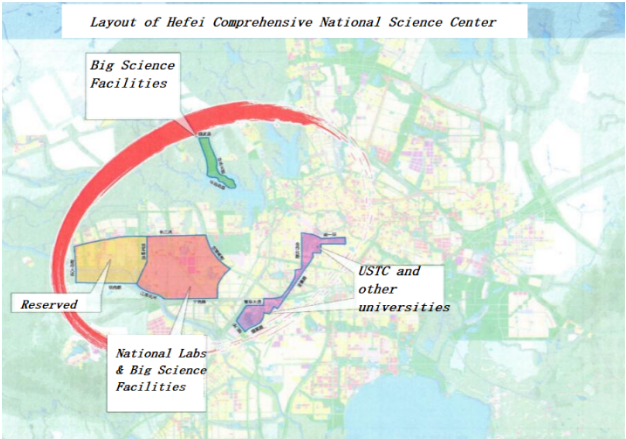


Figure 5: Hefei Comprehensive National Science Center has already reserved space for HIEPA in national labs.

CONCLUSION AND FUTURE WORK

The proposal that construct a super tau-charm collider in Hefei during the 14th and 15th Five-Year Plan sounds attractive, but there is still lots of work to do. We should pay a lot more attention to accelerator physics and key technologies. A preliminary conceptual study project for the new tau charm factory will be beneficial.

Meanwhile, the team is now notably short of hands. Experienced accelerator physicists and engineers are needed all around the world, therefore, besides worldwide recruitment, we should also set up a full system of training and education of accelerator physics and technologies.

REFERENCES

- [1] Z. Zhao, “Introduction to Future High Intensity Collider @ 2-7 GeV in China” , in *Workshop on Physics at Future High Intensity Collider @ 2-7GeV in China*, Hefei, China, Jan 2015, unpublished.
- [2] Q. Luo, “Preliminary Conceptual Study of Next Generation Tau Charm Factory accelerator at China” , in *Proc. 8th International Particle Accelerator Conf. (IPAC’17)*, Copenhagen, Denmark, May 2017, pp. 3436-3438
- [3] M. Biagini, “Super τ /charm project in Italy”, *Presented for the super τ /charm study group*, USTC, Hefei, China, 30 Sept. 2014
- [4] W. Lu, “Key Physics of Plasma Based Acceleration and its Implication to gamma-gamma Collider”, *The Mini-workshop on Future Gamma-gamma collider*, Beijing, April 23-26 2017

DIFFERNET OPTICS WITHIN LARGE ENERGY REGION AT BEPCII

C. H. Yu^{†, 1}, Y. Zhang¹, Q. Qin, J. Q. Wang, G. Xu, C. Zhang, D. H. Ji, Y.Y. Wei, J. Xing, X. H. Wang, X.M. Wen, Z. Duan, Y. Jiao, N. Wang, Y. M. Peng, Y. Y. Guo, S. K. Tian, Y. S. Sun, J. Wu, Y. Bai, S.

C. Jiang, C. C. Du, Key Laboratory of Particle Acceleration Physics and Technology,
Institute of High Energy Physics, Chinese Academy of Sciences, Beijing 100049, China

¹also at University of Chinese Academy of Sciences, Beijing 100049, China

Abstract

BEPCII is designed at the beam energy of 1.89 GeV. According to the requirements of high energy physics, BEPCII has been operated in the energy region from 1.0 GeV to 2.3 GeV since 2009. The energy region is quite large so that it is very important to select optics for the optimized luminosity. Different optics within different energy region at BEPCII will be introduced in detail in this paper.

INTRODUCTION

Beijing Electron-Positron Collider (BEP) has been well operated not only for high energy physics, but also for synchrotron radiation application for more than 15 years since 1989. Its upgrade scheme BEPCII is a double-ring collider which two beams have same energies. It aims at the research of τ -charm physics with a designed luminosity of $1.0 \times 10^{33} \text{ cm}^{-2} \text{ s}^{-1}$, which is about two orders higher than BEP at the beam energy of 1.89 GeV. The two new rings have been built in the existing BEP tunnel while keeping the machine as a synchrotron radiation source. According to the requirements of high energy physics, BEPCII has been operated in a large energy region from 1.0 GeV to 2.3 GeV since 2009.

OPTICS OPTIMIZATION AT 1.89 GeV

The main parameters of designed lattice is shown in Table 1. The commissioning of BEPCII at the energy of 1.89 GeV started on June 22nd, 2008. The horizontal tune was moved from 6.530 to 6.505 on May 5th, 2009 for higher luminosity. The data taking at the energy of 1.89 GeV started from the beginning of 2010. The beam current and luminosity were improved step by step, together with the control of detector background and the luminosity optimization systematically. The maximum beam current and luminosity reached 750 mA and $6.49 \times 10^{32} \text{ cm}^{-2} \text{ s}^{-1}$, respectively until April 28th, 2011. There are two limitations to restrict the luminosity further improvement. One is the beam current, and the other is beam-beam parameter. It's very hard to increase the beam current, especially above 700 mA due to heating problem, which were mainly caused by synchrotron radiation power and high order mode. Several serious hardware failures were happened during the operation, such as kicker magnet, RF coupler, SR monitor, bellows, feedback system, etc. The beam-beam parameter was limited obviously under 0.033 at any bunch current shown in Fig. 1. Bunch lengthening effect was considered to explain the phenomenon.

[†] yuch@ihep.ac.cn

Table 1: Main Design Parameters of BEPCII

Parameters	Values
Operation energy	1.0~2.1 GeV
Optimized energy	1.89 GeV
Beam current	910 mA
Bunch current	9.8 mA
Circumference	237.5 m
Number of particles	4.5×10^{12}
β function at IP β_x/β_y	1.0 m/1.5 cm
Horizontal emittance	144 nm-rad
Working point ν_x/ν_y	6.53/5.58
Harmonic number	396
Bunch number	93
Bunch spacing	2.4 m
RF voltage	1.5 MV
RF frequency	499.8 MHz
RF cavity number per ring	1
Energy loss per turn	121 keV
Synchrotron radiation power	110 kW
Damping time $\tau_x/\tau_y/\tau_E$	25/25/12.5 ms
Natural energy spread	5.16×10^{-4}
Momentum compaction	0.0235
Natural bunch length	1.35 cm
Crossing angle at IP	$11 \times 2 \text{ mrad}$
Beam-beam parameter	0.04
Luminosity	$1.0 \times 10^{33} \text{ cm}^{-2} \text{ s}^{-1}$

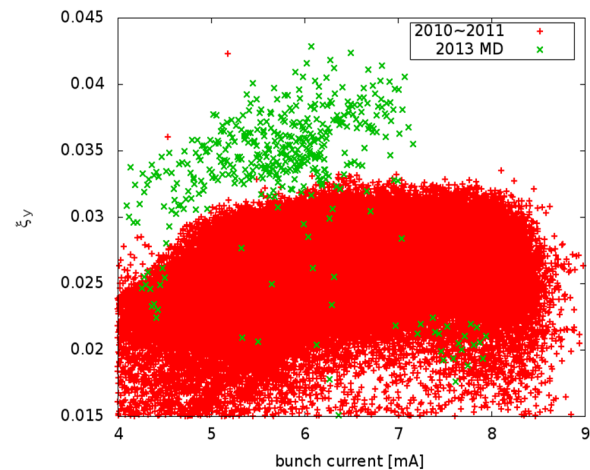


Figure 1: Comparison of beam-beam parameter with the schemes of different bunch lengths.

Table 4: Main Lattice Parameters for Low Energy Region

Parameters	Values
Beam energy	1.0 GeV
β function at IP β_x/β_y	1.0 m/1.2 cm
Horizontal emittance	54 nm-rad
Working point ν_x/ν_y	6.505/5.580
Momentum compaction	0.0286
Natural bunch length	0.6 cm

Table 5: Main Lattice Parameters for High Energy Region

Parameters	Values
Beam energy	2.3 GeV
β function at IP β_x/β_y	1.0 m/1.5 cm
Horizontal emittance	144 nm-rad
Working point ν_x/ν_y	7.505/5.580
Momentum compaction	0.017
Natural bunch length	1.5 cm

During the past years, data taking at 173 high energy points have been finished. The realized peak luminosity at different beam energies are shown in Fig. 3. Red dot means the data taking time is relatively longer.

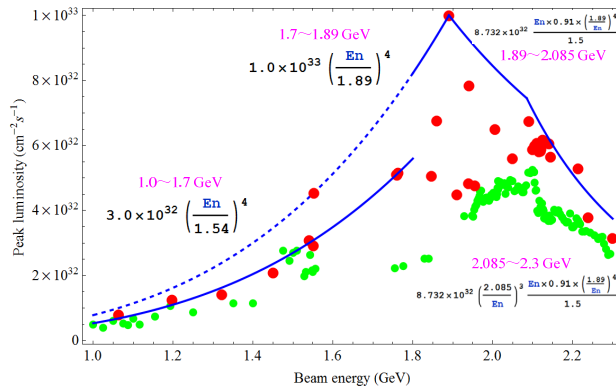


Figure 3: The peak luminosity from 1.0 GeV to 2.3 GeV.

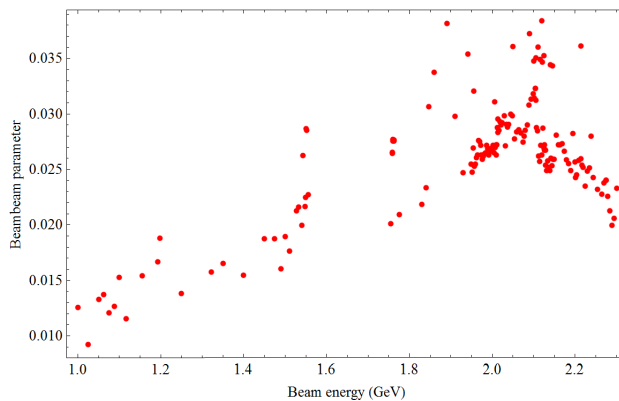


Figure 4: The achieved beam-beam parameter.

The RF system can support a maximum 110 kW beam power. For the operation of high energy region the beam current can't be higher due to the limitation of RF power. Moreover, the bunch length and emittance could not be well controlled so that the beam-beam parameter was lower. For the operation of low energy region the multi-

bunch instability was very serious. The beam current was limited by the ability of feedback system. The statistic of beam-beam parameter, beam power, beam current and bunch number are shown in Fig. 4 and Fig. 5.

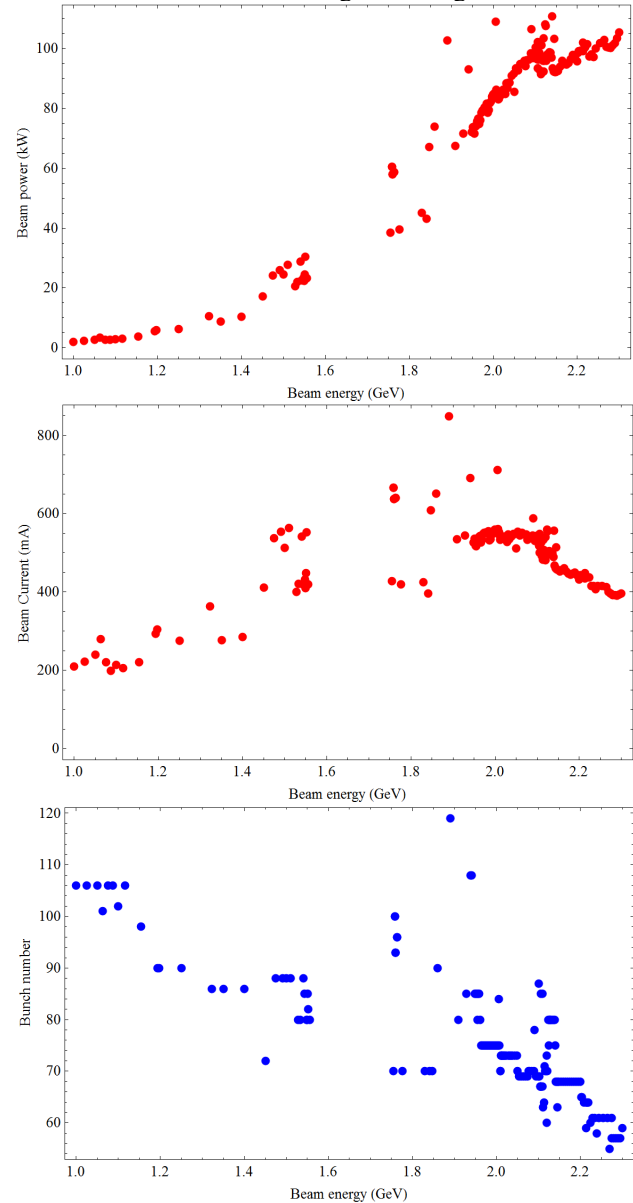


Figure 5: Statistic of beam power, beam current and bunch number.

CONCLUSION

BEPCII is in a good performance for high energy physics with different optics within energy region 1.0~2.3 GeV. The upgrade to take data at the energy 2.3~2.45 GeV is undergoing. The operation with beam energy up to 2.35 GeV is feasible right now. For much higher energy it will be feasible after the summer shutdown of 2019.

REFERENCES

- [1] Yuan Zhang *et al.*, in *Proc. IPAC'14*, paper THPRI007.

HIGH CURRENTS EFFECTS IN DAΦNE

C. Milardi[†], D. Alesini, S. Bini, A. Drago, A. Gallo, A. Ghigo,
S. Guiducci, M. Serio, A. Stella, M. Zobov, LNF-INFN, Frascati, Italy
F. Marcellini, PSI, Villigen, Switzerland
P. Raimondi, ESRF, Grenoble, France

Abstract

DAΦNE, the Italian lepton collider, operates routinely with high intensity electron and positron colliding beams. The high current multi-bunch beams are stored in two independent rings, each of them 97 m long, and are distributed into 100÷110 contiguous buckets out of the 120 available, spaced by only 2.7 ns.

Since its construction, DAΦNE has been operated in different configurations which, overall, allowed to store currents up to 1.4 A and 2.45 A in the positron and in the electron beam respectively. To this day DAΦNE holds the record for the highest electron beam current ever stored in particle factories and modern synchrotron radiation sources.

The DAΦNE experience, in terms of beam dynamics optimization aimed at achieving the high intensity beams, is presented with special emphasis on the *e-cloud* related issues which represent the dominant effect limiting the positron beam current.

INTRODUCTION

DAΦNE [1, 2] is an accelerator complex consisting of a double ring lepton collider working at the energy of the Φ -resonance, (1.02 GeV) and an injection system. The collider includes two independent rings, each ~97 m long.

The two rings share an interaction region (IR), where the detector on duty is installed. A full energy injection system, including an S-band LINAC, 180 m long transfer lines, and an accumulator/damping ring provides fast and high efficiency electron–positron injection in topping-up mode.

Since its construction DAΦNE has been manly operated in two configurations, differing essentially for the approach to the beam-beam interaction. In fact, till 2006, the main rings shared two ~10 m long interaction regions, although only one detector at a time was taking data. Due to the common beam pipe, the two beams collided with a rather small horizontal angle, of the order of 25 mrad, which was also compliant with the Piwinski criterion [3]. During this initial phase, the collider performances have been significantly improved by several progressive upgrades and a wide program of machine measurements and studies, aimed at pointing out the physics processes limiting the maximum achievable current and luminosity, has been undertaken. This activity largely contributed to define a proposal for an original collision scheme based on large Piwinski angle and *Crab-Waist* (*CW*) compensation of the beam-beam interaction [4, 5]. In 2006 the novel approach to collision has been implemented on DAΦNE during a six months shutdown planned to install a compact detector

without longitudinal magnetic field, offering an optimal simplified environment to test the new configuration: the SIDDHARTA experiment.

The parameter of the DAΦNE collider in the nominal and in the *CW* configurations are reported in Table 1.

Table 1: DAΦNE Beam Parameters

	DAΦNE native (2000÷2006)	DAΦNE CW Since 2007
Energy (MeV)	510	
β_y^* (cm)	1.8	0.85
β_x^* (cm)	160	23
σ_x^* (μm)	760	250
σ_y^* (μm) <small>low current</small>	5.4	3.1
σ_z (cm)	2.5	1.5
Bunch spacing (ns)	2.7	
Damping times τ_E, τ_x (ms)	17.8/36.0	
Cros. Angle $\theta_{cross}/2$ (mrad)	12.5	25
Pwinski Angle ψ (mrad)	0.6	1.5
ϵ (mm mrad)	0.34	0.28
RF frequency [MHz]	368.26	368.667
Harmonic number	120	
$L \cdot 10^{32}$ (cm ⁻² s ⁻¹)	1.5	4.36

HIGH CURRENT DESIGN STRATEGY

The efforts aimed at achieving high intensity beams and at optimizing beam quality have been comparable to the ones invested in the beam-beam interaction approach.

Since the design stage all the main ring vacuum components have been specified in order to store large total current in a large number of bunches, which required special emphasis on vacuum and collective effect related topics.

Each ring vacuum chamber [6] consists of 4 arcs and straight sections. The chamber of the arcs is made by a special Al-Mg alloy (Al 5083 H321), while the straight section ones use a slightly different composition Al-Si alloy (Al 6082 T6). The dipole and wiggler beam pipes in the arcs are all equipped with antechambers and synchrotron radiation absorbers in order to improve pumping efficiency.

It is well known that collective instabilities in accelerators mostly come from an intense particle beam electromagnetically interacting with its vacuum chamber environment. This interaction, which can easily drive the beam to instability, is described by the wakefield (time domain) and beam-coupling impedance (frequency domain) concepts. Hence the need for a detailed evaluation of the impedance impact on single and multibunch dynamics [7]. Since the

[†] catia.milardi@lnf.infn.it

very beginnings the machine design approach aimed at reducing as much as possible the number of vacuum chamber elements trapping parasitic High Order Mode (HOM) able to drive multi-bunch instabilities, and at pointing out technical solutions suitable to damp HOMs and instabilities as well. This approach has been primarily pursued by properly designing the RF cavities [8]. They integrate a system of waveguides coupled to HOMs resonant fields that allow to absorb the power released by the beam into the trapped modes. The residual excitation of beam oscillation is damped by a bunch-by-bunch digital feedback system.

The most relevant resonating volumes and discontinuities such as bellows, pumping ports, spherical beam pipe at the interaction point etc. have been shielded with screens.

The resistive wall impedance and the contribution to the impedance of the main inductive elements have been carefully evaluated as well as their contribution to the power losses.

New designs and novel ideas were adopted for almost all principal vacuum chamber components: RF cavities [9, 10], shielded bellows [11], longitudinal feedback kickers [12], BPMs [13], DC current monitors [14], injection kickers [15], transverse feedback kickers and others [16]. For example, longitudinal feedback kickers similar to those developed for DAΦNE are routinely used in more than ten operating colliders and synchrotron radiation sources.

The transverse mode coupling instability threshold has been evaluated and, according to simulations, was an order of magnitude higher than the nominal bunch current.

HIGH CURRENT EXPERIENCE

Despite the careful design efforts beam measurements taken during commissioning outlined some relevant differences between e^- and e^+ beam dynamics.

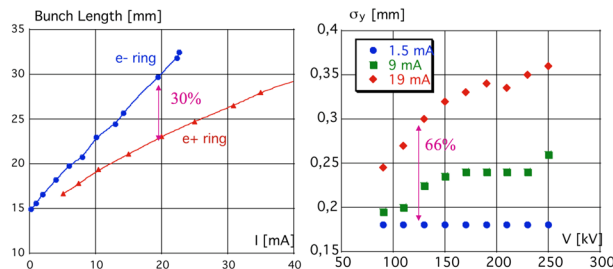


Figure 1: Comparison between e^- (blue dots) and e^+ (red dots) bunch length measurements as a function of the bunch current (left); measured vertical e^- beam size blow-up (right) as a function of the RF cavity voltage for different values of the bunch current.

First of all, at the nominal bunch current of 20 mA the e^- bunches were by about 30% longer than e^+ ones, as shown in Fig. 1. This had a direct impact in terms of geometric luminosity reduction due to the well-known hour-glass effect [17]. Moreover, for beams colliding with a horizontal crossing angle, as it is the DAΦNE case, synchro-betatron beam-beam resonances become stronger for longer

bunches due to a larger Piwinski angle, thus limiting the maximum achievable beam-beam tune shift parameter.

The ring impedance has been estimated through bunch length measurements as a function of bunch current. Numerical fits based on a broadband model have shown that the beam coupling impedance of the two DAΦNE rings were different by approximately a factor of two. The measured impedance of the positron ring was $Z/n = 0.54 \Omega$ to be compared with 1.1Ω of the electron one. This difference produced several harmful consequences affecting the collider performances.

During ordinary operations also a transverse beam size blow-up, mainly in the vertical plane, was observed beyond the microwave instability threshold, see Fig. 2. This effect, which also exhibited a heavy dependence on the RF cavity voltage, as shown in Fig. 1, was clearly correlated with the longitudinal microwave instability, since it had the same threshold, the threshold was higher for larger values of the α_c parameter, see Fig. 2, and it was more harmful for the e^- ring which had a higher coupling impedance.

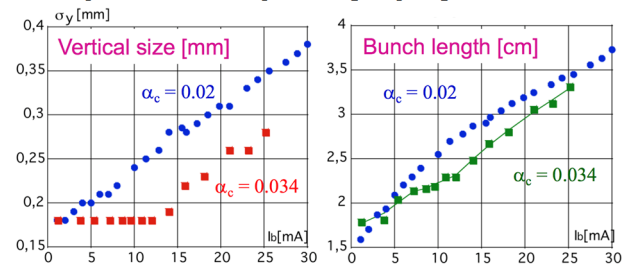


Figure 2: Measured vertical e^- beam size blow-up (left) and bunch length (right) as a function of bunch current for different momentum compaction (α_c) values.

Furthermore there was evidence of single bunch instability, mainly a longitudinal quadrupole oscillation, appearing at lower bunch current in the e^- ring. The quadrupole longitudinal instability has been controlled by a special technique implemented at DAΦNE [18] in the synchrotron (dipole) feedback system. The new technique consisted in shifting the Quadrature Phase Shift Keying (QPSK) modulated signal driving the feedback back end in order to damp both dipole and quadrupole beam motions.

NEGATIVE MOMENTUM COMPACTION

As far as high current issues are concerned, it is worth recalling the experimental test done at DAΦNE implementing a lattice with negative momentum compaction (α_c) in both rings [19].

In such configuration a considerable bunch shortening has been measured as predicted by numerical simulations. High single bunch currents have been stored in both beams, notably in the e^+ ring current up to 40 mA has been measured with large negative chromaticities, without any evidence of head-tail instability.

Concerning multi bunch dynamics, stable currents of the order of 1 A have been stored in both rings without any problem for RF cavities and feedback systems operation. Remarkably feedbacks were not necessary to store currents

up to 400 mA in the e^- ring. The 1 A current limit was essentially due to saturation in the injection process that, due to the major lattice modifications, required careful optimization.

The encouraging results led to test collisions with the negative α_c lattice configuration. At first a comprehensive collision tuning allowed to reproduce the same values in terms of convoluted dimension of the interacting bunches at the IP, as for the positive α_c optics ($\Sigma_y \sim 8.2 \mu\text{m}$ and $\Sigma_x \sim 1 \text{ mm}$). Then currents have been progressively increased looking at the beam-beam phenomenology. The best luminosity results have been obtained with currents of the order of 300 mA in both beams, which gave a luminosity $L = 2.5 \times 10^{31} \text{ cm}^{-2} \text{ s}^{-1}$ corresponding to a specific luminosity of the order of $2.5 \cdot 10^{28} \text{ cm}^{-2} \text{ s}^{-1} \text{ mA}^{-2}$, a rather higher value if compared with the one ordinary measured with positive α_c optics; unfortunately the promising results were not confirmed at high currents. To our knowledge DAΦNE is the only collider to have implemented and studied collision with negative α_c .

BEAM DYNAMICS OPTIMIZATION

Years 2001÷2006

In order to cancel out the differences between e^- and e^+ rings the electrodes (ICEs) originally installed in the wiggler beam pipes of the e^- ring with the aim of neutralizing the ions of the residual vacuum, were removed. The activity was carried on during the shutdown propaedeutical to the installation of the FINUDA detector in 2006.

Beam measurements, after ICEs removal, confirmed that the e^- beam dynamics was almost comparable to that of the e^+ beam [20]. The e^- bunch length was 25÷30 % shorter, see Fig. 3, and there was no evidence of either quadrupole instability threshold or vertical beam blow-up at the operating bunch current ($\sim 15 \text{ mA}$).

This resulted in about 50% specific luminosity increase during the run for the FINUDA experiments [21].

Concerning multibunch operations, since 2002 it became possible to store current in 100 consecutive bunches after reducing the impact of parasitic crossing in the IR1 by: moderately reducing β_x^* and beam emittance, slightly increasing the crossing angle, varying $\theta_x/2$ from 12.5 to 14.5 mrad, and optimizing transverse and longitudinal feedback systems [22].

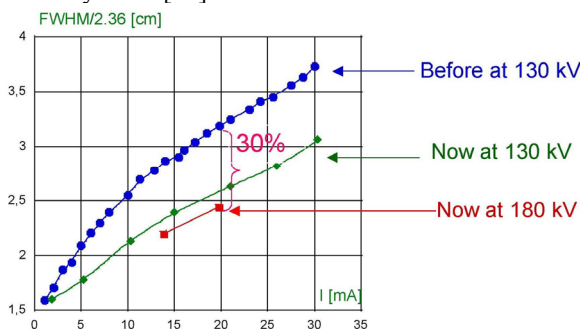


Figure 3: Bunch lengthening before (blue dots) and after (green and red dots) ICEs removal.

By the end of 2006, after the FINUDA run, also thanks to significant improvements to the non-linear optics [23, 24], the maximum stored currents were $I^- = 2.4 \text{ A}$ and $I^+ = 1.4 \text{ A}$; while the maximum luminosity was achieved at current of the order of 1.5 A and 1.1 A for the e^- and the e^+ beam respectively, (see Table 2).

Crab-Waist Upgrade

By the end of 2006, in the framework of upgrades aimed at implementing the innovative *Crab-Waist* Collision Scheme [25] several vacuum elements were modified once again.

A new crossing section providing complete separation between the two beams replaced the second IR.

A new IR was designed [26] in order to implement a full separation between the two ring beam pipes just after the first defocusing quadrupole of the low- β , paying great attention to avoid all the possible discontinuities so as to keep the ring coupling impedance low. The number of bellows was also limited to the minimum necessary to compensate thermal strain and mechanical misalignments. There were four bellows per ring both in IR and in the crossing region. The vacuum chamber of the IR consisted of straight pipes merging in a Y shaped section. Special attention has been paid to the *Y-section* design since beam induced electromagnetic fields can generate trapped high order modes (HOM). Simulations have pointed out four possible HOMs, among them only the first was trapped and, even in the worst case, assuming the beam spectrum in full coupling with the trapped mode, the estimated released power was less than 200 W. Nevertheless, the *Y-section* was equipped with a cooling system to remove the heating due to the HOM [27].

Newly designed bellows were installed in the new IR and in the ring crossing section. The inner radius of bellows convolutions was $\approx 65 \text{ mm}$, the outer one 80 mm and the length $\approx 50 \text{ mm}$, see Fig. 4. They exploited innovative RF shield [28], necessary to prevent the discontinuity from acting as a cavity for the beam. The new RF shield was implemented by means of Ω shaped Be-Cu strips, installed all around two cylindrical aluminium shells fixed at the bellows ends.

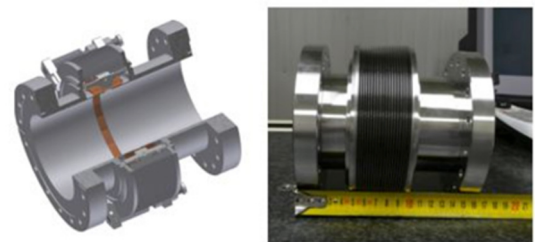


Figure 4: Copper-Beryllium strip shielded bellows, mechanical design (left) and real device (right).

These shields replaced the old ones realized by using contiguous mini bellows. Electromagnetic simulations performed with the HFSS code in the frequency range from DC to 5 GHz showed that the new design reduced bellows contribution to the ring coupling impedance.

The injection kickers, two in each ring, were replaced with new devices [29] based on tapered strips embedded in a rectangular cross section vacuum chamber allowing injection rate, in principle, up to 50 Hz, see Fig. 5.



Figure 5: The new injection kicker under test (left) and installed on the electron ring (right).

Moreover, a smooth beam pipe and tapered transitions reduced the kickers contribution to the total ring coupling impedance. All these features were intended to improve the maximum storable currents, colliding beams stability and background on the experimental detector during injection.

The vacuum chamber components modifications for the CW experiment brought another relevant factor in the coupling impedance reduction.

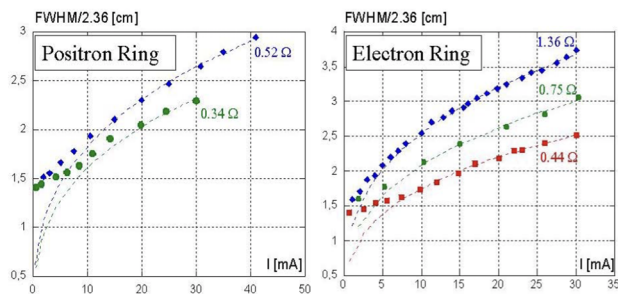


Figure 6: Bunch lengthening for the e^+ beam (left) before (blue) and after (green) the CW upgrade; bunch lengthening for the e^- beam (right) for the native ring setup (blue), after ICEs removal (green) and after CW upgrade (red).

As one can see in Fig. 6 by comparing the green and red curves, bunches in the electron ring were by about 20% shorter with respect to the previous FINUDA run.

During the test run for the CW configuration with the SIDDHARTA experiment the maximum currents that have been stored were $I^- = 2.2$ A and $I^+ = 1.2$ A; while the peak luminosity, which was three times larger than in the past [30, 31], was achieved at current of the order of 1.47 A and 1.0 A for the e^- and the e^+ beam respectively, (see Table 2).

Crab-Waist for the Large KLOE-2 Detector

The remarkable improvements in terms of instantaneous and integrated luminosity achieved during the CW test opened new perspectives for physics research at DAΦNE, and a new run was planned for the upgraded KLOE-2 detector.

Several activities were undertaken [32] in view of the KLOE-2 preliminary run in 2010.

A new IR was designed [33] to cope with the requirements of the KLOE detector, which included a high intensity longitudinal field strongly perturbing beam

dynamics and coupling the transverse betatron oscillations of the stored beams.

The leftover old-style bellows were replaced with new ones having lower impedance and providing long lasting shield contour uniformity when compressed.

Few ion clearing electrodes, still present in the electron ring and no longer used, were removed.

New electrodes (ECE) have been installed in the e^+ ring to mitigate the *e-cloud* induced effects.

The Collimator rectangular vacuum chambers, (20 mm high and 90 mm wide), were replaced by square ones (55 mm) to optimize their contribution to the ring impedance. Moreover, the new design allowed to move the blades closer to the beam, improving their effectiveness in intercepting the background otherwise hitting the experimental detector.

The new kicker developed for the transverse horizontal positron feedback was also used as a beam dumper. It was installed in the opposite section with respect to the IR and was intended to dump the beam in a controlled way reducing the radiation level in the area and avoiding dangerous detector trips.

Also in this case the ring impedance was estimated relying on bunch length measurements as a function of bunch current. Results have shown a bunch lengthening reduction of the order of 10% at a current of 20 mA with respect to the values attained during the test run with the CW scheme.

Bunch length is neither affected by the insertion of the beam collimators nor, on the positron ring, by the presence of the new electrodes for electron clearing, see Fig. 7. ECEs contribution to the inductive component of the ring impedance is negligible, as emphasised by bunch lengthening with current that, in the e^+ ring, was even lower than in the e^- one.

The RF cavity hardware was also reviewed developing a direct RF feedback system in the low-level RF. This allowed to reduce the cavity detuning angle, increasing the overall efficiency and limiting the reduction of the coherent ‘0-mode’ synchrotron frequency with beam current. The power of the ring RF station was limited to ≈ 60 KW, with respect to the 180 kW nominal value, by decreasing the klystron HV in order to reduce the power consumption. The reduced RF power was nevertheless sufficient to sustain the stored current.

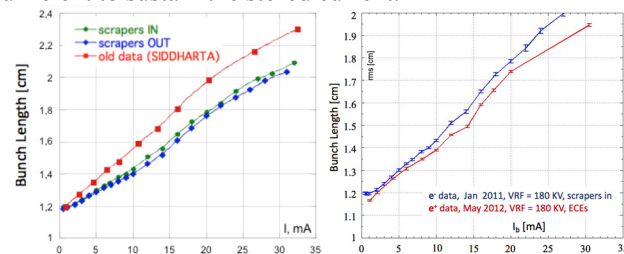


Figure 7: e^- beam bunch lengthening as a function of the bunch current for different e^- ring configurations (left); comparison between e^- and e^+ bunch lengthening after the CW upgrade for the KLOE-2 run (right).

The four wigglers installed in each ring have been modified [34] to reduce the higher order multipoles of the magnetic field, and by removing a purpose built sextupole component, which had been efficiently used to implement a smooth and distributed chromaticity control.

Unfortunately, the preliminary run outlined a major fault in some bellows in the IR, which had lost electrical continuity causing anomalous beam induced heating of one of the two defocusing quadrupoles, ultimately resulting in a harmful random vertical tune-shift. For this reason, during the shutdown of 2013, intended to upgrade the detector, the vacuum chamber around the interaction point was replaced [35]. The new one had tapered transition between the thin ALBEMET sphere and the Al beam pipes, and included reshaped bellows with new designed RF contacts. Two cooling coils were added on the tapers and new semi-cylindrical thin (35 mm) beryllium shields were placed inside the sphere.

Thereafter during collider operations, the e^- beam was still exhibiting the effects due to a microwave instability threshold appearing above a current of the order of ~ 10 mA per bunch, resulting in a widening of the transverse beam sizes. Such effect was quite moderate in single beam operation and became sometimes more harmful in collision due to the beam-beam interaction [36]. There was a plan to cure this effect by using an optics with higher momentum compaction α_c , but there was no time to implement it.

Furthermore, the quality of the e^- beam depended heavily on the mitigation of the effect induced by the ions of the residual vacuum, such effect is counteracted by leaving a suitable empty gap in the batch. The width of such gap is a compromise between opposite requirements posed by e^- beam dynamics and high luminosity. It depends greatly on the vacuum condition which improves with the stored beam dose. In fact, the best results in terms of luminosity have been achieved, by the second half of the run, through collisions of 106 consecutive bunches.

In general beam dynamics was affected by all the modifications implemented in the two rings.

Beam currents, especially the e^- one, were affected by longitudinal quadrupole oscillations. This instability was successfully kept under control by the QPSK based techniques as in the past. The environmental RF and DC noise coming from pickups, and leading to undesirable vertical beam size growth, was minimized by installing a low noise front end, designed in collaboration with SuperKEK feedback team, on the vertical feedback.

E-cloud Related Issues

Since the beginning of high current operations, the e^+ beam dynamics has been shown to be dominated by the *e-cloud* induced instabilities. The e^+ current was limited by several factors all related to the *e-cloud* phenomenology, such as: fast horizontal instability at high current, increase in the vertical beam size, tune-spread along the batch, and anomalous vacuum pressure rise with current in the arcs. Measurements and simulations showed how horizontal

instability was triggered by the *e-cloud* formation in the dipoles and in the wigglers vacuum chambers [37].

The DAΦNE collider has been designed much before than the accelerator scientific community recognized the impact of the *e-cloud* on beam dynamics, for this reason some project options were not properly optimized as, for instance, the choice of Al for the vacuum chamber. In fact, Al has very high Secondary Electron Yield (SEY). Nevertheless, some other features played a positive role to contain the *e-cloud* formation. It is the case of the antechamber and the synchrotron radiation absorbers integrated in the dipole and wiggler vacuum chamber nominal design. It must also be considered that DAΦNE operates at rather low energy with high intensity multi-bunch beams, and very low bunch spacing, of the order of ~ 2.7 nsec. The energy emitted by synchrotron radiation each turn is of the order of 9.7 KeV which, due to the short ring circumference, corresponds to a quite high energy density.

Beside design concepts several countermeasures were adopted while operating DAΦNE, tuning rings and beam parameters, installing new devices, potentiating bunch-by-bunch transverse feedback systems, and last but not least securing optimal dynamic vacuum conditions, for instance, sublimating frequently the ring vacuum chambers.

A positive result was obtained lengthening the bunch by reducing the voltage of the RF cavity of the e^+ ring. Fig. 8 presents the behaviour of the pressure rise with the stored current, measured by two vacuum gauges installed on different arcs, as a function of the RF cavity voltage. Positive effects were obtained also moving ring chromaticity toward high positive values, and tuning the octupole magnets.

As far as devices are concerned, solenoidal coils were wound all around straight sections. The transverse horizontal feedback power was doubled (500 W now) providing $\sim 40\%$ increase in the kick strength. The horizontal feedback kicker was replaced with a device having double stripline length and reduced plate separation, providing larger shunt impedance at the low frequencies typical of the unstable modes.

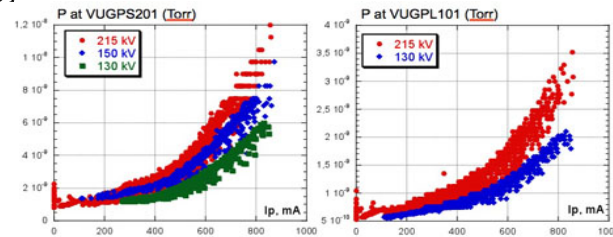


Figure 8: Pressure rise versus stored e^+ current in 2 different arcs as a function of the RF cavity voltage.

Moreover, the kicker was moved in a lattice position having a higher β_x value. On purpose designed electrodes [38] were installed inside dipole and wiggler vacuum chambers. The electrodes were checked in 2012, during the KLOE preliminary run. Several measurements and tests demonstrated their effectiveness in thwarting the *e-cloud* effects [39, 40]. Moreover, ECEs made possible a number

of unprecedented measurements (*e-cloud* instabilities growth rate, transverse beam size variation, tune shifts along the bunch train) where the *e-cloud* contribution was clearly evidenced by turning ECEs on and off. Tests with ECEs also provided a useful framework to benchmark simulation codes.

The vertical beam size enlargement has been measured at the synchrotron light monitor by gradually turning off all the electrodes as shown in Fig. 9. The vertical size increased from about 110 μm with electrodes on to more than 145 μm with the electrodes off. This trend clearly indicated that the single bunch *e-cloud* instability was responsible for the vertical beam size growth.

The tune modulation along the batch induced by the *e-cloud* density variation [41] is reported in Fig. 10.

The fractional tunes progressively increase and reaches a steady state regime after ~ 20 bunches. In the horizontal plane the head-tail tune spread is about 0.006–0.008.

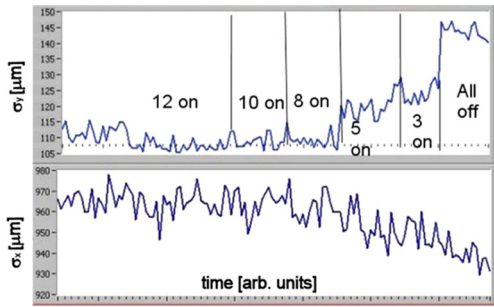


Figure 9: Beam dimension at the SLM turning progressively off all ECEs ($I^+ = 500\div 600$ mA, 100 bunches).

Relying on simulations, this tune shift should correspond to an *e-cloud* density, in the wiggler sections, of the order of 10^{14} m^{-3} , a value significantly different than the one predicted by simulation. However, such discrepancy is consistent with a local *e-cloud* density in the vacuum chamber centre, close to the beam trajectory, higher by an order of magnitude with respect to the average density foreseen by the theoretical model.

When the ECEs are switched on the tune shift reduces by a factor of 2–3, but they do not cancel completely the tune spread. This can be explained reminding that the electrodes in the wigglers cover only 67% of their total length. In turn, as it is seen in Fig. 10(b), the vertical tune spread is notably smaller than the horizontal one and the ECEs almost completely cancel it. Still some vertical tune variation is observed while turning on and off the ECEs. This behaviour can be explained with the residual orbit variation observed during the measurements. In fact, the presence of high strength CW sextupoles leads mainly to the vertical tune shift of all bunches in the batch.

These first studies were all done by polarizing the stripline with a positive voltage in the range $0\div 250$ V. However, simulations indicated that a factor two higher voltage was required to completely neutralize the *e-cloud* density due to a e^+ current of the order of 1 A. For this reason, during the 2013 shutdown the electrode power

supplies were replaced with devices providing a maximum negative voltage of 500 V. The change of polarity was intended to limit the current delivered by the power supplies.

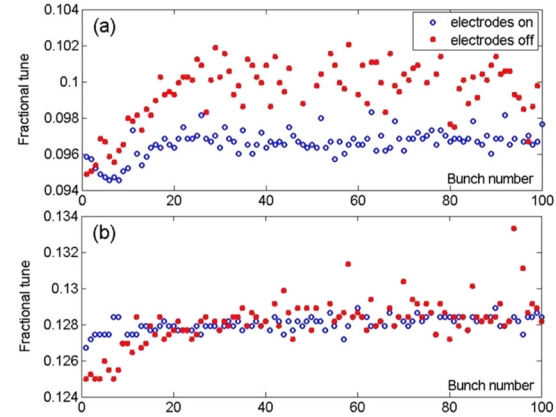


Figure 10: Measurements of horizontal (a) and vertical (b) fractional tunes along the batch at $I^+ \sim 500$ mA.

The new setup has been tested storing a ~ 700 mA current in 90 bunches spaced by 2.7 ns, and measuring the horizontal and vertical tune spread along the batch with the electrodes on and off. Results show a clear reduction of the tune spread in both planes, but especially in the horizontal one. Electrodes have been essential when the vacuum level in the e^+ ring was not optimal yet. At that stage, a careful tuning of each stripline polarization voltage was done in order to avoid sudden variation in the e^+ beam orbit. Then, progressively during the data taking, it was necessary to switched off several ECE due to their faulty behaviour. The KLOE-2 run finished with only 2 ECE fully operative, but, at that point, the benefits coming from the scrubbing process helped in keeping the *e-cloud* instabilities under control. A conclusive explanation of the process leading the ECEs to exhibit a faulty behaviour, after having worked for some time, is under way.

During the whole KLOE-2 run the maximum current stored in the e^+ beam has been of the order of $I^+ \sim 1.2$ A, although, at regime in collision, a current $I^+ > 0.95$ has been rarely injected; a value considerably lower than the one achieved during the previous DAΦNE's run periods.

Table 2: Beam Current Figures

	DAΦNE native (2001-2006)	DAΦNE CW SIDDHARTA (2007-2009)	DAΦNE CW KLOE-2 (2010-2018)
$L_{\text{peak}} \cdot 10^{32} (\text{cm}^{-2}\text{s}^{-1})$	1.5	4.4	2.38
$I^- \text{ at } L_{\text{peak}} (\text{A})$	1.5	1.47	1.18
$I^+ \text{ at } L_{\text{peak}} (\text{A})$	1.2	1.0	0.87
$I_{\text{MAX}} (\text{A})$	2.4	2.2	1.7
$I^+_{\text{MAX}} (\text{A})$	1.4	1.2	1.1
N_{bunches}	111	105	106

CONCLUSION

During the whole period of operations DAΦNE succeeded in providing and maintaining high intensity stable beams, thanks to the relevant design effort and to the

- [36] C. Milardi *et al.*, “DAFNE tune-up for the KLOE-2 experiment”, IPAC11, pp. 3687-3689, 2011.
- [37] T. Demma *et al.*, “A Simulation Study of the Electron Cloud Instability at DAΦNE”, PAC09, pp. 4695-4697.
- [38] D. Alesini *et al.*, “Design and Test of the Clearing Electrodes for e-Cloud Mitigation in the e^+ DAΦNE Ring”, IPAC10, pp. 15151517, 2010.
- [39] M. Zobov *et al.*, “Operating Experience with Electron Cloud Clearing Electrodes at DAΦNE”, ECLLOUD12, 2012.
- [40] D. Alesini *et al.*, “DAΦNE operation with electron cloud clearing electrodes”, *Phys. Rev. Lett.*, Vol. 110, p. 124801, Mar. 2013.
- [41] A. Drago, <http://indico.cern.ch/event/306551/>

ion ring impedance budget. The ion-ring impedance at the collision scenario is thus estimated as:

$$L \approx 97.6 \text{ nH}, |Z_{\parallel}/n| \approx 0.08 \Omega, k_{\parallel} \approx 8.6 \text{ V/pC}, |Z_{\perp}| \approx 80 \text{ k}\Omega/\text{m}.$$

Table 1: Impedance-Generating Components in JLEIC

Elements	e-Ring	Ion-Ring	e-Cooler
Flanges (pairs)	1215	234	104
BPMs	405	214	49
Vacuum Ports	480	92	62
Bellows	480	559	74
Vacuum valves	23	14	-
Tapers	6	6	26
Collimators	16	16	-
Forks	0	0	4
Fast kickers	0	0	2
DIP screen slots	470	-	-
Crab cavities	2	8	0
RF/SRF cavities	32	40	2
RF/SRF bellows	0	60	0
RF/SRF valves	68	24	-
Feedback kickers	2	2	-
IR chamber	1	1	-

As the JLEIC design improves and getting more complete, the counts for certain elements in Table 1, such as the collimators, feedback kickers, and ion-clearing electrodes, will be further modified. In addition, some special components unique to the JLEIC design, such as the crab cavities and IR chamber, require detailed impedance modelling and cannot use reference of impedances from the existing machines. Accurate impedance budgets of both the electron and ion rings require careful electromagnetic field calculations, which can generate the full impedance spectrum for each impedance-generating components.

SINGLE BUNCH INSTABILITIES

In this section, we discuss the beam stability at the collision scenarios for the electron beam at energies $E_e=3, 5, 10$ GeV and for the proton beam at $E_p=100$ GeV.

Longitudinal Microwave Instability (LMWI)

With the Boussard approximation, the LMWI instability threshold is given by the Keil-Schnell criterion:

$$\left| \frac{Z_{\parallel}(n)}{n} \right|^{\text{th}} \approx \frac{2\pi\beta^2 |\eta| E \sigma_{\delta}^2}{e I_{\text{peak}}}$$

For JLEIC baseline parameters in Table 2, the estimation of LMWI impedance thresholds are listed in Table 3 and compared with the expected machine impedances $|Z_{\parallel}/n|^{\text{ring}}$, where “s”, “u”, and “m” denote stable, unstable and marginal respectively. It is interesting to note that unlike PEP-II LER, which is a separate ring and has different dipole configuration from that in HER, here the JLEIC e-ring uses the same dipole configuration for a

wide range of beam energy, with both the dipole strength and the energy spread from synchrotron radiation scaling with the beam energy. As a result, the energy spread for beam at 3 GeV in the JLEIC e-ring is much smaller than that for the PEP-II LER beam; so the former is vulnerable to LMWI while the latter is not. This estimation indicates the necessity to apply suppression mechanisms against the microwave instability for the JLEIC e-ring at low energy. Examples of such mechanisms include use of an alternative dipole configuration, the split dipole concept in the eRHIC design [8], or damping wigglers. For the ion ring, the machine impedance is expected to be much smaller than the threshold impedance, so the beam is safe from this instability. For the electron ring, detailed simulations are to be conducted to study the bunch lengthening due to potential-well distortion below the LMWI threshold, and the turbulent bunch lengthening and energy-spread increase beyond the instability threshold.

Transverse Mode-Coupling Instability (TMCI)

The impedance threshold for the transverse mode-coupling instability (TMCI) is roughly approximated by

$$|Z_{\perp}|^{\text{th}} \approx F E v_s / e \langle \beta_{\perp} \rangle I_{\text{peak}},$$

with F the bunch form factor ($F = 2\pi$ for short bunches). The threshold results are obtained from parameters in Table 2 and listed in Table 4 for both the JLEIC electron and proton beams at selected collision energies, and are compared with the expected upper limits of the machine transverse impedances $|Z_{\perp}|^{\text{ring}}$. These results show that the beams are stable with regard to TMCI. Here the machine impedances are estimated using impedance budgets of existing machines. Since there are large uncertainties in both the machine transverse impedance and the simple back-of-envelope formula, detailed studies of TMCI will be carried out when more accurate JLEIC impedance model becomes available. Such studies include solving the eigenvalue problem of the Vlasov equation [9] or macroparticle tracking that takes into account of potential-well distortion in the longitudinal phase space and many other effects [10]. Additionally, special attention needs to be paid to the Christmas-tree-like equilibrium longitudinal charge distribution for the proton bunch under strong electron cooling, which has a very dense core with long tails [11]. Space-charge effects on TMCI will also be assessed, especially for the ion bunches during their formation process [12].

Table 2: Parameters Used for Instability Estimations

	PEP-II (LER)	JLEIC e-Ring			JLEIC p-Ring
E [GeV]	3.1	3	5	10	100
I_p [A]	113	59.0	59.0	50.6	15.6
η (10^{-3})	1.31	1.09			6.22
σ_{δ} (10^{-4})	7.7	2.78	4.64	9.28	3.0
v_s (10^{-2})	3.7	0.88	1.46	2.51	5.3

$\langle \beta_{\perp} \rangle$ [m]	20	13	18
-------------------------------------	----	----	----

Table 3: Longitudinal Microwave Instability (LMWI)

	PEP-II (LER)	JLEIC e-Ring			JLEIC p-Ring
E [GeV]	3.1	3	5	10	100
$ Z_{\parallel}/n ^{\text{ring}}$ [Ω]	0.1	≤ 0.1 (expectation)			0.1
$ Z_{\parallel}/n ^{\text{th}}$ [Ω]	0.145	0.02 7	0.125	1.16	22.5
LMWI	s	u	m	s	s

Table 4: Transverse Mode-Coupling Instability (TMCI)

	PEP-II (LER)	JLEIC e-Ring			JLEIC p-Ring
E [GeV]	3.1	3	5	10	100
$ Z_{\perp} ^{\text{ring}}$ [M Ω /m]	≤ 0.1	≤ 0.1 (expectation)			≤ 0.5
$ Z_{\perp} ^{\text{th}}$ [M Ω /m]	0.28	0.22	0.60	2.4	119
TMCI	s	s			s

COUPLED BUNCH INSTABILITIES

Narrowband impedances from RF cavities can cause longitudinal or transverse coupled bunch instabilities (LCBI or TCBI). The JLEIC electron ring is expected to use the PEP-II RF cavities, with the RF HOM parameters listed in Tables 1 and 2 of Ref. [13]. For the JLEIC ion ring, an initial RF cavity design is recently developed, featuring low-cost 2-cell cavity with coaxial couplers for HOM damping. The corresponding HOM parameters for the JLEIC ion ring are listed in Table 5 and 6. In addition to HOM, we also include the resistive wall impedance and broadband impedance $(Z_{\parallel}^{BB})_0 = 2\Omega$ in this study.

Combining the above impedances with the JLEIC machine and beam parameters, we can estimate the growth rate for the coupled-bunch instabilities by ZAP [14] (using Sacherer-Zotter's formulas) under the assumption of even bunch filling pattern. This assumption gives an upper bound of the instability growth rate for general filling patterns. Since the growth rates are much faster than the natural damping rate, the design will rely on fast feedback systems (FBS) to mitigate the coupled-bunch instabilities. Consequently, we will assess the beam stability by comparing the instability growth time with the damping times (\sim millisecond) of advanced fast feedback systems. Here a nonzero chromaticity of $\xi = 1$ and a finite betatron tune spread of $3e-04$ are assumed for the TCBI calculations for both the electron and the proton beams.

Table 5: Longitudinal HOM Parameters (p-Ring)

f [MHz]	R_s [Ω]	Q
940.8	7.98e06	2.98e06
1771.9	2.25e04	5643.9
1814.0	1.00e05	5265.5
2894.8	3.33e04	9172.4

3079.4	2.23e02	2.65e04
--------	---------	---------

Table 6: Transverse HOM Parameters (p-Ring)

f [MHz]	Polarization	R_{\perp} [k Ω /m]	Q
1169.8	V	17.9	82.2
1170.1	H	18.0	90.3
1183.8	H	28.1	91.3
1183.9	V	32.3	96.5
1286.7	H	110	501.6
1290.0	V	100	474.5
1315.5	H	357	697.9
1318.7	V	503	970.5
1390.0	H	1930	36348.4
1390.2	V	27700	539455
1572.7	H	1.20	64.2
1575.2	V	2.87	94.1
1627.6	H	1.96	51.2
1629.1	V	0.43	54.1
1865.1	V	3.54	84.7
2517.1	V	7.80	9707.1
2517.1	H	2.36	8531.8

In Table 7 and 8, $\tau_{a=1}^{\parallel}$ and $\tau_{a=2}^{\parallel}$ are the growth time for the longitudinal dipole and quadruple modes respectively, and $\tau_{a=0}^{\perp}$ and $\tau_{a=1}^{\perp}$ correspond to the growth time for the transverse rigid and dipole modes. Here $\tau_{\text{damp}}^{\parallel}$ (or $\tau_{\text{damp}}^{\perp}$) for the e-ring represents the natural longitudinal (or transverse) damping time due to synchrotron radiation, while $\tau_{\text{damp}}^{\parallel}$ and $\tau_{\text{damp}}^{\perp}$ for the p-ring are the damping times for the proton beam due to the strong electron cooling [15] in the JLEIC design. Note that for the electron ring, the lowest energy beam ($E_e = 3$ GeV) has the fastest growth time, $\tau_{a=1}^{\parallel} = 2.9$ ms for LCBI and $\tau_{a=0}^{\perp} = 1.6$ ms for TCBI, which are manageable by FBS as operated in modern electron storage rings. For the electron beam, even though the resistive wall and broadband impedances have negligible effects on the LCBI growth rate, the resistive wall has significant effect on $\tau_{a=0}^{\perp}$ while the broadband impedance has significant effect on $\tau_{a=1}^{\perp}$. For the proton beam, because of its high energy, the fast growth times of LCBI, $\tau_{a=0}^{\parallel} = 6.0$ ms and $\tau_{a=1}^{\parallel} = 6.0$ ms, would require much stronger kicker strength for the longitudinal FBS than those found in existing proton-ring FBS. This further implies higher broadband impedance due to the demand of more kicker cavities. Recently a new RF cavity design using waveguide coupler was proposed [16], and for the p-ring it can prolong the LCBI growth time to $\tau_{a=0}^{\parallel} = 31$ ms. However, due to resistive wall impedance, the qua-

drupole mode growth time $\tau_{a=1}^{\parallel} = 6.2$ ms remains short. More topics for TCBI need to be addressed by computer modelling, such as (1) effects of realistic uneven bunch pattern (with injection/ejection gaps and/or ion clearing gaps), (2) the joint effects of HOMs from both the accelerating/focusing RF cavities and the crab cavities, and (3) the Landau damping effect on transverse coupled-bunch instability, from either the chromaticity or the beam-beam tune shift spread.

Table 7: LCBI in JLEIC

	e-Ring			p-Ring
E [GeV]	3	5	10	100
$\tau_{a=1}^{\parallel}$ [ms]	2.9	4.1	72.8	6.0
$\tau_{a=2}^{\parallel}$ [ms]	31	43	466	6.0
$\tau_{\text{damp}}^{\parallel}$ [ms]	187	40.5	5.1	> 30 min

Table 8: TCBI in JLEIC

	e-Ring			p-Ring
E GeV	3	5	10	100
$\tau_{a=0}^{\perp}$ [ms]	1.6	2.7	64	23.1
$\tau_{a=1}^{\perp}$ [ms]	12.8	19.6	39.8	501
$\tau_{\text{damp}}^{\perp}$ [ms]	375	81	10	> 30 min

ELECTRON CLOUD IN THE ION RING

In an ion ring, the ionization of residual gas and the beam-loss induced surface emission provide the source for the primary electrons, while the electron cloud build-up comes mainly from the secondary electron production [17]. For different stages of ion bunch formation, the build-up of electron cloud and its impact on the ion bunch stability can behave very differently. Unlike the trailing-edge effect of electron cloud for long ion bunches found in conventional ion rings, here the high rep rate and short bunches of the ion beam in JLEIC during collision render the electron cloud build-up process similar to those in positron rings of modern lepton colliders. For the proton beam at $E_p = 100$ GeV, the electron cloud density rapidly rises up and then saturates at around the neutralization density of

$$\rho_{\text{sat}} = \frac{N_b}{\pi b^2 L_{\text{sep}}} = 2 \times 10^{12} \text{ m}^{-3},$$

as modelled in Ref. [18] for a similar set of parameters. The threshold for the electron-cloud induced single-bunch transverse mode-coupling instability (TMCI) can be estimated using the two-particle model [19],

$$\rho_{\text{th}} = \frac{2\gamma Q_s}{\pi r_p C \langle \beta_y \rangle} = 1.7 \times 10^{13} \text{ m}^{-3}.$$

With $\rho_{\text{sat}} < \rho_{\text{th}}$, the bunch is stable from the electron-cloud induced strong head-tail instability. The electron-cloud induced coupled-bunch instability for the JLEIC ion beam can cause more concern, which is yet to be studied by detailed simulations.

ION EFFECT IN THE ELECTRON RING

The ionization scattering of the electron beam with residual gas molecules in the vacuum chamber can cause ion trapping in the electron ring. The trapped ions can cause many undesirable effects for the electron beam, such as emittance growth, tune shift, halo formation, and coherent coupled-bunch instabilities. For symmetric bunch pattern, the critical mass for the ions to be trapped in either x -motion or y -motion is given by [20]

$$A_{x,y}^{\text{trap}} = \frac{r_p N_b L_{\text{sep}}}{2\sigma_{x,y}(\sigma_x + \sigma_y)}.$$

The critical ion masses for the JLEIC electron ring are listed in Table 9, which shows that all ion molecules ($A \geq 2$) will be trapped for even bunch fill. Here constant rms bunch sizes are assumed in the estimation.

Table 9: Critical Ion Mass for Trapped Ion

E_e [GeV]	3	5	10
L_{sep} [m]	0.63	0.63	2.52
σ_x [mm]	0.15	0.26	22.2
σ_y [mm]	0.07	0.12	0.51
A_x^{trap}	0.5	0.2	0.24
A_y^{trap}	1.1	0.4	0.4

Bunch clearing gaps in electron rings are often used to clear the ions so as to prevent them from accumulating turn after turn [21]. Typically a gap in the bunch train, with a length of a few percent of the ring circumference, will help clear up the ions. However, even with the ions being cleared after each turn by a clearing gap (or gaps under multi-train operation), there is still the fast beam-ion instability (FBII) [22] that could cause coupled transverse dipole motion of the electron bunches, with the dipole amplitude increases in time and along the bunch train. Under the assumptions that (1) the force between the ion and electron beam is linear to their dipole offsets and (2) constant frequency for all ion oscillations, the FBII is characterized by the growth time τ_g by

$$y_b(t) \propto \left(t/\tau_g\right)^{-1/4} e^{\sqrt{t/\tau_g}},$$

$$\tau_g^{-1} [\text{s}^{-1}] = 5p[\text{Tor}] \frac{N_b^{3/2} n_b^2 r_p^{1/2} L_{\text{sep}}^{1/2} c}{\gamma \sigma_y^{3/2} (\sigma_x + \sigma_y)^{3/2} A^{1/2} \omega_\beta}.$$

For realistic beams, Landau damping is considered as a result of ion oscillation frequency spread due to horizontal charge distribution. The dipole amplitude growth is then characterized by the e-folding time [23, 24]

$$y_b \propto e^{t/\tau_e}, \quad \tau_e^{-1} \approx \tau_g^{-1} \frac{c}{4\sqrt{2}\pi L_{\text{sep}} n_b a_{bt} f_i}$$

for f_i being the coherent ion oscillation frequency, and a_{bt} the ion frequency variation. For the JLEIC electron ring, τ_g and τ_e are shown in Table 10 (for $a_{bt} = 0.5$) for a single bunch train. Here for $E_e = 10$ GeV, the growth

Table 10: Growth time of FBII for JLEIC e-Ring

CONCLUSIONS

ACKNOWLEDGEMENT

REFERENCES

- ## Beam instability

STUDY TO MITIGATE ELECTRON CLOUD EFFECT IN SuperKEKB

Y. Suetsugu[†], H. Fukuma, K. Ohmi, M. Tobiyama, K. Shibata

High Energy Accelerator Research Organization (KEK), 305-0801, Tsukuba, Japan

Abstract

During Phase-1 commissioning of the SuperKEKB from February to June 2016, electron cloud effect (ECE) was observed in the positron ring. The electron clouds at high-beam-current region were found to be in the beam pipes in drift spaces of the ring, where antechambers and titanium nitride (TiN) film coating were prepared as countermeasures against ECE. Permanent magnets and solenoids to generate magnetic fields in the beam direction were attached to the beam pipes as additional countermeasures. Consequently, during Phase-2 commissioning from March to July 2018, experiments showed that the threshold of current linear density for exciting ECE increased by a factor of at least two when compared to that during Phase-1 commissioning. While the countermeasures were strengthened, the effectiveness of the antechambers and TiN film coating had to be re-evaluated. By performing various simulations and experiments during Phase-2 commissioning, it was found that the antechamber was less effective than anticipated with regards to reducing the number of photoelectrons in the beam channel. The TiN film coating, on the other hand, had low secondary electron yield as expected.

INTRODUCTION

The SuperKEKB is an electron-positron collider with asymmetric energies in KEK that aims for an extremely high luminosity of $8 \times 10^{35} \text{ cm}^{-2} \text{ s}^{-1}$ [1]. The main ring (MR) consists of two rings, i.e. the high-energy ring (HER) for 7-GeV electrons and the low-energy ring (LER) for 4-GeV positrons. Each ring has four arc sections and four straight sections, as shown in Fig. 1.

Electron cloud effect (ECE) is a serious problem in the SuperKEKB LER [2]. The threshold density of electrons ($n_{e,th}$ [m^{-3}]) at which ECE is excited was estimated to be $\sim 3 \times 10^{11} \text{ m}^{-3}$ by various simulation studies [3]. Hence, highly effective countermeasures against ECE were required for the SuperKEKB LER [4], which are summarized in Table 1. Beam pipes with antechambers for suppressing the effect of photoelectrons and a TiN film coating for reducing the secondary electron yield (SEY) were used for in the majority of the new beam pipes, most of which were made of aluminum (Al) -alloy. A schematic of a typical beam pipe at arc sections is presented in Fig. 2. The beam pipes for bending magnets have longitudinal grooves in the beam channel along with the TiN film coating in order to further reduce the SEY. Clearing electrodes were installed in the beam pipes for wiggler magnets instead of the TiN film coating, but they also have the antechambers. The beam pipes for wiggler magnets were made of copper. Approximately 90% of the beam pipes in the ring possess the

antechambers and TiN film coating. Magnetic fields are applied in the beam direction by solenoids to the beam pipes in drift spaces between electromagnets, such as quadrupole magnets and bending magnets. With these all countermeasures, an electron density (n_e [m^{-3}]) of approximately $2 \times 10^{10} \text{ m}^{-3}$ was expected at the designed beam parameters, i.e. a beam current of 3.6 A at a bunch fill pattern of one train of 2500 bunches, with a bunch spacing of 2 RF-buckets (referred to 1/2500/2RF hereafter). Here, one RF-bucket corresponds to 2 ns. This value of n_e is sufficiently lower than the $n_{e,th}$, $3 \times 10^{11} \text{ m}^{-3}$. It must be noted that the magnetic fields in the beam direction (B_z [G]) at drift spaces were not prepared before Phase-1 commissioning, since the maximum stored beam current was not expected to be so high during the commissioning, i.e. approximately 1 A at the maximum.

The n_e around the beam orbit in an Al -alloy beam pipe with antechambers was measured via electron current monitors, which were also used in the previous KEKB experiments [5]. Two electron monitors were set up at the bottom of the beam channel of a test beam pipe. The voltage applied to the electron collector was 100 V, while that applied to the grid (repeller) varied from 0 V to -500 V. These two electron monitors were attached to the same beam pipe: one in the region with TiN film coating (as in the other typical beam pipes in the ring) and one in the region without the TiN film coating (i.e. bare Al surface). The test beam pipe was placed in an arc section of the ring. The line density of photons of the synchrotron radiation (SR) is $1 \times 10^{15} \text{ photons s}^{-1} \text{ m}^{-1} \text{ mA}^{-1}$, i.e. 0.16 photons $\text{posi.}^{-1} \text{ m}^{-1} \text{ turn}^{-1}$. This line density is almost same as the average value of arc sections.

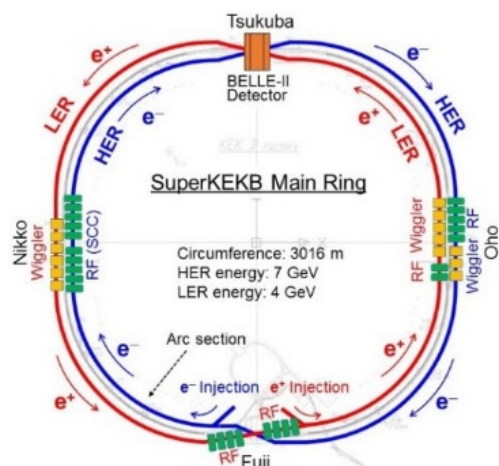


Figure 1: Layout of the SuperKEKB Main Ring (MR). One ring consists of four arc sections and four straight sections.

[†] yusuke.suetsugu@kek.jp

Content from this work may be used under the terms of the CC BY 3.0 licence (© 2018). Any distribution of this work must maintain attribution to the author(s), title of the work, publisher, and DOI.

Table 1: Countermeasures used to minimize the ECE in the SuperKEKB LER. The circles indicate the countermeasures applied for each main section in the ring [4].

Sections	Length [m]	n_e (circular) [m ⁻³]	Countermeasures					n_e (expected) [m ⁻³]
			Antechamber (1/5)	TiN coating (3/5)	Solenoid (B_z) (1/50)	Groove (1/2)	Electrode (1/100)	
Drift space (arc)	1629	8×10^{12}	○	○	○			2×10^{10}
Corrector mag.	316	8×10^{12}	○	○	○			2×10^{10}
Bending mag.	519	1×10^{12}	○	○		○		6×10^{10}
Wiggler mag.	154	4×10^{12}	○	○*			○	5×10^9
Quadrupole and Sextupole mag.	254	4×10^{10}	○	○				5×10^9
RF cav. section	124	1×10^{11}		○	○			1×10^9
IR	20	5×10^{11}		○	○			6×10^9
Total	3016							
Average		5.5×10^{12}						2.4×10^{10}

*Except for beam pipes with clearing electrodes.

Abbreviations;

RF cav. section: Beam pipes around RF cavities, IR: Interaction region.

n_e (circular): Density of electrons expected for circular beam pipe (copper).

n_e (expected): Density of electrons expected after applying countermeasures.

Antechamber: Antechamber scheme, Solenoid: Solenoid winding, but it means actually a magnetic field in the beam direction (B_z).

Groove: Beam pipe with grooves, Electrode: Beam pipe with clearing electrodes

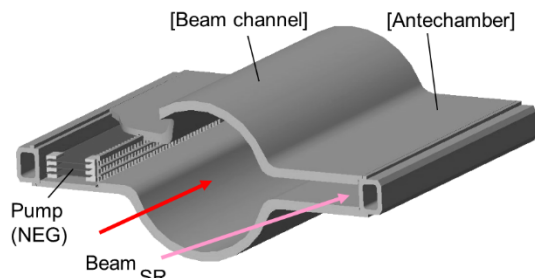


Figure 2: Typical cross section of a beam pipe at arc sections for LER.

ECE IN PHASE-1 COMMISSIONING

ECE at Early Stage

The ECE was first observed during Phase-1 commissioning from a beam current (I [mA]) of approximately 600 mA at a bunch fill pattern of 1/1576/3.06RF despite the implementation of the various countermeasures described above [6, 7]. The vertical beam size began to blow up from this I as shown in Fig. 3 ([without PM at bellows]). The pressure in an arc section (P [Pa]) abnormally increased with an increase in I due to the multipactoring of electrons. This abnormal blow up of beam size and rise in pressure are the typical phenomena of ECE.

The blow up of the vertical beam size for bunch fill patterns of 4/150/2RF, 4/150/3RF, 4/150/4RF, and 4/150/6RF are shown in Fig. 4(a) as a function of the current linear density (I_d [mA bunch⁻¹ RF-bucket⁻¹]), i.e. the bunch current divided by the bunch spacing. The threshold of I_d ($I_{d,th}$ [mA bunch⁻¹ RF-bucket⁻¹]) at which the ECE is excited, i.e. the blow up of beam size begins, was approximately 0.1–0.12 mA bunch⁻¹ RF-bucket⁻¹.

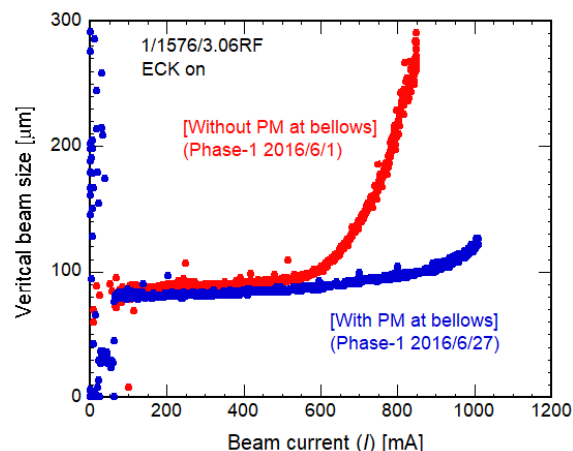


Figure 3: Behaviors of vertical beam size without and with PM units on Al-alloy bellows chambers for a bunch fill pattern of 1/1576/3.06RF.

It was finally found that this ECE was caused by the electrons in the Al-alloy bellows chambers without TiN film coating. They are 200 mm long and are located at an average of every 3 m around the ring. There are approximately 830 bellows chambers in total, and their total occupied length is ~5% of the circumference of the ring. However, the n_e in the test beam pipe at the region without TiN film coating was found to be on the order of 10^{13} m^{-3} , which is more than 10 times greater than the $n_{e,th}$ of $3 \times 10^{11} \text{ m}^{-3}$.

To counteract the ECE, two units of permanent magnets (PM), where 16 PM were attached to C-shaped iron plates (yokes), were placed at the top and bottom of each Al-alloy bellows chamber. A B_z of approximately 100 G was formed in most regions of the PM units, although the polarity reversed locally just near the magnets. After attaching the PM units to all Al-alloy bellows chambers,

the abnormal blow up of beam size disappeared at an I value of 600–700 mA as shown in Fig. 3 ([with PM at bellows]). A simulation by CLOUDLAND [8] showed that the n_e around the beam orbit in the Al-alloy bellows chamber with the PM units would be in the order of 10^{10} m^{-3} even for the designed beam parameters, i.e. a beam current of 3.6 A at a bunch fill pattern of 1/2500/2RF, where the maximum SEY (δ_{max}) was assumed to be 2.0.

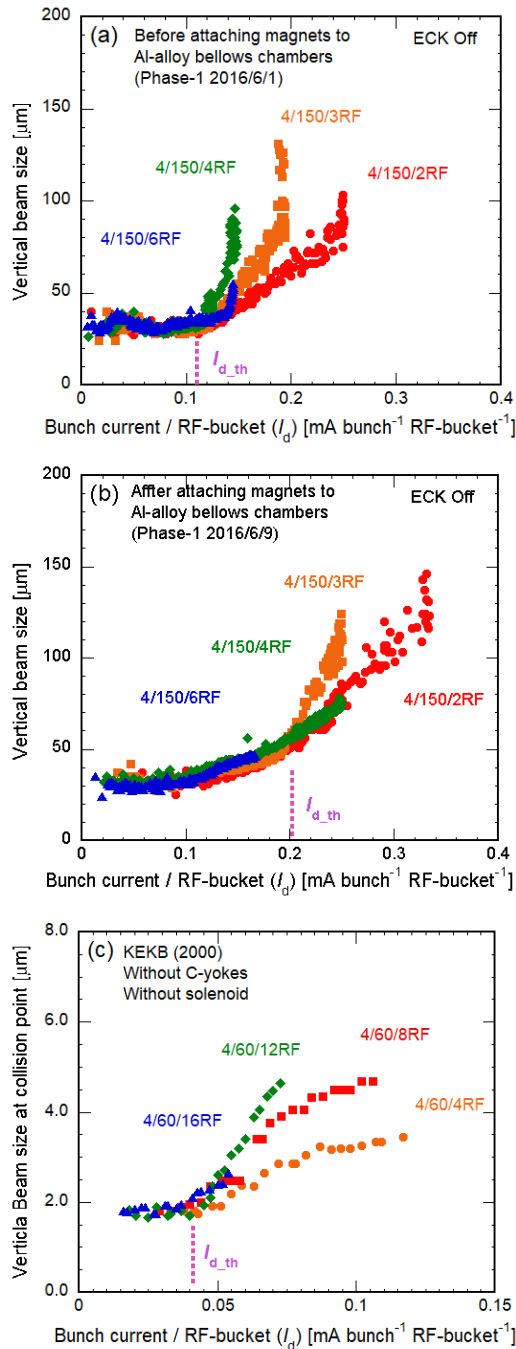


Figure 4: Vertical beam sizes as a function of the current line density (I_d) for several bunch fill patterns measured (a) before and (b) after attaching PM units to Al-alloy bellows chambers in Phase-1 commissioning of SuperKEKB, and (c) in the early stage of KEKB era.

ECE at High Current

With an increase in the operation beam current, the ECE began to appear again at an I value of approximately 900 mA at a bunch fill pattern of 1/1576/3.06RF. The blow up of beam size started from this I value, as shown in Fig. 3 ([with MP at bellows]). Figure 4(b) shows the dependence of the vertical beam size on I_d for bunch fill patterns of 4/150/2RF, 4/150/3RF, 4/150/4RF, and 4/150/6RF. The $I_{d,th}$ was $0.2 \text{ mA bunch}^{-1} \text{RF-bucket}^{-1}$ for 2 and 3 RF-buckets spacings, which corresponded to I of approximately 900 mA for a bunch fill pattern of 1/1576/3.06RF. Furthermore, the modes of the transverse coupled bunch instabilities were measured and analyzed using a bunch-by-bunch beam feedback system [9]. The modes excited by the electrons at the drift space [10, 11] were clearly observed.

It was observed that the n_e in the test beam pipe at the region with TiN film coating was close to the $n_{e,th}$, i.e. approximately $3 \times 10^{11} \text{ m}^{-3}$. Furthermore, PM units with iron yokes, similar to those used for Al-alloy bellows chambers, were partially attached for tests around several beam pipes at drift spaces. As a result, the abnormal pressure rise was suppressed in the region. From these observations, the electron cloud was considered to exist in the beam pipes at drift spaces.

It should be noted that the $I_{d,th}$ of $0.2 \text{ mA bunch}^{-1} \text{RF-bucket}^{-1}$, after suppressing ECE caused by the Al-alloy bellows chambers, is much higher than that in the case at the early stage of KEKB without any countermeasures, i.e. $0.05 \text{ mA bunch}^{-1} \text{RF-bucket}^{-1}$ as shown in Fig. 4(c) [12]. The beam pipes and bellows chambers of KEKB had a simple circular cross section and were made of pure copper or stainless steel without any internal coating. This indicated that the antechambers and TiN film coating in the SuperKEKB effectively suppressed ECE to some extent. However, the excitation of ECE also meant that the countermeasures in Phase-1 commissioning were still insufficient, implying the necessity of additional countermeasures before starting the next commissioning. Furthermore, a re-evaluation of the effectiveness of antechambers and TiN film coating in the real ring was required to check whether they were working as expected.

ADDITIONAL COUNTERMEASURES

As additional countermeasures against the ECE, permanent magnets (PM) units and solenoids were attached to most of the beam pipes at drift spaces in LER. The PM units with C-shaped iron yokes (Type-1 unit) were placed in series around the beam pipe as shown in Fig. 5, which produced a B_z of approximately 60 G. A simulation showed that the n_e around the beam orbit in the unit reduced to approximately $1/10^{\text{th}}$ of the $n_{e,th}$ even for the designed beam parameters. However, the Type-1 unit cannot be used near electromagnets, such as quadrupole and sextupole magnets, because the iron yokes affect their magnetic fields. Hence, another type of PM units (Type-2 unit), which consists of Al-alloy cylinders with PM inside and Al-alloy supports, were placed close to the

electromagnets, as also shown in Fig. 5. The B_z inside the Type-2 units was approximately 100 G. For the beam pipes that had been used from the KEKB era, solenoid windings were revived [12].

Before starting Phase-2 commissioning, approximately 86% of the drift spaces (approximately 2 km) was covered with B_z larger than 20 G.

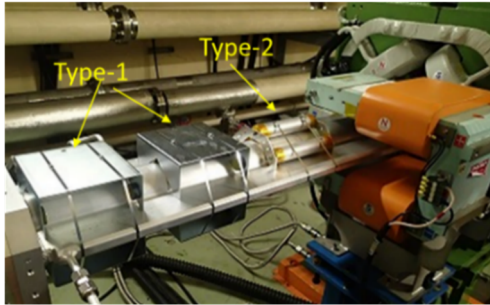


Figure 5: Type-1 and Type-2 units at drift space.

ECE IN PHASE-2 COMMISSIONING

During Phase-2 commissioning from March to July 2018, the vertical beam sizes and increases in pressure were measured in the same way as Phase-1 commissioning.

Figure 6 shows the dependence of the vertical beam size on I_d for bunch fill patterns of 4/120/2RF, 4/120/3RF and 4/120/4RF. As shown in Fig. 6, the blow up was not observed until the I_d value of 0.4 mA bunch⁻¹ RF-bucket⁻¹. The $I_{d,th}$ for exciting ECE increased by at least twice when compared to the case of Phase-1 commissioning (Fig. 4(b)). Since the n_e in the test beam pipe at the region with TiN film coating did not change from that observed in Phase-1 commissioning, the improvement of the $I_{d,th}$ should be attributed to the B_z applied after Phase-1 commissioning.

In the case of Phase-1 commissioning, the pressure at arc sections abnormally increased with I when the I value was higher than 300 mA at bunch fill patterns of 2-RF bucket spacings. But the pressure was almost proportional to I in the case of Phase-2 commissioning.

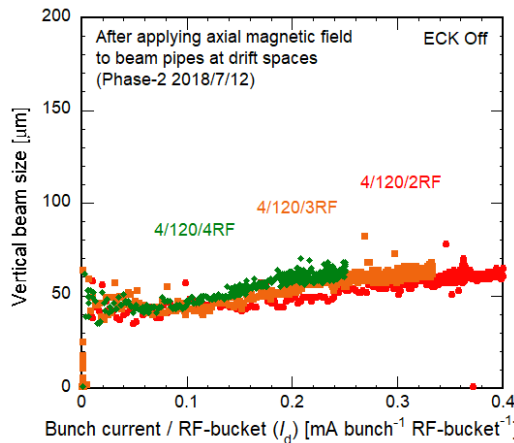


Figure 6: Vertical beam sizes as a function of current linear density (I_d) for several bunch fill patterns during Phase-2 commissioning.

The unstable modes excited by the electrons at drift spaces were not detected. Instead, the modes excited by electrons near the inner wall which were trapped by the B_z were observed. Furthermore, the growth rates of the modes were much slower than those observed during Phase-1 commissioning.

From these observations, it can be concluded that the additional countermeasures, i.e. the application of B_z by PM units and solenoids to the beam pipes at drift spaces, contributed well towards suppressing ECE in Phase-2 commissioning.

RE-EVALUATION OF THE EFFECT OF ANTECHAMBER AND TIN COATING

Firstly, as a measure of effectiveness of a beam pipe with an antechamber with regards to suppressing photoelectrons, the reduction rate of the number of photoelectrons in the beam channel relative to a simple circular beam pipe (α) is defined as follows.

$$\alpha \equiv \frac{p_b + \beta \times p_a}{p_b + p_a} \quad (1)$$

Here, the p_b and p_a are the number of photoelectrons generated in the beam channel and the antechamber, respectively. Hence, the total number of photoelectrons at the location is $p_b + p_a$, and β is the probability of the electrons in the antechamber exit to the beam channel. A small value of α implies a high effectiveness of antechamber.

On the other hand, the maximum SEY (δ_{max}) was used as a measure of the effectiveness of TiN film coating with regards to reducing secondary electrons.

Calculation of β

At first, β in Eq. (1) was estimated from a simulation to calculate the motion of electrons. The electric field due to electron cloud in the beam channel was calculated by a band-matrix solver. The force from a positron beam was calculated by using the Basatti-Erskine equation or the beam potential for an electron inside or outside of $10 \sigma_x$, respectively, where the σ_x is the transverse beam size. Photoelectrons were assumed to be generated only at the innermost wall of the antechamber. Furthermore, the emission angle of photoelectrons followed the cosine law.

In the case where the space charge effect and the reflection of electrons were neglected, i.e. n_e was low, β was approximately 0.07. On the contrary, in the case where the space charge was taken into account by assuming a bunch current of 1 mA bunch⁻¹, bunch spacing of 3 RF-buckets, δ_{max} of 1.2, and a reflection rate of electrons of 0.7, i.e. n_e was high, β was 0.03 – 0.04. In the following discussions, a β value of 0.05 was assumed.

Relationship between α and δ_{max}

The n_e in the order of 10^{11} m^{-3} , where the space charge effect is small, is determined not only by the SEY (i.e. δ_{max}) but also the number of photoelectrons in the beam channel (i.e. α). More concretely, the n_e is almost proportional to

the number of photoelectrons for a constant δ_{\max} . From the observations made during Phase-1 commissioning, the ECE was excited at an I value of approximately 900 mA for a bunch fill pattern of 1/1576/3.06RF. This implies that the n_e should be approximately $3 \times 10^{11} \text{ m}^{-3}$ at these beam parameters. Under this condition, the δ_{\max} was calculated as a function of the number of photoelectrons in the beam channel by using the CLOUDLAND simulation code, where a circular beam pipe was used as a model, and the result is presented in Fig. 7. The α value corresponding to the number of photoelectrons are also plotted in Fig. 7. Here, the bunch fill pattern was 1/150/3RF, the number of positrons in a bunch was $3.13 \times 10^{10} \text{ bunch}^{-1}$ (corresponds to $0.5 \text{ mA bunch}^{-1}$), and the line density of photons of SR was $0.16 \text{ photons posi}^{-1} \text{ m}^{-1} \text{ turn}^{-1}$. This line density is equal to the average value of the arc sections as described before. The quantum efficiency was assumed to be a constant, 0.1. Furthermore, the photoelectrons were emitted uniformly inside the beam channel.

If the value of α was estimated from simulations or measurement, the δ_{\max} of the surface can be deduced using Fig. 7. For example, the value of α was estimated to be 0.01 in the experiment during the KEKB commissioning where a test beam pipe with an antechamber made of pure copper was used [13]. By using this value, δ_{\max} is estimated to be approximately 1.4 from Fig. 7. This value of δ_{\max} is higher than that obtained for TiN film coating (1.0 – 1.2) after sufficient electron bombardment in a laboratory [14]. Hence it is required that the α value of a real beam pipe should be estimated to evaluate the actual δ_{\max} .

Note that the re-evaluated values of α and δ_{\max} here are the average of those measured in the ring because the ECE is excited by the average value of n_e . However, ~90% of the beam pipes in the ring have antechambers and TiN film coating. Most of other parts are simple circular beam pipes, but are located in straight sections where the intensity of SR is small.

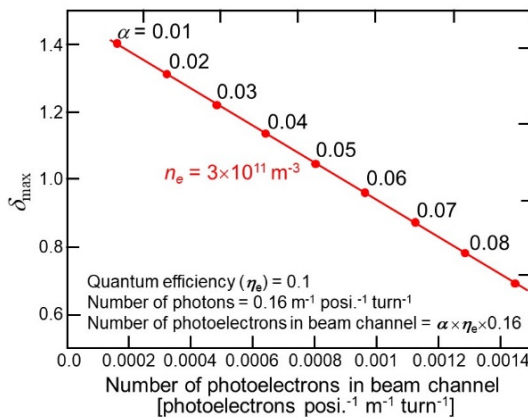


Figure 7: Combinations of δ_{\max} and number of photoelectrons in a beam channel that give the same density of electrons (n_e) of $3 \times 10^{11} \text{ m}^{-3}$ at 900 mA for a bunch fill pattern of 1/1576/3.06RF calculated by CLOUDLAND. The values of α corresponding to the number of photoelectrons are also mentioned in the plot.

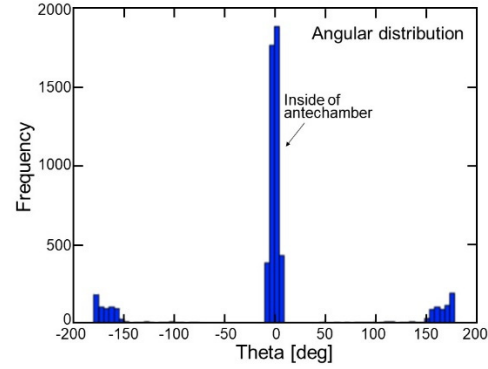


Figure 8: Angular distribution of absorbed photons, where 0° corresponds to the inner most side of the antechamber, calculated by using the Synrad3D simulation code.

Hence, the re-evaluated values can be considered to represent those of beam pipes having antechambers and TiN film coating.

Re-evaluation of α and δ_{\max}

The α and δ_{\max} values were re-evaluated from three methods by using simulations and experiments during Phase-2 commissioning.

(i) From photon distribution

Using the cross section and the surface roughness of a real beam pipe, the number of photons inside the beam pipe was calculated by using the Synrad3D simulation code [15]. The innermost wall of the antechamber, where the SR is directly irradiated, was roughened by using the glass beads blast (GBB) method. On the other hand, the surface of beam channel is that of an extruded Al pipe. Considering the measured surface roughness of these surfaces, the distribution of photons absorbed by the inner wall of beam pipe was calculated under the real layout of electromagnets at the location where the n_e was measured. The scattered photons from upstream of the location were taken into account in the calculation assuming that a TiN film with a thickness of 200 nm was coated on Al surface.

Figure 8 is the angular distribution where the “Theta = 0” corresponds to the inner most part of the antechamber. The line density of total photons absorbed at the location was $0.16 \text{ photons posi}^{-1} \text{ m}^{-1} \text{ turn}^{-1}$. On the other hand, the line density of photons absorbed in the beam channel was $0.00956 \text{ photons posi}^{-1} \text{ m}^{-1} \text{ turn}^{-1}$. The number of photoelectrons can be obtained by multiplying the quantum efficiency with the number of absorbed photons. Assuming a constant value for the quantum efficiency, the following equation is derived:

$$\frac{p_b}{p_b + p_a} = \frac{0.00956}{0.16} = 0.06 \quad (2)$$

Assuming the value of β as 0.05, the α value of 0.11 was calculated from Eqs. (1) and (2). Then, the value of δ_{\max} was evaluated as 0.5–0.6 from the extrapolated line in Fig. 7.

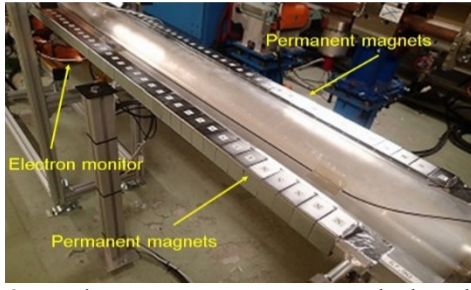


Figure 9: Weak permanent magnets attached to the antechambers of the test beam pipe with electron monitors to prevent the photoelectrons generated in the antechamber from entering the beam channel.

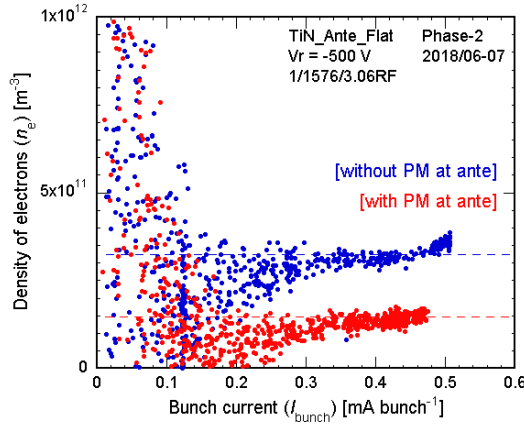


Figure 10: Measured density of electrons (n_e) near the beam orbit with and without permanent magnets (PM) at antechambers.

(ii) From measured n_e

If the n_e value is almost proportional to the number of photoelectrons in the beam channel, the ratio of n_e in the case that the electrons from antechamber can be negligible (n_{e0}) and that under usual condition (n_e) can be written as follows:

$$\frac{n_{e0}}{n_e} = \frac{p_b}{p_b + \beta \times p_a} \quad (3)$$

Hence, if the n_{e0} is measured, the α value can be deduced using Eqs. (3) and (1).

The value of n_{e0} was measured during Phase-2 commissioning by attaching weak permanent magnets along the ends of the antechambers of the test beam pipe, as shown in Fig. 9. These magnets generate weak vertical magnetic fields (B_y [G]) along the antechamber and confine the emitted photoelectrons inside. The B_y value close to the permanent magnets was approximately 100 G, but that in the beam channel was less than 0.5 G, which is the same order to the terrestrial magnetism. In the simulation, the B_y of this order of magnitude had no effect on the n_e in the beam channel and was experimentally found to have little effect on the measurement of n_e by the present electron monitors.

The measured values of n_{e0} and n_e at a bunch fill pattern of 1/1576/3.06RF during Phase-2 commissioning are presented in Fig. 10. The ratio n_{e0}/n_e was 1.5/3.3 at a bunch current of 0.45 mA bunch⁻¹. Assuming the value of β as

0.05, the ratio p_b/p_a was calculated to be 0.04 from Eq. (3). The value of α was then calculated as 0.08 from Eq. (1). Consequently, using the relation described in Fig. 7, the δ_{\max} was estimated to be approximately 0.7 – 0.8.

(iii) From the behavior of n_e against I

Here the α and δ_{\max} were estimated from the behaviors of the measured n_e values against I_d values by comparing them with the values obtained from the simulations. Figure 11(a) shows the dependence of n_e measured at the region with TiN film coating of the test beam pipe (without PM units) on I_d at a bunch fill pattern of 4/150/2RF during Phase-2 commissioning. On the other hand, Fig. 11(b) shows the dependence of n_e calculated using the PyECLOUD simulation code [16] at a bunch fill pattern of 1/150/2RF for the combinations of $(\delta_{\max}, \alpha) = (0.8, 0.09)$, $(1.0, 0.06)$, $(1.2, 0.04)$, and $(1.4, 0.01)$, where a circular beam pipe was again used as a model. These combinations of (δ_{\max}, α) give the same n_e values of approximately $3 \times 10^{11} \text{ m}^{-3}$ at a bunch current of 0.5 mA bunch⁻¹ and a bunch fill pattern of 1/150/3RF, which almost follows the relation indicated by the line in Fig. 7. The calculated behavior of n_e was consistent with the measured values for the cases of $\alpha = 0.03 - 0.06$ and $\delta_{\max} = 1.2 - 1.0$. Similar results were obtained for other bunch fill patterns of 3 and 4 RF-buckets spacings.

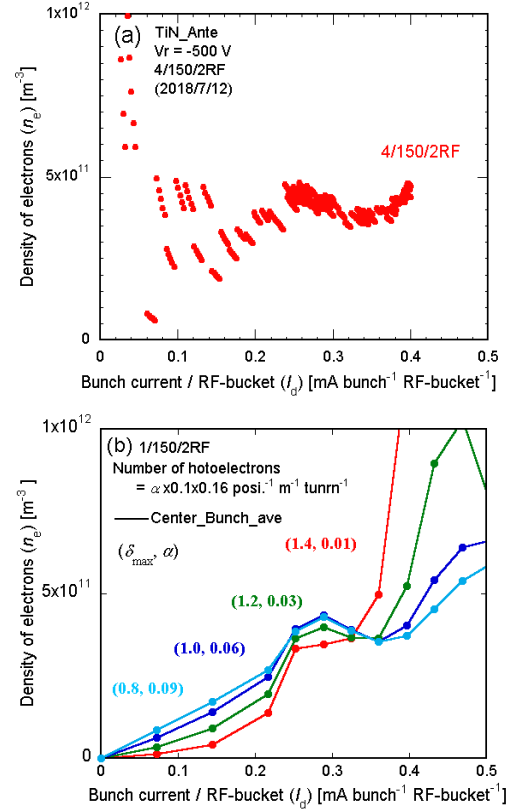


Figure 11: (a) Measured density of electrons (n_e) near the beam orbit and (b) calculated ones by using PyECLOUD for several combinations of (δ_{\max}, α) as a function of the current linear density (I_d) at bunch fill patterns of 2 RF-buckets spacings.

Results of Re-evaluation

The following is the summary of the above results:

- (i) $\alpha = 0.11$ and $\delta_{\max} = 0.5 - 0.6$
- (ii) $\alpha = 0.09$ and $\delta_{\max} = 0.7 - 0.8$
- (iii) $\alpha = 0.03 - 0.06$ and $\delta_{\max} = 1.0 - 1.2$

It must be noted that the first evaluation by the method (i) assumed the same quantum efficiencies for both the antechamber (rough surfaces and no TiN film coating) and the beam channel (smooth surface and TiN film coating) to obtain the number of photoelectrons. This point is a difference between this and the other methods (ii) and (iii) where the number of photoelectrons is directly used. This difference could explain the relatively high value of α in method (i). If the quantum efficiency of the TiN film coating is lower than that of the Al surface, for example [17], the value of α should be smaller than the obtained value.

Although the results are relatively scattered, all the values of α are larger than that obtained in the KEKB experiments, i.e. 0.01 [13]. This difference will be explained by the followings: (a) the location of experimental set up, i.e. just downstream (KEKB) and seven meters downstream (SuperKEKB) of a bending magnet, (b) the material of beam pipe, i.e. copper (KEKB) and Al-alloy (SuperKEKB), (c) the height of antechamber, i.e. 18 mm (KEKB) and 14 mm (SuperKEKB), (d) the treatment of the innermost surface of antechamber where the SR is directly irradiated, and so on. Especially, it should be noted that some portion of photons from upstream hit the beam channel due to the vertical spread and scattering far downstream of the bending magnets in the real machine.

As for δ_{\max} of the TiN film, the values are closer to or are somewhat lower than those obtained in the laboratory [14]. The TiN film coating seems to be working as well as expected with regards to reducing the emission of secondary electrons.

SUMMARY

The ECE was excited in the SuperKEKB LER during Phase-1 commissioning. The ECE observed at the high current region was caused by the electron cloud in the beam pipes at drift spaces, which have TiN film coating and antechambers. Additional countermeasures, i.e. application of PM units and solenoids to generate a B_z of several ten gauss, worked well during Phase-2 commissioning, and the ECE was not observed until an I_d of 0.4 mA bunch⁻¹ RF-bucket⁻¹. Although the value of I_d of the designed parameters is 0.7 mA bunch⁻¹ RF-bucket⁻¹, the countermeasures in the SuperKEKB have been working almost as expected so far.

The effectiveness of the antechamber (α) and TiN film coating (δ_{\max}) was re-evaluated by using simulations and experiments during Phase-2 commissioning, while the countermeasures were strengthened. The α value of the real beam pipe in the ring was found to be larger than expected. The value of δ_{\max} , on the other hand, was less when compared to the values obtained in the laboratory. The

results obtained here indicates the importance of suppressing photoelectrons for ECE.

The next Phase-3 commissioning of the SuperKEKB will begin at the start of 2019, and the beam current will be increased further. Before starting Phase-3 commissioning, more PM units will be added to aim for a coverage of 95% of the drift spaces with a B_z higher than 20 G. Careful observation of the ECE should be continued during Phase-3 commissioning.

ACKNOWLEDGEMENTS

The authors would like to thank all the staff of the KEKB accelerator division for their cooperation and continuous encouragement during the commissioning phase.

REFERENCES

- [1] Y. Ohnishi, "Report on SuperKEKB phase 2 commissioning," in *Proc. IPAC'18*, Vancouver, Canada, April 29 – May 4, 2018, pp. 1–5.
- [2] K. Ohmi and F. Zimmermann, "Head Tail Instability Caused by Electron Clouds in Positron Storage Rings," *Phys. Rev. Lett.* 85, p. 3821, 2000.
- [3] Y. Susaki *et al.*, "Electron cloud instability in SuperKEKB low energy ring," in *Proc. IPAC'10*, Kyoto, May 23–28, 2010, pp.1545–1547.
- [4] Y. Suetsugu *et al.*, "Results and problems in the construction phase of the SuperKEKB vacuum system," *J. Vac. Sci. Technol. A*, 34, p. 021605, 2016.
- [5] K. Kanazawa *et al.*, "Measurement of the electron cloud density around the beam," in *Proc. PAC'05*, Knoxville, USA, May 16–20, 1995, pp. 1054–1056.
- [6] Y. Suetsugu *et al.*, "First Commissioning of the SuperKEKB Vacuum System," *Phys. Rev. Accel. Beams*, 19, p. 121001, 2016.
- [7] Y. Suetsugu *et al.*, "Achievements and problems in the first commissioning of SuperKEKB vacuum system," *J. Vac. Sci. Technol. A*, 35, p. 03E103, 2017.
- [8] L. Wang *et al.*, "A perfect electrode to suppress secondary electrons inside the magnets," in *Proc. EPAC 2006*, Edinburgh, Scotland, June 26 – 30, 2006, pp.1489–1491.
- [9] M. Tobiyama *et al.*, "Coupled bunch instability caused by electron cloud," in *Proc. PAC'05*, Knoxville, USA, May 16–20, 1995, pp. 943–945.
- [10] S. S. Win *et al.*, "Numerical study of coupled-bunch instability caused by an electron cloud," *Phys. Rev. Spe. Top. – Accel. Beams*, 8, p. 094401, 2005.
- [11] K. Ohmi, *et al.*, "ELECTRON CLOUD STUDIES IN SUPERKEKB PHASE I COMMISSIONING," in *Proc. IPAC2017*, Copenhagen, Denmark, May 14–19, 2017, pp. 3104–3106.
- [12] H. Fukuma *et al.*, "Status of Solenoid System to Suppress the Electron Cloud Effects at the KEKB," *AIP Conference Proceedings* 642, 2002, pp.357–359.
- [13] Y. Suetsugu *et al.*, "R&D of copper beam duct with antechamber scheme for high current accelerators," *Nucl. Instrum. Method Phys. Res. A*, 538, p. 206, 2005.

- [14] K. Shibata *et al.*, “Development of TiN coating system for beam ducts of KEK B-factory,” in *Proc. EPAC'08*, Genoa, Italy, June 23–27, 2008, pp. 1700–1702.
- [15] G. Dugan *et al.*, “SYNRAD3D photon propagation and scattering simulations,” in *Proc. the Joint INFN-CERN-EuCARD-AccNet Workshop on Electron-Cloud Effects: ECLLOUD'12* (CERN Yellow Report CERN-2013-002), Isola d’Elba, Italy, 2012, June 5–9, pp. 117–129.
- [16] G. Ladarola, G. Rumolo, “PyECLLOUD and build-up simulations at CERN,” in *Proc. the Joint INFN-CERN-EuCARD-AccNet Workshop on Electron-Cloud Effects: ECLLOUD'12* (CERN Yellow Report CERN-2013-002), Isola d’Elba, Italy, 2012, June 5–9, pp. 189–194.
- [17] Y. Suetsugu *et al.*, “Continuing study on the photoelectron and secondary electron yield of TiN coating and NEG (Ti–Zr–V) coating under intense photon irradiation at the KEKB positron ring,” *Nucl. Instrum. Method Phys. Res. A*, 556, p. 399, 2006.

BENCHMARKING OF SIMULATIONS OF COHERENT BEAM-BEAM INSTABILITY WITH SUPERKEKB MEASUREMENT

K. Ohmi*, K. Hirosawa, H. Ikeda, H. Koiso, Y. Ohnishi, M. Tobiyama,
KEK/Soken-dai, Tsukuba, Japan,
D. E. Khechen, CERN, Geneva, Switzerland

Abstract

Coherent beam-beam instability in head-tail mode has been predicted in collision with a large crossing angle. The instability is serious for design of future e^+e^- colliders based on the large crossing angle collision. It is possible to observe the instability in SuperKEKB commissioning. Horizontal beam size blow-up of both beams has been seen depending on the tune operating point. We report the measurement results of the instability in SuperKEKB phase II commissioning.

INTRODUCTION

Coherent beam-beam instability in head-tail mode has been studied for Phase II commissioning of SuperKEKB. β_x^* is squeezed to ~ 3 cm in the SuperKEKB design. The instability was seen in $\beta_x^* \sim 24$ cm ($8\times$ of the design) but not in 12 cm ($4\times$) at the design bunch population N_{\pm} [1] in strong-strong beam-beam simulation. The instability is serious for large β_x^* , because two beams correlate proportional to β_x^* .

β_x^*/β_y^* were squeezed step-by-step in Phase II commissioning. During the squeezing β^* , we had the chance to measure the instability. Table 1 shows the parameters of SuperKEKB. Beam-beam collision was established with the expected β^* in Phase II. The bunch population was 50-60% of the design, and the beam-beam parameter is limited for electron beam $\xi_y = 0.02$ [2]: that is, positron beam enlarges in vertical, increasing the bunch currents. Tune operating point is $(\nu_x, \nu_y) = (44.569, 46.609)$ and $(45.541, 43.608)$ for LER and HER, respectively. Any instability signal has not been seen in this operating point, but by changing the horizontal tune of one beam, the horizontal beam sizes of the both beams increase simultaneously. We present the experimental results and the beam-beam simulations in this paper.

Table 1: Parameters for SuperKEKB

parameter	design		Phase-II	
	LER	HER	LER	HER
$N_{\pm} (10^{10})$	9	6.5	4.8	4.0
$\varepsilon_{x/y} \text{ (nm/pm)}$	3.2/8.64	4.6/13	2.1/21	4.6/30
$\beta_{x/y}^* \text{ (mm)}$	32/0.27	25/0.3	200/3	100/3
ν_z	0.0247	0.028	0.022	0.026
ξ_x	0.0028	0.0012	0.0073	0.0025
$\sigma_z \theta_c / \sigma_x$	24.7	19.4	10	10

* ohmi@post.kek.jp

STUDY USING STRONG-STRONG BEAM-BEAM SIMULATION

Figure 1 shows the instability simulation for SuperKEKB commissioning before starting Phase II. Two cases of $\beta_{x,y}^*$ with $(8\times, 8\times)$ and $(4\times, 8\times)$ of the design were examined. The instability was seen in $(8\times, 8\times)$, but not in $(4\times, 8\times)$. Horizontal and synchrotron tunes are $\nu_x = 0.53$ and $\nu_z = 0.025$ for both rings.

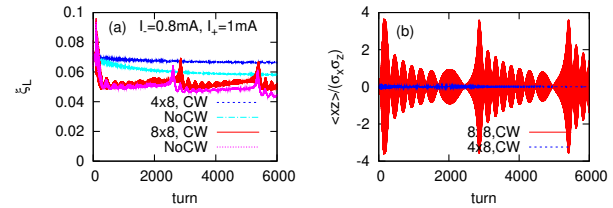


Figure 1: Strong-strong simulation results for SuperKEKB [1]. (a) and (b) show the beam-beam parameter and head-tail motion $\langle xz \rangle$, respectively, at the commissioning stage with IP beta, $(8\times, 8\times)$, and $(4\times, 8\times)$.

In reality, synchrotron tunes of two beams are different, $\nu_x^{(+)} = 0.0247$ and $\nu_z^{(-)} = 0.028$ for LER and HER respectively. Complex head-tail mode coupling between two beams can occur with combination of head-tail modes of two beams [3]. Figure 2 presents variation of tune and growth rate of beam-beam head-tail mode, where the horizontal tune is $\nu_x^{(\pm)} = 0.53$ for both beams. The threshold of the instability is very low ($0.05\times$ of the design bunch population). Mode coupling between $\nu_x^{(+)} + \nu_z^{(+)}$ and $\nu_x^{(-)} - 3\nu_z^{(-)}$ is seen in the right plot of Fig. 2.

Strong-strong simulations using the code (BBSS) have been performed for collision with different synchrotron tunes. Figure 3 presents the evolution of luminosity, dipole moment $\langle x \rangle$, beam size σ_x and correlation of $\langle xz \rangle$, where the horizontal tune is 0.53 for both beams. The horizontal beta function of IP is 4 times of the design, $\beta_x^* = 128/100$ mm. Instability was not seen for equal synchrotron tune ($\nu_z = 0.025$) as shown in Fig. 1. Oscillation in $\langle xz \rangle$ was seen in 1000 turns, but disappeared after that. Horizontal beam size of two beams increased about two times. Small coherent motion in $\langle x \rangle$ remained after 10,000 turns.

Table 2 summarizes simulation results for several horizontal tunes. The horizontal beam size is normalized by the design value. The width (range) of the luminosity and beam size represents lower and upper value; namely presence of a coherent oscillation. Even without coherent oscillation, the

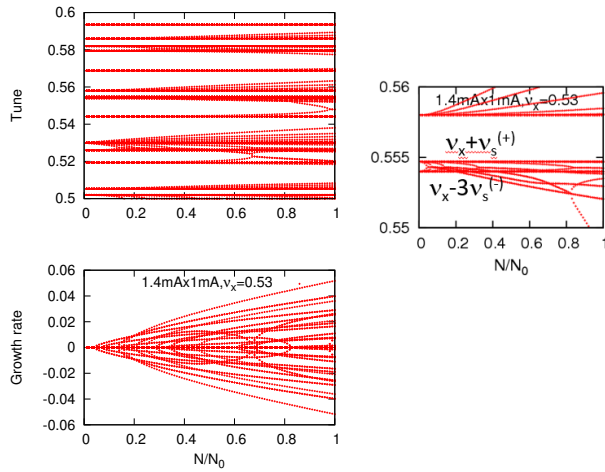


Figure 2: Variation of tune (top left) and growth rate (bottom left) of beam-beam head-tail mode as function of bunch population normalized by the design value. Right plot shows detailed tune behavior near $\nu = 0.55 - 0.56$.

beam size may become large. Stable condition is realized only for $\nu_x = 0.535$ and $\beta^* = (4\times, 8\times)$.

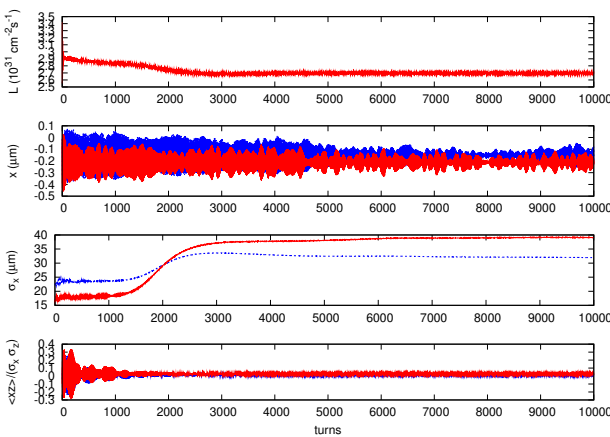


Figure 3: Evolution of luminosity, dipole moment $\langle x \rangle$, beam size σ_x and correlation of $\langle xz \rangle$ given by the strong-strong simulation. Those of positron and electron beams are plotted with red and blue lines, respectively. Tune is $\nu_x^{(\pm)} = 0.53$, $\nu_z^{(+)} = 0.0247$ and $\nu_z^{(-)} = 0.028$.

INSTABILITY MEASUREMENT IN PHASE-II COMMISSIONING

Machine experiments were held to study the beam-beam instability two times, July 7 and 13, 2018. Tune scan was performed to find instability condition in 7 July. Beam current was $(I_{+,tot}, I_{-,tot}) = (270, 225), (220, 180)$ and $(200, 160)$ mA. Bunches of 395 were stored with 25 ns spacing. Horizontal tune of LER and HER was scanned near the usual operating point $(\nu_x^{(+)}, \nu_x^{(-)}) = (0.567, 0.542)$, where the integer part is removed. Figure 4 presents log data

Table 2: Summary of the strong-strong simulation

ν_x	$8 \times 8 \times$			
	L/L_0	σ_x (L)	σ_x (H)	osc.
0.53	0.58-0.66	6.5	4.5	Y
0.535	0.70-0.95	2.5-6.2	1.4-4.0	Y
0.54	0.75-0.95	2.5-6.0	1.4-4.0	Y
0.545	0.83	7.2	1.2	N
	$4 \times 8 \times$			
0.53	0.75-1.0	3.0-7.5	2.2-6.2	Y
0.535	1.04	1.2	1.0	N
0.54	1.05	2.1	1.1	N
0.545	0.94	5.2	1.7	N
0.55	0.75-0.77	8.6	3.5	N

of beam current, luminosity, beam sizes and tunes during the measurement. Horizontal beam size increase of both beams is seen for decreasing horizontal tune of e^+ beam to 0.551. The size was recovered when ν_x of e^- beam increased $\nu_x^{(-)} = 0.54 \rightarrow 0.546$ with keeping $n_x(e^-) = 0.553$. Further decreasing, $\nu_x^{(+)} = 0.553 \rightarrow 0.543$, beam size increased at $\nu_x^{(-)} = 0.546$. Then increasing $\nu_x^{(+)} = 0.543 \rightarrow 0.553$ and decreasing $\nu_x^{(-)} = 0.548 \rightarrow 0.542$, the horizontal beam size blow-up was seen. The beam size enlargement appeared at condition $\nu_x^{(+)} + \nu_x^{(-)} = \text{constant}$. The beam size increase was not observed in single beam for scanning the horizontal tune. The beam size increase was not seen at (170, 142) mA.

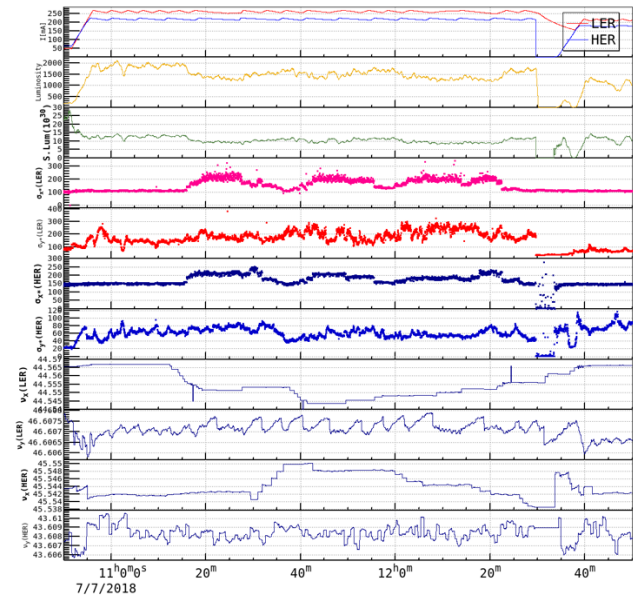


Figure 4: Log of operating condition during the measurement.

Figure 5 shows horizontal beam size as function of $\nu_x(e^\pm)$ at (270,225) mA.

Figures 6 and 7 present horizontal beam size as function of $\nu_x(e^\pm)$ at (220,180) and (200,160) mA, respectively.

Another machine experiment was held to observe beam oscillation in the horizontal blow-up on 13 July. Figure 8

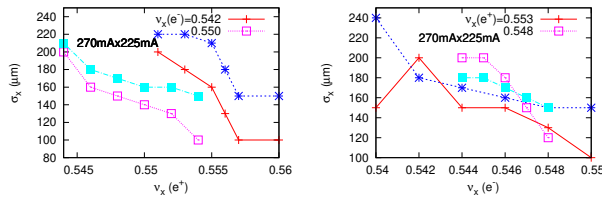


Figure 5: Horizontal beam size of two beams as function of $\nu_x(e^\pm)$ at (270, 225) mA.

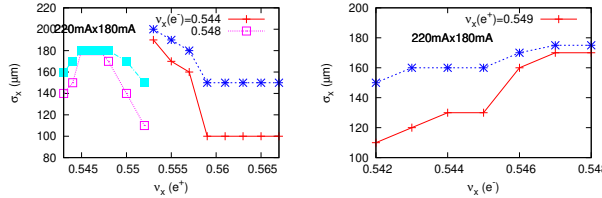


Figure 6: Horizontal beam size of two beams as function of $\nu_x(e^\pm)$ at (220, 180) mA..

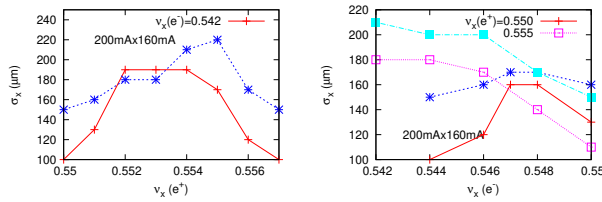


Figure 7: Horizontal beam size of two beams as function of $\nu_x(e^\pm)$ at (200, 160) mA.

shows beam size variation during the measurement. Horizontal tune of e^+ beam was scanned from $0.565 \rightarrow \sim 0.55$. e^- beam is aborted at 17:24 due to background increase induced by the instability. Beam current is increased to (300, 250) mA. for the measurement. Bunch oscillation and snap shot using streak camera were taken at 0.552, 0.5435, when a strong beam size blowup was seen.

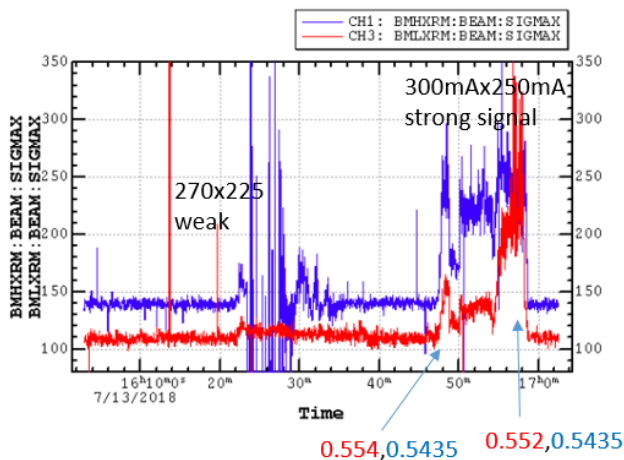


Figure 8: Log of beam size at an machine experiment held on 13 July.

Figure 9 presents FFT amplitude of Bunch Oscillation Recorder for LER. Clear signals at $\nu = 0.564$ and its side-band 0.585 were seen. Since noise level of HER data was high, clear oscillation was not seen.

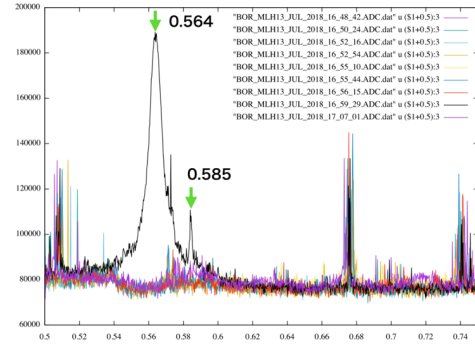


Figure 9: FFT amplitude of Bunch Oscillation Recorder for LER, when a strong beam size blowup was seen.

Figure 10 presents results for streak camera measurement. Shot-by-shot (left) and average (right) of the horizontal beam size were plotted. No clear signal was seen. Probably, the resolution is not sufficient.

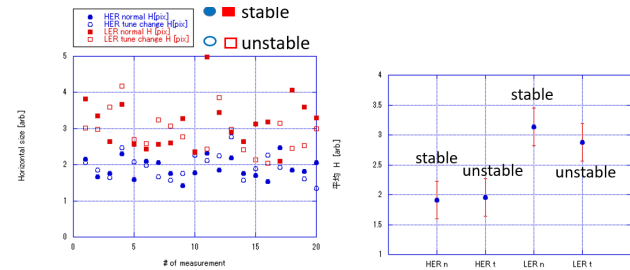


Figure 10: Beam size measured by streak camera. Left is shot-by-shot and right is averaged.

SUMMARY

Coherent beam-beam instability due to head-tail mode coupling of two beams has been predicted in collision with a large crossing angle. Experiments to verify the instability were held in SuperKEKB commissioning. Horizontal beam size of both beams increased when horizontal tune of e^- beam was scanned. This observation can be evidence of the beam-beam instability.

REFERENCES

- [1] K. Ohmi, N. Kuroo, K. Oide, D. Zhou, F. Zimmermann, *Phys. Rev. Lett.* 119, 134801 (2017).
- [2] Y. Ohnishi et al., presented at eeFACT2018, Hong Kong, Sept. 2018, paper MOXAA02, in this conference.
- [3] N. Kuroo, K. Ohmi, K. Oide, D. Zhou, F. Zimmermann, *Phys. Rev. AB* 21, 031002 (2018).

BEAM-BEAM EFFECTS AT HIGH ENERGY e^+e^- COLLIDERS*

D. Shatilov[†], Budker Institute of Nuclear Physics, 630090 Novosibirsk, Russia

Abstract

One of the main requirements for future e^+e^- colliders is high luminosity. If the energy per beam does not exceed 200 GeV, the optimal choice will be a circular collider with “crab waist” collision scheme. Here, to achieve maximum luminosity, the beams should have a very high density at the IP. For this reason, radiation in the field of a counter bunch (BS – beamstrahlung) becomes an appreciable factor affecting the dynamics of particles. In particular, in the simulations for Further Circular Collider (FCC), new phenomena were discovered: 3D flip-flop and coherent X-Z instability. The first is directly related to BS. The second can manifest itself at low energy (where BS is negligible), but at high energies BS substantially changes the picture. In the example of FCC-ee, we will consider the features of beam-beam interaction at high-energy crab waist colliders, and optimization of parameters for high luminosity.

INTRODUCTION

FCC-ee is a double-ring e^+e^- collider to be built at CERN and operate in the wide energy range from Z-pole (45.6 GeV) to $t\bar{t}$ (up to 185 GeV). At such energies, beam-beam effects can get an extra dimension due to BS [1, 2]. FCC-ee apparently will be the first collider where BS plays a significant role in the beam dynamics. For this to happen, two conditions must be fulfilled: high energy and high charge density in the bunch. For example, the energy in LEP was large enough, but the charge density too small, so the effect was negligible. BS increases the energy spread (and hence the bunch length) and creates long non-Gaussian tails in the energy distribution, which can limit the beam lifetime due to a possible escape of particles beyond the energy acceptance.

The collider has a two-fold symmetry and two Interaction Points (IP) with a horizontal crossing angle and “crab waist” collision scheme [3, 4]. The luminosity per IP for flat beams ($\sigma_y \ll \sigma_x$) can be written as:

$$L = \frac{\gamma}{2e r_e} \cdot \frac{I_{tot} \xi_y}{\beta_y^*} \cdot R_H, \quad (1)$$

where I_{tot} is the total beam current which is determined by the synchrotron radiation power 50 MW. Therefore L can be increased only by making ξ_y larger and β_y^* smaller while keeping R_H reasonably large. We assume that ξ_y can be easily controlled by N_p (number of particles per

bunch), that implies adjusting the number of bunches to keep I_{tot} unchanged. The hour-glass factor R_H depends on L_i/β_y^* ratio, where L_i is the length of interaction area which in turn depends on σ_z and Piwinski angle ϕ :

$$\phi = \frac{\sigma_z}{\sigma_x} \tan\left(\frac{\theta}{2}\right), \quad (2)$$

$$L_i = \frac{\sigma_z}{\sqrt{1+\phi^2}} \Rightarrow \frac{2\sigma_x}{\theta}. \quad (3)$$

Here θ is the full crossing angle, and expressions after \Rightarrow correspond to $\phi \gg 1$ and $\theta \ll 1$, see Fig. 1.

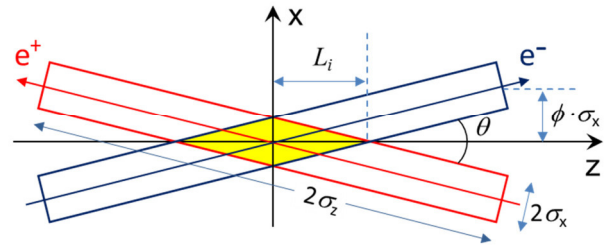


Figure 1: Sketch of collision with large Piwinski angle.

The beam-beam parameters for $\sigma_y \ll \sigma_x$ and $\theta \neq 0$ become [5]:

$$\xi_x = \frac{N_p r_e}{2\pi\gamma} \cdot \frac{\beta_x^*}{\sigma_x^2 (1+\phi^2)} \Rightarrow \frac{N_p r_e}{\pi\gamma} \cdot \frac{2\beta_x^*}{(\sigma_z \theta)^2} \quad (4)$$

$$\xi_y = \frac{N_p r_e}{2\pi\gamma} \cdot \frac{\beta_y^*}{\sigma_x \sigma_y \sqrt{1+\phi^2}} \Rightarrow \frac{N_p r_e}{\pi\gamma} \cdot \frac{1}{\sigma_z \theta} \sqrt{\frac{\beta_y^*}{\epsilon_y}}$$

In particular, $\xi_x \propto 1/\epsilon_x$ (in head-on collision) transforms to $\xi_x \propto \beta_x^*/\sigma_z^2$ when $\phi \gg 1$, and ξ_y dependence on σ_x vanishes. Further, because of the symmetry, we consider a model with one IP (that is a half ring of FCC-ee).

HIGH ENERGY

At very high energies (e.g. $t\bar{t}$ production, 175÷185 GeV) the beam lifetime is mainly determined by single BS photons [2], which imposes another limitation on the luminosity. An example is shown in Fig. 2. The black curve corresponds to the Gaussian distribution with σ_8 increased by 30% due to BS. As is seen, within 3-4 sigma the real distribution agrees well with it, but at large amplitudes there are long non-Gaussian tails. Their asymmetry is related to the fact that the damping time is comparable

* Work supported by Russian Science Foundation, N 14-50-00080.

[†] email: shatilov@inp.nsk.su

to the period of synchrotron oscillations. Therefore, the optimized momentum acceptance also should be asymmetrical, as proposed and implemented in [6, 7].

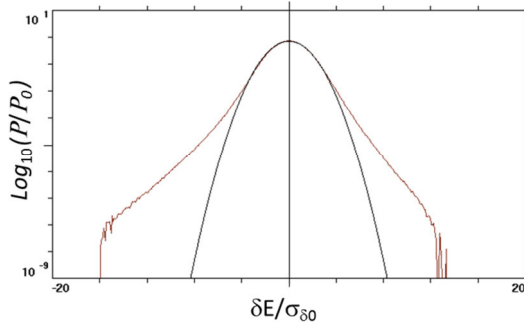


Figure 2: Energy distribution at 182.5 GeV in the logarithmic scale, black line: Gauss with $\sigma_8 = 1.3 \sigma_{80}$.

A rough estimate for the beamstrahlung lifetime can be found in [8]:

$$\tau_{BS} \propto \exp\left(\frac{2\alpha\eta\rho}{3r_e\gamma^2}\right) \cdot \frac{\rho\sqrt{\eta\rho}}{L_i\gamma^2}, \quad (5)$$

where α is a fine structure constant, η is the energy acceptance (which should be maximized), and ρ is the bending radius of particle's trajectory in the field of oncoming bunch. Evidently, ρ is inversely proportional to the absolute value of transverse electro-magnetic force acting on the particle. Its dependence on the transverse coordinates for flat beams is shown in Fig. 3.

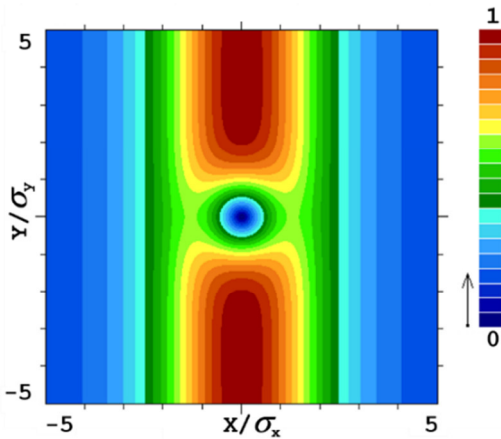


Figure 3: Absolute value of the transverse force for flat beams, in relative units.

The minimum values of ρ correspond to the particles with $|x| < \sigma_x/2$ and $|y| > 2\sigma_y$. However, during collision particles traverse the opposite bunch horizontally because of the crossing angle. This means that the maximum force acting on a particle at the IP depends mainly on the vertical coordinate, and ρ is inversely proportional to the surface charge density in the horizontal plane:

$$\frac{1}{\rho} \propto \frac{N_p}{\gamma\sigma_x\sigma_z} \propto \frac{\xi_y}{L_i} \sqrt{\frac{\epsilon_y}{\beta_y^*}} \propto L \sqrt{\frac{\epsilon_y}{\beta_y^*}}. \quad (6)$$

These relations are valid for both head-on and crossing angle collisions; the last transformation is based on (1) and assumption that $L_i \approx \beta_y^*$.

Our goal is to increase L while keeping the lifetime (and therefore ρ) large enough. It follows that ϵ_y (i.e. both the betatron coupling and ϵ_x) should be minimized, and β_y^* should be *increased*. For example, increase in β_y^* (together with L_i) by a factor of k may result in the luminosity gain by $k^{1/2}$ with ρ unchanged. In fact, as is seen from (5), τ_{BS} is inversely proportional to L_i provided that $\rho = \text{const}$. Therefore, to keep $\tau_{BS} = \text{const}$ when L_i is increased, we need to slightly increase ρ . However, τ_{BS} dependence on L_i is much weaker than the dependence on ρ (because the argument of \exp is $\gg 1$), so the gain in luminosity will be *almost* $k^{1/2}$. All these manipulations mean an increase in σ_x and N_p , but other than that, ξ_y will also rise by $k^{3/2}$. Consequently, we may perform such optimization only as long as ξ_y remains below the beam-beam limit.

This can be formulated in a different way. If there are multiple limiting factors, the maximum performance is achieved when all limits are reached simultaneously. In our case it means that β_y^* (together with L_i) should be adjusted in such a way that both τ_{BS} and ξ_y achieve their limits. This implies that, if the balance shifts towards "limit by the BS lifetime" (e.g. decrease in η or increase in γ , ϵ_y), the luminosity optimization will require some increase in L_i (together with β_y^*).

Note that in collision with large Piwinski angle, an increase in L_i means an increase in σ_x rather than σ_z . Since ϵ_y should be small, L_i is controlled by β_x^* which is made quite large, unlike lower energies, where the choice of β_x^* is determined by other factors.

3D FLIP-FLOP

When energy decreases, the lifetime limitation due to BS weakens. This is easy to understand from the following considerations. Assuming that the lattice is not changed, emittances drop quadratically and σ_x , L_i – linearly with energy. If we keep ξ_y and β_y^* unchanged then, as follows from (5) and (6), ρ remains constant and τ_{BS} grows significantly because its dependence on γ is very strong. Hence at lower energies we may allow some reduction in η , and for higher luminosity we need to decrease β_y^* and ρ . On the other hand, since the bending radius in the arc dipoles remains unchanged, the relative contribution of BS to the energy spread grows and the bunch lengthening becomes larger.

For example, when the parameters of FCC-ee are optimized for high luminosity, σ_z increases due to BS almost 3.5 times at 45.6 GeV and only 1.3 times at 182.5 GeV. Why then we do not see this effect in low energy colliders? Because they have much higher magnetic field in the

dipoles or, which is the same, much smaller bending radius in the arcs.

As seen from (4), the bunch lengthening leads to a decrease in ξ_y and L . Therefore, to achieve high luminosity, it is necessary to increase N_p . That, in turn, strengthens BS and causes additional lengthening. As a result, the equilibrium σ_z with account of BS can increase several times, and this is fraught with the appearance of instability. The threshold depends on asymmetry in population of colliding bunches, but even in a symmetrical case the instability arises (with higher N_p).

Briefly, the problem is that the weakening of BS for one bunch leads to its shortening, as a result ξ_x and ξ_y for the opposite bunch grow and all three of its sizes are increasing; this even more weakens the BS for the first bunch. In this way we obtain a positive feedback in the following chain:

- 1) Asymmetry in the bunch currents leads to asymmetry in the bunch lengths (due to BS).
- 2) In collisions with $\phi \gg 1$, asymmetry in σ_z enhances synchrotron modulation of the horizontal kick for a longer bunch, thus amplifying synchro-betatron resonances. Besides, ξ_x^w grows quadratically and ξ_y^w – linearly with decrease of σ_z^s , so the footprint expands and can cross more resonances. All this leads to increase in both emittances of the weak bunch.
- 3) An increase in ϵ_x^w has two consequences: a) weakening of BS for a strong bunch, which makes it shorter, and b) growth of ϵ_y^w due to the betatron coupling, which leads to asymmetry in the vertical beam sizes.
- 4) As seen in Fig. 3, the greatest BS is experienced by the particles with the vertical coordinates $|y^w| > 2\sigma_y^s$. When $\sigma_y^w > \sigma_y^s$, the number of particles in the weak bunch experiencing strong BS increases while the number of such particles in the strong bunch decreases. Thus, asymmetry in the vertical beam sizes leads to further increase in σ_z asymmetry.
- 5) Now we go back to point 2, and the loop is closed. In the beginning, all three beam sizes grow slowly until the footprint touches strong resonance, then the “weak” bunch blows up.

An example is shown in Fig. 4. The top row corresponds to a stable situation, though some acceptable bloating of the weak bunch is seen. In the bottom row asymmetry is the same, but N_p increased by 5%. As a result, the strong bunch shrank to unperturbed sizes, while the weak one became swollen in all three dimensions.

Another example can be found in [9], where the strength of “crab” sextupoles was not optimal. In this case ξ_y^w exceeds the limit, which leads to bloating of σ_y^w . Thus we come to asymmetry in σ_y , and instability begins to develop in the longitudinal and vertical dimensions. At the same time, ξ_x^w grows rapidly with decreasing σ_z^s , and when the footprint overlaps horizontal synchro-betatron resonance, σ_x^w also increases, making the whole process even faster. In the end, we again get 3D flip-flop.

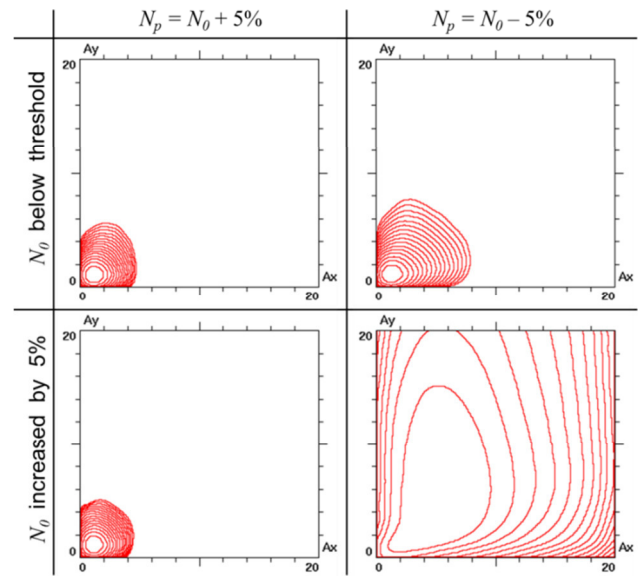


Figure 4: Example of 3D flip-flop. Equilibrium density contour plots ($\sqrt{\epsilon}$ between successive lines) in the space of normalized betatron amplitudes are shown for stable (top) and unstable (bottom) cases.

In the best case, when crab sextupoles are optimal and ξ_y below the limit, the 3D flip-flop is usually initiated by the horizontal synchro-betatron resonances – satellites of half integer. This is its similarity with another instability, which will be discussed below.

COHERENT X-Z INSTABILITY

This instability [10, 11] develops in the horizontal plane and is manifested by wriggle of the bunch shape. If we imagine that the bunch is sliced longitudinally in many pieces, the amplitudes of X-displacement of slices depend on their Z-coordinates and vary on every turn. An example is presented in Fig. 5, where coordinates of centers of slices are shown at some turns. Red line corresponds to unperturbed state, green – to the stage of development of instability (oblique part of the curve in Fig. 6), and blue – to the final stage with ϵ_x blown up.

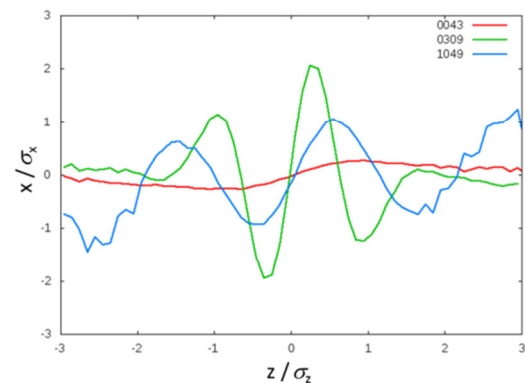


Figure 5: Coherent X-Z instability, the bunch shape in the horizontal plane at different (43, 309 and 1049) turns.

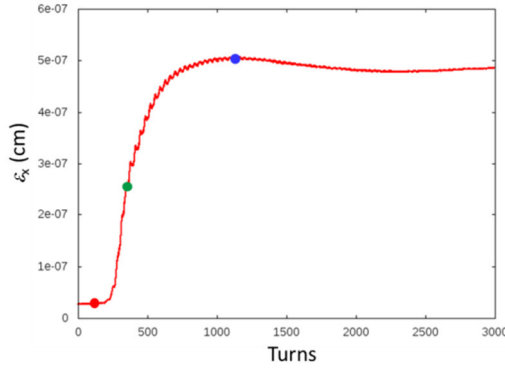


Figure 6: Evolution of the horizontal emittance. The colour dots correspond to the turns shown in Fig. 5.

In collision schemes with $\phi \gg 1$, an increase in ε_x itself does not have a noticeable impact on luminosity. However, this leads to a proportional increase in ε_y due to the betatron coupling, so eventually the luminosity will drop several times. The instability does not cause dipole oscillations and therefore cannot be suppressed by feedback. We need to look for conditions under which it does not arise.

The most effective is to reduce β_x^* , which means a decrease in ξ_x . However, in FCC-ee at 45.6 GeV, β_x^* can only be reduced to 15 cm [7, 12], and this is not enough to suppress the instability. The next step is to reduce ξ_x with the given β_x^* . In fact ξ_x is important not itself, but in comparison with the synchrotron tune ν_s . As we shall see later, the greatest danger arises from the synchro-betatron resonances $2\nu_x - 2m \cdot \nu_s = 1$, the distance between them is just ν_s . Our task is to make ξ_x noticeably smaller than ν_s , then we can put the working point and the whole footprint between resonances. Herewith, by decreasing ξ_x we should preserve the luminosity, i.e. ξ_y . In assumption that $\beta_{x,y}^*$ and ε_y were already minimized and therefore are not free parameters, from (4) it follows that the only way to reduce the ξ_x/ξ_y ratio is to increase the bunch length (we assume that N_p also should grow proportionally, to keep ξ_y unchanged).

This is best done by increasing the momentum compaction factor α_p . An advantage is that ν_s grows together (and by the same factor) with σ_z . In addition, larger α_p increases the threshold of microwave instability to an acceptable level. The main drawback of this approach is that emittances also grow in the power of 3/2 with respect to α_p , and yet we were forced to double α_p at 45.6 GeV [7, 12].

Further optimization requires a proper choice of the working point. For this we performed a scan of betatron tunes in a simplified model: linear lattice without explicit betatron coupling. The beam-beam effects were implemented in a weak-strong approximation; therefore coherent instabilities are not manifested here. The simulation results are presented in Fig. 7. Since $\xi_x \ll \xi_y$, the footprint looks like a narrow vertical strip, bottom edge resting on the working point.

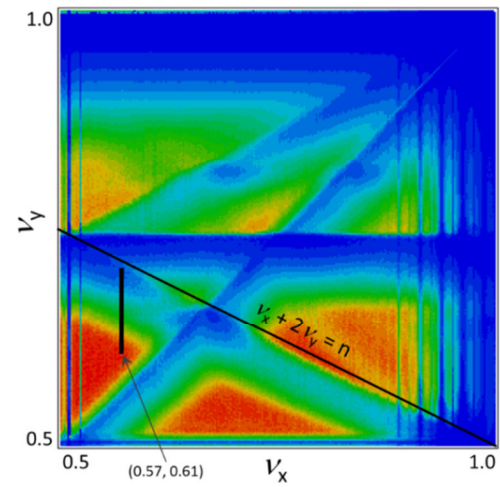


Figure 7: Luminosity for FCC-ee at 45.6 GeV, depending on the betatron tunes. The colour scale from zero (blue) to $2.3 \cdot 10^{36} \text{ cm}^{-2} \text{ c}^{-1}$ (red). The black narrow rectangle shows the footprint at (0.57, 0.61).

The good region is reduced to a red triangular area bounded by the main coupling resonance $\nu_x = \nu_y$, sextupole resonance $\nu_x + 2\nu_y = n$, and half-integer resonance $2\nu_x = 1$ with its synchrotron satellites. All other higher-order coupling resonances are suppressed by the crab waist, and therefore are not visible. As seen from the plot, the range of permissible ν_x for large ξ_y is bounded on the right by 0.57 – 0.58.

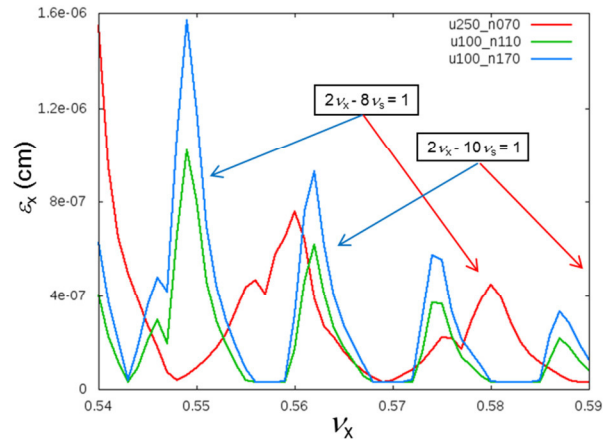


Figure 8: Growth of ε_x due to coherent X-Z instability, depending on ν_x , for FCC-ee at 45.6 GeV. Red line corresponds to $U_{\text{RF}} = 250 \text{ MV}$, $N_p = 7 \cdot 10^{10}$, green and blue lines – $U_{\text{RF}} = 100 \text{ MV}$, $N_p = 1.1 \cdot 10^{11}$ and $1.7 \cdot 10^{11}$.

Then we performed a numerical scan of ν_x in quasi-strong-strong model, in which coherent instabilities and flip-flop can be observed. The results are presented in Fig. 8, and synchro-betatron resonances are clearly seen. As the order of resonances increases, their strength weakens. Zones free from instability can be detected starting from the region between $2\nu_x - 8\nu_s = 1$ and $2\nu_x - 10\nu_s = 1$,

so the “good” ν_x are determined by the synchrotron tune. As seen, the first window for $U_{RF} = 250$ MV is located around 0.59 – too much for large ξ_y . And here we are helped by the reduction of U_{RF} , thereby decreasing ν_s (while ξ_x/ν_s not changed) and increasing the order of resonances located in the region of interest ($\nu_x < 0.58$).

Here it is appropriate to recall the semi-analytical scaling law obtained from other considerations for the threshold bunch intensity [12]:

$$N_{th} \propto \frac{\alpha_p \sigma_\delta \sigma_z}{\beta_x^*}, \quad (7)$$

where σ_δ is the energy spread. In respect that $\alpha_p \sigma_\delta \propto \nu_s \sigma_z$ and $\xi_x \propto N_p \beta_x^* / \sigma_z^2$, this is nothing else than a condition on the ratio ξ_x / ν_s . We obtained a similar relation from the simple requirement to “squeeze” the footprint in between synchro-betatron resonances. It should be noted that the proposed solution also solves the problem with 3D flip-flop, since it helps to avoid resonances which are crucial for both instabilities.

Consider now the influence of BS on these processes. In our range of parameters, where σ_z is defined mainly by BS, it scales as $\sigma_z^2 \propto N_p$. The rationale for this dependence is not so obvious, but in the simulation it was confirmed with good accuracy. As a result, ξ_x does not depend on N_p . This is clearly seen in Fig. 8 comparing the green and blue lines, which differ only in the bunch population. Thus, if we stay in a “good” area, N_p can be increased until it is limited by other factors – energy acceptance or ξ_y . The reverse side of this coin is that getting rid of instability (e.g. if ν_x is not optimal) simply by reducing N_p will be quite difficult. To do this, it is necessary to descend to the region where the dependence $\sigma_z^2 \propto N_p$ is violated, which means a significant decrease in the luminosity.

BOOTSTRAPPING

Another problem is how to bring bunches into collision, since “before collision” they are too short. Consequently, $\xi_{x,y}$ will be far above the limits, and the beams will be blown up and killed on the transverse aperture before they are stabilized by BS. To avoid this, we must gradually increase the bunch population during collision, so we come to *bootstrapping*.

An example is presented in Fig. 9. We start with approximately one quarter of the final bunch population, and then alternately add small portions to both beams. In fact, the injection cycle will last about 2 minutes, but in simulations it was reduced to ~ 2 damping times to avoid unnecessary time-consuming calculations.

As is seen, the bunch after injection (added portion) becomes “strong” and its length reduces because the opposite bunch elongates due to the increased beamstrahlung, while the asymmetry remains moderate all the time.

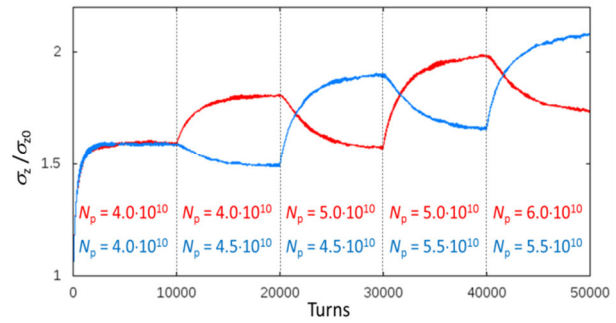


Figure 9: Simulated bootstrapping for Z-pole operation in FCC-ee: length of colliding bunches vs. time. The first few steps towards the nominal $N_p = 1.7 \cdot 10^{11}$ are shown.

The benefit of this procedure is especially great at low energies, where it can double the luminosity. But also at high energies the luminosity can be raised using this method and avoiding large asymmetry in the population of colliding bunches.

PARAMETER OPTIMIZATION SUMMARY

With increasing energy, Piwinski angle decreases and damping becomes stronger, so the coherent instabilities weaken. In addition, when considering the optimization of parameters, it is necessary to take into account that a resonant depolarization (which may be required for energy calibration) imposes a restriction on the synchrotron tune [13].

Here we briefly describe the selection of parameters associated with the beam-beam interaction at four FCC-ee operating points (see also in [7, 14]). The current table can be found in [15].

Z-pole (45.6 GeV)

The biggest problems at this energy are associated with the 3D flip-flop and coherent X-Z instability. To combat them, the following steps were taken: increase α_p , decrease β_x^* and U_{RF} , choice of ν_x between synchro-betatron resonances in the range from 0.56 to 0.58.

W^\pm Pair Production Threshold (80 GeV)

Here we may allow smaller α_p to decrease emittances, while the instabilities are mitigated by low β_x^* and U_{RF} . However, in this case ν_s will be too small. In order to make a resonant depolarization possible, we were forced to use the lattice with large α_p (same as at Z-peak) and the maximum possible U_{RF} , which is determined by the RF staging scenario. A small β_x^* and proper choice of betatron tunes are sufficient to avoid instabilities.

HZ Production (120 GeV)

At this and the next energy points we do not care about polarization, therefore α_p should be small to minimize emittances, while U_{RF} is determined by the energy loss per turn – there is not much freedom for optimization.

The coherent instabilities at 120 GeV are much weaker but still exist; the remedy is the same as above: a small β_x^* and a neat choice of the working point.

ttbar Threshold (175 – 182.5 GeV)

The coherent instabilities are suppressed by very strong damping, but another problem becomes dominant: the lifetime limitation by single high-energy BS photons. Therefore, in contrast to other energies, optimization requires an increase in β_x^* .

It is worth recalling that the condition $\beta_y^* \approx L_i$ should be met at all points, which actually means an increase in β_y^* with energy.

ACKNOWLEDGEMENTS

The author would like to thank K. Oide and K. Ohmi for many useful discussions.

REFERENCES

- [1] J. Augustin *et al.*, “Limitations on performance of e^+e^- storage rings and linear colliding beam systems at high energy”, *eConf C781015*, 009, 1978.
- [2] V. Telnov, “Restriction on the energy and luminosity of e^+e^- storage rings due to beamstrahlung”, *Phys. Rev. Lett.* vol. 110, p. 114801, Mar. 2013.
- [3] P. Raimondi, D. Shatilov, and M. Zobov, “Beam-beam issues for colliding schemes with large Piwinski angle and crabbed waist”, LNF-07-003-IR, Jan. 2007, e-Print: physics/0702033.
- [4] M. Zobov *et al.*, “Test of crab waist collisions at DAFNE Phi factory”, *Phys. Rev. Lett.* vol. 104, p. 174801, Apr. 2010.
- [5] P. Raimondi and M. Zobov, “Tune shift in beam-beam collisions with a crossing angle”, DAFNE Tech. Note G-58, Apr. 2003.
- [6] K. Oide, “Optics for Compton scattering”, 64th FCC-ee Optics Design meeting, CERN, Nov. 2017, <https://indico.cern.ch/event/683544/>.
- [7] K. Oide, “FCC-ee optics design”, ICFA Beam Dyn. Newslett. 72, p. 19, Dec. 2017.
- [8] A. Bogomyagkov, E. Levichev, and D. Shatilov, “Beam-beam effects investigation and parameters optimization for a circular e^+e^- collider at very high energies”, *Phys. Rev. ST Accel. Beams*, vol. 17, p. 041004, Apr. 2014.
- [9] K. Ohmi, “CEPC and FCCee parameters from the viewpoint of the beam-beam and electron cloud effects”, IAS High Energy Physics Conf., Hong Kong, Jan. 2018.
- [10] K. Ohmi, “Study of coherent head-tail instability due to beam-beam interaction in circular colliders based on crab waist scheme”, in *Proc. eeFACT2016*, Daresbury, UK, Oct. 2016, paper TUT1BH2, pp. 61-65.
- [11] K. Ohmi, *et al.*, “Coherent beam-Beam instability in collisions with a large crossing angle”, *Phys. Rev. Lett.* vol. 119, p. 134801, Sep. 2017.
- [12] K. Oide *et al.*, “Progress in the design of beam optics for FCC-ee collider ring”, in *Proc. IPAC2017*, Copenhagen, Denmark, May 2017, paper TUOCB1, pp. 1281-1284.
- [13] I. Koop, “Polarization studies for FCC-ee and CEPC”, presented at FCC Week 2018, Amsterdam, Netherlands, Apr. 2008, <https://indico.cern.ch/event/656491/contributions/2938716/>.
- [14] D. Shatilov, “FCC-ee parameter optimization”, ICFA Beam Dyn. Newslett. 72, p. 30, Dec. 2017.
- [15] D. Shatilov, “IP beam parameter optimization for FCC-ee”, presented at FCC Week 2018, Amsterdam, Netherlands, Apr. 2008, <https://indico.cern.ch/event/656491/contributions/2939184/>.

BEAM-BEAM BLOWUP IN THE PRESENCE OF X-Y COUPLING SOURCES AT FCC-EE

D. El Khechen*, K. Oide¹, F. Zimmermann, CERN, Geneva, Switzerland
¹ also at High Energy Accelerator Research Organisation, Tsukuba, Ibaraki, Japan

Abstract

FCC-ee, the lepton version of the Future Circular Collider (FCC), is a 100 Km future machine under study to be built at CERN. It acquires two experiments with a highest beam energy of 182.5 GeV. FCC-ee aims to operate at four different energies, with different luminosities to fulfill physics requirements. Beam-beam effects at such a high energy/luminosity machine are very challenging and require a deep understanding, especially in the presence of x-y coupling sources. Beam-beam effects include the beamstrahlung process, which limits the beam lifetime at high energies, as well as dynamic effects at the Interaction point (IP) which include changes in the beta functions and emittances. In this report, we will define the beam-beam effects and their behaviours in the FCC-ee highest energy lattice after introducing x-y coupling in the ring.

INTRODUCTION

Beam-beam effects including beamstrahlung have been studied for FCC-ee. Dynamic effects including dynamic β functions and dynamic emittances were simulated in the presence of vertical misalignments of the sextupoles. Tracking was performed in SAD [1] with a beam-beam element present at both IPs of the FCC-ee highest energy lattices (175 and 182.5 GeV). The beam-beam is represented by a weak-strong beam beam simulation (BBWS) [2] which is implemented in SAD. Beam blowup was observed by tracking in the presence of beam-beam and without beam beam. We will report on the different simulations and discuss the results.

DYNAMIC β FUNCTIONS AND EMITTANCES

Dynamic effects are the change of the Twiss parameters (β functions and emittances) at the IP due beam beam quadrupolar focusing. These dynamic effects are enhanced by running at half integer or integer resonance tunes and thus affecting the luminosity.

Analytical Estimations

Dynamic beta functions can be easily calculated by the half turn matrix as given in Eq. (1), where β , β_0 , μ , μ_0 are the dynamic β , the design β , the shifted betatron tune after beam beam and the design betatron tunes respectively and $\frac{1}{f}$ being the beam beam strength. Solving Eq. (1), we can obtain the dynamic beta function given in Eq. (2) where

$\xi_{x,y}$ is the so-called beam beam parameter and expressed in terms of β function and beam-beam force as given in Eq. (3)

$$\begin{pmatrix} \cos \mu & \beta \sin \mu \\ -\frac{1}{\beta} \sin \mu & \cos \mu \end{pmatrix} = \begin{pmatrix} 1 & 1 \\ -\frac{1}{2f} & 0 \end{pmatrix} \begin{pmatrix} \cos \mu_0 & \beta_0 \sin \mu_0 \\ -\frac{1}{\beta_0} \sin \mu_0 & \cos \mu_0 \end{pmatrix} \begin{pmatrix} 1 & 1 \\ -\frac{1}{2f} & 0 \end{pmatrix} \quad (1)$$

$$\beta = \frac{\beta_{x,y}}{\sqrt{1 - (2\pi\xi_{x,y})^2 + 4\pi\xi_{x,y}\cot(\mu_{0x,y})}} \quad (2)$$

$$\xi_{x,y} = \frac{\beta_{0x,y}}{4\pi f_{x,y}} \quad (3)$$

Analytical estimations of dynamic emittance require longer calculations. One way to calculate the dynamic horizontal emittance is given in [3]. The calculation of the dynamic vertical emittance is not straight forward since it requires the knowledge of the errors and corrections of the lattice.

Simulations of Dynamic Effects

The dynamic β functions and emittance were also simulated by an insertion of a thin quadrupole at both IPs representing the linear beam-beam. The thin quadrupole gives a kick as given in Eq. (4).

$$KL = \frac{4\pi f_{x,y}}{\beta_{0x,y}} \quad (4)$$

The beam beam parameters in this case are given to be (0.095,0.157) in the horizontal and vertical plane respectively. It is important to mention that the vertical emittance in the lattice is generated by vertically misaligned sextupoles to achieve an xy coupling of 0.2%. Furthermore, the values of the betatron tunes for the given lattice are $(\nu_x, \nu_y) = (0.553, 0.59)$. The new values of β functions and emittance, after the insertion of the thin quadrupole, are then extracted. The results of the simulations for the dynamic β perfectly match with the analytical estimations and the results of the dynamic effects are summarized in the Table. 1. It is important here to highlight that the values of the dynamic emittance depend essentially on the way the xy coupling is introduced in the lattice.

TRACKING AND BLOWUP

Tracking with Beam Beam

Tracking was also considered to study the beam beam dynamic effects. This was performed by inserting two beam

* dima.el.khechen@cern.ch

Table 1: Values of dynamic β functions and emittances for one given random generator

Twiss functions	Design values	Dynamic values
β_x (m)	1	0.49
β_y (mm)	2	1.12
ϵ_x (nm)	1.34	2.14
ϵ_y (pm)	2.7	3.83

beam elements at both IPs of the lattice. Tracking of 10^4 macroparticles beam initially generated at the IP was performed over 500 turns (50 turns= 1 longitudinal damping period). Every turn, the β functions and the emittances of the tracked beam were calculated at the IP. In the following section, the vertical emittance is introduced by vertically misaligning the sextupoles to achieve an xy coupling of 0.2%. For the time being, only one seed is used for the random misalignments of the sextupoles. Tracking in the presence of the beam beam elements showed a blowup in the vertical (from 2.7 pm to 3.83 pm) and horizontal (from 1.34 nm to 2.14 nm) emittances as shown in Figs. 1 and 2. Such a blowup in the vertical emittance was not observed in the simulations without misalignments [4]. To verify the source of the blowup, a tracking was performed without a beam beam element.

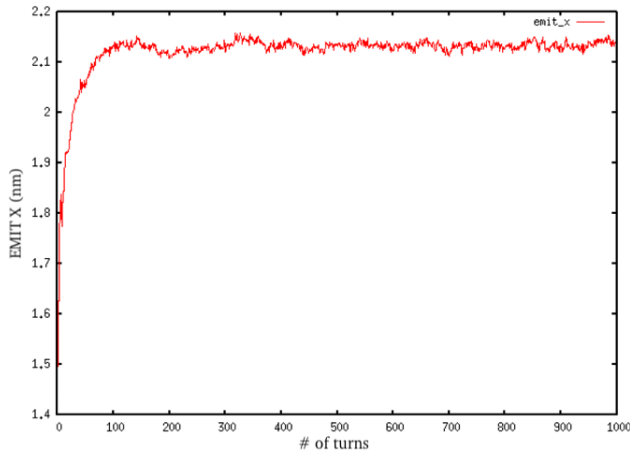


Figure 1: Evolution of horizontal emittance in the presence of the beam beam element.

Tracking Without Beam Beam

Beam beam elements are removed and a simple tracking was performed in the presence of vertical misaligned sextupoles to achieve 2.7 pm vertical emittance. The same seed used for the sextupole misalignments for tracking with the beam beam was also used for this tracking. Unexpected emittance blowup of the vertical emittance was observed (from 2.7 pm to 5 pm). This blowup is shown in Fig. 3. A possible reason for such a blowup could be related to the dispersions and xy coupling induced by the sextupole misalignments in the ring.

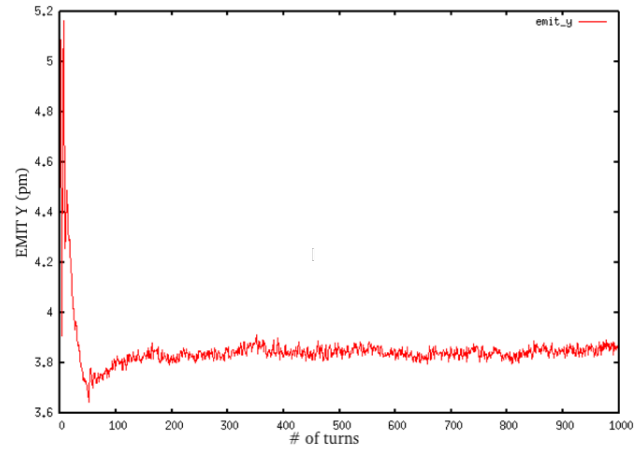


Figure 2: Evolution of vertical emittance in the presence of the beam beam element.

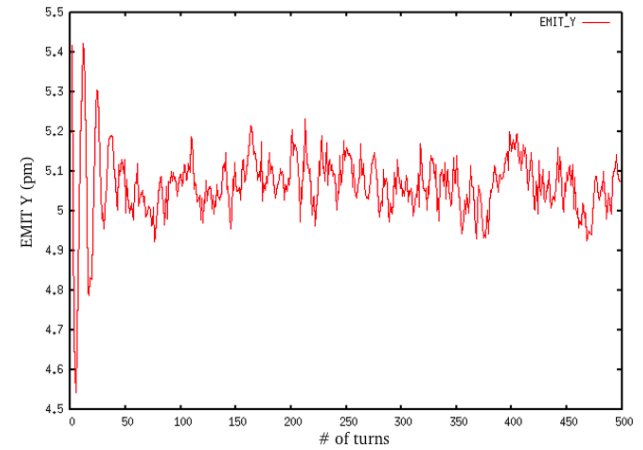


Figure 3: Evolution of the vertical emittance in the absence of beam beam element.

MORE SAMPLES TRACKING

For a better understanding, different seed generators for sextupole misalignments have been produced and tracking was performed with and without the beam beam element. Results showed the clear dependence of the blowup on the seed number.

With Beam Beam

Twelve different samples were simulated and tracking of the beam was performed in the presence of the beam beam element, over 500 full turns. The vertical emittance was then averaged over the different samples and the result is shown in Fig. 4 along with error bars. The error bars are big, this is explained by the variation of the amount of the vertical emittance blowup for different random generator seeds shown in Fig. 5.

Without Beam Beam

The same procedure was done in the absence of the beam beam element, the result of the average emittance is shown in Fig. 6. The individual seeds are shown in Fig. 7.

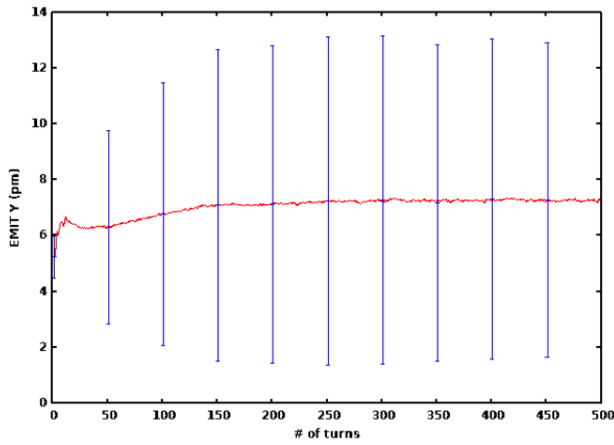


Figure 4: The evolution of the average vertical emittance over twelve samples in the presence of beam beam element.

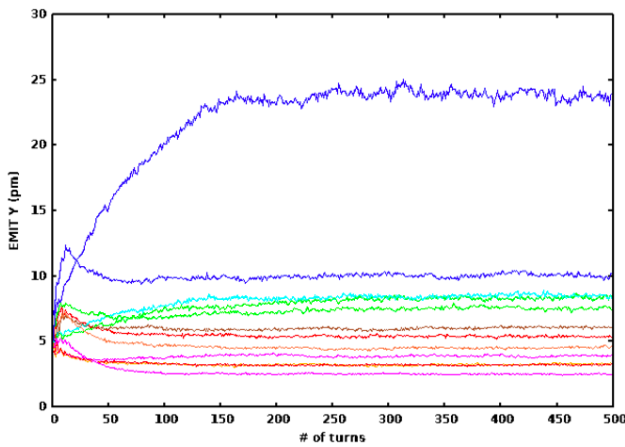


Figure 5: The evolution of the vertical emittance of the twelve different samples in the presence of the beam beam element.

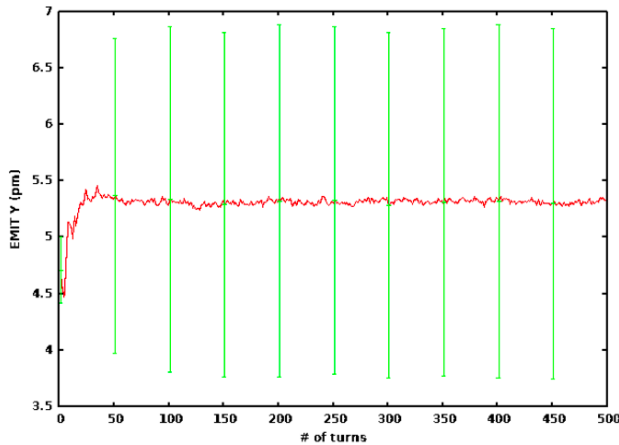


Figure 6: The evolution of the average vertical emittance over twelve samples in the absence of beam beam element.

Compare Optics

Among the twelve different seeds simulated we choose the best and the worst seed and we compare their optics.

TUYBA03

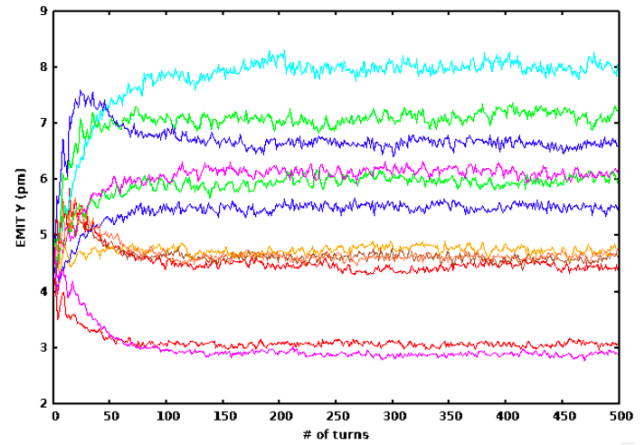


Figure 7: The evolution of the vertical emittance of the twelve different samples in the absence of the beam beam element.

The best seed is number 13 which didn't result in a vertical emittance blowup in both cases, with and without beam beam (Fig. 8), however the largest blowup was induced by seed number 25 (Fig. 9). We compare the vertical dispersion functions and R2 coupling parameters in the lattice for the two seeds since the vertical emittance depends strongly on these parameters. We notice that the dispersion functions are globally similar for both seeds (Fig. 10), however the coupling parameter R2 is larger for seed 25 than for seed 13 (Fig. 11). The vertical dispersions and R2 coupling values are also checked at the IP, and results are reported in Table. 2. As predicted, R2 values at IPs are higher for seed 25 than for seed 13 which is obviously resulting in a vertical emittance blowup.

Other simulations have been carried on, where the vertical emittance blowup was found to be dependent on the symmetry of the skew quads and the values of the betatron and synchrotron tunes [5].

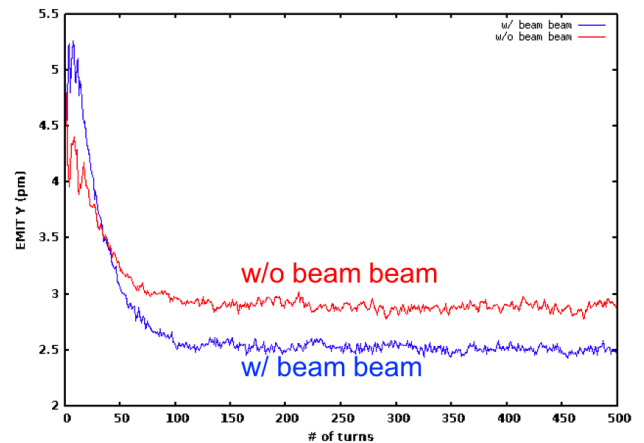


Figure 8: The evolution of the vertical emittance with (blue) and without (red) beam beam element for seed 13.

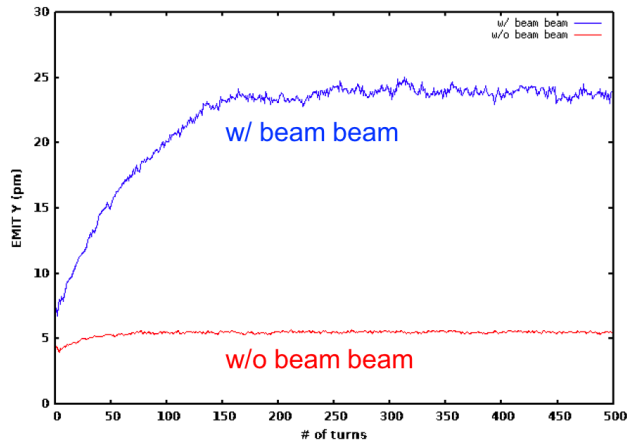


Figure 9: The evolution of the vertical emittance with (blue) and without (red) beam beam element for seed 25.

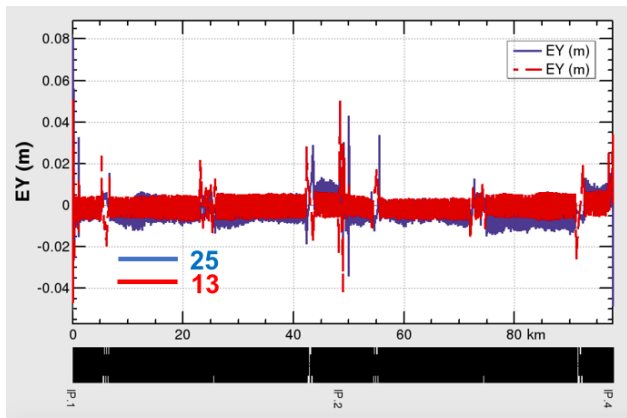


Figure 10: The vertical dispersion in the lattice for seed 13 in red and seed 25 in blue.

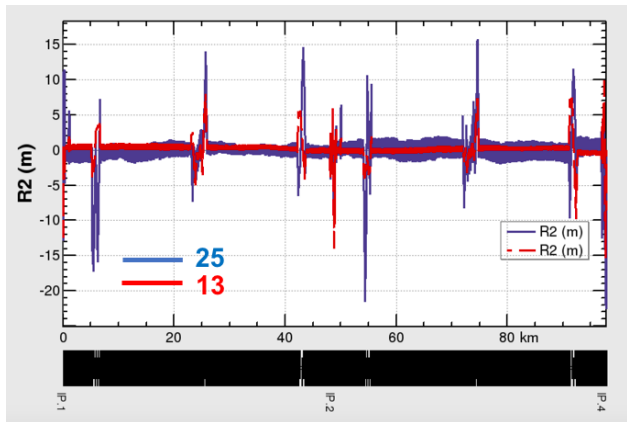


Figure 11: The R2 coupling parameter in the lattice for seed 13 in red and seed 25 in blue.

Table 2: Dispersion and coupling values at IP1 and IP2 for seeds 13 and 25

Seed	η_y at IP1 / IP2 (μm)	R2 at IP1 / IP2 (mm)
13	-15 / 17	0.15 / -0.03
25	5.3 / -22.1	0.5 / 1

CONCLUSION

Beam blowup was observed by tracking with and without beam beam in the presence of xy coupling sources in the ring represented by vertical misalignments of sextupoles. This blowup was observed to be dependent of the random generator used for the sextupole misalignments. High R2 coupling parameter values seemed to be responsible for such a blowup. Further simulations are undergoing considering corrected lattice, however this blowup will set further conditions on the low emittance tuning and the choice of the tunes.

ACKNOWLEDGEMENTS

The authors thank M. Benedikt, A. Blondel, M. Boscolo, E. Levichev, K. Ohmi, D. Shatilov, D. Zhou and the entire FCC-ee Collaboration Team for encouraging the research, useful discussions, and suggestions.

REFERENCES

- [1] SAD: <http://acc-physics.kek.jp/SAD/SADHelp.html#L288>
- [2] K. Ohmi, D. Zhou, D. Shatilov, Y. Zhang, "BEAM-BEAM SIMULATION STUDY FOR CEPC", THPRI003, *IPAC14 proceeding*, Dresden, Germany.
- [3] A. V. Otboev and E. A. Perevedentsev, "Self-consistent Beta functions and emittances of round colliding beams", *PHYSICAL REVIEW SPECIAL TOPICS - ACCELERATORS AND BEAMS*, VOLUME 2, 104401 (1999) IEEE Periodicals, Piscataway, NJ, USA, Oct. 2014, pp. 34–52.
- [4] D. Zhou, presented at FCC Week 2016, 11-15 April 2016, Rome, Italy(2016).
- [5] K. Oide, "BEAM BLOWUP DUE TO SYNCHRO-BETA RESONANCE WITH/WITHOUT BEAM-BEAM EFFECTS", presented at eeFACT2018, Hong Kong, Sept. 2018, paper WEXBA03, in this conference.

SOME ISSUES ON BEAM-BEAM INTERACTION AT CEPC^{*†}

Y. Zhang^{†1}, N. Wang, J. Wu¹, Y. Wang, D. Wang, C. Yu¹

Institute of High Energy Physics, CAS, 100049 Beijing, China

¹also at University of Chinese Academy of Sciences, 100049 Beijing, China

Abstract

In this paper, the beam-beam study in CEPC CDR is briefly introduced. Some issues related with beam-beam interaction will be emphasized. The bunch lengthening caused by impedance and beamstrahlung is simulated in a more self-consistent method. The initial result shows that the stable collision bunch current is lower considering the longitudinal wake field. During the coures of dynamic aperture optimization, it is found that there exist some disagreement between dynamic aperture and beam lifetime. We try to define the so-called diffusion map analysis to explain the difference between different lattices. Some initial result for different lattice solution is shown.

INTRODUCTION

The circular Electron Positron Collider(CEPC) is a large international scientific project initiated and housed by China. It was presented for the first time to the international community at the ICFA Workshop “Accelerators for a Higgs Factory: Linear vs. Circular”(HF2012) in November 2012 at Fermilab. The Conceptual Design Report (CDR, the Blue Report) was published in September 2018 [1]. The CEPC is a circular e⁺e⁻ collider located in a 100-km circumference underground tunnel. The CEPC center-of-mass energy is 240 GeV, and at that collision energy will server as a Higgs factory, generating more than one million Higgs particles. The design also allows operation at 91 GeV for a Z factory and at 160 GeV for a W factory. The number of Z particles will be close to one trillion, and W⁺W⁻ pairs about 15 million. Theses unprecedented large number of particles make the CEPC a powerful instrument not only for precision measurments on these important particles, but also in the search for new physics.

Beam-beam interactions are one of the most important limitation to luminosity. Beamstrahlung is synchrotron radiation excited by the beam-beam force, which is a new phenomenon in such high energy storage ring based e⁺e⁻collider. It will increase the energy spread, lengthen the bunch and may reduce the beam lifetime due to the long tail of photon spectrum [2, 3]. In this paper, we’ll first briefly show some simulation result in CEPC CDR. And then some initial result with self-consistent longitudinal wake field and beam-beam interaction is shown. In the end, we’ll discuss some disagreement between dynamic aperture and beam lifetime. We also did some attempt to define the so-called

diffusion map analysis to explain the cause of more halo particles in some lattice.

BEAM-BEAM STATUS IN CDR

The main parameters of CEPC CDR is shown in Table 1. There are two options for Z, where the detector solenoid strength is 3T or 2T. The 3T options is ignored in Table 1.

Table 1: Main Parameters (CDR)

	Higgs	W	Z(2T)
C ₀ (km)		100	
IP		2	
E (GeV)	120	80	45.5
U0/turn (GeV)	1.73	0.34	0.036
θ (mrad)		16.5×2	
Piwinski Angle	3.48	7.0	23.8
N _p (10 ¹⁰)	15	12	8
Bunch Number	242	1524	12000
SR Power (MW)	30	30	16.5
β _x [*] /β _y [*] (m/mm)	0.36/1.5	0.36/1.5	0.2/1.0
ε _x /ε _y (nm/pm)	1.21/2.4	0.54/1.6	0.18/1.6
ξ _x /ξ _y	0.018/0.109	0.013/0.123	0.004/0.079
RF Voltage (GV)	2.17	0.47	0.1
f _{RF} (MHz)		650	
σ _{z0} (mm)	2.72	2.98	2.42
σ _z (mm)	4.4	5.9	8.5
ν _s	0.065	0.04	0.028
σ _p (10 ⁻⁴)	13.4	9.8	8
L (10 ³⁴ cm ⁻² s ⁻¹)	3	10	32

According to the LEP2 experience, the achieved maximum beam-beam parameter strongly depdens on the SR damping decrement. Figure. 1 shows the beam-beam performance of CEPC and LEP2. The design beam-beam parameter is nearly 2-3 times higher that of LEP2 experience, which is the contribution of crab-wasit scheme [4]. The crab-waist scheme helps to suppress the nonlinear betatron resonance with large Piwinski angle collision and crab-waist transformation. It has been tested in DAΦNE with new detector SIDDHARTA, where the peak luminosity increases with a factor of about 3. In a more complicated physics running with detector KLOE2, the peak luminosity increase about 50% [5].

Higgs

Figure. 2 shows the luminosity versus horizontal tune. There exist strong instability near the resonance ν_x - mν_s = n/2, where the new found coherent X-Z instability causes xz moment oscillation and horizontal beam size blow up [6].

^{*} Work supported by National Key Programme for S&T Research and Development (Grant NO. 2016YFA0400400) and NSFC Project 11775238.

[†] zhangy@ihep.ac.cn

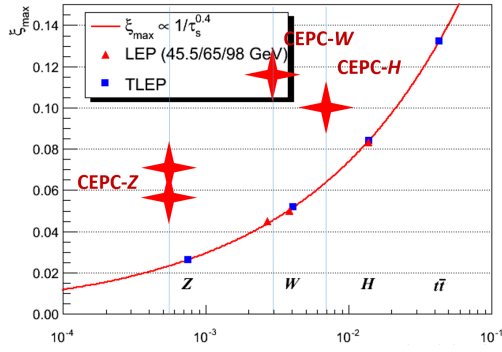


Figure 1: Comparison of beam-beam parameter between CEPC and LEP2. The horizontal axis is the damping decrement between IP.

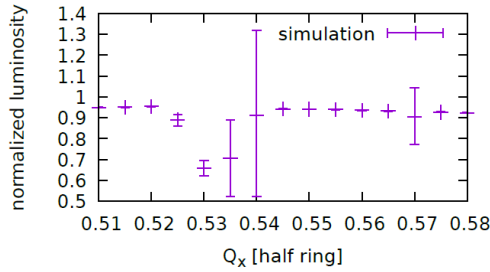


Figure 2: The normalized luminosity versus horizontal tune(half ring) at Higgs. The error bar shows the turn-by-turn luminosity distortion.

We define the achieved beam-beam parameter with luminosity to evaluate the performance and check the margin between design and maximum values,

$$\xi_y = \frac{2r_e\beta_y^0 L}{N\gamma f_0} \quad (1)$$

where N the bunch population, f_0 the revolution frequency, r_e electron classical radius, β_y^0 the vertical β function, and L the bunch luminosity. Figure. 3 shows the beam-beam parameter versus bunch population. It seems we have enough margin to ensure the reliability.

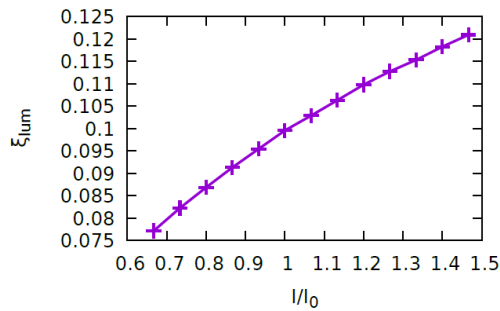


Figure 3: Beam-beam performance versus bunch population at Higgs.

The beamstrahlung lifetime is a serious issue in a higgs factory. The lifetime is evaluated as [3]

$$\tau_{bs} = \frac{\tau_z}{2Af(A)} \quad (2)$$

where A is the boundary of momentum acceptance in action, $f(J)$ is the distribution of action with beam-beam $\int_0^\infty f(J)dJ = 1$, and τ_z is the longitudinal damping time. Figure. 4 shows the beamstrahlung lifetime versus the bunch population. To ensure 100 minutes lifetime limited by momentum acceptance, it require about 1.3% with design bunch current, while nearly 1.6% with bunch population 22×10^{10} . Considering the present dynamic aperture optimization result and possible machine error tolerance, it is reasonable to choose the design value. In one words, the bunch population is mainly limited by beamstrahlung lifetime at Higgs mode of CEPC.

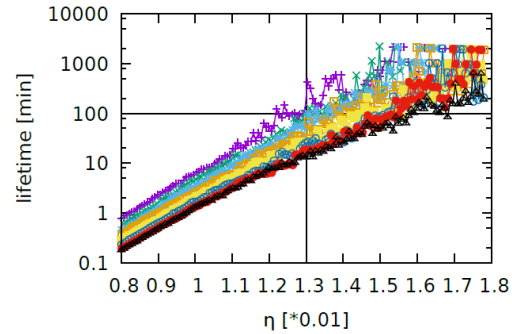


Figure 4: Beamstrahlung lifetime estimated with strong-strong beam-beam interaction at Higgs. Different line represent different bunch population from 15×10^{10} to 22×10^{10} .

W

Since the horizontal beam size blow up is the most prominent phenomenon caused by the x-z coherent instability, the 2D tunes scan result in Fig. 5. Figure. 6 shows the turn-by-turn evolution of σ_x . The simulation shows that there exist very narrow stable working point space ($\nu_x = 0.552-0.555$) with CDR parameters at W. The parameters is to be optimized further, such as squeezing β_x^* or increasing RF voltage [7], to suppress the instability.

Z

The luminosity performance at Z is limited by HOM of RF cavity and electron cloud instability instead of beam-beam interaction. However we still simulate the beam-beam interaction at different bunch intensity, shown in Fig. 7. With same beam current, comparing to 3T detector solenoid, weaker solenoid (2T) reduces the vertical emittance and allow squeeze β_y^* , luminosity increase by a factor of 2. If we increase the bunch population from 8×10^{10} to 12×10^{10} and keep the beam current constant, the luminosity will increase 20%.

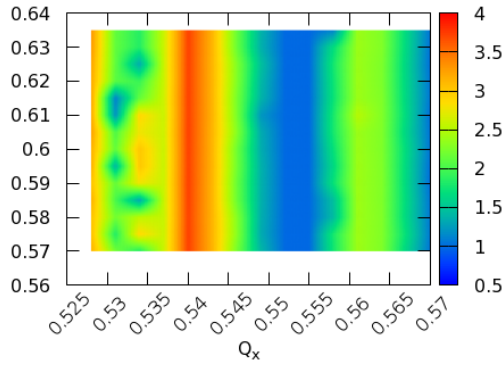


Figure 5: Normalized horizontal beam size versus the tune(half ring) at W.

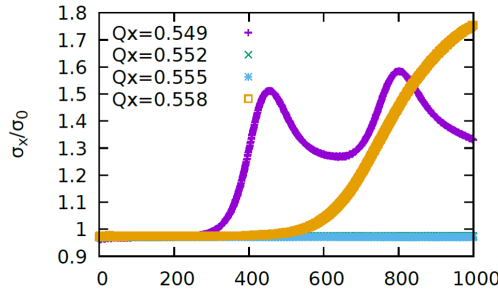


Figure 6: Horizontal bunch size evolution at different tune($v_y = 0.59$)(half ring) at W.

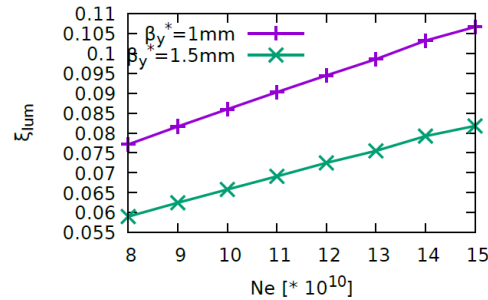


Figure 7: Beam-beam performance at Z ($\beta_y^* = 1.5\text{mm}$ for 3T and 1mm for 2T).

LONGITUDINAL IMPEDANCE

In conventional e^+e^- storage ring colliders, we only use lengthend bunch length in beam-beam simulation instead for considering impedance directly. It is no problem since the longitudinal dynamics is not sensitive to beam-beam interaction. But it is different since the bunch will also be lengthend during beam-beam interaction by beamstrahlung effect. It is very natural and more self-consistent to include the longitudinal impedance in the beam-beam simulation. The longitudinal kick along the bunch $V(t)$ is calculated each turn [8],

$$I(t) = \int_{-\infty}^{\infty} \frac{d\omega}{2\pi} e^{-i\omega t} \tilde{I}_{||}(\omega), \quad \tilde{V}(\omega) = -\tilde{I}(\omega) \tilde{Z}_{||}(\omega) \quad (3)$$

where $I(t)$ is the bunch distribution. Here we only consider the Higgs mode.

Figure. 8 shows the rms bunch length without/with beam-beam interaction. The bunch length obtained with IBB [9] is shorter than that of ELEGANT [10] with beam-beam off. Smooth approximation is adopted in our code, while there is local RF cavity in ELEGANT. With beam-beam, we simulate 3 cases:

- the conventional method, initialize the bunch using the length calculated by ELEGANT
- the conventional method, initialize the bunch using the length calculated by IBB
- self-consistent method, initialize the bunch using the zero-current natural bunch length, considering the longitudinal impedance

It is found that the bunch length saturate near bunch population 19×10^{10} . We also check the transverse dimension, shown in Figure. 9. It is found that there exist transverse blowup. We do not find any dipole or coherent x-z instability so far. The beam-beam parameter saturate near 19×10^{10} , as shown in Fig. 10, when we consider the longitudinal kick from impedance.

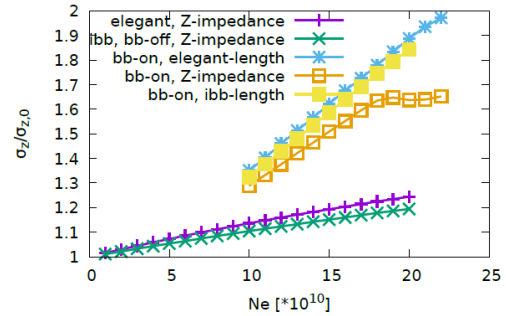


Figure 8: Bunch length with and without longitudinal impedance.

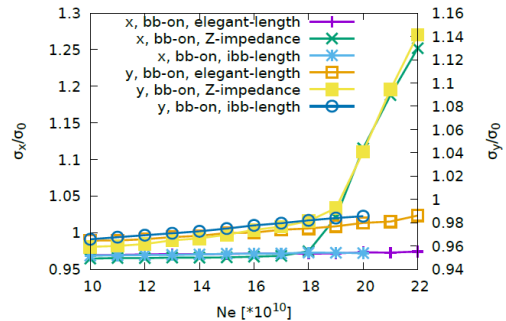


Figure 9: Transverse beam size with and without longitudinal impedance.

DYNAMIC APERTURE & LIFETIME

After dynamic aperture optimization, we usually do the many particle(1000) and long turns(10^5) tracking with the

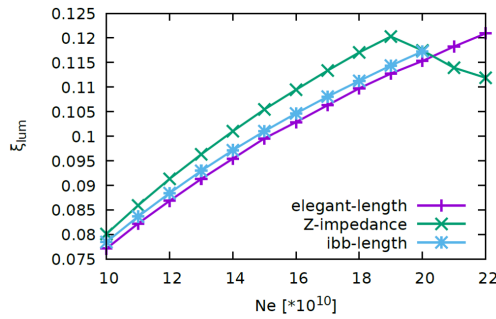


Figure 10: Beam-beam parameter with and without longitudinal impedance.

lattice and beam-beam interaction to check if the beam lifetime is long enough. It is found that larger dynamic aperture does not ensure longer lifetime, as shown in Fig. 11. It should be mentioned that the beam-beam interaction is on during the tracking of dynamic aperture and lifetime.

There exist strong nonlinearity, strong synchrotron radiation (even dependent on amplitude), strong beam-beam interaction and beamstrahlung effect in CEPC. The popular frequency map analysis [11] method does not work now. Following some work [12–15], we attempt to define the figure of merit of diffusion as

$$D \equiv \log_{10} \left(\sum_{turn} \sigma_a^2 \right) \quad (4)$$

where $\sigma_a^2 = \sigma_{ax}^2 + \sigma_{ay}^2 + \sigma_{az}^2$, with A_i the normalized amplitude,

$$A_i = \sqrt{2J_i/\epsilon_i}, \quad i = x, y, z \quad (5)$$

We track 200 particles, 25 turns with same initial transverse amplitude, and scan the transverse amplitude space to calculate the diffusion. The diffusion map analysis for 4 different lattices is shown in Fig. 12. It seems the result coincides well with the lifetime tracking result.

SUMMARY

We briefly present the beam-beam simulation result for CEPC CDR. The beam-beam performance is limited by

beamstrahlung effect at Higgs. It nearly reaches the beam-beam limit at W. The limitation of luminosity performance at H is not limited at Z.

The very initial simulation shows that the beam-beam performance is reduced when considering the longitudinal impedance. We attempt to use the diffusion map analysis method to explain the lifetime difference of different sextupole configurations. The initial result shows good agreement. It is expected that we could add some constraint during dynamic aperture optimization to ensure long lifetime.

ACKNOWLEDGEMENTS

The first author would like to thank K. Ohmi (KEK), D. Shatilov (BINP), K. Oide (CERN) and D. Zhou (KEK) for their continuous help and support.

REFERENCES

- [1] CEPC Study Group, arXiv:1809.00285 [physics.acc-ph]
- [2] V.I. Telnov, *Phys. Rev. Lett.*, 110, 114801, 2013
- [3] K. Ohmi, et al., “Beam-beam Simulation Study for CEPC”, in *Proc. IPAC’14*.
- [4] M. Zobov, et al., *Phys. Rev. Lett.*, 104, 174801, 2010.
- [5] C. Milardi, presented at eeFACT2018, Hong Kong, Sep 2018, paper MOYAA02, in this conference.
- [6] K. Ohmi, et al., *Phys. Rev. Lett.*, 119, 134801, 2017.
- [7] D. Shatilov, presented at eeFACT2018, Hong Kong, Sep 2018, paper TUYBA02, in this conference.
- [8] A. Chao, “Physics of collective beam instabilities in High Energy Accelerators”, 1993.
- [9] Y. Zhang, K. Ohmi, et al., *Phys. Rev. ST-AB.*, 8, 074402, 2005.
- [10] ELEGANT, <https://ops.aps.anl.gov/elegant.html>
- [11] J. Laskar, *Icarus*, 88, 266, 1990.
- [12] D. Shatilov, et al., *Phys. Rev. ST-AB.*, 14, 014001, 2011.
- [13] K. Ohmi, et al., in *Proc. APAC’04*.
- [14] G. Stancari, et al., FERMILAB-CONF-13-054-APC.
- [15] K. Oide, et al., *PRAB* 19, 111005, 2016.

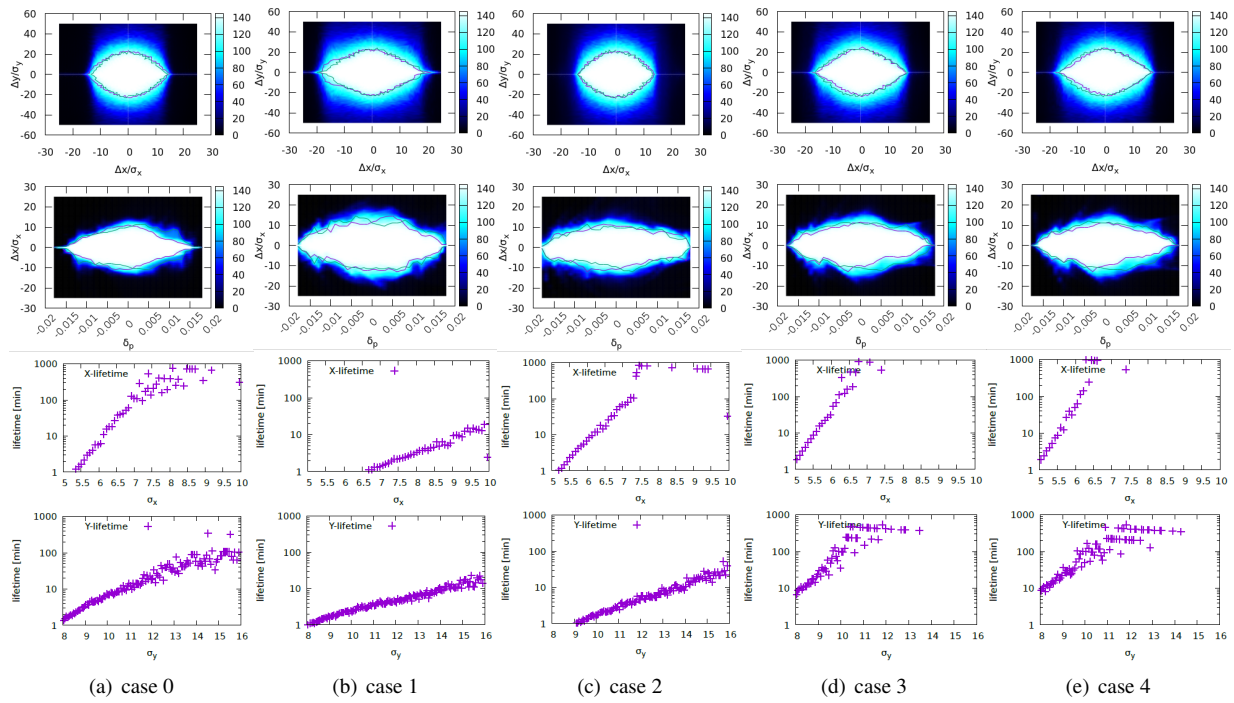


Figure 11: Dynamic aperture and lifetime of 5 different sextupole configurations.

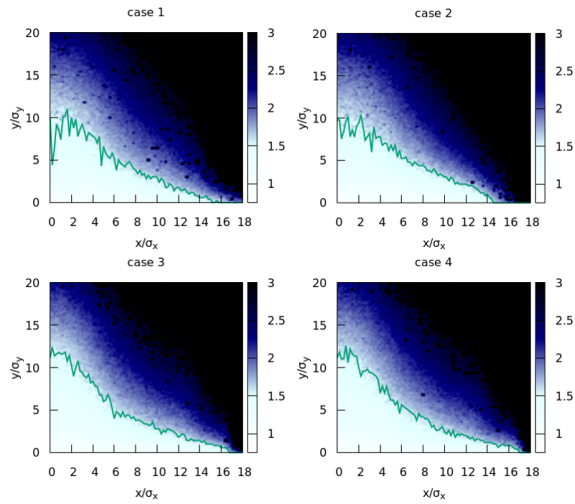


Figure 12: Diffusion map analysis of 4 different sextupole configurations.

KEKB INJECTION DEVELOPMENTS

K. Furukawa*, Injector Linac group

High Energy Accelerator Research Organization (KEK), Tsukuba, 305-0801, Japan
SOKENDAI (The Graduate University for Advanced Studies), Tsukuba, 305-0801, Japan

Abstract

The e^-/e^+ SuperKEKB collider is now under commissioning. As e^-/e^+ beam injection for SuperKEKB greatly depends on the efforts during the previous KEKB project, the injection developments during KEKB are outlined as well as the improvements towards SuperKEKB. When KEKB was commissioned, approximately ten experimental runs per day were performed with e^-/e^+ injections in between. As another collider PEP-II had a powerful injector SLAC, the KEKB injector had to make a few improvements seriously, such as injection of two bunches in a pulse, continuous injection scheme, eventual simultaneous top-up injections, as well as many operational optimizations. The design of SuperKEKB further required the beam quality improvements especially in the lower beam emittance for the nano-beam scheme, as well as in the beam current for the higher ring stored current and the shorter lifetime.

INTRODUCTION

The energy-asymmetric electron-positron collider, KEKB B-Factory, had been operated successfully for 11 years from 1999 to 2010. It had contributed to the intensity frontier of particle physics by achieving the world highest luminosity at the time. During that period the operation of the collider became much advanced compared with the previous project TRISTAN [1].

In order to meet the beam injection requirements to the collider the injector went through a major reconstruction. The goal was essentially a higher injection rate with a full-energy injection and was mainly achieved by increasing the electron injection energy from 2.5 GeV up to 8 GeV. As the injection aperture became rather small down to 30 ps, the ring RF frequency was modified to have an integer relation between the injector and the ring [2]. The injector accomplished substantial progress during the KEKB period as well. Challenges from many different viewpoints were made to improve the machine. While many of them did not immediately provide meaningful contributions, accumulation of those trials brought significant difference in the performance of injector operation [3].

The collider has been upgraded for the SuperKEKB project since 2010 and is expected to be able to further elucidate the flavor physics of elementary particles with 40-fold improved luminosity, by doubling the stored beam current and also by the nano-beam scheme to shrink the beam size down to a twentieth at the interaction point [4, 5].

The upgrade for SuperKEKB was again a major challenge at the injector. The nano-beam scheme demands fairly small

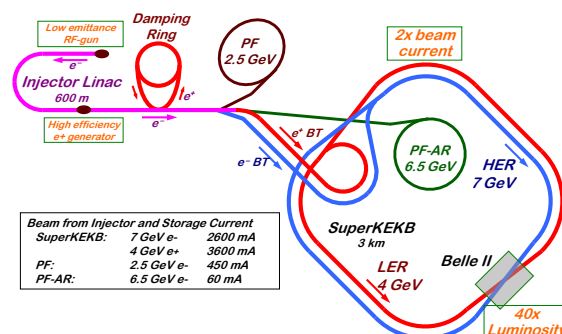


Figure 1: Layout of electron/positron accelerator complex with beam properties from the injector linac into four storage rings of SuperKEKB-HER, LER, PF and PF-AR.

transverse and longitudinal phase space as well as several times higher beam charge of the injection beams. The electron beam would be realized employing a newly designed RF gun [6]. The positron beam would be achieved with combination of a newly installed flux concentrator and a damping ring [7, 8].

Figure 1 shows the accelerator complex configuration at KEK. The injector linac delivers the beams not only to the SuperKEKB high-energy ring (HER) and low-energy ring (LER) but also to light sources of photon factory (PF) and photon factory advanced ring (PF-AR). Even during the SuperKEKB upgrade construction the injector was required to inject the beam into two light source storage rings [9].

Those injection developments during KEKB operation and SuperKEKB upgrade are described in this paper.

KEKB OPERATION

Two B factories of PEP-II and KEKB were operational at the same time [10]. While the SLAC injector to PEP-II was powerful enough, every endeavor at injector was made to satisfy the stable injection into KEKB.

For example, as the beam fluctuation was large in the early stage of the KEKB project, many stabilization loops were installed for beam properties like energies and orbits [11]. For energy stabilization a simple PI (proportional-integral) loop was applied between BPMs (beam position monitors) and RF systems as in Fig.2. Many of those loops were dependent on the beam modes where the beams were injected. Thus, a feedback loop management tool was constructed to supervise those many closed loops as in Fig. 3.

The construction of beam dumps at the middle of the both electron and positron beam transports to HER and LER have assisted the beam quality measurement without injection. It was extremely useful and used everyday.

* kazuro.furukawa@kek.jp

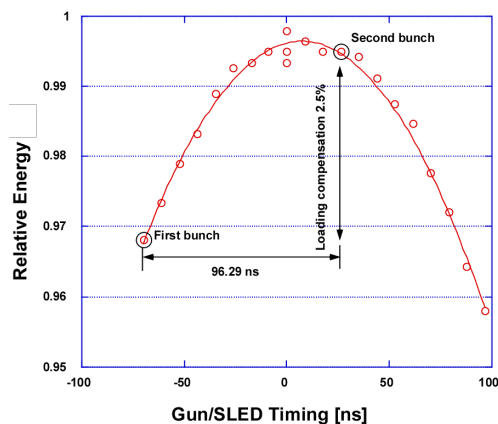


Figure 6: Beam loading compensation to equalize bunch energies in two-bunch acceleration.

tion were important to evaluate the properties of those two bunches separately and simultaneously without losing the accuracy. Among several beam properties, BPMs, a bunch monitor (streak camera) and wire scanners were improved. Transverse and longitudinal wakefield compensations were crucial. Figure 6 shows an example how energies of those two bunches were equalized by changing the RF pulse timing. Those energies were observed continuously and equalized by a closed loop [14].

While timings of gun and RF systems were carefully tuned, properties of those bunches had slight discrepancies. Nevertheless, the injection rate was improved at least by 65%.

Three-bunch acceleration was once considered for SuperKEKB by flattening RF pulses. It turned out to be cost ineffective.

CONTINUOUS INJECTION

If it was possible to eliminate the period with the detector HV turned off, the integral luminosity should be significantly improved. Such an experimental mode is called top-up (top-off) injection or continuous injection. However, the effect of injection beam background had to be suppressed. The injection beam background to Belle detector was carefully examined in order to realize the continuous injection. While the both KEKB and Belle were improved, central drift chamber (CDC) and time of flight (TOP) detectors as well as the data taking system were especially improved. The data acquisition was vetoed for 2 ms just after the injection.

Figure 7 and 8 show the machine status history for 8 hours before and after the introduction of the continuous injection to the KEKB operation. The detector HV was always applied in the latter case. This new injection mode was another major step forward in early 2004, and approximately 26% gain was achieved in the integral luminosity [15].

In the continuous injection made the run length optimization became meaningless, and shorter switching time between electron and positron injections was pursued. Figure 9 plots the number of beam mode transitions per year between injections into four storage rings of KEKB-HER, KEKB-LER, PF and PF-AR.

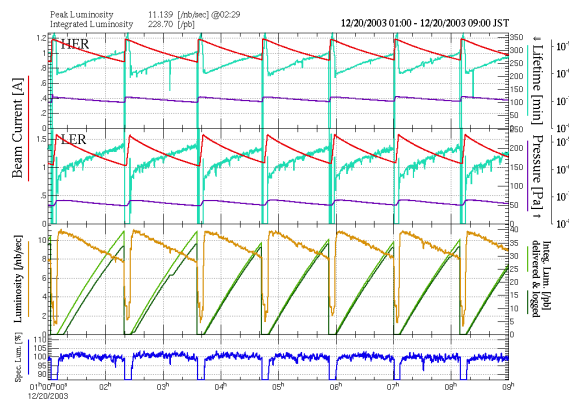


Figure 7: Storage beam currents and luminosity for 8 hours before the continuous injection was applied.

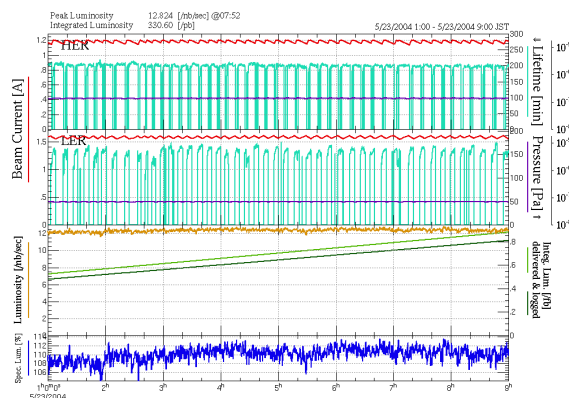


Figure 8: Machine history for 8 hours after the continuous injection was applied. Nearly 30% increase in integral luminosity was achieved.

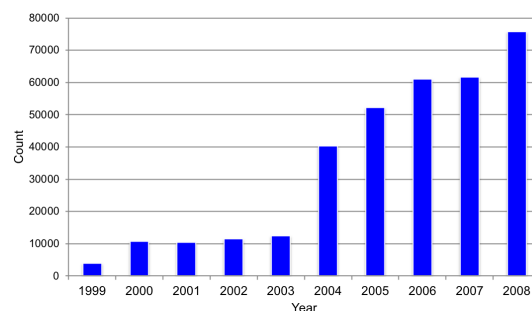


Figure 9: Beam mode transitions per year between injections into KEKB-HER, KEKB-LER, PF and PF-AR.

KEKB-LER, PF and PF-AR. At the beginning it took several minutes to change 500 device parameters. Later, the devices and the software as well as quality assurance measures were improved and the transition time was shortened down to 20 seconds, and the modes were switched about 360 times per day in 2008.

SIMULTANEOUS TOP-UP INJECTIONS

Even faster beam mode transition had been examined since 2005 just after the continuous injection was introduced.

characterized as a stealth beam mode. As the beam quality requirement for SuperKEKB is demanding, the arrangement of stealth beam mode would be indispensable in the near future.

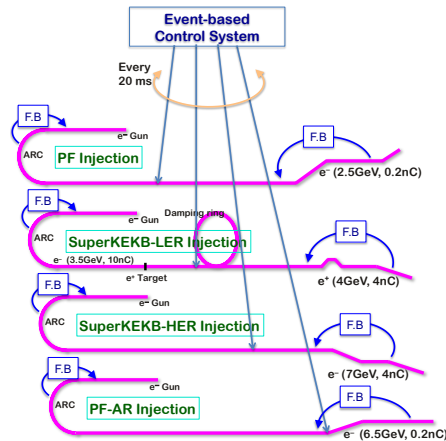


Figure 12: Single injector linac behaves as four virtual accelerators (VAs) to inject their beams into four separate storage rings. Each VA would be associated with several beam stabilization loops.

CONCLUSION

We learned a lot during KEKB injection operation. It contributed to achieve the world highest luminosity. Injection into SuperKEKB is another challenge with higher beam charge and lower transverse/longitudinal emittance. Steady progress towards designed injection beam would be achieved in steps. Then, we may need to improve the injection further with stealth beam measurement and optimization for example.

ACKNOWLEDGEMENTS

The author is grateful to all the staff and operators in KEKB/SuperKEKB project for their suggestions and continuous encouragement.

REFERENCES

- [1] K. Oide, “KEKB B-Factory, The Luminosity Frontier”, *Prog. Theor. Phys.*, vol. **122**, pp. 69–80, 2009, doi:10.1143/PTP.122.69
- [2] I. Abe, *et al.*, “The KEKB Injector Linac”, *Nucl. Instrum. Meth.*, vol. **A 499**, pp. 167–190, 2003, doi:10.1016/S0168-9002(02)01787-4
- [3] M. Akemoto, *et al.*, “The KEKB injector linac”, *Prog. Theor. Exp. Phys.*, vol. **2013**, p. 03A002, 2013, doi:10.1093/ptep/ptt011
- [4] Y. Ohnishi *et al.*, “Accelerator Design at SuperKEKB”, *Prog. Theor. Exp. Phys.*, vol. **2013**, p. 03A011, 2013, doi:10.1093/ptep/pts083
- [5] K. Akai, K. Furukawa, H. Koiso, “SuperKEKB Collider”, *Nucl. Instrum. Meth.*, vol. **A 907**, pp. 188–199, 2018, doi:10.1016/j.nima.2018.08.017

- [6] M. Yoshida *et al.*, “Generation and Acceleration of Low-emittance, High-current Electron Beams for SuperKEKB”, in *Proc. LINAC’14*, Geneva, Switzerland, Sep. 2014, paper MOIOB03, pp. 21–25, url:jacow.org/LINAC2014/papers/moiob03.pdf
- [7] T. Kamitani *et al.*, “SuperKEKB Positron Source Construction Status”, in *Proc. IPAC’14*, Dresden, Germany, Jun. 2014, paper MOPRI004, pp. 579–581, doi:10.18429/JACoW-IPAC2014-MOPRI004
- [8] M. Kikuchi *et al.*, “Design of Positron Damping Ring for Super-KEKB”, in *Proc. IPAC’10*, Kyoto, Japan, May. 2010, paper TUPEB054, pp. 1641–1643, url:jacow.org/IPAC10/papers/tupeb054.pdf
- [9] K. Furukawa *et al.*, “Upgrade of KEK Electron/positron Linac Control System for the both SuperKEKB and Light Sources”, in *Proc. ICALEPCS’17*, Barcelona, Spain, Oct. 2017, paper THMPL02, pp. 1257–1260, doi:10.18429/JACoW-ICALEPCS2017-THMPL02
- [10] J. Seeman, “PEP-II and KEKB Operational Status”, in *Proc. PAC’05*, Knoxville, USA, May 2005, paper MOAA003, pp. 276–280, url:jacow.org/p05/PAPERS/MOAA003.pdf
- [11] K. Furukawa *et al.*, “Beam Switching and Beam Feedback Systems at KEKB Linac”, in *Proc. LINAC’00*, Monterey, USA, Aug. 2000, paper TUE10, pp. 633–635, url:jacow.org/100/papers/TUE10.pdf
- [12] Y. Ogawa *et al.*, “High-Intensity, Two-Bunch Acceleration for Doubling Positron Production at the KEKB Linac”, in *Proc. HEACC’01*, Tsukuba, Japan, Mar. 2001, paper P1hlf05.
- [13] S. Ohsawa *et al.*, “Increase of Positrons by a High-Intensity Two-Bunch Acceleration Scheme at the KEKB Linac”, in *Proc. PAC’01*, Chicago, USA, Jun. 2001, paper RPPH026, pp. 3284–3286.
- [14] K. Furukawa *et al.*, “Beam Feedback Systems and BPM Read-Out System for the Two-Bunch Acceleration at the KEKB Linac”, in *Proc. ICALEPCS’01*, San Jose, USA, Nov. 2001, paper WECT006, pp. 266–268.
- [15] T. Abe, *et al.*, “Commissioning of KEKB”, *Prog. Theor. Exp. Phys.*, vol. **2013**, p. 03A010, 2013, doi:10.1093/ptep/pts101
- [16] A. Akiyama, *et al.*, “Accelerator Control System at KEKB and the Linac”, *Prog. Theor. Exp. Phys.*, vol. **2013**, p. 03A008, 2013, doi:10.1093/ptep/pts081
- [17] K. Furukawa *et al.*, “Rejuvenation of 7-GeV SuperKEKB Injector Linac”, in *Proc. IPAC’18*, Vancouver, Canada, Apr. 2018, paper MOPMF073, pp. 300–303, doi:10.18429/JACoW-IPAC2018-MOPMF073
- [18] Y. Seimiya *et al.*, “Low Emittance Beam Transport for e^-e^+ LINAC”, presented at *eeFACT’18*, Hong Kong, Sep. 2018, paper TUPAB02, this conference.
- [19] K. Furukawa *et al.*, “Beam Feedback System Challenges at SuperKEKB Injector Linac”, in *Proc. ICALEPCS’13*, San Francisco, USA, Oct. 2013, paper FRCOBAB04, pp. 1497–1500, url:jacow.org/ICALEPCS2013/papers/frcobab04.pdf

LOW EMITTANCE BEAM TRANSPORT FOR e⁻/e⁺ LINAC

Y. Seimiya*, N. Iida, M. Kikuchi, T. Mori, KEK, Tsukuba, Japan

Abstract

Design luminosity of SuperKEKB is $8 \times 10^{35} \text{cm}^{-2} \text{s}^{-1}$, which is 40 times higher than that of KEKB achieved. To achieve the design luminosity, the beam have to be transported to the SuperKEKB main ring with the high bunch charge (4 nC) and low emittance: 40/20 μm for horizontal/vertical electron beam emittance and 100/15 μm for positron beam emittance in Phase 3 final. In the LINAC and the beam transport line, the emittance growth is mainly induced by residual dispersion, beam phase space jitter, wake-field in acceleration structure, and radiation excitation. In the Phase 2 operation, we have evaluated and, if possible, corrected these effects on the emittance. Results of the emittance measurement is described.

INTRODUCTION

SuperKEKB is e-/e+ collider for high energy particle physics in KEK. The design luminosity of SuperKEKB is 40 times higher than that of KEKB achieved [1]. This high luminosity can be realized by both doubling the current and making the beam size a one-twentieth compared with that of KEKB. The Phase 2 commissioning was finished in July 2018. The LINAC was developed for SuperKEKB [2]. During the operation in Phase 2, collimator tuning to reduce background of Belle-II detector, β squeezing for small beam size at the collision point, collision tuning to maximize the high luminosity, and so on have been done [3]. The physics run is scheduled to start in March 2019 as the Phase 3. Required beam-parameters for Phase 2 and Phase 3 (final) are shown in Fig. 1. In Phase 3 final, requirement to the beam charge is 4 nC for both beams. Required horizontal/vertical emittance is 100/15 μm for positron beam and 40/20 μm for electron beam. We have to convey this high-quality beam to the main ring without emittance degradation as far as possible. Otherwise, the injection rate would be worse and the luminosity would not be able to reach the target value.

A footprint of the LINAC and the beam transport line (BT) is shown in Fig. 2. The LINAC is composed of Sector A, B, J-ARC, C, and 1-5. The LINAC has two kinds of electron gun; a thermionic gun to obtain high-current beam used for positron production and a photocathode RF gun for low emittance electron beam. The large emittance of the positron beam emittance for LER is reduced by a damping ring (DR), which is placed beside the end of Sector 2. The beam is extracted from the end of Sector 2 to the LTR line at 1.1 GeV and injected to the DR. After two cycles of the LINAC pulse, the damped beam is, through the RTL line, resumed to the start of Sector 3 in the LINAC. Positron beam is accelerated up to 4 GeV and transported through the positron BT line and finally reaches the low energy ring

Stage	Phase 2 (Mar. – Jul. 2018)		Phase 3 (Mar. 2019 –)	
	e+	e–	e+	e–
Beam				
Bunch charge (nC)	1.5	1	4	4
Norm. Emit. ($\gamma\beta\epsilon$) (μm)	200/40 (Hor./Ver.)	150	100/15 (Hor./Ver.)	40/20 (Hor./Ver.)
Energy spread	0.16%	0.1%	0.16%	0.07%

Figure 1: Required beam-parameters for SuperKEKB injector LINAC and the beam transport line.

(LER). Low emittance electron beam is accelerated up to 7 GeV and transported through the electron BT line and finally reaches the high energy ring (HER). To maintain the low emittance, fine tuning is necessary in every place of the system.

SOURCES OF EMITTANCE GROWTH

We have evaluated several conceivable kinds of sources of the emittance growth.

Residual Dispersion

Through the residual dispersion, the energy spread converts to the beam size. First, an example of the dispersion correction at J-ARC section in the LINAC are shown in Fig. 3. where the horizontal axis shows path length along the beam line, blue and red lines show horizontal and vertical dispersion function, respectively. Before correction, large residual dispersion had emerged after the J-ARC as shown in the left inset of Fig. 3. By tuning the strength of quadrupole magnets, horizontal/vertical residual dispersion became small from 0.429/0.092 m to 0.024/0.017 m as shown in the right inset of Fig. 3.

In the same manner, we corrected dispersion in the RTL. In the RTL, there are two ARCs. For example, Fig. 4 shows before and after the dispersion correction in first ARC. The bottom figure in Fig. 4 shows residual dispersion. Blue and red lines show horizontal and vertical residual dispersion, respectively. After the dispersion correction, residual dispersion became smaller. Figure 5 shows values of residual dispersion before and after correction. In both ARCs, residual dispersion became smaller after the dispersion correction. But, the residual dispersion in the first ARC is still not small enough. We need more studies in detail on this issue.

Figure 6 shows improvement of the emittance due to dispersion correction. The emittance was measured with wire scanner (WS). First, we corrected the dispersion in the second ARC. By the correction, emittance was improved from

* seimiya@post.kek.jp

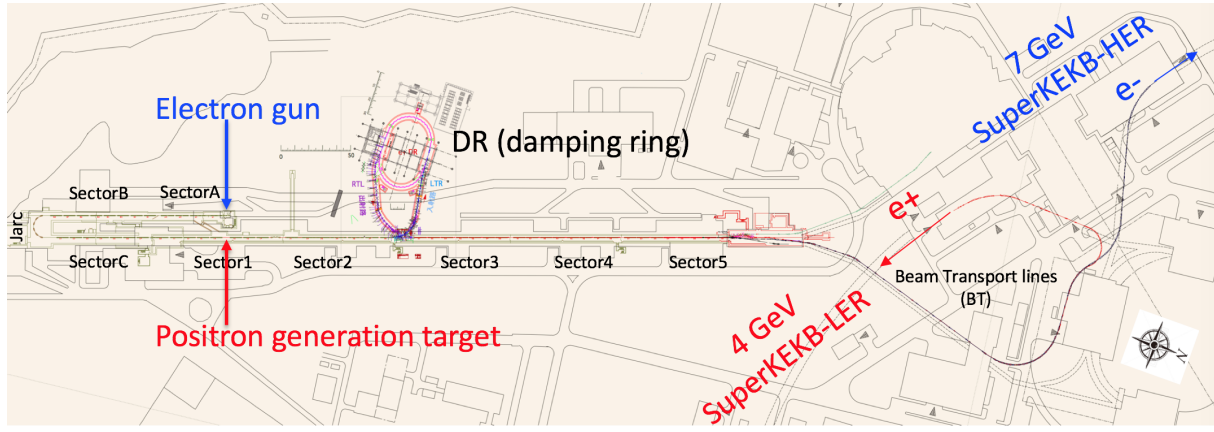


Figure 2: A footprint of SuperKEKB injector LINAC and the beam transport line.

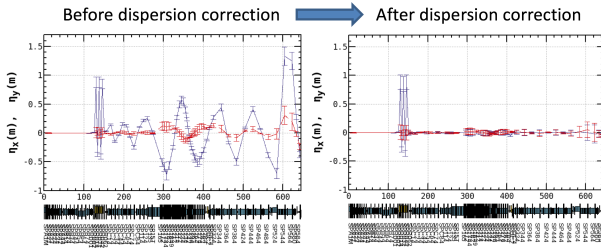


Figure 3: Dispersion measurement before and after the dispersion correction in the LINAC.

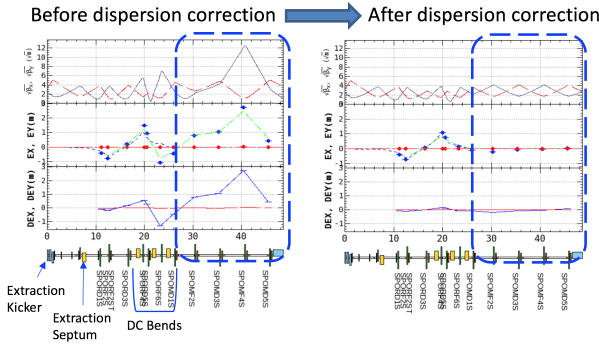


Figure 4: Dispersion measurement before and after the dispersion correction in the RTL.

about $300 \mu\text{m}$ to $200 \mu\text{m}$. Then, we corrected the dispersion in the first ARC. By the correction, emittance was improved to $130 \mu\text{m}$. Though the horizontal emittance became less than half, it is still twice as large as design value. Reference [4] mention this issue.

In the same manner, we corrected dispersion in each ARC of the BT. Figure 7 shows residual dispersion before and after correction for electron and positron beam. The order of ARC names are from the upstream to downstream of the BT. In the upstream of the WSs, dispersion correction was done. In some ARCs, dispersion correction is not completed.

e+	$\langle \eta x^2 \rangle^{1/2}$ [m]		$\langle \eta y^2 \rangle^{1/2}$ [m]		Fudge Factor of Quad.
Correction	Before	After	Before	After	[%]
2 nd ARC	0.079	0.019	0.0094	0.0077	-4.5
1 st ARC	1.05	0.09	0.02	0.01	-8.2

Figure 5: Residual dispersion before and after correction in the RTL.

e+ 0.7 [nC]	Horizontal Dispersion at Straight section after the Arcs			DR design emittance
	Before Correction	After Correction in 2 nd arc	After Correction in 1 st arc	Fudge Factor of Quads [%]
$\langle \eta x^2 \rangle^{1/2}$ [m]	0.079	0.019	0.09	-4.5
	1.05			-8.2
Measured Emittance in Sector 3				
$\gamma \beta \epsilon_x$ [μm]	293 ± 44.5	192 ± 22.4	126 ± 8.2	64.3
$\gamma \beta \epsilon_y$ [μm]	1.84 ± 0.163	2.01 ± 0.363	1.5 ± 0.1	

Figure 6: Emittance improvement due to dispersion correction.

Beam Phase Space Jitter

The extent of the transported beam to the main ring must be stable so that the beam can be injected inside the main ring acceptance. The emittance that includes beam phase space jitter, called as effective emittance, must satisfy the requirement. We evaluated the emittance growth due to the beam phase space jitter and investigated their sources.

To evaluate the emittance growth due to beam phase space jitter, we introduce following effective emittance,

$$\begin{aligned} \epsilon_{eff} &= \sqrt{\langle X^2 \rangle \langle X'^2 \rangle - \langle X X' \rangle^2} \\ &= \sqrt{\epsilon_0^2 + \epsilon_j^2 + 2\epsilon_0 \epsilon_j B_{mag}}, \end{aligned}$$

where

$$\begin{aligned} X &= x + \Delta x, \quad X' = x' + \Delta x', \\ \epsilon_0 &= \sqrt{\langle x^2 \rangle \langle x'^2 \rangle - \langle x x' \rangle^2}, \\ \epsilon_j &= \sqrt{\langle \Delta x^2 \rangle \langle \Delta x'^2 \rangle - \langle \Delta x \Delta x' \rangle^2}, \\ B_{mag} &= \frac{\gamma_0 \beta - 2\alpha_0 \alpha + \beta_0 \gamma}{2}, \end{aligned}$$

e ⁻		$\langle\eta x^2\rangle^{1/2}$ [m]		$\langle\eta y^2\rangle^{1/2}$ [m]		Fudge Factor of Quadrupole	[%]
Correction		Before	After	Before	After		
Slope 1		0.13	0.11	0.05	0.01	1.0~5.9	
Bte 0 th ARC		0.11	0.02	0.01	0.02	0~6.7	BT-WS placed
Bte 1 st ARC		0.102	0.038	0.029	0.036	2.37	
Bte 2 nd , 3 rd ARC		0.066	0.029	0.037	0.034	2.52	
Slope 2		0.104	0.091	0.192	0.116	3.55	Inj. point to MR
Bte 4 th ARC		-	-	-	-	-	

e ⁺		$\langle\eta x^2\rangle^{1/2}$ [m]		$\langle\eta y^2\rangle^{1/2}$ [m]		Fudge Factor of Quadrupole	[%]
Correction		Before	After	Before	After		
Btp 0 th ARC		0.27	0.02	0.01	0.03	-26~12.9	BT-WS placed
Btp 1 st ARC		0.037	0.047	0.126	0.102	2.5	
Slope 1		-	-	-	-	-	
Btp 2 nd , 3 rd ARC		-	-	-	-	-	
Slope 2		-	-	-	-	-	Inj. point to MR
Btp 4 th ARC		-	-	-	-	-	

Figure 7: Residual dispersion before and after correction for both electron and positron beam in the BT.

ϵ_0 and ϵ_j are nominal emittance and emittance growth induced by beam phase space jitter (jitter emittance), respectively. B_{mag} is a phase space mismatch between the beam and the jitter. The value is equal to or larger than 1. If $B_{mag} = 1$, there is no mismatch and the effective emittance equals just the nominal emittance plus the jitter emittance. B_{mag} is measured to be about 1-2 in the usual LINAC operation, which is measured with WS. From the beam position, assuming the transfer matrix between two BPMs, beam angle can be estimated. Jitter emittance can thus be derived from the beam position jitter and beam angle jitter.

We have measured the beam position jitter at BPM in the LINAC. Figure 8 shows the beam position jitter and the jitter emittance. Horizontal axis shows the path length after the electron gun. Position jitter is defined as standard deviation of measured beam position. Around the 140 m point of the figure, there is J-ARC section. Because the J-ARC section is dispersive, beam energy jitter is converted to beam position jitter in this section. Dispersion and position jitter were about 0.8 m and 360 μm at the center of this section, respectively, then energy jitter is estimated to be about 0.045%. In addition to the J-ARC, behind the positron target placed in about 290 m point, beam position jitter and jitter emittance were observed to increase as shown in the left figure in Fig. 8. In this case, horizontal/vertical jitter emittance was about 28/7 μm at the end of the LINAC. Target value of the horizontal/vertical emittance in Phase 3 is 40/20 μm . Therefore, the effect of jitter emittance on effective emittance was very large. On the other hand, after the dispersion correction, horizontal/vertical jitter emittance was decreased to about 1.8/0.9 μm at the end of the LINAC as shown in the right figure in Fig. 8. Beam phase space jitter was successfully reduced by the dispersion correction. Small emittance growth still remains behind the target even after the correction. This result is obtained in case of 1 nC, therefore we should understand origin of the beam phase space jitter to prepare for the 4 nC beam.

Wakefield in Acceleration Structure

Wakefield, generated by a head of bunch, kicks its own tail. Thus if the beam is off-centered in the structure, the transverse wakefield increases beam emittance. This effect can

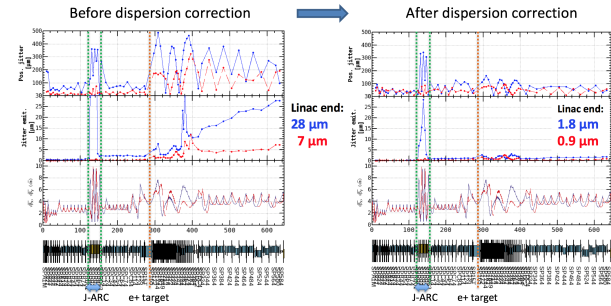


Figure 8: Measured beam position jitter and jitter emittance in the LINAC before and after dispersion correction. The electron beam was 1 nC and generated by RF gun.

Table 1: Basic Parameter Set

Parameter	Value	Unit
Initial emittance	10	μm
Initial bunch length	3/2.35	mm
Initial energy spread	0.004	—
Charge	5	nC
Distribution	Gaussian	—
S-band acc. cavity aperture	$\phi 20$	mm

be minimized by a proper orbit correction. We performed particle tracking simulation to evaluate emittance growth induced by wakefield in acceleration structure. The particle tracking is simulated by the SAD program [5]. Misalignment of the components had been measured by laser-based alignment system [6, 7]. The measured misalignment values were used for this simulation. Table 1 shows basic parameter set of the simulation. Left figure in Fig. 9 shows emittance after orbit displacement was minimized. Blue and red dots show horizontal and vertical emittance, respectively. Blue and red lines show the horizontal and vertical requirements for Phase 3, respectively. As the beam went down to the LINAC end, the horizontal/vertical emittance grew up to 240/120 μm at the end of the LINAC. On the other hand, right figure in Fig. 9 shows emittance minimized at the end of the LINAC. Emittance growth, in this case, occurred at Sector C and corrected at Sector 2. By an orbit correction for emittance preservation, emittance growth induced by an accelerator structure could be cancelled by the other accelerator structure. In this case, the horizontal/vertical emittance is 22/11 μm at the end of the LINAC. These emittances are less than Phase 3 requirements. Especially, the vertical emittance is almost same as initial emittance. In the simulation, transmission rate was almost 1.

Radiation Excitation

Radiation excitation effect on emittance is proportional to both Lorenz gamma to the fifth power and inverse of curvature radius to the third power. Especially, electron beam (7 GeV) is strongly affected by the radiation excitation effect. Particle tracking was performed from beginning to end of the BT. Figure 10 shows the simulation results. Initial

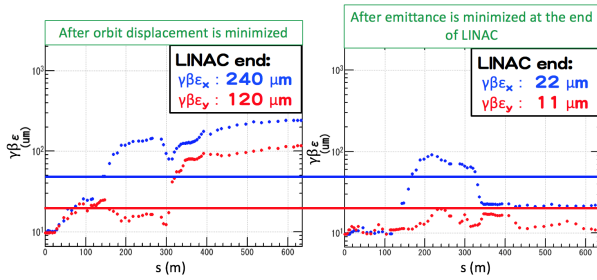


Figure 9: Emittance change due to different orbit correction in the LINAC.

Radiation excitation effect on emittance	Initial particles	With Radiation	Phase-III final requirement
e- (7 GeV) $\gamma\beta\epsilon_x$ [μm]	20	69	40
e+ (4 GeV) $\gamma\beta\epsilon_x$ [μm]	64	77	100

Figure 10: Radiation excitation effect on emittance in the BT.

horizontal emittance of electron/positron beam is 20/64 μm . These emittances are increased by radiation excitation and reach 69/77 μm at the end of the BT. Especially, electron beam emittance at the end of the BT is larger than Phase 3 requirement. We are reconsidering the requirement by taking into account of the actual injection system and beam optics.

EMITTANCE MEASUREMENT

First, we show emittance measurement result of electron beam as Fig. 11. Left and right figures show horizontal and vertical emittance measured at each sector, respectively. Purple dots show emittance of electron beam generated with thermionic gun. Green and blue dots show emittance of electron beam generated with RF gun. Green dots measured in 29 June 2018 and blue dots measured in the next day. Clearly, beam emittance with the RF gun was smaller than that with thermionic gun. Blue and orange dashed lines show Phase 2 and Phase 3 requirement value, respectively. The requirement emittance of electron beam at the end of the LINAC is satisfied for Phase 2, but not for Phase 3. Currently, we performed orbit correction algorithm only to reduce orbit distortion. We will introduce the orbit correction program for emittance preservation in this Winter. Large emittance growth was observed at the BT though dispersion correction was done. This emittance growth is irrelevant to radiation excitation because used WSs in the BT are placed where the total bending angle from the beginning of the BT is small.

Finally, we show emittance measurement result of positron beam in Fig. 12. In Phase 2, the requirement emittance of positron beam at the end of the LINAC was also satisfied though the requirement for Phase 3 was also not satisfied. Emittance was also increased in the BT though dispersion correction was done. Investigations for these un-

known emittance growth sources in the BT are in progress.

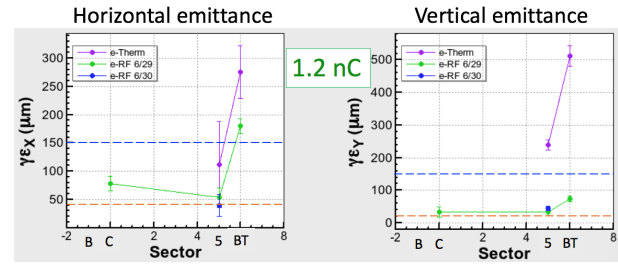


Figure 11: Emittance measurement result for electron beam at each sector.

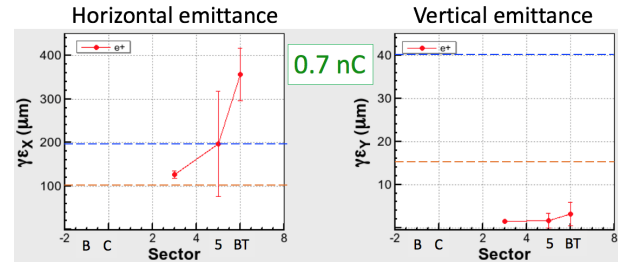


Figure 12: Emittance measurement result for positron beam at each sector.

SUMMARY

In the LINAC and the BT, transport of high current and low emittance beam is necessary for SuperKEKB. In the LINAC, emittance requirement for Phase 2 was satisfied after applying dispersion correction, reduction of beam phase space jitter, and orbit correction. To suppress the emittance growth more, automatic orbit correction for minimizing emittance growth is desired. We plan to introduce such an emittance control program in this Winter. Large emittance growth was observed in the BT. Emittance requirement in Phase 2 was not satisfied in the BT. Investigations of the issues are in progress.

ACKNOWLEDGEMENTS

This work was partly supported by JSPS KAKENHI Grant Number 16K17545.

REFERENCES

- [1] Y. Funakoshi *et al.*, "Achievements of KEKB", *Prog. Theor. Exp. Phys.* 03A001 (2013).
- [2] K. Furukawa *et al.*, "KEKB Injection Developments", in Proc. of eeFACT2018, Hong Kong, China, paper TUPAB01, this conference.
- [3] Y. Ohnishi *et al.*, "Highlights from SuperKEKB Phase 2 Commissioning", in Proc. of eeFACT2018, Hong Kong, China, paper MOXAA02, this conference.
- [4] N. Iida *et al.*, "Commissioning of Positron Damping Ring and Beam Transport for SuperKEKB", in Proc. of eeFACT2018, Hong Kong, China, paper TUPAB07, this conference.

OVERALL INJECTION STRATEGY FOR FCC-ee

S. Ogur^{*†}, F. Antoniou, T. K. Charles[‡], O. Etisken[§], B. Harer, B. Holzer, K. Oide[¶],
T. Tydecks, Y. Papaphilippou, L. Rinolfi, F. Zimmermann, CERN, Geneva, Switzerland,
A. Barnyakov, A. Levichev, P. Martyshkin, D. Nikiforov, BINP SB RAS, Novosibirsk, Russia,
E. V. Ozcan, Bogazici University, Bebek, Istanbul, Turkey,
K. Furukawa, N. Iida, T. Kamitani, F. Miyahara, KEK, Tsukuba, Ibaraki, Japan,
I. Chaikovska, R. Chehab, LAL, Orsay, Paris, France,
S. M. Polozov MEPhI, Moscow, Russia, M. Aiba, PSI, Zurich, Switzerland.

Abstract

The Future Circular electron-positron Collider (FCC-ee) requires fast cycling injectors with very low extraction emittances to provide and maintain extreme luminosities at center of mass energy varying between 91.2-385 GeV in the collider. For this reason, the whole injector complex table is prepared by putting into consideration the minimum fill time from scratch, bootstrapping, transmission efficiency as well as store time of the beams in synchrotrons to approach equilibrium emittances. The current injector baseline contains 6 GeV S-band linac, a damping ring at 1.54 GeV, a pre-booster to accelerate from 6 to 20 GeV, which is followed by 98-km top up booster accelerating up to final collision energies. Acceleration from 6 GeV to 20 GeV can be provided either by Super Proton Synchrotron (SPS) of CERN or a new synchrotron or C-Band linac, distinctively, which all options are retained. In this paper, the current status of the whole FCC-ee injector complex and injection strategies are discussed.

INTRODUCTION

The Future Circular electron-positron Collider (FCC-ee) is designed to provide precision study of Z , W , H bosons and top quark, as a potential first step to the global FCC project of CERN. In 98 km collider, these 4 particles will be studied in 4 different operational modes within the distinct time intervals (i.e. upgrades) of the collider [1].

The injector complex consists of a linac, damping ring, pre-booster and top-up booster, as presented in Fig. 1. Inevitably, this chain requires scheduling of bunches in order to fill the collider within minimum time meanwhile allocating enough time to the beams to approach to the equilibrium emittances of the circular accelerator for their stabilisation before the energy ramp up. On the other hand, the injector complex will have the one tenth of the bucket charge in the collider on average, therefore while topping up into the same collider bucket, we have needed to investigate the fluctuations of the bunch length as well as transverse emittances due to beamstrahlung, also known as boothstrapping [2]. The injection into the proceeding synchrotron (for example

from SPS to top-up booster) is also an important limiting parameter to the synchrotrons determining the required dynamic aperture as well as to the spacing between the bunches or the trains. In Table 1, the injection types have been tabulated. All in all, the FCC-ee injector complex will provide the necessary beams with the same accelerators yet distinct cycles as discussed in details in Table 2.

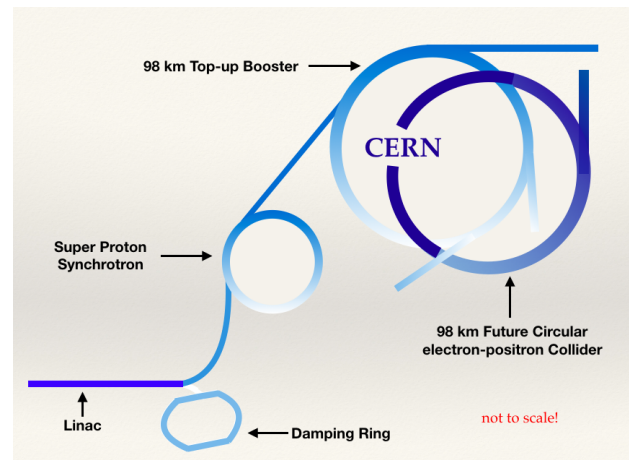


Figure 1: Layout of the FCC-ee.

Table 1: Injection types into the circular accelerators

accelerator	injection type
damping ring	on axis
pre-booster	off-axis
top-up booster	on-axis
collider	off-axis

ELECTRON AND POSITRON PRODUCTION

A low emittance RF-gun has been considered in order to preserve beam transmission and prevent emittance dilution due to wakefields throughout the injector complex. The novel RF-Gun operating at 2856 MHz frequency has been designed to provide 6.5 nC charge in a bunch with

* salim.ogur@cern.ch

† also Bogazici University, Bebek, Istanbul, Turkey

‡ also School of Physics, University of Melbourne, 3010, Victoria, Australia

§ also Ankara University, Ankara, Turkey

¶ also KEK, Tsukuba, Ibaraki, Japan

Table 2: Baseline parameters for the FCC-ee injectors

operation mode	FCCee-Z		FCCee-W		FCCee-H		FCCee-tt	
type of filling	Full	Top-up	Full	Top-up	Full	Top-up	Full	Top-up
energy [GeV]	45.6		80		120		182.5	
lifetime [min]	70	70	50	50	42	42	47	47
τ_{inj} [sec]	122	122	44	44	31	31	32	32
linac bunches	2	2	2	2	1	1	1	1
linac repetition rate [Hz]	200	200	100	100	100	100	100	100
linac RF frequency [MHz]	2856							
linac bunch population [10^{10}]	2.13	1.06	1.88	0.56	1.88	0.56	1.38	0.83
SPS bunch spacing [MHz]	400							
SPS bunches/injection	2	2	2	2	1	1	1	1
SPS bunch population [10^{10}]	2.13	1.06	1.88	0.56	1.88	0.56	1.38	0.83
number of linac injections	1040	1040	500	500	393	393	50	50
number of SPS injections	8	8	2	2	1	1	1	1
SPS supercycle duty factor	0.84	0.84	0.62	0.62	0.35	0.35	0.08	0.08
SPS number of bunches	2080	2080	1000	1000	393	393	50	50
SPS current [mA]	307.15	153.57	130.22	39.07	51.18	15.35	4.77	2.86
SPS injection time [s]	5.9	5.9	5.7	5.7	3.93	3.93	0.5	0.5
SPS ramp time [s]	0.2							
SPS cycle length [s]	6.3	6.3	6.1	6.1	4.33	4.33	0.9	0.9
BR bunch spacing [MHz]	400	400	400	400	400	400	400	400
BR number of bunches	16640	16640	2000	2000	393	393	50	50
BR bunch population [10^{11}]	0.21	0.11	0.19	0.06	0.19	0.06	0.14	0.66
BR cycle time [s]	51.74	51.74	14.4	14.4	7.53	7.53	5.6	5.6
booster ramp time	0.32	0.32	0.75	0.75	1.25	1.25	2	2
number of cycles per species	10	1	10	1	10	1	20	1
transfer efficiency	0.8							
no. of injections/collider bucket	10	1	10	1	10	1	20	1
total number of bunches	16640	16640	2000	2000	393	393	50	50
filling time (both species) [sec]	1034.8	103.48	288	28.8	150.6	15.06	224	11.2
required bunch population [10^{11}]	1.70	0.085	1.5	0.045	1.5	0.045	2.2	0.066

the normalised transverse emittance of $3\text{ }\mu\text{m}^1$, and $\sigma_z=1.5$ mm bunch length with 0.6% energy spread at 10 MeV. The designed RF-Gun [3,4] is shown in Fig. 2.

Apart from RF gun, a thermionic gun will also be utilized in order to supply 10 nC of bunch charge. Actually, the whole injector complex is designed to accelerate 3.4 nC (i.e. 2.13×10^{10}) electron or positron in a bunch or bucket, the charge extracted from the electron sources are intentionally designed to be higher in order to have safety margins for unforeseen transmission loss, positron production, last but not least, to be able to send higher charge for the first fill of the collider.

The creation of the positrons will be done by impinging electrons on a target inside the linac at 4.46 GeV. Regarding the probable transmission loss in the capture and acceleration of positrons inside the remaining 1.54 GeV part of the linac, some safety margin is allocated for the incident electron charge into the positron target. In other words, the FCC-ee injectors can impinge the target with up to 10 nC of

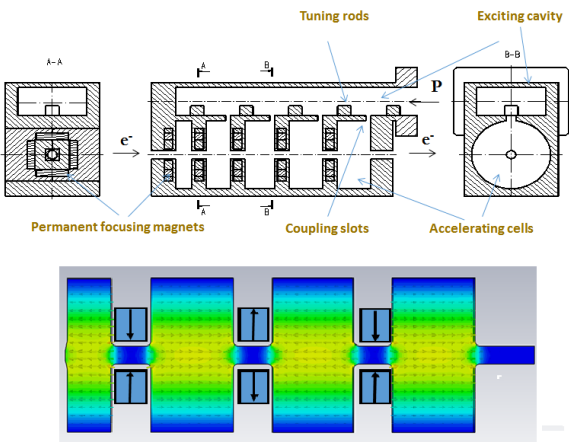


Figure 2: Sketch of S-Band RF-gun using parallel coupling accelerating structures with permanent magnets in the irises and its corresponding electromagnetic simulations.

electron bunch at 4.46 GeV in order to achieve 3.4 nC of positrons at 1.54 GeV at the end of 6 GeV linac. The target

¹ Instead of π .mm.mrad, the unit of the emittance is said to be μm , and this notation is followed through the paper.

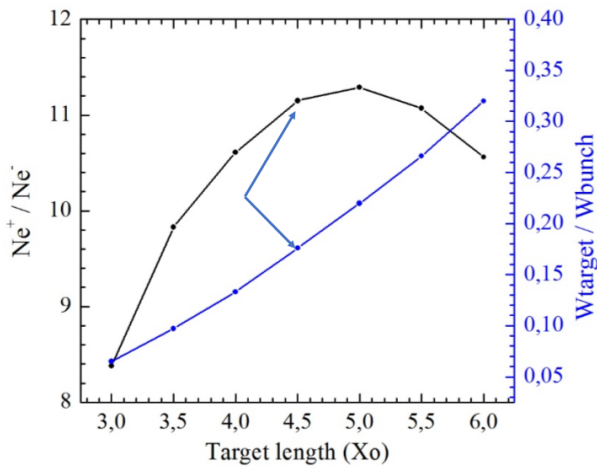


Figure 3: Optimisation of conventional positron target thickness with positron yield (left vertical axis), and total energy deposition in tungsten target is normalised by the total electron bunch energy (right vertical axis).

simulations are retained for both conventional and hybrid targets [5]. In Fig. 3, the conventional target length versus positron production yield has been presented, and the target thickness would suffice the FCC-ee needs determined to be 16 mm thick tungsten foil where the tungsten radiation length is denoted as X_0 corresponding to 3.5 cm. The power deposited in the target is calculated to be 2.8 kW per pulse. For max e^- charge of 8.8 nC (i.e. net of transmission loss out of 10 nC e^- in a bunch sent from the thermionic gun), e^- beam energy is 76 J (2 bunches per RF pulse with 200 Hz of linac repetition), in other words, the average e^- beam power on the target is 15 kW [6].

The optimisation of positron targets, flux concentrator as well as accelerating structures surrounded by the solenoids and triplets are currently on going [7,8]. Meanwhile, the e^+ beam used in the FCC-ee injector simulations are taken from KEK, which the positrons simulated from the conversion target up to 1.1 GeV in the linac [9].

LINACS

6 GeV S-Band linac operating at 2856 GHz has been finalised excluding positron optics. The linac has a branching point at 1.54 GeV for emittance cooling in the damping ring. The space charge in the RF gun as well as in the first 75 MeV part of the linac have been taking into account (i.e. up to 85 MeV). The misalignments have been randomly distributed and the automatic orbit steering algorithm has successfully transmitted the beam with transverse emittance dilution below 15% with perfect transmission, leaving more than an order of magnitude safety margin for the injected emittance into the pre-booster. The linac basics and former versions have been already presented in [10], yet some modifications and updates have been done and presented in this chapter.

The 1.54 GeV electrons will be injected into damping ring (DR) for 25 ms, and then injected back to the linac after

emittance cooling via a bunch compressor (BC), which DR and BC will be discussed in the following sections. Therefore, the linac is continued from 1.54 GeV up to 6 GeV using S-Band cavities, where its optics and some parameters are presented in Fig. 4 and Table 3, respectively.

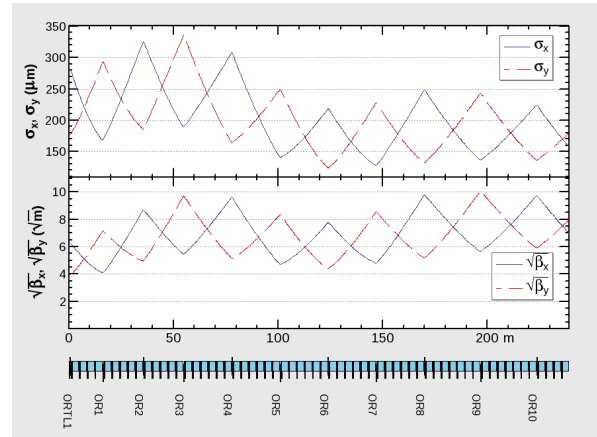


Figure 4: Optics of 1.54-6 GeV linac.

Table 3: Some parameters of the 1.54-6 GeV linac.

Parameter	Value
length	239.1 m
frequency	2856 Hz
repetition	200 Hz
number of bunches per RF pulse	2-4
number of quad./cavity	12, 60
injection-extraction energy	1.54 GeV-6 GeV
injected emittance (h/v)	1.86/0.39 nm
average extracted emit. (h/v)	0.55/0.11 nm
final emittance w/o blowup (h/v)	0.48/0.10 nm
transmission for 3.4 nC	100%

The 6 GeV linac will accelerate both beams alternatively. During the electron beam delivery into boosters, the linac will send 2 bunches per RF pulse, however, during positron beam creation, there will be 2 e^+ bunches followed by 2 high charge e^- up to 4.46 GeV part of the linac to create new positron bunches which will be sent into the DR.

The FCC-ee injector baseline foresees utilisation of the CERN SPS or a new synchrotron as a pre-booster. On the other hand, high gradient C-Band linac can be also a compelling alternative for 6-20 GeV acceleration interval. The C-Band accelerating structures of 1.8 m length will have an aperture of 16 mm with 50 MV/m unloaded cavity gradient. The main parameter of the C-Band linac has been given in Table 4. The short-range wakefields [11] have been included in the simulations together with misalignments of quadrupoles and cavities, misinjection, and BPM readout errors, as in the case of S-Band linac. The optics of C-Band cavities is preceded by the S-Band 1.54-6 GeV linac in Fig. 4, and therefore it continues starting from the 'QC0' quadrupole in Fig. 5.

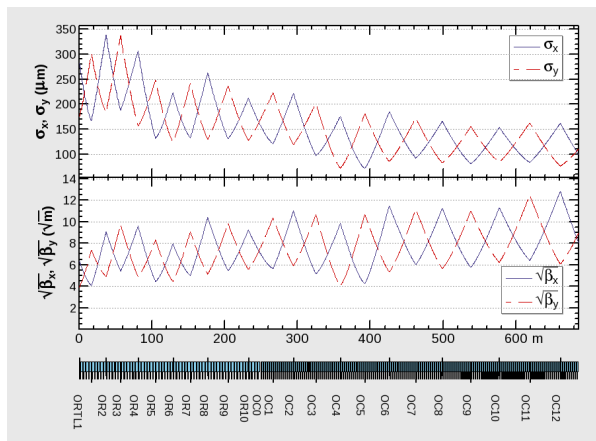


Figure 5: Optics of 1.54-20 GeV linac. Note that C-Band accelerating structures starts at 'QC0' after S-Band structures.

Table 4: Some parameters of the C-Band 6-20 GeV linac

Parameter	Value
length	446.9 m
frequency	5712 Hz
repetition	200 Hz
number of bunches per RF pulse	2
number of quad./cavity	13, 156
average extracted emit. (h/v)	1.18/0.05 nm
final emittance w/o blowup (x/y)	0.15/0.03 nm
transmission for 3.4 nC	100%

C-Band structure has brought 447 meter additional length to S-Band 6 GeV linac in order to reach 20 GeV. Moreover, the extracted emittance values 1.18/0.05 nm, which are calculated for 12 random seeds, are quite compatible with the injection emittance to the booster. Moreover, thanks to utilisation of DR for emittance cooling of both species, the energy spread of the beams at 20 GeV is around $\pm 0.7\%$ in total, allowing safe direct injection into the top-up booster, as the beam profile of tracking can be seen in Fig. 6.

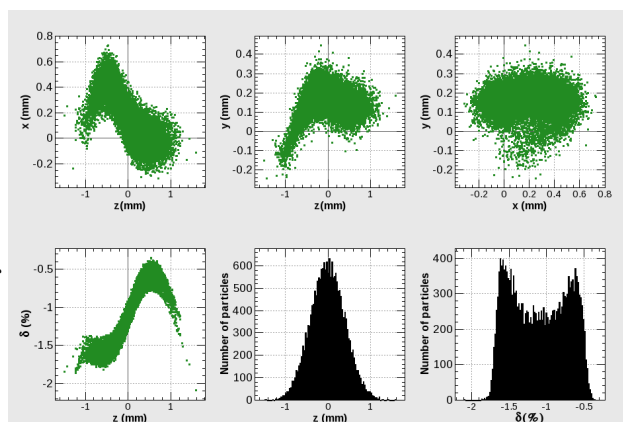


Figure 6: Beam profile at the end of S-Band plus C-Band linac at 20 GeV

DAMPING RING

The primary intend of using damping ring for FCC-ee is the emittance cooling of the positrons, yet for the compatibility of both species, the DR is planned to be used for the e^- beam as well without bringing any additional delay to the e^- beam delivery to the collider. The damping ring is designed to be at least 240 meter (i.e. about 800 ns for relativistic $\beta \approx 1$) in order to be able to host 5 trains separated by 100 ns due to kicker rise/fall times, and each train has 2 bunches RF pulse coming from linac separated by approximately 60 ns due to long range longitudinal wakes, as discussed in details in [10]. The DR optics has been changed slightly to mitigate the impact of Intra-beam scattering (IBS), which is done by creating 20% x-y coupling in the optics. The optics have been shown in Fig. 7 and some corresponding parameters of DR is tabulated in Table 5.

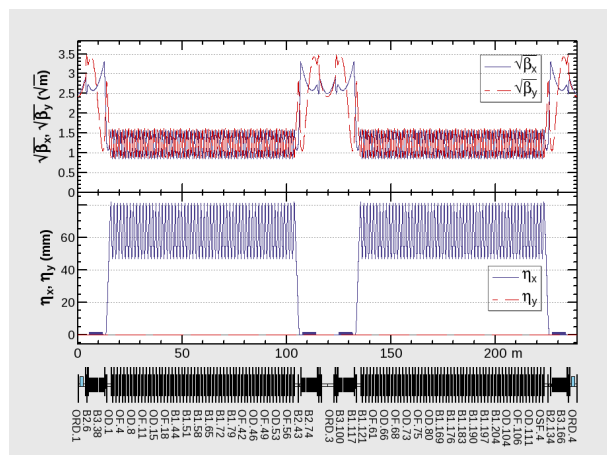


Figure 7: Damping ring optics.

Table 5: 1.54 GeV damping ring parameters with IBS and 20% coupling

parameter	value
circumference	241.8 m
bending radius	7.75 m
no. trains, bunches/train	5, 2
train, and bunch spacings	100 ns, 61 ns
FODO cell phase advance (h/v)	69.5/66.1 deg
betatron tune (h/v)	24.19/23.58
equilibrium emittance (h/v)	1.38/0.28 nm
longitudinal equilibrium emittance	1.73 um
damping time (h/v/l)	10.5/10.9/5.5 ms
no. of wigglers, theirs fields	4, 1.8 T
energy loss per turn	0.23 MeV
RF voltage, frequency	4 MV, 400 MHz

The dynamic aperture(DA) of the DR has been calculated to be around $\pm 7\%$, therefore it rules out usage of an energy compressor since the positrons have an energy spread of $\pm 5\%$ after the collimation of the long tail particles. Therefore, they can be injected into the DR directly by a mere transverse

matching. The DA achieved in transverse and longitudinal directions is shown in Fig. 8.

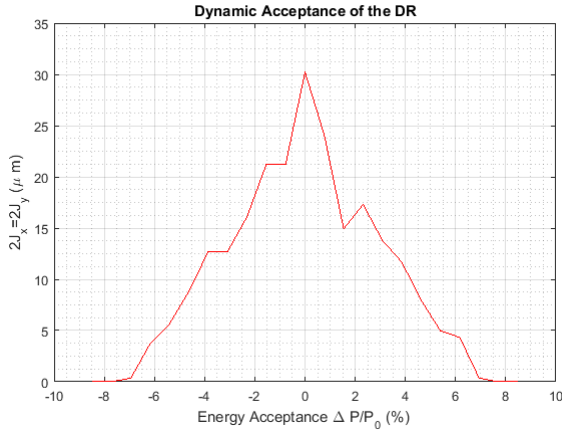


Figure 8: Dynamic acceptance for 1000 turns with synchrotron radiation.

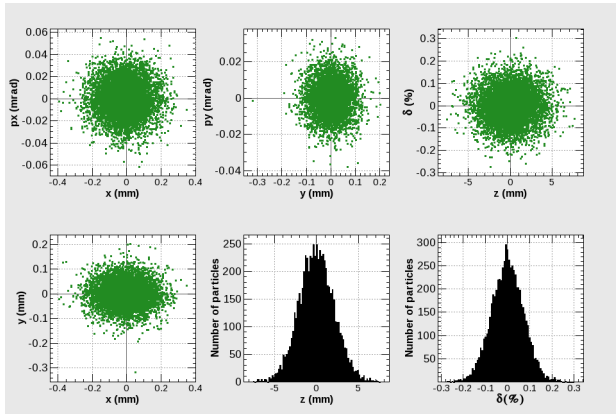


Figure 9: Positron beam profiles after tracking in the ideal DR for the allocated beam store time of 45 ms.

All in all, the DR tracking results are outstandingly close to the analytic calculations and equilibrium emittance of the DR, as presented in Table 6.

Table 6: DR tracking results of positron beam for 45 ms in the ideal machine with 20% coupling to mitigate IBS

direction	injected emittance	extracted emittance
horizontal	1.26 μm	1.48 nm
vertical	1.21 μm	0.38 nm
longitudinal	75.5 μm	1.48 μm

However, a bunch compressor after DR is required to reduce the RMS bunch length from 5 mm (assuming the cavity voltage of the DR is reduced in order to prevent CSR kick, actually $\sigma_z=2.2$ mm in Fig. 9) to 0.5 mm, prior to injection into the linac. A dogleg bunch compressor comprised of two

triple bend achromat (TBAs) can achieve this compression. The full details of which can be found in [12].

The longitudinal dispersion properties of the bunch compressor are: $R_{56} = 0.40$ m, $T_{566} = 61.8$ mm, and $U_{5666} = -23.5$ mm, where T_{566} and U_{5666} are the second- and third-order longitudinal dispersion respectively. Sextupole magnets placed in the dispersive region not only optimize of the second-order longitudinal dispersion, T_{566} , to linearize the longitudinal phase space distribution, but also correction the chromaticity.

Left unchecked, CSR has the potential to significantly degrade the quality of the beam. This is true despite the relatively long bunch length ($\sigma_{z,f} = 0.5$ mm) because the reasonably large R_{56} value required necessitates a large degree of bending. Fortunately, CSR cancellation techniques [12–17] can mitigate the emittance growth to an acceptable level (less than 10 %). Careful control of β_x and α_x at the center of each dipole, as well as the phase advance between each dipole can allow us to cancel out the CSR kicks (Δx_k and $\Delta x'_k$) almost completely. To compensate for the CSR kicks, an additional quadrupole magnet is needed in the section between the TBAs. Figure 10 compares of the emittance growth through the bunch compressor when this CSR kick analysis is applied and when it is not.

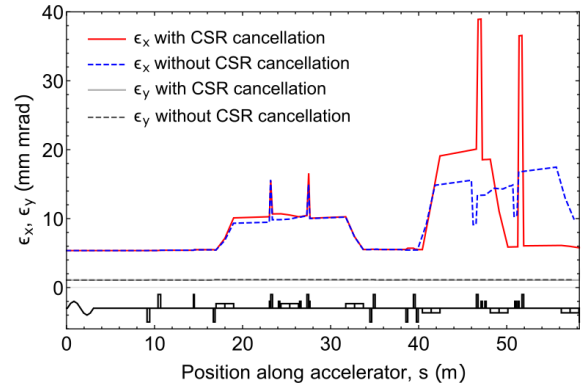


Figure 10: Emittance along the bunch compressor, before CSR cancellation technique applies (blue, dotted) and after (red, solid).

The positron beam of KEK has been simulated through matching section to the DR, 45 ms in the DR, then these particles are gone through BC, finally another matching has been done to the linac at 1.54 GeV. This overall tracked beam has been used in Linac simulations presented in the former chapter.

PRE-BOOSTERS

Two different options are considered as a pre-booster before the bunches transferred to the high-energy booster: using the existing Super Proton Synchrotron (SPS) or designing completely a new ring. The initial basic parameters for the FCC-ee pre-injector were established in order to satisfy the collider flux requirements and using the CERN SPS as

a pre-booster ring (PBR) [18]. Since there can be issues on using the SPS as pre-injector due to machine availability, synchrotron radiation and RF system requirements, a "green field" alternative pre-booster ring design is also considered [19]. The purpose of this study is to present the necessary modifications on the existing SPS and the conceptual design of an alternative accelerator ring with injection and extraction energies of 6 and 20 GeV, respectively.

SPS as Pre-booster

Damping wiggler and Robinson wiggler magnets are proposed to be installed in the straight sections of the SPS, in order to achieve the required emittance like in the case of the CLIC damping rings design [20].

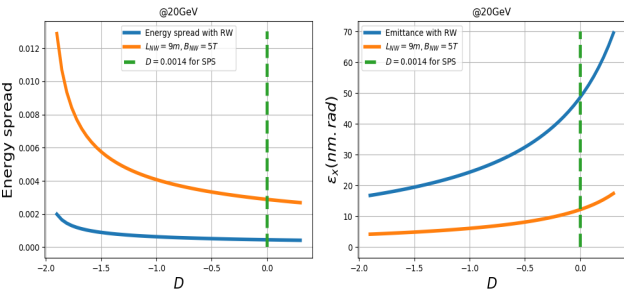


Figure 11: Parametrization of the energy spread (left) and emittance (right) with the normal wiggler (NW) and Robinson wiggler (RW) magnet at 20 GeV for SPS

For the existing SPS, the achievable emittance and damping time are around 48 nm and 1.7 s, respectively, even if the phase advance for one FODO cell is arranged to around 135 degree. However, the horizontal emittance can be significantly decreased by adding a Robinson wiggler yet it introduces a growth in the energy spread [21–23], as it can be seen in Fig. 11. The preliminary results have concluded the emittance to be reduced to 12 nm from around 48 nm by deploying damping wiggler magnet with 9 m and 5 T. Then, the emittance is further reduced to required 5 nm by introducing a Robinson wiggler. In conclusion, the damping time becomes much lower than the required 0.1 s thanks to these proposed wiggler magnets.

Alternative Ring Design

The structure of alternative ring has been provided based on the analytic calculations and simulations. A FODO type cell is chosen for the ring which has 4 arcs and 4 straight sections. Wiggler magnets are planned to be placed in one of the straight sections to be able to have 0.1 s damping time at 6 GeV. Each arc has 35 FODO cells with sextupole magnets in each main cell, whereas each straight section has two matching cells and there are 10 cells in the straight section. One straight section contains 2 T and 8.1 m long wiggler magnet which is based on the wiggler design of CLIC [24]. A cell contains two 5.31 m long dipoles located between quadrupoles with 30 cm length. The chromaticity is controlled by two families of 20 cm long sextupoles. The

total circumference turns out to be 2908 m and the general parameters of the ring can be seen in Table 7. A scan has been performed to determine the optimum phase advances in terms of the emittance. Accordingly, $\mu_x, \mu_y = 0.363/2\pi, 0.1/2\pi$ are chosen for achieving minimum emittance. For the phase advance in the straight section, it is planned to be chosen around 90 degree to provide minimum beta function with maximum efficiency for injection and extraction elements.

Table 7: General parameters of the alternative PBR at injection and extraction energies, respectively.

Parameters	Values (inj./ext.)
energy	6 / 20 GeV
circumference	2908 m
equilibrium emittance	0.19 / 4.88 nm
energy loss/turn	1.12 / 57.8 MeV
natural chromaticity (h/v)	-69 / -123
hor. damping times	0.096 / 0.006 s

Dynamic aperture (DA) calculations, according to the tracking results of MADX-PTC [25], gives around 7 mm in horizontal and vertical directions.

BOOSTER

The last stage of the FCC-ee injector chain is a 98 km full energy injector housed in the same tunnel as the collider. This rapid cycling booster synchrotron is designed to ramp the beam energy up from 20 GeV to the beam energy of the collider in the range of 45.6 to 182.5 GeV and provide top-up injection every 5.6 to 51.74 seconds.

The booster will follow the footprint of the FCC hadron collider, while the collider rings are placed about 1.2 m on the outside. In the experimental cavern the collider's interaction region layout with crossing angle and local chromaticity compensation creates an offset of the interaction point of about 11 m, which leaves sufficient space for the booster to bypass the detector on the inside.

The magnetic lattice is of FODO structure. Two optics are used for the collider. First, a $90^\circ/90^\circ$ optics has been chosen for the operation at 120 GeV and 182.5 GeV. Secondly, a $60^\circ/60^\circ$ optics are designed for the operation at the lower beam energies 45.5 and 80 GeV, since this optics provides larger momentum compaction factor for longer bunches to mitigate the microwave instability [26]. The horizontal emittance evolution of each collider staging and the corresponding optics have been summarised in Table 8. In the arcs the cell length is about 54 m driven by the required horizontal equilibrium emittance. A comparison of the emittance values of booster and collider is given in Table 2. In the straight sections the cell length is 50 m except in the straight sections with the RF installation, where the cell length has been increased to create more room for the cryomodels. 566 m long section with smaller curvature at the beginning and at the end of each arc have been designed to house the

Table 8: Horizontal equilibrium emittances of the booster compared to the values of the collider for all four beam energies. The 60° optics is used for 45.5 GeV and 80 GeV operations while the 90° optics will be used for 120.0 GeV and 182.5 GeV.

beam energy (GeV)	booster emittance (nm)	collider emittance (nm)
45.5	0.24	0.24
80.0	0.73	0.84
120.0	0.55	0.63
182.5	1.30	1.48

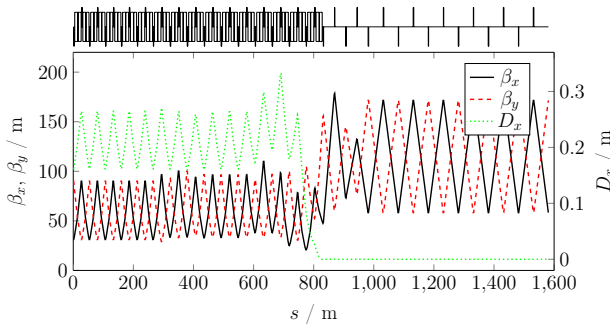


Figure 12: Beta functions and horizontal dispersion function of the transition from the arc lattice into a straight section with RF installation. The first five cells are regular arc FODO cells with a length of 54 m. The following section of 566 m consists of ten FODO cells with different bending angle to fit the geometry of the dispersion suppressor of the hadron collider. They also serve as quadrupole-based dispersion suppressor and matching section to the optics of the straight FODO cells with 100 m length.

dispersion suppressor of the FCC hadron collider. In these sections, the cell length is 56.6 m and a quadrupole-based dispersion suppressor scheme was chosen for the booster. Figure 12 shows the betafuncions in the transition of the periodic solution of arc 2 via the FCC-hh dispersion suppressor section into the straight section with the RF installation [27].

At 20 GeV beam energy the horizontal equilibrium emittance shrinks down to only $\epsilon_x = 15$ pm with the 90°/90° optics. As a consequence intra-beam scattering would blow up the emittance blow-up of a factor 48. In addition, the transverse damping time is $\tau_x = 10$ s, which would not allow to reach the equilibrium before the ramp-up. Therefore, 16 wiggler magnets are installed at the beginning and at the end of the straight sections with the RF system. The damping time is decreased $\tau_x = 0.1$ s and the horizontal equilibrium emittance is increased to $\epsilon_x = 300$ pm and $\epsilon_x = 296$ pm for the 60°/60° optics and the 90°/90° optics respectively. The wigglers have a length of $L_w = 9.1$ m with a period length of $\lambda_w = 0.23$ m. The wiggler have been chosen to be normal-conducting as they have to be switched off during the

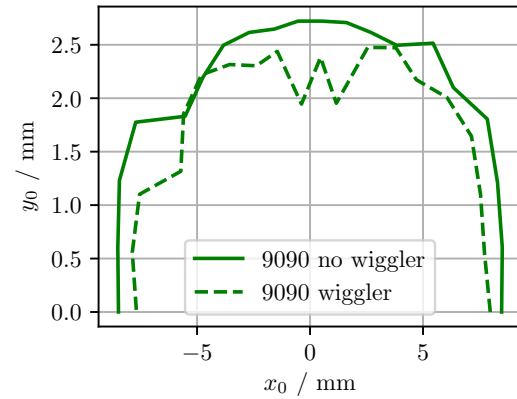


Figure 13: Dynamic aperture of the FCC-ee booster with 90°/90° optics at 20 GeV beam energy with and without wiggler magnets for a beta-function of 100 m.

energy ramp-up. Otherwise the energy loss by synchrotron radiation would exceed the capacities of the RF system. The pole tip field is $B = 1.8$ T, the actual wiggler field is then $B_w = 1.45$ T. The characteristics of the synchrotron radiation light fan created by the wigglers is currently under investigation by the vacuum group.

From the different sextupole schemes that were studied a non-interleaved sextupole scheme provided the largest DA for both optics. Tracking studies showed that the wigglers do not decrease the dynamic aperture significantly as shown in Fig. 13. The DA was determined by the survival of the particles after 1000 turns.

CONCLUSION

The RF-gun is ready for prototyping and positron study is continuing. The linacs up to 20 GeV (except 1.54 GeV positron linac part) have been finalized. They promise a nearly perfect transmission with low emittance to be safely injected into the pre-booster or booster. All in all, linac consists of 318 meters S-Band to reach 6 GeV, and 488 m C-Band to reach additional 14 GeV acceleration.

The damping wiggler and Robinson wiggler magnets will be inserted into the SPS lattice. The insertion of both type of wigglers will lead SPS to reach at the targeted equilibrium emittance with an acceptable energy loss per turn. The DA optimization for alternative pre-booster and simulations of Robinson wiggler for SPS are ongoing. The DA of top-up booster is fairly enough for safe acceptance of the beam from pre-boosters or C-Band linac. Additionally, final 6D tracking studies including wigglers and transverse quadrupole misalignments are under way. The instability study of the booster, such as microwave and transverse mode coupling instabilities, is also ongoing.

Each of the FCC-ee injectors has been designed with alternative options. The injector baseline satisfies all requirements, even with large safety margins. In particular, it supports the proposed bootstrapping injection mode of

the collider. With the proposed injector, the collider can be filled from zero in about 17 minutes at the Z pole, and even much faster at higher energies. The bunch schedules have been optimized for maximum average luminosity in operation.

REFERENCES

- [1] K. Oide *et al.*, "Design of beam optics for the future circular collider e^+e^- collider rings", *Phys. Rev. Accel. Beams*, vol. 19, p. 111005, Nov. 2016.
- [2] S. Ogur *et al.*, "Bunch Schedules for the FCC-ee Pre-injector", Proceedings of Int. Particle Accelerator Conf. (IPAC'18), Vancouver, Canada, Apr.-May 2018, MOPMF001.
- [3] A. V. Andrianov *et al.*, "Development and low power test of the parallel coupled accelerating structure", *JINST* 11 P06007, 2016.
- [4] Y. D. Chernousov *et al.*, "Accelerating structure with parallel connection". Patent for invention (Russia), No. RU2472244C1, BI. 01/10/2013, № 1.
- [5] I. Chaikovska *et al.*, "Experimental Activities on High Intensity Positron Sources Using Channeling", *Proceedings of IPAC'17*, Copenhagen, Denmark, WEPIK002, 2017.
- [6] P. Martyshkin, "Preliminary result of FCC positron source simulation", CERN, Geneva, Switzerland, accessed in September 2018, <https://indico.cern.ch/event/623025/contributions/2576145/attachments/1452960/2241145/Presentation2.pdf>
- [7] I. Chaikovska *et al.*, "Positron source", talk presented at the FCC-week 2017, Berlin, Germany, accessed in March 2018, https://indico.cern.ch/event/556692/contributions/2590440/attachments/1468997/2272259/e_FCCweek2017_IC.pdf
- [8] P. Martyshkin, "FCC-ee Flux Concentrator Computer Models", CERN, Geneva, Switzerland, accessed in September 2018, <https://indico.cern.ch/event/749013/contributions/3098680/attachments/1699198/2735883/FCC-FC.pdf>
- [9] N. Iida *et al.*, "Beam Dynamics in Positron Injector Systems for the Next Generation b-Factories", *Proceedings of IPAC 2011*, THYA01, San Sebastian, Spain, 2011.
- [10] S. Ogur *et al.*, "Layout and Performance of the FCC-ee Pre-injector Chain", Proceedings of Int. Particle Accelerator Conf. (IPAC'18), Vancouver, Canada, Apr.-May 2018, MOPMF034.
- [11] K. Yokoya, "Short-Range Wake Formulas for Infinite Periodic Pill-Box", 1998.
- [12] T. K. Charles, et al. "Bunch Compression and Turnaround Loops in the FCC-ee Injector Complex," 9th International Particle Accelerator Conference IPAC2018, Vancouver, BC, Canada, 2018, THPAF037, 3044-3047.
- [13] D. Douglas, "Suppression and Enhancement of CSR-Driven Emittance Degradation in the IR-FEL Driver," *Technical Report JLAB-TN-98-012*, 1998.
- [14] S. Di Mitri, M. Cornacchia, and S. Spampinati, "Cancellation of coherent synchrotron radiation kicks with optics balance," *Phys. Rev. Lett.*, 110, 014801, 2013.
- [15] S. Di Mitri and M. Cornacchia, "Electron beam brightness in linac drivers for free-electron-lasers," *Phys. Rep.*, 539, 2014.
- [16] R. Hajima, "A first-order matrix approach to the analysis of electron beam emittance growth caused by coherent synchrotron radiation," *Japanese Journal of Applied Physics, Part 2: Letters*, 42, pp. 974-976, 2003.
- [17] Y. Jiao, X. Cui, X. Huang, and G. Xu, "Generic conditions for suppressing the coherent synchrotron radiation induced emittance growth in a two-dipole achromat," *Phys. Rev. STAB*, 17, 060701, 2014.
- [18] Y. Papaphilippou *et al.*, "Design Guidelines for the Injector Complex of the FCC-ee", in *Proc. 7th Int. Particle Accelerator Conf. (IPAC'16)*, Busan, Korea, May 2016, paper THPMR042, pp. 3488-3491, ISBN: 978-3-95450-147-2, doi:10.18429/JACoW-IPAC2016-THPMR042.
- [19] O. Etisken *et al.*, "Pre-Booster Ring Considerations for the FCC e^+e^- Injector", in *Proc. 9th Int. Particle Accelerator Conf. (IPAC'18)*, Vancouver, BC, Canada, Apr. 4, pp. 83-86, doi:10.18429/JACoW-IPAC2018-MOPMF002.
- [20] Y. Papaphilippou *et al.*, "The SPS as an Ultra-Low Emittance Damping Ring Test Facility for CLIC", in *Proc. 4th Int. Particle Accelerator Conf. (IPAC'13)*, Shanghai, China, May 2013, paper TUPME042, ISBN: 978-3-95450-122-9.
- [21] The LEP injector study group, "The LEP injector chain", in *LEP design report*, CERN-SPS/63-26, 1983.
- [22] Y. Baconnier *et al.*, "Emittance Control of the PS e^+e^- Beams Using a Robinson Wiggler", *Nuclear Instrument and Methods in Physics Research A234* (1985) 244-252, North-Holland, Amsterdam, 1984.
- [23] T. Goetsch *et al.*, "Status of the Robinson Wiggler Project at the Metrology Light Source", in *Proc. 6th Int. Particle Accelerator Conf. (IPAC'15)*, Richmond, VA, USA, May 2015, pp. 132-134, doi:10.18429/JACoW-IPAC2015-MOPWA019.
- [24] F. Antoniou, "Optics Design of Intrabeam Scattering Dominated Damping Rings", CLIC Note 989, CERN-Thesis-2012-368.
- [25] CERN-BE/ABP Accelerator Beam Physics Group, MAD-Methodical Accelerator Design. <http://mad.web.cern.ch/mad/>
- [26] E. Belli *et al.*, "Single Bunch Instabilities in FCC-ee", in *Proceedings of IPAC2018*, Vancouver, BC, Canada, pp. 3336-3339.
- [27] B. Harer *et al.*, "Status of the FCC-ee Top-Up Booster Synchrotron", Proceedings of Int. Particle Accelerator Conf. (IPAC'18), Vancouver, Canada, Apr.-May 2018, MOPMF059.

OVERALL DESIGN OF THE CEPC INJECTOR LINAC*

J. R. Zhang[†], Y. L. Chi, J. Gao, X. P. Li, C. Meng, G. X. Pei¹, S. L. Pei, D. Wang, C. H. Yu¹
Institute of High Energy Physics, 100049 Beijing, China
¹also at University of Chinese Academy of Science, 100049 Beijing, China

Abstract

The CEPC injector consists of linac and booster. To meet the requirement of the booster, the linac should provide 10 GeV electron and positron beam at a repetition frequency of 100 Hz. In this paper, the overall design of the linac has introduced. For the linac one-bunch-per-pulse is adopted and bunch charge should be larger than 3 nC in the design. A 1.1 GeV damping ring with 75.4 m circumference has adopted to reduce the transverse emittance of positron beam to suitably small value.

INTRODUCTION

Circular Electron-Positron Collider (CEPC) [1] is a 100 km ring e^+e^- collider for a Higgs factory. It has proposed by the Institute of High Energy Physics (IHEP) of the Chinese Academy of Sciences (CAS) in collaboration with a number of institutions from various countries. The CEPC accelerator is composed of linac, booster, collider and the transports lines. The energy of the collider is 120 GeV. The CEPC booster provides 120 GeV electron and positron beams to the CEPC collider and is in the same tunnel as the collider. The energy of the linac is 10 GeV. The layout of CEPC accelerator shows in Fig. 1.

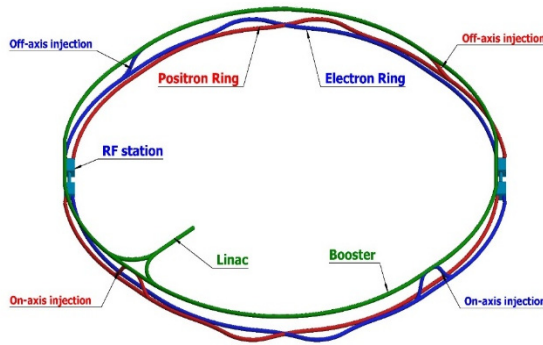


Figure 1: Layout of CEPC accelerator.

OVERVIEW OF THE LINAC

The linac is a normal conducting S-band linac with frequency in 2860 MHz and provide electron and positron beams at an energy up to 10 GeV. The main requirements of the booster to Linac shows in Table 1. Single bunch mode has adopted and the repetition frequency is 100 Hz.

Simplicity and high availability are the design principles. The layout baseline design is the linear scheme and there are 15% backups of the klystrons and accelerating structures. Considering the potential to meet higher requirements and the ability to update in the future, the bunch charge is designed to larger than 3 nC, which is important for positron source design.

Table 1: The requirements of the Booster to the Linac

Parameters	Value	Unit
e^-/e^+ beam energy	10	GeV
Repetition rate	100	Hz
e^-/e^+ bunch population	>1.5	nC
Energy spread (e^-/e^+)	$<2 \times 10^{-3}$	-
Emittance (e^-/e^+)	<120	nm

The linear scheme of linac layout as the baseline design shows in Fig. 2. The linac is composed of electron source and bunching system (ESBS), the first accelerating section (FAS) where electron beam is accelerated to 4 GeV, positron source and pre-accelerating section (PSPAS) where positron beam is accelerated to larger than 200 MeV, the second accelerating section (SAS) where positron beam is accelerated to 4 GeV and the third accelerating section (TAS) where electron and positron beam are accelerated to 10 GeV. Electron bypass transport line (EBTL) scheme has considered for bypass electron beam in electron mode. A 1.1 GeV damping ring at SAS is introduced to reduce the positron beam emittance. The short-range wakefields have considered in the simulation of beam dynamics.

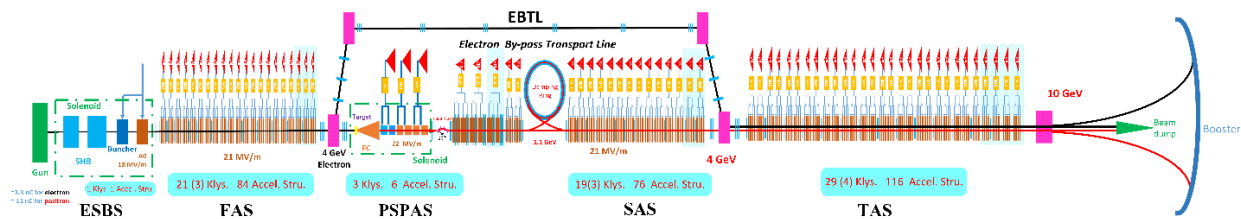


Figure 2: Layout of CEPC Linac.

* Work supported by NSFC (11705214)

[†] zhangjr@ihep.ac.cn

ELECTRON LINAC

ESBS

The ESBS contains the electron source and a bunching system. Two operation modes of the electron source are required; one is to provide a 3.3 nC bunch charge for electron injection and the other is to provide a 11 nC bunch charge as the primary electron beam for positron production. The bunching system consists of two sub-harmonic bunching cavities with frequency in 143 MHz and 572 MHz, an S-band buncher and an S-band accelerating structure with frequency in 2860 MHz. The transverse focussing element in the bunching system is solenoid. Beam distribution at exit of the ESBS and normalized rms emittance along the beam direction is shown in Fig. 3. The normalized rms emittance at the ESBS exit is 80 mm-mrad and the transmission efficiency is about 90%.

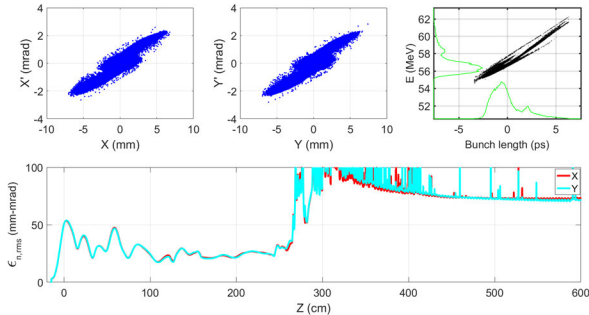


Figure 3: Beam distribution at the exit of ESBS (top) and normalized rms emittance (below) along the beam direction.

Electron Linac Mode

The electron Linac is composed of FAS, EBTL and TAS. The horizontal distance between EBTL and the Linac is 2 m. The EBTL adopt local achromatic design and dispersion function is controlled within 0.5 m. The optical functions are shown in Fig. 4. The start-to-end dynamics simulation results of electron Linac with the bypass section are shown in Fig. 5, where the rms energy spread is 0.11% and the rms emittance is about 5 nm at the Linac exit. All the results can meet the requirements of the booster.

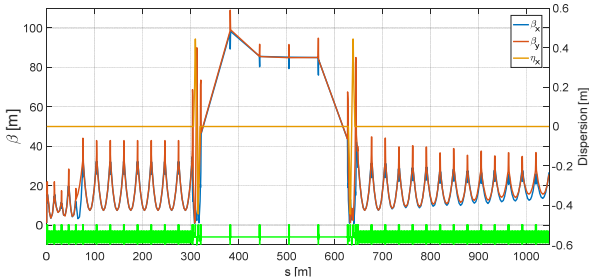


Figure 4: Optical functions of the electron linac.

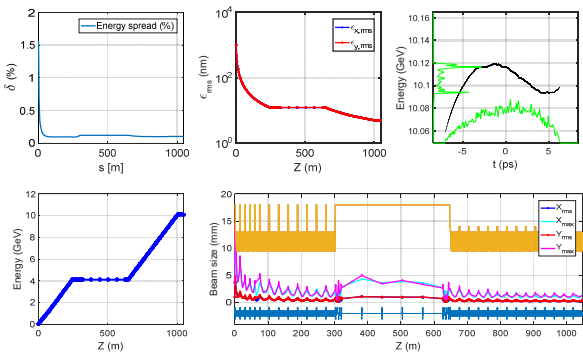


Figure 5: Beam dynamic simulation results for the electron linac, including energy spread (top-left), emittance (top-middle), longitudinal beam distribution (top-right), energy (bottom-left) and beam size (bottom-right).

POSITRON LINAC

PSPAS

A schematic of the positron source and pre-accelerating section (PSPAS) is shown in Fig. 6, including the target, flux concentrator (FC) which is an adiabatic matching device (AMD), caputre accelerating structures (blue), pre-accelerating structures (orange) and a chicane system. All the accelerating structures are same and each klystron drive two accelerating structures. The chicane systme is designed to dump the electron beam and photons. To achieve larger than 3 nC bunch charge positron beam at linac exit, a 4 GeV primary electron beam with an intensity of 10 nC/bunch is required. The length of the tungsten target is 15 mm and the RMS beam size of electron beam is 0.5 mm. The average electron beam power is 4 kW.

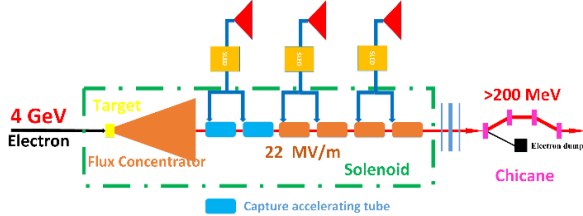


Figure 6: The layout of CEPC positron source.

The magnetic field of AMD is a pseudo-adiabatically changing solenoid field from peak 6 T to 0.5 T, which is a flux concentrator superimposed on a 0.5-T DC solenoid field. Comprehensive consideration of positron capture efficiency, emittance control and accelerating structure design, the aperture of accelerating structure has chosen as 25 mm. Figure 7 shows the positron yield at the second capture accelerating structure exit with different accelerating gradient and input phase corresponding to RF phase. There are two phase range where have higher positron yield: deceleration mode and acceleration mode. According to positron yield and consideration on beam energy, the accelerating gradient has chosen as 22 MV/m.

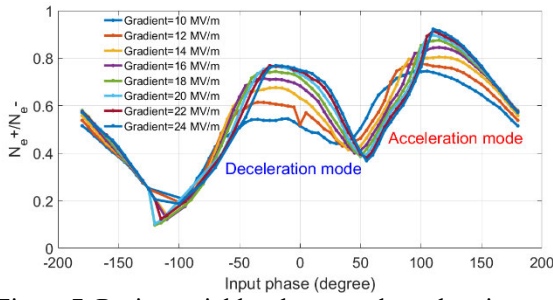


Figure 7: Positron yield at the second accelerating structure exit with different accelerating gradient and phase.

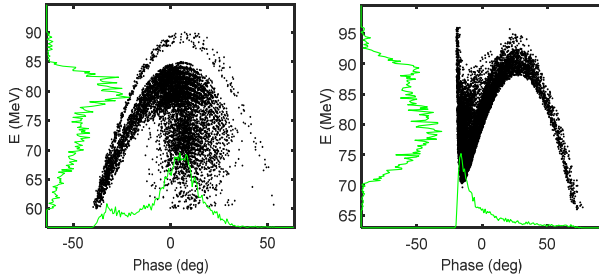


Figure 8: Beam distribution at the second accelerating structure exit, left is deceleration mod and right is acceleration mod.

The longitudinal beam distributions of deceleration mode and acceleration mode at the capture accelerating structure exit show in Fig. 8. From the simulation results acceleration mode have more compact phase spectrum, so the acceleration mode has adopted in the simulation. The deceleration mode is also possible in the operation of linac, same as KEKB [2]. The envelope from target exit to pre-accelerating section exit shows in Fig. 9. The distribution at pre-accelerating section exit shows in Fig. 10, where the energy cut off range is from 235 MeV to 265 MeV and the phase cut off range is from -8° to 12° . In this cut off condition the positron beam yield (N_{e^+}/N_e) is about 0.55, which can meet the bunch charge requirement.

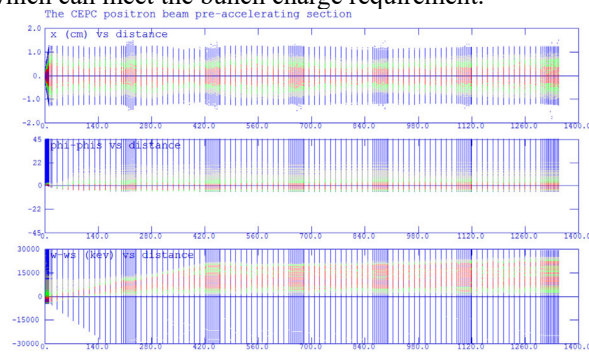


Figure 9: Beam envelope from target exit to pre-accelerating section exit.

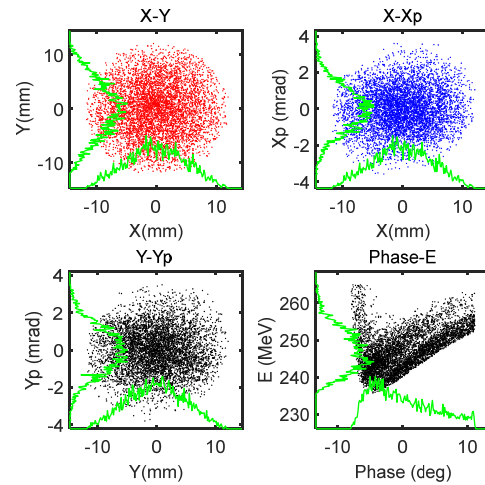


Figure 10: The distribution at pre-accelerating section exit.

Damping Ring

The energy of DR is 1.1 GeV and the circumference is 75.4 m [3]. The DR has a racetrack shape and the arcs have designed with 60 degrees FODO cell. Figure 11 shows the twiss parameters of the DR and the main parameters show in Table 2.

The injected emittance (normalized) for DR is 2500 mm-mrad and the injected energy spread is smaller than 0.2%. The positron beam will be stored in DR for 20 ms according to the 100 Hz repetition rate and two-bunch storage scheme. The extracted emittance is better to be smaller than one quarter of the injected emittance. Considering the issue of injection efficiency, the transverse acceptance of DR should be larger than five times of the injection beam size.

Before damping ring, the energy spread of the positron bunch should be reduced in order to match the RF acceptance of damping ring. After damping ring, longitudinal bunch length control must be provided to minimize energy spread in the linac. Reducing bunch length in the ring to the required value will need very high (~ 40 MV) RF voltage, so we add a bunch compressor system after the damping ring.

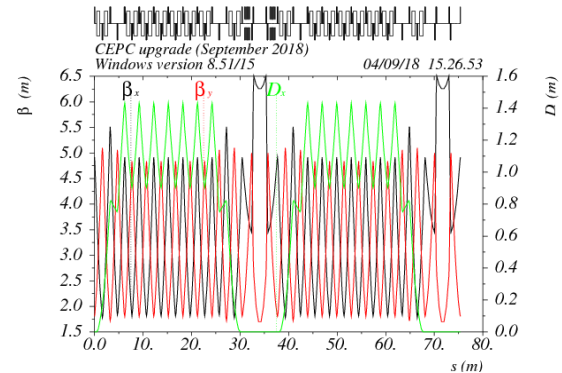


Figure 11: Twiss parameter for the whole ring.

Table 2: Main Parameters of Damping Ring

Parameters	Value	unit
Energy	1.1	GeV
Circumference	75.4	m
Bending radius	3.6	m
Dipole strength B ₀	1.03	T
U ₀	36.3	keV/turn
Damping time x/y/z	15.2/15.2/7.6	mS
δ ₀	0.05	%
ε ₀	376.7	mm.mrad
injection σ _z	5	mm
Extract σ _z	7.5	mm
ε _{inj}	2500	mm.mrad
ε _{ext} x/y	530/180	mm.mrad
δ _{inj} /δ _{ext}	0.18/0.05	%
Energy acceptance by RF	1.0	%
f _{RF}	650	MHz
V _{RF}	2.0	MV

Positron Linac Mode

The positron Linac is composed of SAS and TAS. Simulations are performed over an energy range from 200 MeV to 10 GeV. The third accelerating section accelerates both prositron and electron beams from 4 GeV to 10 GeV. Because the emittance of the positron beam is larger than the electron beam, the lattice of the TAS is based on the positron beam requirements. In the low-energy part of the SAS, the focusing structure is FODO and the quadrupoles nest on the accelerating structure. As the emittance decreases with energy increase and the damping ring the focusing structures are varied to decrease the number of quadrupole: one-triplet-one-accelerating-structure, one-triplet-four-accelerating-structures and one-triplet-eight-accelerating-structures. Four focusing structures shows schematically in Fig. 12.

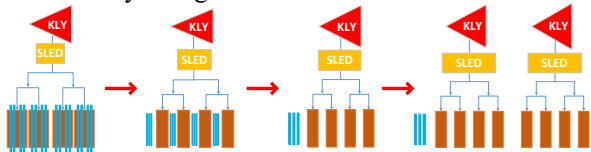


Figure 12: The focusing structures of positron linac.

Beam simulation results are shown in Fig. 13. At linac exit the energy spread is 0.16% and the rms emittance is 30/10 nm with the damping ring, which all meet the requirements of booster. The break in the plots is at the position of the DR.

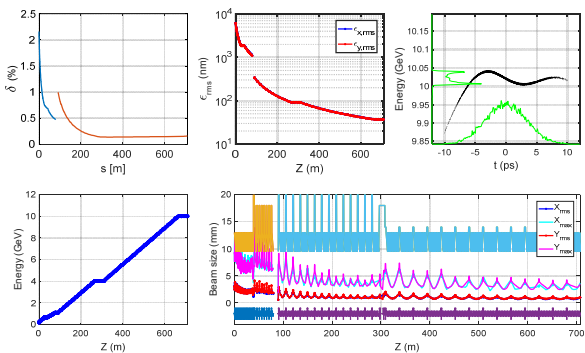


Figure 13: Beam dynamic simulation results for the positron linac, including energy spread (top-left), emittance (top-middle), longitudinal beam distribution (top-right), energy (bottom-left) and beam size (bottom-right).

CONCLUSION

The linac provides 10 GeV electron and positron beam with single bunch mode to the booster. A bypass section has been designed for the e- to make the e+ target simple. A fixed tungsten target has used in the positron source system. The e- beam on the target is 4 GeV & 10 nC. A damping ring is in the position of 1.1 GeV to reduce the positron emittance. The lianc design is meet the requirments of the booster.

ACKNOWLEDGEMENTS

The authors would like to thank the professor T. Kamitani and K. Furukawa for their helpful discussions.

REFERENCES

[1] Y.F. Wang, “A proposal on ring-based Higgs factory in China”, 2nd Symposium on Accelerator-based HEP Strategy and Development in China, Beijing, 2012.

[2] Takuya Kamitani, “SuperKEKB positron source status”, POSIPOL 2016, Orsay, France, Sep. 2016.

[3] D. Wang *et al.*, “Design Study on CEPC Positron Damping Ring System”, in *Proc. Linac18*, Beijing, China, Sep. 2018, paper THPO001.

AN ON-AXIS INJECTION DESIGN FOR CEPC

X. Cui[†], C. Yu, Y. Zhang, J. Zhai, IHEP, Beijing 100049, China

Abstract

Considering the requirement on the dynamic aperture in the main collider, an on-axis injection method is needed for the Higgs energy at CEPC. A swap-out on-axis injection scheme using the booster as an accumulation ring is given in this paper. Some dynamical problems concerning the effectiveness of this injection scheme is also discussed.

INTRODUCTION

The CEPC is a circular e^+e^- collider with a 100-km circumference [1]. Its center-of-mass energy is 240 GeV, and it will serve as a Higgs factory at that collision energy. The design also allows operation at 160 GeV as a W factory and 91 GeV as a Z factory. The CEPC accelerator complex consists of a double-ring collider, a booster, a linac and several transport lines. The collider and booster are located in the same underground tunnel, while the linac is built at ground level. Electrons and positrons are generated and accelerated to 10 GeV in the collider, and then are injected into the booster ring. The beams are then accelerated to full-energy and injected into the collider. The geometry of the CEPC complex is shown in Fig. 1, and some key parameters of the booster and collider are shown in Table. 1.

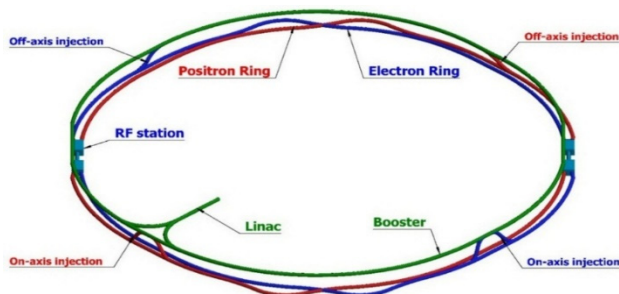


Figure 1: The geometry of the CEPC complex.

For the simplicity and robustness of the injection system, a conventional horizontal off-axis injection is chosen as the baseline design for Higgs, W, and Z mode. However, in the Higgs energy, when the errors and beam-beam effects are considered, the dynamic aperture in the collider may be not enough for an off-axis injection. To relax the requirements on dynamic aperture, an on-axis injection scheme, which is similar to the swap-out injection in HEPS [2], is proposed.

ON-AXIS INJECTION PROCESS

The idea of this on-axis injection is to use the booster as an accumulator ring, and inject the large bunch in the collider into the booster, not the other way around. Thus

off-axis injection and bunch merge are performed in the booster, whose dynamic aperture is large enough. A diagrammatic sketch of this injection process is shown in Fig. 2. In the injection, first fill the booster with small bunches whose bunch charge are 3% of the bunch charge in the collider. Ramp the booster up to 120 GeV, then several circulating bunches of the collider are injected back into the booster ring. After 4 damping times, the injected bunches will merge with the small bunches in the booster with the help of synchrotron radiation damping. Then the merged bunches will be injected back into the same buckets left empty from the last injection. This bunch exchange between the booster and collider ring can repeat until the booster is empty.

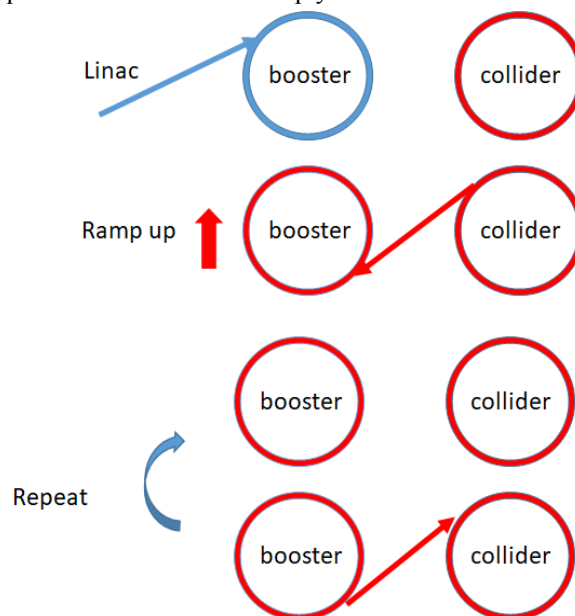


Figure 2: A sketch of the on-axis injection process.

With this on-axis injection scheme, the required horizontal dynamic aperture in the collider is reduced from $13\sigma_x$ to $8\sigma_x$. The number of exchanged bunches between the collider and booster every time is limited by the total current in the booster. With a 1mA booster current threshold, the time structure of the booster is shown in Fig 3. It is shown that the time needed for every on-axis injection is about 35s, which is less than the 47s required by the beam lifetime in the collider [1].

[†] cuixh@ihep.ac.cn

Content from this work may be used under the terms of the CC BY 3.0 licence (© 2018). Any distribution of this work must maintain attribution to the author(s), title of the work, publisher, and DOI.

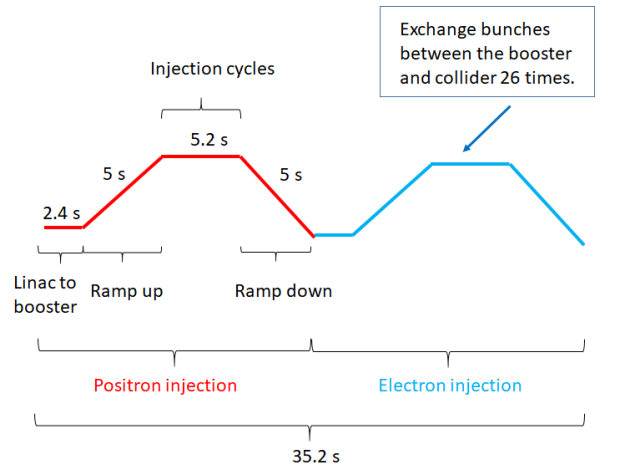


Figure 3: Time structure of the booster in on-axis injection.

Table 1: Some Key Parameters of CEPC

	Collider (Higgs energy)	Booster (Higgs energy)
Beam energy (GeV)	120	120
Circumference (km)	100	100
Bunch number	242	242
EBunch charge (nC)	24	0.72
Current (mA)	17.4	0.52
Emittance x/y (nm.rad)	1.21/0.0024	3.57/0.0178
Bunch length sz (mm)	4.4	2.8
Energy spread (%)	0.134	0.094
Damping time tx/ty/tz (ms)	46.5/46.5/23.5	52/52/26
Lifetime (hour)	0.43	/

SOME DISCUSSIONS

longitudinal Matching

In the on-axis injection scheme, the exchange bunches should be injected back to the right buckets of their own in the collider, so a longitudinal matching is needed. This problem is simplified by the same circumference of the booster and collider. Nevertheless, due to the different paths traveled by the injection beam and the circulating beam, a longitudinal deviation is introduced, as seen in Fig. 4. The length of the transport line is 261.2 meters, and the path difference between the injected beam and the circulating beam is only 0.011 meters, or 0.037 ns in time. This is equivalent to a 17 degree phase shift in the booster, and is in the stable region. This phase shift can be damped by synchrotron radiation. And if any longitudinal mismatch occurs, we could move the RF phase in the

booster to fit this problem. An experiment at BEPC II shows that the 200ms injection time is enough for this purpose.

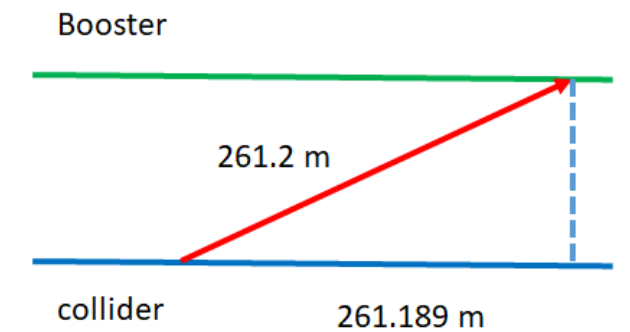


Figure 4: A sketch of the path length traveled by the injection beam and the circulating beam.

Beam Loading

Transient beam loading in the booster by the injection of large bunch and larger total beam current are considered [3]. With 7 large bunches (0.07mA) evenly distributed among the other small bunches. Max cavity voltage drop is 0.48 %. Max phase shift is 0.63 deg. With 13 large bunches in a very short bunch train. The maximum cavity voltage drop is 5.8%, and the maximum phase shift is 7.7 deg.

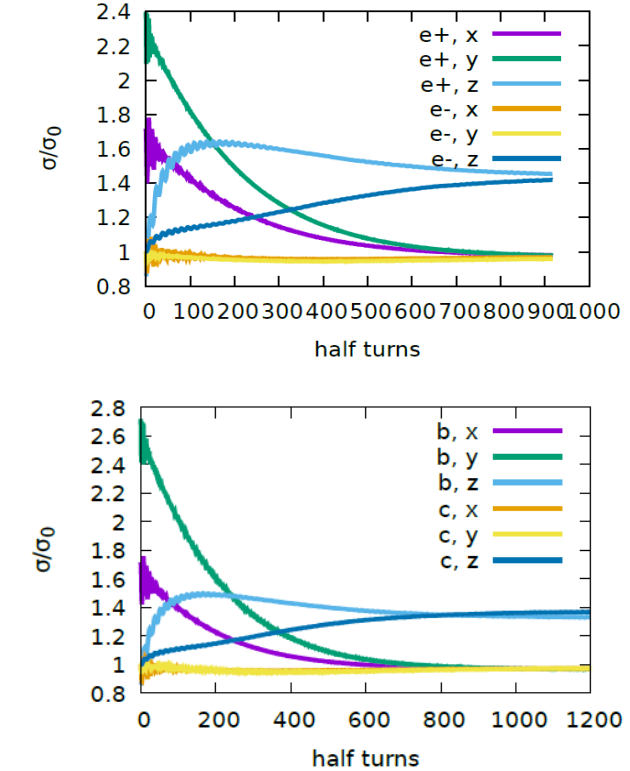


Figure 5: Simulation results without bunch condition difference (top) and with a 9 % σ_x horizontal offset, a 50 % σ_y vertical offset and 3% Intensity difference between colliding bunches.

Flip-flop Instability

A beam-beam simulation is done for the bunch instability due to the absence of several bunches in the collider. The results are shown in Fig. 5. It shows that there is no flip-flop instability even with a transverse offset and 3% Intensity difference between the colliding beams.

Injection Efficiency

In the on-axis injection we need to transfer the whole bunch into the booster and back into the collider, it is needed and challenging to have a very high injection efficiency in this process. Some preliminary results on effect of the beam position and energy errors are shown in Fig. 6. More work are still needed when more error sources are included.

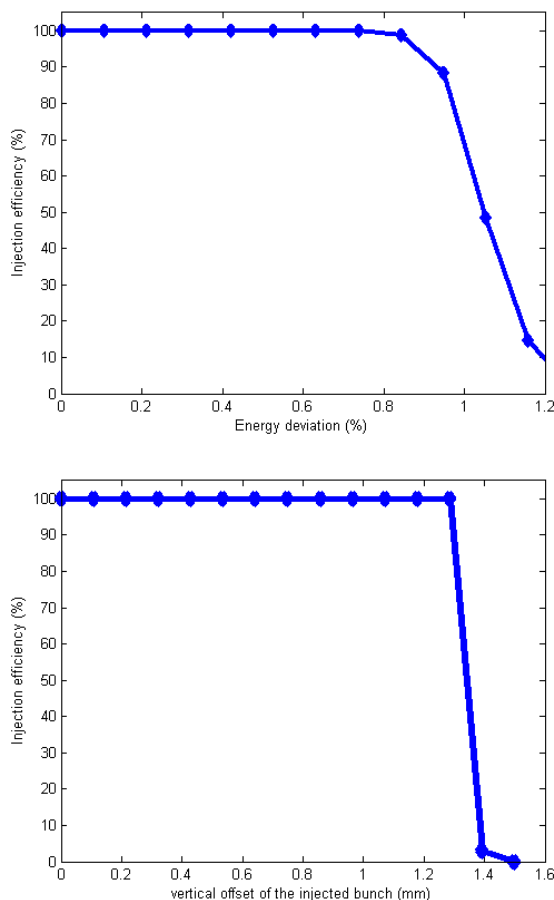


Figure 6: effect of the beam position errors (top) and energy deviation (bottom) on the injection efficiency.

CONCLUSION

An on-axis injection scheme for CEPC is shown in this paper. With this injection, the requirement on the horizontal dynamic aperture in the collider can be reduced significantly. Several problems concerning this injection are discussed. Efforts to improve the injection efficiency are needed in the future to make this on-axis injection a solid design.

REFERENCES

- [1] The CEPC Study Group, "CEPC Conceptual Design Report", Volume I- Accelerator, IHEP-CEPC-DR-2018-01, IHEP-AC-2018-01, August 2018.
- [2] Z. Duan, *et. al.*, "The Swap-out Injection Scheme For The High Energy Photon Source", in *Proc. IPAC'18*.
- [3] J. Zhai, *et. al.*, "HOM Simulations and Damping Scheme for CEPC Cavities", in *Proc. IPAC'17*.

DESIGN AND BEAM DYNAMICS OF THE CEPC BOOSTER*

D. Wang[†], C. Yu¹, X. Cui, D. Ji, J. Zhai, Y. Liu, Y. Zhang¹, C. Meng, N. Wang, J. Gao,
IHEP, 100049 Beijing, China

¹also at University of Chinese Academy of Sciences, 100049 Beijing, China

Abstract

The CEPC booster needs to provide electron and positron beams to the collider at different energy with required injection speed. A 10 GeV linac is adopted as the injector for CDR. Then the beam energy is accelerated to specific energy according to three modes of CEPC collider ring (H, W and Z). The geometry of booster is designed carefully in order to share the same tunnel with collider. The design status of booster including parameters, optics and dynamic aperture is discussed in this paper.

INTRODUCTION

The CEPC baseline design for CDR is a 100km double ring scheme with a same size booster whose energy starts from 10 GeV [1]. The booster provides electron and positron beams to the collider at different energies. Both the injection from zero current and the top-up injection should be fulfilled. Figure 1 shows the overall layout of CEPC injection chain. The booster is in the same tunnel as the collider, placed above the collider ring except in the interaction region where there are bypasses to avoid the two detectors on collider ring.

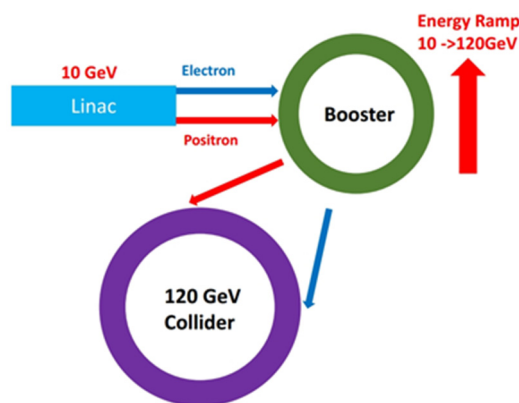


Figure 1: Overall layout of the CEPC injection chain.

BOOSTER PARAMETERS

Booster Design Requirements

The beam quality requirements in the booster are determined by the collider ring and the total beam current in the booster is limited by the RF power which is 1.0mA for Higgs, 4.0 mA for W and 10mA for Z. The energy acceptance of booster should be larger than 1% at four ener-

gy modes and the booster emittance at 120GeV should be lower than 3.6 nm in order to fulfill the requirement of injection to collider ring. The coupling of booster should be controlled under 0.5% which is defined by the requirement of Higgs on-axis injection scheme [1]. We assume 3% current decay for top up injection and the total efficiency of CEPC injection chain is 90%. With the limit for total beam current and the assumption of current decay in collider ring, the top up injection for Higgs mode and W mode needs only one cycle, and needs two cycles for Z mode. The top up injection time structures for the three energy modes are shown in Fig. 2. Furthermore, the dynamic aperture should be large enough for both injection and extraction to guarantee the required transfer efficiency which will be discussed in the last chapter.

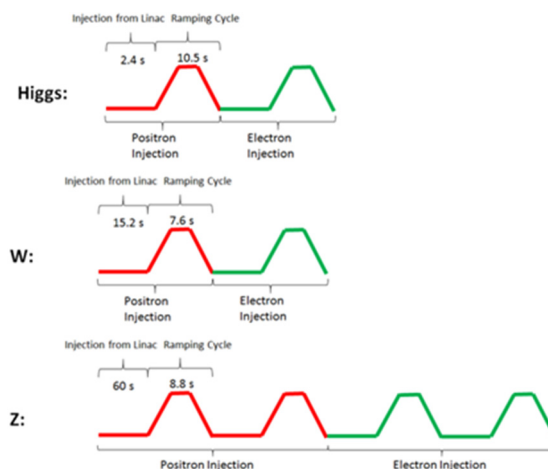


Figure 2: Top up injection time structure for Higgs, W and Z modes.

Beam Parameters at Different Energy

The main booster parameters at injection and extraction energies are listed in Table 1 and Table 2. The beam is injected from linac to booster by on-axis scheme and then injected from booster to collider at three different energies by off-axis scheme. Also the on axis injection from booster to collider for Higgs has been designed in case the dynamic aperture of collider ring at Higgs energy is not good enough for the off-axis injection.

After energy ramping, the booster emittance for Higgs and W approaches the value small enough to inject into the collider. The beam emittance for Z mode after energy ramping still cannot fulfil the collider injection requirement and further damping (5s) is needed before extraction from the booster. The emittance evolution in the booster for three energy modes is show in Fig. 3.

The top up injection time is 25.8 seconds for Higgs off-axis mode, 35.4 seconds for Higgs on-axis mode, 45.8

* Work supported by the National Key Programme for S&T Research and Development (Grant NO. 2016YFA0400400) and the National Natural Science Foundation of China (11505198 and 11575218).

[†] wangd93@ihep.ac.cn

seconds for W and 4.6 minutes for Z. When the collider is injected from zero current, the beam lifetime is much longer than the top up injection. At that time, the beam lifetime in collider is dominated by the Touschek effect which is about 695 hours for Higgs, 75 hours for W and about 33 hours for Z. The full injection time from 0 current for both beams is 10 minutes for Higgs, 15 minutes for W and 2.2 hours for Z (bootstrapping start from half of the design current).

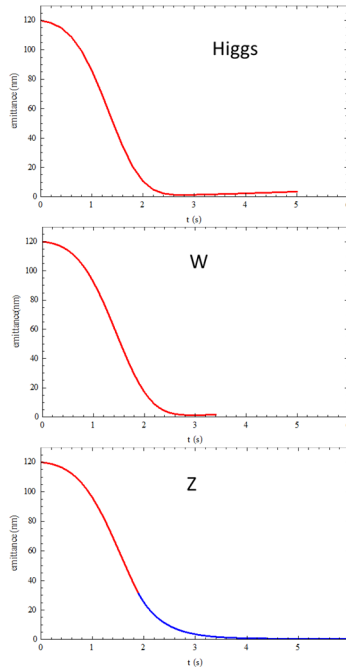


Figure 3: Emittance evolution in the booster from injection to extraction (top: Higgs, middle: W, bottom: Z).

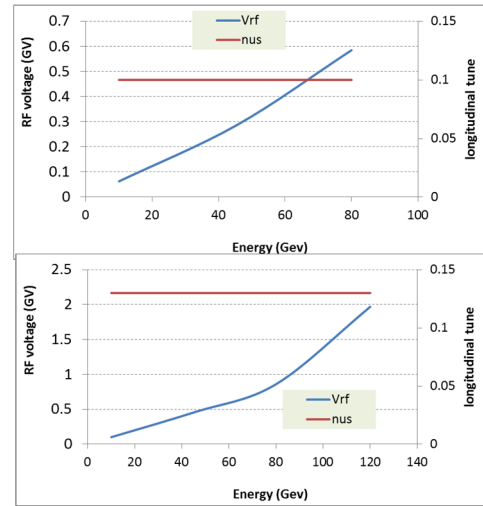


Figure 4: Booster RF ramping curve (top: Z & W, bottom: Higgs).

The RF voltage and longitudinal tune of the booster during ramping for the three energy modes are shown in Fig. 4. The longitudinal tune is constant (0.1) during ramping for Z and W. The longitudinal tune is 0.13 for Higgs to get larger energy acceptance for the on axis injection scheme. The beam lifetime is long enough during the ramping process which is 4.0×10^9 hours at 10 GeV, dominated by the transverse quantum lifetime, and is 7.8×10^{17} hours at 120 GeV, dominated by the longitudinal quantum lifetime.

Table 1: Main Parameters for the Booster at Injection Energy

		<i>H</i>	<i>W</i>	<i>Z</i>
Beam energy	GeV		10	
Bunch number		242	1524	6000
Threshold of single bunch current	μA		25.7	
Threshold of beam current (limited by coupled bunch instability)	mA		100	
Bunch charge	nC	0.78	0.63	0.45
Single bunch current	μA	2.3	1.8	1.3
Beam current	mA	0.57	2.86	7.51
Energy spread	%		0.0078	
Synchrotron radiation loss/turn	keV		73.5	
Momentum compaction factor	10^{-5}		2.44	
Emittance	nm		0.025	
Natural chromaticity	H/V		-336/-333	
RF voltage	MV		62.7	
Betatron tune $\nu_x/\nu_y/\nu_s$			263.2/261.2/0.1	
RF energy acceptance	%		1.9	
Damping time	s		90.7	
Bunch length of linac beam	mm		~ 1.0	
Energy spread of linac beam	%		0.2	
Emittance of linac beam	nm		< 120	

Table 2: Main Parameters for the Booster at Extraction Energy

		<i>H</i>	<i>W</i>	<i>Z</i>
		Off axis injection	On axis injection	Off axis injection
Beam energy	GeV	120		80
Bunch number		242	235+7	1524
Maximum bunch charge	nC	0.72	24.0	0.58
Maximum single bunch current	μA	2.1	70	1.7
Threshold of single bunch current	μA	300		
Threshold of beam current (limited by RF power)	mA	1.0		4.0
Beam current	mA	0.52	1.0	2.63
Injection duration for top-up (Both beams)	s	25.8	35.4	45.8
Injection interval for top-up	s	47.0		153.0
Current decay during injection interval			3%	
Energy spread	%	0.094		0.062
Synchrotron radiation loss/turn	GeV	1.52		0.3
Momentum compaction factor	10 ⁻⁵		2.44	
Emittance	nm	3.57		1.59
Natural chromaticity	H/V		-336/-333	
Betatron tune ν_x/ν_y			263.2/261.2	
RF voltage	GV	1.97		0.585
Longitudinal tune		0.13		0.10
RF energy acceptance	%	1.0		1.2
Damping time	ms	52		177
Natural bunch length	mm	2.8		2.4
Injection duration from empty ring	h	0.17		0.25

BOOSTER OPTICS

The design goal for the booster optics is to make sure the geometry is the same as the collider and satisfy the requirements of beam dynamics. The total number of magnets and sextupole families is minimized taking into account capital and operating costs. The maximum cell length and hence the maximum emittance in the booster is limited by the collider injection requirements.

Survey Design

Figure 5 shows the geometry of booster compared with the collider and Fig. 6 shows the cross section of the tunn

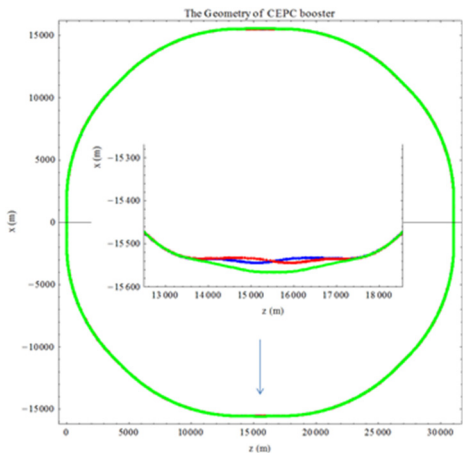


Figure 5: Booster vs. collider layouts.

el. Both CEPC collider and booster are located inside the same tunnel, and booster is on the top of collider. The horizontal position of the booster has been designed in the center of collider two beams. The horizontal position error of booster was controlled under ±0.17m. To do it, the precision of element length and bending angle has to be controlled carefully.

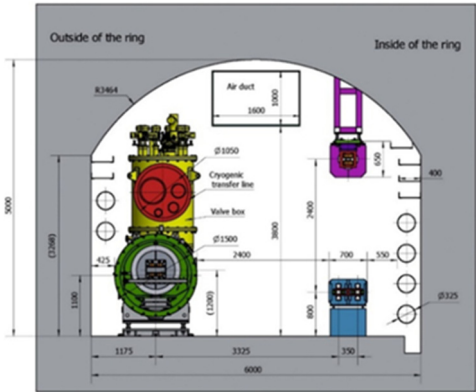


Figure 6: The cross section of CEPC tunnel.

Arc Region

Standard FODO cells have been chosen for the booster lattice [2]. The length of two FODO cells in the booster corresponds to three FODO cells in the collider. The phase advance of each cell is 90/90 degrees in the horizontal and vertical planes. The length of each bend is 46.4 m including ten short dipole magnets. The length of each

quadrupole is 1.0 m, while the distance between each quadrupole and the adjacent bending magnet is 1.6 m. Thus the total length of each FODO structure is 101 m. 97 FODO structures make up an octant. At the two ends of each octant, there are dispersion suppressors and straight sections. We need to adjust bend strength in the dispersion suppressors in order to match the geometry of collider ring. Figure 7 shows the twiss functions of the FODO cell and Fig. 8 shows twiss functions of the dispersion suppressor.

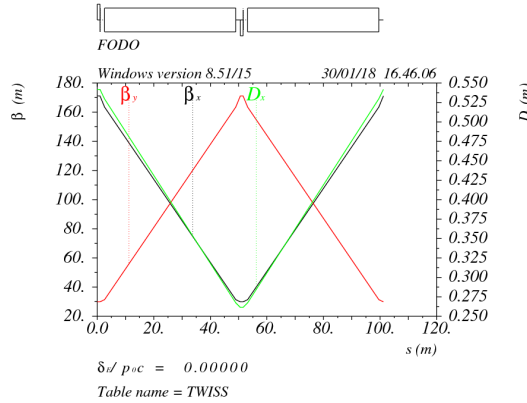


Figure 7: The Twiss functions of the FODO cell.

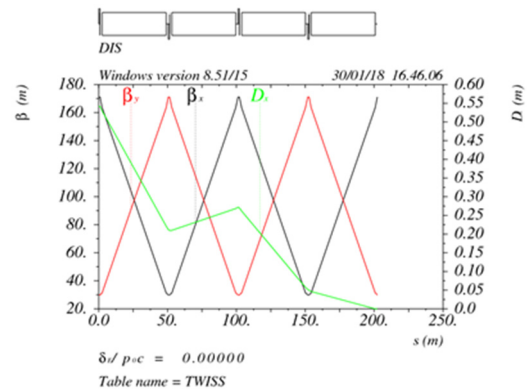


Figure 8: The Twiss functions of the dispersion suppressor.

Injection Region

The length of the straight sections for injection/extraction is exactly the same as in the collider. Figure 9 shows the lattice functions in the injection/extraction region. The phase advance in the injection straight section is tunable for adjusting the working point of the entire ring and also optimizing the off-momentum DA.

RF Region

In the RF section, dedicated optics with a lower beta function is designed to reduce the multi-bunch instability due to the RF cavities. Two matching sections whose phase advances are tunable at the two ends of the RF straight section transfer the beta function from the standard arc to the low beta section. Figure 10 shows the lattice functions in the RF region. The length of the low beta

section is 1.6 km and the total length of the RF straight section is 3.4 km which is exactly same as the collider ring.

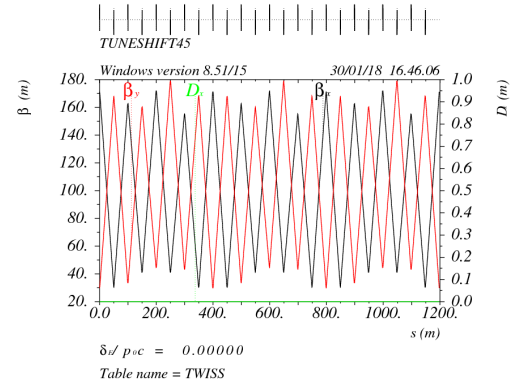


Figure 9: The Twiss functions of injection straight section.

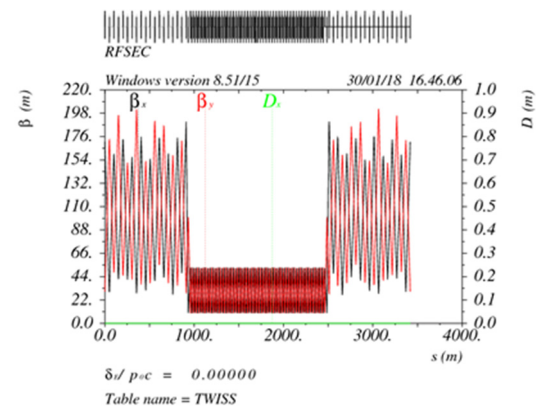


Figure 10: The Twiss functions of RF straight section.

IR Region

The geometry of booster is same as collider ring except for the IR. In the IR region, the booster is bypassed from the outer side to avoid a conflict with the CEPC detectors. The separation between the detector center and booster is 25 m considering the requirements of civil engineering and the radiation protection. Figure 11 shows the lattice functions in the IR.

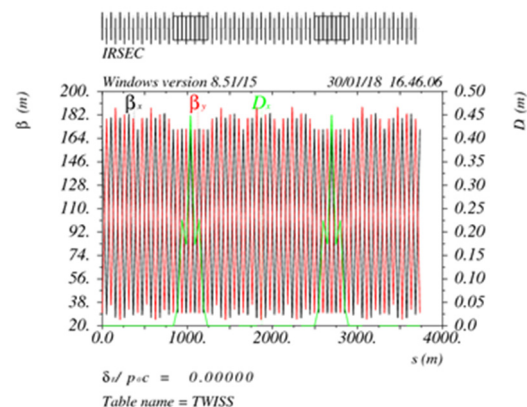


Figure 11: The Twiss functions of IR bypass.

Table 3: Error Analysis Settings

Parameters	Dipole	Quadrupole	Sextupole	Parameters	BPM (10Hz)
Transverse shift x/y (μm)	50	70	70	Accuracy (m)	1×10^{-7}
Longitudinal shift z (μm)	100	150	100	Tilt (mrad)	10
Tilt about x/y (mrad)	0.2	0.2	0.2	Gain	5%
Tilt about z (mrad)	0.1	0.2	0.2	Offset after BBA(mm)	30×10^{-3}
Nominal field	3×10^{-4}	2×10^{-4}	3×10^{-4}		

Dynamic Aperture

A non-interleave scheme and two sextupole families are adopted for linear chromaticity correction. Both the phase advances between sextupole pairs and the ones between octants are optimized carefully in order to achieve larger dynamic aperture. The thick black line in Fig. 16 shows the dynamic aperture of bare lattice; the purple line is the DA with errors and orbit corrections; the red line is the DA with errors; the thin black line in the upper plot is the beam stay clear region at 10GeV and the blue line in the lower plot is the DA with orbit corrections, radiative damping and sawtooth effect at 120GeV.

With errors and orbit corrections, the dynamic aperture of the booster is nearly two thirds of that for the bare lattice as shown in Fig. 16. At 10GeV, the DA with errors should be larger than the beam stay clear region. At 120GeV, the radiative damping effect and sawtooth effect is also considered except for the error effect, and the according DA result including damping and sawtooth is shown as the blue line in the lower plot of Fig. 16. The DA requirement and the real DA results which have been realized are listed in Table 4. Where the DA requirement at 10GeV is determined by the beam stay clear region and is determined by the re-injection process from the collider in the on-axis injection scheme at 120GeV.

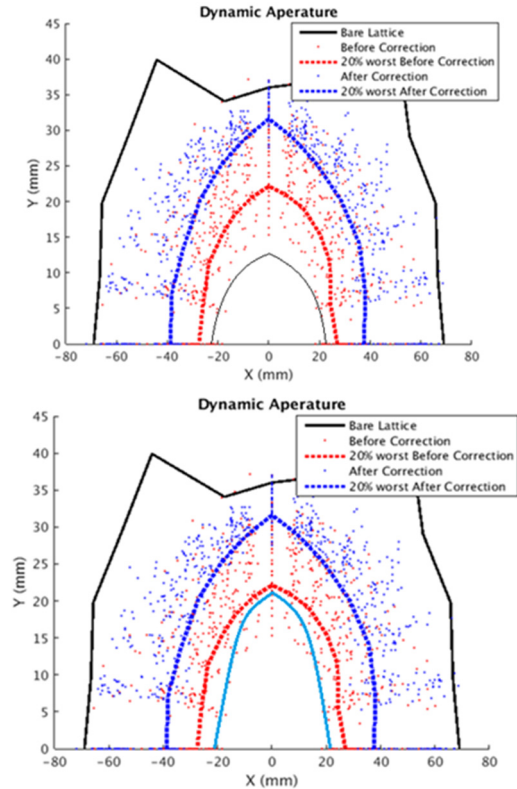


Figure 16: Dynamic aperture of booster (top: 10GeV, bottom: 120GeV).

Table 4: Summary of Booster DA Results

	DA requirement		DA results	
	H	V	H	V
10GeV ($\epsilon_x = \epsilon_y = 120\text{nm}$)	$4\sigma_x + 5\text{mm}$	$4\sigma_y + 5\text{mm}$	$7.7\sigma_x + 5\text{mm}$	$14.3\sigma_y + 5\text{mm}$
120GeV ($\epsilon_x = 3.57\text{nm}$, $\epsilon_y = \epsilon_x \cdot 0.005$)	$6\sigma_x + 3\text{mm}$	$49\sigma_y + 3\text{mm}$	$21.8\sigma_x + 3\text{mm}$	$779\sigma_y + 3\text{mm}$

SUMMARY

The design status of CEPC 100km booster has been introduced and so far it can meet the injection requirements at three energy modes. Both parameters and optics design was explained in detail. The design goal for the optics is to make sure the geometry of booster can match the one of collider and satisfy the requirements of beam dynamics. A lot of efforts for geometry design and nonlinearity optimization with special sextupoles arrangement have been done. Error studies were also included. The DA results shown the errors in the booster are tolerable.

ACKNOWLEDGEMENT

The authors thank Professors K. Oide, Y. Cai and M. Koratzinos for their helpful discussions.

REFERENCES

- [1] The CEPC Study Group, “CEPC Conceptual Design Report”, Volume I- Accelerator, IHEP-CEPC-DR-2018-01, IHEP-AC-2018-01, August 2018.
- [2] T. Bian, “Nonlinearity optimization for CEPC booster”, Ph.D. thesis, IHEP, Beijing, China, 2018 (in Chinese).
- [3] D. Wang, *et al.*, “DA studies in CEPC by downhill method”, ICFA Mini-Workshop on Dynamic Apertures of Circular Accelerators, Nov. 2017, IHEP, Beijing.

COMMISSIONING OF POSITRON DAMPING RING AND THE BEAM TRANSPORT FOR SuperKEKB

N. Iida*, Y. Funakoshi, H. Ikeda, T. Ishibashi, H. Kaji, T. Kamitani,
M. Kikuchi, T. Kobayashi, H. Koiso, F. Miyahara, T. Mori, Y. Ohnishi,
Y. Seimiya, H. Sugimoto, H. Sugimura, R. Ueki, Y. Yano, D. Zhou,

High Energy Accelerator Research Organization (KEK), Tsukuba, Ibaraki 305-0801, Japan

Abstract

The Positron Damping Ring (DR) for SuperKEKB successfully started its operation in February 2018, and the commissioning was continued until the end of SuperKEKB Phase 2 in July without serious troubles. This paper describes achievements of the beam commissioning of injection and extraction lines (LTR and RTL) between the LINAC and DR. In the LTR commissioning, the positron beam with high emittance, wide energy spread, and high charge were transported and injected into the DR. In the RTL commissioning, special cares were necessary to preserve the low emittance. The observed emittance growth in the RTL was not a problem for Phase 2, but it should be resolved in the coming Phase 3. In this paper, brief results of the commissioning of the DR is also reported.

INTRODUCTION

SuperKEKB [1] is a double-ring asymmetric collider of 7-GeV electron ring (HER) and 4-GeV positron ring (LER) with the Belle II detector installed in the interaction region. The KEKB accelerator [2], the predecessor had been in operation from 1998 to 2010, with the then world’s highest luminosity of $2.1 \times 10^{34} \text{ cm}^{-2} \text{ s}^{-1}$. To increase the luminosity by 40 times of KEKB, a new collision scheme called “Nano beam scheme” are adopted as well as two times high stored current is required. Since the stored beam has low emittance and high current, the lifetime is short, and the charge of the injection beam must also be high. We adopted an RF gun [3, 4] for generating the low-emittance electron beam. For positrons a flux concentrator [5](FC) as well as a damping ring had been adopted. The FC is a pulsed solenoid installed in right after the positron target to collect positrons generated at the target with high efficiency. The longitudinal phase distribution of the positron is huge, requiring some schemes for efficiently transporting the beam to DR as written in [6].

SuperKEKB is divided in three phases in its operation. In February 2016, we succeeded in operation of Phase 1 [7, 8] for about 5 months without Belle II detector, without collision. Completing construction of super-conducting final quadrupoles in a year and a half further, commissioning of DR and the collider with Belle II (Phase 2 [9]), in which a part of innermost detectors were unmounted, have commenced on January and March 2018 respectively. The required parameters for the positron injection beam of

SuperKEKB-LER are shown in Table 1. It should be noted that these values are defined as “ultimate” parameters in each stage that should be realized in harmony with a development of collision performance.

As shown in Fig. 1, the DR, a 1.1-GeV storage ring with a circumference of about 135.5 m has been constructed at 120 m downstream the positron target of the LINAC [10]. The positron beam is extracted from the end of Sector 2 of the LINAC whose energy is 1.1 GeV, and injected into the DR. Since the enormous energy spread from FC exceeds the energy acceptance of the DR, an energy compression system (ECS) is installed utilizing the first arc of the LTR. The damped beam from the DR is returned to the entrance of Sector 3 of the LINAC. The acceleration frequency of the DR is about 508.9 MHz, which is same as that of SuperKEKB, the resulting bunch length is too long to be accepted to the LINAC with acceleration frequency 2856 MHz (S-band). Thus a bunch compression system (BCS) in the second arc of RTL was installed. Figure 2 shows the particle distribution before and after the DR in the longitudinal phase space simulated with the parameters on Table 2. The parameters from the DR are modified from the initial design [11] to match the changes in the RF voltage from the design value of 1.4 to 1.0 MV, with the emittance accordingly changed from $89 \mu\text{m}$ to $64.3 \mu\text{m}$. As shown in Fig. 2, since positrons from

Table 1: Required parameters of injection beam for SuperKEKB-LER Phase 2 and 3

	DR Extraction	Phase2	Phase3–
$\gamma\epsilon_x [\mu\text{m}]$	64.3	< 200	< 100
$\gamma\epsilon_y [\mu\text{m}]$	3.2	< 40	< 15
$\sigma_\delta [\%]$	0.055	0.16	0.10
Charge [nC]	1.5	1.5	4.0

Table 2: Design Parameters of the Injection and Extraction Beam for DR (* shows a full width.)

Parameters	ECSin	ECSout =DRin	BCSin =DRout	BCSout
$\gamma\epsilon_x [\mu\text{m}]$		2800	64.3	
$\gamma\epsilon_y [\mu\text{m}]$		2600	3.2	
$\sigma_z [\text{mm}]$	$\pm 8^*$	$\pm 30^*$	6.6	1.3
$\sigma_\delta [\%]$	$\pm 5^*$	$\pm 1.5^*$	0.055	0.8
$R_{56} [\text{m}]$	–0.61			–1.05
$V_c [\text{MV}]$	41			21.5

* naoko.iida@kek.jp

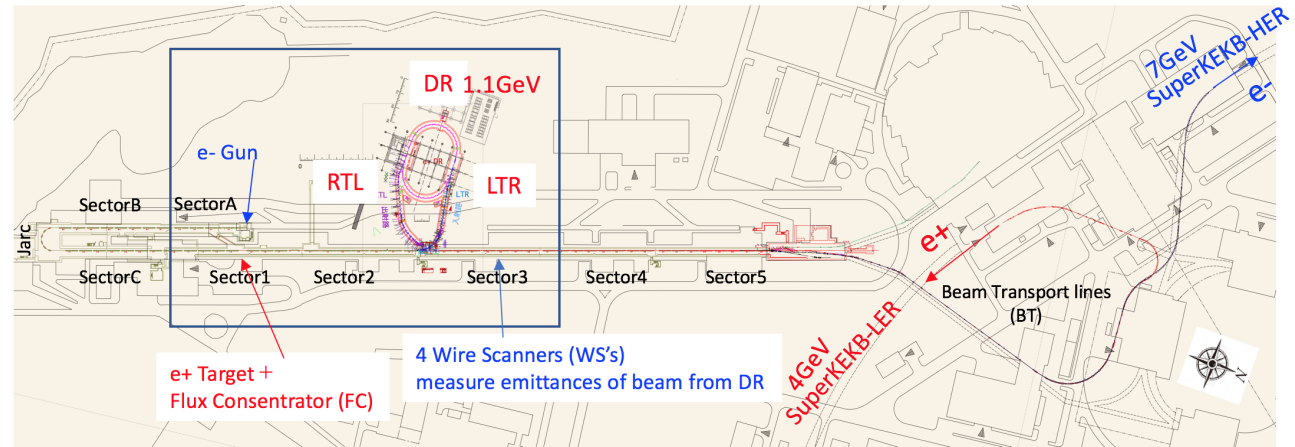


Figure 1: The LINAC consists of eight sectors from Sector A, B, C, and 1 to 5 starting from the electron sources. The electron and positron beams are accelerated up to 7 GeV and 4 GeV, respectively, and are injected into the HER and LER of SuperKEKB via each beam transport line (BT). Both of the injection/extraction lines for the DR (LTR/RTL) have two arc sections with straight sections between them.

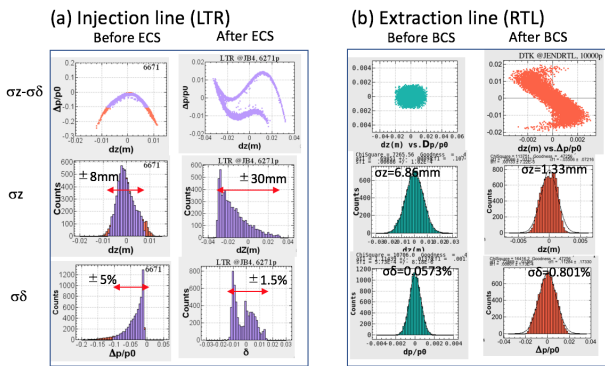


Figure 2: Simulated distributions of longitudinal phase space before and after ECS, and those of BCS.

the FC have a long energy-tail, which cannot be accepted in the DR even with ECS, we installed four collimators in the arc section of the LTR to prevent the tail particles with an energy deviation larger than 5% from passing through the LTR. The energy spread of remaining particles is compressed to $\pm 1.5\%$, the DR bucket height. The bunch length of the extracted beam from the DR is compressed from 6.6 mm to 1.3 mm with the BCS. Although for $V_c = 18.4$ MV, the bunch length is compressed to the minimum at the BCS exit, the voltage 21.5 MV was adopted, since the simulation shows that the energy spread at the injection point to LER is optimum, owing to gymnastics in the longitudinal plane in the downstream. Because the bunch length of the beam in the BCS and ECS is not negligible with respect to the frequency of S-band, an effect of RF curvature is visible as in “After ECS/BCS” in Fig. 2. With the parameters (R_{56} , V_c) as in Table 2, the beam can be transported without notable loss.

COMMISSIONING OF LTR

LTR commissioning was started on Jan. 23rd, 2018. Initially the beam was guided by inserting a beam shutter at the

end of the LTR to prevent the beam from going to the DR, and on the next day, reached the beam shutter. At that time, the FC was out of operation and the charge was 0.75 nC. The beam loss in the DR, LTR and RTL had to be strictly controlled because of the radiation limit. Figure 3 shows the beam optics of the LTR.

Tuning of LTR

Since the energy distribution is far from symmetry as shown in Fig. 2-(a), the information from beam position monitors (BPMs), which is the center of gravity of the beam, should be used with care for steering. Therefore, we first made core “Ginjo” [12] beam by using the four collimators. As shown in the upper row in Fig. 4, the highest energy could be definitely identified observing the profile monitor, and the energy peak of the beam was adjusted so as to be placed at the center of the vacuum chamber using the energy

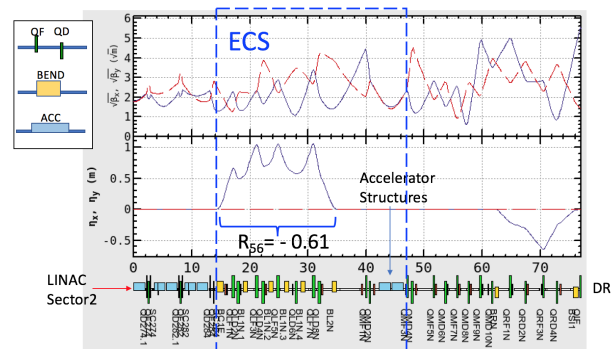


Figure 3: Beam optics of the LTR. The upper graph shows the horizontal (blue) and vertical (red) beta functions. The lower graph shows the horizontal dispersion. The horizontal axis is the distance in meter from the end of Sector 2 in the LINAC. R_{56} of the first arc of the LTR and V_c of the downstream accelerating structure constitute the ECS.

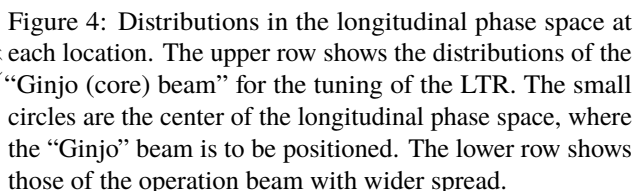


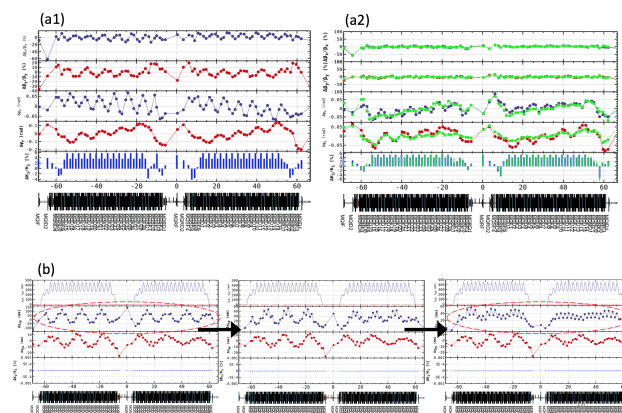
Figure 1 consists of two parts. Part (a) is a scatter plot showing the charge at the 2nd arc in nanocoulombs (nC) on the y-axis (ranging from 0 to 0.8) versus the SPEAR3W value in red on the x-axis (ranging from 0 to 10). The data points are blue circles, and a red line indicates the beam energy from the LINAC to the LTR. A blue arrow points to the right, labeled 'Beam Energy from LINAC to LTR'. A red arrow points to the left, labeled 'Energy Acceptance of LTR: $\pm 5\%$ '. A blue hatched area on the left is labeled 'Cut by the Collimators'. Part (b) is a schematic diagram of the LTR showing the beam energy and acceptance at various points. The diagram shows a central oval representing the LTR, surrounded by various components. The beam energy is indicated by a blue arrow pointing to the right, and the energy acceptance is indicated by a red arrow pointing to the left. The diagram also shows the charge at the 2nd arc and the SPEAR3W value at various points.

Measured energy acceptance of the LTR 1st arc by using the “Ginjo” beam is shown in Fig. 5-(a). It is cut by the collimator during operation where the low energy beam of the 1st arc passes indicated by the hatching on the left side of the figure. Parameters of ECS and injection to the DR were searched only using the “Ginjo” beam, and once determined, these parameters were maintained during operation unless the machine is unexpectedly changed. After tuning process using “Ginjo” beam is completed, we returned to the ordinary beam, opened the collimators, and increased the beam energy by +5% with respect to the “Ginjo” beam. By this tuning, the beam is rotated in the longitudinal phase space around a center, where the “Ginjo” beam sits on, and in the physical space, the beam with energy spread of $\pm 5\%$ is placed around the center of beam pipe. Other basic beam-based measurements, such as 3-BPM measurements, local bump study, beam based alignment (BBA), and single kick response measurement, had been performed.

Table 3: Measured emittances by wire scanners at the straight section of LTR when the FC is stand-by and on.

	FC: Stand-by	FC: 5kV
$\gamma\epsilon_x$ [μm]	2350	2760
$\gamma\epsilon_y$ [μm]	2310	2450
Charge [nC]	0.75	1.5

COMMISSIONING OF DR



The first commissioning of the DR and the beam transportation to the end of LINAC were done in three days. That includes tunings of timing for the injection septum, kickers and BPMs in the DR, orbit tuning, RF capturing, tunings of timing for the extraction septum, kickers and BPMs in the RTL, orbit tuning, BCS of the RTL, and LINAC tuning. The optics corrections of the DR were made with the results shown in Fig. 6. As shown in Fig. 6-(a2), the β -functions are somewhat improved by the correction, but phase advances

have systematic slopes. After the β correction the dispersion corrections were made, but a pattern of horizontal dispersion remained. Further investigation is necessary.

In the first stage of operation a model parameter of fringe field was wrongly assigned. Even after the correction the fudge factors of 5% still exists in the arc quads. Calibration of bends and quads in the field measurement might be a reason.

COMMISSIONING OF RTL

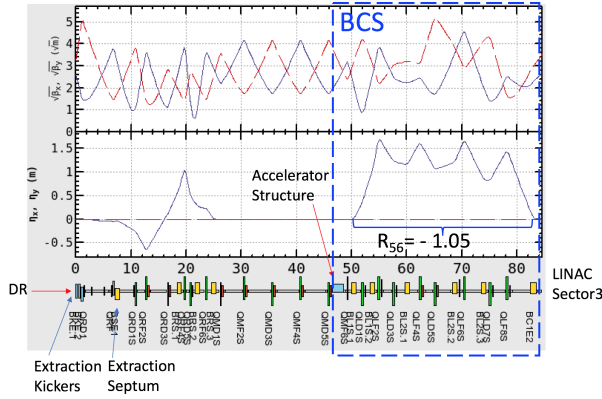


Figure 7: Beam optics of the RTL. The BCS consists of V_c of the S-band acceleration tube installed in the straight section of RTL and R_{56} of the second arc. The notations are same as Fig. 3.

Tuning of BCS from RTL to the End of LINAC

On February 8th, as the beam revolved around the DR, it was extracted to the RTL at the same time, and on February 10th the beam after tuning of the BCS was transported to the beam dump at the end of the LINAC. The low emittance beam from the DR has fewer worries of beam loss unlike at the time of the LTR, but there is a difficulty in keeping the low emittance during the transportation. Since the beam distribution from the DR is clearly Gaussian, it is already “Ginjo” beam. Figure 7 shows the optics of the RTL.

Tuning procedures of BCS paralleled with those of ECS; RF of BCS was set to standby first, the orbit was corrected, and the RF was turned on, finding the zero-cross phase. Since a streak camera in Sector 3 was not ready at that time, we identified a proper phase between two possibilities of 0 and π observing screen monitors where the horizontal dispersion exists. Actually however, it can also be confirmed by the fact that in the wrong phase, the beam does not pass well to Sector 5. After setting the phase of the BCS, we adjusted the RF phase of Sector 3 to 5. The energy spread at the end of LINAC was measured to be $\pm 0.3\%$ in full width with the screen monitor, which satisfies the requirement in Table 1.

EMITTANCE GROWTH

The emittances of the positron beam from the DR and RTL are measured at Sector 3 in LINAC with four wire scanners

as shown in Table 4. Assuming that the horizontal emittance is same as the design value of the DR, the emittance ratio of the DR is presumed to be less than 2.3%. The major issue is that the measured horizontal emittance at Sector 3 is larger than the design by a factor of 2.

Table 4: Measured emittances by wire scanners at Sector 3

	Measured Emittance	DR Design
$\gamma\epsilon_x$ [μm]	126 ± 8.2	64.3
$\gamma\epsilon_y$ [μm]	1.5 ± 0.1	

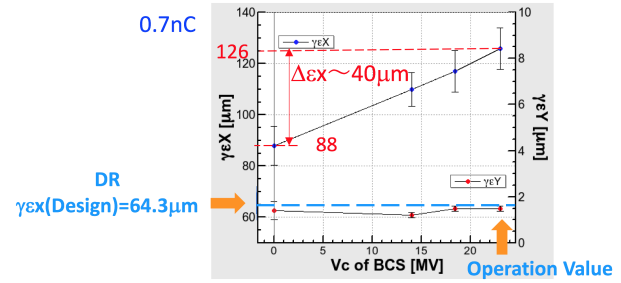


Figure 8: BCS-voltage dependence of the horizontal emittance. The blue and red dots show the measured normalized horizontal and vertical emittances. The blue dashed line shows the design emittance of the DR. The operation voltage of the BCS is 23 MV.

Table 5: Bunch charge dependence of the horizontal emittance

Charge [nC]	V_{BCS} [MV]	$\gamma\epsilon_x$ [μm]	$\gamma\epsilon_y$ [μm]
0.7	0	88 ± 7.6	1.4 ± 0.4
1.5	0	104 ± 7.4	3.7 ± 0.5

The measured emittances depend on BCS voltage as well as the bunch charge as shown in Fig. 8 and Table 5. The measured horizontal emittance depends on the bunch length and/or energy spread. The $\gamma\epsilon_x$ measured at Sector 3, even minimum of them, is larger than the design value of the DR. Furthermore, the larger emittances in both the horizontal and vertical planes are observed with higher bunch charge. We have checked a possibility that the emittance is caused by coherent synchrotron radiation (CSR) in the bending magnets at the arc sections of the RTL. The wake potential of the CSR is shown in Fig. 9 [15]. The resulting emittance growth by tracking simulation is shown in Table 6. The effect of the CSR on the emittance growth is negligibly small. Other possibilities are residual dispersion at the wire scanners, and the transverse wake field in Sector 3. Anyway, the measurement of the emittance in the DR is also necessary.

CONCLUSION

The commissioning of the LTR, DR, and the RTL for SuperKEKB were successfully done for a short time. No

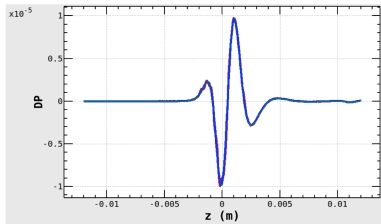


Figure 9: The wake potential of the longitudinal CSR of single-bunch effects in RTL. The vertical scale is the relative momentum change, $\Delta p/p$ for bunch charge 4 nC. The blue and red lines show the wake potential from the theoretical calculation and simulation, respectively.

Table 6: The effects of CSR on emittance

V_{BCS} [MV]	Q [nC]	$\Delta\epsilon_x/\epsilon_x$
21.5	0.7	3.2×10^{-6}
21.5	4.0	3.1×10^{-5}
0	4.0	1.1×10^{-8}

serious trouble occurred. The emittance of DR should be measured in the next run. An emittance growth from the DR to Sector 3 was observed. It depends on the BCS-voltage and bunch charge. More investigations should be done before Phase 3 operation.

REFERENCES

[1] Y. Ohnishi *et al.*, “Accelerator design at SuperKEKB”, *Prof. Theor. Exp. Phys.*, vol. 2013, no. 3, P. 03A011, Mar. 2013.
[2] T. Abe *et al.*, “Achievements of KEKB”, *PTEP* 2013(2013)03A001 DOI: 10.1093/ptep/pts102.
[3] M. Yoshida *et al.*, “Generation and Acceleration of Low-emittance, High-current Electron Beams for SuperKEKB”, in *Proc. LINAC’14*, Geneva, Switzerland, Sep.2014, pp. 21–25.

[4] T. Natsui *et al.*, TUT2H2 “Injector Linac Upgrade and New RF Gun Development for SuperKEKB”, *Proc. eeFACT2016*, Daresbury, UK, Oct. 24-27, 2016.
[5] T. Kamitani *et al.*, MOPRI004, “SuperKEKB Positron Source Construction Status”, *Proc. IPAC’14*, Dresden, Germany, Jun. 15-20, 2014.
[6] N. Iida *et al.*, THYA01, “Beam Dynamics in Positron Injector Systems for the Next Generation B-Factories”, *Proc. IPAC’11*, San Sebastian, Spain, Sep. 4-9, 2011.
[7] Y. Ohnishi *et al.*, TUT2H2, “Commissioning of the Phase-1 SuperKEKB B-Facility and Update on the Overall Status”, *Proc. NAPAC2016*, Chicago, USA, October. 24-27, 2016.
[8] M. Satoh *et al.*, THPOY027, “Commissioning Status of SuperKEKB Injector Linac”, *Proc. IPAC2016*, Busan, Korea, May. 9-13, 2016.
[9] Y. Ohnishi *et al.*, MOXAA02, “Highlights from SuperKEKB Phase 2 Commissioning”, *Proc. eeFACT2018*, Hong Kong, China, this workshop.
[10] K. Furukawa *et al.*, TUPAB01, “KEKB Injection Developments”, *Proc. eeFACT2018*, Hong Kong, China, this workshop.
[11] M. Kikuchi *et al.*, TUPEB054, “Design of Positron Damping Ring for Super-KEKB”, *Proc. IPAC’10*, Kyoto, Japan, May. 23-28, 2010.
[12] <https://www.sake-talk.com/rice-polishing-ratio/>
[13] N. Iida *et al.*, “Recent Progress of Wire Scanner Systems for the KEKB Injector LINAC and Beam Transport Lines”, *Proc. IPAC2000*, Vienna, Austria, pp. 1738-1740.
[14] H. Ikeda *et al.*, MOPA02, “Beam Diagnostics for SuperKEKB Damping Ring in Phase-II Operation”, *Proc. IBIC’18*, Shanghai, China, 2018.
[15] D. Zhou and Y. Seimiya, Private communication.

PERFORMANCE OF THE FCC-ee POLARIMETER

N. Y. Muchnoi*,

Budker Institute of Nuclear Physics, 630090 Novosibirsk, Russian Federation
also at the Novosibirsk State University, 630090 Novosibirsk, Russian Federation

Abstract

Inverse Compton scattering is the classical way to measure the electron beam polarization. Eligibility of the approach at high energy domain has been demonstrated by LEP [1, 2], HERA [3] and SLD [4] experiments. Fast measurement of beam polarization allows to apply the resonant depolarization technique for precise beam energy determination [5, 6]. The distinctive feature of the FCC-ee polarimeter is the registration of scattered electrons along with scattered photons. Polarimeter is designed to measure the transverse polarization of the non-colliding pilot bunch with 1% accuracy every second. Furthermore the same apparatus allows to measure the beam energy, longitudinal beam polarization (if any) and transverse beam positions/sizes at the place of installation.

INTRODUCTION

The illustration for the process of Inverse Compton Scattering (ICS) is presented in Fig. 1.

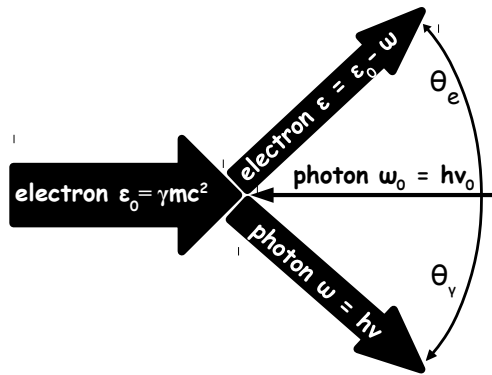


Figure 1: Inverse Compton scattering: the thickness of every arrow qualitatively reflects the energy of each particle. ω_0, ε_0 and ω, ε are the energies of the photon and electron in their initial and final states correspondingly, while θ_γ and θ_e are the scattering angles of photon and electron.

Considering an ultra-relativistic case ($\varepsilon_0, \varepsilon, \omega \gg \omega_0$) we introduce the universal scattering parameter

$$u = \frac{\omega}{\varepsilon} = \frac{\theta_e}{\theta_\gamma} = \frac{\omega}{\varepsilon_0 - \omega} = \frac{\varepsilon_0 - \varepsilon}{\varepsilon}, \quad (1)$$

bearing in mind the energy and transverse momenta conservation laws while neglecting the corresponding impacts of initial photon. Parameter u lies within the range $u \in [0, \kappa]$

and is limited from above by the longitudinal momenta conservation: κ is twice the initial energy of the photon in the rest frame of the electron, expressed in units of the electron rest energy:

$$\kappa = 4 \frac{\omega_0 \varepsilon_0}{(mc^2)^2} = 2 \times 2\gamma \frac{\omega_0}{mc^2}. \quad (2)$$

If the electron-photon interaction is not head on, the angle of interaction $\alpha \neq \pi$ affects the initial photon energy seen by the electron, and κ parameter becomes¹

$$\kappa(\alpha) = 4 \frac{\omega_0 \varepsilon_0}{(mc^2)^2} \sin^2 \left(\frac{\alpha}{2} \right). \quad (3)$$

Almost any experimental application of the backscattering of laser radiation on the electron beam for any reason implies the use of the scheme shown in Fig. 2. Laser radiation is inserted into the machine vacuum chamber, directed and focused to the interaction point where scattering occurs. The dipole is used to separate scattered photons (and electrons) from the electron beam, propagating in the machine's vacuum chamber. x -axis and z -axis define the coordinate system in the interaction point, the plane of the figure is the plane of machine, the vertical y -axis is perpendicular to the plane of figure. After the dipole, the coordinate system (x', z') is rotated by the beam bending angle θ_0 .

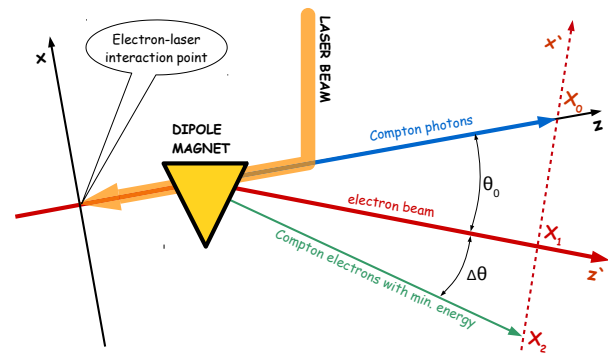


Figure 2: Regular layout of ICS experiments realization.

For the FCC-ee polarimeter we assume the interaction of laser radiation with electrons in the electron energy range $\varepsilon_0 \in [45 : 185]$ GeV. The energy of the laser photon ω_0 is coupled with the radiation wavelength in vacuum λ_0 : $\omega_0 = hc/\lambda_0$, where $hc = 1.239\,841\,93\,\text{eV} \cdot \mu\text{m}$. In particular when $\lambda_0 = 1\,\mu\text{m}$, $\varepsilon_0 = 100\,\text{GeV}$ and $\alpha = \pi$ one obtains the “typical” value of κ parameter for the FCC-ee case, $\kappa \approx 1.9$. Maximum energy of backscattered photon ω_{max} obviously

¹ this is correct when $\tan(\alpha/2) \gg 1/\gamma$.

* N.Yu.Muchnoi@inp.nsk.su

corresponds to the minimal energy of scattered electron ε_{min} , both values are easily obtained from definitions Eq. (1) – Eq. (3) when $u = \kappa$:

$$\omega_{max} = \frac{\varepsilon_0 \kappa}{1 + \kappa} \quad \text{and} \quad \varepsilon_{min} = \frac{\varepsilon_0}{1 + \kappa}. \quad (4)$$

Note that $\omega_{max} = \varepsilon_{min}$ when $\kappa = 1$. It's not hard to show that the scattering angles of photon θ_γ and electron θ_e (see Fig. 1) depend on u and κ as:

$$\theta_\gamma = \frac{1}{\gamma} \sqrt{\frac{\kappa}{u} - 1} \quad \text{and} \quad \theta_e = \frac{u}{\gamma} \sqrt{\frac{\kappa}{u} - 1}. \quad (5)$$

The electron scattering angle θ_e can not exceed the limit $\max(\theta_e) = \kappa/2 \cdot \gamma = 2\omega_0/mc^2$ and we see that this value does not depend on ε_0 .

ICS Cross Section

ICS cross section depends on polarization states of all initial and final particles [7]. It is common to average the polarization terms of the final states, then the cross section depends solely from the initial photon and electron polarizations. In order to describe polarization states of the laser and electron beams in the coordinate system x, y, z , presented in Fig. 2, let's introduce modified Stokes parameters.

- $\xi_\perp \in [0 : 1]$ and $\varphi_\perp \in [0 : \pi]$ are the degree of laser linear polarization and its azimuthal angle.
- $\xi_\cup \in [-1 : 1]$ is the sign and degree of circular polarization of laser radiation: $\sqrt{\xi_\perp^2 + \xi_\cup^2} = 1$.
- $\zeta_\perp \in [0 : 1]$ and $\phi_\perp \in [0 : 2\pi]$ are the degree of transverse e^\pm beam polarization and its azimuthal angle.
- $\zeta_\cup \in [-1 : 1]$ is the sign and degree of longitudinal spin polarization of the electrons: $\sqrt{\zeta_\perp^2 + \zeta_\cup^2} \in [0 : 1]$.

Then, the ICS cross section is described by the sum of three terms: $d\sigma = d\sigma_0 + d\sigma_\parallel + d\sigma_\perp$. These terms are: $d\sigma_0$ – unpolarized electron; $d\sigma_\parallel$ – longitudinal electron polarization; $d\sigma_\perp$ – transverse electron polarization:

$$\begin{aligned} \frac{d\sigma_0}{du d\varphi} &= \frac{r_e^2}{\kappa^2(1+u)^3} \left(\kappa(1 + (1+u)^2) - 4\frac{u}{\kappa}(1+u)(\kappa-u) \left[1 - \xi_\perp \cos(2(\varphi - \varphi_\perp)) \right] \right), \\ \frac{d\sigma_\parallel}{du d\varphi} &= \frac{\xi_\cup \zeta_\cup r_e^2}{\kappa^2(1+u)^3} u(u+2)(\kappa-2u), \\ \frac{d\sigma_\perp}{du d\varphi} &= \frac{-\xi_\cup \zeta_\perp r_e^2}{\kappa^2(1+u)^3} 2u\sqrt{u(\kappa-u)} \cos(\varphi - \phi_\perp). \end{aligned} \quad (6)$$

In Eq. (6) r_e is the classical electron radius and φ is the observer's azimuthal angle. As one can see from Eq. (6), the last term $d\sigma_\perp$, most important for FCC-ee polarimeter, can not modify the total cross section, which in absence of longitudinal polarization of electrons is obtained by integration

of $d\sigma_0$ only:

$$\begin{aligned} \sigma_0(\kappa) &= \frac{2\pi r_e^2}{\kappa} \left[\left(1 - \frac{4}{\kappa} - \frac{8}{\kappa^2} \right) \log(1 + \kappa) + \right. \\ &\quad \left. + \frac{1}{2} \left(1 - \frac{1}{(1 + \kappa)^2} \right) + \frac{8}{\kappa} \right]. \end{aligned} \quad (7)$$

In case when $\kappa \ll 1$ Eq. (7) tends to Thomson cross section $\sigma_0 = \frac{8}{3}\pi r_e^2 (1 - \kappa)$.

The above expressions are enough e. g. to start Monte-Carlo generator and allow further analysis of scattered particles distributions. The probability distribution of u is defined by the cross section Eq. (6). Then the required properties, like ω , ε , θ_e or θ_γ are obtained using Eq. (1) and Eq. (5). However, the influence of bending magnet in Fig. 2 on scattered electrons is not yet considered.

Bending of Electrons

Let's describe the dipole strength by the parameter B , assuming for the sake of brevity that it is proportional to the integral of magnetic field along the electron trajectory. The electron with energy ε will be bent to the angle $\theta = B/\varepsilon$ under the assumption that B is the same for all energies under consideration². By Eq. (1) we express the energy ε of scattered electron through the ICS parameter u : $\varepsilon = \varepsilon_0/(1 + u)$. This electron is bent by the dipole to the angle

$$\theta = \frac{B}{\varepsilon} = \frac{B}{\varepsilon_0} + u \frac{B}{\varepsilon_0} = \theta_0 + u\theta_0, \quad (8)$$

i. e. θ is the sum of the beam bending angle θ_0 and the bending angle $\Delta\theta = u\theta_0$, caused by electron energy loss in ICS. Both θ_0 and $\Delta\theta$ are shown in Fig. 2 for the maximum possible u value $u = \kappa$. Note that $\kappa\theta_0$ does not depend on ε_0 as well as $\max(\theta_e)$. In ref. [8] it was suggested to use the ratio $\Delta\theta/\theta_0 = \kappa$ for beam energy determination at ILC.

Let us introduce a new designation $\vartheta_x \equiv \gamma(\theta - \theta_0) = u\theta_0$ which is the angle $\Delta\theta$, measured in units of $1/\gamma$. The electron scattering angle in ICS, expressed in the same units, is $\vartheta = u\sqrt{\kappa/u - 1}$ as it follows from Eq. (5). Combining bending and scattering angles and splitting ϑ into x and y components we get:

$$\begin{aligned} \vartheta_x &= \sqrt{u(\kappa - u)} \cos \varphi + u\vartheta_0, \\ \vartheta_y &= \sqrt{u(\kappa - u)} \sin \varphi. \end{aligned} \quad (9)$$

Since backscattered photons are not bent by the dipole, the photon transverse angles (Eq. (5)) in the same space and in the same units, according to similar considerations, are the following:

$$\begin{aligned} \eta_x &= -\sqrt{\kappa/u - 1} \cos \varphi - \vartheta_0, \\ \eta_y &= -\sqrt{\kappa/u - 1} \sin \varphi. \end{aligned} \quad (10)$$

² The validity of this assumption will be discussed on page 3.

POLARIMETER

The polarimeter will be installed in the FCC-ee section shown in Fig. 3. After the dispersion suppressing dipole magnet, about 100 m of free beam propagation without multipole magnets is reserved for separation of the ICS photons and electrons from the beam. The interaction of the pulsed

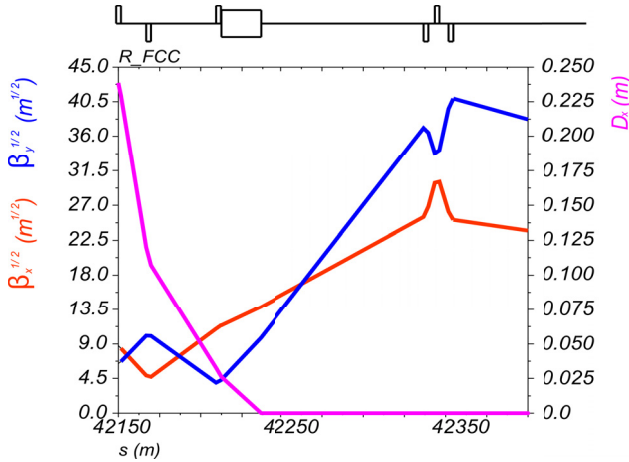


Figure 3: Polarimeter location with respect to FCC-ee lattice.

laser beam with the electron beam occurs just between the dipole and preceding quadrupole, where there is a local minimum of vertical β -function. In Fig. 4 there is the sketch of the polarimeter apparatus arrangement in horizontal plane.

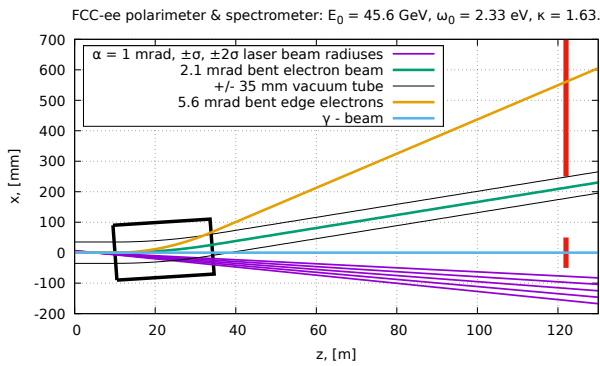


Figure 4: Sketch of the polarimeter: dipole ($L = 24.12$ m, $\theta_0 = 2.13$ mrad, $B = 0.0135$ T, $R_0 = 11302$ m), vacuum chamber, particle trajectories. Red vertical bars on the right side show the location of the scattered particles detectors – 100 m away from the center of the dipole.

The laser radiation $\lambda_0 = 532$ nm is inserted to the vacuum chamber from the right and focused to the interaction point ($z=5$ m). The laser spot transverse size at i. p. is $\sigma_0 = 0.25$ mm. According to Fig. 4, laser-electron interaction angle is $\alpha = \pi - 0.001$ and the relative difference between κ from Eq. (2) and $\kappa(\alpha)$ from Eq. (3) is as small as $2.5 \cdot 10^{-7}$.

Spectrometer

Figure 4 helps to understand how much could be the difference of the B-field integral, seen by the electrons with

different energies. All of the electrons enter the dipole of length L along the same line – the beam orbit. Then, the radius of trajectory will be dependent on the electron energy. Let R_0 to be the radius of an electron with energy ε_0 and $\theta_0 = L/R_0$ is the beam bending angle. The minimal radius of an electron after scattering on the laser light will be $R_0/(1 + \kappa)$. After passing the dipole these two electrons will have the difference $\Delta x \approx \kappa L \theta_0 / 2$ in transverse horizontal coordinates. With the parameters of Fig. 4 this difference is $\Delta x \approx 43$ mm. The length of the trajectories of these two electrons inside the dipole will be also different, i. e. even in case of absolutely uniform dipole their field integrals will not be the same. With rectangular pole shape exact expression for relative difference of the lengths of trajectories is:

$$\frac{\Delta L}{L} = \frac{1}{1 + \kappa} \frac{2}{\theta_0} \arcsin \left(\frac{\theta_0}{2} (1 + \kappa) \sqrt{1 + \left(\frac{\kappa \theta_0}{2} \right)^2} \right) - \frac{2}{\theta_0} \arcsin \left(\frac{\theta_0}{2} \right). \quad (11)$$

As we see this relative difference depends on θ_0 and κ only. With the set of parameters taken from Fig. 4, i. e. $\theta_0 = 2.13$ mrad and $\kappa = 1.63$, $\Delta L/L = 2.63 \cdot 10^{-6}$.

The result of this section is the proof of the validity of assumption about the equality of the integrals of the magnetic field for the electron beam and scattered electrons. This assumption was found to be rather accurate for the dipole with perfectly uniform field, however *shorter dipole is much more preferable* in order to decrease Δx and hence have less concerns about the field quality.

Scattered Photons & Electrons

The Monte-Carlo generator was created to obtain the 2D (x, y) distributions of scattered photons and electrons at the detectors, located as it was shown in Fig. 4. The ICS parameters are: $\varepsilon_0 = 45.6$ GeV and $\omega_0 = 2.33$ eV. The spectrometer configuration is described by the beam bending angle $\theta_0 = 2.134$ mrad, the lengths of the dipole $L = 24.12$ m and two spectrometer arms. First arm $L_1 = 117$ m is the distance between laser-electron IP and the detector. Second arm $L_2 = 100$ m is the distance between the longitudinal center of the dipole and the detector.

The impact of the electron beam parameters is accounted by introducing the angular spreads according to the beam emittances $\epsilon_x = 0.27$ nm and $\epsilon_y = 1$ pm. The horizontal and vertical electron angles x' and y' in the beam are described by normal distributions standard deviations $\sigma_x = \sqrt{\epsilon_x/\beta_x}$ and $\sigma_y = \sqrt{\epsilon_y/\beta_y}$. The generator is arranged as follows:

- raffle $u \in [0, \kappa]$ and $\varphi \in [0 : 2\pi]$ according to 2D function $d\sigma(u, \varphi)$ Eq. (6)),
- raffle x' and y' according to corresponding normal distributions,
- obtain photon X_γ, Y_γ and electron X_e, Y_e transverse coordinates at the detection plane:

$$\begin{aligned} X_y &= x' L_1 - \frac{L_1}{\gamma} \sqrt{\kappa/u - 1} \cos \varphi - \theta_0 L_2, \\ Y_y &= y' L_1 - \frac{L_1}{\gamma} \sqrt{\kappa/u - 1} \sin \varphi, \\ X_e &= x' L_1 + \frac{L_1}{\gamma} \sqrt{u(\kappa - u)} \cos \varphi + u \theta_0 L_2, \\ Y_e &= y' L_1 + \frac{L_1}{\gamma} \sqrt{u(\kappa - u)} \sin \varphi. \end{aligned} \quad (12)$$

The results of such a simulation for an electron beam with $\zeta_{\perp} = 25\%$ vertical ($\phi_{\perp} = \pi/2$) spin polarization are presented in Fig. 5 and Fig. 6. The difference between the figures is the laser polarization $\xi_{\cup} = +1$ (Fig. 5) and $\xi_{\cup} = -1$ (Fig. 6). The 2D distributions for both photons and electrons are plotted along the same horizontal axis x , where $x = 0$ corresponds to the position of the electron beam. The detectors for scattered particles are located outside the machine vacuum chamber. The scattered electrons distribution starts from $x = 40$ mm: this is the radius of the vacuum chamber.

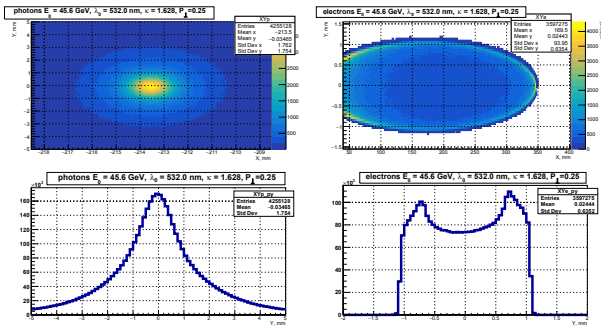


Figure 5: MC results, $P_{\perp} = \xi_{\cup} \zeta_{\perp} = 0.25$ and $\phi_{\perp} = \pi/2$.

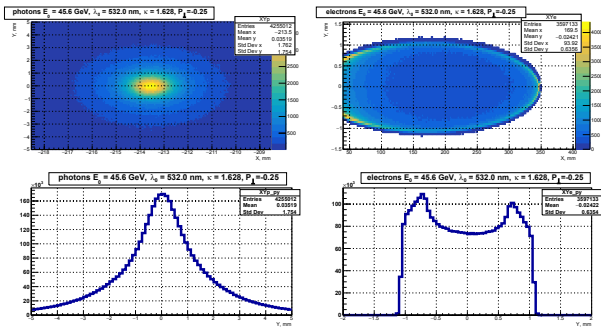


Figure 6: MC results, $P_{\perp} = \xi_{\cup} \zeta_{\perp} = -0.25$ and $\phi_{\perp} = \pi/2$.

The 1D distributions in the bottom of each figure are the projections of 2D distributions to the vertical axis y . The mean y -values of these distributions are shifted up or down from zero according to the presence of beam polarization and corresponding asymmetries in ICS cross section. In Fig. 7 all distributions are obtained by subtraction of corresponding distributions from Fig. 5 and Fig. 6. Detecting the up-down asymmetry in the distribution of laser backscattered photons is a classical way to measure the transverse polarization of the electron beam. In [9] it was proposed to use the up-down asymmetry in the distribution of scattered electrons for the

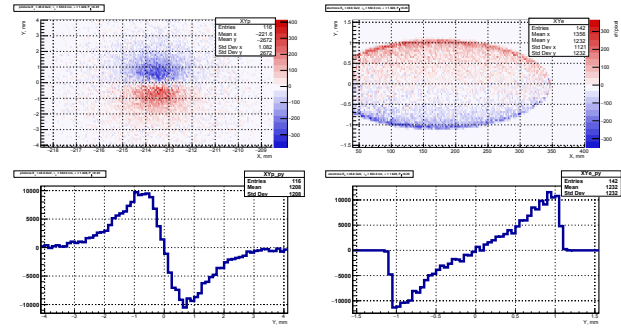


Figure 7: The difference between corresponding distributions in Fig. 5 and Fig. 6.

transverse polarization measurement at the ILC. It was suggested to measure the distribution of scattered electrons by silicon pixel detector.

Maximum up-down asymmetry in the distribution of scattered electrons occurs at the scattering angles of $\theta_e^* = \pm 2\omega_0/mc^2$, which is approximately $\pm 9 \mu\text{rad}$ (see Eq. (5) and Eq. (6)). Asymmetry can be observed only if the distribution is not blurred by the electron beam emittance. On the other hand, maximum up-down asymmetry in the distribution of scattered photons occurs at the scattering angles of $\theta_{\gamma}^* \approx 1/\gamma$ which is almost the same as θ_e^* in our particular case. But e. g. when beam energy is about 5 GeV, θ_{γ}^* is ten times larger than θ_e^* and the measurement of beam polarization by photons looks like more preferable. What are the benefits of scattered electrons against scattered photons for the FCC-ee polarimeter?

- Scattered electrons propagate to the inner side of the beam orbit, i. e. there is no direct background from high energy synchrotron radiation.
- Unlike photons, charged electrons are ready to be detected by ionization losses. The photons need to be converted to e^+e^- pairs: this leads either to low detection efficiency either to decrease in spatial resolution.
- Despite the fact that the fluxes of scattered photons and electrons are the same, the flux density of electrons is much lower due to bending and corresponding spatial separation by energies. Simultaneous detection of multiple scattered electrons thus is much easier.
- Analysis of the scattered electrons distribution allows to measure the longitudinal beam polarization as well as the transverse one.
- As one can observe from Figs. 5–7, change of laser circular polarization leads to a redistribution of the scattered electron density within a fixed elliptic shape of distribution. This fact potentially provides better systematic accuracy for beam polarization determination.

Nevertheless both photon and electron distributions are going to be measured by the polarimeter. First, to exploit

directly the LEP and HERA experience. Second, to be able to measure the center of the photon distribution in both x and y dimensions. The latter is required for direct beam energy determination, which will be discussed below.

SCATTERED ELECTRONS

This section owes its origin to the successful application of the method of direct electron beam energy determination by backscattering of laser radiation. The approach is based on the measurement of ω_{max} (see Eq. 4) in cases when this energy can be measured with good accuracy and in absolute scale. For the last years, the positive experience with this approach was accumulated at the low energy colliders VEPP-4M, BEPC-II and VEPP-2000 [10]. Despite the fact that this method is not directly applicable in FCC-ee case, let us try to figure out what can be learned from the elliptical shape of the distribution of scattered electrons, obtained by MC simulations above.

We return to the consideration of the spatial distribution of the scattered electrons. From Eq. (9) we obtain the square equation on u :

$$(\vartheta_x - u\vartheta_0)^2 + \vartheta_y^2 = u(\kappa - u), \quad (13)$$

with the roots $u^\pm =$

$$\frac{\kappa + 2\vartheta_0\vartheta_x \pm \sqrt{\kappa^2 - 4(\vartheta_x^2 + \vartheta_y^2(1 + \vartheta_0^2) - \kappa\vartheta_0\vartheta_x)}}{2(1 + \vartheta_0^2)}. \quad (14)$$

The average value of u and its limiting value for the large values of ϑ_0 do not depend on ϑ_y :

$$\langle u \rangle = \frac{u^+ + u^-}{2} = \frac{\kappa/2 + \vartheta_0\vartheta_x}{1 + \vartheta_0^2} \xrightarrow{\vartheta_0 \gg 1} \frac{\vartheta_x}{\vartheta_0}. \quad (15)$$

In the ϑ_x, ϑ_y plane all the scattered electrons are located inside the ellipse (what we have seen in Figs. 5, 6), described by the radicand in Eq. (14). The center of the ellipse is located at the point $[\vartheta_x = \kappa\vartheta_0/2; \vartheta_y = 0]$, its horizontal semiaxis is $A = \kappa\sqrt{1 + \vartheta_0^2}/2$ while the vertical (along ϑ_y) is $B = \kappa/2$. In particular, this means that

$$\vartheta_x^{max} = \frac{\kappa}{2} \left(\vartheta_0 + \sqrt{1 + \vartheta_0^2} \right) \xrightarrow{\vartheta_0 \gg 1} \kappa\vartheta_0. \quad (16)$$

Recall that according to notation introduced above, ϑ -s are the angles measured in units of $1/\gamma$, while θ -s are the angles in radians. In radians expression Eq. (16) looks like

$$\Delta\theta = \frac{\kappa}{2} \left(\theta_0 + \sqrt{1/\gamma^2 + \theta_0^2} \right) \xrightarrow{\theta_0 \gg 1/\gamma} \kappa\theta_0, \quad (17)$$

where $\Delta\theta$ and θ_0 were presented in Fig. 2. In order to rewrite the ICS cross section (Eq. 6) in ϑ_x, ϑ_y variables we calculate the Jacobian matrix $\mathbf{J} = \partial(\vartheta_x, \vartheta_y)/\partial(u, \varphi)$:

$$\mathbf{J} = \begin{bmatrix} \vartheta_0 + \frac{\kappa/2 - u}{\sqrt{u(\kappa - u)}} \cos \varphi & -\sqrt{u(\kappa - u)} \sin \varphi \\ \frac{\kappa/2 - u}{\sqrt{u(\kappa - u)}} \sin \varphi & \sqrt{u(\kappa - u)} \cos \varphi \end{bmatrix}. \quad (18)$$

The determinant of \mathbf{J} is:

$$\begin{aligned} \det(\mathbf{J}) &= \kappa/2 - u + \vartheta_0 \sqrt{u(\kappa - u)} \cos \varphi = \\ &= \sqrt{\kappa^2/4 - \vartheta_x^2 - \vartheta_y^2(1 + \vartheta_0^2) + \kappa\vartheta_0\vartheta_x}. \end{aligned} \quad (19)$$

Hence $dud\varphi = 2d\vartheta_x d\vartheta_y / \det(\mathbf{J})$, where “2” is due to the sum of “up” and “down” solutions of Eq. (14). Let us perform another change of variables: instead of ϑ_x, ϑ_y we introduce x and y . With these new variables the cross section exists inside the circle of radius $R = 1$ centered at $(x = 0; y = 0)$:

$$x = \frac{2\vartheta_x/\kappa - \vartheta_0}{\sqrt{1 + \vartheta_0^2}}, \quad y = \frac{\vartheta_y}{\kappa/2}. \quad (20)$$

Then:

$$\begin{aligned} dud\varphi &= \frac{\kappa dx dy}{\sqrt{1 - x^2 - y^2}}, \\ u = \langle u \rangle &= \frac{\kappa}{2} \left(1 + \frac{x\vartheta_0}{\sqrt{1 + \vartheta_0^2}} \right), \\ \sin(\varphi) &= \frac{y\kappa}{2\sqrt{u(\kappa - u)}}. \end{aligned} \quad (21)$$

In Eq. (21) the vertical transverse electron polarization ($\phi_\perp = \pi/2$) is assumed, then $\cos(\varphi - \phi_\perp) = \sin(\varphi)$. Considering backscattering of circularly polarized laser radiation ($\xi_\cup = \pm 1$) on the electron beam, where both vertical transverse ($\zeta_\perp \neq 0, \phi_\perp = \pi/2$) and longitudinal ($\zeta_\cup \neq 0$) polarizations are possible, we rewrite the cross sections Eq. (6):

$$\begin{aligned} \frac{1}{r_e^2} \frac{d\sigma_0}{dx dy} &= \frac{1 + (1 + u)^2 - 4(u/\kappa)(1 + u)(1 - u/\kappa)}{\kappa(1 + u)^3 \sqrt{1 - x^2 - y^2}}, \\ \frac{1}{r_e^2} \frac{d\sigma_\parallel}{dx dy} &= \xi_\cup \zeta_\cup \frac{u(u + 2)(1 - 2u/\kappa)}{\kappa(1 + u)^3 \sqrt{1 - x^2 - y^2}}, \\ \frac{1}{r_e^2} \frac{d\sigma_\perp}{dx dy} &= -\xi_\cup \zeta_\perp \frac{uy}{\kappa(1 + u)^3 \sqrt{1 - x^2 - y^2}}. \end{aligned} \quad (22)$$

Due to the term $\sqrt{1 - x^2 - y^2}$ in the denominator of Eq. (22) the cross section has singularity at the edge of a circle (ellipse), which however is integrable.

Fitting the Distribution

The detectors for scattered photons and electrons are going to be installed as it was shown in Fig 4. For the detection of scattered electrons we consider a position measurement using a silicon pixel detector (as in [9]) placed at the distance $L_1 = 117$ m from the Compton IP and $L_2 = 100$ m from the center of bending dipole. The active dimension of the detector is 400×4 mm², it is shifted horizontally 40 mm away from the beam axis, assuming the given size of vacuum chamber. The size of the pixel cell taken is 2×0.05 mm², i. e. there are 200 pixels in x and 80 pixels in y .

The pixel detectors for photons (with thin converter) and electrons will measure the x and y positions of each particle according to the scheme shown in Fig 8.

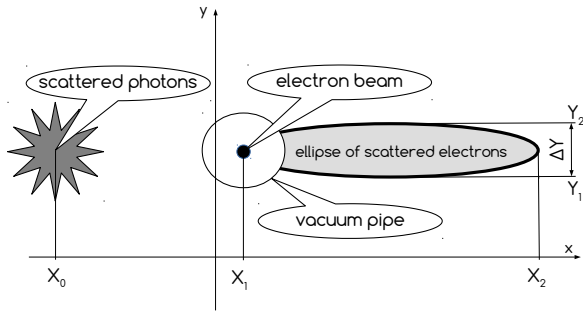


Figure 8: The xy plane of particle detection. X_0 is the horizontal center of gravity in the scattered photons distribution. X_1 is the electron beam position and at the same time – the left edge of the scattered electrons ellipse, while X_2 is the right side of the ellipse. Vertical size $\Delta Y = L_1 \cdot (4\omega_0/mc^2)$.

We will fit the MC distribution of scattered electrons by theoretical cross section Eq. (22). This cross section has a very sharp edge at $x^2 + y^2 = 1$ so the integrals of Eq. (22) over each pixel are required for fitting. The cross section dependencies on u and y are much smoother so it was found to be enough to take the integral

$$I_{xy} = \int_{x_0}^{x_1} \int_{y_0}^{y_1} \frac{dx dy}{\sqrt{1 - x^2 - y^2}} \quad (23)$$

over a rectangular pixel limited by $[x_0, x_1]$ in x and $[y_0, y_1]$ in y which is not difficult to do analytically.

The second step is to calculate the convolution of I_{xy} with the two-dimensional normal distribution of initial electrons: $P(x, y) = \frac{1}{2\pi\sigma_x\sigma_y} \exp\left(-\frac{x^2}{2\sigma_x^2} - \frac{y^2}{2\sigma_y^2}\right)$. It is not hard to show, that σ_x and σ_y are the RMS electron beam sizes (due to betatron and synchrotron motion) at the plane of detection. The last step is to account for the cross section dependencies on u and y parameters in Eq. (22).

The $F(x, y)$ function was built based on these considerations in order to describe the shape of the scattered electrons distribution, see Fig. 9. It has nine parameters except normalization:

- The first parameter is κ , defined in Eq. (2). This parameter is fixed according to approximate value of the beam energy cause $F(x, y)$ weakly depends on κ , $\pm 1\%$ changes does not matter on the fit results.
- The next four parameters are X_1, X_2, Y_1, Y_2 – positions of the ellipse edge, see Fig. 8.
- The sixth and seventh are responsible for polarization sensitive terms $P_\perp = \xi_\cup \zeta_\perp$ and $P_\parallel = \xi_\cup \zeta_\cup$. In the example below the fixed conditions are $\phi_\perp = \pi/2$ and $\zeta_\cup = 0$.
- The eighth and ninth are σ_x and σ_y – the electron beam sizes at the azimuth of the detector.

Fig. 9 shows the results of numerical experiment with the initial parameters $\varepsilon_0 = 45.6$ GeV, $\lambda_0 = 532$ nm, $P_\perp = 0.1$ and $2 \cdot 10^7$ scattering events. The distribution of scattered electrons was then fitted by the function $F(x, y)$.

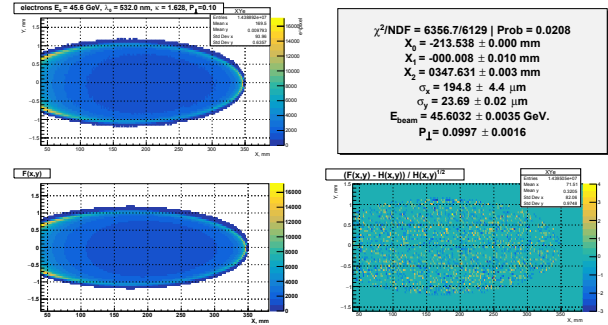


Figure 9: *Top-left*: MC distribution of scattered electrons $H(x, y)$. *Bottom-left*: function $F(x, y)$ after fitting. *Bottom-right*: normalized difference: $(F(x, y) - H(x, y))/\sqrt{H(x, y)}$. *Top-right*: the $F(x, y)$ parameters obtained by fitting (except X_0 , which is the mean x value of the photons distribution).

The parameters obtained directly from the fit are the ellipse edge positions X_1, X_2, Y_1, Y_2 , beam transverse sizes σ_x and σ_y and the beam polarization degree P_\perp . In this experiment P_\perp is measured with 1.6% accuracy (0.16% absolute accuracy). The beam energy, E_{beam} in Fig. 9, and its measurement accuracy (≈ 80 ppm) were evaluated from X_0, X_1 and X_2 :

$$E_{beam} = \frac{(mc^2)^2}{4\omega_0} \cdot \frac{X_2 - X_1}{X_1 - X_0}. \quad (24)$$

SCATTERING RATE

Consider CW TEM₀₀ laser radiation propagating along z -axis. If laser light of wavelength λ_0 is focused at $z = 0$ to the waist size of σ_0 , the beam size will evolve along z :

$$\sigma(z) = \sigma_0 \sqrt{1 + \left(\frac{z}{z_R}\right)^2}, \quad (25)$$

where $z_R = 4\pi\sigma_0^2/\lambda_0$ is the Rayleigh length. The optical intensity $[W/cm^2]$ in a Gaussian beam of power P [W] is:

$$I(r, z) = \frac{P}{2\pi\sigma(z)^2} \exp\left(-\frac{r^2}{2\sigma(z)^2}\right). \quad (26)$$

Far field divergence is $\theta = \sigma_0/z_R = \lambda_0/4\pi\sigma_0$. Laser radiation power is the number of photons emitted per second:

$$P = dE/dt = h\nu \cdot dN/dt \quad [J s^{-1}]. \quad (27)$$

Thus the longitudinal density of laser photons along z is: $\rho_\parallel = dN/dz = P\lambda_0/hc^2$ $[cm^{-1}]$. Consider an electron ($v/c \approx 1$) propagating towards the laser head sea with small incident angle α as illustrated by Fig. 10. The photon target

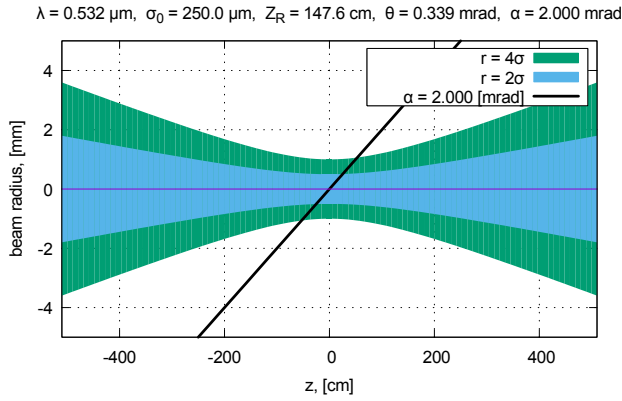


Figure 10: An electron (the black sloping line) passing through the laser beam waist.

density for this electron is defined as:

$$\rho_{\perp} = \rho_{\parallel} \frac{(1 + \cos \alpha)}{2\pi\sigma_0^2} \int_{-\infty}^{\infty} \frac{\exp\left(-\frac{z^2 \tan^2 \alpha}{2\sigma(z)^2}\right)}{1 + (z/z_R)^2} dz \quad [\text{cm}^{-2}]. \quad (28)$$

Scattering probability W is determined by the product of ρ_{\perp} and the scattering cross section. The latter is defined by Eq. (7) and depends on κ parameter, see Fig. 11.

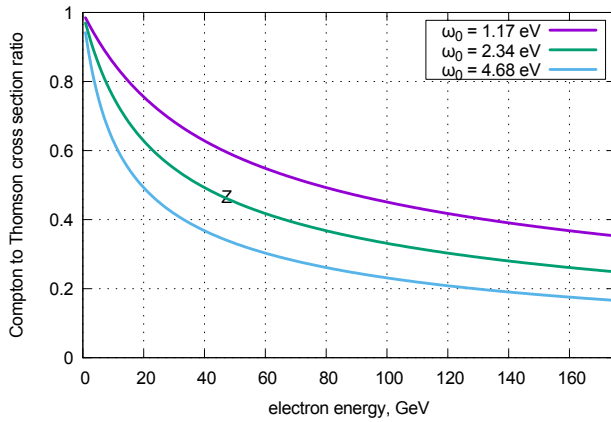


Figure 11: The ratio of the ICS cross section to Thomson cross section vs electron energy.

Maximum scattering probability W_{max} is reached in case $\alpha = 0$ and at low energy with Thomson cross section $\sigma_T = 0.665$ barn.

$$W_{max} = \frac{\sigma_T}{\pi\sigma_0^2} \frac{P\lambda_0}{hc^2} \int_{-\infty}^{\infty} \frac{dz}{1 + (z/z_R)^2} = \frac{4\pi\sigma_T P}{hc^2} = \frac{P}{P_c}, \quad (29)$$

where $P_c = \hbar c^2 / 2\sigma_T \approx 0.7124 \cdot 10^{11}$ [W] is the power of laser radiation required for 100% scattering probability. We see that W_{max} depends neither on the radiation wavelength λ_0 nor the waist size σ_0 , but on the laser power only. A low energy electron bunch with $0.7 \cdot 10^{11}$ population colliding

head-on with 1 W of laser radiation will produce one Compton scattering event – this is true if the transverse sizes of the electron bunch is much smaller than the laser ones.

The loss in scattering probability when $\alpha \neq 0$ is defined by the ratio of angle α to the laser divergence angle $\theta = \sigma_0/z_R$. Since the mirror is required in order to deliver the laser beam to IP, θ should be always smaller than α : this ratio finely will describe the laser and electron beam separation at the place of mirror installation (see Fig. 4). If we define the “Ratio of Angles” as $R_A = \alpha/\theta$, probability loss will be expressed as:

$$\eta(R_A) = \frac{W(\alpha)}{W_{max}} = \frac{1}{\pi} \int_{-\infty}^{\infty} \exp\left(-\frac{x^2 R_A^2}{2(1+x^2)}\right) \frac{dx}{1+x^2}. \quad (30)$$

The result of numerical integration is presented in Fig. 12.

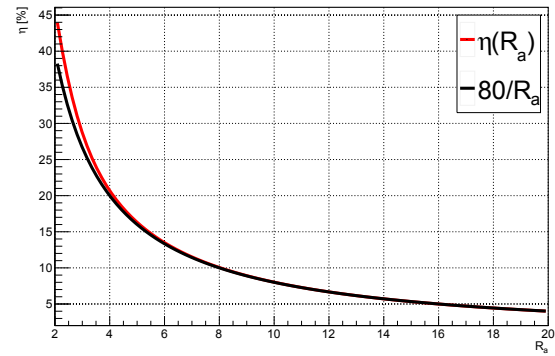


Figure 12: $\eta(R_A)$ vs R_A by Eq. (30) and its approximation.

At the FCC-ee there will be polarized pilot bunches for regular beam energy measurement by resonant depolarization. So the laser system should provide the backscattering on a certain electron bunch: the laser operation in CW mode is thus not possible. The FCC-ee revolution frequency ≈ 3 kHz is comfortable for solid-state lasers operating in a Q-switched regime. The laser pulse propagation can be described as:

$$\rho_{\parallel}(s, t) = \frac{N_{\gamma}}{\sqrt{2\pi}c\tau_L} \exp\left(-\frac{1}{2}\left(\frac{s-ct}{c\tau_L}\right)^2\right), \quad (31)$$

where τ_L and E_L are pulse duration and energy, $N_{\gamma} = E_L \lambda / hc$. Scattering probability for $\alpha = 0$ is:

$$W = \frac{P_L}{P_c} \cdot \int_{-\infty}^{\infty} \frac{\exp\{-2(xR_L)^2\}}{\pi(1+x^2)} dx, \quad (32)$$

where $P_L = E_L / \sqrt{2\pi}\tau_L$ is the instantaneous laser power and $R_L = z_R / c\tau_L$ is the “Ratio of Lengths”. The scattering probability for an arbitrary α is:

$$W = \frac{P_L}{P_c} \cdot \eta(R_L, R_A), \quad \text{where} \quad \eta(R_L, R_A) = \int_{-\infty}^{\infty} \frac{\exp\left(-x^2 \left(2R_L^2 + \frac{R_A^2}{2(1+x^2)}\right)\right)}{\pi(1+x^2)} dx. \quad (33)$$

The map of the efficiency $\eta(R_L, R_A)$, obtained by numerical integration of Eq. (33), is presented in Fig. 13.

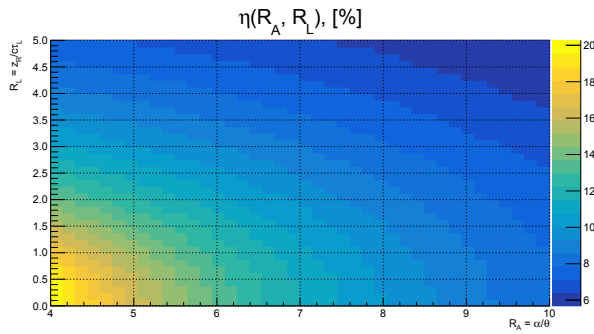


Figure 13: $\eta(R_L, R_A)$ color map.

Now we have enough instruments to estimate the flux of backscattered photons, obtained from one FCC-ee bunch in the configuration, shown in Fig. 4.

- Beam electron energy $E_{beam} = 45.6$ GeV.
- Laser wavelength $\lambda_0 = 532$ nm.
- Cross section (letter Z on Fig. 11): $R_x \approx 50\%$.
- Waist size $\sigma_0 = 0.25$ mm, $z_R = 148$ cm.
- Far field divergence $\theta = 0.169$ mrad.
- Interaction angle $\alpha = 1.0$ mrad (horizontal crossing).
- Laser pulse: $E_L = 1$ [mJ], $\tau_L = 5$ ns, $f = 3$ kHz.
- Instantaneous power: $P_L = 80$ kW, $P_L/P_c = 1.1 \cdot 10^{-6}$.
- Ratio of angles $R_A = 5.9$, ratio of lengths $R_L = 0.98$.
- $\eta(R_L, R_A) \approx 13\%$ (see Fig. 13).
- Scat. probability $W = P_L/P_c \cdot R_x \cdot \eta(R_L, R_A) \approx 7 \cdot 10^{-8}$.
- $N_e = 10^{10}$ e^\pm /bunch: $\dot{N}_\gamma = f \cdot N_e \cdot W \approx 2 \cdot 10^6$ [s $^{-1}$].
- Average laser power is $P = f \cdot E_L \approx 3$ W.

The influence of the electron beam sizes on the above estimations was not considered cause here it is nonessential.

SUMMARY

The electron beam polarimeter for the FCC-ee project has been considered. With the laser system parameters, described in the latter section, it allows to measure transverse beam polarization with required 1% accuracy every second. With the suggested scheme, this apparatus can also measure the beam energy, longitudinal beam polarization, beam position and transverse beam sizes at the place of installation. The statistical accuracy of direct beam energy determination is $\Delta E/E < 100$ ppm within 10 s measurement time. The

possible sources of systematical errors require additional studies. The best case of such studies would be the experimental test of the suggested approach on low-emittance and low-energy electron beam.

REFERENCES

- [1] M. Placidi and R. Rossmanith, “ e^+e^- polarimetry at LEP”, *Nucl. Instrum. Meth.*, A274:79, 1989.
- [2] L. Knudsen, J.P. Koutchouk, M. Placidi, R. Schmidt, M. Crozon, J. Badier, A. Blondel, and B. Dehning, “First observation of transverse beam polarization in LEP”, *Physics Letters B*, 270(1):97–104, nov 1991.
- [3] D.P. Barber, H.-D. Bremer, M. Böge, R. Brinkmann, W. Brückner, Ch. Büscher, M. Chapman, K. Coulter, P.P.J. Delheij, M. Düren, E. Gianfelice-Wendt, P.E.W. Green, H.G. Gaul, H. Gressmann, O. Häusser, R. Henderson, T. Janke, H. Kaiser, R. Kaiser, P. Kitching, R. Klanner, P. Levy, H.-Ch. Lewin, M. Lomperski, W. Lorenzon, L. Losev, R.D. McKeown, N. Meyners, B. Micheel, R. Milner, A. Mücklich, F. Neunreither, W.-D. Nowak, P.M. Patel, K. Rith, Ch. Scholz, E. Steffens, M. Veltri, M. Vetterli, W. Vogel, W. Wander, D. Westphal, K. Zapfe, and F. Zetsche, “The HERA polarimeter and the first observation of electron spin polarization at HERA”, *Nuclear Instruments and Methods in Physics Research Section A: Accelerators, Spectrometers, Detectors and Associated Equipment*, 329(1-2):79–111, may 1993.
- [4] M. Woods, “The Scanning Compton polarimeter for the SLD experiment”, In *High-energy spin physics. Proc. 12th International Symposium, SPIN 96, Amsterdam, Netherlands, September 10-14, 1996*, pages 843–845, 1996.
- [5] Aleksandr N Skriskii and Yurii M Shatunov, “Precision measurements of masses of elementary particles using storage rings with polarized beams”, *Soviet Physics Uspekhi*, 32(6):548–554, 1989.
- [6] L. Arnaudon, L. Knudsen, J.P. Koutchouk, R. Olsen, M. Placidi, R. Schmidt, M. Crozon, A. Blondel, R. Aßmann, and B. Dehning, “Measurement of LEP beam energy by resonant spin depolarization”, *Physics Letters B*, 284(3-4):431–439, jun 1992.
- [7] V.B. Berestetskii, E.M. Lifshitz, and L.P. Pitaevskii. *Quantum Electrodynamics*. Butterworth-Heinemann, 1982. pp. 354–368.
- [8] N. Muchnoi, H.J. Schreiber, and M. Viti, “ILC beam energy measurement by means of laser compton backscattering”, *Nuclear Instruments and Methods in Physics Research Section A: Accelerators, Spectrometers, Detectors and Associated Equipment*, 607(2):340–366, aug 2009.
- [9] Itai Ben Mordechai and Gideon Alexander, “A Transverse Polarimeter for a Linear Collider of 250 GeV e^\pm Beam Energy”, In *Helmholtz Alliance Linear Collider Forum: Proc. the Workshops Hamburg, Munich, Hamburg 2010-2012, Germany*, pages 577–590, Hamburg, 2013. DESY.
- [10] M. N. Achasov and N. Yu. Muchnoi, “Laser backscattering for beam energy calibration in collider experiments”, *JINST*, 12(08):C08007, 2017.

RESONANT DEPOLARIZATION AT Z AND W AT FCC-EE

I. A. Koop[†]

Budker Institute of Nuclear Physics,
also at Novosibirsk State University,

Novosibirsk State Technical University, [630090] Novosibirsk, Russia,

Abstract

Both future 100 km in circumference electron-positron colliders CEPC and FCC-ee need know beams energies with the extreme precision of 1–2 ppm. This can be done only with the help of Resonant Depolarization (RD) technique. Still, some beam parameters of these machines, like energy spread and damping decrements, are so high near 80 GeV per beam, that it is required special consideration and tricks to overcome the difficulties.

The author has written simple spin tracking code, which simulates main features of the RD process in presence of continuous energy diffusion due to synchrotron radiation fluctuations.

It was shown by this study, that the applicability of the RD method is limited by the effect of widening of the central and side band peaks of the spin precession spectrum when the synchrotron tune Q_s is chosen too low, say below $Q_s=0.05$. In this case spin precession lost its resonant nature due to overlap of the wide central spectrum peak with the nearby synchrotron side bands.

Dependencies of the spectrum peaks width from various beam parameters and a new RD-procedure recipe are presented.

INTRODUCTION

Beam emittances in FCCee are so small, that all spin resonances with the betatron motion frequencies are suppressed and their influence on the spin motion is negligible. Truly, at 80 GeV beam energy (spin tune $\nu_0 = \gamma a = 181.5$) the horizontal and the vertical beam emittances are expected to be $\varepsilon_x = 0.84$ nm and $\varepsilon_y = 1.7$ pm, respectively [1]. At Z ($\nu_0 = 103.5$) these emittances are of the same order, but optics for Z is slightly different [2].

The code ASPIRRIN [3, 4] provides reliable estimation of the strengths of the so-called “intrinsic” resonances $\nu_0 = \nu_{\pm k} = Q_y \pm k$. In Fig.1 are presented the modules of few resonance harmonics in the vicinity of Z-peak, while same plot for the W energy range is shown in Fig.2.

One can see that the maximal spin perturbation value does not exceed $w_k = 8 \cdot 10^{-5}$. This is much below of the critical level $(w_k)_{crit} = 0.01$ - a value which may shift the fractional part of the spin tune by $\delta\nu \approx (w_k)_{crit}^2 = 0.0001$ —the wanted accuracy of the fractional part of the tune measurement ($\Delta\nu = \nu_0 \cdot \Delta E/E = (100 \div 180) \cdot 10^{-6} \approx 10^{-4}$).

Taking all this into account, we concentrate now our attention on a study of integer resonances and their

synchrotron side band satellites. These resonances are driven by the closed orbit distortions or by the longitudinal magnetic field. The last is just the case in the detector region.

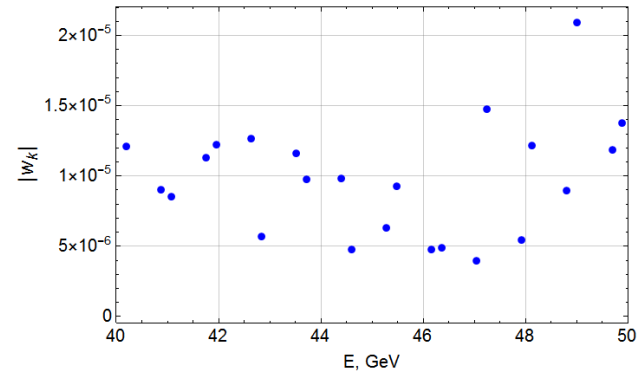


Figure 1: The strengths of few intrinsic resonances in vicinity of Z-peak beam energy.

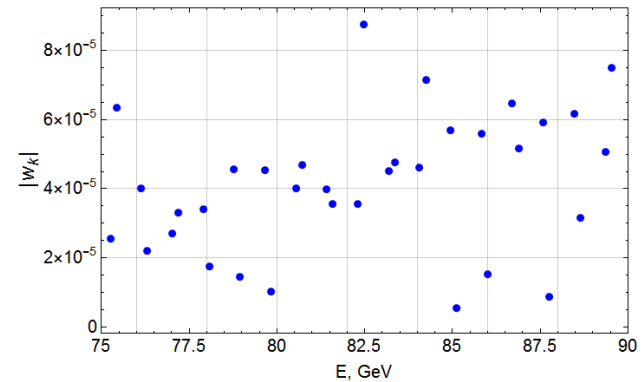


Figure 2: The strengths of few intrinsic resonances near the W-threshold beam energy.

CLOSED ORBIT DISTORTIONS

Sensitivity to misalignment of quads is very high in future electron-positron colliders. This can be expressed via the so-called spin-orbit response function $F_3(\theta)$, which defines the strength of the integer spin resonance $\nu_0 = k$ via the convolution of $F_3(\theta)$ with the dimensionless vertical orbit curvature $\Delta K_x(\theta)$ [3, 4]:

$$w_k = \frac{1}{2\pi} \int_0^{2\pi} F_3(\theta) \cdot \Delta K_x(\theta) d\theta.$$

In Fig.3 as example is plotted the module of $F_3(\theta)$ function for FCC-ee at 45.6 GeV calculated by the code ASPIRRIN. Its average value in arcs is about 250 and

[†] koop@inp.nsk.su

increases to about 1500 in the final focus and few other quads. With such high sensitivity the average errors of the arc's quads alignment should be much smaller than the expected level $\sigma_y = 0.05 \div 0.10$ mm to have all integer harmonics below the critical value $(w_k)_{crit} = 0.01$. But we, in fact, shall suppress only two most dangerous harmonics: say with $k=103$ and $k=104$, if $\nu_0 \approx 103.5$. This can be done with the well-known technique of harmonic spin matching [5, 6].

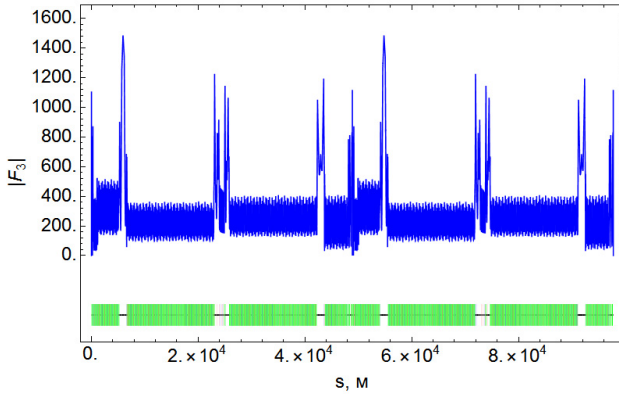


Figure 3: Spin response function $|F_3|$ for the vertical orbit distortions in FCC-ee at 45.6 GeV.

SPIN TRACKING CODE ALGORITHM

Author has written a simple code which performs a Monte-Carlo simulation of the spin motion of ensemble of particles, which are subjected to synchrotron oscillations with their amplitude variation due to radiation damping and quantum fluctuations of SR. I do not consider the betatron oscillations due to reasons discussed above. This greatly simplifies the task. Now we are interesting only by the synchrotron motion parameters and not by any details about the ring lattice.

I do in fact the turn by turn matrix transformation of the synchrotron and spin variables. The synchrotron map is described as follows. We start from the equation:

$$w_k = \frac{1}{2\pi} \int_0^{2\pi} F_3(\theta) \cdot \Delta K_x(\theta) d\theta.$$

It describes the evolution of the relative energy deviation $\delta = \Delta E/E$ with the constant damping decrement λ and

the synchrotron frequency $Q_s = \sqrt{Q_0^2 - \lambda^2}$. The solution at the azimuth θ is:

$$\begin{pmatrix} \delta(\theta) \\ q(\theta) \end{pmatrix} = e^{-\lambda\theta} \begin{pmatrix} \cos(Q_s\theta) & \sin(Q_s\theta) \\ -\sin(Q_s\theta) & \cos(Q_s\theta) \end{pmatrix} \begin{pmatrix} \delta(0) \\ q(0) \end{pmatrix}.$$

Here $q(\theta) = (\delta'(\theta) + \lambda\delta(\theta))/Q_s$ is the conjugate variable for the energy deviation $\delta(\theta)$. The synchrotron tune Q_s is small. Therefore we typically choose $\theta=2\pi$ as a period for spin and energy mapping.

We place the random Gaussian law energy jumps at the beginning of each turn. Their sigma value is adjusted so, as to receive the required equilibrium energy distribution.

Particles spins are rotated two times per turn. First time at the beginning of each turn θ_j by the spin perturbation frequency w_j :

$$w_j = w_0 + w_{RF} \cdot \cos(\nu_{RF}\theta_j).$$

Here w_0 states for the static rotation around the longitudinal or radial axis, while w_{RF} is the spin rotation amplitude generated by the RF flipper/depolarizer operated at frequency tune ν_{RF} . The second rotation represents the spin transformation done in the arc. In this stage each particle is rotated individually, according to its energy, around the vertical axis.

DEPOLARIZATION RATES EVALUATIONS

Running the spin tracking code with different spin tunes, I got the depolarization rate dependence from this tune, see Fig.4. The results in this plot are presented in the form of asymptotic polarization degree attainable in presence of the depolarization effects due to radiative diffusion caused by the quantum fluctuations of SR.

The equilibrium is established between two opposite processes: the Sokolov-Ternov - polarizing one and the concurrent - depolarizing due to chromatic nature of spin perturbation, which was chosen be $w=0.001$. The polarization degree was calculated as the ratio:

$$P = 92.6\% \left(1 + \tau_{ST}/\tau_{Dep}\right)$$

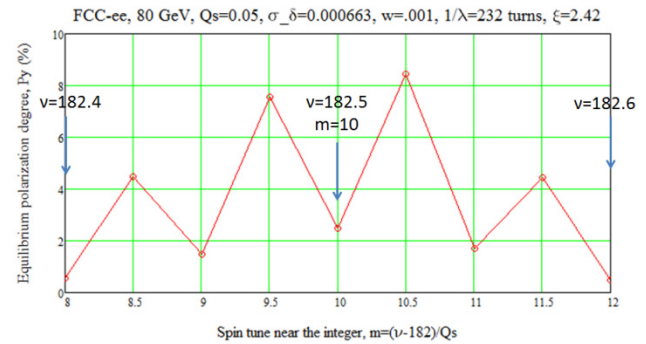


Figure 4: Equilibrium Sokolov-Ternov polarization degree in FCC-ee at 80 GeV with the spin perturbation harmonic $w=0.001$ and the synchrotron tune $Q_s=0.05$.

We see that polarization drops down at all synchrotron side band resonances $\nu_0 = k \pm mQ_s$, where the integer m is the order of a satellite. Also it is interesting that region near the half-integer spin tunes looks most favourable to get the highest polarization degree.

SINGLE PARTICLE PRECESSION SPECTRUM

One can ask the question: how looks the precession spectrum for a single particle? To answer this question I run my code for 40000 turns and got the plot presented in the Fig.5. The average particle's energy was set to 80.41 GeV, which corresponds to the spin tune $\nu_0 = 182.481$.

This peak is the highest at the plot. But just nearby one can see the mirror symmetric side band satellite $\nu = \{\nu_0\} + Q_s = 0.531 \rightarrow 0.469$. This complicates a task of finding of the central peak in measurements with RD.

Other beam parameters in this run are: energy spread $\sigma_\delta = 0.000663$, synchrotron tune $Q_s = 0.05$, the decrement of synchrotron oscillations $\lambda = 1/232$.

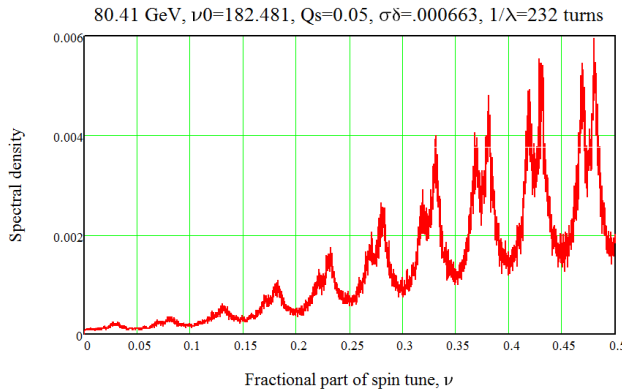


Figure 5: Spectrum of spin precession of a single particle which makes 40000 revolutions around the ring.

Besides of difficulties with presence of many peaks in the spectrum, there appears another problem for RD – each peak became very wide and beam became depolarized before RF-flipper's frequency crossed the centre of the spectrum central peak.

To overcome this difficulty, I propose to change slightly the standard RD procedure. Instead of continues scan by the RF-flipper's frequency, we can switch it on for short time periods to depolarize a beam partially. Then one shifts the flipper's frequency by a large step and turns it on again, and so on and forth. The result of the simulation of this depolarization procedure is shown in Fig.6.

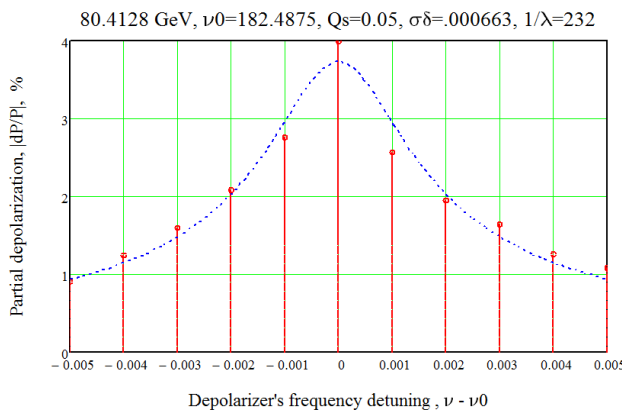


Figure 6: Tune scan by the depolarizer, which produces only the partial depolarizations at the selected frequency points.

The line shape fitting function (dotted blue) is:

$$f(\nu) = A \frac{\Delta}{\Delta^2 + (\nu - \nu_0)^2}$$

It has three free parameters A, Δ, ν_0 . But we are mainly interesting only by the centre of a peak position ν_0 .

The overall accuracy of presented here procedure is highly determined by the sensitivity of the polarimeter and from a level of the initial polarization degree. We will not discuss it here.

Finally, I will present below the functional dependence of the spectral line width Δ from the main beam parameters. I do not pretend on very high precision of the found fitting function, but it shows more or less well - which parameters are most important to make the spectrum peaks as narrow as possible.

$$\Delta = 0.0035 \frac{\lambda}{0.000686} \left(\frac{\nu_0 \sigma_\delta}{182.425 \cdot 0.00663} \right)^{2.5} \left(\frac{0.05}{Q_s} \right)^3$$

Obviously, the peak's width is proportional to the synchrotron decrement λ , but depends much stronger from the spin tune ν_0 , beam relative energy spread σ_δ and from the synchrotron tune Q_s . For given accelerator without wigglers the energy dependence is very strong:

$$\Delta \sim E^8$$

Therefore, this effect plays important role only at W threshold and not at Z !

Unfortunately, we have not a freedom to vary the machine and beam parameters as we want. They have very large influence also on the other collider's properties, like the attainable luminosity et cetera. Therefore it is very important to support any RD measurement by the full computer model of that procedure.

CONCLUSION

Spin tracking of the motion of a single particle reveals the dependence of the spectrum line width from the synchrotron tune and other beam parameters. This width becomes very large for chosen value of the synchrotron tune $Q_s = 0.05$ at W and the standard RD procedure becomes not applicable. The proposed above new RD procedure (by steps) works well even in cases when a width of the spin resonance became very large. That is just the case with $Q_s = 0.05$. Still the accuracy of a method needs to be studied further. The second order terms in orbital motion also contribute to the line width [7] and even can lead to systematic errors in beam energy determination by the RD [8].

ACKNOWLEDGEMENTS

We thank A.V. Otboev for help with the ASPIRRIN code calculations.

REFERENCES

- [1] M. Boscolo, talk at FCC Weak 2018, Amsterdam, 2018.
- [2] K. Oide, talk at FCC Weak 2017, Berlin, 2017. Also see: K. Oide *et al.* "Design of Beam Optics for the FCC-ee Collider Ring", DOI: 10.18429/JACoW-IPAC2016-THPOR018 Conference: C16-05-08, p. THPOR018 Proceedings.

BEAM INSTRUMENTATION AT SUPERKEKB

G. Mitsuka*, M. Arinaga, J. W. Flanagan, H. Fukuma, H. Ikeda, H. Ishii,
S. Iwabuchi, K. Mori, E. Mulyani, M. Tejima, and M. Tobiyama,
KEK Accelerator Laboratory, 1-1 Oho, Tsukuba 305-0801, Japan

also at Graduate School for Advanced Study (SOKENDAI), 1-1 Oho, Tsukuba 305-0801, Japan
G. S. Varner, U. Hawaii, Dept. Physics and Astronomy, 2505 Correa Rd., Honolulu HI 96822, USA
G. Bonvicini, Wayne State U., 135 Physics Bldg., Detroit MI 48201, USA

Abstract

Phase 2 commissioning of the SuperKEKB electron-positron collider has been performed with final focus optics from February 8 to July 17, 2018. The main aims of Phase 2 commissioning were to verify the novel nano-beam collision scheme and achieve the machine luminosity $O(10^{34} \text{ cm}^{-2}\text{s}^{-1})$. The beam instruments including the bunch-by-bunch feedback and orbit feedback systems, which are central to the beam diagnostics at SuperKEKB, were successfully operated throughout Phase 2. In this talk, we will present the commissioning results focusing on beam diagnostics and show prospects for the final phase of commissioning from next spring.

INTRODUCTION

The SuperKEKB collider (2016–) is a major upgrade to the KEKB collider (1998–2010) at KEK. Colliding 7 GeV electrons in the high energy ring (HER) and 4 GeV positrons in the low energy ring (LER), with a factor of two higher beam currents and the novel nano-beam scheme [1], will provide 40 times larger luminosity than KEKB.

Commissioning of SuperKEKB has been proceeded along the following three periods. *Phase 1* from February 1 to June 28, 2016 aimed to perform scrubbing run for new vacuum chambers and low emittance tuning for new arc lattice. After closing Phase 1, the superconducting final quadrupoles (QCS) and the Belle II detector except for the inner silicon-based VXD tracking system were installed. *Phase 2* started on February 8, 2018 with commissioning of the positron damping ring (DR) and was followed by commissioning of the HER and LER from March 19 to July 17, 2018. The main parameters of the HER, LER, and DR at Phase 2 are summarized in Table 1. *Phase 3* physics operation is scheduled from March 2019 with the complete Belle II detector.

Main tasks of Phase 2 are first to achieve electron-positron collisions, second to verify the nano-beam collision scheme, and finally to establish control of beam-induced backgrounds resulting from low beta functions at the interaction point (IP).

Beam instruments at SuperKEKB are designed for beam diagnostics, e.g. establishing the circulating orbit, finding the beam-beam kick, accumulating large beam currents, etc. In the rest of this paper, we present the performance of beam instrumentation at Phase 2 and prospects for Phase 3.

* gaku.mitsuka@kek.jp

BEAM INSTRUMENTATION AT DR

Beam Position Monitor

There are totally 83 beam position monitors (BPMs) in the DR [2]. A BPM consists of four button electrodes with a diameter of 6 mm, where two electrodes are attached each other in one flange (see Fig. 1). We use the detection circuit VME 18K11 L/R that employs a log-ratio amplifier.

Figure 2 shows a schematic diagram of the BPM timing system. First, the main frequency divider generates bunch revolution timing that is synchronized with the injection bunch timing. Second, the 32 channel digital delay unit inserted between the main frequency divider and 18K11 further adjusts the timing offset. The second timing adjustment is needed for the timing differences $\sim 200 \text{ ns}$ owing to the BPM locations relative to the injection point and sizable cable lengths.

Table 1: Main parameters of the SuperKEKB HER, LER, and DR at Phase 2

	HER	LER	DR
Energy (GeV)	7	4	1.1
Circumference (m)		3016	135
Max. current (mA)	800	860	12
Bunch length (mm)	5	6	6.6
RF frequency (MHz)		508.877	
Harmonic number		5120	230
Betatron tune (H/V)	44.54/ 46.56	45.54/ 43.56	8.24/ 7.17
Synchrotron tune	0.02	0.018	0.025
T. rad. damp time (ms)	58	43	12
x-y coupling (%)	0.27	0.28	10
Emittance (nm)	3.2	4.6	29
Peak luminosity ($\text{cm}^{-2}\text{s}^{-1}$)		5.5×10^{33}	
Beam position monitor	486	444	83
Turn-by-turn monitor	69	70	83
Trans. FB system	2	2	1
Visible SR monitor	1	1	1
X-ray size monitor	1	1	0
Betatron tune monitor	1	1	1
DCCT	1	1	1
Bunch current monitor	1	1	1
Beam loss monitor	105 (IC) and 101 (PIN)		34

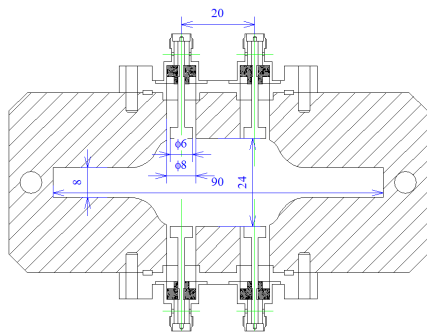


Figure 1: Cross section of the DR BPM.

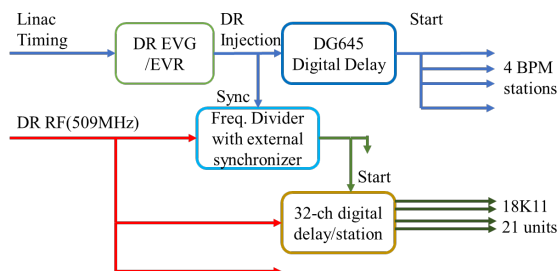


Figure 2: Block diagram of the DR BPM timing system.

The BPM block positions relative to the quadrupole magnets were surveyed using FARO 3D-ARM. The mean and 1σ standard deviation values for horizontal and vertical directions are (0.07 ± 0.47) mm and (-0.25 ± 0.29) mm, respectively. Gain difference among four electrodes was estimated as $< 8\%$ by the beam-based gain mapping method. The mean position resolution of the BPM system, 2–10 μ m (horizontal) and 2–3 μ m (vertical), was obtained using the 3-BPM method with 2k sample for 1 nC/bunch (see Fig. 3).

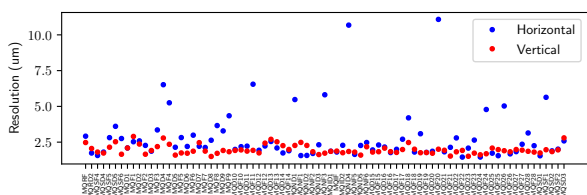


Figure 3: Position determination resolution of the DR BPMs.

Beam Size Monitors

Longitudinal and transverse beam sizes from injection to extraction were measured by a streak camera and a fast gated camera. Figure 4 shows examples of measured bunch lengths after the injection.

Beam Loss Monitors

Totally 34 ion chambers are installed along the DR and two beam transport lines. These monitors are sensitive to possible beam losses and inhibit the injection in case the loss exceeding the pre-defined threshold. We use the fast sample ADCs with digital peak hold circuit to monitor the integrated loss within 1 second.

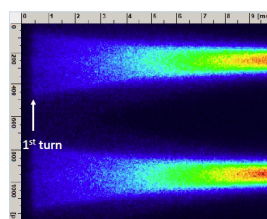


Figure 4: Measured bunch lengths in the DR after injection.

BEAM INSTRUMENTATION AT MAIN RINGS

Gated Turn-by-turn Monitor

The gated turn-by-turn monitor (GTBT, Fig. 5) is developed mainly for measurements of beam optics using a non-colliding bunch and injection beam orbit [3]. Four independent channels are each connected to a fast RF switch, a log-ratio beam signal detector, and a 14-bit ADC.

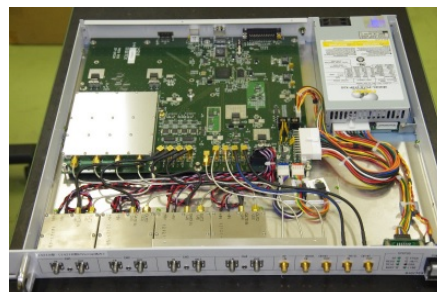


Figure 5: Photo of the gated turn-by-turn detector.

At SuperKEKB, optical functions such as betatron functions, x-y couplings and dispersions are usually measured by narrow-band BPMs using single kick method. Additionally, the GTBTs serve for measurements of the phase advances between the GTBTs. It is advantageous particularly around at the IP where the BPM gain and the BPM position relative to the QCS location are rather unreliable owing to fairly complex mechanical structure and large gain loss of the coaxial cables.

In the early stage of Phase 2, the GTBTs started the operation with the signal timing gate fully opened and successfully detected the injection beam orbit. Additional 19 GTBTs since Phase 2, located mainly around at the HER injection points and at the IP, contributed to smooth beam circulations. After beam storage we finely adjusted the ADC and gate timing. Note that the beam timing (definition of the bucket 0) was shifted wildly from Phase 1 mainly due to the insertion of the DR in the injection timing path.

Towards Phase 3, we plan to develop data processing software in the GTBTs' EPICS IOCs, such as a fast Fourier transform, correction for one-turn delay, etc. It enables quick optics measurements and GTBT data analyses in situ.

Photon Monitors

X-ray monitors (XRM) are installed one to each main ring primary for vertical beam size measurements [4]. Since the silicon pixel detectors and the fast readout systems developed under the US-Japan collaboration were not in time, we instead measured the vertical beam sizes by analyzing the X-ray-induced images projected on the scintillator screens (Fig. 6).

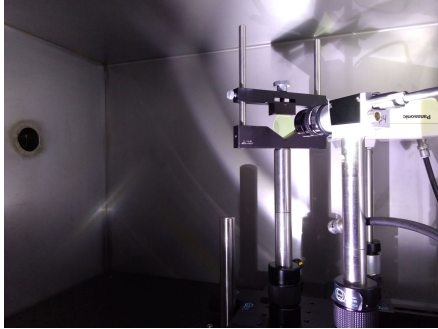


Figure 6: CCD camera and scintillator screen inside the XRM detector box.

At Phase 1 the LER XRM results on the vertical emittance (ε_y) agreed well with the optics estimation. However, in the HER, the XRM data gave 3.5 times larger ε_y compared with the optics estimation. The large ε_y might be caused by smearing effects $\sim 32 \mu\text{m}$ remaining in the HER XRM system.

For Phase 2, we replaced the Be filter 16 mm in thickness with 0.2 mm in thickness in the HER to reduce small angle scatterings through the Be filter. Such scatterings might result in large smearing effects. Additionally, β_y at the X-ray source point was changed from 7.6 m to 28 m. The Phase 2 measurements show that the smearing effects are reduced to $6.6 \mu\text{m}$, indicating that the measurable beam size in the HER can be down to $7 \mu\text{m}$. Detailed analyses are ongoing.

Another photon monitor, visible synchrotron radiation monitor (SRM), is also installed one to each main ring [5]. A SRM is essentially an interferometer and simultaneously measures horizontal and vertical beam sizes. After Phase 1, the diamond extraction mirrors located on the upstream of the visible SR lines in the both rings were replaced to gain 200 % large aperture, and baffles were added to reduce the stray light in the visible SR line. At Phase 2, beam size measurements worked well in the HER, but in the LER the SR spot seemed staggering as the beam current increased. We plan to open the mirror chamber for inspection.

The bunch lengths were measured using the streak camera in the both main rings. Figure 7 shows the measured bunch lengths in the HER and the LER. The bunch lengthening behavior in the HER is consistent with the KEKB, because most of the vacuum chambers in the arc and straight sections at SuperKEKB were inherited from KEKB. Though the bunch lengthening in the LER became moderated compared with Phase 1, it still shows unexpected larger lengthening with bunch current.

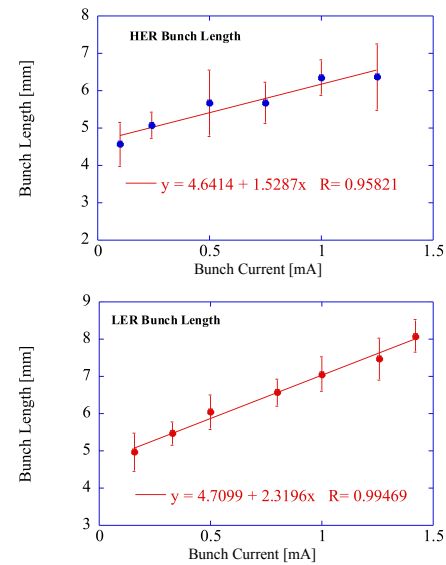


Figure 7: Measured bunch lengths in the HER (upper) and the LER (bottom) as a function of the bunch current.

Bunch Feedback System

Figure 8 shows the block diagram of the bunch-by-bunch feedback systems installed in the HER and LER [6]. The system consists of position detection systems, high speed digital signal processing systems with a base clock of 509 MHz (iGp12 [7]), and wide-band kickers. As we experienced at Phase 1, there was very strong transverse coupled-bunch instabilities in the early stage of Phase 2, which limited the maximum beam currents. By tuning the timing and phase of the transverse feedback systems, we successfully suppressed the coupled-bunch instabilities up to the maximum beam current $\sim 800 \text{ mA}$ with the minimum bunch separation of 4 ns.

We obtained many transient domain data in the LER during the beam study on electron cloud effects (ECEs). Figure 9 shows an example of growing and damping transients with the 4 ns bunch separation and the beam current of 300 mA in the vertical plane. The distribution of the unstable modes and the growth time show drastic changes compared with those in Phase 1. For example, the fitted growth time constant to the mode 2550 was about 3.9 ms, which is much slower than at Phase 1 ($\sim 0.8 \text{ ms}$). This tendency is presumably due to the counter measure to suppress ECEs in the drift space. The damping time constant is estimated as $< 1 \text{ ms}$, which is consistent with Phase 1.

Concerning longitudinal coupled-bunch instability, we could increase the threshold current from 660 mA (Phase 1) to 800 mA for the nominal collision (3.06 spacing). However, we still encountered the longitudinal coupled-bunch instability in the LER during the ECE study and a challenge to high beam current operation at the very end of Phase 2. The mode and threshold seemed depending on the head position of the vertical collimator nearest to the IP.

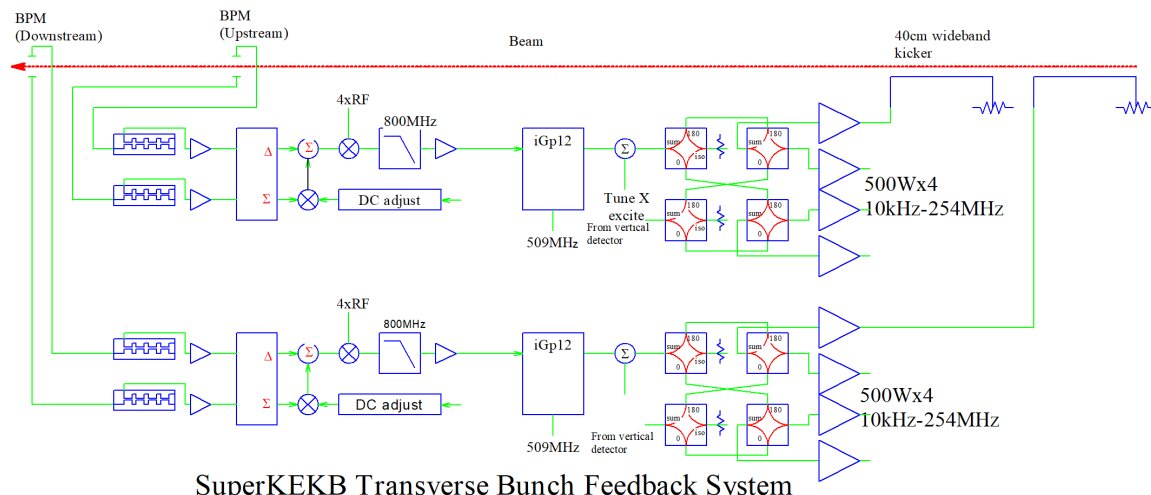


Figure 8: Block diagram of the transverse bunch feedback systems.

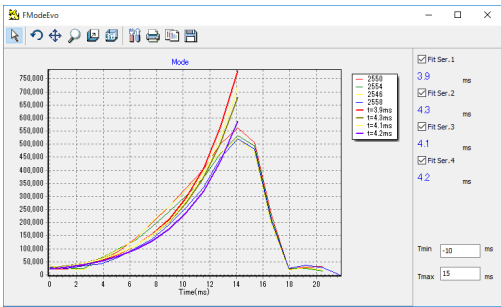


Figure 9: Evolution of the vertical unstable modes with by-2 pattern in the LER at a current of 300 mA.

The longitudinal bunch-by-bunch feedback systems in the LER were not fully functioning at Phase 2 simply due to lack of tuning time. Towards Phase 3 we add two more longitudinal feedback cavities with 1 kW of wide band feedback amplifiers per each cavity. The longitudinal system will be tuned in the early stage of Phase 3.

CONCLUSION

At Phase 2 we could successfully realize the first collision at SuperKEKB and achieve the luminosity $5.55 \times 10^{33} \text{ cm}^{-2} \text{ s}^{-1}$. It indicates no significant issue found in the nano-beam scheme. All the beam instrumentation systems at SuperKEKB showed excellent performances throughout Phase 2. Particularly newly operated system in the DR since Phase 2 enabled smooth beam commissioning. Further improvements of the instrumentation system are ongoing towards forthcoming Phase 3 physics operation.

ACKNOWLEDGEMENTS

The authors would like to thank the SuperKEKB commissioning group for their help in the operation. This work is partly supported by the US-Japan collaboration in High Energy Physics (R&D for SuperKEKB and the next generation high luminosity colliders).

REFERENCES

- [1] P. Raimondi in *2nd LNF Workshop on SuperB*, Frascati, Italy, March 16–18 2006. <http://www.lnf.infn.it/conference/superb06/>
- [2] H. Ikeda *et al.*, in *Proc. IBIC' 18*, Shanghai, China, MOPA02 (2018).
- [3] M. Tobiyama *et al.*, in *Proc. IBIC 2013*, MOPF32, 2013, Oxford, GB.; in *Proc. IBIC 2014*, WEPD05, 2014, Monterey, CA, U.S.A.
- [4] E. Mulyani and J.W. Flanagan, in *Proc. IBIC 2015*, Melbourne, p.377 (2015); in *Proc. IBIC 2016*, TUPG72, 2016, Barcelona, Spain.
- [5] T. Abe *et al.*, Technical Design Report of SuperKEKB, in preparation and to be published as a KEK report. An preliminary version is seen in <https://kds.kek.jp/indico/event/15914/>
- [6] M. Tobiyama *et al.*, in *Proc. PASJ2016*, TUOM06, Chiba, Japan.
- [7] Dimtel, Inc., <http://www.dimtel.com/>

FAST LUMINOSITY MONITORING ON THE SUPERKEKB COLLIDER (LUMIBELLE2 PROJECT)

P. Bambade, S. Di Carlo, D. Jehanno, V. Kubytskyi, C.-G. Pang, Y. Peinaud,
LAL, Univ. Paris-Sud, CNRS/IN2P3, Université Paris-Saclay, 91400 Orsay, France
Y. Funakoshi, S. Uehara, KEK, 305-0801 Tsukuba, Japan

Abstract

LumiBelle2 is a fast luminosity monitoring system prepared for SuperKEKB. It uses sCVD diamond detectors placed in both the electron and positron rings to measure the Bhabha scattering process at vanishing photon scattering angle. Two types of online luminosity signals are provided, Train-Integrated-Luminosity signals at 1 kHz as input to the dithering feedback system used to maintain optimum overlap between the colliding beams in horizontal plane, and Bunch-Integrated-Luminosity signals at about 1 Hz to check for variations along the bunch trains. Vertical beam sizes and offsets can also be determined from collision scanning. This paper will describe the design of *LumiBelle2* and report on its performance during the Phase-2 commissioning of SuperKEKB.

INTRODUCTION

SuperKEKB uses the so-called *nano-beam scheme* to reach a very high instantaneous luminosity of $8 \times 10^{35} \text{ cm}^2 \text{ s}^{-1}$ [1]. It consists of using a large crossing angle at the interaction point (IP) to enable colliding 2500 ultra-low emittance bunches with very small beam sizes (design value $\sigma_y \sim 50 \text{ nm}$). The luminosity is very sensitive to beam-beam offsets, e.g. caused by vibration of mechanical supports induced by ground motion. In order to maintain the optimum beam collision condition, orbit feedback systems are essential at the IP [2]. At SuperKEKB, the beam-beam deflection method is used for orbit feedback in the vertical plane, while in the horizontal plane, a dithering orbit feedback system using the luminosity as input, similar to that operated in the past at PEP-II, has been adopted [3,4].

For this purpose, a fast luminosity monitor based on sCVD diamond detectors, named *LumiBelle2*, was developed and tested during the Phase-2 commissioning of SuperKEKB. By measuring the rate of Bhabha events on each side of the IP at vanishing photon scattering angle, *LumiBelle2* can provide both Train-Integrated-Luminosity (TIL) signals and Bunch-Integrated-luminosity (BIL) signals simultaneously, over a large range of luminosities. The TIL signals are needed by the dithering orbit feedback system at 1 kHz, with relative precisions better than 1% [5]. BIL signals are important to probe potential luminosity differences between the numerous bunches along the trains. Another luminosity monitoring system named ZDLM (Zero Degree Luminosity Monitor) is also installed in the immediate vicinity. It uses Cherenkov and scintillator detectors [6], providing important complementary measurements. In addition, the ECL-LOM (Electro-

magnetic Calorimeter Luminosity On-line Measurement) is operated in the backward and forward end-caps of the Belle II detector, measuring the coincidence rates of back-to-back Bhabha events in the opposite sectors, with the ability to provide absolute values of the luminosity after proper internal calibration [7].

In this paper, we describe the design of *LumiBelle2*, including results of detector tests with a ^{90}Sr electron isotope source, the experimental set-up and the DAQ based on a FPGA, and then report on obtained luminosity monitoring performances, based on simulation and measurements pursued during the Phase-2 commissioning period, both with colliding beams, and with single beams, for background evaluations.

DESIGN AND LAYOUT

The placement of the *LumiBelle2* detectors was carefully studied to ensure sufficient signal rates while limiting the background contamination, taking also into account space constraints on the beam line. This resulted in choosing locations 10 and 29 m downstream of the IP in the Low Energy Ring (LER) and High Energy Ring (HER), to measure, respectively, Bhabha scattered positrons and photons [8]. To increase the rate of extracted positrons, a custom made beam pipe section with a depression of 15 mm and 45° inclined windows is used in the LER, see Fig. 1. A Tungsten radiator with an effective thickness of 4 Radiation Lengths (1 RL = 3.5 mm) was added to enhance the electromagnetic showers and boost the detection efficiency [9].

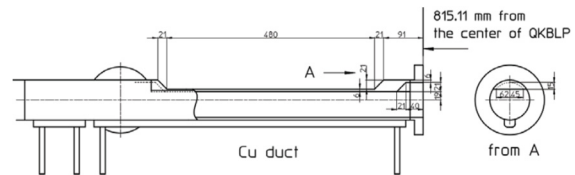


Figure 1: *LumiBelle2* LER window shaped beam pipe.

The RF of SuperKEKB is about 500 MHz, with bunches stored nominally almost every other bucket (so-called quasi 2-bucket fill pattern), which implies collisions every 4 ns. For BIL monitoring at high counting rate, signals from neighbouring bunches must be separated. A new diamond detector with a thickness of $140 \mu\text{m}$, coupled with a broadband 2 GHz 40 dB current amplifier from CIVIDEC [10] at the front-end, are used for this purpose. Low attenuation half-inch HELIAX coaxial cables are used to avoid signal broadening during the transfer to the data acquisition system in the Belle II Electronics Hut located about 100 m away.

Diamond Detector Test

Signal amplitudes and charge in the diamond detector were compared using data acquired with an oscilloscope, integrating the signal peaks to determine the charge, see Fig. 2. The good observed linearity makes it possible to sum signal amplitudes turn by turn to evaluate integrated relative Bhabha scattering rates for each bunch crossing.

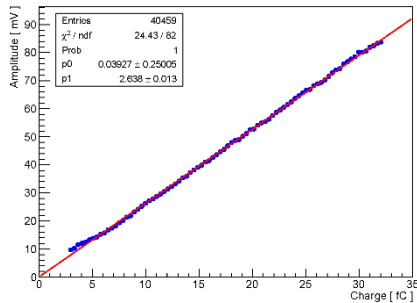


Figure 2: Relationship between signal amplitude and charge generated in the diamond detector.

The Constant Fraction Discrimination (CFD) method was used to study the timing performance of the diamond detector, using a fraction of 5%. As can be seen in Fig. 3, the signal rise time peaks at 0.88 ns, and most signals (more than 98%) are within 4 ns. The small impact from these partially overlapping pulses is at present neglected, but could in principle be considered as a correction.

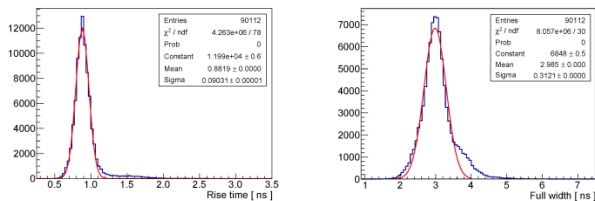


Figure 3: Distribution of rise times (l.h.s) and full widths (r.h.s) of the signal in the diamond detector.

Mechanical Set-up

The experimental layout for luminosity monitoring during the Phase-2 commissioning is shown in Fig. 4. It consists of pillars supporting three *LumiBelle2* diamond detectors and the ZDLM counters in both rings [6]. One of the *LumiBelle2* diamond sensors in each ring has a remotely controlled motor to enable scans in the horizontal plane over a range of 25 mm.

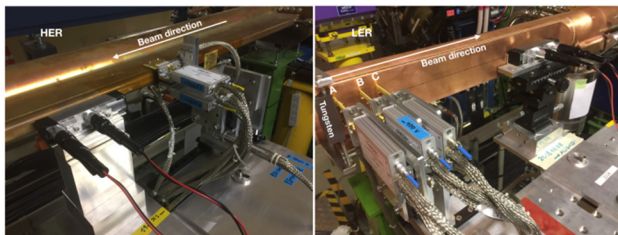


Figure 4: Experimental layout of *LumiBelle2* and ZDLM sensors in both rings (l.h.s. for HER and r.h.s. for LER).

Data Acquisition System

The DAQ developed for *LumiBelle2* is located in the Belle II Electronics Hut. A functional diagram is shown in Fig. 5. Four among the six provided signals are selected by connecting the corresponding cables to a GSPS 10-bit AC-coupled ADC board (FMC126, 4 DSP), requiring a clock at 1 GHz (twice the RF frequency). The four ADC digital outputs are then fed to a VIRTEX-7 FPGA board (VC707, Xilinx), which calculates the Train Integrated Luminosity (TIL), Bunch Integrated Luminosity (BIL), COUNT (event rate) and RAW SUM (direct summing all of samples) in real time, at a rate of up to 1 kHz, simultaneously for the four incoming inputs. The DAQ includes also a 16-bit DAC, providing eight analog outputs with 1 kHz bandwidth that can be configured independently to convert to any TIL, BIL, COUNT or RAW SUM values, from any of the four input channels.

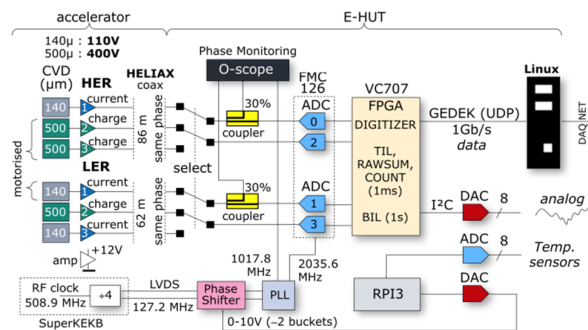


Figure 5: *LumiBelle2* DAQ functional diagram.

The DAQ was initially designed to handle a maximum rate of one bunch every 2 ns, corresponding to train patterns with all or almost all buckets filled. It makes use of two principles: (1) the luminosity is proportional to the amplitudes and rates of signal peaks, and (2) the pulses and RF clock are synchronous, to enable sampling all peaks simultaneously. As the ADC is AC-coupled, the mean value of the pulse train is always centred at 0 V, requiring therefore sampling also the pedestals between subsequent pulses. For bunches separated by 2 ns, this implies sampling at twice the RF frequency. As illustrated in Fig. 6, the current amplifiers used for the Phase-2 commissioning are fast enough only for the 4 ns bunch spacing used nominally at SuperKEKB. One sample (1) is then positioned on the peak (using the Phase Shifter shown on Figure 5 to find the optimum timing) and the pedestal is obtained from the third sample (+3). The luminosity process integrates over 1 ms the sum of all differences $\text{Diff}(n)$ between these samples above a defined threshold to provide the TIL value. The same process provides 5120 sums each second corresponding to the BIL value for each bucket. The COUNT value gives the total number of pulses during 1 ms, and therefore the ratio TIL/COUNT represents the mean pulse amplitude. The RAW SUM value calculates the sum of all samples above a defined threshold and is intended for some channels which use Charge Amplifiers with a 10 ns FWHM, and

that cannot be handled easily in terms of TIL and BIL. All the real time data are uploaded to a Linux machine through the GEDEK protocol (ALISE) over a UDP link at 1 GB/s, then converted into ROOT ntuple files and saved together with a number of related relevant machine parameters available through the EPICS protocol and important for the offline analysis. A subset of the *LumiBelle2* data were also uploaded to EPICS at a rate of about 1 Hz, for continuous display in the accelerator and Belle II control rooms. Moreover, for the purpose of the IP dithering orbit feedback, analog information from the DAC based on the 1 kHz TIL data was directly fed to the lock-in amplifier used by that system.

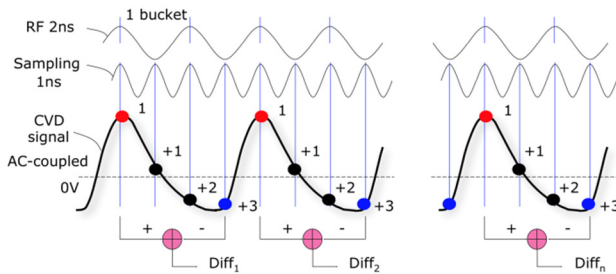


Figure 6: Illustration of DAQ signals processing for 4 ns bunch spacing.

RESULTS IN PHASE-2

The Phase 2 commissioning of SuperKEKB started with single beam testing and tuning in March 2018. Beam collisions were first achieved on April 25, 2018, followed by luminosity and background tuning and studies until July 17, 2018.

Background Evaluation

During single beam operation, *LumiBelle2* measured single beam loss rates, mainly resulting from Bremsstrahlung accompanying scattering of beam particles on the nuclei of the residual gas in the straight section upstream of the sensors, and from Touschek scattering [11]. Figure 7 gives an example of background rates measured by *LumiBelle2* together with the beam currents and pressures during successive fills in both rings.

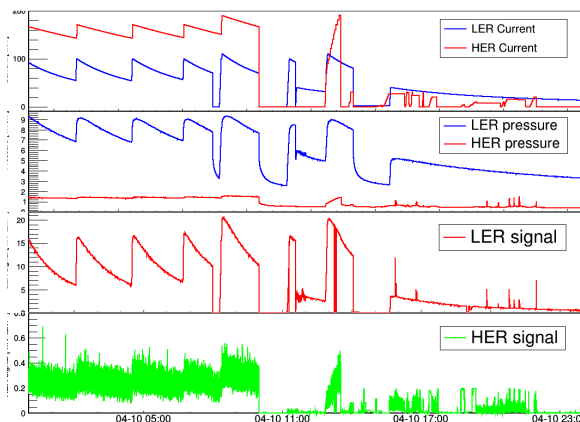


Figure 7: Example of background rates in *LumiBelle2* during single beam testing in 2018.

Good correlation was found between the measured background rates and key machine parameters in each ring. A detailed simulation of single beam loss rates was developed based on generating the basic processes and tracking final state particles with SAD, followed by modelling the signal collection in the detectors using GEANT4. Rather realistic estimates of the vacuum profile along the relevant parts of the interaction region, obtained by reweighting the measured vacuum levels using a detailed vacuum simulation [12], were obtained and used for the Bremsstrahlung process. Comparisons between simulation and *LumiBelle2* measurements as function of the product of current and pressure in each ring are shown in Figure 8. The simulation overestimates the loss rates in both rings by about 10% to 20%. This bias can be explained by the imperfect knowledge of the exact vacuum pressure in the narrow 1 cm radius beam pipe used at the IP, where most of the Bremsstrahlung scatters which can reach *LumiBelle2* sensors are produced. Also, the thresholds for signal detection used for the real and simulated data were not yet fully calibrated.

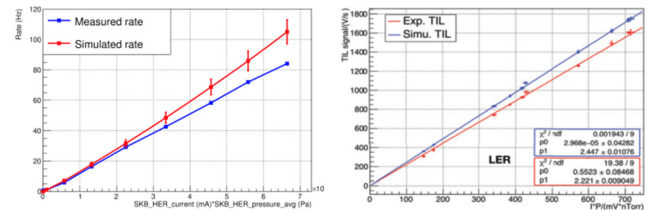


Figure 8: Comparison between the simulation and measurement in HER (lhs) and LER (rhs).

The linear dependence in Figure 8 indicates that the Bremsstrahlung process dominates the background loss rates in *LumiBelle2* in both rings. A dedicated “Touschek study” was pursued at the end of the Phase-2 commissioning period, consisting of taking single beam loss data as a function of varying vertical emittances (with $\beta_x^* = 200/100$ mm for LER/HER and $\beta_y^* = 3$ mm) to enable convenient extraction of the Touschek component from the background signals [11]. The Bremsstrahlung and Touschek processes represented about 87% and 13% fractions of the measured *LumiBelle2* single beam loss rates in this experiment, respectively, consistent with the prediction from the simulation for the corresponding beam parameters.

Train Integrated Luminosity Monitoring

LumiBelle2 and ZDLM luminosity monitors observed Bhabha scattering signals in both LER and HER when beams were collided for the first time on April 26, 2018 [6]. The luminosity monitors were then used for machine tuning and luminosity optimization during the entire commissioning.

While the Train-Integrated-Luminosity signal integrates the signals' amplitude at 1 kHz to meet the requirements of the dithering feedback system, integrating and recording this luminosity signal at 1 Hz provides relative lumi-

nosity information which is quite useful for collision tuning and studies in the accelerator control room. Figure 9 gives an example of the *LumiBelle2* luminosity signals, together with the beam currents and pressures in both rings. In general, the luminosity signals follow the changes in the product of beam currents in both rings.

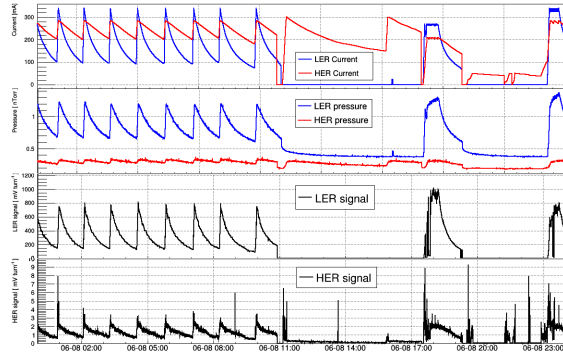


Figure 9: Example of *LumiBelle2* luminosity signals along with beam currents and pressures in both rings.

Thanks to the custom made beam pipe section with a depression of 15 mm and 45° inclined windows installed on the LER side, the corresponding Bhabha scattering positron signal collection was much more efficient than for the photons in the HER, see Figure 10 (lhs), while still reasonably proportional to each other. The LER signals were typically proportional to the product of the beam currents, as illustrated in Figure 10 (rhs), although vertical beam offsets at the IP can have a major impact, e.g. due to ground motion or other effects.

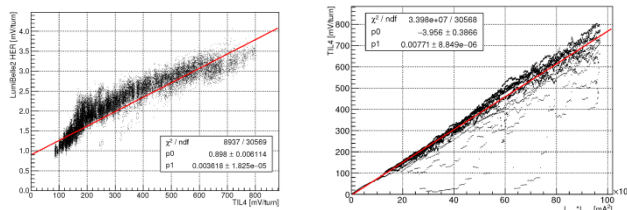


Figure 10: Luminosity signals in HER vs that in LER (lhs) and LER luminosity signal as function of product of beam currents in both rings.

Luminosity signals from ZDLM and ECL-LOM were compared with *LumiBelle2* in the LER, see Figure 11, showing good overall consistency. The ECL-LOM measurement has poor statistics because of the much lower Bhabha rates at finite scattering angle in the Belle II detector end-caps. Studying the short term fluctuations in the 1 kHz TIL data, the statistical precision for the luminosity measurement in the LER was found to be 2.27% for a luminosity of $1.85 \times 10^{33} \text{ cm}^{-2} \text{ s}^{-1}$. A relative precision of 1% can thus be expected when luminosities reach $10^{34} \text{ cm}^{-2} \text{ s}^{-1}$. The 1 kHz relative luminosity signal was also used to test the performance of the dithering orbit feedback system, by deliberately introducing a horizontal beam-beam offset. The results show that the feedback

system can correct the beam orbit at the IP. Details can be found in [13].

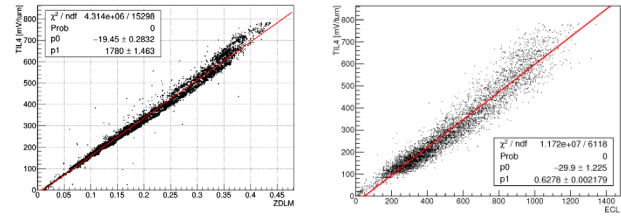


Figure 11: Comparison between luminosity signals from different monitors, *LumiBelle2* vs ZDLM (lhs) and *LumiBelle2* vs ECL-LOM (rhs).

Using the dependence of the TIL signal when scanning the vertical position of one beam across the other, average vertical beam size information and optimum collision position can be estimated. Figure 12 gives an example of *LumiBelle2* luminosity signal when scanning the vertical position of the electron beam. Fitting a Gaussian function, the optimum vertical offset was $0.19 \mu\text{m}$ while the second moment of the distribution was $\Sigma_y = 0.51 \mu\text{m}$. Assuming both beams have Gaussian charge distributions and equal vertical beam sizes, and that beam blow-up from the beam-beam interaction can be neglected, then the vertical beam size could be evaluated as $\sigma_y = \Sigma_y / \sqrt{2}$. This latter assumption is only valid for very low beam intensities, and beam blow-up from the beam-beam interaction must in general be taken into account. The vertical beam offset scans enable also the SNR to be estimated by comparing the signal at peak position with that when the two beams are completely separated. During the above scan, the maximum luminosity provided by ECL-LOM was $1.3 \times 10^{32} \text{ cm}^{-2} \text{ s}^{-1}$ and the observed SNR was 65. From simulation, the SNR was estimated to be 42 under the same conditions. Some overestimation of the simulated background may explain this difference, while it still needs to be studied in detail.

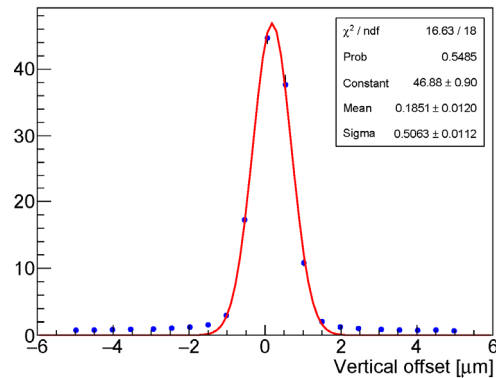


Figure 12: Relative luminosity signal with respect to the vertical offset of electron beam (arbitrary units).

Bunch Integrated Luminosity Monitoring

The specified number of bunches circulating in each ring is nominally about 2500. Variations in the bunch transverse positions and sizes are in principle possible,

through a variety of effects, and should be monitored, just like the bunch currents. The *LumiBelle2* BIL signal prepared for this purpose is illustrated in Figure 13 for the beam conditions at the end of the Phase-2 commissioning, when the instantaneous luminosity was $\sim 1.6 \times 10^{33} \text{ cm}^{-2} \text{ s}^{-1}$, with 395 bunches circulating in each ring, separated by 32 ns (corresponding to sixteen RF buckets). The observed spread in bunch integrated luminosity signals was about 9.3%, dominated by the measured spread in the product of bunch currents, which was found to be about 8.7% using the bunch-by-bunch current monitor [14]. In comparison, the relative precision in the corresponding 1 kHz TIL data was 2.35%, from which the average relative precision of BIL signals at 1 Hz could be estimated at the level of 1.5% (by simple scaling in the assumption of uniform bunch current and alignment of the bunches along the trains in both rings).

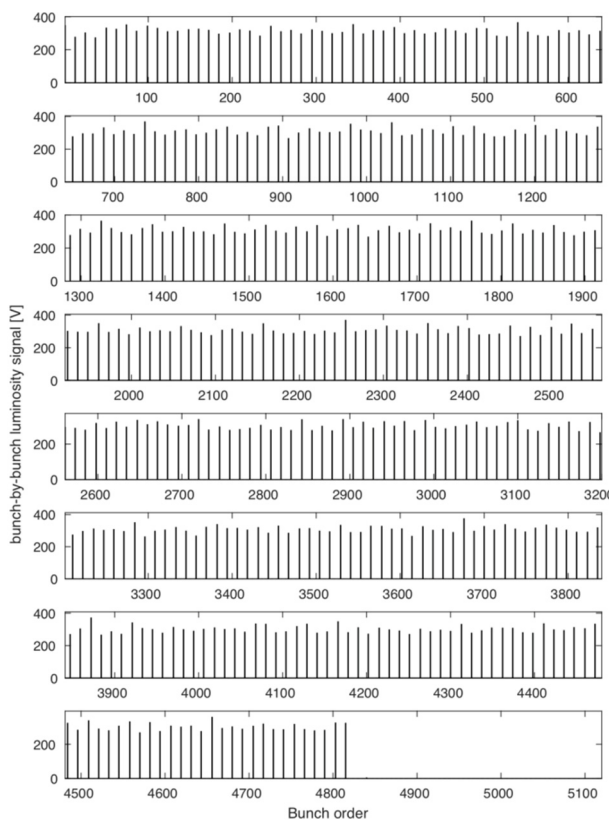


Figure 13: Bunch-by-bunch relative luminosity signals from *LumiBelle2* for 395 bunches circulating in each ring and colliding.

CONCLUSION AND NEXT PLANS

Fast luminosity monitoring based on diamond sensors was developed and employed during the Phase-2 commissioning of SuperKEKB. Several months of operational experience in both single and colliding beam modes have demonstrated good general performance and reliability.

With the expected increases in luminosity and evolution of the machine in future years, some improvements and further studies are needed, in particular:

- Optimising the combination and positions of sensors and amplifiers to ensure sufficient relative precision over the full range of expected luminosities from low ones during tuning to the specified nominal value while minimizing accumulated radiation doses.
- Shielding to mitigate activation of the beam pipe and radiator on the LER side.
- Equipping a new station for scattered Bhabha photon measurements with higher rates on the HER side.
- Upgrading the DAQ for long-term operation.

The dithering orbit feedback system was tested successfully but more tests and studies will be needed during the next phase of commissioning to ensure smooth operation in the future when beam sizes become much smaller.

Potential variations in luminosity along the bunch trains from collective effects or other mechanisms can be studied using the provided bunch-by-bunch luminosity signals together with existing bunch current data in both rings.

ACKNOWLEDGEMENT

This work was supported by the H2020 RISE E-JADE project of the European Commission, grant agreement No. 645479, by the China Scholarship Council (CSC) and by the Toshiko Yuasa France Japan Particle Physics Laboratory (TYL-FJPPL). The authors would like to express their warm thanks to the BEAST and KEK colleagues for fruitful discussions and support.

REFERENCES

- [1] Y. Ohnishi et al., "Accelerator design at SuperKEKB", *Prog. Theor. Exp. Phys.* Vol. 2013, pp. 03A011, 2013. doi:10.1093/ptep/pts083
- [2] Y. Funakoshi et al., "Orbit feedback system for maintaining an optimum beam collision", *Phys. Rev. ST Accel. Beams*, vol. 10 pp. 101001, 2007. doi:10.1103/PhysRevSTAB.10.101001
- [3] A. S. Fisher et al., "Commissioning of the fast luminosity dither for PEP-II", *Stanford Linear Accelerator Center*, Stanford, CA 94309, USA, Rep. SLAC-PUB-12608, July 2007, <http://www.slac.stanford.edu/cgi-wrap/getdoc/slac-pub-12608.pdf>
- [4] Y. Funakoshi et al., "Interaction Point Orbit Feedback System at SuperKEKB", in *Proc. 6th Int. Particle Accelerator Conf. (IPAC'15)*, Richmond, VA, USA, May 2015, pp. 921-923. doi:10.18429/JACoW-IPAC2015-MOPHA054.
- [5] C.G. Pang et al., "Simulation study on luminosity feedback horizontal beam stabilization at SuperKEKB", in *Proc. 9th Int. Particle Accelerator Conf. (IPAC'18)*, Vancouver, Canada, May 2018, pp. 2250-2253. doi:10.18429/JACoW-IPAC2018-WEPAL037.
- [6] C.G. Pang et al., "First tests of SuperKEKB fast luminosity monitors during 2018 Phase-2 commissioning", in *Proc. 9th Int. Particle Accelerator Conf. (IPAC'18)*, Vancouver, Canada, May 2018, pp. 2254-2257. doi:10.18429/JACoW-IPAC2018-WEPAL038.
- [7] Belle-ECL et al., "Electromagnetic calorimeter for Belle II", *J. Phys.: Conf. Ser.*, vol. 587, pp. 012045, 2015. doi:10.1088/1742-6596/587/1/012045

- 62th ICFA ABDW on High Luminosity Circular e^+e^- Colliders
ISBN: 978-3-95450-216-5
- eeFACT2018, Hong Kong, China JACoW Publishing
doi:10.18429/JACoW-eeFACT2018-TUPBB06
- [8] D. El Khechen et al., "First Tests of SuperKEKB Luminosity Monitor During 2016 Single Beam Commissioning", in Proc. 7th Int. Particle Accelerator Conf. (IPAC'16), Busan, Korea, May 2016, pp. 81-83. doi:10.18429/JACoW-IPAC2016-MOPMDB006.
- [9] C.G. Pang et al., "Preparation of CVD Diamond Detector for fast Luminosity Monitoring of SuperKEKB", in Proc. 8th Int. Particle Accelerator Conf. (IPAC'17), Copenhagen, Denmark, May 2017, pp. 135-138. doi:10.18429/JACoW-IPAC2017-MOPAB027.
- [10] CIVIDEC, <https://cividec.at/>
- [11] D. El Khechen, PhD thesis "Fast Luminosity Monitoring Using Diamond Sensors for SuperKEKB", Université Paris-Sud, 2016.
- [12] M. Ady, "Monte-Carlo simulation of ultra high vacuum and synchrotron radiation for particle accelerators", PhD thesis, École polytechnique Fédérale de Lausanne (EPFL), July 2016.
- [13] Y. Funakoshi *et al.*, "Early Observations of IP Dither Luminosity Feedback at SuperKEKB", Presented at this conference

Content from this work may be used under the terms of the CC BY 3.0 licence (© 2018). Any distribution of this work must maintain attribution to the author(s), title of the work, publisher, and DOI.

HIGH PRECISION EXPERIMENTS IN THE J/ψ , $\psi(2S)$ AND τ SECTOR

I. B. Nikolaev* on behalf of the KEDR Collaboration
Budker Institute of Nuclear Physics, 630090, Novosibirsk, Russia
Novosibirsk State University, 630090 Novosibirsk, Russia

Abstract

High precision experiments in charmonium sector require beam energy calibration. VEPP-4M [1] storage ring with energy measurement by resonant depolarization (RD) method provided high precision mass measurement of J/ψ - and $\psi(2S)$ - mesons with KEDR detector with accuracy 2×10^{-6} [2]. This narrow resonances can be used for calibration of energy scale of other accelerators such as BEPC-II or future Super Charm-Tau Factories equipped with Compton backscattering (CBS) energy measurement system.

BEAM ENERGY MEASUREMENT

Resonant Depolarization Method

The resonant depolarization (RD) method [3] is the most accurate technique of beam energy measurement. The accuracy achieved is about 10^{-6} . The method was successfully applied in the high precision measurements of the mass of elementary particles from ϕ -meson to Z -boson.

The method is based on the measurement of the spin precession frequency Ω , which depends on the beam Lorentz factor γ and well-known normal μ_0 and anomalous μ' parts of the electron magnetic moment:

$$\Omega = \omega_r \left(1 + \gamma \frac{\mu'}{\mu_0} \right), \quad (1)$$

where ω_r is the beam revolution frequency in the storage ring. The spin precession frequency is determined by the moment of resonant destruction ($\Omega = n\omega_r \pm \omega_d$, where $n \in \mathbb{Z}$) of the beam polarization in an external electromagnetic field with a frequency ω_d .

The beam polarization could be measured in several ways: using intensity of intra-beam scattering (Touschek effect) [4]; intensity of synchrotron light [5]; asymmetry of Compton backscattering [6]; scattering asymmetry on internal target [7]. At the VEPP-4M beam polarization is determined by intra-beam scattering [8]. The beam is depolarized by a TEM wave which is created by two matched striplines. They are connected to a high frequency generator with tunable frequency, which is computer controlled. The generator frequency ω_d and the VEPP-4M revolution frequency ω_r are stabilized by a rubidium atomic clock with an accuracy 10^{-10} . A polarized beam is prepared in the VEPP-3 booster with polarization time 1.3 hours at $E=1.55$ GeV or 0.6 hours at $E=1.85$ GeV then injected into VEPP-4M. In order to suppress beam size and orbit instabilities a relative count rate difference $\Delta = \dot{N}_{pol}/\dot{N}_{unpol} - 1$ of the polarized and unpolarized bunch is under observation.

The depolarization frequency is measured with an accuracy better than 10^{-6} . Double energy calibrations with opposite directions are performed in order to suppress dangerous side 50 Hz resonances. The determination of center of mass energy at the interaction point (IP) requires taking into account following effects: vertical orbit distortions and spin precession frequency width; solenoid field of the detector; coherent energy loss asymmetry; electron and positron energy difference and beam separation in parasitic IP; β -function chromaticity and beam potential [9, 10]. Corrections and errors are about few keV. Between calibrations VEPP-4M energy is reconstructed [11] by using some parameters of VEPP-4M storage ring: field of bending magnet measured by nuclear magnetic resonance method; environment and storage ring temperatures; beam orbits.

Compton Backscattering

The RD method meets problem with beam polarization near τ -lepton production threshold ($E = 1777$ MeV) due to close vicinity to $\Omega_s/\omega_r - 1 = 4$ spin resonance [12]. An additional method of energy monitor for τ mass measurement experiment is required. The process of Compton backscattering (CBS) allows one to determine beam energy by measuring maximum energy of scattering photon:

$$E = \frac{\omega_{max}}{2} \left(1 + \sqrt{1 + \frac{m_e^2}{\omega_0 \omega_{max}}} \right), \quad (2)$$

ω_0 is the initial energy of laser photon; m_e is the electron mass. For the first time this method was realized in [13] and firstly applied in particle experiments for tau mass measurement at VEPP-4M [14]. The scattered photons are registered by high purity germanium detector (HPGe). The detector is calibrated by number of well known γ -sources. The achieved accuracy of the method in beam energy range $E = 1.7 - 1.9$ is about 60 keV. Absolute calibration of the CBS method was done via comparison with RD. The experience of system exploitation at VEPP-4M helped with same systems at BEPC-II [15] and at VEPP-2000 [16] colliders.

HIGH PRECISION EXPERIMENTS AT VEPP-4M WITH KEDR DETECTOR

The data analysis of J/ψ and $\psi(2S)$ mass measurement is based on three J/ψ scans with integrated luminosity 0.7 pb^{-1} and on four $\psi(2S)$ scans with integrated luminosity 1.0 pb^{-1} [2]. Each scan has several points with different energies which cover resonance shape. The beam energy is calibrated before and after data acquisition in each scan point. The resonance masses were determined by fitting

* I.B.Nikolaev@inp.nsk.su

the inclusive hadronic cross sections as a function of the e^+e^- center-of-mass energy. Special investigation were performed to understand stability of VEPP-4M and reliability of energy reconstruction between RD energy calibrations. The total energy drift during day-night is about 50 keV [17]. The energy reconstruction accuracy during the experiments of J/ψ and $\psi(2S)$ mass measurements is about 6 – 8 keV [2, 10]. The achieved accuracy of mass measurement is about 2×10^{-6} which is the best in the world and will remain so for decades.

For tau mass measurement we use CBS method as beam energy monitor together with RD technique. For energy calibration by RD we injected polarized beam at $E = 1.85$ GeV and then deaccelerated energy to tau threshold. The energy was reconstructed by using VEPP-4M parameters as mention before and compared with the CBS energy monitor. CBS monitor itself is calibrated at the moment of energy measurement by RD. We achieved best world accuracy at that time [18]. Later this result was improved at BEPC-II collider with BES-III detector [19] where CBS energy measurement system was installed [15] which calibrated by location of J/ψ and $\psi(2S)$ resonances. This year integrated luminosity about 130 pb^{-1} had been collected again to improve accuracy of tau mass measurement. Data analysis is in progress.

Measurement of Γ_{ee} for J/ψ - and $\Gamma_{ee} \times \mathcal{B}_{\mu\mu}$ for $\psi(2S)$ -mesons are based on 0.23 pb^{-1} and 6.5 pb^{-1} integrated luminosity respectively. High precision mass measurement of J/ψ and $\psi(2S)$ with beam energy spread determination and RD energy calibration allow us to measure this parameters with best or world comparable accuracy [20, 21]. Measurement of the mass of $\psi(3770)$ -meson is based on 2.6 pb^{-1} integrated luminosity. The resonance is located on the $\psi(2S)$ slope and new measurement [22] allowed to discover sufficient role of resonance-continuum interference which affects on resonance shape. With resonant depolarization method the masses of D^0 and D^+ mesons ($\int L = 0.9 \text{ pb}^{-1}$) are measured with best accuracy [23] in 2010. A new measurement was done in 2017 and now data analysis is in progress.

SUMMARY

The resonant depolarization method of beam energy calibration at VEPP-4M allows us to measure masses of the J/ψ - and $\psi(2S)$ - mesons with high accuracy (2×10^{-6}). Moreover we had measured masses of τ lepton, D^{*-} , D^0 -mesons, parameters of the $\psi(3770)$ -mesons and leptonic width of the J/ψ and $\psi(2S)$ mesons. Together with Compton backscattering method of beam energy calibration this lays the foundation of high precision experiments at other e^+e^- colliders.

REFERENCES

[1] V. E. Blinov *et al.*, “The status of VEPP-4,” English, *Physics of Particles and Nuclei Letters*, vol. 11, no. 5, pp. 620–631, 2014, issn: 1547-4771. doi: 10.1134/S1547477114050082.

[2] V. V. Anashin *et al.*, “Final analysis of KEDR data on J/ψ and $\psi(2S)$ masses,” *Phys. Lett.*, vol. B749, pp. 50–56, 2015. doi: 10.1016/j.physletb.2015.07.057.

[3] A. D. Bukin *et al.*, “The phi Meson: Precision Measurement of Its Mass, Observation of the omega phi Interference,” *Yad. Fiz.*, vol. 27, pp. 976–984, 1978, [Sov. J. Nucl. Phys. 27, 516 (1978)].

[4] V. N. Baier and V. A. Khoze, “Effects of particle scattering inside the beams of polarized particles in the storage rings,” *At. Energ.*, vol. 25, pp. 440–442, 1968. doi: 10.1007/BF01239705.

[5] V. Korchuganov, G. Kulipanov, N. A. Mezentsev, E. Saldin, and A. Skrinsky, “Using synchrotron radiation for rapid measurement of the absolute energy of electrons in the storage ring,” *BNP preprint*, vol. 77-83, 1977.

[6] V. N. Baier and V. A. Khoze, “Determination of the transverse polarization of high-energy electrons,” *Sov. J. Nucl. Phys.*, vol. 9, pp. 238–240, 1969.

[7] M. V. Dyug *et al.*, “Moller polarimeter for VEPP-3 storage ring based on internal polarized gas jet target,” *NUCLEAR INSTRUMENTS AND METHODS IN PHYSICS RESEARCH SECTION A-ACCELERATORS SPECTROMETERS DETECTORS AND ASSOCIATED EQUIPMENT*, vol. 536, no. 3, pp. 338–343, 10th Workshop on Polarized Sources and Targets, Russian Acad Sci, Budker Inst Nucl Phys, Siberian Branch, Novosibirsk, RUSSIA, SEP 22-26, 2003, issn: 0168-9002. doi: 10.1016/j.nima.2004.08.095.

[8] V. Blinov *et al.*, “Absolute calibration of particle energy at VEPP-4M,” *Nucl. Instrum. Meth.*, vol. A494, pp. 81–85, 2002. doi: 10.1016/S0168-9002(02)01449-3.

[9] A. Bogomyagkov, S. Nikitin, I. Nikolaev, A. Shamov, A. Skrinsky, and G. Tumaikin, “Central Mass Energy Determination in High Precision Experiments on VEPP 4M,” in *Particle Accelerator Conference PAC07 Jun 2007*, Albuquerque, New Mexico, 2007, pp. 63–65.

[10] V. M. Aulchenko, S. Balashov, I. Nikolaev, *et al.*, “New precision measurement of the J/ψ - and ψ' - meson masses,” *Phys. Lett.*, vol. B573, pp. 63–79, 2003. doi: 10.1016/j.physletb.2003.08.028. {hep-ex/0306050}.

[11] V. E. Blinov *et al.*, “Review of beam energy measurements at VEPP-4M collider: KEDR/VEPP-4M,” *Nucl. Instrum. Meth.*, vol. A598, no. 1, pp. 23–30, 2009, issn: 0168-9002. doi: 10.1016/j.nima.2008.08.078.

[12] A. Bogomyagkov *et al.*, “Research of Possibility to use Beam Polarization for Absolute Energy Calibration in High-precision Measurement of Tau Lepton Mass at VEPP-4M,” in *9th European Particle Accelerator Conference (EPAC 2004)*, Lucerne, Switzerland.

[13] I. C. Hsu, C.-C. Chu, and C.-I. Yu, “Energy measurement of relativistic electron beams by laser Compton scattering,” *Phys. Rev. E*, vol. 54, no. 5, pp. 5657–5663, doi: {10.1103/PhysRevE.54.5657}.

[14] N. Y. Muchnoi, S. A. Nikitin, and V. N. Zhilich, “Fast and precise beam energy monitor based on the Compton backscattering at the VEPP-4M collider,” in *European Particle Accelerator Conference (EPAC 06)*, Edinburgh, Scotland, 2006, pp. 1181–1183.

[15] E. V. Abakumova *et al.*, “The beam energy measurement system for the Beijing electron-positron collider,” English, *NUCLEAR INSTRUMENTS AND METHODS IN PHYSICS RESEARCH SECTION A-ACCELERATORS SPECTROMETERS DETECTORS AND ASSOCIATED EQUIPMENT*,

- vol. 659, no. 1, pp. 21–29, ISSN: 0168-9002. DOI: 10.1016/j.nima.2011.08.050.
- [16] E. V. Abakumova *et al.*, “A system of beam energy measurement based on the Compton backscattered laser photons for the VEPP-2000 electron-positron collider,” *NUCLEAR INSTRUMENTS AND METHODS IN PHYSICS RESEARCH SECTION A-ACCELERATORS SPECTROMETERS DETECTORS AND ASSOCIATED EQUIPMENT*, vol. 744, pp. 35–40, ISSN: 0168-9002. DOI: 10.1016/j.nima.2014.01.020.
- [17] A. Bogomyagkov *et al.*, “Study of the energy stability in the VEPP-4M storage ring,” Prepared for 8th European Particle Accelerator Conference (EPAC 2002), Paris, France, 3-7 Jun 2002, Paris, France.
- [18] V. V. Anashin, V. Aulchenko, I. Nikolaev, *et al.*, “Measurement of the tau lepton mass at the KEDR detector,” *JETP Lett.*, vol. 85, pp. 347–352, 2007. DOI: 10.1134/S0021364007080012.
- [19] M. Ablikim *et al.*, “Precision measurement of the mass of the tau lepton,” *PHYSICAL REVIEW D*, vol. 90, no. 1, ISSN: 1550-7998. DOI: 10.1103/PhysRevD.90.012001.
- [20] V. V. Anashin *et al.*, “Measurement of $\Gamma_{ee} \times B_{\mu\mu}$ for $\psi(2S)$ meson,” *Physics Letters B*, vol. 781, pp. 174–181, 2018, ISSN: 0370-2693. DOI: 10.1016/j.physletb.2018.03.079. %7Bhttp://www.sciencedirect.com/science/article/pii/S0370269318302752%7D
- [21] V. V. Anashin *et al.*, “Measurement of $\Gamma_{ee}(J/\psi)$ with KEDR detector,” *Journal of High Energy Physics*, vol. 2018, no. 5, p. 119, ISSN: 1029-8479. DOI: 10.1007/JHEP05(2018)119. %7Bhttps://doi.org/10.1007/JHEP05(2018)119%7D
- [22] V. V. Anashin *et al.*, “Measurement of $\psi(3770)$ parameters,” *Physics Letters B*, vol. 711, no. 3–4, pp. 292–300, 2012, ISSN: 0370-2693. DOI: 10.1016/j.physletb.2012.04.019. %7Bhttp://www.sciencedirect.com/science/article/pii/S0370269312004224%7D
- [23] V. V. Anashin *et al.*, “Measurement of D-0 and D+ meson masses with the KEDR detector,” *Physics Letters B*, vol. 686, no. 2-3, pp. 84–90, 2010, ISSN: 0370-2693. DOI: 10.1016/j.physletb.2010.02.046. http://www.sciencedirect.com/science/article/pii/S0370269310002339

POLARIZATION ISSUES AT CEPC

Sergei Nikitin*, BINP SB RAS, Novosibirsk

Abstract

We study a possibility of obtaining transversely polarized electron/positron beams at the CEPC collider. At the beam energy of 45 GeV, this requires the use of the special wigglers to speed up the radiative self-polarization process. A numerical estimation of the depolarizing effect of the collider field errors is made, taking into account the modulation of the spin precession frequency by synchrotron oscillations. In addition, we consider an alternative possibility of obtaining polarization by accelerating the polarized particles in the booster and then injecting them into the main ring. This option saves time spent on the polarization process, and can also be crucial for obtaining longitudinal polarization.

INTRODUCTION

This work is devoted to obtaining transverse and longitudinal polarizations within the framework of the CEPC Collider project and is based on materials presented by the author in [1, 2].

Particle transverse polarization at least of 10% is needed to apply the resonant depolarization technique [3] in the experiment on precise Z-pole mass measurement. Because of too long time of radiative polarization in the basic version of the magnetic structure of CEPC, it becomes necessary to use strong non-uniform wiggler magnets to speed up the polarization process. Such wigglers can cause a significant increase in the spread of the spin precession frequency. In turn, this leads to an intensification of the depolarizing effect of quantum fluctuations in the presence of the guiding field imperfections. The calculations of this effect should take into account the synchrotron modulation of the spin tune. We consider the main obstacles to obtaining the radiative self-polarization at CEPC with 45 and 80 GeV. It is necessary to determine the critical level of errors in the CEPC magnet alignment by calculating their response in the spin motion.

In addition, we are trying to imagine an alternative way of obtaining polarization at CEPC. The rate is made for acceleration of polarized electrons in the booster using the Partial Siberian Snake technique [4] for crossing spin resonances. Injection into the collider can provide for two modes - with transverse and longitudinal polarizations. The kinematic scheme of longitudinal polarization can include the restoration of vertical polarization in the arcs and two spin rotators at the ends of the section with IP.

SPEEDING UP POLARIZATION PROCESS

The well-known Sokolov-Ternov mechanism of radiation self-polarization of particles in an ideal storage ring is characterized by the time τ_p of polarization build-up to the extent

$$P_0 = 0.92 [5]:$$

$$\frac{1}{\tau_p} = \frac{5\sqrt{3}}{8} \frac{r_e \Lambda_e c \gamma^5}{R^3} \langle K^3 \rangle, \quad (1)$$

where r_e , Λ_e , γ are the electron radius, Compton wave length and relativistic factor respectively; K is the orbit curvature in units of the inverse machine radius R ; $\langle \dots \rangle$ is averaging over the storage ring azimuth (ϑ). The design time of the radiative polarization in the 100 km CEPC is huge: 260 hrs at 45 GeV! At 80 GeV, this time falls as $(45/80)^5$ to 16 hrs. To speed up the polarization process, it is possible to apply the long-known method [5] based on the use of N_w special wiggler magnets (the so-called shifters) with such a distribution of the vertical field along the orbit that $\int B_w ds = 0$ and $\int B_w^3 ds \neq 0$. Let every shifter consist of three bending magnets. The field of edge magnets (B_-) is much smaller in magnitude than the field of the central one (B_+) and opposite in sign to it. The field of the latter is directed like the bending field in the arcs. Since $|B_+|^3 \gg |B_-|^3$, the equilibrium degree of polarization in the ideal case is close to the maximum (P_0). The shifters decrease the polarization time in accordance with the equation (L_- and L_+ are the corresponding magnet lengths):

$$\tau_p^w = \tau_p \left[1 + N_w \frac{B_+^3 L_+ + 2|B_-|^3 L_-}{2\pi R < B_0 > B_0^2} \right]^{-1}. \quad (2)$$

The fraction of radiation energy loss enhancement is

$$u = N_w \frac{B_+^2 L_+ + 2B_-^2 L_-}{2\pi R < B_0 > B_0}. \quad (3)$$

The harmful effect of the shifters is an increase in the beam energy spread:

$$\frac{\Delta E_w}{\Delta E} = \left[\frac{\tau_p}{\tau_p^w} \cdot \frac{1}{1+u} \right]^{1/2}. \quad (4)$$

The effectiveness of the described system as applied to CEPC can be judged by its parameters in Table 1. The Eqs. (2-4) are written in the isomagnetic approximation (the characteristic field in the CEPC magnets is $B_0 \approx 0.013$ T at 45.6 GeV, the averaged-over-azimuth field $\langle B_0 \rangle \approx 0.01$ T). At the same time, the calculated data presented in the table refer to the detailed design structure.

The reduction of τ_p by an order, down to $30 \div 20$ hours, means that it becomes possible to polarize the beams up to 10% in a few hours. This degree of polarization is quite sufficient for its observation by a laser polarimeter under the conditions of application of the resonant depolarization technique for determining the energy of the particles [6]. As the analysis below shows, a further increase in the field of wigglers and their number leads to an undesirable increase of depolarizing effects due to the large energy spread.

* nikitins@inp.nsk.su

Table 1: Parameters of the wiggler system (45.6 GeV)

N_w	B_+ T	L_+ m	B_- T	L_- m	$\frac{\tau_p}{\tau_w}$	u	$\frac{\Delta E_w}{\Delta E}$
10	0.5	1	0.125	2	8.3	0.20	2.6
10	0.6	1	0.15	2	13.6	0.29	3.3

DEPOLARIZATION FACTOR

Non-Resonant Spin Diffusion

Quantum fluctuations lead to the scattering of particle trajectories in the beam relative to the equilibrium orbit. In turn, this causes diffusion of the vertical projection of the spins in the presence of the guide field perturbations. The corresponding depolarizing effect is characterized by the depolarization time τ_d . As a result, an actual equilibrium polarization degree $P < P_0$ is established with a relaxation time $\tau_{rel} = (1/\tau_p + 1/\tau_d)^{-1} < \tau_p$. The depolarization factor

$$G = P/P_0 = \tau_{rel}/\tau_p \quad (5)$$

depends on the distributed radial magnetic and vertical electric fields which perturb the trajectories of particles in the vertical plane. The strongest depolarizing effect is produced by the sources that cause vertical distortions $y + 0(\vartheta) = y_0(\vartheta + 2\pi)$ of the closed orbit. Their influence increases with the approach to integer spin resonances $\nu = k$. Here, k is a natural number; $\nu = \gamma a$ is the spin tune averaged over the beam particles. In general, ν is a real number of spin precession cycles per one turn of particle (γ and a are the Lorentz factor and the anomalous part of the gyromagnetic ratio of electron, respectively). Because of synchrotron oscillations with frequency ν_γ , the spin tune is modulated by the law

$$\tilde{\nu} = \nu + \Delta \cdot \cos \psi_\gamma, \quad (6)$$

Δ is the amplitude related to the amplitude of energy oscillations. The distribution function of Δ is $f(\Delta) = (\Delta/\sigma_\nu^2) \exp[-\Delta^2/(2\sigma_\nu^2)]$; $\sigma_\nu = \nu\sigma_\gamma = (\Delta^2/2)^{1/2}$ is the spin tune spread due to the beam energy spread σ_γ . Modulation Eq. (6) leads to the appearance of the dependence of the factor G on the detuning from the modulation resonances $\nu = k + m\nu_\gamma$ (m is integer).

To estimate an actually achievable polarization degree with accounting the synchrotron modulation one can use the known formula [7]

$$G \approx \left\{ 1 + \frac{11\nu^2}{18} \sum_{k,m} \frac{|w_k|^2 I_m(\sigma_\nu/\nu_\gamma) \exp(-\sigma_\nu/\nu_\gamma)}{[(|\nu - k| - m\nu_\gamma)^2 - \nu_\gamma^2]^2} \right\}^{-1}. \quad (7)$$

Here $I_m(x)$ is the modified Bessel function; w_k is the k th azimuthal Fourier harmonic amplitude of the spin perturbations related to radial magnetic and vertical electric fields.

Approximately, the harmonic amplitude is determined as

$$w_k \approx \left\langle \nu \frac{d^2 y_0}{d\vartheta^2} \exp(-ik\vartheta) \right\rangle, \quad (8)$$

$y_0 = y_0(\vartheta)$ is the vertical closed orbit distortion in units of R . In Eq. (7) the following expansion in series in terms of Bessel functions is used:

$$w_k \exp \left[-i \frac{\Delta}{\nu_\gamma} \sin \psi_\gamma \right] = w_k \sum_{l=-\infty}^{l=\infty} J_l \left(\frac{\Delta}{\nu_\gamma} \right) \exp(-il\psi_\gamma). \quad (9)$$

In the strict sense, the expansion Eq. (9) and then Eq. (7) for G are valid if [8]

$$\sigma_\nu^2 \Lambda_\gamma < \nu_\gamma^3, \quad (10)$$

Λ_γ is the radiation decrement of the synchrotron oscillations in units of inverse turns. The diffusion coefficient of the energy can be expressed as

$$D_\gamma = \frac{1}{2} \frac{d}{dt} \overline{\left(\frac{\delta\gamma}{\gamma} \right)^2} = \frac{11}{18\tau_p} \quad (11)$$

The diffusion rate of the spin precession phase is written in the form

$$D_\Psi = \frac{d}{dt} \overline{(\delta\Psi)^2} = \frac{\nu^2}{\nu_\gamma^2} D_\gamma \quad (12)$$

The parameter [1]

$$\Gamma = \frac{11\nu^2}{18\nu_\gamma^3 \tau_p f_0} = \frac{D_\Psi}{\nu_\gamma f_0} = \frac{\sigma_\nu^2 \Lambda_\gamma}{2\nu_\gamma^3} \quad (13)$$

characterizes the precession phase increment due to diffusion per the period of synchrotron oscillations $(\nu_\gamma f_0)^{-1}$. The condition Eq. (10) is almost equivalent to the condition

$$\Gamma \ll 1, \quad (14)$$

which means that such an increment is negligibly small. Under the condition

$$\Gamma \gtrsim 1, \quad (15)$$

the spectrum of spin perturbations becomes blurry, i.e. must differ from the strictly linear spectrum Eq. (9). In Table 2, the data of LEP and CEPC on the Z pole energy are presented, which allow them to be compared by the parameter Γ . In the case of LEP, as well as of CEPC without the use of wigglers, this parameter is small, the expansion Eq. (9) is quite applicable. When $\Gamma \gtrsim 1$, the results obtained on the basis of this approximation are of an evaluative nature.

Calculation Examples for LEP and CEPC

In Fig. 1, the polarization at the colliders LEP and CEPC is calculated from Eq. (7) for the magnitude of the resonance harmonic of random perturbations of a closed orbit $w_k = 2 \times 10^{-3}$ in dependence on the beam energy (and also on the spin tune, in the example for LEP). Only two nearest

Table 2: Precession phase diffusion increment (Γ) in 45 GeV LEP and CEPC. Star indicates cases with special wigglers

	σ_v	v_γ	f_0 kHz	τ_p hr	Γ
LEP	0.061	0.083	11	5	0.054
CEPC	0.039	0.028	3	268	0.103
	0.128	0.028	3	19.7*	1.40
	0.103	0.028	3	32.3*	0.860

integer spin resonances with $k = 103$ and $k + 1 = 104$ are taken into account in the calculation. For simplicity, we put $|w_k| = |w_{k+1}|$. The red curves respond to the case without consideration of the modulation when (in the approximation $|\nu - k| \gg \max(\sigma_v, v_\gamma)$)

$$G \approx \left[1 + \frac{11\nu^2}{18} \sum_k \frac{|w_k|^2}{(\nu - k)^4} \right]^{-1} \quad (16)$$

The estimate for LEP for the harmonic amplitude $|w_k| = 2 \cdot 10^{-3}$ is correlated with the real data on the observation of the polarization at that facility. According to [9], the polarization at LEP reached 40% at 44.7 GeV ($\nu = 101.46$). This approximately corresponds to the calculation at the spin tune of 103.46. In the LEP polarization simulations [10], performed long before the LEP activity started, the same polarization degree at the mentioned energy was obtained for the 50 μm random vertical displacements of the LEP quads.

The plots for CEPC in Fig. 1 relate to two cases. First case (a bottom left graph) is that of the current CEPC design in the luminosity mode. It is characterized by $v_\gamma = 0.028$ and the moderate spreads of beam energy and spin tune. The maximal equilibrium polarization degree is close to 50%. The modulation resonances can be neglected. With that a time to build up polarization is too large: $\tau_{rel} \approx 0.5\tau_p = 134$ hrs. In the point of view of obtaining polarization, this mode is relevant if only using injection of polarized beams from the CEPC booster. In this case, the relaxation of the polarization occurs to a level of 50%, which guarantees the preservation of a high degree of polarization for the whole life time of the injected beam.

Another case is an example of CEPC using the special wigglers to speed up the polarization process more than 8 times in accordance with Table 1 (see a bottom right graph in Fig. 1). The energy and spin tune spreads are increased approximately 3 times. This reduces approximately twice the degree of polarization at the maximum.

In order to increase the equilibrium degree of radiation polarization in the wiggler mode, it is necessary to decrease the harmonic amplitudes of the two nearest integer spin

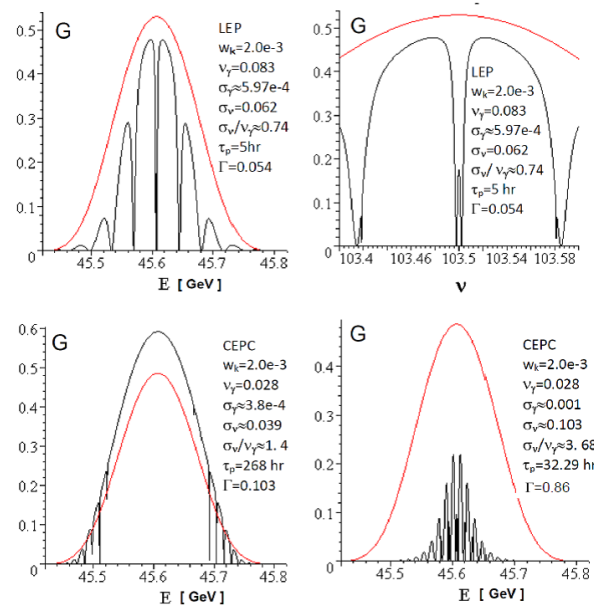


Figure 1: Polarization at LEP and CEPC at the same spin harmonic amplitude $|w_k| = 2 \cdot 10^{-3}$ vs. energy and spin tune. The red curves correspond to the case of no consideration of synchrotron modulation, see Eq. (16).

resonances (in this case, $k = 103$ and $k = 104$) due to a special correction of the vertical closed orbit. Estimates show that in the case of CEPC, one should reduce the harmonic to a level of $|w_k| = 10^{-3}$ or even less. It is also necessary to limit the field of wigglers, since the increase in the spin tune spread caused by them leads to a drop in the degree of polarization. As can be seen from Fig. 2, the field of wigglers 0.5 Tesla is preferable in comparison with the field of 0.6 Tesla, so it gives a 7-fold greater degree of polarization.

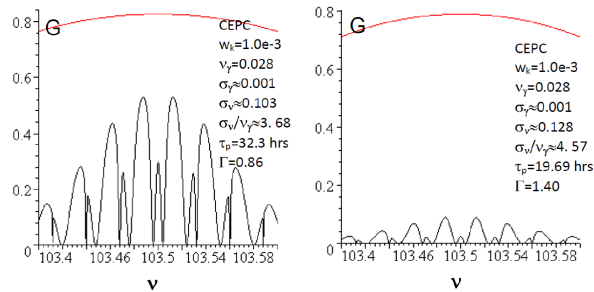


Figure 2: Polarization at 45 GeV CEPC at $|w_k| = 10^{-3}$ vs. the spin tune in two cases of the special wiggler parameters from Table 1: $B^+ = 0.5$ T (left) and $B^+ = 0.6$ T (right).

With increasing beam energy, the depolarizing effects of the guiding field imperfections intensify. At the threshold energy of the W pair production, in order to obtain polarization, an even more thorough correction of the spin harmonics associated with the distortions of the vertical closed orbit is needed. But, as will be shown below, the wigglers will not be needed to speed up the polarization process. The dependence of the polarization on the energy/spin tune in

the region of the W-threshold is plotted in Fig. 3 for the harmonic amplitude $|w_k| = 5 \cdot 10^{-4}$.

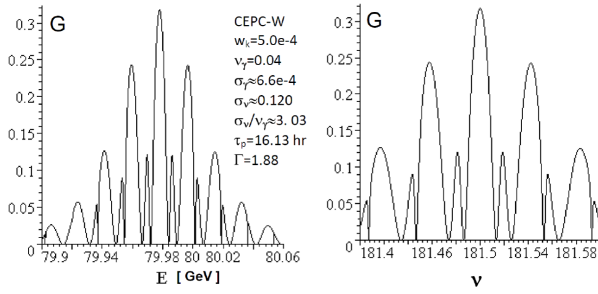


Figure 3: CEPC polarization near the W pair production threshold vs. the beam energy (left) and the spin tune (right).

SPIN RESPONSE TO MISALIGNMENTS

Spin Response Function

In electron-positron storage rings, as well as in proton rings with flat torsion-free orbit, the power of the depolarizing resonances associated with the action of transverse perturbations on the particle is determined by the so-called spin response function ($\nu \gg 1$) [7]:

$$F^\nu(\theta) = \frac{\nu e^{i\nu\theta}}{2} \left[f_y \int_{-\infty}^{\theta} \bar{f}_y' K e^{-i\nu\phi} d\theta' - \bar{f}_y \int_{-\infty}^{\theta} f_y' K e^{-i\nu\phi} d\theta' \right], \quad (17)$$

where $f_y e^{-i\nu\theta}$ is the vertical Floquet function; ν_y is the vertical betatron tune; the bar means a complex conjugation; $\phi = \int_0^\theta K d\theta$. This function has a period of $2\pi/m_p$ with m_p , the number of the magnetic structure super-periods (at CEPC, $m_p = 2$). It varies nonmonotonically with the beam energy and increases indefinitely in magnitude with approach to the resonances $\nu \pm \nu_y = k$.

Estimate of Resonance Harmonics

The amplitudes of integer spin resonance harmonics can be estimated using the calculated values of F^k ($\nu = k!$) at the azimuths of the field error location. For the random vertical offsets of the orbit in N_q quads with the spread δy :

$$|w_k^{(1)}|^2 = (\delta y)^2 \left(\frac{\nu}{2\pi} \right)^2 \sum_{i=1}^{N_q} \left(\frac{\partial H_y}{\partial x} \cdot \frac{l}{HR} \right)_i^2 |F_i^\nu|^2. \quad (18)$$

For the tilts of the N_b bending magnets around their axis with the angular spread $\delta\chi$:

$$|w_k^{(2)}|^2 = (\delta\chi)^2 \left(\frac{\nu}{2\pi} \right)^2 \sum_{i=1}^{N_b} \left(\frac{H_y l^2}{HR} \right)_i |F_i^\nu|^2. \quad (19)$$

For the tilts of the N_q quads (η_x is the horizontal dispersion):

$$|w_k^{(3)}|^2 = (\delta\chi)^2 \left(\frac{\nu}{2\pi} \right)^2 \sum_{i=1}^{N_q} \left(\frac{\partial H_y}{\partial x} \cdot \frac{l\eta_x}{HR} \right)_i^2 |F_i^\nu|^2. \quad (20)$$

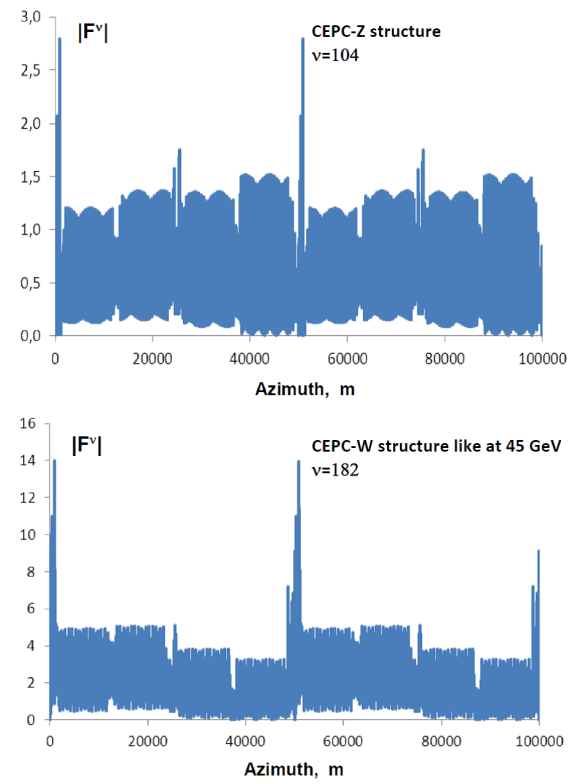


Figure 4: Spin response function for the integer resonance harmonics from the regions of Z-pole and W threshold.

In Eqs. (18-20), l_i is a length of the i th magnetic element, H_y is a vertical magnetic field, $HR = \langle B_0 \rangle R$ is the machine magnetic rigidity. The generalized amplitude is

$$|w_k|^2 = |w_k^{(1)}|^2 + |w_k^{(2)}|^2 + |w_k^{(3)}|^2 \cdot (k - \nu)^2. \quad (21)$$

In Eq. (21), the factor $(k - \nu)^2$ takes into account the difference of the latter case from the first two in the power-law dependence of the depolarization effect on the resonance detuning. The beam energy in Z-pole peak corresponds to the detuning of approximately 0.5 from two nearest spin resonances with $k = 103$ and $k = 104$. Fig. 4 and Fig. 5 shows the azimuthal distributions of the spin response at the CEPC main ring calculated using Eq. (17) for these two values of the harmonic number [2]. In Table 3, the expected values of the resonance harmonic amplitudes, estimated from Eq. (18-21), are given for the typical magnitudes of the misalignments mentioned above. The resulting amplitudes are about 3 and 1.5 times larger than desirable one (10^{-3}), which indicates the need for correction of the harmonics.

At the energy of the W pair production threshold, $|F^\nu|$ is noticeably larger than that at Z pole energy (Fig. 4) This means higher requirements to the quality of correction for obtaining polarization at 80 GeV.

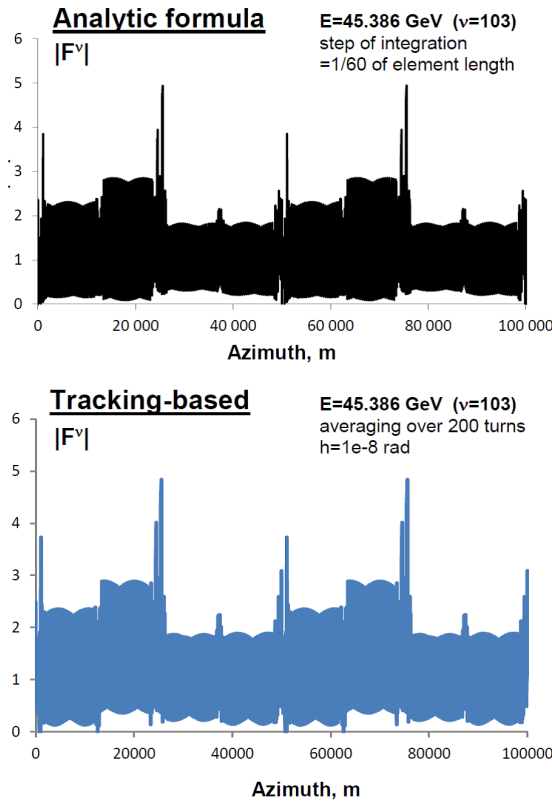


Figure 5: Comparison of the analytic-based and tracking-based calculations of F^ν .

Table 3: Spin integer resonance harmonic amplitudes at $N_q = 5368$, $N_b = 2458$, $\delta y = 50 \mu\text{m}$, $\delta \chi = 3 \cdot 10^{-4}$

k	103	104
$ w_k^{(1)} $	2.7×10^{-3}	1.2×10^{-3}
$ w_k^{(2)} $	7.4×10^{-4}	4.1×10^{-4}
$ w_k^{(3)} $	2.8×10^{-3}	2.9×10^{-3}
$ w_k $	2.9×10^{-3}	1.5×10^{-3}

Comparison of Spin Response Calculations by Analytic- and Tracking-Based Methods

In view of the importance of these results, a calculation [2] of the spin response function was carried out using an alternative method [11] basing on the particle tracking simulation. In this method, the probe particle experiences a vertical kick $h \ll 1$ at an arbitrary azimuth θ_0 , where the spin response is calculated, and begins to oscillate in the fields of a storage ring. The increment $\delta S_\perp^{(j)} = \delta S_x^{(j)} + i\delta S_z^{(j)}$ of the transverse component of the spin vector \vec{S} ($|\vec{S}| = 1$) acquired to the j -th turn is found by multiplying the spinor matrices corre-

sponding to the perturbed spin motion. In a conventional storage ring, this motion is described by the equations (the orth system $\vec{e}_x \times \vec{e}_z = \vec{e}_y$ is used):

$$\begin{aligned} d\vec{S}/d\theta &= \vec{W} \times \vec{S} \\ W_x &= (1 + \nu)y'' \\ W_z &= (1 + a)K'y + (a - \nu)Ky' \\ W_y &= \nu K - (1 + \nu)x''. \end{aligned} \quad (22)$$

It can be shown that

$$F^\nu(\theta_0) = \left\langle -\frac{ie^{-i2\pi j}}{\nu h} \cdot \delta S_\perp^{(j)} \right\rangle - 1 \quad (23)$$

where averaging is done over a large number of turns. Comparison of the graphs in Fig. 5 demonstrates the practically complete agreement between the two methods.

Influence of Betatron Oscillations

Because of the very small emittance of the beam, the contribution of betatron oscillations to the kinetics of the radiation polarization is expected to be negligible. In particular, this is indicated by the calculation of the depolarizing factor for the case of random tilts of quadrupoles (Fig. 6). The calculation is based on the approach [10] in which $F^\nu(\theta)$

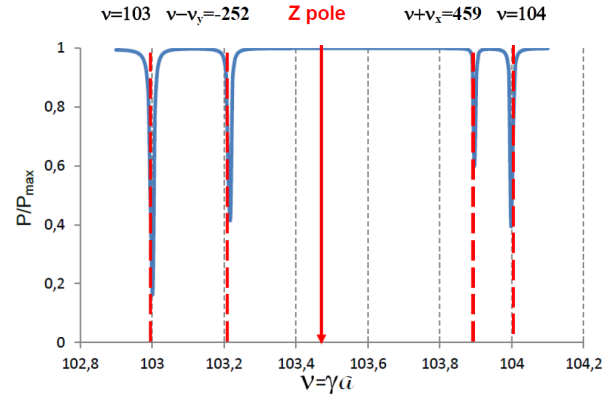


Figure 6: Depolarizing effect of the CEPC quadrupole tilts with the spread $\delta \chi = 6 \times 10^{-4}$ rad ($\nu_x/\nu_y = 355.1/355.21$).

is used. Three types of resonances appear in the linear approximation. Integer resonances are associated with harmonics whose amplitude $w_k^{(3)}$ is estimated like in Eq. (20). Resonances $\nu \pm \nu_x = k$ arise from the betatron coupling. Resonances $\nu \pm \nu_y = m_p k$ are owing to the feature of the spin response function. Synchrotron oscillations are not taken into account, since the corresponding modulation resonances are even narrower than the main ones.

TIME TO REACH 10% POLARIZATION

The polarization increases in time according to the law $P(t) = GP_0[1 - \exp(-t/\tau_{rel})]$. Let us define the operation time we should spent to reach the certain polarization degree of $\eta = P(t_\eta)$ percentages in the conditions under consideration:

$$t_\eta = -\tau_{rel} \ln \left(1 - \frac{\eta}{92G} \right). \quad (24)$$

Here, $\tau_{rel} = G\tau_p$ or $\tau_{rel} = G\tau_p^w$ depending on whether special wigglers are used or not. Based on the maximum values of factor G in Fig. 2 and Fig. 3, a table of parameters for obtaining polarization at Z-pole and W pair production threshold is compiled, including the time t_η , which in the considered cases considered ranges from 2 to 4 hours (see Table 4).

Table 4: Parameters of obtaining polarization at CEPC. * and ** indicate the cases $B_+ = 0.5$ T and $B_+ = 0.6$ T.

E GeV	$ w_k $	G_{max}	ν_γ	τ_{rel} hr	η %	t_η hr
45.602	10^{-3}	0.53	0.028	17.1*	10	3.93
45.602	10^{-3}	0.09	0.028	1.8**	6	2.28
79.978	.0005	0.32	0.040	4.8	10	2.14

POLARIZATION SCENARIO AT Z- POLE

About 100 pilot electron/positron bunches of relatively small total current I_p are stored to be partially polarized up to 10% in 2.5 hrs using 10 shifter magnets with the field of 0.6 T. The SR power from each shifter magnet is 3 kW at $I_p = 2$ mA (of the order of 1% of the main train) When the polarization process ends the shifter magnets turn off. Then the main bunch train is stored. The pilot bunches are not in collision. Their lifetime is about 10^5 s due to scattering of particles on thermal radiation photons [12]. The polarized bunches are used one by another for the RD calibration of beam energy every 15 min. So, a single polarized bunch train is spent per day while taking data in detector occurs. A qualitatively similar scenario was proposed some time ago for the FCCee project.

ALTERNATIVE APPROACH

Acceleration of Polarized Beam in Booster

In [1] we drew attention to one more way to obtain the polarization at the CEPC collider. It seems reasonable to accelerate in the CEPC booster the electrons of (60 ÷ 80)% polarization degree coming from the 10 GeV linac with a photo-gun source, taking measures to preserve the polarization (Fig. 7). Obviously, in the case of positrons, this will require the creation of a 10 GeV damping ring. In general, preservation of the particle polarization during acceleration in the booster saves a time spent on the process of radiative polarization, and can also be decisive for obtaining the longitudinal polarization in the collider.

Without special measures, such an acceleration is possible if the total depolarization effect at fast crossing a system of

spin resonances, estimated with the help of the Froissart-Stora formula, is small:

$$\varepsilon' = \frac{d\varepsilon}{d\theta} \gg \pi \sum_k |w_k|^2 \sim \pi N_{res} |w_{char}|^2. \quad (25)$$

Here, ε' is a rate of change in the detuning $\varepsilon = \nu - \nu_k$ from the k -th spin resonance (integer or spin-betatron one) with the harmonic amplitude w_k . The particle energy in the booster rises from 10 to 45 GeV in 2 seconds. This corresponds to a rather high rate of change in the detuning: $\varepsilon' \approx 2 \cdot 10^{-3}$. With $N_{res} = 80$, the number of intersected

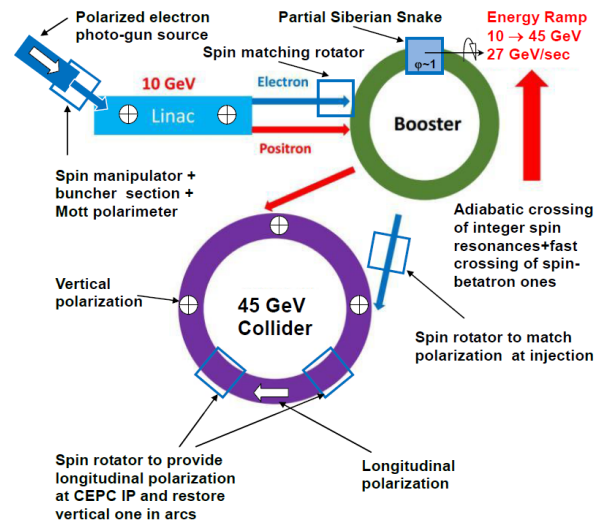


Figure 7: Sketch of obtaining longitudinal polarization using acceleration of polarized electrons in booster .

integer resonances in the mentioned range, we obtain from Eq. (25) an estimate for the admissible characteristic magnitude of the harmonics : $|w_{char}| \ll 0.003$. At the same time, the typical amplitude for integer spin resonances, due to magnet alignment errors, is of the order of at least 10^{-3} . The amplitudes for the intrinsic resonances $\nu_k = k \pm \nu_{x,y}$ are much smaller but the amount of such resonances is 4 times larger ($N_{res} \approx 320$).

In view of the unreliability of the maximally simplified approach, one should apply the well-known Partial Siberian Snake (PSS) method [4] to maintain the polarization in the booster. Let us consider an example with a helix snake [8, 13] rotating the spin through an angle $\varphi = 0.4$ rad around the particle velocity. In this case, there will be an adiabatically slow intersection of the energy levels related to the integer resonances , since $\varphi^2 \gg 4\pi^2 \varepsilon'$. In the presence of PSS, the equilibrium polarization direction is not vertical and changes with the booster energy. By this reason, it is required to match the beam polarization at injection as well as at ejection using appropriate spin rotators in the beamlines. In the case of ejection, the rotator should have two modes - one for the transverse and the other for longitudinal polarization in the collider.

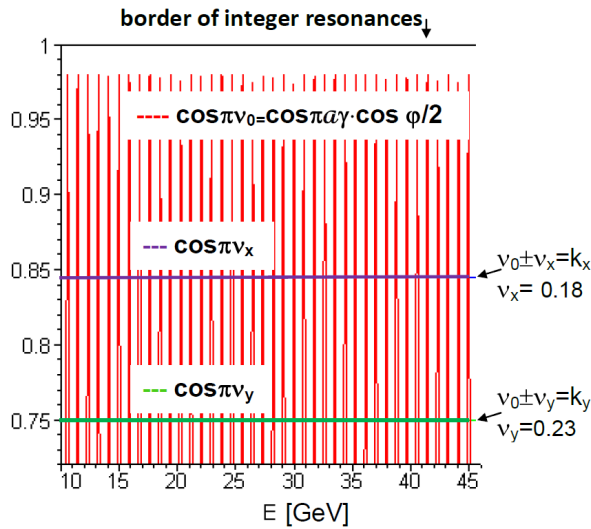


Figure 8: Diagram of the main spin resonance intersections as function of energy at $\varphi = 0.4$ rad.

The adiabatic mode mentioned above ensures to keep the particle polarization oriented along the equilibrium polarization direction during acceleration. The effective frequency of spin precession (ν_0) is determined from the equation $\cos \pi \nu_0 = \cos \pi a \gamma \cdot \cos \frac{\varphi}{2}$. This function, oscillating with energy during acceleration, is shown in Fig. 8. Its module does not equal 1 anywhere, which means that the spin tune averaged over the beam does not intersect any integer spin resonance. At the same time, this function curve intersects at certain points the horizontal lines of the intrinsic spin resonances $\nu_0 \pm \nu_{x,y} = k_{x,y}$. The rate of the effective detuning change at these points is

$$\varepsilon'_0 = \varepsilon' \frac{\sqrt{\cos^2 \varphi/2 - \cos^2 \pi \nu_{x,y}}}{\sin \pi \nu_{x,y}} \approx \varepsilon'. \quad (26)$$

Fast crossing these resonances will occur with a small loss of the polarization if the characteristic resonant harmonic amplitude of the corresponding perturbations satisfies the condition Eq. (25) at $N_{res} = 320$: $w_{char} \ll 10^{-3}$. From a practical point of view, this is easily done for beams with a small emittance and an appropriately compensated betatron coupling.

With $\varphi = 0.4$ rad, the helix snake can have the following parameters: transverse field=0.9 T, length=8.6 m, number of twists=4. The closed orbit makes the transverse excursions inside the snake and restores at exit. The maximum orbital deviations from the axis $Y_{max} = 5$ mm, $X_{max} = 3.7$ mm at 10 GeV and $Y_{max} = 1.1$ mm, $X_{max} = 0.8$ mm at 45 GeV. In cardinal case $\varphi = \pi$, absolutely all spin resonances are avoided. But this leads to an unacceptable increase of radiation losses. For instance, at the helix snake field of 1.78 T, its length of 8.6 m ($\varphi = \pi/2$) the losses due to the snake at 120 GeV are comparable with that from the booster main field. At 10 GeV, they exceed the nominal losses by 25 times. For comparison, the solenoid-based snakes do not increase

radiation losses. But an advantage of helix snakes is compact arrangement. The required integral of the solenoid field in the full Siberian snake ($\varphi = \pi$) is 104 T·m at 10 GeV and 474 T·m at 45.6 GeV. At the same time, the necessary helix snake field integral does not depend on energy at $\varphi = \text{const}$.

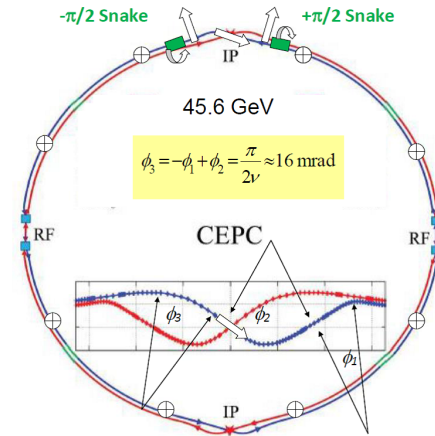


Figure 9: Kinematic scheme of longitudinal polarization.

On Longitudinal Polarization

In one of the ways [5] to organize longitudinal polarization, the equilibrium direction of polarization in the arcs remains vertical, and in a certain region evolves due to the use of spin rotators, taking the direction along the velocity at IP (Fig. 7). As rotators, for example, solenoids can be used in combination with magnets with a vertical field. The examples of a detailed calculation of such systems including the radiative kinetics of polarization are given in [14, 15].

In [1] attention is drawn to the fact that the S-shaped twist of the orbit in median plane in the CEPC section with IP (Fig. 9) can be a base to design a kinematic scheme of longitudinal polarization with minimization of the depolarization effect of quantum fluctuations. For this, two conditions must be met. First, the rotators should be distinguished by signs of rotation of the spin around the velocity vector by an angle of $\pi/2$. With a field of 8 T, the length of corresponding solenoid should be about 30 m at 45 GeV. Second, the angles of the orbit twist to the left and right of IP (between the solenoids) are equal in magnitude to $\pi/(2\nu)$ and opposite in sign (Fig. 9). As a result of this antisymmetry of the system of rotators as a whole, the main contributions to the spin-orbit coupling which are due to chromaticity of spin rotation in the solenoids as well as in the magnets between them cancel each other out [16]. This sharply reduces the depolarizing effect of quantum fluctuations in the arcs. In the top injection mode, the average in time degree of polarization of electrons in the collider will be close in magnitude to the degree of polarization of injected particles.

MORE ISSUES

There are two more issues that need to be studied. First of them concerns a depolarizing influence of SR in the inter-

action area where beams intersect the 3T detector solenoid axis at a large angle (of about 15 mrad). Another is the resonance spin diffusion at a large spin tune spread in framework of a model basing on the radiative excitation and damping. In principle, the latter can be actual in the mode using the strong wigglers to speed up polarization. For particles from the distribution function tail, the amplitude of spin tune modulation by synchrotron oscillations can overlap the distance to a closest integer spin resonance.

CONCLUSION

- Depolarization effect of the different misalignments of the CEPC magnets has been estimated in comparison with the LEP case taking into account modulation of the spin precession frequency by synchrotron oscillations. With a large spin tune spread, this modulation significantly enhances the depolarization effect.
- The proposed parameters of the special wigglers in the number of 10 pieces to speed up polarization at 45 GeV are quite moderate.
- Sensitivity of spin motion to transverse field imperfections is determined through Spin Response Function. In order to self-test, this function has been calculated in two ways: in the analytic approach and by partial tracking simulation. The results are in full agreement.
- At Z-pole, the spin harmonic related to the sources of vertical closed orbit distortions should be corrected to the levels of $\lesssim 10^{-3}$. Similar problem was successfully solved in past at LEP. At the W pair production threshold energy, requirements for the spin harmonic matching are significantly tightened because of the increased spin response in the existing version of the magnetic structure.
- If the proper spin harmonic matching is done, it is possible to reach polarization in range $(6 \div 10)\%$ in time of $2 \div 4$ hours at 45 GeV CEPC, and 10% polarization in 2 hours at the W^\pm threshold energy.
- Because of very small beam emittance, accounting for betatron oscillations in the radiative kinetics of spins leads to very narrow depolarization resonances. This is demonstrated by the calculation of the effect of random tilts of the CEPC quadrupoles.
- There is an alternative possibility of obtaining polarization by accelerating the polarized particles in the CEPC booster and then injecting them into the main ring. To ensure non-zero detuning from the integer resonances in the booster, we suggest to apply the 0.9 T 4-fold twist helix snake of about 9 m in length with a small angle of spin rotation around velocity. Intersection of the main spin-betatron resonances will occur in the fast crossing mode. This option saves time spent on the polarization process, and can also be crucial for obtaining longitudinal polarization.

- The design twist of the CEPC orbit at the IP section allows one to try one of the known methods of organizing longitudinal polarization with the restoration of vertical polarization in the arcs while minimizing the depolarizing effect of the spin rotators.

ACKNOWLEDGMENT

Author is grateful to Prof. Jie Gao for initiating the discussion on the polarization at CEPC; Anatoly Kondratenko for notable conversations on spin dynamics; Ivan Koop, Nikolay Muchnoi, Dmitry Shatilov for useful discussions on FCCee polarization program; Dou Wang and Yiwei Wang for technical help.

REFERENCES

- [1] S.A. Nikitin, Talk at IAS Program on High Energy Physics 2018, Hong Kong (Jan. 2018).
- [2] S.A. Nikitin, Talk at Workshop on the Circular Electron Positron Collider, Universita degli Studi Roma Tre, 25 May 2018.
- [3] A.D. Bukin et al., *Proc. V-th Int. Symp. on High Energy Physics and Elementary Particle Physics*, Warsaw, 1975, pp. 138-162.
- [4] Y.S. Derbenev et al., *Proc. Of the Tenth Int. Conf. on High Energy Charged Particle Accelerators*, vol.2, Serpukhov, 1977, p.76
- [5] Y.S. Derbenev et al., *Particle accelerators* V. 8, No. 2, pp. 115-126 (1978).
- [6] L.Knudsen et al., *Physics Letters B*, Vo. 270, Issue 1, 7 November 1991, pp. 97-104.
- [7] Y.S. Derbenev, A.M. Kondratenko, A.N. Skrinsky. *Particle accelerators*, V.9, No. 4, pp. 247-265 (1979).
- [8] A.M. Kondratenko, Doctoral Dissertation, Novosibirsk, 1982.
- [9] R. Assmann et al., PAC 1995.
- [10] S.A. Nikitin, E.L. Saldin, M.V. Yurkov, *Nucl. Instr. and Meth. A* 1983, vol. 213, No.3, pp. 317-328.
- [11] S.A. Nikitin, Talk at the XX International Symposium on Spin Physics SPIN 2012, Dubna, 20 sept. 2012.
- [12] V.I. Telnov, *NIM(A)* 260 (1987) 304.
- [13] Y.S. Derbenev, A.M. Kondratenko, AIP Con. Proc. 51, 292 (AIP, NY, 1979).
- [14] S.A. Nikitin, E.L. Saldin, M.V. Yurkov, Preprint INP 81-116 (1981); Internal Report, DESY L-Trans-286 (1984).
- [15] S.A. Nikitin, SB-NOTE-ACC-2008-001 (2008) (Preprint at LNL, Frascati).
- [16] I.A. Koop, The 40th ICFA Advanced Beam Dynamics Workshop on High Luminosity e^+e^- factories (FACTORIES '08). 14-16 Apr. 2008, Novosibirsk.

IDEAS FOR LONGITUDINAL POLARIZATION AT THE Z/W/H/TOP FACTORY

I. A. Koop^{†,2}, A. V. Otboev, Yu. M. Shatunov¹,

Budker Institute of Nuclear Physics, [630090] Novosibirsk, Russia

¹also at Novosibirsk State University, [630090] Novosibirsk, Russia

²also at Novosibirsk State Technical University, [630090] Novosibirsk, Russia

Abstract

Different schemes for getting the longitudinal polarization at FCC-ee are considered. Depolarization rates for rings with spin rotators are evaluated and methods of acceleration of polarized beams in a booster synchrotron are proposed.

INTRODUCTION

First ideas on how the stable longitudinal polarization of colliding electrons and positrons can be achieved were proposed in 70-th [1–4]. In this paper we analyse the possibilities to use 90° spin rotators which are installed at proper bending angle relative to the Interaction Point (IP) of the FCC-ee collider [5].

The crab-waist collision scheme assumes an operation with extremely small vertical beam emittance. Therefore only the solenoid type spin rotators with a compensated x – y coupling can be used for spin manipulations in a ring. Also due to strong Synchrotron Radiation (SR) and associated with that fast energy diffusion the schemes which utilises the idea of Siberian Snake can't be used. Restoration of the vertical spin direction in main arcs of FCC-ee is mandatory. Only then the spin-orbit coupling effects and the depolarization rates are minimised to the acceptable level.

LONGITUDINAL POLARIZATION

Near the Z-peak (beam energy around 45.6 GeV) the spin tune $\nu_0 = \gamma a$ is equal to $\nu_0 = 103.5$. Here γ is the Lorentz factor and $a = q/q_0 = 0.0016$ states for the anomalous magnetic moment of an electron. Hence, if spin is directed longitudinally at IP, it shall be rotated two times by 90° —first by a bend in the horizontal plane and then by a solenoid around the longitudinal axis, see Fig.1.

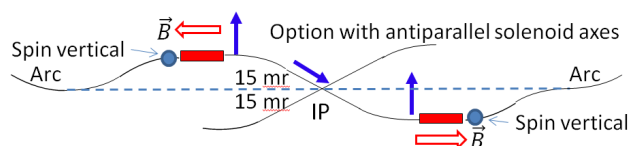


Figure 1: The proposed spin and velocity rotation sequences for achieving the longitudinal polarization at Z.

The corresponding velocity vector bending angle is $\phi = 0.5\pi/\nu_0 \approx 0.015$, while the needed longitudinal field integral is $BL = 0.5\pi BR/(1+a) \approx \pm 235$ T·m per rotator. Remind, that due to antisymmetric layout of all spin rotations in this scheme, the net spin rotation is zero. There-

fore the equilibrium spin direction in main arcs is the same as without spin rotators and, moreover, it is independent on the particle's energy. This is very important, because guaranties the cancelation of spin-orbit coupling in arc's dipole magnets. Spin direction is chromatic only in the chicane magnets, which rotate spin in the horizontal plane. But their contribution to radiative depolarization by quantum fluctuations of SR is negligible. Another remark: the global spin precession frequency is not affected by such an insertion and can be used for beam energy determination applying the Resonant Depolarization (RD) method.

Unfortunately, the accumulated bending angle distribution in FCC-ee experimental straight section is not fully antisymmetric relative to IP—at the left side bends with negative curvature are much weaker compared to bends on the right side from IP, see Fig.2.

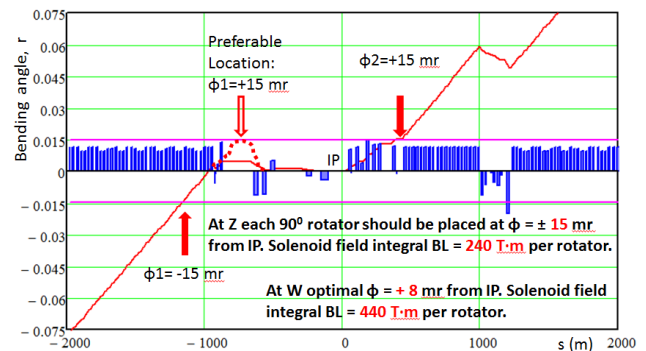


Figure 2: The accumulated bending angle distribution in FCC-ee experimental straight section (red solid curve). The dotted curve shows the desirable bending angle dependence optimal for the operation with longitudinal polarization at Z. The alternative place for inserting of the left side spin rotator is $\phi_1 = -15$ mr—seems easier for realization.

Therefore, for realization of the discussed above the ideal spin rotation scheme shown in Fig.1, the geometry of bends on the left side of the straight section should be changed so, as to provide empty drifts at $\phi = +15$ mr from IP. This is schematically shown in Fig.2 by the dotted red line. The alternative place for inserting the left side spin rotator, shown at Fig.2 by the red arrow, is $\phi = -15$ mr. This option, probably, is easier for realization, because all changes in the ring layout should be done at much larger distance from IP, thus not affecting the background problems from SR near detector. In this option the angle between axis of the left and the right rota-

[†]koop@inp.nsk.su
WEXAA04

tors is near $\phi=30$ mr and, correspondingly, spin makes half turn around the vertical axis by such bend between rotators at some specific spin tune, say at $\nu_0 = 101.4$. The difference in depolarization rates between two options is not large. At the Fig.3 are plotted the dependences of modules of the spin-orbit coupling vector $d = |\gamma \partial \vec{n} / \partial \gamma|$ on the spin tune for two discussed above layouts: with zero integral bend between rotators and with $\phi=31$ mr (spin rotation is exactly by π at $\nu_0 = 101.4$). In both cases the same spin perturbation $w=0.01$ is introduced at some ring azimuth. There one can see many minimums, roughly $d = 10 \div 12$, near half-integer spin tunes—optimal energy points for preserving beams polarization.

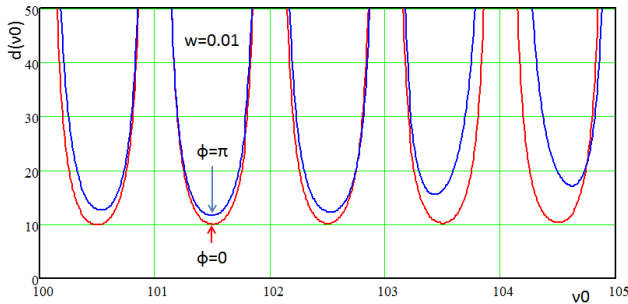


Figure 3: Module of the spin-orbit coupling vectors in arcs of FCC-ee for two options: spin rotations by bends between left and right spin rotators are $\phi=0$ and $\phi=\pi$ at $\nu_0 = 101.4$. In both cases the same spin perturbation $w=0.01$ is introduced at some ring azimuth.

The depolarization rate τ^{-1} depends on the average value of the d -factor as [6]:

$$\tau^{-1} = \tau_{ST}^{-1} \left(1 + \frac{11}{18} d^2 \right),$$

where $\tau_{ST} = 260$ hours at Z is the Sokolov-Ternov self-polarization time. Obviously we can reduce it, say, to $\tau = 0.5 \div 1.5$ hours—the expected luminosity life-time. Hence, the permissible value of the d -factor is about $d = 17 \div 30$, correspondingly the spin perturbation value should not exceed $w = 0.017 \div 0.03$. This goal can easily be reached applying the well-known harmonic spin matching technique [7, 8], because even with $\sigma_Q = 50 \mu\text{m}$ the average accuracy of quadrupole lenses alignment reaches only $w=0.02$ according our estimations.

MAKING BEAMS POLARIZED

The injector chain of FCC-ee consists of 6 GeV linac, conversion system to produce positrons, two 1.54 GeV damping rings for cooling electrons and positrons, 6–20 GeV pre-booster synchrotron and finally the main booster synchrotron for acceleration of beams from 20 up to 182.5 GeV [9].

The polarized electron beam of full intensity can be achieved from the polarised electron gun, as it was al-

ready demonstrated in many labs, experiments and proposals. Here we will discuss only a problem of how a positron beam can be made polarized via the Sokolov-Ternov mechanism in a special wiggler-ring with asymmetric bending fields. An example of parameters for such storage ring is presented in the Table 1.

The radiative polarization time is inverse proportional to fifth power of beam energy and cubic power of the modulus of an orbit curvature [4]:

$$\tau_p^{-1} = \frac{5\sqrt{3}}{8} \lambda_e r_e c \gamma^5 \langle |K|^3 \rangle.$$

Obviously, to get a short polarization time it is desirable to use very high average bending field and choose beam energy as high as possible. In our example we consider the racetrack ring comprised with two 25 m arcs and two 5 m straight sections. Each of 20 FODO cells is comprised of 4 asymmetric wigglers. The positive $B1=10.5$ T pole has a length $L1=10$ cm, while two negative poles of a wiggler have the field $B2=-1.796$ T and a length $L2=-18$ cm. Each wiggler bends beam by 4.5° .

Table 1: Preliminary Specifications of Polarizing Positrons Wiggler-Ring

Parameter	Value	Dimension
Beam energy, E	1.54	GeV
Circumference, C	60	m
Bending radii: $r1, r2$	0.49, -2.86	m
Bending fields, $B1, B2$	10.5, -1.8	T
Energy loss/turn, ΔE	2.925	MeV
Momentum spread, $\sigma_{\Delta E/E}$	0.00166	
Bunch population, N	$2 \cdot 10^{10}$	
Number of bunches, N_b	20	
Bunch spacing, Δt	10	ns
Total beam current, I	0.32	A
SR power, P	937	kW
RF frequency, f_0	400	MHz
RF harmonic number, h	80	
RF voltage, V_{RF}	4	MV
Bucket size, $A_{\Delta E/E}$	1	%
Synchrotron tune, ν_s	0.0235	
Bunch length, σ_s	16.5	mm
Polarization time, τ_p	9.8	s
Polarization degree, P	77.5%	after 20 s

In such a ring 77.5% polarization degree will appear in 20 seconds (after two polarization time), while the asymptotic polarization level is 89%.

A sequence of injections/extractions looks as follows. A fresh, unpolarised bunch of positrons is extracted every second from the low emittance 1.54 GeV damping ring and injected into the wiggler-ring. There each bunch is becoming polarized being stored in this ring for 20 s, or approximately for two polarization time. After that the polarized bunch is returned to the main damping ring for cooldown, simultaneously be replaced by a new unpolarized bunch from it. Assuming the beam lifetime

$\tau_{beam} = 4000$ s and the production rate $\dot{N}_{e^+} = 2 \cdot 10^{10}$ positrons per second, we can store in the collider ring 500 of the full intensity bunches with the nominal bunch population $N = 1.7 \cdot 10^{11}$ positrons per bunch. This corresponds to a luminosity of $L = 0.7 \cdot 10^{35} \text{ cm}^{-2} \text{ s}^{-1}$ for experiments with doubly polarized beams near Z-peak. But FCC-ee collider can handle up to 16640 bunches of such intensity. So, all extra collisions, beyond of 500 doubly polarized, will proceed in the un-polarized mode, or with polarized electron bunches only.

To reach the higher luminosity, one should increase the ring circumference and proportionally the number of wigglers. This looks at first glance not very reasonable but more difficult for realization.

ACCELERATION OF POLARIZED BEAMS IN A BOOSTER

Let's now discuss problems of how one can preserve polarization during acceleration of beams in the main booster synchrotron. The nominal ramping speed is 25 GeV in 0.32 s, or equivalently: $d\nu/dN = 0.056$ spin rotations per turn. We have performed the spin tracking simulations of how polarization will be lost during the acceleration process. First option, presented on Fig.4, assumes fast crossing of many integer resonances in presence of a local spin perturbation with some reasonable strength $w=0.02$. We limit the range of spin tune ramp by the diapason $89 < \nu_0 < 104$. One can see that polarization loss for this option is unacceptably high—each crossing of integer resonance kills about 10–20 % of the polarization degree.

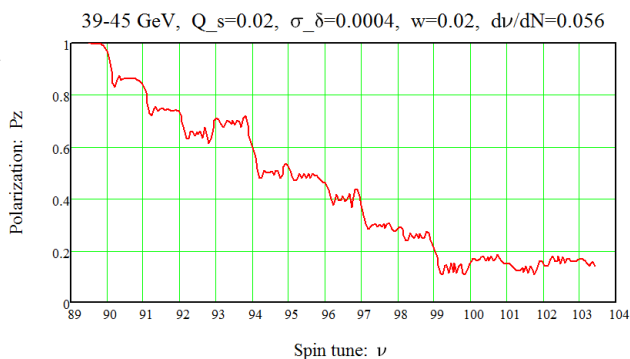


Figure 4: Drop of beam polarization during “fast” crossing of many integer resonances. Local spin perturbation is chosen $w=0.02$.

The second option assumes acceleration in presence of a weak Partial Snake. Results of same simulations are shown in Fig.5. In this option all spins are reversing coherently their vertical component when crossing each integer resonance and polarization is preserved quite well. On our opinion this option is most favourable for acceleration up to Z peak. Solenoids of a snake can be kept static, while all quads inside the snake's insertion will be ramped in such a way, that matrix of the insertion will be kept constant and fully uncoupled. The need longitudinal

field integral is about $BL = 200 \text{ T}\cdot\text{m}$. Then at 20 GeV we will have $w=0.5$ (full snake!) and $w=0.22$ at 45.6 GeV. 45.6 GeV, $Q_s=0.02$, $\sigma_\delta=0.0004$, $w=0.2$, $d\nu/dN=0.056$

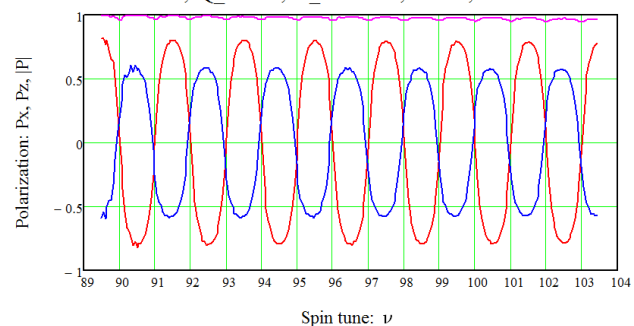


Figure 5: Acceleration in a booster ring with Partial Snake strength $w=0.2$. Polarization loss is only 3.5%.

Unfortunately, the Partial Snake scheme does not work for beam acceleration up to W threshold. Then beam is subjected to rather fast depolarization. For this energy interval is mandatory to avoid any crossing of integer resonance. Also d -factor should be as small as possible—means spin should be vertical in arcs. All this is accomplished in a third option [10–11], which assumes preservation of polarization with the use of even numbers of full Siberian Snakes. They divide a booster ring in unequal bending arcs, see Fig.6. Stable spin direction is vertical everywhere, but changes the sign after passing through each snake. The global spin tune became very low in this option. For example: with the asymmetry parameter $\chi=0.002$ the spin tune reaches the value $\nu = \chi\nu_0 = 0.363$ for $\nu_0 = 181.5$ ($E=80 \text{ GeV}$).

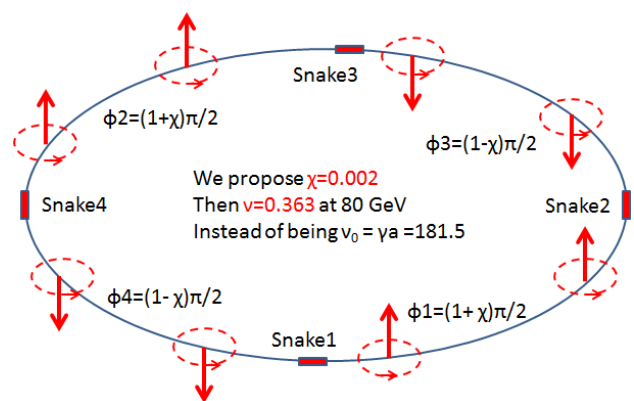


Figure 6: Four Siberian Snakes divide a ring in four unequal arc segments. The stable spin direction is vertical and changes a sign after each Snake.

This makes possible acceleration of polarized beams up to very high energy, say up to 80 GeV. The only problem now is that all solenoids should be ramped proportionally to the beam energy. That is an issue, which we leave for future technical studies. As an example, beam depolarization at 80 GeV induced by high localized spin perturbation $w=0.1$ is shown on Fig.7.

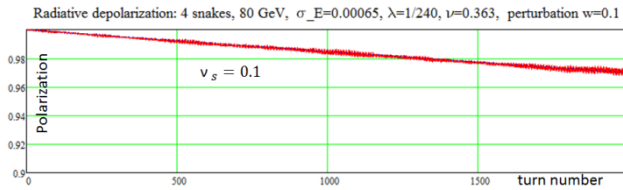


Figure 7: Spin tracking results for study of beam depolarization at 80 GeV ring with 4 Siberian Snakes. Spin perturbation value is $w=0.1$.

The observed depolarization time 18 s is sufficiently large and a polarized beam can be accelerated in 10 s without significant loss of the polarization from 20 GeV up to 80 GeV.

SOLENOID TYPE SPIN ROTATORS

Most robust lattice design of the solenoid type spin rotators is presented in the Fig.8.

For decoupling should be $T_x = -T_y$ [Litvinenko, Zholentz, 1980](#)

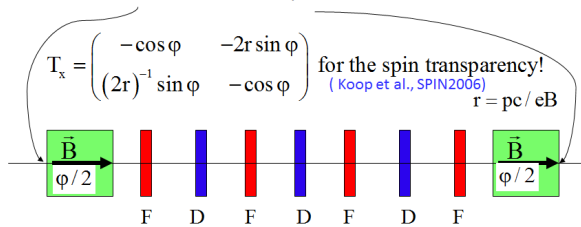


Figure 8: Optimal scheme of the solenoid type spin rotators.

Two identical solenoids and 7 quadrupole lenses in between comprise an insertion with the specified optical properties. Namely, their two-dimensional matrix blocks should satisfy the condition $T_y = -T_x$ to cancel x - y coupling [12]. Moreover, for spin transparency it is desirable to fulfil one extra condition [13]:

$$T_x = -T_y = \begin{pmatrix} -\cos \varphi & -2r \sin \varphi \\ (2r)^{-1} \sin \varphi & -\cos \varphi \end{pmatrix}, \quad r = Br/B$$

Seven quadrupole lenses, combined into four families, provide very good flexibility for achieving of the desired transformation properties of the insertion optics. It is remarkable that all quads in this scheme don't need to be made of skew type! The required optical solution can be found practically for any arbitrary solenoid strength. In particular, solenoids can be switched off, if polarization not needed at all.

CONCLUSION

At Z the longitudinal polarization looks feasible, but some changes in IR lattice are required to insert rotators at $\phi = \pm 15$ mr from IP.

At W both rotators should be moved to other drifts located at $\phi = \pm 8$ from IP. Depolarization rate will be roughly the same as without spin rotators, if their axes are parallel each other, and will be slightly higher, if the left side rotator will be placed at negative bending angle $\phi = -8$ mr.

In any case fast acceleration of pre-polarized electron and positron beams has to be foreseen. Partial Snake with static solenoids will preserve polarization during ramping up to Z-peak energies. But acceleration up to W requires use of few Siberian Snakes installed in the main booster.

ACKNOWLEDGEMENTS

We thank S.R. Mane for useful discussions and his help with running and providing of the new ASPIRRIN code.

REFERENCES

- [1] Ya. S. Derbenev *et al.*, Preprint IYaf SO AN SSSR 2-70, Novosibirsk, 1970.
- [2] N. Christ, F. J. M. Farley, H. G. Hereward, 1974. 5 pp. "On the feasibility of colliding beam experiments with longitudinally polarized electrons", Published in *NIM* 115 (1974), 227–231.
- [3] Ya. S. Derbenev and A. M. Kondratenko, Preprint IYaf SO AN SSSR 76-84, Novosibirsk, 1976. Proc. of V-th All-Union Conf. on Charged Particle Accelerators, Dubna, 1976.
- [4] Ya. S. Derbenev *et al.* "Radiative Polarization: Obtaining, Control, Using", *Part.Acc.* 8, 115, 1978.
- [5] K. Oide *et al.* "Design of Beam Optics for the FCC-ee Collider Ring", DOI: 10.18429/JACoW-IPAC2016-THPOR018 Conference: C16-05-08, p. THPOR018 Proceedings.
- [6] Ya. S. Derbenev, A.M. Kondratenko, "Polarization kinematics of particles in storage rings", *Sov. Phys. JETP* 37:968-973, 1973, *Zh. Eksp. Teor.Fiz.* 64:1918–1929, 1973.
- [7] D.P. Barber *et al.*, DESY 85-044 (1985).
- [8] R. Assmann *et al.*, "Polarization studies at LEP in 1993", CERN SL/94-08 (AP).
- [9] Y. Papaphilippou, talk at FCC Weak 2018, Amsterdam, 2018.
- [10] A. M. Kondratenko, Doktor degree thesis, Novosibirsk, 1982 (in russian).
- [11] S. R. Mane, in arXiv: 1406.0561v1 physics.acc-ph, 3 Jun 2014.
- [12] A. A. Zholents and V. N. Litvinenko, "On The Compensation Of Solenoid Field Effects By Quadrupole Lenses", DESY-L-TRANS-289, Mar 1984. 9pp. Translation of Novosibirsk preprint IYF-81-80 (translation).
- [13] I. A. Koop, A.V. Otboev, P. Yu. Shatunov, Yu. M. Shatunov, "Orbit and Spin transparent Siberian Snake and Spin Rotator with Solenoids", *SPIN2006*, Nagoya, Japan, 2006.

IR DESIGN ISSUES FOR HIGH LUMINOSITY AND LOW BACKGROUNDS*

M. K. Sullivan[†], SLAC National Accelerator Laboratory, 94025 Menlo Park, CA, USA

Abstract

New e^+e^- accelerator designs aim for factory-like performance with high-current beams and high luminosities. These new machines will push interaction region designs to new levels and require a careful evaluation of all previous background sources as well as introduce possibly new background sources. I present here a summary of standard background sources and also suggest a new possible background source for Synchrotron Radiation (SR) namely, specular reflection. In addition, one will have to pay closer attention to the beam tail particle distribution as this may become a significant source of SR background from the high-current and high-energy beams of these new designs.

INTRODUCTION

The Interaction Region (IR) of a colliding beam e^+e^- accelerator is always one of the more challenging aspects of the collider design. In order to obtain a high luminosity, usually done by having many beam bunches, nearly all designs now have a separate storage ring for each beam. This in turn means that the collision has a crossing angle (only the PEP-II B-factory had separate storage rings and a head-on collision through the use of strong bending magnets close to the Interaction Point (IP)). Crossing angles for new or recently completed designs range from ± 15 mrad (FCCee [1,2]) to ± 41.5 mrad (superKEKB [3]). The demand for high-luminosity ($\sim 10^{34}$ - 10^{36} cm $^{-2}$ s $^{-1}$) requires the final focus magnets to be close to the IP (~ 1 m) in order to get the necessary small spot size at the collision point. I will first discuss some of the standard layout issues for a collision point and how these affect the background studies. Then I will concentrate on the various background issues related to SR and, in particular, discuss the potential for specular reflection to become a possible new SR background source. I will then look more closely at the issue of the beam tail particle distribution and how this distribution can become an important source of SR backgrounds. Finally, I will mention the standard beam particle backgrounds that must always be studied along with some of the other accelerator related issues that must be evaluated before an IR design can be accepted.

THE IR DESIGN

Final Focus Quadrupoles

As mentioned above, modern factory designs have a

* Work supported by the U.S. Department of Energy, Office of Science, Office of Basic Energy Sciences, under Contract No. DE-AC02-76SF00515 and HEP

[†] sullivan@slac.stanford.edu

crossing angle between the beams at the collision point. The crossing angle is imposed by the requirement that the focusing elements in each beam are independent (i.e. there are no shared magnets – no quadrupoles that have both beams). In addition, the Final Focus (FF) magnets are placed close to the IP. The short L^* values (~ 1 -2 m) in these designs mean that these FF quadrupoles are quite strong and that the beta functions in these quads tend to be large. This makes the FF magnets an important source of SR production. This is especially true of the high-energy (FCCee and CEPC) designs. Here the FF magnets are focusing a very high-energy beam and the SR energy spectrum from these magnets is well into the MeV range. The photons from this higher energy spectrum need to be masked and the high energy of these photons make this more difficult. Figures 1a and 1b illustrate the masking issues for SR that comes from the FF magnets.

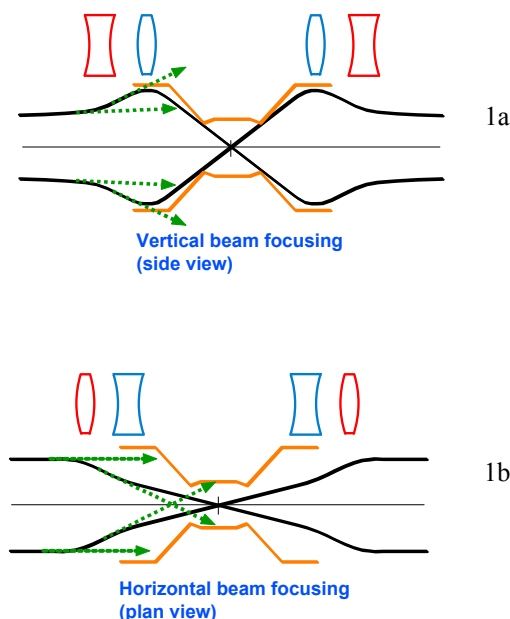


Figure 1: Illustration of the primary issues in shielding a central beam pipe from the SR coming from final focus magnets. 1a: Vertical view of the FF magnets and IP. The SR generated in the vertical comes from the beam when it is defocused in X-focusing magnet (red outline) which is usually before the Y-focusing magnet (blue outline) the last magnet before the IP. The X-focusing magnet generates fans of SR that are between the two green dashed arrows in the drawing. There is another fan from the Y-focusing magnet that is between the outside green dashed arrows and the beam envelope that hits the IP. This radiation is easier to shield than the radiation shown in 1b. 1b: Plan view showing the horizontal radiation fans generated by the beam in the X-focusing magnet which is before the Y-focusing magnet. This radiation is more difficult to shield.

shield as the SR fans cross-over the beam axis because of the over-focusing nature of this magnet. The horizontally focusing magnet must over-focus in order to compensate for the defocusing that comes from the Y-focusing magnet. This can be seen from the outline of the beam envelope (black lines) in the drawings.

The close FF quadrupoles will obscure more of the low angle acceptance of the detector. In order to minimize this the outer radius of these quadrupoles is minimized. The large beam size in these magnets and the need to minimize the outer radius tends to push the magnet design to a cold bore configuration. This can be okay, but the SR generated by the upstream FF magnets must then not strike the inner bore of the downstream FF magnets in each beam line. If masking the downstream magnet bores is needed, this mask can become a backscatter source of SR photons for the detector and care must be taken to minimize this potential source of background.

OTHER SR BACKGROUNDS

Secondary SR Sources

Once primary strikes of SR photons on the central beam pipe have been masked away it becomes necessary to consider all possible cases of secondary radiation coming from one bounce and/or mask tip scattering. The high-energy beams of new accelerator designs have higher energy photon spectra, and this will increase the rate of secondary sources. In addition, the high-current beams of all designs also increase the secondary source rates.

Tip scattering is an unavoidable source of secondary SR background. The SR photons that strike near an edge or near the corner of a mask have a chance of scattering through the mask material and striking the central detector beam pipe. The tip scattering rate increases as the incident photon energy increases (higher energy photons have a greater chance of scattering through the material). Figure 2 illustrates this source of SR background.

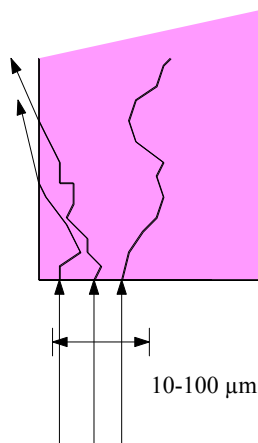


Figure 2: The SR photons that strike a mask either near a tip or near an edge have a chance of scattering through the material. Some fraction of these forward-scattered photons will strike the central beam pipe.

Tip scattering can be minimized through material selection for the mask. A high Z material is usually better, and this choice is also usually better for beam particle backgrounds. When possible, moving the mask tip back away (in Z) from the central beam pipe reduces the solid angle acceptance to the central beam pipe for the scattered photons. This can sometimes be done with an upstream mask intercepting the majority of the incident radiation and the closer mask then receiving a reduced incident photon rate.

Backscatter from either downstream beam pipe surfaces or downstream masks can be a serious source of detector background from SR. Here again, keeping these sources as far away as possible from the IP will reduce the solid angle acceptance back to the central beam pipe and keep these backgrounds low. Also, the choice of mask material can be tailored to a specific photon energy spectrum and this can help reduce the rate from this downstream secondary source.

Coating the central beam pipe (which is invariably made of Be) with a thin layer of high Z material (i.e. Au), can significantly cut down the penetration rate of incident photons if the photon energy is low enough (usually <10-20 keV). However, at the very high energy machines (i.e. the FCCee at the top energy), it is not so clear that a thin layer of high Z material helps since the photon energies are so much higher. In this case, a lower Z material (i.e. Cu) may be selected for conductivity issues rather than for SR photon absorption. The lower Z material of course reduces the track multiple scattering – a feature generally desired by the detector team.

Upstream Last Bend Magnet

The last bend magnet before the IP always sends SR into the IR. This radiation must always be masked away from the central chamber. All designs strive to make this last bend magnet weak and as far from the IP as reasonable. The number of photons decreases with increasing distance and the energy spectrum of the SR photons diminishes linearly with the magnetic field strength. A soft energy photon spectrum is much easier to mask away from the central beam pipe but the increase in low energy photons and the large distance from the IP together can make a possible new source of detector background (see below).

Specular Reflection

When the photon energy spectrum is soft, and the angle of incidence is small many of the incident photons can actually mirror reflect (specular reflection) off of a surface. See Fig. 3. The number of mirror-reflected photons can be much higher than the number of photons that scatter out of the incident surface. I have found one reference where a surface of *unpolished* Cu had a reflection coefficient of nearly 20% for incident photons up to 25 keV at an incident angle of 3.5 mrad [4]. The material tested was similar to the type of inside surface found in a Cu beam pipe.

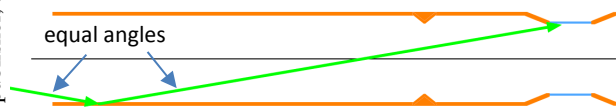


Figure 3: Photons from specular reflection off of a beam pipe surface that is far upstream of the IP might be able to avoid the local masking scheme and strike the central beam pipe.

This background source is particularly difficult to simulate. One has to know a great deal about the inner surface of the vacuum chamber as well as some information on the reflection coefficient as a function of incident photon energy and incident photon angle. Special cases have been simulated and work is ongoing to put specular reflection into several codes [5-8].

The best procedure to check for specular reflection is by inspecting the geometry of the design. If it is possible for reflected photons to strike the central beam pipe, then proceed to install masking or rearrange the geometry so that specular reflection photons can no longer strike the central chamber. This may have to include the study of multiple bounces as parallel beam pipe surfaces may be able to “pipe” the reflected photons over long distances [9].

BEAM TAILS

All stored beams have a non-gaussian beam tail. The particle distribution comes about from several different factors, 1) quantum fluctuations in SR emission, 2) beam-beam interactions, 3) beam-gas interactions, 4) Inter-beam scattering to name a few. This tail distribution can contribute to detector backgrounds by two methods: 1) the high sigma particles may get lost inside the IR and 2) the high sigma particles can emit SR inside the final focus quads generating steep angle photons that have a chance of getting around the masking scheme and either hitting the central detector beam pipe directly or hit nearby surfaces that can one bounce to the central beam pipe. The number of beam particles in the tail distribution should not be more than about 1-2% of the total. Anything much above this number would start to be noticeable as a discrepancy in the calculation of the luminosity since the tail particles do not contribute to the luminosity [10]. On the other hand, there cannot be too many particles at very high sigma or out where there is a physical aperture as these particles would be scrapped off and cause beam lifetimes that are too short. M. Sands [11] has made an estimate of the particle density at an aperture limit as a function of lifetime and concludes that a particle density equivalent to the 6σ value of the standard beam gaussian sets a lifetime of about 1 day. New accelerators accept lifetimes of less than 1 hr and in some cases as little as 10 min. This means the particle density at an aperture limit (like a collimator) can be quite a bit higher. Figures 4a and 4b show plots of the tail distributions used by the SR background simulation program SYNC_BKG [12]. The tail is a second flatter gaussian compared to the primary

beam gaussian (shown with a blue line). In addition, the plot shows the particle density levels for several beam lifetime estimates based on the calculation made by Sands.

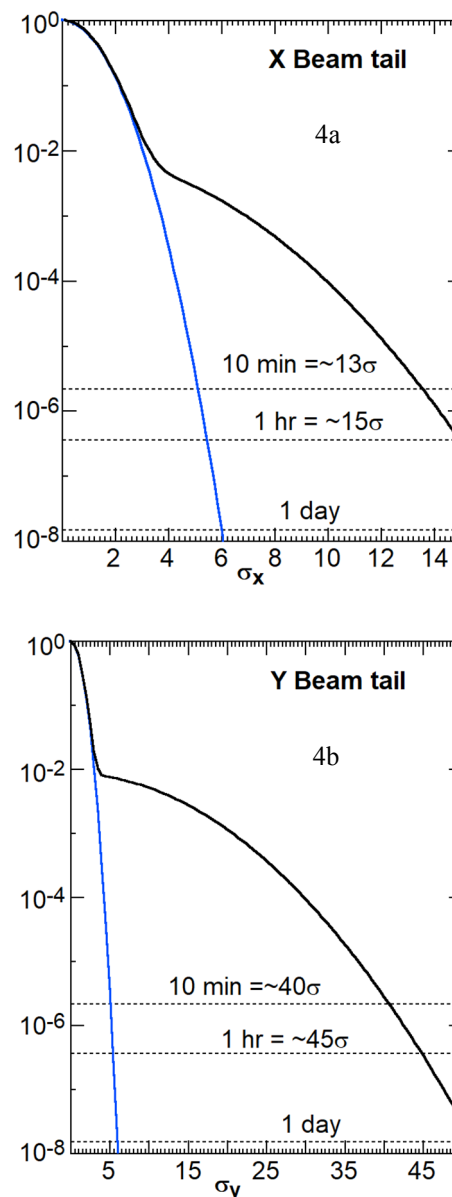


Figure 4: Figure 4a is a plot of the X tail distribution with dashed horizontal lines indicating approximate beam lifetimes based on the estimate by M. Sands. The blue lines in 4a and 4b are the profile of the main beam gaussian. Figure 4b is the vertical tail distribution. Here we assume the main beam bunch vertical sigma is smaller than the horizontal sigma and subsequently increase the aperture out to about 50σ . The vertical tail is consequently depicted as being flatter than the horizontal beam tail. The 2D integral of the tail distribution shown in these plots above leads to a sum of about 0.3% or almost 10 times lower than the estimated upper limit.

The estimates listed previously concerning the possible range of the beam tail distribution still leaves a lot of room. The tail distributions above might be called too

small for an initial commissioning accelerator since there is a lot of outgassing from any new machine when beam is first stored in a ring and this should contribute significantly to the beam tail. The background study for an IR should include rather conservative estimates of the beam tail (i.e. a low lifetime or close to our 2% upper limit for the integral or perhaps both).

Equation (1) is the formula used to generate the core and tail distributions shown above where $a = 8.5 \times 10^{-3}$ for both plots and $b = 0.3$ for the X plot and 0.1 for the Y plot.

$$e^{-\left(\frac{x^2}{2\sigma^2}\right)} + ae^{-\left(\frac{b^2x^2}{2\sigma^2}\right)} \quad (1)$$

LUMINOSITY BACKGROUNDS

The initial B-factories (PEP-II and KEKB) were the first machines to encounter issues from luminosity related backgrounds in e^+e^- circular colliders. There are two main luminosity backgrounds; radiative Bhabhas and low-energy e^+e^- pair production with the primary beam particles from the interaction going down the outgoing beam pipes and not being seen by the detector.

Radiative Bhabhas

The radiative Bhabhas produce a photon which lowers the energy of the outgoing beam particle that radiated. This off-energy beam particle is then mis-focused in the downstream final focus magnets and can be lost in the nearby downstream beam pipe. The PEP-II and KEKB B-factories both had designs with shared outgoing quadrupole magnets which meant that the outgoing beam was bent by the quadrupole field due to the beam being offset in this downstream quad. The off-energy radiative Bhabha beam particles were then swept out of the beam pipe close to the detector causing a significant increase in the overall background rate. All present and future IR designs for e^+e^- ring colliders do not have any shared magnets for this reason. Figure 5 illustrates the radiative Bhabha process.

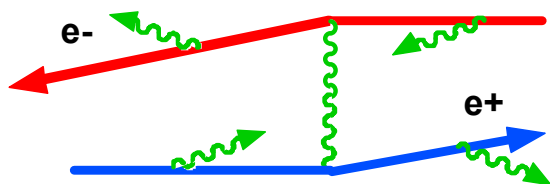


Figure 5: Depiction of the radiative Bhabha process. A radiative Bhabha interaction has only one photon in the final state. We show here the first four Feynman diagrams together for brevity. The interactions that occur from this process with a small scattering angle are the ones that tend to contribute to detector backgrounds.

Low-energy e^+e^- Pair Production

The 2nd luminosity background is the soft e^+e^- pair production. Here the low energy e^+e^- pair tend to curl up in

the detector solenoid field. However, if the energy of the pair is high enough then these low-energy electrons can get just outside of the central beam pipe and then travel in a path that runs through the first layer of the vertex tracker. This small-radius helical track will leave an enormous amount of ionization in the first layer effectively disabling large sections of the inner layer of the vertex tracker. The rate for this process tends to set the minimum radius of the central beam pipe. This rate is also dependent on the strength of the detector magnetic field. Figure 6 shows the Feynman diagram for this process.

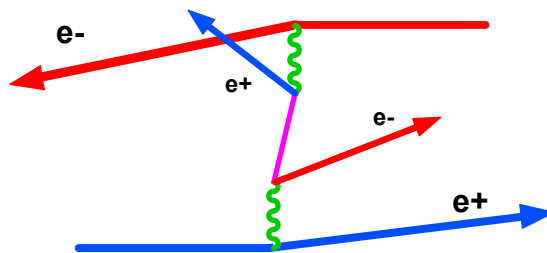


Figure 6: Illustration of the Feynman diagram for the low-energy e^+e^- pair production.

Of course, both of these luminosity backgrounds increase as the luminosity increases.

BEAM PARTICLE BACKGROUNDS

There are several general beam particle interactions that are standard detector background sources from stored beams. They are: 1) Beam-Gas interactions (BGB) where a beam particle interacts inelastically with a gas molecule and a high energy photon traveling along the beam particle trajectory is emitted along with an off-energy beam particle, 2) Coulomb scattering where a beam particle interacts elastically with a gas molecule resulting in a beam particle that is close to or outside of the storage ring phase space or dynamic aperture, 3) Inter-Bunch scattering (IBS) and Touschek scattering, interactions inside the beam bunch that kick beam particles out to high sigma values, 4) Beam-beam scattering where the interaction is at the collision point causing a shift in the tune of the stored beam particle which pushes it out to high sigma values (usually in the vertical plane), and 5) injection backgrounds where the injected bunch is inserted several beam sigmas off-axis with respect to the stored beam.

All of the beam particle interactions mentioned above generate beam particles out at high sigma values. The BGB and Coulomb scattering interactions are a linear function of the gas pressure and beam current. The IBS and Touschek interactions depend on the particle density in a bunch. High single bunch current and low emittance designs increase these interactions. However, low emittance and high single bunch current are directions machine people use to increase the luminosity. The backgrounds from beam-beam scattering due to the collision of course will tend to increase as the luminosity increases which usually means the tune shift increases.

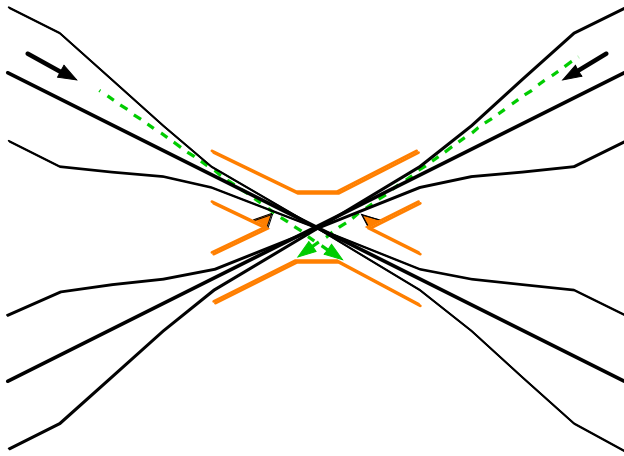


Figure 10: In order to mask the SR from the over-focused beam in the X plane, one must install very aggressive masking as close to the beam-stay-clear envelope as possible. Then the SR from the X-focusing quad will either hit the mask tip or will go past the central beam pipe. In this drawing we see the SR (dashed green lines) that just misses the mask tips and then is shown to just go past the central beam pipe.

The superKEKB accelerator at KEK has a crossing angle of 83 mrad (± 41.5 mrad) which is the largest collision crossing angle to date. Consequently, the design has followed the above description and has installed SR masking that tips starting at 0.245 m from the IP and have a radius of 4.5 mm. However, the superKEKB design calls for very small emittances and this means that this small radius mask tip is still more than 40σ away from the beam in the X plane.

OTHER IMPORTANT IR ISSUES

There are several more issues that need to be studied for all IR designs and some of these will need to be looked at more carefully due to the large beam currents and high beam energies. I will list some of these below with some comments.

HOM Heating

When the beams pass through the IR, they go from separate beam pipes to a shared beam pipe at the collision point. This means that there is a place on either side of the central beam pipe where the two separate beampipes join together. This region where the separate pipes come together always produces a region where the vacuum cross-section reaches a local maximum. The central beam pipe is usually as small as can be achieved based on backgrounds and other considerations which means we have two separate vacuum regions with a local maximum. This region will trap Higher-Order-Mode (HOM) RF energy with wavelengths that are too large to be able to travel down the outgoing beam pipes. This trapped RF power must be absorbed locally, and it is important to develop an absorbing mechanism [14]. This is especially true for high-current designs.

Image Current Heating

In addition to HOM heating there are heating issues coming from image currents. These currents travel along the inside wall of the beam pipe and can deposit power into the beam pipe material based on the I^2R losses in the material. Aside from the DC component in the power loss which is based on the average beam current, there is also an AC component related to the bunch length and to the bunch spacing. The AC part has a penetration depth into the material called the skin depth. For most accelerators this is on the order of a few microns. These losses are coming from both beams and that means that we can have a phase difference between the beams. In general, one does not know exactly what the phase difference will be between the beams, the best thing to do is to assume the power loss from each beam adds up in the central beampipe. Cooling for the central chamber is almost always necessary. For very high-energy configurations where the beam currents are significantly lower (i.e. FCCee running at the top energy) the power loss from both HOM and image current may be low enough to make beam pipe cooling unnecessary and this might allow for the possibility of installing an especially thin central beam pipe for this segment of machine running.

Vacuum Pressure

As mentioned earlier, it is important that the vacuum pressure upstream of the IP, between the collision point and the last upstream bend magnet, needs to be as low as reasonable. Preferably below 1×10^{-9} Torr. The vacuum pressure right at the IP does not need to be especially low as the volume of vacuum with a higher pressure is quite small and any beam-gas interactions from this region do not have a big impact on the detector background rate. This same argument is true for the downstream beam pipes.

Injection Backgrounds

The injected bunch that enters the stored beam comes in off-axis (either in X or in Y). This off-axis sub-bunch (usually less than 10% of the stored bunch, especially for continuous injection) damps down into the stored bunch after several turns. During the damping time, this part of the stored beam usually generates significantly higher backgrounds in the detector and in many cases, this particular stored beam bunch is blanked out from the detector trigger and data acquisition. For continuous injection designs it is important to estimate this increase in background and make sure that the added background levels are tolerable with regards to integrated radiation dosage.

CONCLUSION

There are always a large number of conflicting issues that need to be addressed in order for an IR design in a new accelerator to become feasible. The detector needs to be able to efficiently collect the physics and the accelerator needs to be able to achieve the luminosity. Both of these requirements are crucial in order for the overall

design to be a success. High luminosity and large beam currents together with high-energy beams increase the importance of checking and cross-checking detector backgrounds as well as engineering feasibility of any particular IR design. The new factories (primarily Higgs factories) will push collider and IR designs into a new regime and new source terms for detector backgrounds as well as new issues affecting accelerator performance may come to light. It is important to continue to review past design decisions and to explore possible new issues that may come up especially as the overall design matures. Small changes in the accelerator running conditions can produce a significant impact on the IR design by requiring changes in the SR masking design or in the size of the central beam pipe or in the collimator scheme designed to protect the IR from beam related backgrounds.

ACKNOWLEDGMENTS

I would like to thank the organizers of this workshop for the opportunity to write up this summary of IR issues for high-luminosity e^+e^- circular colliders. I would especially like to thank M. Boscolo for presenting this summary to the workshop.

REFERENCES

[1] M. Koratzinos, *et. al.*, “The FCC-ee Study: Progress and Challenges”, <https://arxiv.org/abs/1506.00918>

[2] M. Koratzinos, *et. al.*, “FCC-ee accelerator parameters, performance and limitations”, *37th International Conference on High Energy Physics (ICHEP)*, (2015), <https://doi.org/10.1016/j.nuclphysbps.2015.09.380>

[3] Y. Ohnishi, *et.al.*, “Accelerator Design at SuperKEKB”, *Prog. Theor. Exp. Phys.* 2013, 03A011 (2013), <https://doi.org/10.1093/ptep/pts083>

[4] D. H. Bilderback and S. Hubbard, “X-ray Mirror Reflectivities from 3.8 to 50 keV”, Pt. II, *NIM* 195 pgs. 91-95, (1982)

[5] H. Burkhardt, https://indico.cern.ch/event/497514/contributions/1177065/attachments/1231011/1804574/G4dev_FW_Options_2016_02_18.pdf

[6] R. Cimino, V. Baglin, F. Schäfers, “Potential Remedies for the High Synchrotron-Radiation-Induced Heat Load for Future Highest-Energy-Proton Circular Colliders”, *Phys. Rev. Lett.* **115**, 264804, <https://doi.org/10.1103/PhysRevLett.115.264804>

[7] G. Dugan and D. Sagan, “Simulating synchrotron radiation in accelerators including diffuse and specular reflections”, *Phys. Rev. Accel. Beams* **20**, 020708, <https://doi.org/10.1103/PhysRevAccelBeams.20.020708>

[8] G. F. Dugan, K. G. Sonnad, R. Cimino, T. Ishibashi, and F. Schäfers, “Measurements of x-ray scattering from accelerator vacuum chamber surfaces, and comparison with an analytical model”, *Phys. Rev. ST Accel. Beams* **18**, 040704, <https://doi.org/10.1103/PhysRevSTAB.18.040704>

[9] L. Jones, T. Dershem, “Synchrotron Radiation from protons in a 20 TeV, 10 Tesla superconducting super collider”, *Prod. Of the 12th International Conference on High-Energy Accelerators*, 1983, pg 138

[10] Ewan Patterson. Private communication.

[11] M. Sands, “Physics of Electron Storage Rings an Introduction”, SLAC-121 (1979) sect. 5.7 pg. 141.

[12] M. Sullivan, “A suite of simulation programs used to model Synchrotron Radiation emission from magnets close to the Interaction Region in electron beam accelerators”, in preparation.

[13] H. Burkhardt was one of the first to mention this possible new source of neutrons as a background issue.

[14] A. Novokhatski, E. Belli, M. G. Costa, R. Kersevan, M. Sullivan, “Unavoidable trapped mode in the interaction region of colliding beams”, *Phys. Rev. Accel. Beams* **20**, 111005, <https://doi.org/10.1103/PhysRevAccelBeams.20.111005>

MACHINE DETECTOR INTERFACE FOR THE e^+e^- FUTURE CIRCULAR COLLIDER

M. Boscolo*, O.R. Blanco-Garcia, INFN/LNF, Frascati, Italy
N. Bacchetta¹, E. Belli², M. Benedikt, H. Burkhardt, M. Gil Costa, K. Elsener,
E. Leogrande, P. Janot, H. Ten Kate, D. El Khechen, A. Kolano, R. Kersevan,
M. Lueckhof, K. Oide, E. Perez, N.A. Teherani, O. Viazlo, Y. Voutsinas and
F. Zimmermann, CERN, Geneva, Switzerland
M. Dam, Niels Bohr Institute, Copenhagen, Denmark
A. Blondel, M. Koratzinos, DPNC/Geneva University, Geneva, Switzerland
A. Novokhatski, M. Sullivan, SLAC, Menlo Park, California, USA
A. V. Bogomyagkov, E. B. Levichev, S. Sinyatkin, BINP SB RAS, Novosibirsk, Russia
F. Collamati, INFN-Rome1, Rome, Italy
¹also INFN-Padova, Padova, Italy
²also at University of Rome Sapienza and INFN-Roma1, Rome, Italy

Abstract

The international Future Circular Collider (FCC) study [1] aims at a design of p-p, e^+e^- , e-p colliders to be built in a new 100 km tunnel in the Geneva region. The e^+e^- collider (FCC-ee) has a centre of mass energy range between 90 (Z-pole) and 375 GeV ($t\bar{t}$). To reach such unprecedented energies and luminosities, the design of the interaction region is crucial. The crab-waist collision scheme [2] has been chosen for the design and it will be compatible with all beam energies. In this paper we will describe the machine detector interface layout including the solenoid compensation scheme. We will describe how this layout fulfills all the requirements set by the parameters table and by the physical constraints. We will summarize the studies of the impact of the synchrotron radiation, the analysis of trapped modes and of the backgrounds induced by single beam and luminosity effects giving an estimate of the losses in the interaction region and in the detector.

LAYOUT AND DESIGN CRITERIA

The FCC-ee collider with 100 km circumference and a wide range of beam energies, from 45.6 to 182.5 GeV, aims at unprecedented levels of energies and luminosities. The requirements at the collision point for the accelerator and detector make the interaction region (IR) one of the most challenging parts of the overall design, this region is named machine detector interface (MDI). Table 1 summarizes the most relevant beam parameters for the MDI design.

To reach the target luminosity of $2.3 \times 10^{36} \text{cm}^{-2}\text{s}^{-1}$ at the Z-pole the crab-waist collision scheme is a necessary ingredient together with pushing the beam current to the limit, obtainable with double rings. The baseline optics for the FCC-ee double-ring collider is described in Ref. [3]. The main characteristics of the optics design are two interaction points (IPs) per ring, horizontal crossing angle of

Table 1: FCC-ee beam parameters most relevant for the IR design

Parameter	Z	W ⁻ W ⁺	ZH	$t\bar{t}$
E _{beam} (GeV)	45.6	80	120	182.5
Luminosity ($10^{34} \text{cm}^{-2}\text{s}^{-1}$)	230	28	8.5	1.55
Beam current (mA)	1390	147	29	5.4
Particles/bunch (10^{11})	1.7	1.5	1.8	2.3
Horiz. emittance (nm)	0.27	0.84	0.63	1.46
Vert. emittance (pm)	1.0	1.7	1.3	2.9
β_x^* (m)	0.15	0.2	0.3	1.0
β_y^* (mm)	0.8	1.0	1.0	1.6
σ_x^* (μm)	6.4	13	13.7	38.2
σ_y^* (nm)	28	41	36	68
SR bunch length (mm)	3.5	3	3.15	1.97
total bunch length (mm)	12.1	6	5.3	2.54
RF Acceptance (%)	1.9	2.3	2.3	3.36
DA energy accept. (%)	1.3	1.3	1.7	-2.8/+2.4
Rad. Bhabha Lifetime (min)	68	59	38	40
Beamstr. Lifetime (min)	> 200	> 200	18	18

30 mrad at the IP and the crab-waist scheme with local chromatic correction system. A so-called tapering of the magnets scales all the magnetic fields with the local beam energy as determined by the SR. This optics is being improved and modified, for instance one of the most relevant modification for the IR design is the reduction of β_x^* to 15 cm at the Z to mitigate the coherent beam-beam instability [4]. Nominal emittances are very small and especially in the vertical plane the target value of $\epsilon_y = 1 \text{ pm}$ at the Z-pole poses stringent requirements on misalignment tolerances as well as on coupling correction. The design restricts the total synchrotron radiation (SR) power at 100 MW, thus the stored current per beam varies from 1.4 A at Z to 5.4 mA at $t\bar{t}$. Following the LEP2 experience where the highest local critical energy was 72 keV for photons emitted 260 m from the IP [5] the FCC-ee optics design maintains critical energies from bending

* manuela.boscolo@lnf.infn.it

magnets below 100 keV starting from 100 m from the IP; critical energy from the first bend after the IP is higher, being 691 keV at $t\bar{t}$. An asymmetric optics has been designed to meet these goals on the critical energy. The asymmetry allows each beam to come from the inner ring to the IP, to be bent strongly after the IP and to be merged back close to the opposite ring. Outside the IR, the FCC-ee and FCC-hh trajectories are on the same footprint while an additional tunnel is necessary for 1.2 km around the IP in order to allow for the crab-waist collision scheme with large crossing angle. The collider layout is shown in Fig. 1 with the two beam trajectories.

Figure 2 shows an expanded horizontal view for the region ± 3 m from the IP. The free length between the interaction point (IP) and the first final focus quadrupole (QC1) L^* is 2.2 m. The IR is symmetric and the two beam pipes are merged together at about 1 m from the IP and the distance between the magnetic centres of the two QC1 for the two beams is only few cm. In Fig. 2 are also shown the main components such as the first focusing quadrupole named QC1 in yellow. The first element at about 1 m from the IP is the luminosity counter, magenta in the plot and in red and blue the instrumentation and cables, followed by the compensating solenoid in light green and by the screening solenoid starting at about 2 m and out of this plot. The High Order Mode (HOM) absorber is in dark yellow, the Tungsten shielding outside the vacuum pipe is in light blue. The detector solenoid, a cylinder with half-length 4 m and a diameter of around 3.8 m, is outside this picture. Its peak value is 2 T. To reduce multiple scattering effects in the luminosity monitor the vacuum chamber from ± 0.9 m from the IP will be made of Beryllium followed by a Copper vacuum chamber throughout the final focus doublet. Synchrotron radiation mask tips are also shown in the plot, they are placed in the

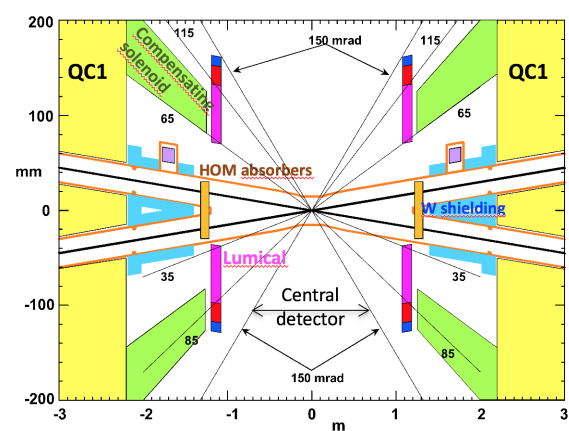


Figure 2: IR layout top view (x-z plane); note the expanded scale for the ordinate (± 200 mm) with respect to the abscissa (± 3 m).

horizontal plane just in front of QC1 at 2.1 m from the IP to intercept SR scattered particles. At the mask tips the horizontal aperture will be reduced from 15 mm to 12 mm. The beam pipe will be at room temperature and water cooling is foreseen throughout the IR, including inside the superconducting final focus quadrupoles. The compactness of the MDI design, as result of the available space to host all the necessary components is a challenge. An integration study with an assembly concept is in progress, to study the feasibility of this design. In addition to the elements shown in Fig. 2, also beam position monitors, flanges, bellows, cryostat, vacuum pump need to be placed.

SOLENOID COMPENSATION SCHEME

The crab-waist collision scheme requires very small vertical beam sizes at the IP which implies the first final focus quadrupole to be strong and close to the IP. It needs to be so close to the IP that it is located inside the main detector solenoid. The additional ingredient for the crab-waist scheme is the large crossing angle, which brings the two beam trajectories to pass off-axis from the detector solenoid, inducing also an increase of the vertical emittance. To handle this unwanted effect, the detector solenoid field maximum is set at 2 T and, on the other hand, a compensation solenoid is foreseen as close as possible to the IP. A screening solenoid is also needed to surround QC1 to avoid transverse beam coupling. A compact design is needed to leave a large physics detector acceptance; the accelerator components are required to stay below an angle of 100 mrad from the beam axis. This design gives an overall emittance blow-up estimate of 0.3 pm for two IPs at the Z-pole.

The stringent requirements of the final focus quadrupoles can be satisfied by using canted-cosine-theta (CCT) technology. It is an iron-free design with crosstalk and edge effect compensation, giving a field quality of better than one unit for all multipoles. Dipole and skew quadrupole correctors can be incorporated without increasing the length

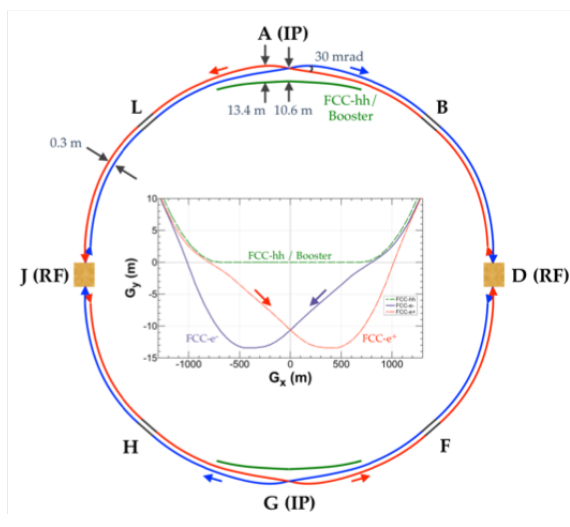


Figure 1: Schematic layout of the FCC-ee collider rings. The green line indicates the beamline of the FCC-ee booster and hadron collider FCC-hh. The plot in the middle shows the two beams trajectories at the IP.

of the magnetic system. The vertical emittance blow-up due to residual magnetic field has been estimated with SAD, finding an increase of 0.3 pm. A full mechanical and thermal engineering analysis has been performed as well. In order to prove feasibility, a prototype of this design is under construction at CERN.

IR TRAPPED MODES AND HIGH ORDER MODE ABSORBER

The high beam currents produce electromagnetic waves in the IR. The geometry of the beam pipe in the IR is as constant and smooth as possible to avoid unwanted electromagnetic trapped modes and heating problems. However, in the IR the two beams may generate electromagnetic waves where the vacuum chambers are combined into one near the collision point [6]. This region is shown in Fig. 3. The high order

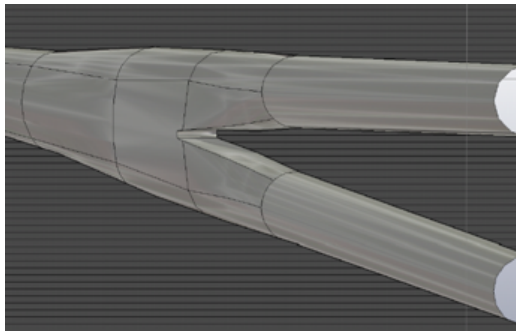


Figure 3: 3D CAD view of the IR vacuum chamber in the region where two beam pipes are merged together.

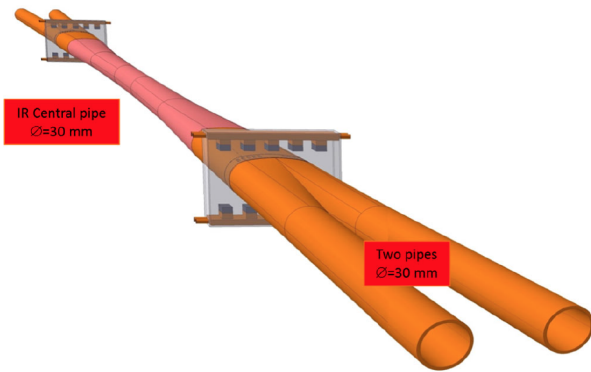


Figure 4: HOM absorbers design.

modes (HOM) that interact with a beam particle may cause local heating in the IR and typically their frequencies are in the range of several GHz. Other electromagnetic waves, excited by the beam, with a frequency above the cutoff will travel away from the IR and may cause heating downstream the ring. 3D calculations have been carried out using CST [7] and HFSS [8] codes. The numerical simulations show that there is a trapped mode with a frequency of 3.459 GHz

Table 2: Summary table of the SR coming from the last soft bend upstream the IP. Second column gives the incident number of photons in the central beam pipe per second.

E_{beam} GeV	E_{critical} keV	γ rate on central pipe (Hz)
182.5	113.4	1.18×10^8
175	100	1.25×10^8
125	36.4	1.01×10^7
80	9.56	7.02×10^5
45.6	1.77	9.58×10^3

and 2.91 kW power. This effect can be mitigated by HOM absorbers, with slots oriented perpendicular to the HOM electric field, allowing the mode field to easily propagate through these slots and, at the same time, the beam field, will not pass. Water cooled absorbers are above and below the slots. They will be placed in the region where the two beam pipes are split in two, and just after the luminosity calorimeter, symmetrically from the IP. Fig. 4 shows the HOM absorbers design, which includes a water cooling system to avoid heating.

SYNCHROTRON RADIATION

The large crossing angle together with the high beam energy may induce high SR in the IR and consequently into the detector. We can state that the SR in the IR drives the layout design. One of the most significant constraints is the requirement on the critical energy and power of the synchrotron radiation generated upstream of the IR that may shine into the detector. An additional constraint of the FCC-ee layout is the compatibility with FCC-hh, which drives the infrastructure design. In order to combine the two requests of a large crossing angle and the need to prevent high energy SR fans from going into the IP, the IR optics have been designed asymmetrically so that the incoming beam from both sides comes from the inner ring and the outgoing beam exits to the outer ring. In this way the outgoing beams are more strongly bent than the incoming beams thereby lowering the SR energy from the incoming beams. Independent approaches are used to evaluate the main source of the SR background in the IR region coming from photons emitted by beam particles passing through the last bending magnets and by higher amplitude particles in the final focus quadrupoles.

MDISim, SYNC_BKG and SYNRAD+ are used to evaluate the radiation critical energy, the SR fans and to design the IR layout including masks, shieldings and the beam pipe. MDISim [9] is a toolkit that combines existing standard tools MAD-X [10], ROOT [11] and GEANT4 [12, 13]. It reads the MAD-X optics files, and uses its twiss output file to generate the geometry and the magnetic field information in a format which can be directly imported in GEANT4 to perform full tracking, including the generation of secondaries and detailed modelling of the relevant processes. SYNC_BKG

traces beam macroparticles through sliced magnets and is a modified version of a code developed at LBNL by Al Clark (see ref. [14] for a detailed description of the two methods and studies). SYNRAD+ [15] is used to perform a full simulation of the optical interaction, including reflection as well as absorption, of the incident radiation with the beam pipe material. It takes as input a geometry either from CAD or STL format and the magnetic fields and it generates and tracks SR photons starting from a given beam distribution.

To reduce SR backgrounds to tolerable limits the first criteria was to set a minimum distance for the bending magnets from the IP and the maximum critical energy for incoming beam. The synchrotron radiation flux reaching the detectors can be further reduced by the combination of fixed and movable masks (collimators), as well as by optimizing surface to reduce X-ray reflection. We foresee fixed mask tips at 2.1 m upstream of the IP, just in front of the first final focus defocusing quadrupole, in order to intercept this radiation fan and prevent the photons from directly striking the central Be beam pipe. The next level of SR background then comes from photons that strike near the tip of these masks, forward scatter through the mask and then strike the central beam pipe. At the top energy, most of these scattered photons will penetrate the Be beam pipe and then cause backgrounds in the detector. To reduce the effect of this SR source on the experiment we propose to add a thin layer (of the order of $5\text{ }\mu\text{m}$) of high-Z and high conductivity material such

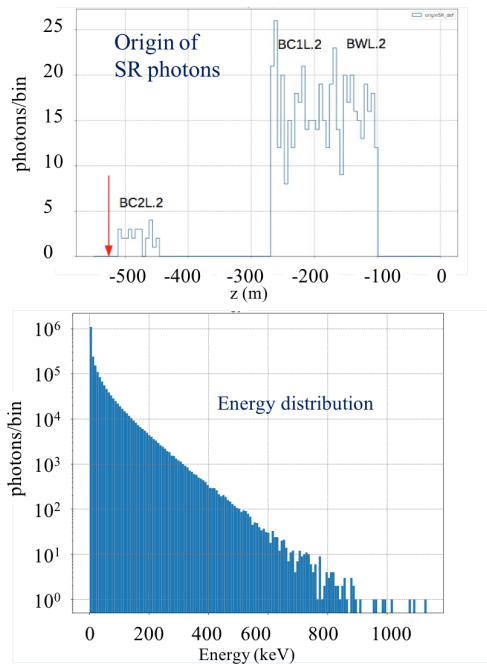


Figure 5: Upper plot: MDISim simulation showing the origin of the photons generated by a beam starting at about -550 m from the IP (see the red arrow); the IP is at $z = 0$ m. Lower plot: energy distribution from the SR produced by the last bend upstream the IP.

as gold inside the Be beam pipe. This will also minimize beam pipe heating from image charge currents. Table 2 is a partial summary of the SR study with details about the photon rate from the last soft bend upstream the IP for all the running beam energies of the FCC-ee. In this study the beam has been considered on-axis. No SR from dipoles or quadrupoles hits directly the central beam pipe. Figure 5 shows the MDISim simulation for the SR generated in the last bending magnets before the IP for the t_{208_nosol} optics for the top energy. The upper plot shows the origin of these photons in the last bending magnets, as generated by a beam starting at the red arrow. The lower plot shows the energy distribution of the SR generated by the last bend before the IP. These SR photons have been tracked into the CLD and IDEA detectors, showing good agreement with the SYNC_BKG simulation and showing the effectiveness of the masking system. Figure 6 shows the hits per bunch crossing with and without the Tungsten shielding.

As a next step more detailed simulations will be performed on the SR, namely using more realistic optics including the solenoidal field, including misalignments and realistic beam distributions that may be slightly off-axis through the final focus quadrupoles. In addition, presently GEANT4 doesn't include SR reflection and this effect will be studied as well. SR collimators to intercept far bends are planned, as from the LEP experience.

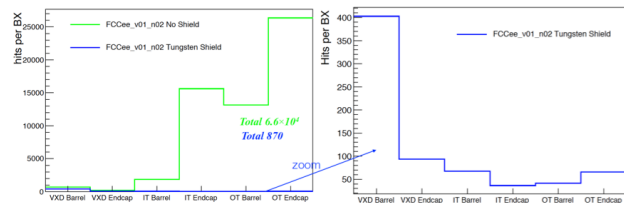


Figure 6: Hits per bunch crossing in the different CLD sub-detectors (see the abscissa) due to SR with (blue line) and without (green line) Tungsten shielding.

BEAM INDUCED AND LUMINOSITY BACKGROUNDS

The deleterious effects of the background is a very important issue in the IR, detector and Machine Detector Interface designs. Beam induced backgrounds are scattering processes leading to particles loss; inelastic beam-gas scattering has been simulated in the MDI region. Scattering of the stored electrons and positrons with thermal photons responsible for single beam particle losses at high energies is also presently under study as from [16]. Luminosity backgrounds are produced at the collision point. Beamstrahlung induced backgrounds have been studied in full simulation. They generate backgrounds at the interaction point and are mostly forward directed leaving the IR. Detailed background studies are in progress to design the MDI region with proper shieldings and collimators. The impact of machine beam

Table 3: Expected particle loss rate both for 1 km of machine section (R_{MDI}), and for the ± 20 m around the IP (R_{ZOOM}), for all the four energy runs

	I [mA]	R_{MDI} [MHz]	R_{ZOOM} [MHz]	R_{MDI}/I [MHz/A]
Z	1390	147	29.2	105
W	147	15.8	3.43	107
H	29	2.96	0.536	102
T	5.4	0.526	0.0959	97

losses in the detector is being considered with full GEANT4 simulation for all the background sources. We briefly describe the study performed for these background sources.

Inelastic Beam-gas Scattering

A precise and effective methodology to perform a detailed study of beam-gas scattering especially in the IR is provided by MDISim. Beam gas induced background has been studied in B-factories (PEP-II and KEKB) and in Super-B factories. SuperKEKB is now starting to benchmark simulation studies with real data [17].

The MDISim toolkit was used to generate the files needed to perform a full GEANT4 simulation for the different beam running energies. A constant beam pipe diameter of 70 mm is considered throughout the ring except for the section from -10 m to 10 m around the IP, shown in Fig. 7. A constant gas pressure of 10^{-7} Pa (or 10^{-9} mbar) is assumed for our study.

The vacuum chamber in QC2 has a diameter of 40 mm, in QC1 of 30 mm. The transition is considered in the simulation with conical tapering from 30 mm to 40 mm as well as from 40 mm to 70 mm (from QC2 to the arcs) in about one meter of longitudinal distance. The beam pipe with magnetic elements was reconstructed in the simulation from ± 850 m from the IP. Primary particles were generated starting at -830 m from the IP, with realistic distributions in transverse phase space, according to the optical parameters of the beam in that point of the machine, and tracked for about 1000 m.

The simulations were performed for a residual gas consisting of N_2 molecules. This represents a worst case, since the

actual residual gas in the beam pipe is expected to contain only a certain fraction of this molecule. Table 3 gives the expected particle loss rates both for the whole simulated machine section and for the ± 20 m around the IP, for all the four energy runs. We predict loss rates of roughly 100 MHz per Ampere of beam current around the IR. As expected, the highest loss rate is found for the Z-pole energy, essentially due to the high current configuration. IR losses are concentrated in the regions where the vacuum chamber gets smaller as the beam approaches the interaction point.

Beam-gas simulation results have been also weighted with a realistic pressure profile evaluated with MolFlow [18] for the *fcc_213* optics at the top energy for about 600 m upstream the IP. About 40% of increase in the expected losses has been found.

First estimates of the background induced by these off-energy scattered particles in the luminosity calorimeter show that the impact is at safe values, mostly thanks to the high-Z shielding [19].

e^+e^- Pairs and $\gamma\gamma \rightarrow$ Hadrons

Beamstrahlung induced backgrounds have been simulated with GuineaPig++ [20] namely coherent and incoherent pair creation (CPC and IPC) and $\gamma\gamma \rightarrow$ hadrons. This effect has been simulated through the detector with full simulation studies [21]. The Coherent Pair Creation (CPC) is strongly focused on the forward direction and is negligible at FCC. The Incoherent Pair Creation (IPC) is expected to be one of the main sources of backgrounds. The impact of this background source has been evaluated for the two FCC-ee proposed detectors CLD (Clic Like Detector) and IDEA. The CLD detector has been derived from CLIC detector model and it has been optimized for FCC-ee experimental conditions. CLD has a 2 T main solenoid field, with vertex detector (VXD) with 3 double layers (barrel) and 4 discs (barrel) and a Silicon tracker. The forward region has a cone of 100 mrad reserved for accelerator use.

The IDEA detector has a vertex detector (MAPS), an ultra-light draft chamber PID (DCH) and 2 T field.

The CLD maximum occupancy per bunch crossing for the IPC and SR is low, being about $\sim 4 \cdot 10^{-4}$ in the VXD for the top energy and $\sim 1.6 \cdot 10^{-4}$ in the tracker. The drift chamber average occupancy results low as well, being ~ 2.9 % for the IPC and ~ 0.2 % for the SR at the top.

Radiative Bhabha and Beamstrahlung Loss Map

Radiative Bhabha and Beamstrahlung are luminosity background sources that can cause beam losses in the IR also due to multitrans effects. GuineaPig++ [20] and BBBREM [22] are used for the radiative Bhabha scattering generator, then multiple turns particle tracking is performed with SAD [23] to determine the IR loss maps. All the beam energies have been considered, from 45.6 GeV to the top energy. At 45.6 GeV, the radiative Bhabhas are all lost up to about 70 m downstream the first IP. At 175 GeV, the radiative Bhabhas are lost mainly in the first half of the ring, and high energy particles that get eventually lost reach the second IP.

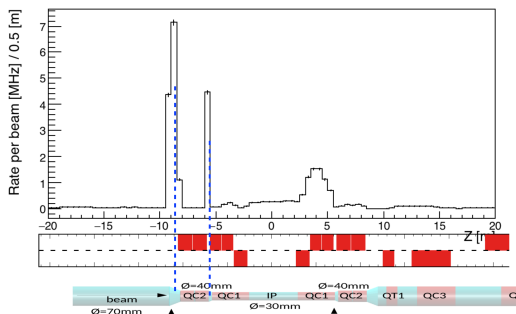


Figure 7: Loss map in the IR. The loss peaks correspond to the restriction of the vacuum chamber between the last drift and final focus quadrupole QC2.

These particles loss distributions are then tracked into the sub-detectors with a full GEANT4 simulation.

For the Beamstrahlung background, the beam-beam element was inserted at both IPs and tracking for a thousand turns with full lattice was considered. Particle losses are mainly concentrated 5 m around the IP in the vertical plane and losses happen mainly in the first few turns. The impact on detector performance is still under investigation although we are expecting it not to be a major issue.

CONCLUSIONS

The FCC-ee Machine Detector Interface baseline conceptual design is ready. Many details have been studied and work is in progress to develop more and more realistic simulations. The solenoid compensation scheme foresees a vertical emittance blow-up of 0.3 pm. Improvements and alternative designs are on-going.

Beam induced and luminosity backgrounds have been studied. Loss maps have been evaluated for inelastic beam-gas scattering, and also for radiative Bhabha and beamstrahlung processes similar study is in progress. Luminosity processes have been directly simulated in the detectors and incoherent pair creation is the dominant effect but always at safe values for both detector designs, CLD and IDEA. At the present level of simulations we find that the SR masking results are very efficient for protecting the detectors and maximum occupancy is under control and at safe values.

ACKNOWLEDGMENTS

We thank the FCC-ee team who contributed to discussions related to the Interaction Region and Machine Detector Interface design.

REFERENCES

- [1] FCC, <https://fcc.web.cern.ch/>
- [2] P. Raimondi, presentation at the 2nd workshop on SuperB Factory, www.lnf.infn.it/conference/superb06/talks/raimondi1.ppt
- [3] K. Oide et al., *Phys. Rev. Accel. Beams* 19, 111005 (2016).
- [4] K. Oide et al., "Progress in the Design of Beam Optics for FCC-ee Collider Ring," doi:10.18429/JACoW-IPAC2017-TUOCB1
- [5] G. von Holtey et al., "Study of beam induced particle backgrounds at the LEP detectors," *Nucl. Instrum. Meth. A* 403 (1998) 205.
- [6] A. Novokhatski, M. Sullivan, E. Belli, M. Gil Costa and R. Kersevan, "Unavoidable trapped mode in the interaction region of colliding beams," *Phys. Rev. Accel. Beams* 20 (2017) 111005. doi:10.1103/PhysRevAccelBeams.20.111005.
- [7] CST User Guide, GmbH, Darmstadt, Germany, [url=https://www.cst.com](https://www.cst.com)
- [8] HFSS, <https://www.ansys.com/products/electronics/ansys-hfss>
- [9] M. Boscolo H. Burkhardt, "Tools for flexible optimisation of ir designs with application to fcc," doi: 10.18429/JACoW-IPAC2015-TUPTY031 pp. 2072–2074.
- [10] MAD-X, methodical accelerator design. <http://mad.web.cern.ch/mad/>.
- [11] Root, <https://root.cern.ch/>.
- [12] S. Agostinelli et al. [GEANT4 Collaboration], "GEANT4: A Simulation toolkit," *Nucl. Instrum. Meth. A* 506, 250 (2003). doi:10.1016/S0168-9002(03)01368-8
- [13] J. Allison et al., "Recent developments in Geant4," *Nucl. Instrum. Meth. A* 835, 186 (2016). doi:10.1016/j.nima.2016.06.125
- [14] M. Boscolo, H. Burkhardt and M. Sullivan *Phys. Rev. Accel. Beams* 20 (2017) 011008. doi:<https://doi.org/10.1103/PhysRevAccelBeams.20.011008>
- [15] R. Kersevan, SYNRAD: a Monte Carlo synchrotron radiation ray-tracing program, *Conf. Proc. C930517* Washington Vol. 5 3848-3850, 1993.
- [16] H. Burkhardt, "Monte Carlo Simulation of Scattering of Beam Particles and Thermal Photons," CERN SL-Note-93-73-OP, <http://cds.cern.ch/record/703373>
- [17] A. Paladino et al., "Beam Background at SuperKEKB during Phase 2 operations", eeFACT2018, Hong Kong, Sept. 2018, paper WEXBA06, in this conference.
- [18] M. Ady and R. Kersevan, "Introduction to the Latest Version of the Test-particle Monte Carlo Code Molflow+," doi:10.18429/JACoW-IPAC2014-WEPME038 <https://molflow.web.cern.ch/>.
- [19] M. Dam, "LumiCal for FCC-ee and beam-background impact", FCCWEEK18, Amsterdam, April 9-13 (2018), <https://indico.cern.ch/event/656491/contributions/2939126/>
- [20] D. Schulte, in 5th Intern. Computational Accel. Physic. Conf., Monterey, CA, USA Spet. 1998, CLIC-NOTE 387.
- [21] G. Voutsinas, N. Bacchetta, M. Boscolo, P. Janot, A. Kolano, E. Perez, M. Sullivan and N. Tehrani, "Luminosity- and Beam-Induced Backgrounds for the FCC-ee Interaction Region Design," doi:10.18429/JACoW-IPAC2017-WEPIK004
- [22] R. Kleiss and H. Burkhardt, "BBBREM: Monte Carlo simulation of radiative Bhabha scattering in the very forward direction," *Comput. Phys. Commun.* 81 (1994) 372 doi:10.1016/0010-4655(94)90085-X
- [23] SAD, <http://acc-physics.kek.jp/SAD/index.html>

BEAM BLOWUP DUE TO SYNCHRO-BETA RESONANCE WITH/WITHOUT BEAM-BEAM EFFECTS*

K. Oide[†], KEK, Tsukuba, Japan
D. El Khechen, CERN, Geneva, Switzerland

Abstract

A blowup of vertical emittance has been observed in particle tracking simulations with beam-beam and lattice misalignments [1]. It was somewhat unexpected, since estimation without lattice errors did not predict such a blowup unless a residual vertical dispersion at the interaction point (IP) is larger than a certain amount. Later such a blowup has been seen in a tracking of lattices without beam-beam effect.

A possible explanation of the blowup is given by a Vlasov model for an equilibrium of quadratic transverse moments in the synchrotron phase space. This model predicts such a blowup as a synchro-beta resonance mainly near the first synchrotron sideband of the main x - y coupling resonance line.

INTRODUCTION

Beam-beam simulations with lattice, with misalignments or x - y coupling sources such as skew quadrupoles are important to estimate the beam lifetime and luminosity evolution under more realistic situation. Such simulations have been tried for FCC-ee collider rings at the energy, 182.5 GeV. As a result, significant blowups are seen, and the magnitudes depend on the random number for the misalignments of sextupoles to generate the vertical emittance. Figure 1 shows an example of such a blowup for two seeds of random numbers of misalignments of arc sextupoles. Note that the residual dispersion at the IP for seed 3 is smaller than the previous criteria given in Table 1, while giving even larger blowup than another seed 19, which has larger dispersions at the IP.

Table 1: Tolerances for residual dispersions at the IP for each energy of FCC-ee, obtained by quasi strong-weak model without lattice given by D. Shatilov [2]. The tolerance $\Delta\eta_y^*$ corresponds to 5% increase of vertical beam size σ_y^* at the IP with beamstrahlung.

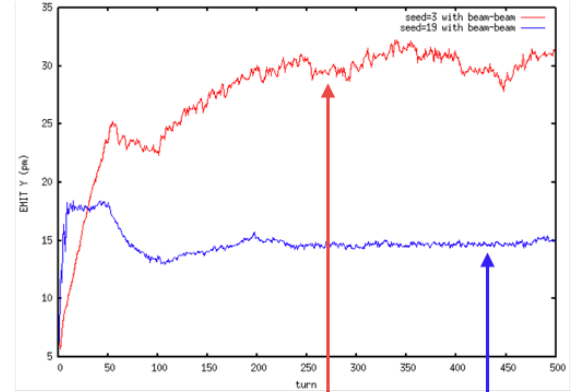
Beam energy [GeV]	45.6	80	120	175
Design σ_y^* [nm]	28	41	35	66
Energy spread ^a [%]	0.13	0.13	0.165	0.185
$\Delta\eta_y^*$ [μm]	1	5	4	6

^a with beamstrahlung

Such a blowup was somewhat unexpected, since the residual dispersion at the interaction point (IP) was not very large

* Work supported by JSPS KAKENHI Grant Number 17K05475. Also supported by the European Commission under Capacities 7th Framework Programme project EuCARD-2, grant agreement 312453, and under the Horizon 2020 Programme project CREMLIN, grant agreement 654166.

[†] katsunobu.oide@cern.ch



Coupling (%)	0.2	0.2
RMS of sext. Offset (°)	11	15
Seed	3	19
η_y @ (IP.1, IP.2) (°)	(-5.3, 4.24)	(-8.9, 8)
$\eta_{py} \times \beta_y^*$ @ (IP.1, IP.2) (°)	(6.8, 1.04)	(35.4, 23)
R2 parameter	(1.8×10^{-3} , 1.8×10^{-3})	(-5.1×10^{-5} , -1.8×10^{-4})

Figure 1: Blowup of vertical emittance measured at the IP by a particle tracking with beam-beam, beamstrahlung, and lattice. The arc sextupoles are vertically misaligned randomly to produce the vertical emittance of the design ratio $\varepsilon_y/\varepsilon_x = 0.2\%$. Two examples for different seeds are shown, corresponding residual vertical dispersions at the IP in the table.

compared to the criteria given by beam-beam simulations without lattice. As well, simulations of beam-beam with lattice but without misalignments or skew quads, did not show such blowups [3].

METHOD AND SETUP

First let us describe the method to examine the effect in this paper:

- Lattice: FCCee_t_217_nosol_2.sad, 182.5 GeV, half ring is simulated assuming a perfect period 2 periodicity. Machine parameters are listed in Ref. [2].
- The vertical emittance around the closed orbit is generated by skew quadrupole added on each sextupole in the arc. Their magnitudes on a pair of sextupoles with the $-I$ transformation between them are parametrized as

$$(k_1 + sk_2, k_2 + sk_1), \quad (1)$$

where $k_{1,2}$ are two random numbers and s is a parameter to represent the symmetry. Then $s = +1/-1$

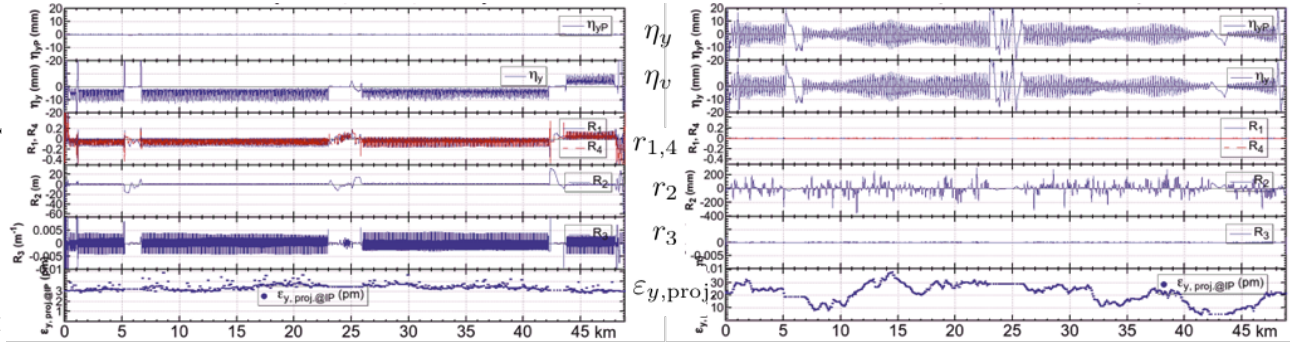


Figure 2: Comparison of beam optics between symmetric (left, $s = +1$) and antisymmetric (right, $s = -1$) skew excitations for a particular seed of random number. The columns are physical vertical dispersion η_y , dispersion in the normal mode η_v , coupling parameters $r_{1,4}$, r_3 , r_4 , and the projected vertical emittance all round the half-ring. Note that the vertical emittance is generated mainly by x - y coupling by the symmetric skew, and dispersion by antisymmetric.

correspond to perfect symmetric/antisymmetric excitations, and $s = 0$ simply random. Examples of the resulting optics are shown in Fig. 2 for $s = \pm 1$ ¹.

- The vertical emittance around the closed orbit is always set to $\varepsilon_y/\varepsilon_z = 0.2\%$ unless specified otherwise.
- Synchrotron radiation, both damping and fluctuation, is turned on in all magnets. Tapering is applied.
- The tracking is done up to 300 half-turns with 1000 particles. The longitudinal damping is 40 turns.
- Optionally simplified beam-beam effects and beamstrahlung are included in the Vlasov model.
- The tracking and the Vlasov model are both done by SAD [4].

Then it was found that such a blowup can occur without beam-beam effects. Figure 3 shows such an example of blowups without beam-beam. The blowup depends on the symmetry of the skew quads as well as the random number. The blowup is well explained by a Vlasov model on *anomalous emittance* with synchro-beta resonances introduced in Ref. [5].

VALIDATION OF THE VLASOV MODEL

The Vlasov model in Ref. [5] obtains the equilibrium distribution of the transverse closed orbit and the quadratic beam distribution matrix in the longitudinal phase space, including the diffusion and damping by synchrotron radiation. It takes all nonlinearities of the transverse transfer matrix and the closed orbit in momentum direction, while only linear parts in transverse planes. To see the validity of the model,

¹ The definition of the coupling parameters are so defined that the uncoupled betatron coordinate is written as

$$\begin{pmatrix} u \\ p_u \\ v \\ p_v \end{pmatrix} = R \begin{pmatrix} x \\ p_x \\ y \\ p_y \end{pmatrix} = \begin{pmatrix} \mu & \cdot & -r_4 & r_2 \\ \cdot & \mu & r_3 & -r_1 \\ r_1 & r_2 & \mu & \cdot \\ r_3 & r_4 & \cdot & \mu \end{pmatrix} \begin{pmatrix} x \\ p_x \\ y \\ p_y \end{pmatrix}. \quad (2)$$

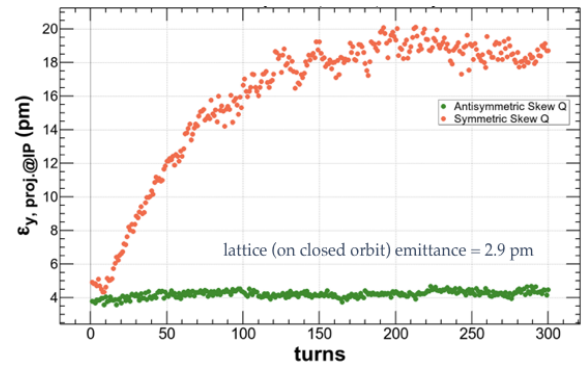


Figure 3: An example of the blowup of the vertical projected emittance at the interaction point (IP) without beam-beam for symmetric (red) and antisymmetric (green) excitations of skew quadrupoles corresponding the optics in Fig. 2. The blowups are quite different between them.

let us see the dependence of the blowup against the vertical tune of the lattice. Figure 4 shows such a tune dependence obtained by the tracking as well as the result of the Vlasov model. The agreement between them is excellent for all ν_y 's in the plot, so we will use the Vlasov mode hereafter, since it is about 1000 times faster than the tracking.

Then let us examine the dependence of the blowup by varying the synchrotron tune ν_z for several betatron tunes. Figure 5 shows such dependences. This tune dependence clearly shows that the most relevant resonance is the first synchrotron sideband $\nu_x - \nu_y - \nu_z = N$ of the main coupling resonance, illustrated in Fig. 6.

SIMPLIFIED BEAM-BEAM EFFECT IN VLASOV MODEL

To estimate the beam-beam effect by the Vlasov model, we implemented a simplified beam-beam effects. It is a thin lens inserted at the IP. First the orbit is kicked at the IP by:

$$\Delta p_{x,y} = -k \frac{\partial U}{\partial (x,y)}, \quad (3)$$

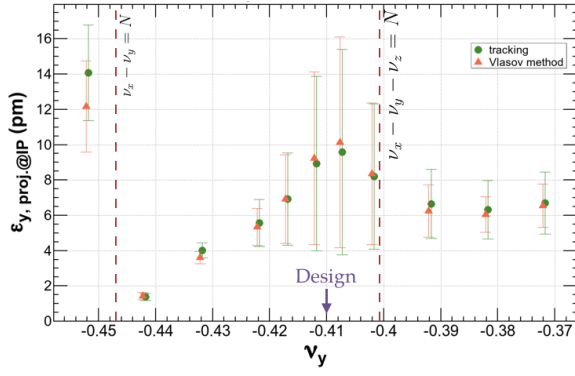


Figure 4: The blowup for different vertical tunes, by tracking (green circle) and the Vlasov model (red triangle). The error bars show the variation with 12 random numbers. Two resonances are shown by vertical dashed lines. This is done for the symmetric skew quad mode without beam-beam.

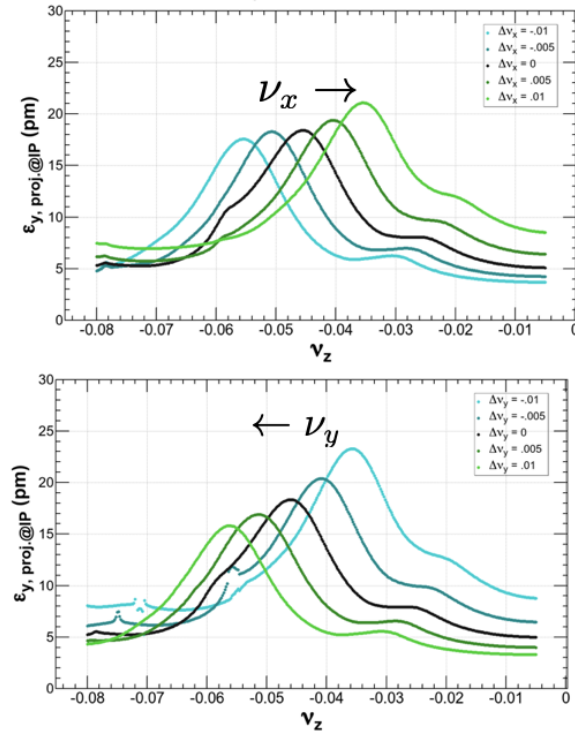


Figure 5: The blowup as a function of synchrotron tune ν_z for various horizontal (upper) and vertical (lower) tunes around the design tune. The shift of the peak indicates that the most relevant resonance is $\nu_x - \nu_y - \nu_z = N$. Obtained by the Vlasov model, for symmetric skew quads. In this case, the skew quads are set to give the design vertical emittance at the design tune, and kept constant for other tunes.

where U is a potential by a Gaussian charge distribution obtained analytically. This has a nonlinear dependence on the closed orbit, which may be important when there is residual dispersion at the IP. Then the associated transfer

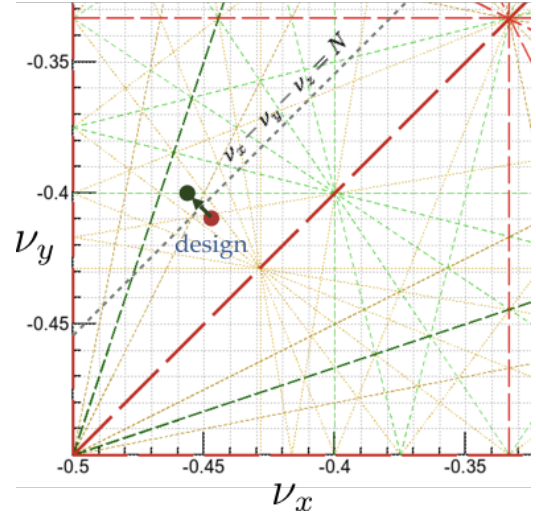


Figure 6: The tune diagram with the design transverse tune (red circle) and an alternative tune (black circle), which will be examined later. The dashed line is the first sideband of the main coupling resonance.

matrix is written as:

$$M_{BB} = \begin{pmatrix} 1 & 0 & 0 & 0 & 0 & 0 \\ -k \frac{\partial^2 U}{\partial x^2} & 1 & -k \frac{\partial^2 U}{\partial x \partial y} & 0 & 0 & 0 \\ 0 & 0 & 1 & 0 & 0 & 0 \\ -k \frac{\partial^2 U}{\partial x \partial y} & 0 & -k \frac{\partial^2 U}{\partial y^2} & 1 & 0 & 0 \\ 0 & 0 & 0 & 0 & 1 & 0 \\ 0 & 0 & 0 & 0 & 0 & 1 \end{pmatrix}, \quad (4)$$

where k and the aspect ratio σ_y/σ_x in U are chosen to the matrix be consistent with beam-beam parameters $\xi_{x,y}$. The beamstrahlung is simplified by damping and excitation matrices at the IP:

$$\Delta M_D = \begin{pmatrix} 0 & 0 & 0 & 0 & 0 & 0 \\ 0 & -d/2 & 0 & 0 & 0 & 0 \\ 0 & 0 & 0 & 0 & 0 & 0 \\ 0 & 0 & 0 & -d/2 & 0 & 0 \\ 0 & 0 & 0 & 0 & 0 & 0 \\ 0 & 0 & 0 & 0 & 0 & -d \end{pmatrix}, \quad (5)$$

$$\Delta \Sigma_{BS} = \begin{pmatrix} 0 & 0 & 0 & 0 & 0 & 0 \\ 0 & 0 & 0 & 0 & 0 & 0 \\ 0 & 0 & 0 & 0 & 0 & 0 \\ 0 & 0 & 0 & 0 & 0 & 0 \\ 0 & 0 & 0 & 0 & 0 & 0 \\ 0 & 0 & 0 & 0 & 0 & \Delta \sigma_\varepsilon^2 \end{pmatrix}, \quad (6)$$

where d and σ_ε is the single-pass relative energy loss and spread due to beamstrahlung. In this design, the numbers are $\xi_{x,y} = (0.0984, 0.1414)$, $d = -7.3 \times 10^{-5}$, and $\sigma_\varepsilon = 3.85 \times 10^{-4}$.

Figure 7 shows the results of blowup at the design tune with/without beam-beam and beamstrahlung against the symmetry parameter s obtained by the Vlasov model. For the

antisymmetric skew, the blowup is smaller than symmetric in the case of no beam-beam. However, with beam-beam the blowup is smaller for the symmetric ones. The beam-beam shrinks the emittance due to the large beam-beam tune shift which makes the betatron tunes off resonance, at least for the symmetric case.

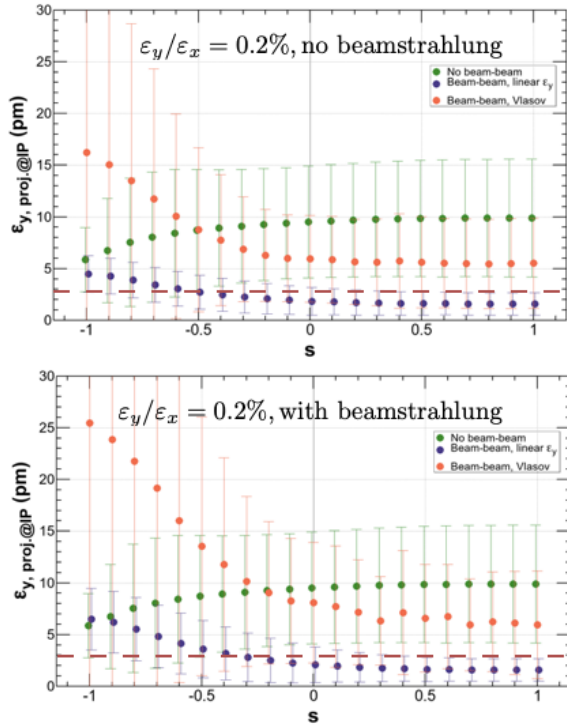


Figure 7: The blowups as a function of the symmetry parameter s with/without beam-beam, without (upper) /with (lower) beamstrahlung. The error bars correspond to the variation of 12 random numbers. The design vertical emittance is shown by the dashed horizontal line. $\varepsilon_y/\varepsilon_x = 0.2\%$ around the closed orbit.

The blowups with smaller vertical emittance, $\varepsilon_y/\varepsilon_x = 0.1\%$, are shown in Fig. 8. The average projected emittance for $s \geq 0$ barely reaches the design value. Considering the variation, The emittance without the blowup should be even smaller than 0.1% .

One may also shift the betatron tunes to reduce the blowup. Figure 9 shows the results for the alternative tune indicated in Fig. 6. Due to other effects concerning the luminosity, the tunes are not freely chosen, and this shift, $\Delta_{x,y} = (-0.01, 0.01)$, is almost the limit.

Several distributions of $\langle y^2 \rangle$ on the synchrotron phase space are shown in Fig. 10, obtained by the Vlasov model. It is seen that large blowups occur at a certain amplitude of the synchrotron motion.

SUMMARY

The synchro-beta resonance accompanied by chromatic x - y coupling and dispersions through the lattice of a collider causes serious beam blowup both with or without beam-

FCCEe_t_217_nosol_2.sad
 $\varepsilon_y/\varepsilon_x = .1\%$, $\Delta\sigma_{\text{eip}} = 0\%$, $\Delta\epsilon_{\text{ip}} = -.0073\%$
Seed = 7 (+2n), GCUT = 3.5, samples = 12,
Design $\nu_{x,y,z} = \{ -.4470, -.4100, -.0462 \}$
 $\varepsilon_{x,y} = \{ .0984, .1414 \}$, IP Correction: OFF

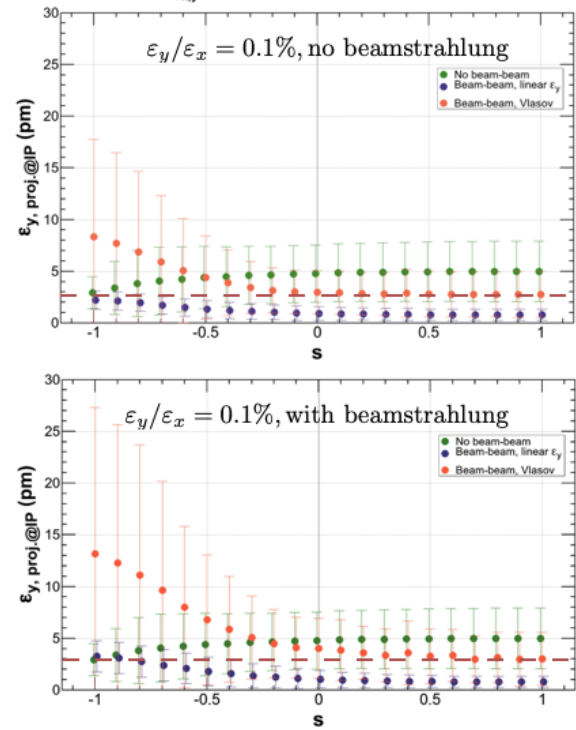


Figure 8: The blowups as a function of the symmetry parameter s with/without beam-beam, without (upper) /with (lower) beamstrahlung. $\varepsilon_y/\varepsilon_x = 0.1\%$ around the closed orbit.

beam effects and beamstrahlung. This phenomenon is well described by a Vlasov model. This will set another criteria on the choice of the tunes and the low emittance tuning.

ACKNOWLEDGEMENT

The authors thank M. Benedikt, A. Blondel, M. Boscolo, E. Levichev, K. Ohmi, D. Shatilov, D. Zhou, F. Zimmermann, and the entire FCC-ee Collaboration Team for encouraging the research, useful discussions, and suggestions.

REFERENCES

- [1] D. El Khechen, "Beam-beam blowup in the presence of x-y coupling sources for FCC-ee", eeFACT2018, Hong Kong, Sept. 2018, paper TUYBA03, in this conference.
- [2] K. Oide, *et al.*, "Several Topics on Beam Dynamics in FCC-ee", eeFACT2018, Hong Kong, Sept. 2018, paper MOYAA01, in this conference.
- [3] D. Zhou, presented at FCC Week 2016, 11–15 April 2016, Rome, Italy(2016).
- [4] <http://acc-physics.kek.jp/SAD/index.html>, <https://github.com/KatsOide/SAD>
- [5] K. Oide and H. Koiso, "Anomalous equilibrium emittance due to chromaticity in electron storage rings", *Phys.Rev. E49* pp. 4474-4479(1994).

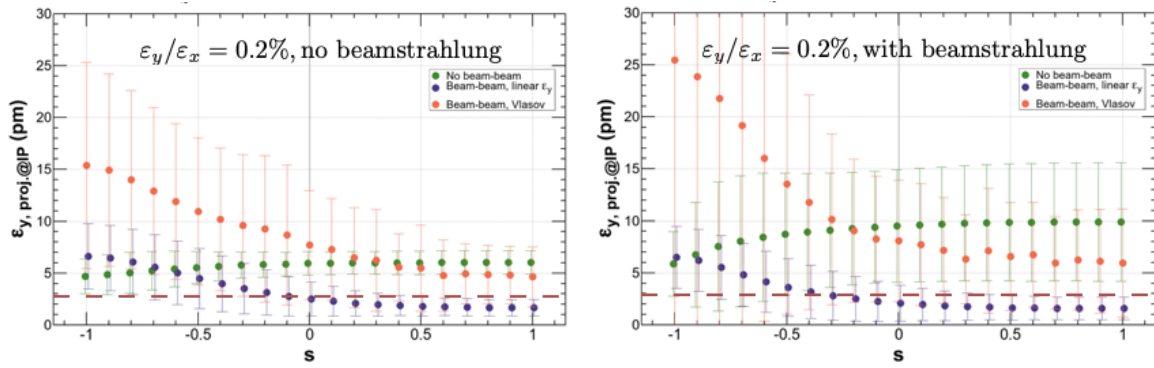


Figure 9: The blowup at the alternative tune shown in Fig. 6, with/without beam-beam, without (left) /with (right) beamstrahlung.

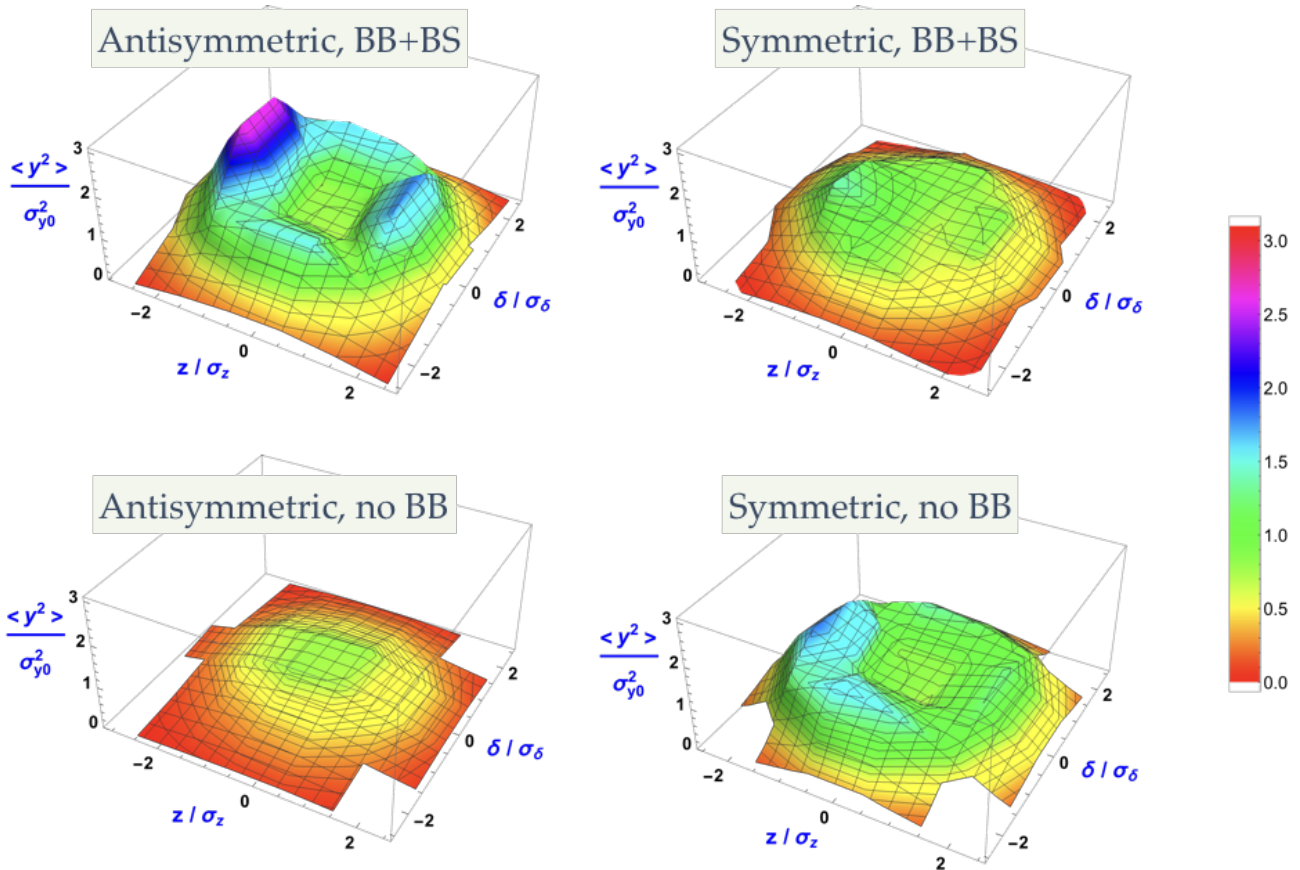


Figure 10: The equilibrium distribution of $\langle y^2 \rangle / \sigma_{y0}^2$ on the synchrotron phase space obtained by the Vlasov model. Upper left: Antisymmetric skew, with beam-beam & beamstrahlung, upper right: symmetric skew, with beam-beam & beamstrahlung, lower left: antisymmetric skew, without beam-beam, lower right: symmetric skew, without beam-beam.

EARLY COMMISSIONING OF THE LUMINOSITY DITHER SYSTEM FOR SUPERKEKB*

Y. Funakoshi[†], T. Kawamoto, M. Masuzawa, S. Nakamura, T. Oki, M. Tobiyama, S. Uehara,
R. Ueki, KEK 305-0801 Tsukuba, Japan
A. S. Fisher, M. K. Sullivan, D. Brown, SLAC, 94025 Menlo Park, U.S.A.
U. Wienands, ANL 60439 Argonne, U.S.A.
P. Bambade, S. Di Carlo, D. Jehanno, C. Pang, LAL, 91898, Orsay, France
D. El Khechen, CERN, CH-1211, Geneva, Switzerland

Abstract

SuperKEKB is an electron-positron double ring collider at KEK which aims at a peak luminosity of $8 \times 10^{35} \text{cm}^{-2} \text{s}^{-1}$ by using what is known as the “nano-beam” scheme. A luminosity dither system is employed for collision orbit feedback in the horizontal plane. This paper reports a system layout of the dither system and algorithm tests during the SuperKEKB Phase 2 commissioning.

INTRODUCTION

The SuperKEKB collider [1] employs a luminosity dither system that was used at SLAC for PEP-II [2] [3] for maintaining the horizontal offset of the two beams at the IP and maximizing luminosity. For this purpose, a collision orbital feedback based on the beam-beam deflection was used in both vertical and horizontal planes at KEKB. With the “nano-beam” scheme, however, the horizontal beam-beam parameters are much smaller than those at KEKB, and detecting a horizontal orbit offset at IP using the beam-beam deflection is not effective at SuperKEKB. Therefore, a dithering method was introduced for SuperKEKB. A good collision condition is sought for by dithering the positron beam (LER, Low Energy Ring), and once a good collision condition is found, it is maintained by an active orbital feedback, which moves the electron beam (HER, High Energy Ring) relative to the LER by creating a local bump at the IP. The algorithm of the system is described elsewhere [4]. The dither system was tested with colliding beams in the SuperKEKB Phase 2 commissioning.

DITHERING SYSTEM

System Layout

The block diagram of the dither system is shown in Fig. 1. The system consists of fast luminosity monitors, a lock-in amplifier, coils for dithering, a programmable amplifier whose functions are gain and phase adjustments for each power supply, actuators (a bump system called “iBump system” which is also used for the fast vertical feedback), a controller for the iBump system, a dither control system (the actual feedback algorithm will be run in an IOC on a PLC) and power supplies of the dithering coils. Those devices are distributed

three different locations, *i.e.* a beam line in the SuperKEKB tunnel, Tsukuba B4 control room which is located near the beam line and Belle 2 Electronics Hut where the Belle 2 data acquisition electronics are assembled. PLC and the iBump system are connected through the EPICS control network and the whole dither system is control by the EPICS system. The system is also connected to the SuperKEKB center control room through the network and can be monitored and controlled therefrom.

Dither Coils

Eight sets of Helmholtz coils for the dithering system were designed and fabricated and their magnetic properties were measured at SLAC [5]. The coils were installed in the SuperKEKB tunnel in June 2015. Each set consists of a pair of coils to provide a horizontal kick and/or another pair of coils to provide vertical kick to the positron beam. The coils are designed to be mounted on the vacuum pipes directly. The coils are installed at 8 locations in the LER, 4 on the right side of the IP (ZD1RP, ZD2RP, ZD3RP and ZD4RP) and another 4 on the left side (ZD1LP, ZD2LP, ZD3LP and ZD4LP), as is shown in Fig. 2. Three types of coils are needed to be designed as the cross sections of the beam pipes vary by location. Two types (ZD1L/RP, ZD2L/RP) are symmetric in shape and have both horizontal and vertical coils while the third type (ZD3L/RP and ZD4L/RP) is asymmetric as this type is mounted on the vacuum pipe ante-chamber and have coils for the vertical kick. Field harmonics were evaluated by a rotating coil system, shown in Fig. 3. The required field uniformity of 0.1% is achieved over a range of ± 10 mm, even with the asymmetric type coil. The LER beam is kicked sinusoidally by the coils in the horizontal direction around the IP at a frequency of 79 Hz. The coils for vertical kick are prepared in order to correct the x-y coupling in the IP bump region.

Luminosity Monitor

Two types of fast luminosity monitors are used for studying dither. They both detect photons, re-coiled electrons, or positrons from radiative Bhabha scattering in the very forward (“zero degree”) direction. One monitoring system is called zero degree luminosity monitor (ZDLM) and is based on Cherenkov and scintillation counters [6]. The other system is developed by LAL, which uses diamond sensors and is called “LumiBelle2” [7]. Required accuracy of the

* Work supported by U.S.-Japan Science and Technology Cooperation Program in High Energy Physics.

[†] yoshihiro.funakoshi@kek.jp

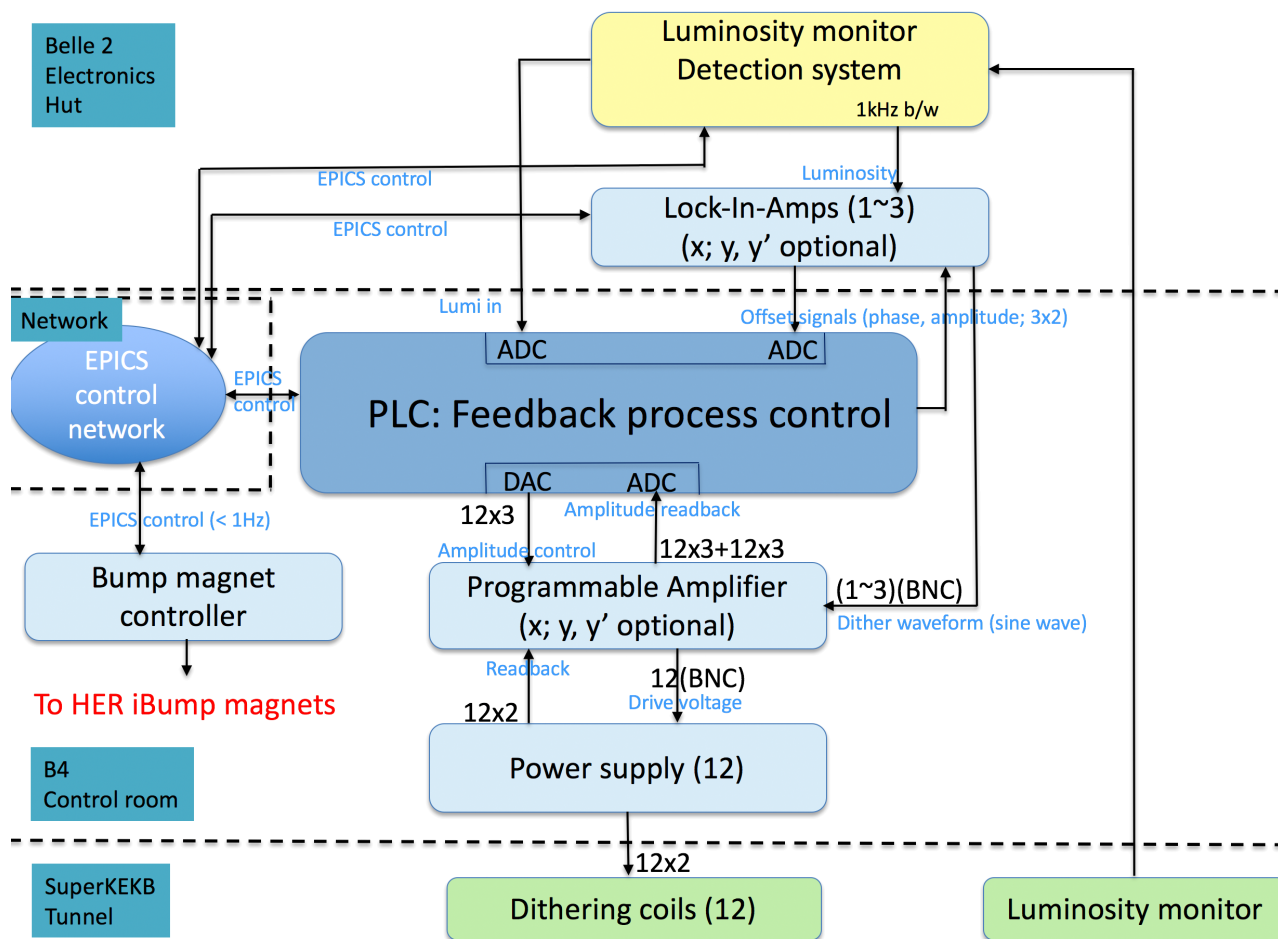


Figure 1: A block diagram of the dither feedback system.

luminosity monitor has been studied by a simulation and is 1% at 1 kHz. The short latency of 1 ms is required so that the monitor can detect a luminosity deviation at a high frequency.

Other Hardwares

A lock-in amplifier (AMETEK ADVANCED MEASUREMENT TECHNOLOGY model 7230) is used to generate a sine wave at a dither frequency. We chose 79 Hz as the dither frequency to avoid interference from the 50-Hz power line and injection frequencies of 1, 2, 5, 12.5, and 25 Hz. The sine wave is used as an input to the power supplies via a programmable amplifier. The luminosity signals are input to the lock-in amplifier, which mixes them with the reference dither signal and then low-pass filtering to provide an output voltage proportional to the dither frequency component of the luminosity together with a phase relation between the dither sine wave and the luminosity modulation signal. The dither feedback acts so that the output of the lock-in amplifier becomes minimum. The programmable amplifier was also designed and fabricated by SLAC [5]. The time delay was adjusted through the programmable amplifier by using the phase-shifter. The fudge factors of each

coil were obtained by analyzing the actual beam orbit. They were used to improve closure of the bump orbit during beam commissioning.

BEAM TEST AND COMMISSIONING

This section summarizes the results from the dithering study with colliding beams. The luminosity signals from ZDLM and LumiBelle2 were used as input to the lock-in amplifier.

Response of Lock-in Amplifier to Luminosity Modulation

We checked the response of the lock-in amplifier twice, *i.e.* on May 5th and July 14th. Figure 4 and 5 show results on May 5th. In the measurement the vertical beta function at the IP was 8mm for both rings and the luminosity was less than $10^{32}\text{cm}^{-2}\text{s}^{-1}$. The dither amplitude at the IP was $40\mu\text{m}$. The output voltage from the lock-in amplifier (magnitude) and the phase are plotted as a function of the horizontal offset at the IP for ZDLM and LumiBelle2. The lock-in amplifier accepts two inputs; Input A for ZDLM and Input B for LumiBelle2 and the polarity of Input B is inverted in the lock-in amplifier. That is why the sign of the phases for the

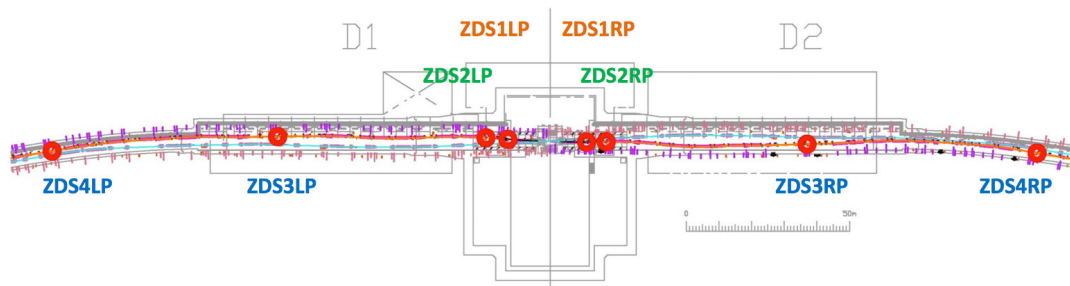


Figure 2: Locations of the dithering coils. Three different types of coils are indicated by three different colors.



Figure 3: Ante-chamber type dithering coil is being measured by a rotating system.

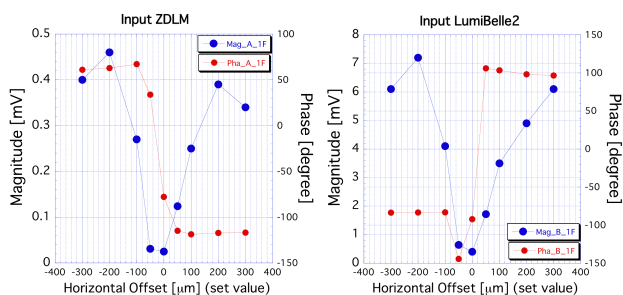


Figure 4: Magnitude (blue) and phase (red) from Lock-in Amp are plotted against the horizontal offset at IP for ZDLM (left) and LumiBelle2 (right).

two inputs is opposite in Fig. 4. The horizontal offset at the IP was created by making horizontal bump orbits at the IP in HER. In this measurement, the dependence of the luminosity on the horizontal offset was not clear in the scan range in the figures, since the IP vertical beta function was not so small and the luminosity was not very high. Nevertheless, the phase jump at around the zero offset was clearly seen in the scan. This shows superiority of this dither method using the lock-in amplifier. In Fig. 5, the product of the magnitude and the sign of the phase using the same data as in Fig. 4 is plotted as a function of the horizontal offset at IP. In the luminosity feedback routine, the quantity shown in Fig. 5 is used as an input value. The feedback acts so as to find the zero cross point of the input and keep it by using the PI algorithm.

The second measurement was done on July 14th. In the measurement the vertical beta function at the IP was 3mm for both rings and the luminosity was around $10^{33}\text{cm}^{-2}\text{s}^{-1}$. The dither amplitude at the IP was $20\mu\text{m}$. Four data sets

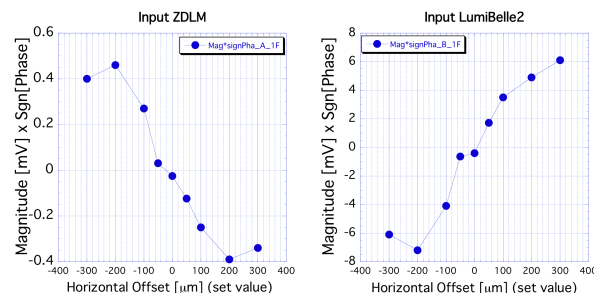


Figure 5: Magnitude times Sgn[phase] is plotted against the horizontal offset at IP for ZDLM (left) and LumiBelle2 (right). The same data as Fig. 4 are used.

were taken using LumiBelle2 and ZDLM alternatively as input to the lock-in amplifier, with varying HER horizontal orbit bump height at the IP, as was done on May 5th. Table 1 summarizes the procedure of the scans. The output voltage (magnitude) from the lock-in amplifier is plotted as a function of the horizontal beam position at QC1LE in Fig. 6 for scans 3 and 4, where the ZDLM signal was used as input to the lock-in amplifier. Here, QC1LE is a final focus quadrupole magnet for the electron ring on the left side of the IP and the beam position is measured value at the BPM attached on the IP side of the magnet. The output voltage becomes zero and the phase jump takes place at $x = -0.95$ mm in both scans, which are consistent with the position of the luminosity peak as is shown below. The plots of the magnitude and the phase for scans 1 and 2 are shown in Fig. 7, where LumiBelle2 was used as input to the lock-in amplifier. When the magnitude is zero, or close to zero, phase jump occurs. However, the beam position is not at $x = -0.95$ mm but at $x = -1.05$ mm. This does not match the beam position where luminosity peaks as is shown below. The magnitude curve is not symmetric with respect to its minimum either, which is not the case with scans 3 and 4. The cause of this mismatch and asymmetric behavior will be investigated during Phase 3 that is scheduled to start in the spring of 2019. Also in this measurement on July 14th, two inputs of the lock-in amplifier are used for ZDLM and LumiBelle2. However, the sign of the phase for the two inputs is same as seen in Figs. 6 and 7, since we set phase offsets properly.

Table 1: Summary of Horizontal Scan (July 14th)

	Input to lock-in amplifier	Scan range (μm)
Scan1	LumiBelle2	-250 \rightarrow +250
Scan2	LumiBelle2	+250 \rightarrow -250
Scan3	ZDLM	-150 \rightarrow +150
Scan4	ZDLM	+150 \rightarrow -150

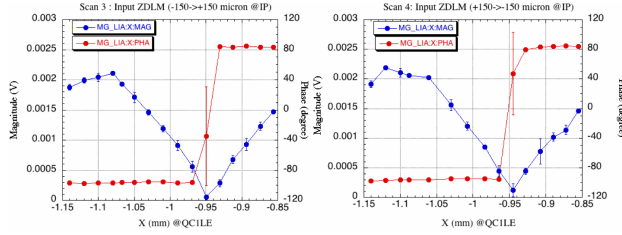


Figure 6: Magnitude (blue) and phase (red) are plotted against the HER beam position x for scans 3 (left) and 4 (right).

Luminosity Response

Figure 8 shows the luminosity response when the bump height at the IP was changed during scan 3, as an example. The luminosity is normalized to its peak for each luminosity monitor. The normalized luminosity is fitted by the following Gaussian functions:

$$L_0 = m_1 + \exp\left(-\frac{(x - m_2)^2}{2m_3^2}\right) \quad (1)$$

where x is the beam position monitored by the beam position monitor (BPM) at QC1LE. The fitted parameters m_2 and m_3 represent the HER beam position where the luminosity peaks and exhibits standard deviation, respectively. Table 2 summarizes the fitted parameters. Luminosity peaks when the HER beam position measured at QC1LE is -0.95 mm for all scans, indicating that the effects of the bump magnet hysteresis and drift of the beam orbits are negligible.

In the Eq. (1), the parameter m_3 corresponds to Σ_x^* for the usual collision scheme. In the "nano-beam scheme", however, we have to use an effective horizontal beam size σ_x^{*eff} instead of the actual horizontal beam size σ_x^* in the

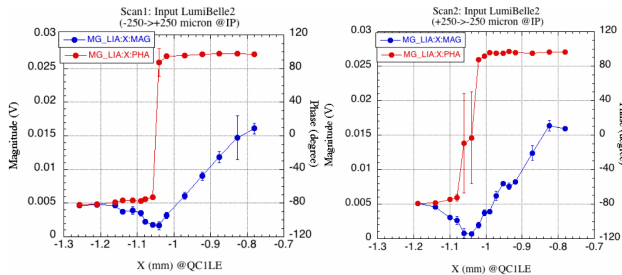


Figure 7: Magnitude (blue) and the phase (red) are plotted against the HER beam position x for scans 1 (left) and 2 (right).

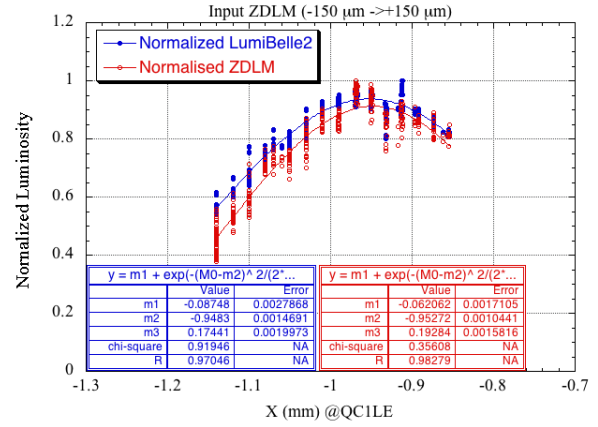


Figure 8: Luminosity is plotted against the beam position measured at the QC1LE BPM during scan 3.

Table 2: Summary of Gaussian-fitted parameters

Detector	LumiBelle2		ZDLM	
	m_2 (mm)	m_3 (mm)	m_2 (mm)	m_3 (mm)
Scan 1	-0.94	0.27	-0.95	0.24
Scan 2	-0.94	0.21	-0.95	0.18
Scan 3	-0.95	0.17	-0.95	0.19
Scan 4	-0.94	0.20	-0.95	0.18

calculation of the luminosity or the beam-beam parameters. The effective horizontal beam size is denoted as follows:

$$\sigma_x^{*eff} = \sigma_z \sin \phi_c \quad (2)$$

where ϕ_c and σ_z are the half crossing angle at the IP (41.5 mrad at SuperKEKB) and the bunch length, respectively. The bunch length was measured to be 5.5 mm for both LER and HER when the bunch current is 0.3 mA [8]. Using 41.5 mrad for ϕ_c and 5.5 mm for σ_z , we obtain ~ 0.23 mm for σ_x^{*eff} and Σ_x^{*eff} is calculated as ~ 0.33 mm. This is $\sim 60\%$ larger than m_3 in Table 2. Luminosity degraded more than expected with a horizontal offset. This can be explained by considering the hourglass effect. When there is a crossing angle at the IP as is in SuperKEKB, a horizontal offset shift introduces a collision point shift in the beam direction, as is indicated in the left side drawing in Fig. 9. The vertical beta-function (β_y) is plotted on the right side. A 100 μm horizontal offset makes β_y larger, which degrades luminosity by approximately 7.2% with β_y^* of 3 mm. If a horizontal offset causes beam blow-up at the IP, an additional degradation in luminosity may take place.

Dither Feedback

A feedback algorithm using the PI control was first tested in May 10th. The magnitude from the lock-in amplifier and the bump height at the IP are plotted in Fig. 10. In this test, we used LumiBelle2 for the input to the lock-in amplifier. The feedback algorithm loop runs in the operation computer system connected through the network in this Phase 2 test.

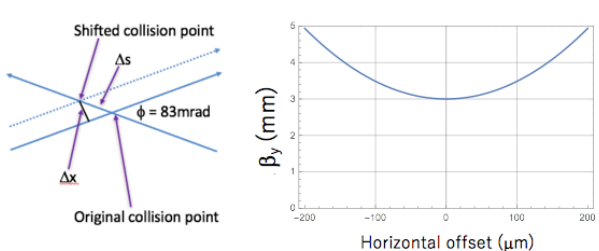


Figure 9: Hourglass effect when there is a horizontal offset at the IP.

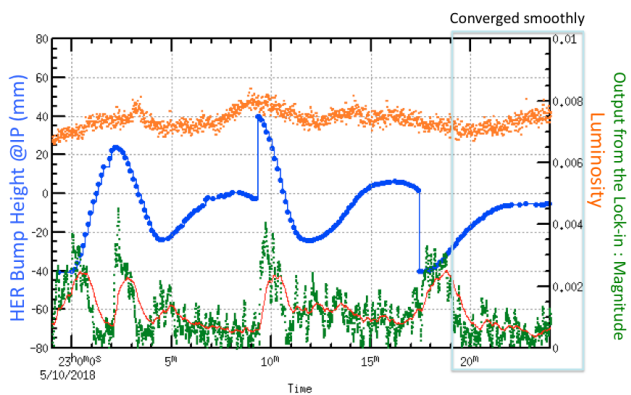


Figure 10: Magnitude (green) and bump height at the IP (blue) are plotted with luminosity (orange) during the dither feedback test.

The feedback cycle was ~ 8 s, which was mainly determined by a data accumulation time in the lock-in amplifier. In the test, the luminosity was around $1 \times 10^{32} \text{cm}^{-2} \text{s}^{-1}$ and we needed a relative long accumulation time for the lock-in amplifier. It determines a proper size and direction of the offset at the IP in the HER. These parameters are then sent to the iBump control system via EPICS to create a bump in the HER. The feedback loop set a bump in the correct direction and made the output from the lock-in amplifier smaller, though there were a couple of overshoots initially. After finding a good feedback parameter set, the feedback converged smoothly to an optimum value without any overshoot and the magnitude was brought to close to zero. The luminosity response was not clear this time, as β_y^* was relatively large (8 mm). The luminosity was not very sensitive to the horizontal beam offset in this test.

SUMMARY AND FUTURE PROSPECTS

The dither feedback system finds the optimum horizontal offset between the LER and HER to maximize luminosity by determining the minimum magnitude of the output of the lock-in amplifier. In the test on July 14th, the optimum horizontal offset was found successfully when ZDLM was used as input to the lock-in amplifier. There was a shift of approximately $100 \mu\text{m}$ between the luminosity maximum offset and the magnitude minimum offset when LumiBelle2 was used as input. This will be investigated during the Phase 3 run first. The test of the dither feedback using LumiBelle2 as input on May 10th was successful. The dependence of luminosity on the horizontal offset agrees with the prediction estimated from the crossing angle, bunch length, horizontal beam size at the IP, and hourglass effect. In the beam operation in Phase 2, the dither feedback was not needed, since the dependence of the luminosity on the horizontal offset was weak. In Phase 3, however, the dither feedback would become indispensable with smaller values of β_y^* .

REFERENCES

- [1] T. Abe *et al.*, “SuperKEKB design report”, in preparation, to be published in KEK Report.
- [2] S. Gierman *et al.*, “New fast dither system for PEP-II”, in *Proc. EPAC’06*, Edinburgh, GB, June 2006, pp. 652-654.
- [3] A.S. Fisher *et al.*, “Commissioning the fast luminosity dither for PEP-II”, in *Proc. PAC’07*, Albuquerque, NM, USA, June 2007, pp. 4165-4167,
- [4] M. Masuzawa *et al.*, “Early Commissioning of the luminosity dither system for SuperKEKB”, in *Proc. IBIC’18*, Shanghai, China,
- [5] U. Wienands *et al.*, “Dither coils for the SuperKEKB fast collision feedback system”, in *Proc. IPAC’15*, Richmond, USA, May 2015, pp. 3500-3502,
- [6] T. Hirai, S. Uehara and Y. Watanabe, “Real-time luminosity monitor for B-factory experiment”, *Nuclear Instruments and Methods in Physics Research*, Section A, pp. 670-676, 11 Feb., 2001,
- [7] S. Di Carlo *et al.*, “Early Phase 2 Results of LumiBelle2 for the SuperKEKB Electron Ring”, in *Proc. IPAC’18*, Vancouver, Canada, April-May 2018, pp. 2934-2935,
- [8] H. Ikeda, private communications.

MACHINE DETECTOR INTERFACE FOR CEPC*

S. Bai^{#1}, C. H. Yu^{1,2}, Y. W. Wang¹, Y. Zhang^{1,2}, D. Wang¹, H. P. Geng¹, Y. S. Zhu¹, J. Gao¹,
Z. H. Liu³, Qi Yang³

¹Institute of High Energy Physics, [100049] Beijing, China

²University of Chinese Academy of Sciences, [100049] Beijing, China

³Huiyu vacuum technology company, [110000] Shenyang, China

Abstract

The Circular Electron Positron Collider (CEPC) is a proposed Higgs factory with center of mass energy of 240 GeV to measure the properties of Higgs boson and test the standard model accurately. Machine Detector Interface (MDI) is the key research area in electron-positron colliders, especially in CEPC, it is one of the criteria to measure the accelerator and detector design performance. In this paper, we will introduce the CEPC superconducting magnets design, solenoid compensation, synchrotron radiation and mask design, detector background, collimator, mechanics assembly etc on, which are the most critical physics problem.

INTRODUCTION

With the discovery of a Higgs boson at about 125 GeV, the world high-energy physics community is investigating the feasibility of a Higgs Factory, a complement to the LHC for studying the Higgs [1]. There are two ideas now in the world to design a future higgs factory, a linear 125×125 GeV e^+e^- collider and a circular 125 GeV e^+e^- collider. From the accelerator point of view, the circular 125 GeV e^+e^- collider, due to its low budget and mature technology, is becoming the preferred choice to the accelerator group in China. MDI is one of the most challenging field in CEPC design, it almost covered all the common problems in accelerator and detector. Background is an important issue in MDI study. Every kinds of background source will increase the initial particles into detector, producing energy deposition in detector, which will make bad influence on the life of detector. Particles which hit the inner wall of beam pipe or collimators may interact with materials, producing lots of secondary particles into detector. These secondary particles will disturb the experiment and make damage to each layers. So it is necessary to reduce lost particles into detector.

The central field strength of CEPC detector solenoid is about 3T, it will introduce strong coupling of horizontal and vertical betatron motion, increasing the vertical emittance and also the vertical orbit. If it is not compensated, the IP beam size will increase, and degrade the luminosity.

In this paper, we will introduce the critical issues of CEPC MDI, including the superconducting magnets design,

solenoid compensation, detector background, collimator design and mechanics assembly etc on.

MDI LAYOUT AND IR DESIGN

The machine-detector interface is about ± 7 m in length in the IR as can be seen in Fig. 1, where many elements need to be installed, including the detector solenoid, luminosity calorimeter, interaction region beam pipe, beryllium pipe, cryostat and bellows. The cryostat includes the final doublet superconducting magnets and anti-solenoid. The CEPC detector consists of a cylindrical drift chamber surrounded by an electromagnetic calorimeter, which is immersed in a 3T superconducting solenoid of length 7.6 m. The accelerator components inside the detector should not interfere with the devices of the detector. The smaller the conical space occupied by accelerator components, the better will be the geometrical acceptance of the detector. From the requirement of detector, the conical space with an opening angle should not larger than 8.11 degrees. After optimization, the accelerator components inside the detector without shielding are within a conical space with an opening angle of 6.78 degrees. The crossing angle between electron and positron beams is 33 mrad in horizontal plane. The final focusing quadrupole is 2.2 m from the IP [2]. The luminosity calorimeter will be installed in a longitudinal location 0.95~1.11 m, with an inner radius of 28.5 mm and outer radius 100 mm. Primary results are got from the assembly, interfaces with the detector hardware, cooling channels, vibration control of the cryostats, supports and so on.

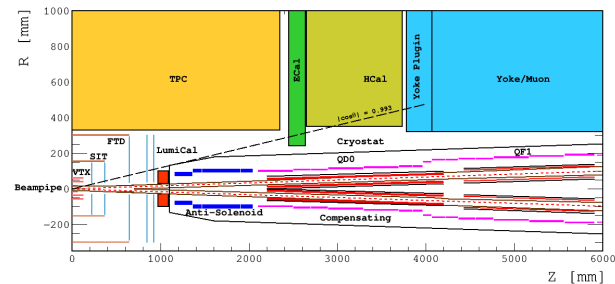


Figure 1: CPEC IR layout.

BEAM PIPE

To reduce the detector background and radiation dose from beam loss, the vacuum chamber has to accommodate the large beam stay clear region. In order to keep precise shaping, all these chambers will be manufactured with

* Work supported by National Key Programme for S&T Research and Development (Grant NO. 2016YFA0400400), and National Natural Science Foundation of China (NSFC, Project 11605210)

baisha@ihep.ac.cn

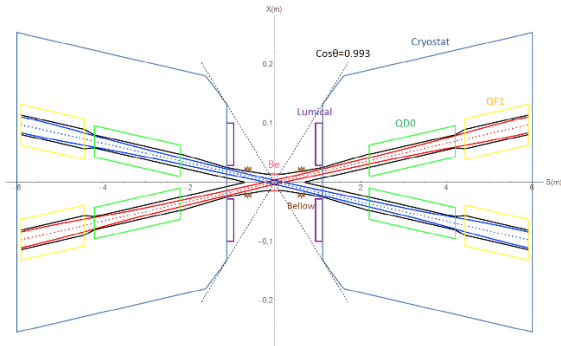


Figure 2: IR layout with beam pipes.

SOLENOID COMPENSATION

To compensate the solenoid field effect to the beam, compensating solenoid & Screening solenoid are installed outside of QD0/QF1 and IP, to make the integral field zero of the beam, and the longitudinal field of FD region zero. $\int B_z ds = 0$ within 0~2.12m; while $B_z < 300$ Gauss away from 2.12m, which is shown in Fig. 3. Anti-solenoid divided into parts according to detector solenoid field in longitudinal. The skew quadrupole coils are designed to make fine tuning of B_z over the QF&QD region instead of the mechanical rotation. [4]

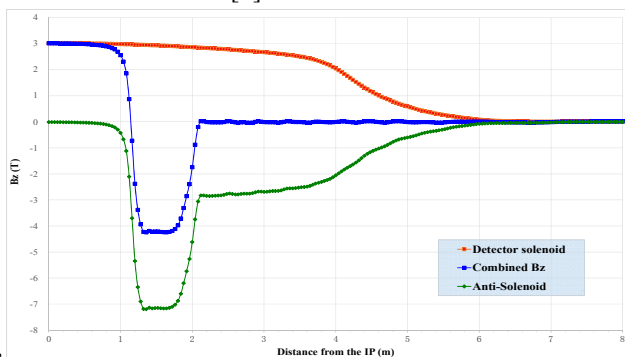


Figure 3: Detector solenoid compensation.

Due to the compensation of solenoid is only the integral field, the fringe field can't be compensated. And the fringe field will cause a vertical closed orbit distortion and excite dispersion in the vertical direction, which contributes to an increase in the vertical emittance. The vertical emittance

growth for Z mode is the most serious among the three operating energies due to the fringe field of the detector solenoid (3T). It is about 1.7%. But for Higgs it can be ignored [4].

SYNCHROTRON RADIATION AND MASK DESIGN

Synchrotron radiation (SR) photons are emitted in a direction tangential to the particle trajectory [5] and contribute to the heat load of the beam pipe and can cause photon background to the experiments. Furthermore, the radiation dose can damage detector components. Therefore the beam optics should be carefully designed in order to prevent the SR photons from directly hitting or scattering into the detector beam pipe.

The maximum designed single beam current is 17.4 mA and the maximum energy is 120 GeV. The fan of SR photons in the IR are mainly generated from the final upstream bending magnet and the IR quadrupole magnets due to eccentric particles.

SR From Bending Magnets

An asymmetric lattice has been selected to allow softer bends in the upstream part of the IP. Reverse bending direction in the final bends avoids SR photons from hitting the IP vacuum chamber. In the upstream part of the IP the SR critical energy is less than 45 keV within 150 m and 120 keV within 400 m. For the downstream part of the IP, there are no bends in the last 50 m and the critical energy is less than 97 keV within 100 m and 300 keV within 250 m. Figure 4. 2. 6. 3 shows the SR fans in the IR produced by the positron beam. The synchrotron radiation generated by electron beam is symmetric.

A significant fraction of these incident photons will forward scatter from the beam pipe surface and hit the central Be beam pipe (a cylinder located ± 7 cm around the IP with a radius of 14 mm). By installing 3 mask tips along the inside of the beam pipe to shadow the inner surface of the pipe the number of scattered photons that can hit the central beam pipe is greatly reduced to only those photons which forward scatter through the mask tips. The optimization of the mask tips (position, geometry and material) is presently under study. The current design calls for at least 3 tips for each incoming beam.

SR In IR Vacuum Chamber

A room temperature beam pipe and conduction cooled superconducting magnet has been adopted. The synchrotron radiation power in QD0 is 2.8 W along 2 m, and in QF1 is 3.1 W along 1.48 m. In the region between QD0 and QF1 it is 36.1 W along 0.23 m, where water cooling is needed. Synchrotron radiation fans in the IR vacuum chamber is shown below in Fig. 4.

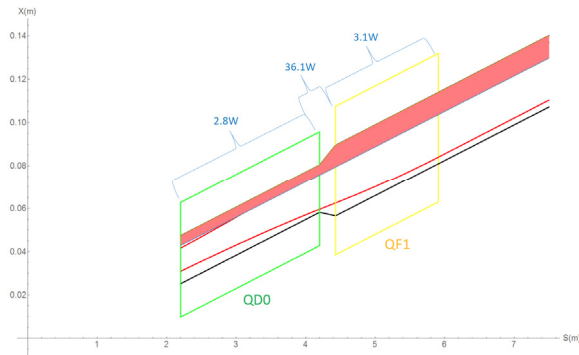


Figure 4: SR photon fans in the IR vacuum chamber.

SR In Final Doublet Quadrupoles

The total SR power generated by the QD0 magnet is 639W horizontally and 165W vertically. The photon critical energy is about 1.3MeV horizontally and 397keV vertically. The total SR power generated by the QF1 magnet is 1567W horizontally and 42W vertically. The photon critical energy is about 1.6MeV horizontally and about 225keV vertically. Below in Fig. 5 shows the synchrotron radiation fans horizontally and vertically from QD0.

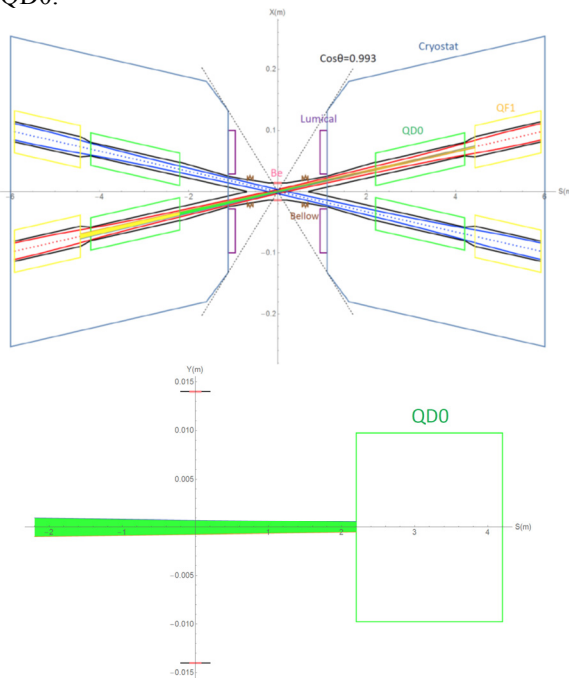


Figure 5: SR photon fans horizontally (up) from QD0 (green) and QF1 (yellow), SR photon fans vertically (down).

There are no SR photons within $10\sigma_x$ directly hitting or once-scattering to the detector beam pipe. There is collimators for the beam loss background, which will be installed in the upstream and downstream ARC far away from IP. These collimators will squeeze the beam to $13\sigma_x$. The SR photons generated from $10\sigma_x$ to $13\sigma_x$ will hit downstream of the IR beam pipe, and the once-scattering photons will not go into the detector beam pipe but goes

even far away from the IP region. Thus the SR photons from final doublet quadrupoles will not damage the detector components and cause background to experiments.

BEAM LOSS BACKGROUND AND COLLIMATOR DESIGN

The beam particles can lose a large fraction of their energy through a scattering processes such as radiative Bhabha, beamstrahlung [6], beam-gas scattering, or beam-thermal photon scattering. After optimizing the lattice, and considering the beam-beam effect and errors, the energy acceptance is about 1.5%. If the energy loss of the beam particles is larger than 1.5%, these particles will be lost from the beam and might hit the vacuum chamber. If this happens near the IR, detectors may be damaged. Beam loss production mechanisms and the associated beam lifetimes are listed in Table 1:

Table 1: CEPC Beam Lifetime

Beam loss mechanism	Beam lifetime	others
Quantum effect	>1000h	
Touscheck effect	>1000h	
Beam-Gas elastic scattering (Coulomb scattering)	>400h	Residual gas CO, 10-7Pa
Beam-Gas inelastic scattering(bremsstrahlung)	63.8h	
Beam-thermal photon scattering	50.7h	
Radiative Bhabha scattering	74min	
Beamstrahlung	80min	

The first three, due to the long lifetime, can safely be ignored. The next four, beamstrahlung, radiative Bhabha scattering, beam-thermal photon scattering and beam-gas inelastic scattering, especially beamstrahlung and radiative Bhabha scattering, due to shorter lifetimes, must be carefully analysed and collimated. Collimators are designed in the ARC which is about 2km far from the IP to avoid other backgrounds generation. Beam loss have disappeared in the upstream of IP for both Higgs and Z factory.

MECHANICS AND ASSEMBLY

IR mechanics assembly typical point is remote vacuum connection. The sealing point is 6m away from the operation point. The Ultrahigh vacuum sealing – Helicoflex is used. The layout is shown in Fig. 6.

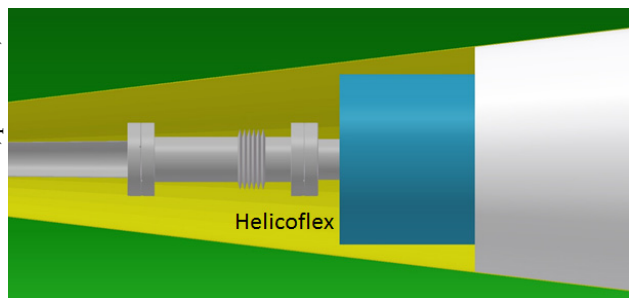


Figure 6: CEPC IR vacuum sealing.

There is no easy solution to install all the critical components in the IR with high precision, which is inspired by the Remote Vacuum Connection (RVC) developed by SuperKEKB [7], which is shown in Fig. 7. We are studying the special installation tools for the remote connection of bellows.

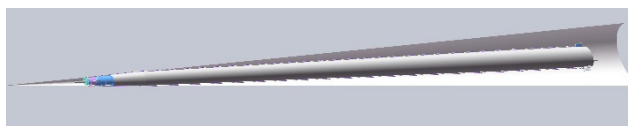


Figure 7: RVC whole layout.

CONCLUSION

The finalization of the beam parameters and the specification of special magnets have been finished. The parameters are all reasonable. The detector solenoid field effect to the beam can be compensated. HOM of IR beam pipe has been simulated and water cooling was considered. Beam lifetime of CEPC double ring scheme is evaluated. The most importance beam loss background is radiative Bhabha scattering and beamstrahlung for the Higgs factory. Collimators are designed in the ARC which is about 2km far from the IP to avoid other backgrounds generation. Beam loss have disappeared in the upstream of IP for both Higgs and Z factory. Preliminary procedures for the installation of IP elements are studying. The boundary between detector and accelerator is still not clear. Very long time is needed to confirm the final scheme. Towards TDR, many of the MDI components are under development.

REFERENCES

- [1] Accelerators for a Higgs Factory: linear vs circular (HF2012). <https://indico.fnal.gov/conferenceDisplay.py?confId=5775>
- [2] Y.W. Wang *et al.*, “Optics Design for CEPC double ring scheme”, WEPIK018, 2017.
- [3] N. Ohuchi *et al.*, “Design and construction of the magnet cryostats for the SuperKEKB Interaction Region”, *Applied Superconductivity*, vol.28, No. 3, April 2018.
- [4] The CEPC-SPPC Study Group, CEPC Conceptual Design Report, Volume I-Accelerator, IHEP-AC-2018-01.
- [5] Synchrotron Radiation and Free Electron Lasers, CERN Accelerator school, CERN-90-03, 1990.
- [6] J.E. Augustin, N. Dikansky, Ya. Derbenev, J. Rees, Burton

Richter *et al.* “Limitations on Performance of e^+e^- Storage Rings and Linear Colliding Beam Systems at High Energy,” *eConf*, C781015:009, 1978.

- [7] K. Kanazawa. *SuperKEKB mechanical assembly at IR*. Presentation in Workshop on the mechanical optimization of the FCC-ee MDI, CERN, Switzerland, Jan 30-Feb 9, 2018.

BEAM BACKGROUND AT SUPERKEKB DURING PHASE 2 OPERATIONS

A. Paladino* on behalf of the BEAST group, KEK - IPNS, Tsukuba, Japan

Abstract

The SuperKEKB accelerator, the upgrade of the KEKB machine, will operate at an unprecedented instantaneous luminosity of $8 \times 10^{35} \text{cm}^{-2} \text{s}^{-1}$, providing the Belle II experiment an expected integrated luminosity of about 50ab^{-1} in ten years of operation. With the increased luminosity, the beam background is expected to grow significantly with respect to KEKB, leading, among other effects, to possible damage of detector components and suppression of signal events. We present studies done during the Phase 2 operation of SuperKEKB to evaluate the contribution of each background source, including the Touschek effect, beam-gas scattering, synchrotron radiation, and injection background. We also present studies performed on collimators and other solutions adopted to mitigate beam backgrounds in the interaction region.

INTRODUCTION

The SuperKEKB [1] asymmetric e^+e^- collider is an upgrade of the KEKB machine that will provide the Belle II experiment [2] an unprecedented instantaneous luminosity of $8 \times 10^{35} \text{cm}^{-2} \text{s}^{-1}$, with an expected integrated luminosity of about 50ab^{-1} in ten years of operation. The upgrade is based on the so called "nano-beam scheme", proposed for the first time by P. Raimondi for the SuperB project [3]. The idea behind the nano-beam scheme is to squeeze as much as possible the vertical beta function of the beams at the IP, maximizing the luminosity, which is given by the following formula, assuming flat beams and equal horizontal and vertical beam sizes for the two beams:

$$L = \frac{\gamma_{\pm}}{2e r_e} \frac{I_{\pm} \xi_{y\pm}}{\beta_{y\pm}^*} \frac{R_L}{R_{\xi_y}} \quad (1)$$

where γ is the Lorentz factor, e the elementary electric charge, r_e the electron classical radius, I_{\pm} the beam current, $\xi_{y\pm}$ the beam-beam parameter, $\beta_{y\pm}^*$ the vertical beta function at the IP, R_L the luminosity reduction factor, R_{ξ_y} the beam-beam reduction factor. + and - indices refer to positron and electron beams respectively. Squeezing the beta-function by a factor 20 with respect to KEKB and doubling the beam currents, a 40 times higher luminosity can be achieved. SuperKEKB basic parameters are summarized in Table 1.

The Belle II detector, an upgraded version of the Belle detector, is placed around the IP. Its vertex reconstruction performance will be improved thanks to the new VerteX Detector (VXD), whose readout electronics can tolerate the 10 Mrad dose expected for the whole period of operation. The purpose of the Phase 2 operation, together with the

commissioning of SuperKEKB in its final configuration, is to verify that the level of backgrounds in the interaction region are compatible with the expectations.

Table 1: Basic parameters for SuperKEKB Phase 2 and Phase 3 operations. The former number refers to the Low Energy Ring (LER), the latter to the High Energy Ring (HER).

	Phase 2	Phase 3
Energy [GeV]	4.0/7.007	4.0/7.007
Beam current [A]	0.327/0.279	3.6/2.6
Number of bunches	789	2500
ε_x [nm]	1.7/4.6	3.2/4.6
$\xi_{y\pm}$	0.028/0.019	0.088/0.081
$\sigma_{y\pm}^*$ [nm]	692/486	48/62
$\beta_{y\pm}^*$ [mm]	3.0/3.0	0.27/0.30
$\beta_{x\pm}^*$ [mm]	200/100	32/25
Luminosity [$\text{cm}^{-2} \text{s}^{-1}$]	2.62×10^{33}	8×10^{35}

BELLE II AND BEAST DETECTORS

For Phase 2, the Belle II detector was used in its final configuration, except for the VerteX Detector (VXD), where only one slice of the final silicon vertex tracker was used, as shown in Fig 1. The remaining volume was occupied by some of the BEAST II detectors:

- FANGS: hybrid silicon pixel detectors.
- CLAWS: plastic scintillators with SiPM readout.
- PLUME: double sided CMOS pixel sensors.

Outside of the VXD volume, other BEAST II detectors were used:

- Diamond sensors for ionizing radiation dose monitoring in the interaction region.
- PIN diodes for ionizing radiation dose monitoring around QCS magnets.
- ^3He detectors for thermal neutron flux measurements.
- TPC detectors for fast neutron flux and direction measurements.

BACKGROUND SOURCES

In this section, the most relevant beam background sources in SuperKEKB are described.

* antonio.paladino@pi.infn.it

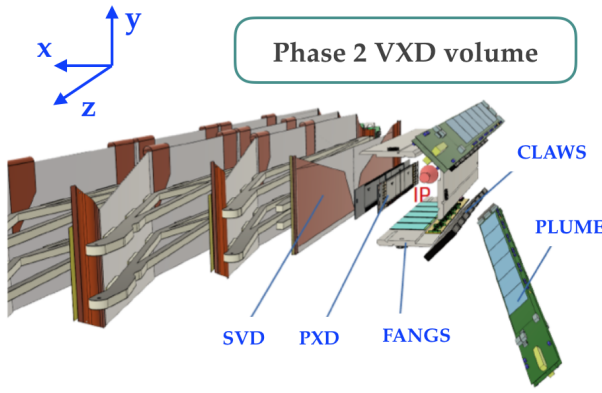


Figure 1: Detectors inside the VXD volume during Phase 2 operations.

Touschek Effect

Touschek effect is a single Coulomb scattering event where a small transverse momentum exchanged by two particles of the same bunch is transformed into a large longitudinal momentum, causing the loss of both particles, one with too much energy, the other one with too less. Lost particles eventually hit the inner surface of the beam pipe generating a shower that, if the hit position is close to the interaction region, can propagate to the detector, causing damage to silicon devices and contributing to generate fake hits that affect the performance of the detector.

The scattering rate of the Touschek effect is proportional to:

$$R_{Tou} \propto \frac{1}{\sigma} E^3 n_b I^2 \quad (2)$$

where σ is the beam size, E the beam energy, n_b the number of bunches, I the beam current.

During Phase 2 operations, beam size scans were performed to evaluate the Touschek component of the background levels. In single beam studies, the vertical beam size has been increased compared to the nominal one changing beam emittance, measuring the background level at each different beam size using BEAST detectors and some of the Belle II sub-detectors. At the beginning, increasing the beam size, a decrease in the background levels was observed, as expected since the Touschek effect is inversely proportional to the beam size. However going to bigger beam sizes during the HER study, an unexpected increase in the background was observed. This background increase could be due to a possible scraping of the beam tails on some structures of the beam pipe, but the hypothesis has to be verified with further studies.

Horizontal collimators are very effective to mitigate the Touschek background, and studies were performed during Phase 2 to find the optimal collimators setting. A description of these studies is given in the dedicated section on "Collimators studies".

Beam-gas Scattering

The second background source in SuperKEKB is the beam-gas scattering that occurs between particles and atoms of the residual gas in the beam pipe. The Coulomb scattering changes the trajectory of the particle, while the bremsstrahlung decreases the particle energy.

The rate of the beam-gas scattering is proportional to:

$$R_{bg} \propto IP \quad (3)$$

where P is the residual pressure inside the beam pipe. In the single beam background studies done during Phase 2, Touschek and beam-gas contributions were evaluated fitting the data with a two-parameters function:

$$P = T \frac{I^2}{\sigma_y n_b} + B I p \quad (4)$$

where T is the parameter for the Touschek component and B is the parameter for the beam-gas component. This function well represents the data of the HER and LER studies at small beam size, as shown in Fig. 2 and in Fig. 3, where the fit of the data taken with the PLUME detector for HER and LER respectively are shown.

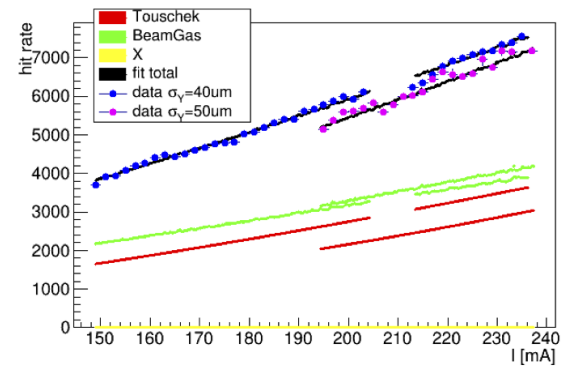


Figure 2: PLUME data of beam size study for HER with Touschek and beam-gas components.

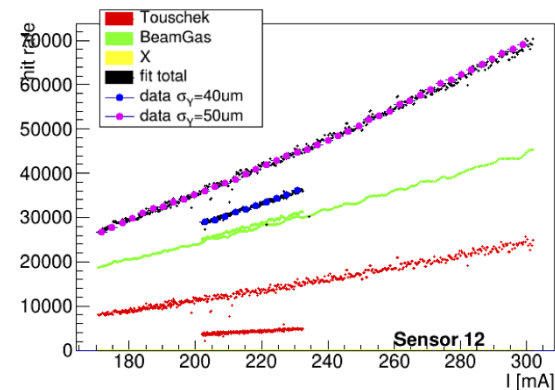


Figure 3: PLUME data of beam size study for LER with Touschek and beam-gas components.

For higher beam sizes an additional term was necessary for HER to fit the data, to take into account the observed increase in background. Touschek and beam-gas components were found to be similar, with the fraction changing depending on the detector.

In Phase 3 the β_y function inside the Final Focus system will be ten times higher than it was at the end of Phase 2, so in Phase 3 we expect that the Coulomb lifetime will be shorter and beam-gas background very high, if not mitigated by good vertical beam collimation. Additional vertical collimators will be placed in the LER to improve the beam-gas background reduction. Some additional heavy-metal shielding are used around the interaction region to lower the effect of the losses due to beam-gas scattering.

Synchrotron Radiation

Another background source is the synchrotron radiation emitted from the beam. The rate of emission is proportional to:

$$R_{bg} \propto E^2 B^2 \quad (5)$$

where B is the magnetic field intensity. This means that the HER contribution to synchrotron radiation is expected to be the main source of this kind of background, with photon energies going from a few keV to tens of keV.

Some countermeasures were taken to protect the detector from synchrotron radiation: the beam pipe is coated with a Au layer (6.6 μm in Phase 2, 10.0 μm in Phase 3), the tapered shape of the beam pipes prevent from direct hits of photons inside the interaction region, and ridge structures are included in the beam pipe shape to prevent forward reflected photons to reach the interaction region.

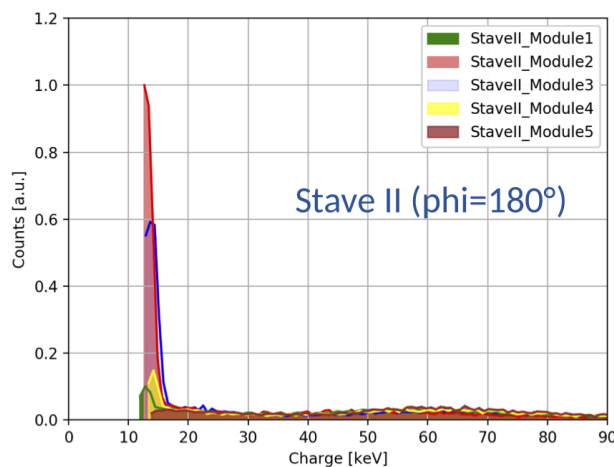


Figure 4: Synchrotron radiation peak observed by the stave n.2 of the FANGS detector, positioned at $\phi = 180^\circ$

Despite the observation of synchrotron radiation was not expected in Phase 2, the PXD detector, located on the outer side of the ring ($\phi = 0^\circ$), and the FANGS BEAST detector, with its Stave 2 located on the inner side of the ring ($\phi = 180^\circ$), observed a peak in the energy spectrum at around 8-10

keV (see Fig 4), with longitudinal distributions that suggest the same mechanism of production for both rings. The origin of this synchrotron radiation peaks seems due to photons produced in the Final Focus region and then reflected by the Tantalum part of the beam pipe. The reflected photons can reach the IR beam pipe and, despite the presence of the Au layer, reach the inner detectors. The simulations has been revised and can now reproduce qualitatively the data, with still some differences in the ratio between the two layers of the PXD.

Luminosity Background

Other background sources comes from the interaction between the two beams, with a rate that is proportional to the luminosity:

1. Electron and positron energies decrease after the Bhabha process, so particles with too much energy difference with respect to the nominal one will be over bent by the Final Focus magnets and lost, hitting the beam pipe and generating electromagnetic showers. The process is mitigated by the fact that in SuperKEKB separate quadrupoles are used for each beam line and for incoming and outgoing beams, but with the very high luminosity of SuperKEKB, this background will still be the dominant one.
2. Photons from the Bhabha process propagate along the beam axis and interact with the iron of the magnets, producing neutrons via the photo-nuclear resonance mechanism. These neutrons are the main background source for the outermost sub-detectors of the experiment.
3. In the two-photon process, low momentum electron-positron pairs are produced and can hit the inner tracking detectors, affecting their tracking performance.

All these background sources depend on the luminosity, so a change in luminosity should decrease the total background level observed by the detectors. Two luminosity studies were performed during Phase 2: in the first one the vertical offset between the beams was changed until luminosity was reduced to zero; in the second study the fill pattern was changed so that the bunches were shifted in time and did not collide. During the first study, when the beams were shifted enough to have no luminosity, an increase of background levels was observed, which is unexpected if collisions do not occur. The origin of the increasing background is still under study. It was challenging to extract the luminosity component of the background from these studies, because the background conditions were not stable between luminosity studies and single beam background studies, making difficult to disentangle the Touschek and beam-gas components from the luminosity one.

Injection Background

During particles injection in the main ring, the injected bunch is perturbed, resulting in particle losses.

collimator study was performed, using the first optimised collimators configuration as a starting point, to see if it was possible to further reduce the background levels. In some cases, like for D06H3 and D06H4, it was possible to further reduce the IR background level. More similar studies are planned for the beginning of Phase 3, especially for horizontal collimators, that are more effective against Touschek background.

A similar study on collimators was done with machine simulation, starting from the fully open configuration and closing one collimator at a time with different steps. A collimator study for Phase 3 using simulation is ongoing, including the collimators that will be added in the early stage of Phase 3.

CONCLUSIONS

BEAST II and BELLE II detectors have been successfully used to study the beam background during the Phase 2 commissioning of SuperKEKB. The studies for Touschek, beam-gas and synchrotron radiation have given useful results, although more investigation is needed to explain some observations. For luminosity background, more effort is needed for Phase 2 data to disentangle the single beam background components and extract the luminosity one.

A general overview of Phase 2 data indicates that the background levels were higher than expected, with LER

storage background around five times HER ones and with HER injection background always higher than LER one. More time should be dedicated at the beginning of Phase 3 to improve background reduction.

ACKNOWLEDGEMENTS

The BEAST group thanks the Belle II collaboration and the SuperKEKB collaboration.

REFERENCES

- [1] Y. Ohnishi *et al.*, “Accelerator design at SuperKEKB”, *PTEP* 2013, 03A011, DOI: 10.1093/ptep/pts083
- [2] T. Abe *et al.* [Belle-II Collaboration], “Belle II Technical Design Report,” arXiv:1011.0352 [physics.ins-det].
- [3] M. Baszczyk *et al.* [SuperB Collaboration], “SuperB Technical Design Report,” arXiv:1306.5655 [physics.ins-det].
- [4] T. Ishibashi, Y. Suetsugu and S. Terui, “Collimators for SuperKEKB Main Ring,” in *Proc. IPAC’17*, paper WEPI009, doi:10.18429/JACoW-IPAC2017-WEPIK009
- [5] H. Nakayama, K. Ohmi, Y. Ohnishi, K. Kanazawa, Y. Suetsugu, H. Nakano and Y. Funakoshi, “Small-Beta Collimation at SuperKEKB to Stop Beam-Gas Scattered Particles and to Avoid Transverse Mode Coupling Instability,” *Conf. Proc. C* 1205201, 1104 (2012).

COMMISSIONING STATUS OF SuperKEKB VACUUM SYSTEM

K. Shibata[†], Y. Suetsugu, T. Ishibashi, K. Kanazawa, M. Shirai, S. Terui, and H. Hisamatsu
 High Energy Accelerator Research Organization (KEK), 305-0817 Tsukuba, Ibaraki, Japan

Abstract

In the upgrade from the KEKB B-factory (KEKB) to the SuperKEKB, approximately 90% and 20% of the beam pipes and vacuum components of the positron ring and the electron ring, respectively, were replaced with new ones. In the Phase-1 commissioning in 2016, vacuum scrubbing and confirmation of the stabilities of new vacuum components at approximately 1 A were carried out, and some problems, such as pressure bursts accompanied with beam losses, were revealed. During the subsequent shutdown, the countermeasures against the problems were taken, and new beam pipes and components, such as beam pipes for the interaction point, and beam collimators were installed. The Phase-2 commissioning, where beam collision tuning was mainly performed, was carried out from March to July 2018. The collimators suppressed the background noise of the particle detector for high-energy physics (Belle II detector) very well, and the frequency of the pressure burst drastically decreased though typical beam currents were lower than those in Phase-1. So far, the vacuum system of the SuperKEKB has been working generally well, and no serious problems have been observed.

INTRODUCTION

The SuperKEKB [1], which is an upgrade of the KEKB, is a high-luminosity electron–positron collider. The main ring (MR) of the SuperKEKB with a circumference of 3016 m is composed of two rings, i.e., the high-energy ring (HER) for 7.0 GeV electrons and the low-energy ring (LER) for 4.0 GeV positrons. Over a period of 10 years, the SuperKEKB project is expected to achieve a 50-fold increase in the integrated luminosity over the original KEKB. The design luminosity is $8.0 \times 10^{35} \text{ cm}^{-2}\cdot\text{s}^{-1}$, which is approximately 40 times the KEKB’s record. In the SuperKEKB, the luminosity will be increased by increasing the beam current to 2.6 A (electrons) and 3.6 A (positrons), which are twice as much as in the KEKB, and adopting a novel “nanobeam” collision scheme, which requires a much smaller emittance beam than the KEKB. In order to achieve this challenging goal, many upgrades are required, among which the upgrade of the vacuum system [2–4] is a crucial requirement.

After more than five years of upgradation work on the KEKB, the commissioning of the SuperKEKB commenced in 2016, and two of three commissioning phases have been completed so far. The first commissioning (Phase-1), which was dedicated to accelerator tuning without the Belle II detector [5], was carried out from February to June 2016 [6]. During the subsequent shut-

down period, the remained upgradation works including the “roll-in” of the Belle II detector [5] to the collision point were performed. The second commissioning (Phase-2), where beam collision tuning was mainly performed, was carried out from March to July 2018.

VACUUM SYSTEM UPGRADATION

Outline of Upgradation

For the LER, in order to realize small beam emittance, the beam optics was drastically changed compared to that of the KEKB, and a large number of magnets need to be rearranged, replaced, and added. Consequently, approximately 93% of the beam pipes and vacuum components were replaced with new ones. On the other hand, in the HER, the wiggler section was newly made to reduce the emittance, but in the arc sections, no replacement of the magnet was performed. Furthermore, because the beam energy of the HER is reduced from 8.0 GeV to 7.0 GeV, the power of the synchrotron radiation (SR) decreases to the tolerance level of a conventional copper beam pipe, in spite of doubling the beam current. Therefore, approximately 80% of the components in the HER can be reused. Only in the interaction region and the new wiggler section, the beam pipes and components were replaced with new ones. Figure 1 shows the location where the vacuum components were replaced in both rings. The reused components of the HER were left undisturbed in the tunnel during the upgradation work keeping vacuum inside although all vacuum pumps were tuned off. However, these components were sometimes exposed to air temporarily when broken components were replaced with new ones.

The target vacuum pressure in the MR is on the order of 10^{-7} Pa at the designed beam current. In the LER, because of the higher beam currents, the SR power and the photon density are consequently higher, and the resultant heat and gas loads are also larger than those of the KEKB. As a solution to this issue, an effectively distributed pumping scheme using a strip-type NEG (ST707, SAES GETTERS Co. Ltd.) was adopted as the main pump for the arc sections of the LER. The expected effective linear pumping speed is approximately $0.14 \text{ m}^3\cdot\text{s}^{-1}\cdot\text{m}^{-1}$ for CO just after the NEG activation. In order to achieve the required pressures, a linear pumping speed of approximately $0.1 \text{ m}^3\cdot\text{s}^{-1}\cdot\text{m}^{-1}$ is required if we assume a photo-desorption coefficient of $1 \times 10^{-6} \text{ molecules}\cdot\text{photon}^{-1}$, which was obtained at a beam dose of $3 \times 10^3 \text{ A}\cdot\text{h}$ in the KEKB and will be accrued after approximately 1 year beam operation at the designed beam current in the case of the SuperKEKB. To evacuate non-active gases and to enable more efficient evacuation in relatively high-pressure regimes, noble-type sputter ion pumps with a nominal pumping speed of $0.4 \text{ m}^3\cdot\text{s}^{-1}$ are provided as an

[†] kyo.shibata@kek.jp

auxiliary pump every 10 m along the ring. The total pressures were measured with approximately 300 cold cathode gauges (CCG, Model C-5, DIAVAC Ltd. Japan) in each ring at pumping ports.

Almost all beam pipes were pre-baked (150 °C, 24 h) [3] in the laboratory before the installation, and no in-situ baking was performed. All beam pipes for the LER were coated with TiN films [7-8] with a thickness of 200 nm to reduce secondary electron yield before the installation as a countermeasure against the electron cloud effect (ECE). To suppress the ECE, additional countermeasures, such as beam pipes with antechambers, a solenoid field, a grooved surface, and an electron clearing electrode, were also adopted in the LER [4].

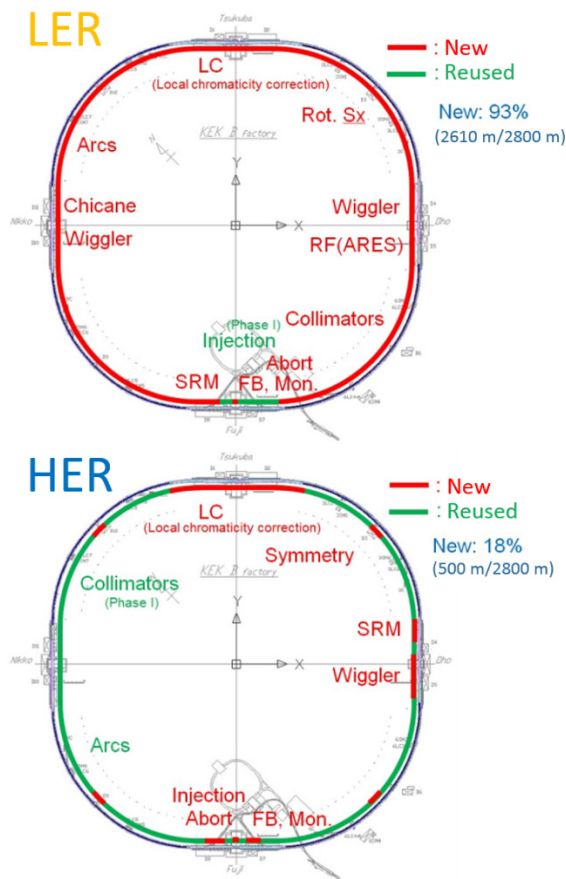


Figure 1: Locations where the vacuum components were replaced in the upgrade from the KEKB to the SuperKEKB.

New Components

Most of the new beam pipes have antechamber structures [3-4, 9], which deal with high power SR due to high beam current, as shown schematically in Fig. 2. SR passes through one or two antechambers at the arc sections or wiggler sections, respectively. At the arc sections, one of the antechambers is used as a pump channel. A screen with many holes with a diameter of 4 mm and a thickness of 5 mm that shields the pump from the beam is installed in the antechamber between the pump and the beam. In the wiggler sections, SR hits both sides of the beam pipe.

The beam pipes have no pumping channel. Instead, the pumping ports are located at the bottom of the antechambers in this case. Cooling channels are provided outside the antechambers to absorb heat deposited by SR, beam-induced wall currents, and higher order modes (HOMs). The antechamber plays a key role as a countermeasure against the ECE by minimizing the impact of photoelectrons on the beam [10]. As a countermeasure against the ECE, the beam pipes in the dipole magnets of the LER have grooved surfaces [11] on the upper and lower sides of the beam channel, as shown in Fig. 3. The material of the new beam pipes in the arc sections is Al-alloy, though copper beam pipes are also used at the locations where the SR power is higher, such as the wiggler sections.

Bellows chambers have to be installed between the beam pipes to ease beam-pipe installation and to absorb thermal deformation during the beam operation. More than 1200 bellows chambers are used in one ring. Newly installed bellows chambers have a comb-type RF-shield [12], as shown in Fig. 4, which has a higher thermal strength than a conventional finger-type shield. A comb-type RF-shield was also used for approximately 40 gate valves.

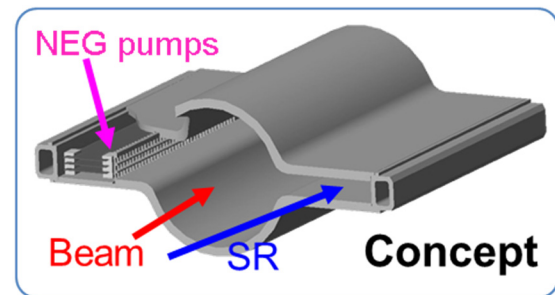


Figure 1: Conceptual drawing of the beam pipe with antechambers for the SuperKEKB.

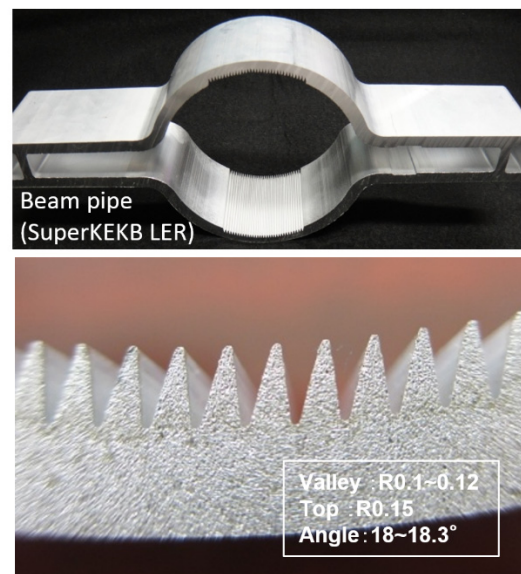


Figure 3: Grooved structure on the top and bottom of the beam channel of the new beam pipe.

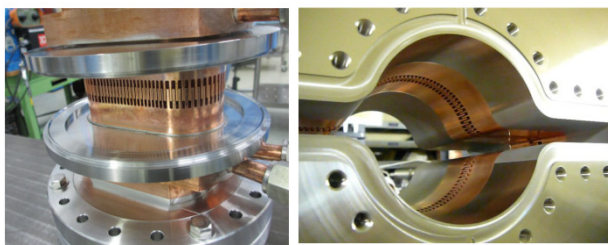


Figure 4: Comb-type RF-shield for new bellows chambers and gate valves for the SuperKEKB.

The beam with a high bunch current ($1.4 \text{ mA-bunch}^{-1}$) and a short bunch length ($6\text{--}7 \text{ mm}$) of the SuperKEKB is likely to excite HOMs. The beam impedance of various vacuum components should be minimized to keep the beam stable and also to avoid excess heating of the components. Gaps or steps at the connection flanges of the beam pipes and the bellows chambers can be significant sources of impedance because the number of flanges is high. As a countermeasure against this issue, step-less Matsumoto–Ohtsuka-type (MO-type) flanges [13], which can provide a vacuum-tight seal at the inner surface while maintaining smooth flow of the wall current across a copper or aluminum-alloy gasket, were adapted to the new components. Figure 5 shows several types of the MO-type flanges adopted in the SuperKEKB. The antechamber is also effective in reducing the impedance of SR masks and pumping ports, which are placed in the antechambers. The SuperKEKB is the first machine that adopted a comb-type RF-shield and step-less MO-type flanges in a large quantity.

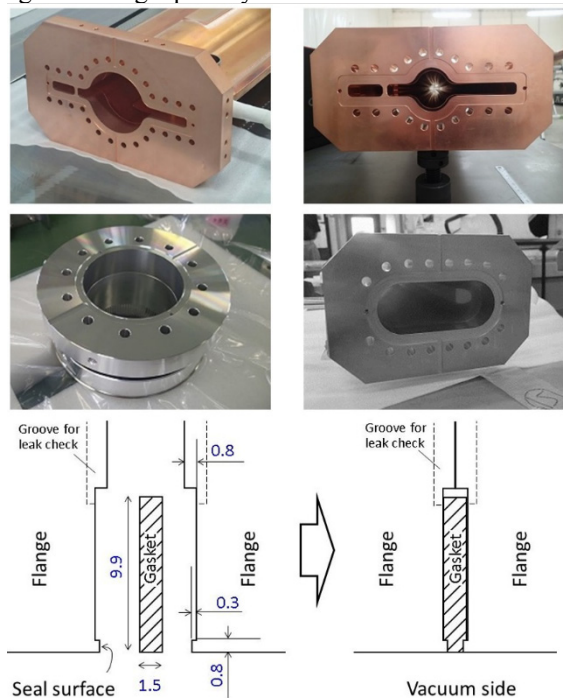


Figure 5: Several types of the step-less MO-type flanges of the SuperKEKB.

New beam collimators [14], which cut off the beam halo and reduce the background noise of the Belle II detector, were installed into the SuperKEKB. These collimators

were newly designed based on those used in PEP II at SLAC with the objective of minimizing the impedance. The conceptual structure of the horizontal collimator is shown in Fig. 6. Two new horizontal beam collimators were installed before the Phase-1 commissioning to test during Phase-1. In the HER, 16 KEKB-type beam collimators [15–16] were reused.

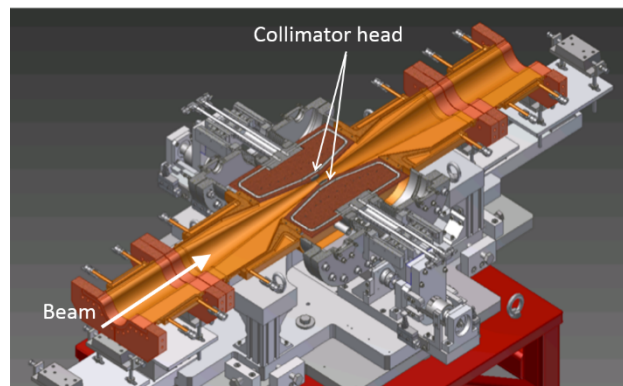


Figure 6: Conceptual structure of new beam collimator (horizontal type).

PHASE-1 COMMISSIONING

Vacuum Scrubbing

The Phase-1 commissioning, which was dedicated to accelerator tuning without the Belle II detector, began in February 2016 and successfully ended in June 2016. Vacuum scrubbing and confirmation of the stabilities of new vacuum components at approximately 1 A were also carried out, and the vacuum system experienced no serious problems during the Phase-I commissioning [17–18]. Figure 7 shows the histories of the average pressure in the whole ring, including that in the straight sections (such as the wiggler sections, beam injection sections, and accelerating cavity sections), average pressure in only the arc sections, and stored beam currents for both rings. The arrows and dates at the tops of Fig. 7 indicate the NEG conditioning times. During Phase-1, the maximum stored beam currents were 1.01 A and 0.87 A and the beam doses were 780 A·h and 660 A·h for the LER and the HER, respectively. For the whole LER, the base pressure (p_{base}) and the average pressure at the maximum beam current (p_{max}) were $5 \times 10^{-8} \text{ Pa}$ and $1 \times 10^{-6} \text{ Pa}$, respectively. The p_{max} of the whole ring and that of the arc sections, where most of the beam pipes were newly fabricated, were almost the same. On the other hand, the p_{base} and p_{max} of the whole HER were $3 \times 10^{-8} \text{ Pa}$ and $2 \times 10^{-7} \text{ Pa}$, respectively. In the arc sections, the p_{max} was $6 \times 10^{-8} \text{ Pa}$, where most beam pipes were reused from KEKB.

Figure 8 shows the average pressures normalized by a unit beam current, i.e., the pressure rise dp/dI [$\text{Pa}\cdot\text{mA}^{-1}$] for the LER and the HER, as functions of the beam doses. In the calculation of dp/dI , the average pressure was used instead of the pressure increase for simplicity. In each graph, the upper axis represents the photon dose D [$\text{photo}\cdot\text{tons}\cdot\text{m}^{-1}$] in the arc sections, and the right axis indicates

the photon stimulated desorption (PSD) rate η [molecules-photon $^{-1}$] in the arc section, evaluated by assuming linear pumping speeds of 0.06 m 3 ·s $^{-1}$ ·m $^{-1}$ and 0.03 m 3 ·s $^{-1}$ ·m $^{-1}$ for the LER and the HER, respectively, considering saturation of the NEG pumping speed [2]. For the arc sections in the LER, at the initial stage, η (1×10^{-3} molecules-photon $^{-1}$) is several times lower than its value in the KEKB (4×10^{-3} molecules-photon $^{-1}$), where circular copper beam pipes without any coating were used [19]. However, at the final stage ($D = 4 \times 10^{24}$ photons·m $^{-1}$), η (7×10^{-6} molecules-photon $^{-1}$) has almost the same value as in the KEKB at the same photon dose. The slope η gradually increases with increasing D . Note that η slightly increased when $D > 6 \times 10^{23}$ photons·m $^{-1}$. The main cause for this increase was a nonlinear increase in the pressure with increasing the beam current due to the gas desorption from electron multipacting in the beam pipe [17-18]. Therefore, the η values in this region do not reflect the real PSD rate. In the HER, on the other hand, the η is lower and shows a steeper decrease in the early stage compared to that in the LER. The η decreases less rapidly at $D > 1 \times 10^{24}$ photons·m $^{-1}$, but this change occurs because the effect of the base pressure is not negligible in the dp/dI calculations. That η in the HER is lower than that in the HER of the KEKB from the beginning [19]. The η at the final stage (1×10^{-7} molecules-photon $^{-1}$) is much lower than that in the case of the KEKB (2×10^{-6} molecules-photon $^{-1}$) at the same D , and its value is almost the same as that in the final stage of the KEKB [19]. Since most of the beam pipes in the arc sections of the HER were reused from the KEKB, their surfaces “remember” the conditions in the KEKB after sufficient vacuum scrubbing (memory effect), even though they were sometimes exposed to air for the vacuum work.

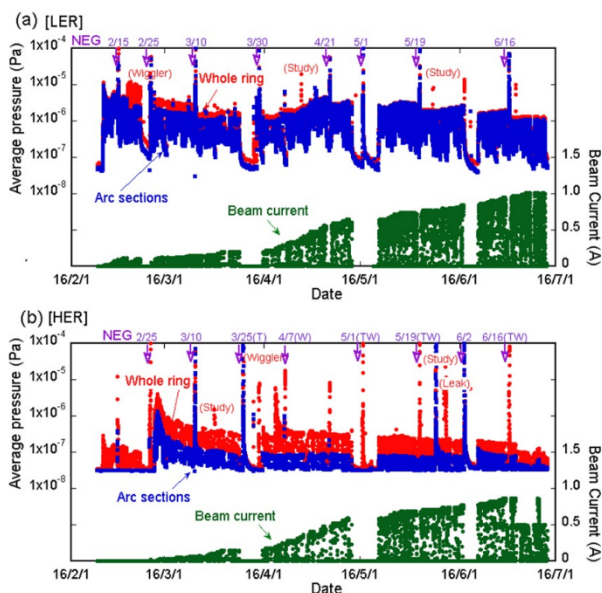


Figure 7: Histories of the average pressures in the whole ring (red), those in the arc sections (blue), and the stored beam currents (green) for (a) the LER and (b) the HER, respectively, during the Phase-1 commissioning.

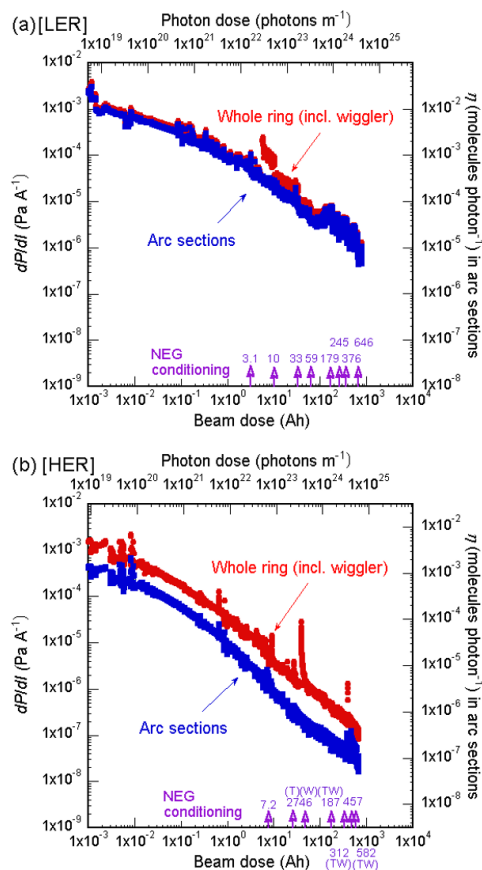


Figure 8: Average pressures normalized by a unit beam current dp/dI for (a) the LER and (b) the HER, respectively, as functions of the beam dose during Phase-1. The PSD rate η in the arc sections as a function of the photon dose is also shown in each graph.

Status of the New Vacuum Components

The SuperKEKB is the first machine to adopt step-less MO-flanges and comb-type RF-shields on a large scale. During the Phase-1 commissioning no overheating, discharging, or abnormal pressure increases were observed in these components. The average temperature increase of these components is less than 4 °C at 1 A. The temperature increases in the bellows chambers located near the beam collimator, where extra HOMs are easily excited, are less than 2 °C, though overheating of the bellows chambers with a conventional finger-type RF-shield was frequently observed in the KEKB.

As for the beam collimators, their operability, heating, and collimator head position accuracy were checked using high beam currents. The effectiveness of the background noise reduction was also confirmed by a preliminary detector installed near the collision point.

Major Problems

One of the major concerns during the Phase-1 commissioning was the localized pressure burst phenomenon accompanied with beam loss in the LER [20-21]. The beam loss monitors triggered beam aborts, and sometimes pressure bursts became obstacles during the beam com-

WORK FOR PHASE-2

Installation of New Components

The most important work in the MR during the shutdown period before the Phase-2 commissioning was to install new beam pipes and components for the Belle II detector and the superconducting final-focusing magnets (QCS magnets) around the collision point.

Six additional beam collimators were installed to suppress the background noise of the Belle II detector, following successful results of the two models used in the Phase-1 commissioning. Including the KEKB-type beam collimators reused in the HER, 5 and 19 beam collimators were prepared for the LER and the HER, respectively, for the Phase-2 commissioning.

The beam pipes at the LER injection region were changed to adapt a low emittance beam injected through the new positron damping ring [23-24].

Countermeasures Against Major Problems

During this shutdown period, we gathered dusts from the beam pipe where bursts were frequently observed by a special tool to clean up the inside of the beam pipes. Actually, we found large-size Al and Al_2O_3 particles in one of the beam pipes where pressure bursts were frequently observed in Phase-1. Furthermore, we knocked most of the beam pipes, in which pressure bursts were frequently observed, and dropped dust particles from their ceilings prior to starting the Phase-2 commissioning.

As for overheating of the connection flanges and air leak in the wiggler sections, new bellows chambers having SR masks at the top and bottom of the antechambers were fabricated for protecting the connection flanges from vertically steered or spreading SR. Two bellows chambers with masks were installed between the beam pipes in the wiggler section. Furthermore, the beam pipes were realigned in the vertical direction with respect to the nearby quadrupole magnets. The beam orbit in the wiggler section was kept as flat as possible during the beam operation in the Phase-2 commissioning. Additionally, the flow rate of cooling water for the overheated beam pipes was increased as much as possible.

PHASE-2 COMMISSIONING

Vacuum Scrubbing

The Phase-2 commissioning began in March 2018 and ended in July 2018. The vacuum system worked generally well and experienced no serious problems again during the Phase-2 commissioning. Figure 10 shows the histories of the average pressure in the whole ring, including that in the straight sections, average pressure in only the arc sections, and stored beam current for both rings. Since the major task of the Phase-2 commissioning was beam collision tuning to verify the novel "nanobeam" collision scheme, typical stored beam currents during Phase-2 were lower than those during Phase-1. However, at the latter in the Phase-2 commissioning, the stored beam currents were increased gradually to confirm the stabilities of

newly installed vacuum components, but the operation time with high currents was not so long. During Phase-2, the maximum stored beam currents were 0.86 A and 0.80 A in the LER and the HER, respectively, and the beam doses were 340 A·h for both rings. For the whole LER, the p_{base} and p_{max} were 5×10^{-8} Pa and 3×10^{-7} Pa, respectively. The p_{max} of the arc sections was 1×10^{-7} Pa. On the other hand, the p_{base} and p_{max} of the whole HER were 3×10^{-8} Pa and 7×10^{-8} Pa, respectively. In the arc sections, the p_{max} was 4×10^{-8} Pa. The lifetime was determined mainly by the Touschek effect in both rings.

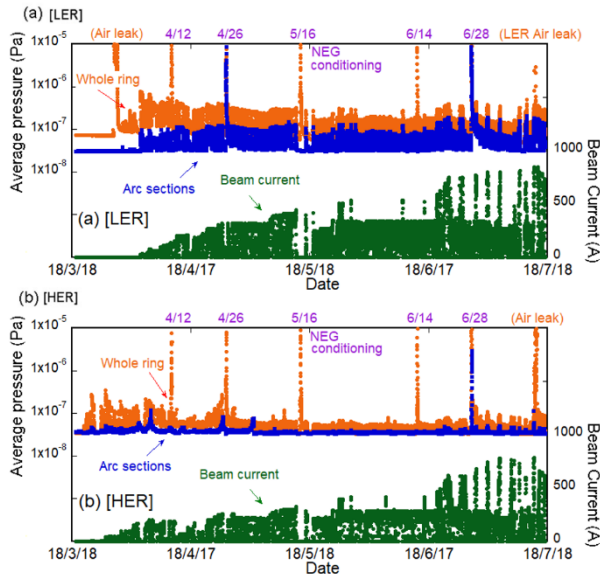


Figure 10: Histories of the average pressures in the whole ring (red), those in the arc sections (blue), and the stored beam currents (green) for (a) the LER and (b) the HER, respectively, during the Phase-2 commissioning.

Figure 11 shows dp/dI for the LER and the HER as a function of the beam dose during the Phase-2 commissioning. At the initial stage, the dp/dI values were high, because vacuum works, such as installation of new beam pipes around the collision point, were carried out during the shutdown period. However, the dp/dI decreased steadily with increasing the beam dose. Figure 12 shows the dp/dI for the whole rings and η in the arc sections for the LER and the HER during the Phase-1 and Phase-2 commissioning. For the LER, it was found that the η values at the last stage of the Phase-2 commissioning are less than those of the Phase-1 commissioning. The decrease in η during Phase-2 is very clear, because a nonlinear pressure increase due to the ECE was suppressed in Phase-2 by the installation of permanent magnets [24]. For the HER, on the other hand, the decrease in η during Phase-2 is not clear, because the p_{max} is too low to calculate the dp/dI accurately.

So far, the total beam dose has been 1113 A·h and 1002 A·h for the LER and the HER, respectively. At the end of the Phase-2 commissioning, the dp/dI values for the whole ring were approximately 3×10^{-7} Pa·A $^{-1}$ and 7×10^{-8} Pa·A $^{-1}$ for the LER and the HER, respectively. In the

arc sections, the total photon doses reached 5.9×10^{24} photons·m $^{-1}$ and 9.3×10^{24} photons·m $^{-1}$, for the LER and the HER, respectively at the end of Phase-2, and η decreased to 1×10^{-6} molecules·photon $^{-1}$ and 7×10^{-8} molecules·photon $^{-1}$ for the LER and the HER, respectively.

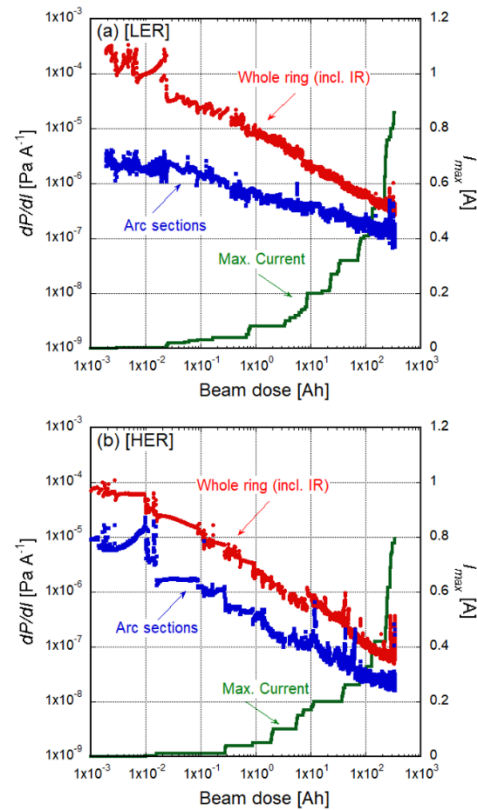


Figure 11: Average pressures normalized by a unit beam current dp/dI and the maximum beam current for (a) the LER and (b) the HER, respectively, as functions of the beam dose during Phase-2.

Status of the New Vacuum Components

The newly installed vacuum components worked well, and vacuum scrubbing of those components processed smoothly as described above.

The tuning of beam collimators watching the detector background and the beam injection rate was carried out. The beam collimators suppressed the background noise of the Belle II detector well and prevented the QCS magnets from quenching caused by the penetration of the particles deviated from their ideal orbit.

Effect of Countermeasures Against Problems in Phase-1

The number of bursts per 50 h of the operation time, beam currents when bursts occurred, and maximum beam currents as functions of the total beam operation time during the Phase-2 commissioning are shown in Fig. 9. The frequency of pressure bursts was greatly reduced in Phase-2. However, the frequency of pressure bursts reduced not only at the locations where the beam pipes were knocked, but also at other locations. Therefore, it

and reinstalled into the SuperKEKB again with the completed Belle II detector. Five new collimators are installed mainly into the LER, and damaged mask heads are replaced with new ones.

The Phase-3 commissioning will commence in March 2019. It is necessary to continue to monitor carefully whether new problems associated with an increase in the beam current in the vacuum system occur.

ACKNOWLEDGEMENTS

The authors would like to thank colleagues in the SuperKEKB team.

REFERENCES

- [1] SuperKEKB, <http://www-superkekb.kek.jp>
- [2] Y. Suetsugu *et al.*, “Design and construction of the SuperKEKB vacuum system”, *J. Vac. Sci. Technol. A*, vol. 30(3), p. 031602, 2012, doi:10.1116/1.3696683.
- [3] Y. Suetsugu *et al.*, “Construction status of the SuperKEKB vacuum system”, *Vacuum*, vol. 121, pp. 238-244, 2015.
- [4] Y. Suetsugu *et al.*, “Results and problems in the construction phase of the SuperKEKB vacuum system”, *J. Vac. Sci. Technol. A*, vol. 34(2), p. 021605, 2016, doi:10.1116/1.4942455.
- [5] Belle II, <https://www.belle2.org>
- [6] Y. Ohnishi *et al.*, “COMMISSIONING OF THE PHASE-1 SuperKEKB B-FACTORY AND UPDATE ON THE OVERALL STATUS”, in *Proc. NAPAC2016*, Chicago, IL, USA, Oct. 2016, pp. 32-36.
- [7] K. Shibata, H. Hisamatsu, K. Kanazawa, Y. Suetsugu, M. Shirai, “DEVELOPMENT OF TiN COATING SYSTEM FOR BEAM DUCTS OF KEK B-FACTORY”, in *Proc. EPAC'08, Genoa*, Italy, June 2008, pp. 1700-1702.
- [8] Y. Suetsugu, K. Kanazawa, K. Shibata, H. Hisamatsu, “Recent studies on photoelectron and secondary electron yields of TiN and NEG coating using the KEKB positron ring”, *Nucl. Instrum. Methods Phys. Res. A*, vol. 578(3), pp. 470-479, 2007, doi:10.1016/j.nima.2007.06.015.
- [9] Y. Suetsugu, K. Shibata, H. Hisamatsu, M. Shirai, K. Kanazawa, “Development of copper beam ducts with antechambers for advanced high-current particle storage rings”, *Vacuum*, vol. 84(5), pp. 694-698, 2010.
- [10] J. A. Crittenden, T. Ishibashi, and Y. Suetsugu, “SYNCHROTRON RADIATION ANALYSIS OF THE SUPERKEKB POSITRON STORAGE RING”, in *Proc. IPAC'15*, Richmond, VA, USA, May 2015, pp. 2222-2225, doi:10.18429/JACoW-IPAC2015-TUPTY080.
- [11] Y. Suetsugu, H. Fukuma, M. Pivi, and L. Wang, “Continuing study on electron-cloud clearing techniques in high-intensity positron ring: Mitigation by using groove surface in vertical magnetic field”, *Nucl. Instrum. Methods Phys. Res. A*, vol. 604(3), pp. 449-456, 2009, doi:10.1016/j.nima.2009.03.011.
- [12] Y. Suetsugu *et al.*, “Development of bellows and gate valves with a comb-type rf shield for high-current accelerators: Four-year beam test at KEK B-Factory”, *Rev. Sci. Instrum.*, vol. 78(4), p. 043302, 2007, doi:10.1063/1.2723747.
- [13] Y. Suetsugu, M. Shirai, and M. Ohtsuka, “Application of a Matsumoto-Ohtsuka-type vacuum flange to beam ducts for future accelerators”, *J. Vac. Sci. Technol. A*, vol. 23(6), pp. 1721-1727, 2005, doi:10.1116/1.2101808.
- [14] T. Ishibashi, S. Terui, and Y. Suetsugu, “LOW IMPEDANCE MOVABLE COLLIMATORS FOR SUPERKEKB” in *Proc. IPAC'17*, Copenhagen, Denmark, May 2017, pp. 2929-2932.
- [15] Y. Suetsugu, T. Kageyama, K. Shibata, and T. Sanami, “Latest movable mask system for KEKB”, *Nucl. Instrum. Methods Phys. Res. A*, vol. 513(3), pp. 465-472, 2003, doi:10.1016/j.nima.2003.06.003.
- [16] Y. Suetsugu, K. Shibata, T. Sanami, T. Kageyama, and Y. Takeuchi, “Development of movable mask system to cope with high beam current”, *Rev. Sci. Instrum.*, vol. 74(7), pp. 3297-3304, 2003, doi:10.1063/1.1583860.
- [17] Y. Suetsugu *et al.*, “Achievements and problems in the first commissioning of superKEKB vacuum system”, *J. Vac. Sci. Technol. A*, vol. 35(3), p. 03E103, 2017, doi:10.1116/1.4977764.
- [18] Y. Suetsugu *et al.*, “First commissioning of the SuperKEKB vacuum system”, *Phys. Rev. ST Accel. Beams*, vol. 19(12), p. 121001, 2016, doi:10.1103/PhysRevAccelBeams.19.121001.
- [19] K. Kanazawa *et al.*, “Experiences at the KEK B-factory vacuum system”, *Prog. Theor. Exp. Phys.*, vol. 2013(3), p. 03A005, 2013, doi:10.1093/ptep/pts068.
- [20] S. Terui *et al.*, “OBSERVATION OF PRESSURE BURSTS IN THE SUPERKEKB POSITRON RING”, in *Proc. IPAC'18*, Vancouver, BC, Canada, April 2018, pp. 2830-2832, doi:10.18429/JACoW-IPAC2018-WEPML058.
- [21] Y. Suetsugu *et al.*, “STATUS OF THE SuperKEKB VACUUM SYSTEM IN THE PHASE-2 COMMISSIONING”, in *Proc. IPAC'18*, Vancouver, BC, Canada, April 2018, pp. 2833-2835, doi:10.18429/JACoW-IPAC2018-WEPML059.
- [22] Y. Suetsugu *et al.*, “Study to Mitigate Electron Cloud Effect in SuperKEKB”, presented at *eeFACT2018*, Hong Kong, China, September 2018, paper TUYAA04, this conference.
- [23] M. Kikuchi *et al.*, “DESIGN OF POSITRON DAMPING RING FOR SUPER-KEKB”, in *Proc. IPAC'10*, Kyoto, Japan, May 2016, pp. 1641-1643.
- [24] K. Shibata *et al.*, “Vacuum system of positron damping ring for SuperKEKB”, *J. Vac. Sci. Technol. A*, vol. 35(3), p. 03E106, 2017, doi:10.1116/1.4979009.

SINGLE BUNCH INSTABILITIES AND NEG COATING FOR FCC-ee

E. Belli*, P. Costa Pinto, G. Rumolo, A. Sapountzis, T. Sinkovits, M. Taborelli,
CERN, Geneva, Switzerland

G. Castorina, M. Migliorati, University of Rome La Sapienza and INFN Sez.Roma1, Rome, Italy
B. Spataro, M. Zobov, INFN/LNF, Frascati (Rome)

Abstract

The high luminosity electron-positron collider FCC-ee is part of the Future Circular Collider (FCC) study at CERN and it has been designed to cover the beam energy range from 45.6 GeV to 182.5 GeV to study the properties of the Higgs boson and other particles. Electron cloud build up simulations on the Z resonance revealed the necessity of minimising the Secondary Electron Yield (SEY) of the pipe walls by applying a Ti-Zr-V Non-Evaporable Getter (NEG) coating in the entire ring. Beam dynamics simulations at 45.6 GeV pointed out that minimising the thickness of this layer is mandatory to reduce the resistive wall (RW) impedance, thus increasing the single bunch instability thresholds and ensuring beam stability during operation. However, reducing the coating thickness can affect the performance of the material and therefore the SEY. For this reason, an extensive measurement campaign was performed at CERN to characterise NEG thin films with thicknesses below 250 nm in terms of activation performance and SEY measurements. This paper also presents the FCC-ee longitudinal impedance model which includes all the current machine components.

INTRODUCTION

In 2014, CERN launched the Future Circular Collider (FCC) study [1] for the design of different circular colliders for the post-LHC era. This study is investigating a high energy proton-proton machine (FCC-hh) to reach a centre-of-mass energy of 100 TeV and a high luminosity electron-positron collider (FCC-ee) as a potential first step to cover a beam energy range from 45.6 GeV to 182.5 GeV, thus allowing to study the properties of the Higgs, W and Z bosons and top quark pair production thresholds with unprecedented precision. Table 1 summarizes the main beam parameters on the Z resonance which represents the most challenging scenario from the beam stability point of view.

Due to the beam parameters and pipe dimensions, electron cloud (EC) and collective effects due to the electromagnetic fields generated by the interaction of the beam with the vacuum chamber can be very critical aspects for the machine by producing instabilities that can limit its operation and performance.

This paper will present an estimation of the EC build up in the main magnets of the positron ring, the contributions of specific vacuum chamber components to the total impedance budget and their effects on single bunch beam dynamics. Special attention has been given to the resistive wall (RW) impedance, whose value is increased by a layer of

Table 1: FCC-ee baseline beam parameters at Z running. SR and BS stand for synchrotron radiation and beamstrahlung.

Beam energy [GeV]	45.6
Circumference C [km]	97.75
Number of bunches/beam	16640
Bunch population N_p [10^{11}]	1.7
Beam current I [A]	1.39
RF frequency f_{RF} [MHz]	400
RF voltage V_{RF} [MV]	100
Energy loss per turn [GeV]	0.036
Momentum compaction α_c [10^{-5}]	1.48
Bunch length $\sigma_{z,SR}/\sigma_{z,BS}$ [mm]	3.5/12.1
Energy spread $\sigma_{dp,SR}/\sigma_{dp,BS}$ [%]	0.038/0.132
Horizontal tune Q_x	269.138
Vertical tune Q_y	269.22
Synchrotron tune Q_s	0.025
Horizontal emittance ϵ_x [nm]	0.27
Vertical emittance ϵ_y [pm]	1.0

Non-Evaporable Getter (NEG) coating which is required to reduce the Secondary Electron Yield (SEY) of the pipe walls for electron cloud mitigation [2, 3]. The studies presented in this paper will show that for the proposed lepton collider at 45.6 GeV the single bunch instability thresholds can be increased by decreasing the coating thickness. For this reason, in parallel to these numerical studies, an extensive measurement campaign was performed at CERN to investigate NEG thin films with thicknesses below 250 nm in terms of activation performance and SEY measurements, with the final purpose of finding the minimum effective thickness satisfying impedance, vacuum and electron cloud requirements.

Besides the RW, other impedance sources have been analyzed and the longitudinal impedance model thus obtained has been used to study the microwave instability and to predict its effects on the stability of the beam.

ELECTRON CLOUD STUDIES

This section presents EC build up studies in the positron ring of the lepton collider at 45.6 GeV. Build up simulations have been performed in the drift space and in all the magnets of the machine (dipoles and quadrupoles in the arcs and final focusing quadrupoles in the interaction region) by using the PyECLOUD [4, 5] code.

The bunch parameters used for simulations are listed in Table 1 while Table 2 summarizes the magnetic parameters of each element. For the beam optics in the arcs and around the interaction point, one can refer to [6]. In the arcs, the

* eleonora.belli@cern.ch

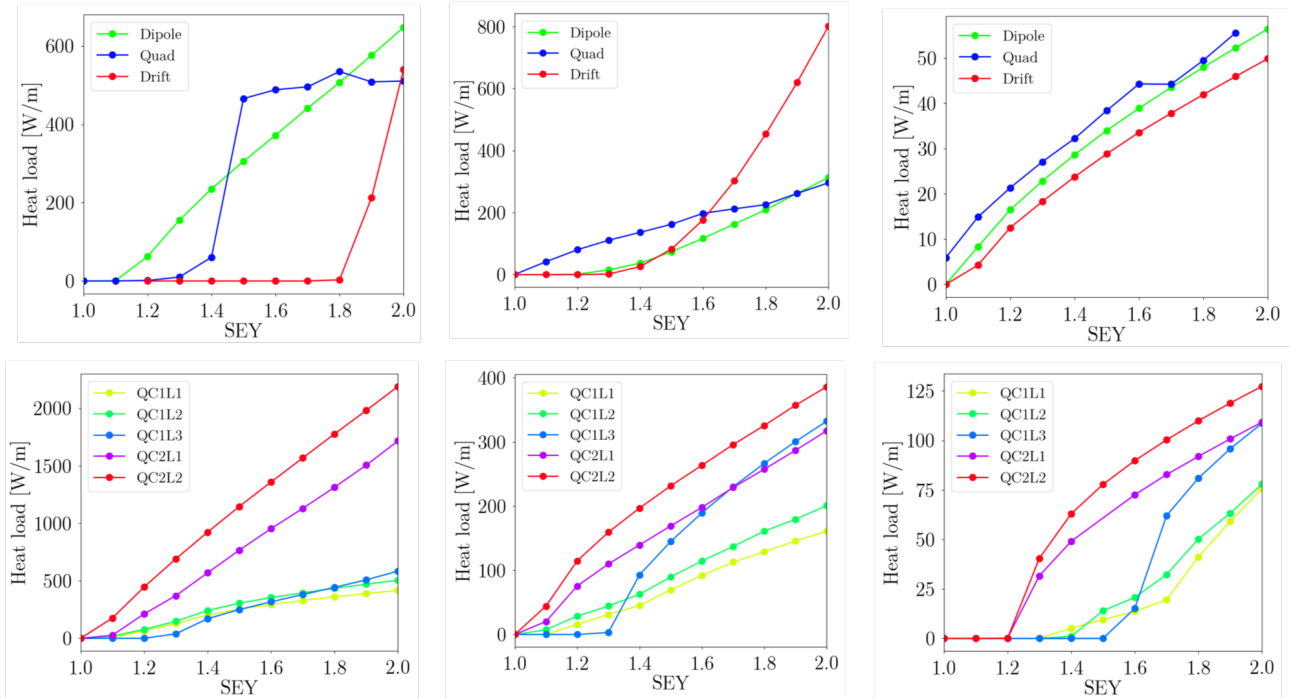


Figure 1: Heat load as a function of SEY for arc components (top) and IR magnets (bottom) in the case of 2.5 ns (left side), 5 ns (center) and 15 ns (right side) bunch spacings.

Table 2: Magnet parameters used for EC build up simulations at 45.6 GeV

Element	Length [m]	Magnetic field
Arc dipole	23.44	0.01415 T
Arc quadrupole	3.1	± 5.65 T/m
Arc drift	-	-
QC1L1	1.2	-96.3 T/m
QC1L2	1.0	50.3 T/m
QC1L3	1.0	9.8 T/m
QC2L1	1.25	6.7 T/m
QC2L2	1.25	3.2 T/m

Table 3: Threshold SEY for multipacting for all the ring components

Element	2.5 ns	5 ns	15 ns
Dipole	1.1	1.1	1.0
Quadrupole	1.2	1.0	<1.0
Drift	1.8	1.3	1.0
QC1L1	1.0	1.1	1.3
QC1L2	1.0	1.0	1.4
QC1L3	1.2	1.3	1.5
QC2L1	1.0	1.0	1.2
QC2L2	1.0	1.0	1.2

vacuum chamber is modelled as a circular pipe with 35 mm radius and two rectangular antechambers on both sides for the installation of synchrotron radiation absorbers, while in the final focusing quadrupoles of the interaction region (IR) the beam pipe is circular with 15 mm radius for the QC1 quadrupole and 20 mm radius for the QC2 quadrupole. According to RF computations [7], bunch spacing of 10 ns and 17.5 ns are not acceptable for the present cavity geometry and filling schemes with at least 100 RF buckets between the first bunches of consecutive trains are preferred. On the basis of these considerations, the EC build up in each element has been simulated by scanning the SEY for different bunch spacing of 2.5 ns, 5 ns and 15 ns and by assuming 4 trains of 80 bunches interleaved with 25 empty buckets at the nominal bunch intensity of $1.7 \cdot 10^{11} e^+$ /bunch. An initial uniform electron distribution of $10^9 e^-/m$ has been assumed in the vacuum chamber to model the survival of electrons between

trains or between turns. The multipacting threshold, defined as the highest SEY without multipacting, has been evaluated for each element and beam and reported in Table 3: these results show that the highest thresholds of EC multipacting are given by the 2.5 ns beam in the arcs and by the 15 ns beam in the IR. Figure 1 shows the EC induced heat load as a function of SEY for different components and bunch spacings. Numerical simulations have also been performed including photoemission seeding [8, 9], showing that the heat load is not affected by photoelectrons. Considering the beam parameters of Table 1, the analytic electron density threshold for the transverse instability [10] at low energy is about $2.29 \cdot 10^{10}/m^3$. Such a low threshold requires a low SEY coating in the entire ring, paying particular attention to the RW impedance seen by the beam.

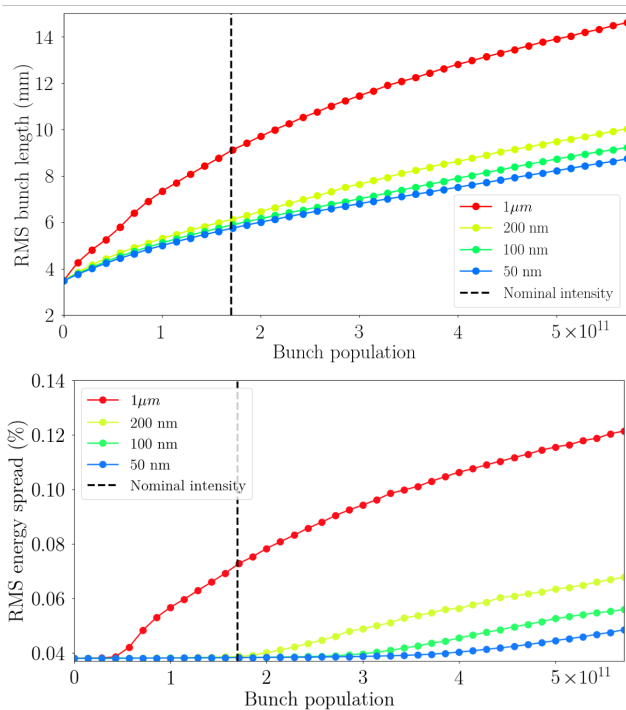


Figure 2: RMS bunch length (top) and RMS energy spread (bottom) as a function of the bunch population given by numerical simulations considering only the RW impedance produced by NEG films with different thicknesses. The dashed black line corresponds to the nominal bunch population.

RESISTIVE WALL IMPEDANCE

For RW impedance studies, the vacuum chamber is assumed to be circular with 35 mm radius and four layers: an outer layer of iron modelling the magnet chamber, then 6 mm of dielectric to consider the gap between the magnet chamber and the beam pipe, an inner layer of copper with 2 mm thickness and a NEG coating of the copper surface whose thickness has been investigated by means of numerical simulations in order to reduce the RW contribution. Analytical and numerical studies for FCC-ee at low energy [8, 9, 11] showed that the single bunch instability thresholds mainly depend on the thickness of the coating and only marginally on its conductivity. Moreover, the RW contribution can be decreased by reducing the film thickness. Simulations with the macroparticle tracking code PyHEADTAIL [12] have been performed considering NEG thin films with thicknesses of 1000 nm, 200 nm, 100 nm and 50 nm and the beam parameters of Table 1.

Microwave Instability

Figure 2 shows the bunch lengthening and the energy spread increase due to the longitudinal RW wakefield as a function of the bunch population for all the thicknesses under study. The instability threshold has been defined as the value of the bunch population corresponding to an increase of the energy spread of about 10% w.r.t. its nominal value.

A standard coating of 1 μm thickness makes the bunch unstable in the longitudinal plane, while thinner films allow to significantly increase the microwave instability threshold. For example, in the case of 100 nm thickness the instability threshold is increased by a factor 7 with respect to 1 μm thickness and it is about 2 times higher than the nominal bunch intensity.

Transverse Mode Coupling Instability

The Transverse Mode Coupling Instability (TMCI) threshold has been evaluated with the analytical Vlasov solver DELPHI [13] by taking into account the bunch lengthening due to the longitudinal wake (Fig. 2). The instability threshold has been defined as the value of the bunch population where the frequencies of two neighboring modes are merging. In the transverse case, the instability threshold is affected to a lesser extent by the coating thickness, because the longitudinal wake produces longer bunches at higher intensities, which increases the TMCI threshold. As shown in Fig. 3, the TMCI threshold is about a factor 2.5 higher than the nominal bunch intensity for both 100 nm and 1 μm thicknesses.

NEG THIN FILMS: EXPERIMENTAL CHARACTERIZATION

Reducing the thickness of NEG coatings for impedance requirements can affect the performance of the material itself and therefore the maximum SEY and related EC mitigation. In order to evaluate the activation performance and SEY, NEG films with thicknesses of 1000 nm, 200 nm, 100 nm and 50 nm were deposited on copper samples by DC magnetron sputtering [14]. More details about the coating process can be found in [8, 9]. The thickness was measured on cross sections of the samples and determined by Scanning Electron Microscopy (SEM) [15], resulting in film thicknesses of 1100 nm, 203 nm, 87 nm and 30 nm, obtained as average values from five measurements. Film composition was measured by energy dispersive X-ray spectroscopy to be 28 at.% Ti, 29 at.% Zr and 43 at.% V.

The surface composition and activation performance were measured by X-ray Photoelectron Spectroscopy (XPS) [16]. The multiplex spectra have been taken at four different steps:

- as received sample, at room temperature
- after 1h heating at 160°C
- after 1h heating at 200°C
- after 1h heating at 250°C

Four activation cycles were performed, with air exposure between two consecutive cycles. The activation performance was evaluated by the reduction of the area of the oxygen peak O1s after the fourth activation cycle. A higher reduction of the oxygen corresponds to a better activation and the results shown in Fig. 4 show that the oxygen surface concentration is increasing for thinner layers.

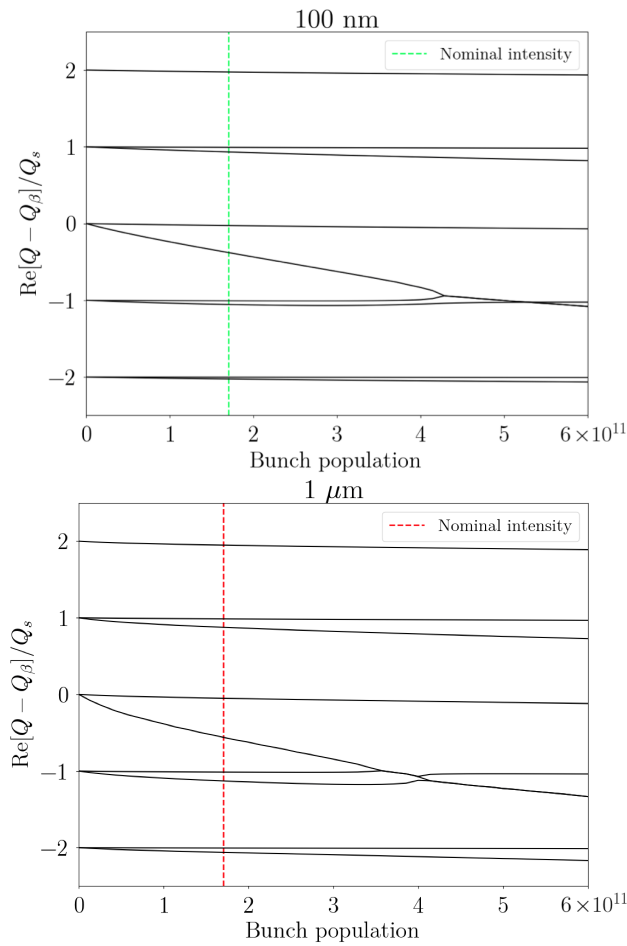


Figure 3: Real part of the tune shift of the first coherent oscillation modes as a function of the bunch population for 100 nm (top) and 1 μm (bottom) thicknesses. The dashed lines correspond to the nominal bunch population.

Figure 5 shows the oxidation state of the metals after the fourth activation cycle. One can observe mainly metallic components on Ti and V and a strong oxide component on Zr for the 87 nm and 30 nm films after activation.

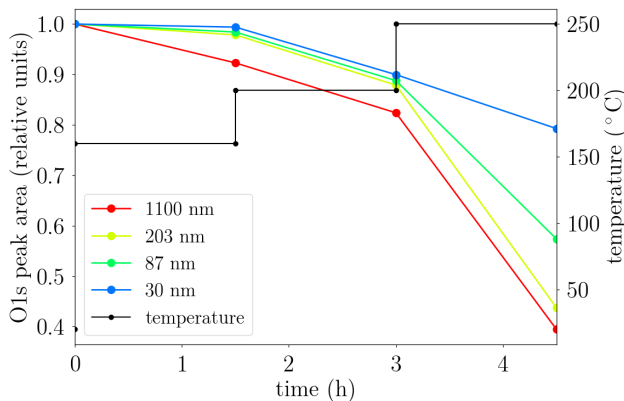


Figure 4: O1s peak area as a function of the activation time and temperature after the fourth activation cycle.

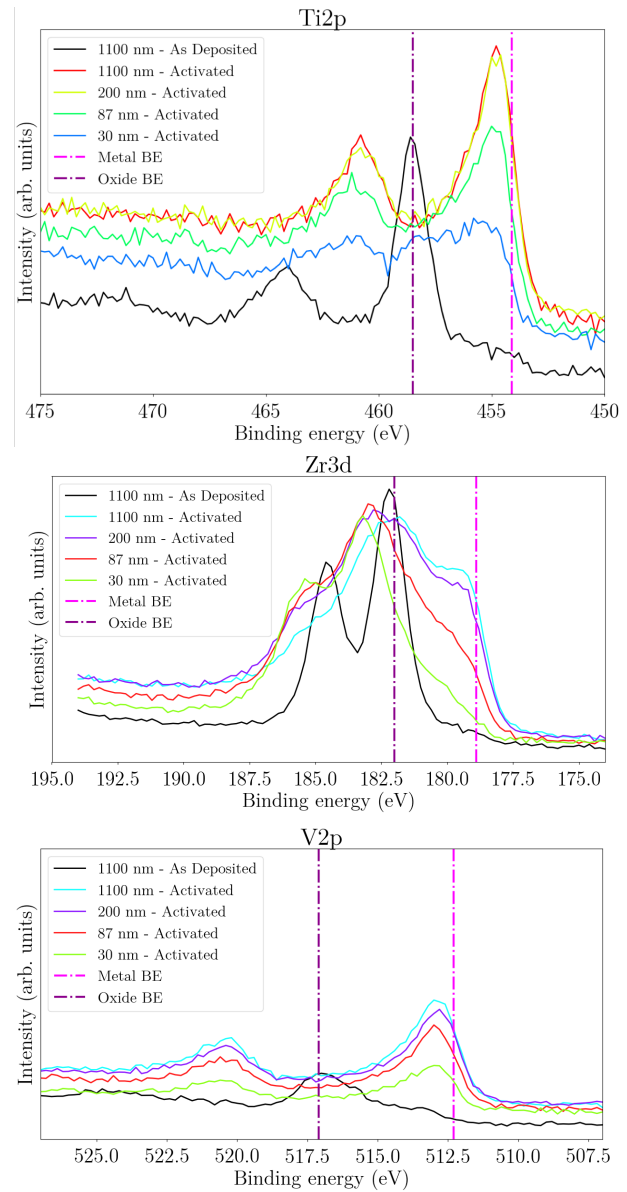


Figure 5: Ti2p (top), Zr3d (centre) and V2p (bottom) photo-peaks obtained by XPS analysis for all the thicknesses under study. 2p and 3d refer to subshells of electronic configuration.

Figure 6 shows the depth profile for each sample after the fourth activation cycle. The oxygen content is decreasing rapidly in all films but while in the 1100 nm sample it decreases below 5% in less than 100 nm, in the thinner samples it is detected in the whole layer. In particular, in the 30 nm film the oxygen concentration goes from 50% at the surface to 30% inside the layer and this big loss in gradient represents the major limiting factor for the material activation, considering that the diffusion of oxygen from the surface oxide to the bulk of the material is faster in case of steep gradient.

SEY measurements were performed by using the experimental set-up described in [8, 9]. Figure 7 shows the SEY

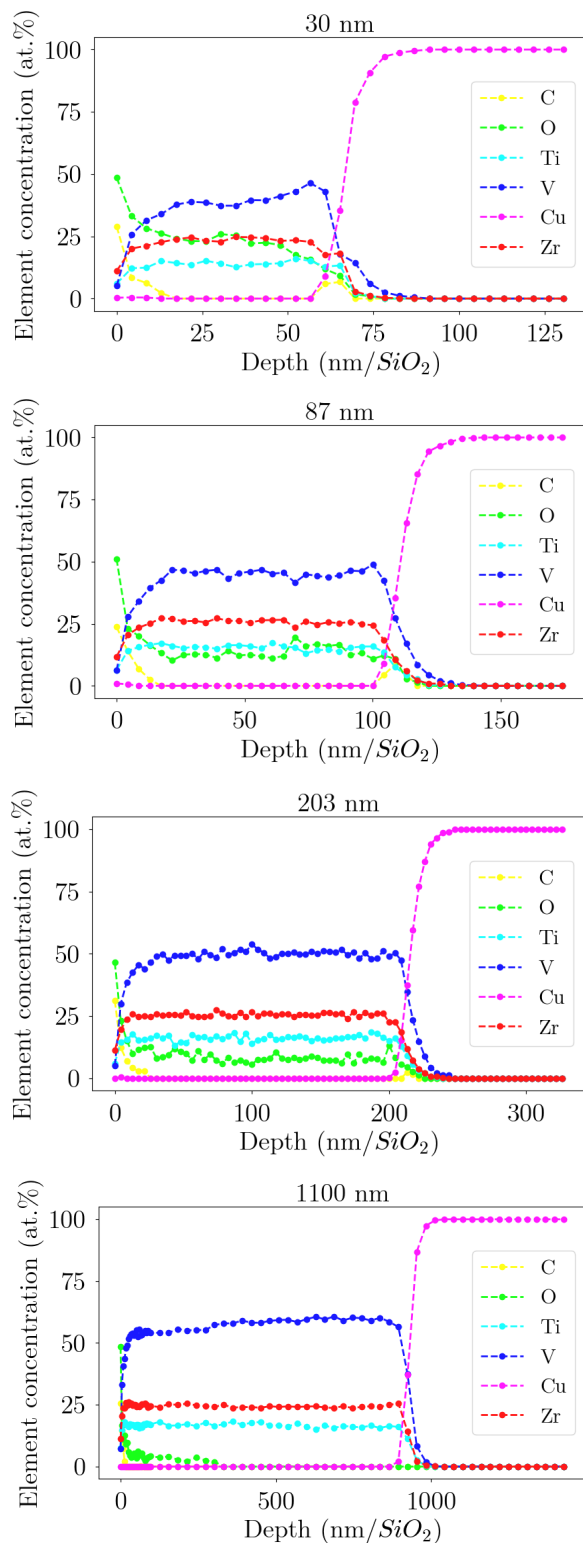


Figure 6: Profile of C, O, Ti, V, Zr and Cu as a function of depth for all the samples.

curves for all the samples under study after the fourth activation cycle, showing that the SEY is increasing for thinner layers. As shown in Fig. 8, elevated concentrations of oxygen in thinner films are responsible for higher SEY. SEY

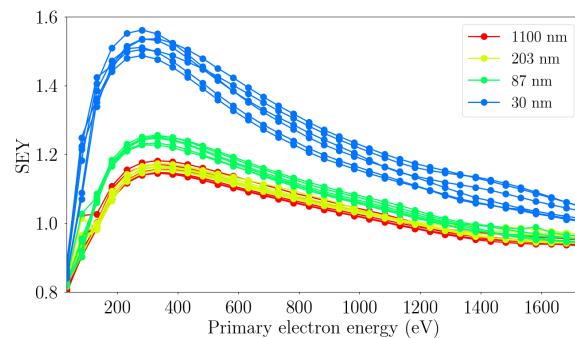


Figure 7: SEY as a function of photoelectrons energy for all the samples under study after the fourth activation cycle of 4 hours up to a temperature of 250°C.

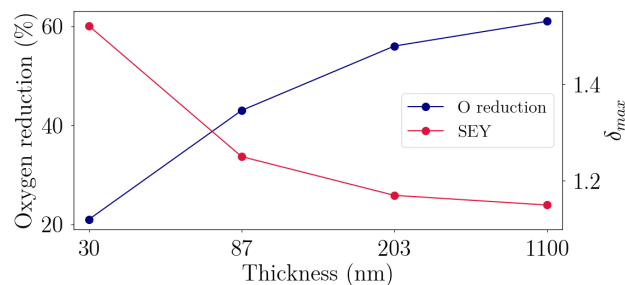


Figure 8: Oxygen reduction and maximum SEY as a function of the coating thickness for all the samples under study after the fourth activation cycle of 4 hours up to a temperature of 250°C.

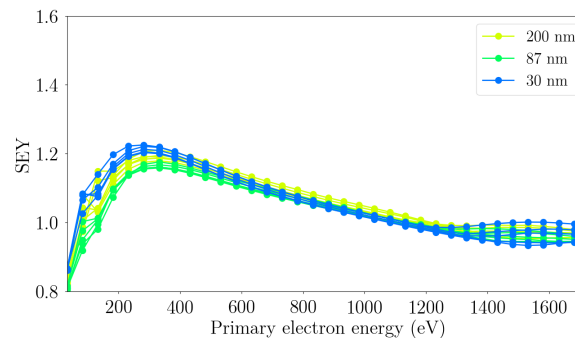


Figure 9: SEY as a function of photoelectrons energy for the thin films after the fourth activation cycle of 24 hours up to a temperature of 250°C.

measurements were also performed after longer activation cycles of 24 hours at the same temperature (see Fig. 9), showing a lower SEY compared to the one obtained after shorter activation times. For example, for the 87 nm sample the SEY was reduced from 1.25 to 1.16.

LONGITUDINAL IMPEDANCE MODEL

The FCC-ee impedance model includes all the current vacuum chamber components: RW (with 100 nm NEG film), vertical and horizontal collimators [17, 18], 400 MHz radio-frequency (RF) cavities [19, 20] with tapers, Beam

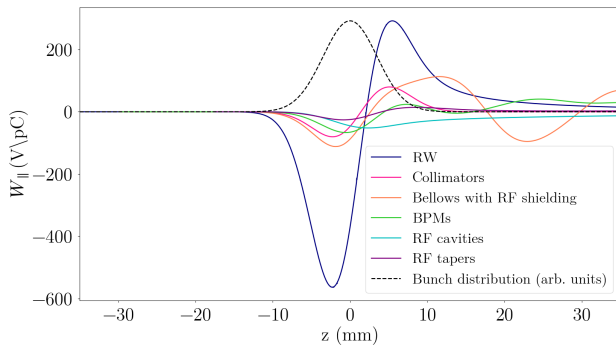


Figure 10: Longitudinal wake potentials for a Gaussian bunch with nominal bunch length $\sigma_z = 3.5$ mm due to the main FCC-ee components compared with the RW contribution (blue line).

Table 4: Power loss contribution of the main FCC-ee components at nominal intensity and bunch length, in the lowest energy case of 45.6 GeV

Component	Number	$k_{loss}[V/pC]$	$P_{loss}[MW]$
Resistive wall	97.75km	210	7.95
Collimators	20	18.7	0.7
RF cavities	56	18.5	0.7
Double tapers	14	26.6	1.0
BPMs	4000	40.1	1.5
Bellows	8000	49.0	1.8
Total		362.9	13.7

Position Monitors [21, 22] and bellows with RF shielding [23]. The contribution of these components to the longitudinal impedance budget has been evaluated by means of ABCI [24] and CST [25] simulations in time domain for a Gaussian bunch with nominal RMS bunch length of $\sigma_z = 3.5$ mm. Figure 10 shows the longitudinal wake potentials of each component while Table 4 summarizes the corresponding loss factors. The major contribution to the machine impedance is given by the RW with a total loss factor at nominal intensity and bunch length of 210 V/pC. The total dissipated power at nominal intensity is 13.6 MW, about a factor 3.6 smaller than the total SR power dissipated by the beam of 50 MW. However, this value of power loss is expected to be lower due to the bunch lengthening effect. From Fig. 11, one can observe that at nominal intensity the bunch length increases of only 7% in case of beamstrahlung while without beamstrahlung the bunch length is twice the nominal value. The MI threshold is about $2.5 \cdot 10^{11}$, a factor of 1.5 larger than the nominal bunch intensity, and is much higher with beamstrahlung.

CONCLUSIONS

This paper analyses the main limitations for the operation of the lepton collider FCC-ee, i.e. EC and collective effects, particularly critical on the Z resonance due to the low energy and the high beam current. EC build up simulations

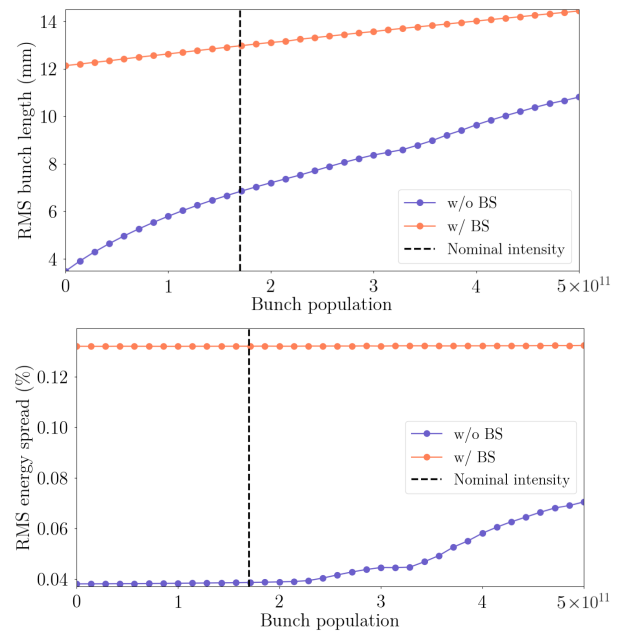


Figure 11: RMS bunch length (top) and RMS energy spread (bottom) as a function of the bunch population given by numerical simulations by considering the impedance contribution of all the machine components. The black dashed line represents the nominal bunch intensity.

have been performed for the main elements of the positron ring, in both the arcs and the IR. Multipacting thresholds and heat load have been evaluated for each component for different bunch spacings of 2.5, 5, 15 ns, indicating that with a low SEY coating ($SEY \leq 1.2$) the 15 ns beam is the preferable option to suppress the EC build up in the IR and to have a lower heat load in the arcs. This coating is also needed to cope with the EC induced single bunch head tail instability, whose electron density threshold on the Z resonance is quite low (about $2.29 \cdot 10^{10}/m^3$). An impedance model was also developed, with special attention to the RW impedance representing the main source of wakefields in the machine. Numerical studies showed that its contribution to the impedance budget can be reduced by decreasing the thickness of NEG coating needed for vacuum requirements and electron cloud mitigation. The minimum effective thickness for NEG activation was examined using XPS. Elevated concentrations of oxygen especially in the thinner films are responsible for reduced activation performance. After four short activation cycles of 4 hours, the thinnest sample of 30 nm was unable to activate effectively and this led to a high maximum SEY of 1.5. Longer activation cycles of 24 hours led to better activation and a lower SEY of 1.21 after the fourth cycle. Numerical simulations and experimental results indicated that a film thickness between 100 nm and 200 nm balancing the limitations of activation and impedance is a good candidate for coating thickness. Further experimental investigation is recommended for SEY and photon-stimulated desorption with a larger number of activation cycles. The impedance has been evaluated for

important machine components, showing that the contribution of these elements is up to 5 times smaller than that of RW. The MI threshold is around $2.5 \cdot 10^{11}$, about a factor 1.5 higher than the nominal bunch intensity. Operation with beamstrahlung will increase the instability thresholds in both planes.

ACKNOWLEDGEMENTS

The authors would like to thank D. Letant-Delrieux, H. Neupert, K. Oide, V. Petit, F. Zimmermann for their help and for the very useful discussions. This work was supported in part by the European Commission under the HORIZON 2020 Integrating Activity project ARIES, Grant Agreement No. 730871.

REFERENCES

- [1] <https://fcc.web.cern.ch>
- [2] P.C. Pinto, S. Calatroni, P. Chiggiato, H. Neupert, W. Volenberg, E. Shaposhnikova, M. Taborelli, and C.Y. Vallgren, Thin film coatings for suppressing electron multipacting in particle accelerators, in *Proceedings of the 2011 Particle Accelerator Conference*, New York, NY (2011), pp. 2096-2098, <https://cds.cern.ch/record/1462768>.
- [3] P.C. Pinto, History and potential of Non Evaporable Getter (NEG) technology, in *Workshop on Advanced Materials and Surfaces*, CERN, Geneva, Switzerland (2013), <https://indico.cern.ch/event/229108/contributions/1539894/>.
- [4] <https://github.com/PyCOMPLETE/PyECLoud>
- [5] G. Iadarola, Electron cloud studies for CERN particle accelerators and simulation code development, CERN Report No. CERN-THESIS-2014-047 (2014).
- [6] K. Oide, Status of optics, in *Proceedings FCC Week 2017 - 31 May 2017, Berlin, Germany*, <https://indico.cern.ch/event/556692/contributions/2590161/>.
- [7] I. Karpov, R. Calaga, and E. Chapochnikova, High order mode power loss evaluation in future circular electron-positron collider cavities, *Phys. Rev. Accel. Beams* vol. 21, p. 071001 (2018).
- [8] E. Belli, et al., Electron cloud buildup and impedance effects on beam dynamics in the Future Circular e^+e^- Collider and experimental characterization of thin TiZrV vacuum chamber coatings, *Phys. Rev. Accel. Beams*, accepted for publication (2018).
- [9] E. Belli, Coupling impedance and single beam collective effects for the Future Circular Collider (lepton option), Ph.D. Thesis, to be published.
- [10] K. Ohmi, Study of electron cloud effects in SuperKEKB, in *Proceedings of IPAC'14*, Dresden, Germany (2014), pp. 1597-1599.
- [11] M. Migliorati, E. Belli, and M. Zobov, Impact of the resistive wall impedance on beam dynamics in the Future Circular e^+e^- Collider, *Phys. Rev. Accel. Beams* vol. 21, p. 041001 (2018).
- [12] <https://github.com/PyCOMPLETE/PyHEADTAIL>
- [13] <https://twiki.cern.ch/twiki/bin/view/ABPComputing/DELPHI>
- [14] P. Chiggiato, P. Costa Pinto, Ti-Zr-V non-evaporable getter films: from development to large scale production for the Large Hadron Collider, in *Thin Solid Films* vol. 515, pp. 382-388 (2006).
- [15] <http://en-dep.web.cern.ch/en-dep/Groups/MME/MM/SEM.htm>
- [16] J. F. Moulder, et al., Handbook of X-ray Photoelectron Spectroscopy, Perkin-Elmer Corporation, Physical Electronics Division, 1992.
- [17] S. DeBarger, et al., The PEP-II movable collimators, No. SLAC-PUB-11752 (2001).
- [18] T. Ishibashi, Low impedance movable collimators for SuperKEKB, in *Proceedings of IPAC'17*, Copenhagen, Denmark (2017), pp. 14-19.
- [19] A. Butterworth, Cavity design and beam-cavity interaction challenges, in *Proceedings FCC Week 2017 - 30 May 2017, Berlin, Germany*, <https://indico.cern.ch/event/556692/contributions/2484361/>.
- [20] S.G. Zadeh, Cavity design approaches and HOM damping for FCC-ee, in *Proceedings FCC Week 2017 - 30 May 2017, Berlin, Germany*, <https://indico.cern.ch/event/556692/contributions/2484333/>.
- [21] F. Marcellini, M. Serio, A. Stella, and M. Zobov, DAPHNE broad-band button electrodes, in *Nucl. Instrum. Meth. A* vol. 402, pp. 27-35 (1998).
- [22] A. Rodrigues, et al., Sirius status report, in *Proceedings of IPAC'16*, Busan, Korea (2016), pp. 2811-2814.
- [23] Y. Suetsugu, M. Shirai, and K. Shibata. Possibility of comb-type rf shield structure for high-current accelerators, *Phys. Rev. ST Accel. Beams* vol. 6, p. 103201 (2003).
- [24] <http://abci.kek.jp/>
- [25] <https://www.cst.com>

CEPC SUPERCONDUCTING MAGNETS*

Y. S. Zhu[†], X. C. Yang, M. Yang, F. S. Chen, W. Kang

Key Laboratory of Particle Acceleration Physics and Technology, Institute of High Energy Physics, Chinese Academy of Sciences, Beijing 100049, China

Abstract

A Circular Electron Positron Collider (CEPC) with a circumference about 100 km, a beam energy up to 120 GeV is proposed to be constructed in China. CEPC will be a double ring collider with two interaction points. Most magnets for CEPC accelerator are conventional magnets, but some superconducting magnets are required in the interaction region. Final focus superconducting high gradient quadrupoles are inside the solenoid field of Detector magnet, so superconducting anti-solenoid is need to minimize the effect of the solenoid field on the beam. In addition, high strength superconducting sextupole magnets are also required. In this paper, the layout and conceptual design of CEPC interaction region superconducting magnets are described, and the R&D plan is presented.

INTRODUCTION

A Circular Electron Positron Collider (CEPC) with a circumference about 100 km is proposed to be constructed in China. It is an important part of the world plan for high-energy physics research. The CEPC center-of-mass energy is 240 GeV, and at that collision energy it will serve as a Higgs factory. The design also allows operation at lower beam energy to be a Z or W factory. The accelerator complex of CEPC consists of a linear accelerator (Linac), a damping ring (DR), the Booster, the Collider and several transport lines [1]. The heart of the CEPC is a double-ring collider with two interaction points.

There are a large number of magnets in the CEPC collider ring, and the magnets occupy over 80% of the circumference. Most magnets for CEPC accelerator are conventional magnets, except some superconducting magnets are needed in the interaction region of CEPC collider ring. Compact high gradient superconducting quadrupole doublet magnets are usually required on both sides of the interaction point (IP) to final focus the beam to achieve high luminosity [2-4]. The CEPC final focus superconducting quadrupoles are inside the solenoid field of Detector magnet, so superconducting anti-solenoid is need to minimize the effect of the solenoid field on the beam. In addition, high strength superconducting sextupole magnets are also required in the CEPC interaction region.

SUPERCONDUCTING MAGNET SYSTEM

The requirements of the final focus quadrupole doublets QD0 and QF1 are based on the circumference 100 km of CEPC, L^* of 2.2 m, and a beam crossing angle of 33 mrad

in the CEPC interaction region. The requirements of the quadrupole magnets are listed in Table 1.

Table 1: Requirements of CEPC Interaction Region Quadrupole Magnets

Magnet	Field gradient (T/m)	Magnetic length (m)	Width of GFR (mm)
QD0	136	2.0	19.51
QF1	110	1.48	27

The crossing angle between the electron and positron beams is 33 mrad in horizontal plane. The final focusing quadrupole is 2.2 m from the IP, and the QD0 and QF1 magnets are designed to be twin aperture quadrupole magnets. They are operated fully inside the solenoid field of the Detector magnet with a central field of 3.0 T. To minimize the effect of the longitudinal detector solenoid field on the accelerator beam, anti-solenoids before QD0, outside QD0 and QF1 are needed. Their magnetic field direction is opposite to the detector solenoid, and the total integral longitudinal field generated by the detector solenoid and anti-solenoid coils is zero. It is also required that the total solenoid field inside the QD0 and QF1 magnet should be close to zero.

The CEPC Machine Detector Interface (MDI) layout at one side of the interaction point is shown in Fig. 1, where QD0, QF1 and Anti-solenoid are the accelerator magnets.

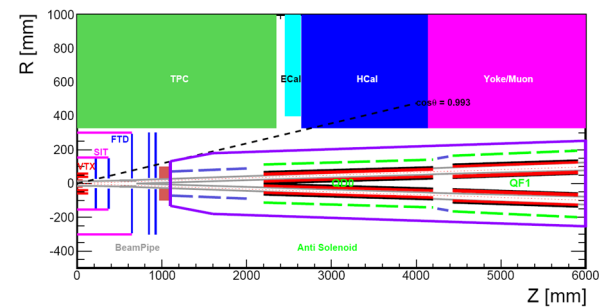


Figure 1: CEPC MDI layout.

According to the layout of the MDI, accelerator devices can only start after $z=1.1$ m along the longitudinal axis, so the available space for the anti-solenoid before QD0 is limited. In addition, the angle of the accelerator magnet seen from the IP point must be small and satisfy the requirement from the Detector. Taking into account the high field strength of twin aperture quadrupole magnet, high central field of anti-solenoid and the limited space, superconducting technology based on NbTi conductor will be used for these interaction region superconducting quadrupole magnets and anti-solenoids.

* Work supported in part by the Yifang Wang scientific Studio of the Ten Thousand Talents Project and in part by the National Natural Science Foundation of China under Grant 11875272.

[†] Email address: yszhu@ihep.ac.cn

Furthermore, there are also 32 superconducting sextupole magnets required in the CEPC interaction region. The requirements of superconducting sextupole magnets for Higgs operation are listed in Table 2.

Table 2: Requirements of CEPC Interaction Region Sextupole Magnets for Higgs

Magnet	Field strength (T/m ²)	Magnetic length (m)	Reference radius (mm)
VSIRD	1635	0.6	8.5
HSIRD	1882	0.8	15.0
VSIRU	1562	0.6	8.5
HSIRU	1999	0.6	15.5

CONCEPTUAL DESIGN

Superconducting Quadrupole Magnet QD0

The final focus QD0 is a double aperture superconducting magnet. The distance from QD0 to the interaction point is 2.2 m, and the minimum distance between two aperture centerlines is only 72.61 mm, so very tight radial space is available for QD0. The outer diameter of single aperture QD0 is determined by the separation of two beams at the IP side.

The design of QD0 is based on two layers cos2θ quadrupole coil using Rutherford cable without iron yoke. The four coils are clamped with the collars made of stainless steel or aluminium. The beam pipe at room temperature is held inside the helium vessel with a clearance gap of 4 mm. In the field calculation, it is assumed that the magnetic field harmonics in the good field region are required to be smaller than 3×10⁻⁴.

2D Field Calculation The QD0 is an iron-free small-aperture long magnet. Its coils will be made of Rutherford cable with a width of 3 mm, a mid-thickness of 0.94 mm, and a keystone angle of 1.8 degrees. The QD0 coil cross section is optimized with four coil blocks in two layers, and there are 23 turns in each pole.

2D magnetic field calculation is performed using OPERA from Cobham Technical Services [5]. Firstly one aperture of QD0 magnet is included in the calculation, and only one quarter is modelled. After optimization, good field quality in the good field region is obtained. The excitation current is 2510A. The number of coil turns, the dimension of the coil and the excitation current are consistent with the expressions of Ampere-Turns for superconducting quadrupole magnets based on sector coils [6]. The magnetic flux lines and magnetic flux density distribution in single aperture are shown in Fig. 2 and Fig. 3, respectively.

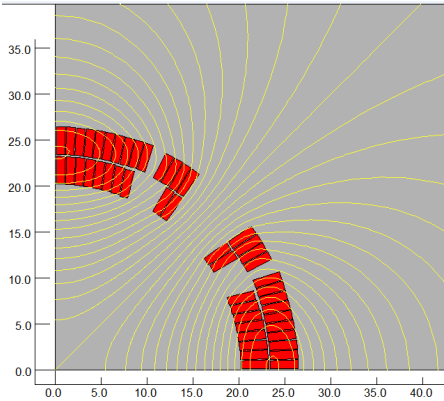


Figure 2: 2D flux lines (One quarter cross section).

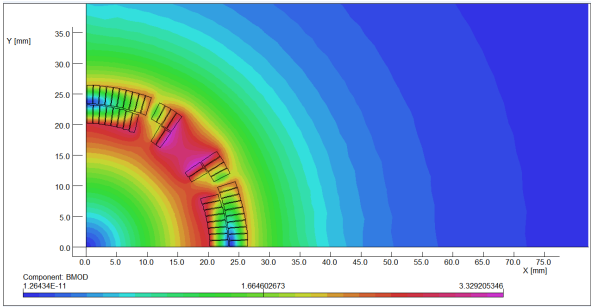


Figure 3: Magnetic flux density distribution.

The calculated relative multipole field contents normalized to the main quadrupole field are smaller than 1×10⁻⁴.

The field in one aperture is affected due to the field generated by the coil in another aperture. Field crosstalk of the two apertures is modelled and studied in OPERA-2D. Figure 4 shows a typical case of flux lines in the two aperture coils.

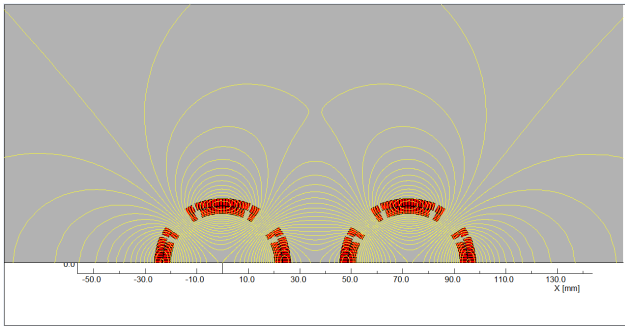


Figure 4: Flux lines of two aperture coils.

The calculated multipole field in one aperture as a function of aperture central distance is presented in Fig. 5 (unit, 1×10⁻⁴).

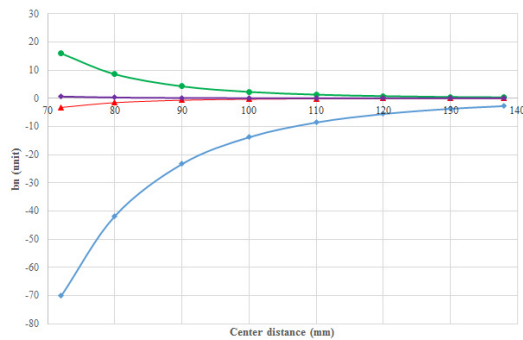


Figure 5: Multipole field in each aperture as a result of field crosstalk.

Since the small distance between the QD0 two apertures, the field crosstalk is serious. The largest multipole field is the sextupole field.

3D Field Calculation QD0 coils are simplified and modelled in OPERA-3D. Firstly the field quality in the single aperture is calculated, and then the multipole fields induced by the field crosstalk of the two apertures are obtained (Figure 6).

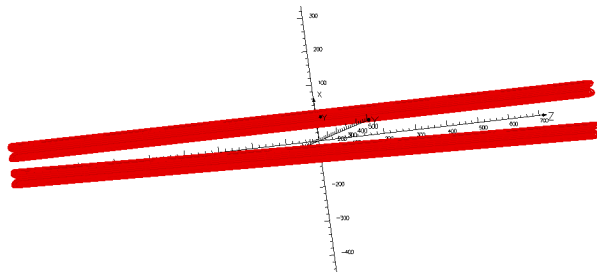


Figure 6: QD0 two aperture coils.

The calculated integrated multipole field contents in one aperture with the twin aperture layout are listed in [7]. The integrated sextupole and octupole field contents in the aperture are very large as a result of the field cross talk, especially the integrated sextupole component of 19×10^{-4} .

A two-layer of shield coil is introduced just outside the quadrupole coil to improve the field quality. The shield coil is not symmetric within each aperture, but the shield coils for two apertures are symmetric. The conductor for the shield coil is round NbTi wire with 0.5 mm diameter, and there are 44 turns for each pole. After optimization, the shield coil in the left aperture is shown in Fig. 7, and each integrated multipole field in each aperture with a shield coil in the twin quadrupole coils layout is smaller than 2×10^{-4} .

To match the fall off of field harmonics caused by the field crosstalk when the distance of two beam lines increases, the conductor lengths of shield coil at each angular positions are different. Therefore, each multipole field is optimized to be smaller than 3×10^{-4} at different longitudinal positions in each aperture.

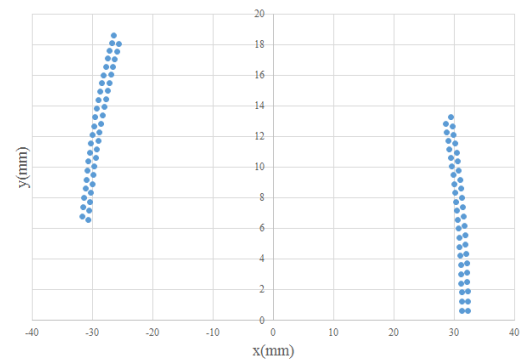


Figure 7: Shield coil in one aperture (half).

The schematic cross-section of single aperture QD0 magnet is shown in Fig. 8.

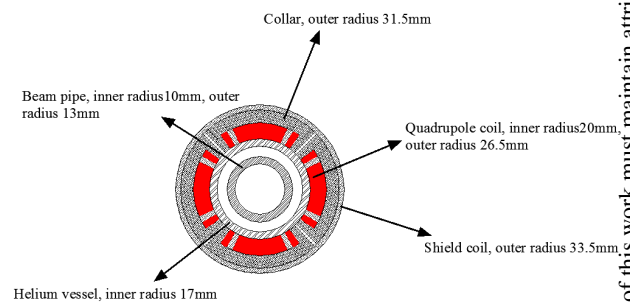


Figure 8: Single aperture QD0 magnet.

Superconducting Quadrupole Magnet QF1

The design of QF1 magnet is similar to the QD0 magnet, except that there is iron yoke around the quadrupole coil for QF1. The used Rutherford cable is similar to that of QD0. One quadrant of QF1 single aperture coil consists of four coil blocks in two layers separated by wedges, with 29 turns for each pole. Since the distance between the two apertures is much larger and the usage of iron yoke, the field cross talk between the two apertures of QF1 is not an issue as it is for QD0.

2D Field Calculation The QF1 cross section is optimized using OPERA-2D. Firstly, only one quarter of single aperture QF1 is modelled. After optimization, the field quality in each aperture is very good. The magnetic flux lines and magnetic flux density distribution are shown in Fig. 9 and Fig. 10, respectively.

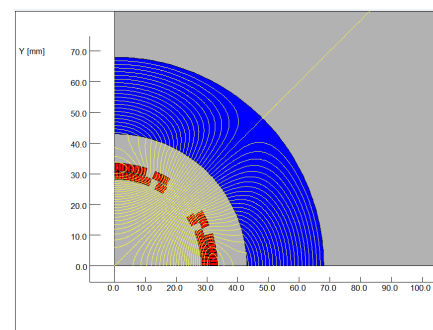


Figure 9: 2D flux lines of single aperture QF1 (One quarter cross section).

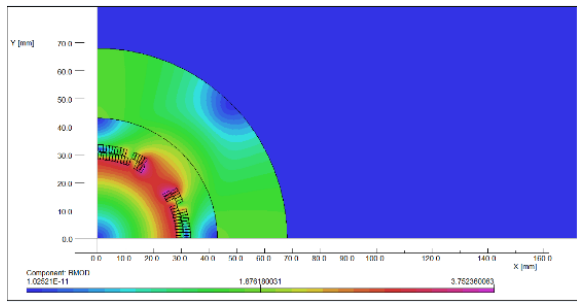


Figure 10: Magnetic flux density distribution of QF1.

Each calculated relative multipole field content in one aperture is smaller than 1×10^{-4} .

Then, field crosstalk of the two apertures in QF1 is modelled and studied in OPERA-2D. Figure 11 shows an example of flux lines in the two aperture coils. The field calculation results show that, the iron yoke can well shield the leakage field of each aperture. The field harmonics from field crosstalk between the two apertures is negligible.

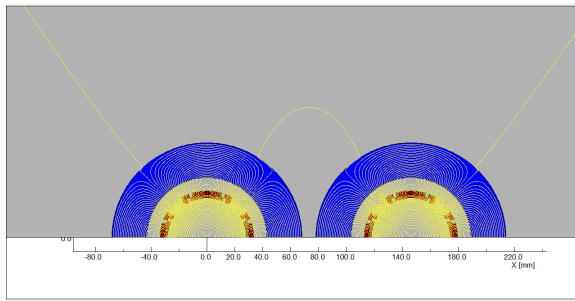


Figure 11: Flux lines of QF1 two aperture coils.

The schematic cross-section of single aperture QF1 magnet is shown in Figure 12.

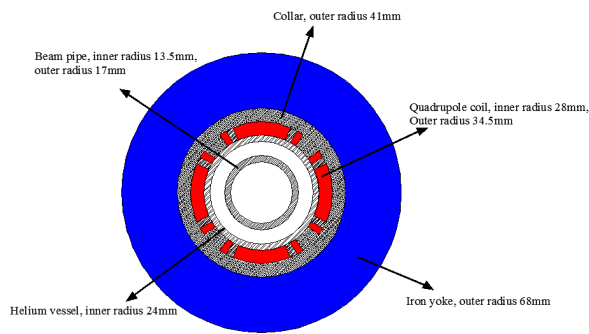


Figure 12: Single aperture QF1 magnet.

Design parameters and forces of QD0 and QF1 are listed in Table 3. The excitation current at W and Z model will decrease correspondingly.

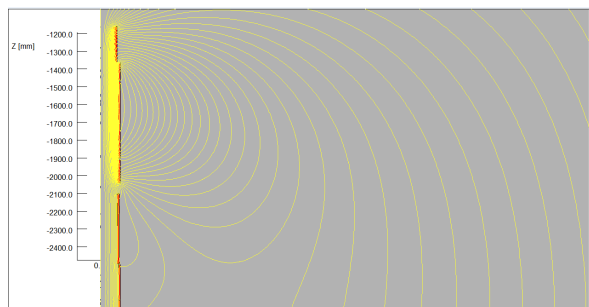


Figure 13: Flux lines of anti-solenoid.

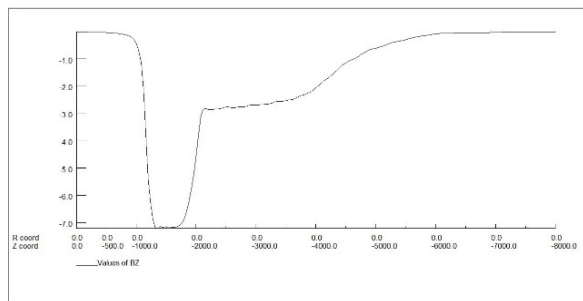


Figure 14: Field distribution of anti-solenoid.

The distribution of total field of Anti-solenoid and Detector solenoid magnet with linear superposition along the longitudinal direction is shown in Fig. 15.

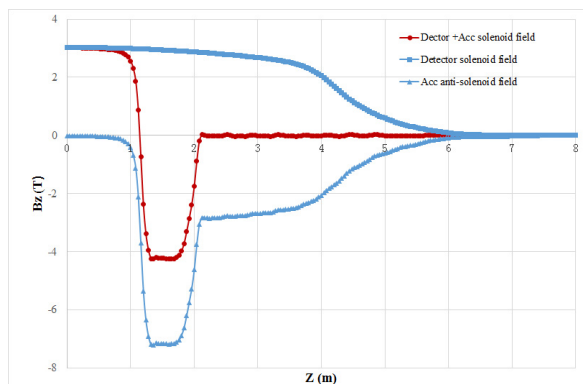


Figure 15: Combined field of Anti-solenoid and Detector solenoid magnet.

The central field of the first section in the anti-solenoid is the strongest, with a peak value of 7.2 T. The combined field distribution of anti-solenoid and Detector solenoid magnet meets the design requirements. Main design parameters of CEPC interaction region anti-solenoids can be found in [1, 7].

Since the field in the last section of anti-solenoid is very low, and to reduce the length of the cryostat, the last section of anti-solenoid will be operated at room-temperature. The superconducting QD0, QF1, and anti-solenoid coils (except the last section) at each side of interaction point are in the same cryostat, and the layout is shown in Fig. 16.

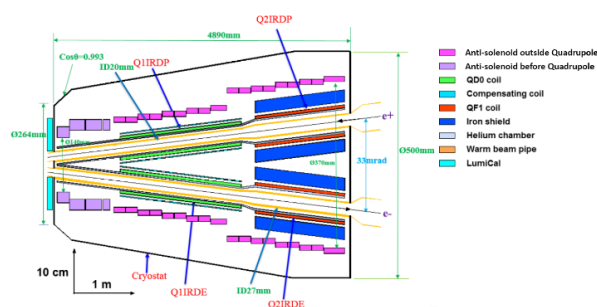


Figure 16: Layout of QD0, QF1, and anti-solenoid.

Preliminary combined field simulation of the Anti-solenoid and Detector solenoid magnet is performed to obtain the force of the Anti-solenoid [Fig. 17].

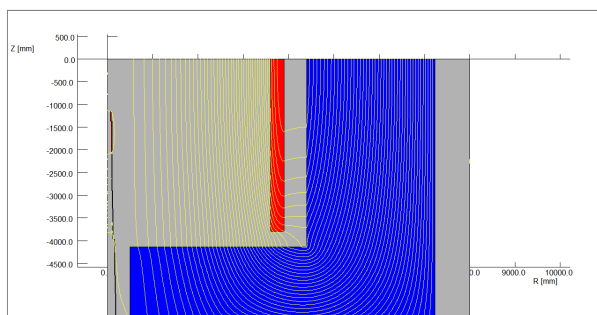


Figure 17: Combined field simulation of Anti-solenoid and Detector solenoid magnet.

QD0 Design Option with Iron Yoke An alternative design option for QD0 with iron yoke is under investigated. Field cross talk of the two apertures in QD0 is studied in OPERA-2D. Figure 18 shows an example of flux lines in the QD0 two aperture with iron yoke, in which the distance between the two aperture is the nearest and the field cross-talk is the most serious. The field calculation results show that, even the size of iron yoke is very limited, it can well shield the leakage field of each aperture, and the field harmonics as a result of field crosstalk between the two apertures is smaller than 1×10^{-4} in the case of Fig. 18. In other cases where the distance between the two apertures becomes larger, the field harmonics will also be smaller. So using the iron yoke, the field harmonics as a result of the field crosstalk is not a problem. In addition, compared with the iron-free design of QD0, the excitation current can be reduced. The main disadvantage of the iron option is that the diameter of QD0 will be larger, and there will be not enough space for multipole corrector coils.

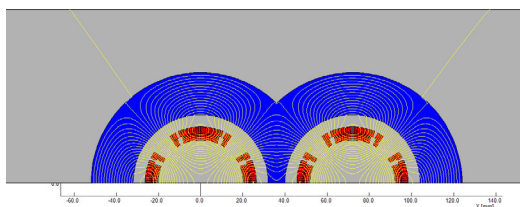


Figure 18: QD0 design option with iron yoke.

Superconducting Sextupole Magnet

The superconducting sextupole magnets have an iron yoke around the coils to enhance the field strength and reduce the operating current. The four type sextupole magnets are designed to have the same cross section. The used Rutherford cable is similar to that of QD0.

The cross section of sextupole magnets is optimized using OPERA-2D. Only one quarter of cross section is modelled. After field optimization, the sextupole coil consists of two coil blocks in two layers, and there are 33 turns in each pole. The field quality in the good field region is very good. The magnetic flux lines and magnetic flux density distribution for type HSIRU sextupole magnet at Higgs operation are show in Fig. 19 and Fig. 20, respectively.

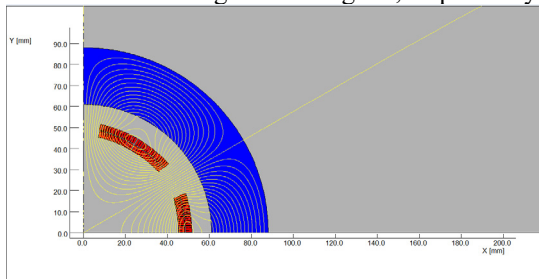


Figure 19: 2D flux lines of sextupole magnet (One quarter cross section).

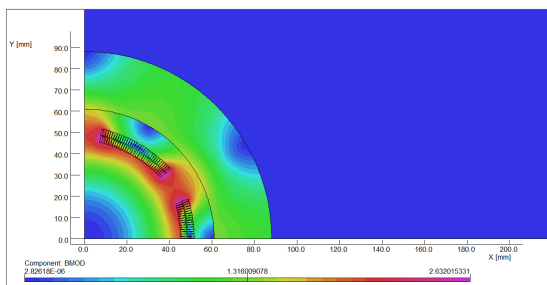


Figure 20: Magnetic flux density distribution.

The calculated relative multipole field contents are all smaller than 1×10^{-4} , and main design parameters of four type superconducting sextupole magnets at Higgs operation are reported in [1].

R&D PLAN

Prior to the construction of CEPC, there will be a five-year R&D period (2018-2022). During this period, prototypes of key technical components will be built.

In the R&D stage of CEPC project, superconducting prototype magnets for the interaction region will be developed in three consecutive steps:

- 1) Double aperture superconducting quadrupole prototype magnet QD0.
- 2) Short combined function superconducting prototype magnet including QD0 and anti-solenoid.
- 3) Long combined function superconducting prototype magnet including QD0, QF1 and anti-solenoid.

The key technical issues of the prototype superconducting magnets to be studied and solved in the R&D are listed below:

- 1) Magnetic and mechanical design of the superconducting quadrupole magnet and anti-solenoids with very high field strength and limited space.
- 2) Fabrication technology of small size Rutherford cable with keystone angle.
- 3) Fabrication procedure of the twin aperture quadrupole coil with small diameter.
- 4) Fabrication procedure of the anti-solenoids with many sections and different diameters.
- 5) Assembly of the combined function magnet including QD0, QF1 and anti-solenoids.
- 6) Development of the long cryostat for the combined function superconducting magnet.
- 7) Development of magnetic field measurement system for small aperture long superconducting magnet.
- 8) Development of quench protection system for combined function superconducting magnet.
- 9) Cryogenic test and field measurement of the small aperture long superconducting magnet.

CONCLUSION

Superconducting magnets in interaction region are key devices for CEPC. Conceptual design of superconducting magnets in CEPC interaction region has been finished. Field crosstalk effect between two apertures in QD0 and QF1 can be reduced to be acceptable. The anti-solenoid is divided into a total of 22 sections with different inner coil diameters, with a max central field of 7.2T. Prototypes superconducting magnets in CEPC interaction region are proposed, and the R&D has started.

REFERENCES

- [1] CEPC Conceptual Design Report, Volume I - Accelerator, http://cepc.ihep.ac.cn/CDR_v6_201808.pdf
- [2] M. Koratzinos, *et al.*, "Progress in the FCC-ee Interaction Region Magnet Design", in *Proc. IPAC2017*, Copenhagen, Denmark, May 2017, pp. 3003-3006.
- [3] Norihito Ohuchi, *et al.*, "Design and Construction of the SuperKEKB QC1 Final Focus Superconducting Magnets", *IEEE TRANSACTIONS ON APPLIED SUPERCONDUCTIVITY*, vol. 25, no.3, p. 4001204, June 2015.
- [4] N. Ohuchi, *et al.*, "Final-focus Superconducting Magnets for SuperKEKB", in *Proc. IPAC2018*, Vancouver, BC, Canada, April 2018, pp. 1215-1219.
- [5] OPERA, Vector Fields Software, Cobham Technical Services, <https://operafea.com/>.
- [6] Yingshun Zhu, *et al.*, "Study on Ampere-Turns of Superconducting Dipole and Quadrupole Magnets Based on Sector Coils", *Nuclear Instruments and Methods in Physics Research A*, vol. 741, 2014, pp. 186-191.
- [7] Yingshun Zhu, "Conceptual Design of CEPC Interaction Region Superconducting Final Focus and Anti-solenoid Magnets", presented at International Workshop on High Energy Circular Electron Positron Collider, Beijing, China, November 6 to 8, 2017, <https://indico.ihep.ac.cn/event/6618/>.

CEPC COLLIDER AND BOOSTER MAGNETS*

Mei Yang[†], Fusan Chen, Wen Kang, Xianjing Sun, Yingshun Zhu

Key Laboratory of Particle Acceleration Physics and Technology, Institute of High Energy Physics, Chinese Academy of Sciences, Beijing 100049, China

Abstract

A Circular Electron Positron Collider (CEPC) with a circumference of about 100 km, a beam energy up to 120 GeV is proposed to be constructed in China. Most magnets for CEPC booster and collider ring are conventional magnets. The quantities of the magnets are large, so the cost and power consumption are two of the most important issues for the magnet design and manufacturing. The dual aperture dipole and quadrupole magnet with low current high voltage are used in the collider ring. Whereas in the booster the dipole magnet works at very low field, so a low packing factor dipole magnet or a coil type without iron design will be investigated and chosen. In this paper, the conceptual design of the CEPC main magnets are described in detailed and the R&D plan is presented.

INTRODUCTION

A Circular Electron Positron Collider (CEPC) is proposed to be constructed in China. It is an important part of the world plan for high-energy physics research. The CEPC will operated at different beam energy of Z, W and Higgs factory. The accelerator complex of CEPC consists of a linear accelerator (Linac), a damping ring (DR), the booster, the collider and several transport lines. The booster and the collider ring are in the same tunnel with a circumference of about 100 km [1].

There are about 9370 magnets in the collider ring and nearly 20000 magnets in the booster ring. Most magnets except some magnets in the interaction region operated at a relatively low field are designed as conventional magnets. A significant effort has been made in optimizing of the power consumption, manufacturing and operation cost of the magnets like that in the LEP and FCC-ee [2-3]. The synchrotron radiation damages to the conductor are considered with more space on the coil windings to place the radiation absorber. All the magnets have been designed using OPERA software [4].

COLLIDER MAGNET SYSTEM

The CEPC collider ring is a double ring collider and most of the dipoles and quadrupoles have similar strength and length. To reduce the cost and power consumption, 2384 dipoles and 2392 quadrupoles are designed as dual aperture magnets to provide magnetic field for both beams whose separation is 350 mm.

Besides the dual aperture magnet design, several special technologies are used to reduce the magnet cost, including

the core steel dilution for dipoles and aluminium conductors instead of copper. To reduce the magnet power consumption, the low current density and high voltage operation mode are used to cut down power consumption of the magnet power supply and the power cables. The main magnet requirements are listed in Table 1. The gap height of the dipoles is 70 mm and the aperture diameter of quadrupoles and sextupoles is 76 mm and 80 mm, respectively.

Table 1: Main Parameters of CEPC Collider Ring Magnets

Magnet	Field strength	Magnetic length	Width of GFR
Dipole	0.0373 T	28.7 m	13.5 mm
Quadrupole	8.42 T/m	2.1 m	12.2 mm
Sextupole	506.2 T/m ²	1.4 m	13.9 mm

Dual Aperture Dipole Magnet

The dipoles are kept as long as possible to limit the synchrotron radiation losses which have a length of 28.7 m. Its iron is divided into five segments for easily fabrication and transportation. The 'I' shape core magnet sharing one coil is chosen to save about 50% power consumption and provide two identical field in the twin apertures. In the first and last segments, the dipole-sextupole combined magnet profile are used to reduce the sextupole strength of the individual sextupoles.

Considering the beam energy saw tooth effect, the trim coils are used for both apertures to adjust the field by the order of $\pm 1.5\%$ independently. 2D field simulation results show that the field quality is sensitive to the position of the aluminium busbars and the trim coil in one aperture has no coupling effect in the other aperture. Figure 1 shows the cross section of the dual aperture dipole magnet with and without the sextupole component.

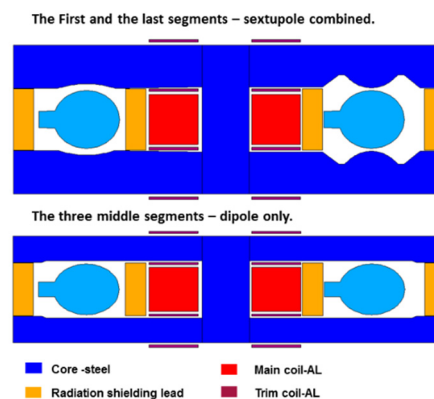


Figure 1: Cross section of the dual aperture dipole.

* Work supported in part by the Yifang Wang scientific Studio of the Ten Thousand Talents Project.

[†] Email address: yangmei@ihep.ac.cn

Dual Aperture Quadrupole Magnet

The dual aperture quadrupoles have different polarities in the twin apertures. The two apertures sharing two racetrack coils made of hollow aluminium cables, compared to eight coils in two independent single aperture quadrupoles, can save nearly 50% of power. The dual aperture quadrupole design gives not only mechanical coupling but also magnetic coupling. To reduce the field coupling between the two apertures, a 50 mm gap filled with stainless steel is inserted into the yoke and separates the yoke into two parts. Trim coils in both apertures have $\pm 1.5\%$ adjustment capability to compensate for the sawtooth effect in beam energy. Figure 2 gives the cross section of the dual aperture quadrupole and Fig. 3 shows the magnetic flux.

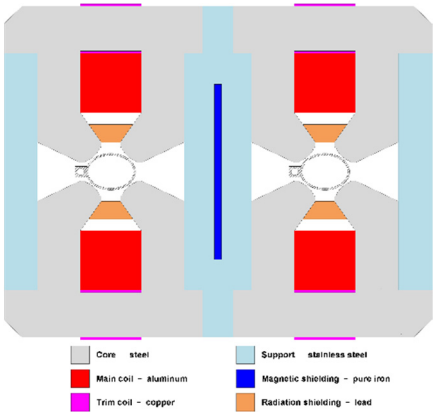


Figure 2: Cross section of the dual aperture quadrupole.

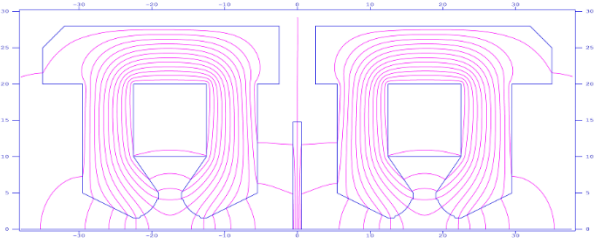


Figure 3: Magnetic flux in the dual aperture quadrupole.

By optimizing the profile of the pole, the systematic harmonics are suppressed to be less than 3×10^{-4} . However, field coupling introduces non-systematic harmonics even if there is a 50 mm gap between the two yokes. To compensate these non-systematic harmonics, a pure iron shielding plate is inserted between the two apertures. Simulation shows that the non-systematic harmonics in both apertures are sensitive to the thickness of the shielding plate. An optimal shielding thickness of 11.52 mm will compensate the non-systematic harmonics and reduce them to close to zero, which does not affect the systematic harmonics in both apertures.

Sextupole SD/SF Magnet

The sextupoles are two individual parallel magnets instead of a dual aperture one. The distance between the e⁺

and e⁻ beam is quite close; therefore the sextupole size is limited and the space between two neighbouring sextupoles is restricted. Figure 4 shows the cross sections and positions of the sextupoles in the two rings.

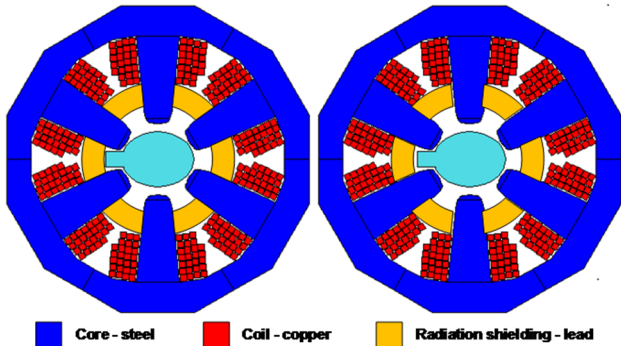


Figure 4: Cross section of two neighbouring sextupoles in the two rings.

Although the two sextupoles are close to each other, the field interference between them is negligible. The pole surface profile is optimized to compensate the harmonics.

BOOSTER MAGNET SYSTEM

The booster has 16320 dipoles, 2036 quadrupoles and 448 sextupoles. The field of the dipole, quadrupole and sextupole magnets will change with the beam energy ranging from 10 GeV to 120 GeV and the field ramping profiled in shown in Fig. 5. The ratio of the maximum field to minimum field of the magnets is 12. The main parameters of the booster ring is represented in Table 2. The dipole magnets have a gap of 63 mm and the aperture diameter of the quadrupoles and sextupoles is 64 mm.

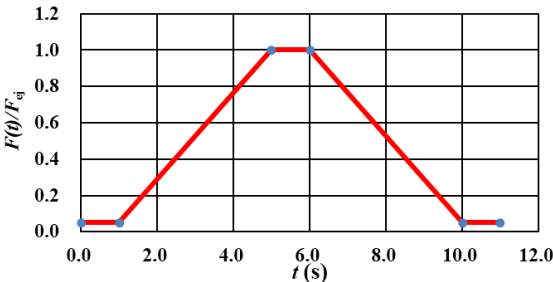


Figure 5: The magnetic field cycle of the booster.

Table 2: Main Parameters of CEPC Booster Magnets

Magnet	Field strength	Magnetic length	Width of GFR
Dipole	0.0338 T	4.7 m	55 mm
Quadrupole	11.07 T/m	1.0 m	28 mm
Sextupole	216 T/m ²	0.4 m	28 mm

Low Field Dipole Magnet

Most dipole magnets are 4.7 m long, the others are 2.4 m and 1.7 m long. The field will change from 29 Gauss to

392 Gauss during acceleration. Due to this very low injection field level, the cores are an H-type structure and composed of a stack of 1 mm thick low carbon steel laminations spaced by 1 mm thick aluminium laminations. Because the magnetic force on the poles is very small, the return yoke of the core can be made as thin as possible. In the pole areas of the laminations, some holes will be stamped to further reduce the weight of the cores as well as to increase the field strength in the stack. The considerations of steel-aluminium core, the thin return yoke and the holes in pole areas can improve the performance of the iron core and considerably reduces the weight and capital cost. Also for economic reasons, the excitation bars are made from 99.5% pure aluminium with a cross section of $30 \times 40 \text{ mm}^2$. Thanks to low Joule loss in the bars, the magnets are cooled by air instead of water.

The integrated field uniformity of the 4.7 m long dipole cores can be optimized within 5×10^{-4} by pole shimming in 2D or end chamfering in 3D. The cross section and magnetic flux of the dipole magnet is shown in Fig. 6.

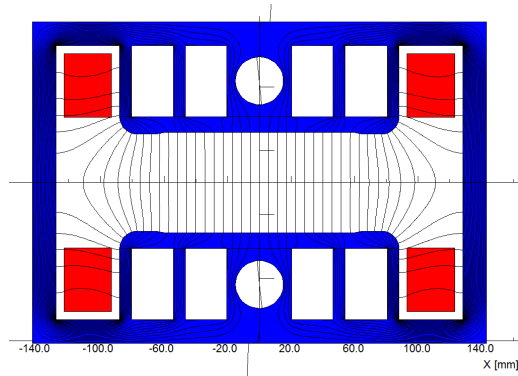


Figure 6: The magnetic flux distribution of the booster dipole magnet.

Quadrupole Magnet

A common design is used for the booster quadrupole magnets. The magnet yoke consists of four pieces (quadrants) made of 0.5 mm thick laminated low carbon silicon steel sheets, which permits installation of the coils between each pole. The assembled magnet can also be split into two halves for vacuum chamber installation. While the hollow aluminium conductor will be chosen for the coil for its lower price and weight. The coil windows leave a certain amount space for radiation shielding blocks.

Due to the length of the magnet is long, 2D magnetic field analysis is sufficient. The pole profiles are designed to introduce positive 12-pole and 20-pole multipole fields to compensate for the end field effects. The cross section and the magnetic flux lines of the quadrupole are shown in Fig. 7.

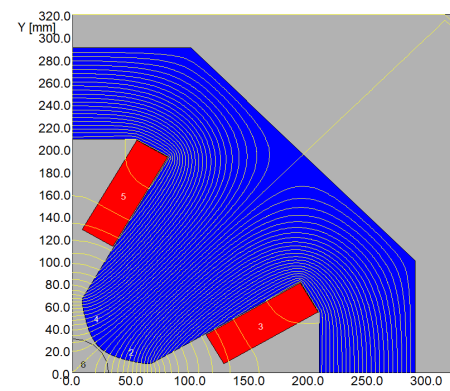


Figure 7: Magnetic flux lines of the booster quadrupole magnet (one quarter).

Sextupole Magnet

The sextupole magnets are divided into two families, focusing or defocusing (horizontal), both of which have the same aperture diameter and magnetic length but have different field strength. The magnetic field will change with the beam energy and the minimum sextupole field strength is 1/12 of the maximum value.

The magnetic core is a two-in-one structure, made of low carbon silicon steel sheets and end plates. By using the end chamfer, the field errors can be reduced to meet the strict field requirements. The coils are wound from solid copper conductors and have a simple racetrack-shaped structure. The cross sections of the sextupole magnets have been designed and optimized using the OPERA-2D and the magnetic flux lines are shown in Fig. 8.

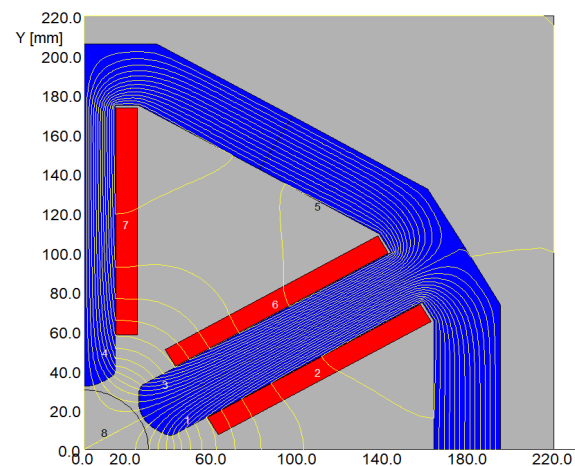


Figure 8: Magnetic flux distribution of the booster sextupole magnet (one quarter).

R&D PLAN

Prior to the construction of CEPC, there will be a five-year R&D period (2018-2022). During this period, prototypes of key technical components will be built.

The field of the dual aperture dipole in the collider is about 140 Gauss at Z mode. The requirements of the field quality is hard to achieve at low field. To study the possible

field distortions for Z running, a short prototype of dual aperture dipole will be developed and tested. The dual aperture quadrupole uses the multi-turn coils made of hollow aluminium and a shielding plate to compensate for the non-systematic harmonics. A dual aperture quadrupole prototype will be built to study the crosstalk.

In the booster, one high precision low field dipole prototype will be developed to study the technical issues of design and production. The oriented low carbon silicon steel laminations with lower coercive force will be used to stack the core. Also the design of dipole magnet without core like the superconducting magnets will be considered and prototypes will be tried.

CONCLUSION

Conceptual design of CEPC collider and booster magnets has been finished. The cross section of the main magnets are represented in this paper. Some technical difficulties have been considered and will be further optimized and studied. The prototypes will be built and measured.

REFERENCES

- [1] CEPC Conceptual Design Report, Volume I - Accelerator, http://cepc.ihep.ac.cn/CDR_v6_201808.pdf
- [2] A. Milanese, "Efficient twin aperture magnets for the future circular e^+e^- collider", *Physical Review Accelerators and Beams*, 112401 (2016).
- [3] LEP Design Report, Volume II-the LEP Main Ring, 1984, <https://cds.cern.ch/record/102083/files/cm-p00047694.pdf>.
- [4] OPERA, Vector Fields Software, Cobham Technical Services, <https://operafea.com/>.

LARGE SCALE SUPERCONDUCTING RF PRODUCTION

Carlo Pagani, INFN-LASA and Università degli Studi di Milano, Milano, Italy

Abstract

The efficient plug to beam power conversion promised by the use of Superconducting RF to accelerate particle beams is still the driving force to pursue the development of this technology. Once the effective gain reached the level to pay for cryogenics, big physics laboratories started to believe on SRF, investing resources and proposing large challenging projects. Since then the cooperation with industry has been crucial to transform a few lab results into reliable SRF cavities and related ancillaries. This process started in the eighties and reached the actual paradigm with the realization of the European XFEL. All the new large scale projects in construction or proposed should start from the analysis of this experience and move forward from there.

INTRODUCTION

Superconducting radiofrequency (SRF) cavities have been in routine operation over the past 30 and more years in a variety of settings, from pushing frontier accelerators for particle physics to applications in nuclear physics and materials science. Used in a number of accelerator based projects, with different frequencies and shapes, they were instrumental in pushing CERN's LEP collider to new energy regimes, in getting high energy and in driving the newly inaugurated European X-ray Free Electron Laser. Nowadays, being the basic technology well understood, almost any type of accelerating structure can be successfully built taking advantage of the technological level that has been reached thanks to the investments done by the big projects in 1980s and 1990s.

At first, it was not clear that superconductivity had much value for RF technology. But it was soon realized that in the practical frequency range of RF accelerators, from hundred MHz to a few GHz, the use of SRF cavities would produce in any case a significant breakthrough due to the increase in the conversion efficiency from plug-to-beam-power, cryogenics included. It was simply a question of developing the technology, and that required investment and big projects.

The High-Energy Physics Lab at Stanford University in the US was a pioneer in applying SRF to accelerators, demonstrating the first acceleration of electrons with a lead-plated single-cell resonator in 1965. Also in Europe, in the late 1960s, SRF was considered for the design of proton and ion linacs at KFK in Karlsruhe, but to really compete with the well-established normal conducting technology the path was still long and tortuous. Following these forerunners since the early 1970s SRF has been introduced in the design of particle accelerators, but results were modest and a number of limiting factors had to be understood and handled. As usual for any new technology a lot of science supported industrial development was needed to reach the current status of the art. In par-

ticular lead and niobium used as superconductor were originally too dirty for SRF. In practice, the different orders of magnitude obtained theoretically with superconductivity in terms of surface resistance were strongly reduced by the normal conductive impurities coming from both the superconductors themselves and the TIG welding electrodes.

However, the pioneering results while not astonishing have been sufficient to convince scientists that was just a question of technology and, once the effective gain reached the level to pay for cryogenics, big physics laboratories started to believe on SRF investing resources and proposing challenging projects. Since then the cooperation with industry has been crucial to transform lab results into reliable items.

SRF TECHNOLOGY AND BIG PROJECTS

The first successful test of a complete SRF cavity at high gradient and with beam was performed at Cornell's CESR facility at the end of 1984, involving a pair of 1.5 GHz, five-cell bulk niobium cavities with a gradient of 4.5 MV/m. This cavity design was then used as the basis for the CEBAF facility to be built at Jefferson Lab in US and convinced KEK in Japan to ask industry to produce a large number of SRF cavities to upgrade the energy of their TRISTAN electron-positron collider.

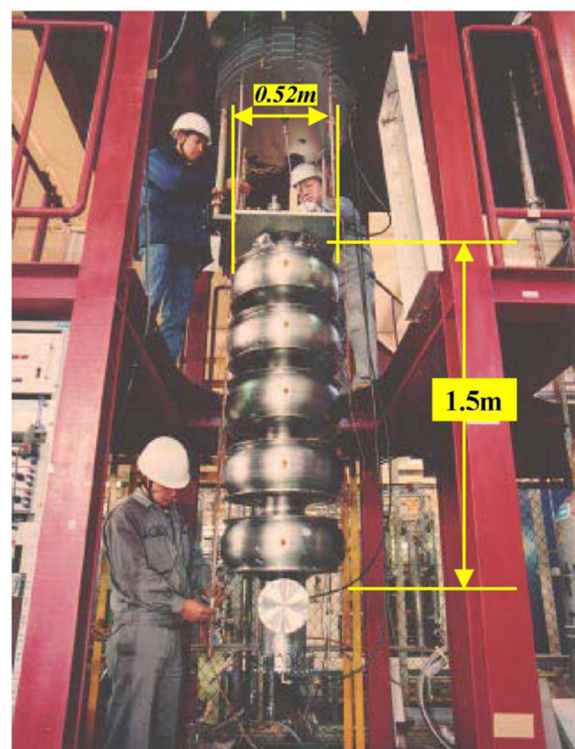


Figure 1: TRISTAN cavity prepared for test at KEK.

In 1989 TRISTAN reached a centre of mass energy of 32 GeV thanks to the installation of 32 large superconducting cavities, 5-cell, 508 MHz, made from bulk niobium sheets [1]. It's important to stress that these cavities were fully produced by industry with the external support of KEK. The consequence has been a fast production of very good cavities for that time (Eacc up to 7-8 MV/m), but the technological know-how was just marginally maintained inside the scientific community and then was rapidly lost by the industry itself because of the marginal expected market. One of the TRISTAN cavity equipped for vertical test at KEK is shown in Fig. 1.

A small number of cavities for other projects were meanwhile designed and built in Europe (HERA at DESY, ALPI at LNL, etc.) and US (ATLAS at ANL, etc.), but their number was too small to really impact technology. All considered it turns out that the biggest contribution to the creation of a reliable and reproducible SRF technology has been mainly given, starting from the end of the eighties, by the only two very large projects based on SRF: LEP2 at CERN and CEFAF in US. The two projects chose quite different ways to successfully develop the SRF technology but the combination of them created the basis for all the steps forward of such a complex system that together with the accelerating cavities includes all the needed ancillaries, like couplers, tuners, cryostats and cryogenic infrastructures.

Because of the size and the novelty, both projects had to locally set up a group of dedicated scientist and a very large infrastructure to completely design and test all the SRF items that were required. CEBAF took care also of the cryogenic plant because the cavity operation at 2 K, i.e. in superfluid Helium, was asking for something new for the global cryogenic industry.

Both projects had to produce and qualify roughly the same number of cavities, about 300, with the respective cryomodules and ancillaries, but the size of these objects was very different. Considering that all the sizes are more or less scaling in a similar way, it's enough to compare the respective cavity active lengths: 0.50 m for CEBAF and 1.70 m for LEP2. For both projects the accelerating gradient and the quality factor were crucial and the quality of the superconducting material was poor at that time. Lead plating was out and the bulk niobium was reasonable just for the smaller sheet sizes requested by the production of the CEBAF cavities. First bulk niobium prototypes of the big 352 MHz cavities for LEP2, asking for sheets close to 1 square meter, turned out to be not sufficiently good to reliably obtain the accelerating field that was justifying the effort. Hopefully, in the middle of the crisis, a scientist of CERN, Cris Benvenuti, developed just in time the magnetron sputtering technique that was depositing on the inner surface of a copper cavity a thin layer of niobium that was good enough to sustain an accelerating field higher than the 5 MV/m originally dreamed [2].

Once reached the goal on house made prototypes, both projects had to face the problem of the series production and the industrialization process had to start.

Because of the small size of the cavities, the large number of people involved in the SRF development and the size of the in house infrastructure, in the case of CEBAF the industrialization process was practically limited to the cavity mechanical fabrication, which was finally performed by an European company. Discussing the pros and cons of this decision are not in the scope of this note, but surely the production of more than 300 bulk niobium cavities for an important National Project in US pushed the Niobium producer to invest on material quality. This effect turned out to be crucial for all the following projects. From then on the niobium available on the marked started to be better and RRR=150 became an available standard.

On the other hand the human and infrastructural resources at CERN, while adequate for the R&D program performed so far, were not consistent with the production in a limited time of a few hundreds of large cavities, with ancillaries and cryostats. Anticipating the industrialization process as much as possible, all the steps of the fabrication of SRF cavities, ancillaries and cryostats was specified in detailed notes and controlled in house. On the basis of this material and with the support of all the CERN SRF group the complete technology was transferred to brother institutions, like INFN and CEA, and finally to three European companies to share the production of 256 + spares, 2.4 m long, accelerating cavities, completed with ancillaries and cryostated in a 4-cavity cryomodule (Fig. 2).



Figure 2: LEP2 cavities in industries during cryostating in large clean rooms of class 100/10.000.

All the process was finally done in industry, from the forming of the half cells to the final ultra-pure water rinsing and module assembly, going through electron beam welding, copper chemistry and magnetron sputtering. Electron beam welding, class 100 clean room assembly and ultra-pure water rinsing became the standard for SRF cavity fabrication and scientific and technical

personnel from CERN, with the support of INFN and CEA, spent an important fraction of their time in the three industries to control the process and make experience of the industrial world with its limits and potentialities. A standard for QC, quality control, and QA, quality assurance has been so implemented at that time and used thereafter for this kind of productions. A qualification RF test in a vertical cryostat of each of the naked cavities was performed at CERN before the module assembly, to control the quality of the niobium coating.

At the end of the 1980s a number of labs were playing with SRF, performing fundamental research but with limited capability to sensibly impact on the SRF technology. The status of the art for the accelerating field reliably obtainable with multi-cell elliptical cavities was 5 to 8 MV/m, and this value was consistent with the production technologies developed both at CERN and Jefferson Lab. While using two different approaches, magnetron sputtering and bulk niobium, these two laboratories were indeed the places where all the production infrastructures and the human expertise were present. Concerning the four industries engaged in the large scale production for LEP-2 and TRISTAN they had to rescale or dismantle infrastructures and human resources according to the lack of large projects asking for SRF, but the process for the SRF industrialization was set and ready to be implemented and eventually improved.

THE TESLA COLLABORATION IMPACT

Was in this context that the TESLA collaboration was set up with the challenging goal of developing the SRF technology at the level needed to be globally accepted as the most promising technology for the future electron-positron collider to be built after LEP2. To understand how hard was the game it is worth remembering that three large collaborations were already competing for the linear collider working hard on three projects, CLIC, JLC and NLC, with somehow different approaches but all working at room temperature. Additionally, to be competitive in term of cost and performances, it was mandatory to improve the established SRF technology by at least a total factor of about 20; namely a factor 5 on the cavity accelerating gradient, from 5 to 25 MV/m, and a factor 4 in the total SRF cost, with ancillaries, cryogenics and power supplies, once expressed in cost per MV installed.

Ten years later, when the TESLA TDR was presented (March 2001), the objective was widely reached and the game with the other competitors was ended in the August 2004 when the ITRP (International Technology Recommendation Panel) chose the TESLA cold technology as the one to be globally adopted for the ILC (International Linear Collider).

INDUSTRY AND THE TESLA SUCCESS

The great success of the TESLA collaboration in opening a new era for the SRF technology had a number of concomitant causes, in addition to the great enthusiasm,

friendship and some ingenuity of the those involved. The fresh experiences from LEP2 and CEBAF was the basis, for instance, plus cryogenic experience from DESY and Fermilab. The bounding MoU helped to inspire a pure scientific research style, with no secrets among the partner institutes and constructive competition to produce the best technology possible. Once the cavity frequency (1.3 GHz) and the number of cells per cavity (nine) had been agreed, we designed the TESLA Test Facility. This central infrastructure at DESY was to treat the active/internal surface of cavities, control and verify each step of the material and cavity production, and finally test the cavities and ancillaries in all conditions, naked and fully dressed, with and without beam. In contrast to the construction of LEP2 and CEBAF, the fabrication of the cavities themselves was handed over to industry. This turned out to be a crucial decision, forcing researchers to a strict collaboration with competing firms and taking advantage of all their expertise and ingenuity.

Niobium material was the first suspected for the modest cavity performances. We started improving its thermal conductivity (identified indirectly through the RRR) heat treating the cavities up to 1400 °C. The process was expensive and detrimental to mechanical robustness but excellent to produce soon two 9-cell prototypes reaching the goal of 25 MV/m. The cavity production was performed in a big company that produces aircrafts and the surface treatment in the new infrastructure set up at DESY collecting all the experience from CERN and CEBAF, but also adding the experience of electronic companies for clean polishing, handling and assembling. Starting from a cavity design challenging for the number of cell but with the simplest possible geometry and at one of the frequency available on the RF market, we put our effort identifying for each step of the production the best available and accessible in industry, avoiding to spend a single minute to “find a better way to warm up the water”. The international enthusiasm and the perspective of a very big project simplified our work. As a typical example, the success with heat treated prototypes together with the availability of a Eddy-current instrument, developed by DESY with industry and able to detect big (100 μm) foreign inclusion on the surface of the niobium sheets to eventually reject them before the cavity fabrication, pushed the niobium producer to do some effort to improve their production and to make cleaner all the steps of the process from the ingot to the sheets delivered. The high temperature heat treatment was then abandoned and the cavity performances remained as good as before. The well-known Fig. 3 shows the status of the stable cavity production at the end of nineties. All the production steps were well defined and documented. A few companies were qualified to deliver niobium according to the specs and a few other companies were able to produce good cavities able to reach the TESLA specs once surface treated at DESY in a well-defined, quasi-industrial way [3].

Two main results from the ongoing R&D in the TESLA collaboration laboratories improved the cavity per-

ILC R&D, the project management decided to implement both the technologies applied so far on the TTF cavity production, respectively based on Buffer Chemical Polishing, BCP, and Electro-Polishing, EP. This was done in spite of the fact that the latter had already demonstrated a better performance in term of maximum accelerating field. The reason was that both process should in principle safely generate cavities with performances higher than the project specifications, namely: $E_{acc} > 23.4$ MV/m at $Q_0 > 1 \times 10^{10}$. Based on the experience done through the past production of about 100 cavities in the TTF/ILC framework, the bulk chemical process that removes the damaged surface layer after all the mechanical processes, was decided to be done by EP in both cases. This decision was also important to have both companies up to date and maintain a competition on the SRF cavity market.

All the details of the technology transfer process and the SRF cavity production for the European XFEL are described in an exhaustive paper published on PRST-AB [5] that, together with the references thereafter, gives a complete picture of the largest and successful SRF cavity production globally done so far. In the same paper also cavity performances and statistics are widely described.

For the scope of this note few concepts that can be taken as useful references follow, meant for future projects that will need large scale cavity production:

- Once a receipt is fully defined and reproducible, with all the steps perfectly documented, a few industries (>1) should be selected, on the basis of the past experience, and helped to set up the required infrastructure. For the E_XFEL this took nearly 2 years, with some defined steps of pre-qualification before the start of the large scale cavity production.
- The use in industry of generic infrastructures and mixing production with an uncomplete R&D preparation phase should be avoided in large projects.
- In qualified industries QA and QC procedures are usually well established and, as a consequence, the results obtained are more stable.
- Industry is reproducing at the best level what the leading lab has transferred.
- In the field of SRF cavities, qualified industries can guarantee the respect of all the specified steps of QA and QC, not the final performances that remain under the responsibility of the project.

As properly shown in ref [6] the usable gradient is typically a few MeV/m lower than the maximum obtained in the vertical test. Field emission and high field Q drop are the principal causes. Looking at the average value on the production of 800 SRF 9-cell cavities an usable gradient of 29.0 MeV/m and 26.3 MV/m was measured respectively for EP and BCP treated cavities. Concerning the cavity quality factor Q_0 an average value of 1.5×10^{10} was obtained for $E_{acc} < 20$ MV/m, slightly higher with BCP. These results widely exceed the E-XFEL goals of $E_{acc} = 23.6$ MV/m at $Q_0 = 1 \times 10^{10}$, but it's important to note that an additional HPR (High Pressure Rinsing) was needed on ca. 40% of the cavities.

THE LESSON LEARNED

The application of SRF in particle accelerator is nowadays well established and a few companies worldwide can deliver reliable SRF cavities, while others can produce niobium material, or build related ancillaries and equipment, all more or less based on what has been developed in the framework of the TESLA Technology Collaboration. The large scale superconducting RF production for the realization, on budget and on time, of the European XFEL set the standard that can be expected by industry on the basis of what was the results of a global R&D effort standing for more than two decades.

The past history teaches that in practice only two choices are viable: either ordering cavities to already qualified industries basing requests on what has been already established, or starting from a lab that has developed in house all the technology and has the time, the personnel and the wish of setting up or promoting a new company.

To conclude it is worthwhile to note that the SRF global market is small with respect to the required technologies and infrastructures, and because it's also very irregular, it cannot sustain many actors. The possible case of a positive decision for the construction in Japan of the 250 GeV ILC could modify this statement but the result would be the same because in this case also global market companies, momentarily in standby, could decide to enter in the market. In reference [7] the excellent results of a batch of cavities produced in Japan a few years ago by the same company that produced in the eighties the SRF cavities for TRISTAN are presented.

REFERENCES

- [1] S. Noguci, "Experience on the Superconducting RF System at TRISTRAN", in *Proc. SRF'95*, Gif sur Yvette, France, Oct. 1995, pp. 163-171.
- [2] C. Benvenuti *et al.*, "Superconducting Cavities produced by Magnetron Sputtering of Niobium on Copper", in *Proc. SRF'87*, Argonne National laboratory, Illinois, USA, Sep. 1987, pp. 445-468.
- [3] B. Aune *et al.*, "Superconducting TESLA cavities", *Phys. Rev. ST AB*, vol. 3, p. 092001, Sep. 2000, doi: 1098-4402/00/3(9)/092001(25)
- [4] TESLA Technical Design Report – The Accelerator, Report: DESY-2001-011; ECFA-2001-209; TESLA 2001-23. http://tesla.desy.de/new_pages/TDR_CD/PartII/accel.html
- [5] W. Singer *et al.*, "Production of superconducting 1.3-GHz cavities for the European X-ray Free Electron Laser", *Phys. Rev. ST AB*, vol. 19, p. 092001, Sep. 2016, doi: 2469-9888/16/19(9)/092001(18)
- [6] D. Resche *et al.*, "Performance in the vertical test of the 832 nine-cell 1.3 GHz cavities for the European X-ray Free Electron Laser", *Phys. Rev. ST AB*, vol. 20, p. 042004, Apr. 2017, doi: 2469-9888=17=20(4)=042004(31)
- [7] K. Sennyu *et al.*, "Industrialization of ILC from a view point of Industry", in *Proc. IPAC'13*, Shanghai, China, May 2013, pp. 2010-2014, ISBN: 978-3-95450-122-9

SRF SYSTEMS FOR KEKB AND SuperKEKB

K. Nakanishi, M. Nishiwaki[#], T. Kobayashi, KEK, Tsukuba, Japan
K. Hirosawa, SOKENDAI, Tsukuba, Japan

Abstract

Eight superconducting accelerating cavities were operated for more than ten years at the KEKB. Commissioning operation of SuperKEKB is ongoing and those cavities are also used to accelerate the electron beam of 2.6 A. There are some issues to address the large beam current and to realize stable operation. One issue is a large HOM power of 37 kW expected to be induced in each cavity module. In particular, the power emitted out to the downstream of the cavity is simulated to be large. To cope with the HOM power issue, we have installed an additional HOM damper to the downstream of the cavity module. Another issue is degradation of Q values of the cavities during the ten years operation. Cause of the degradation was particle contamination. To clean the cavity surface, high pressure rinsing (HPR) is an effective way. Therefore we have developed a horizontal HPR. In this method, a nozzle for water jet is inserted horizontally into the cavity module without disassembly of the cavity. We applied the horizontal HPR to our degraded cavities. The RF performances of those cavities have been successfully recovered. In this report, present status of our cavity will be presented. Additionally, low level RF control issues for SuperKEKB upgrade will be introduced.

Table 1: RF-related Operation Parameters in HER

Parameters	KEKB (operation)	SuperKEKB (design)
Energy [GeV]	8.0	7.0
Beam current [A]	1.4	2.6
Number of bunches	1585	2500
Bunch length [mm]	6~7	5
Total beam power [MW]	~5	8.0
Total RF voltage [MV]	15.0	15.8

OVERVIEW OF KEKB AND SUPERCONDUCTING CAVITY

KEKB accelerator was an electron-positron asymmetric energy ring collider for B-meson physics, consisting of high energy ring (HER) for the electrons and low energy ring (LER) for the positrons. The circumference was around 3 km. The beam energies of HER and LER were 8 and 3.5 GeV, respectively. The maximum beam currents were 1.4 A for HER and 2.0 A for LER. KEKB was operated until June 2010, with a world record luminosity of $2.1 \times 10^{34} / \text{cm}^2/\text{s}$ [1].

One serious concern for high-current storage rings is the coupled-bunch instability caused by the accelerating mode of the cavities. This issue arises from the large detuning of the resonant frequency of the cavities that is needed to compensate for the reactive component of the

beam loading. In order to mitigate this problem, two types of cavities were adopted in KEKB operation [2, 3]: one is a superconducting cavity (SCC) [4, 5], and the other is a normal conducting cavity called ARES [6, 7]. ARES, which is a unique cavity specialized for KEKB, consists of a three-cavity system operated in the $\pi/2$ mode: the accelerating (A-) cavity is coupled to a storage (S-) cavity via a coupling (C-) cavity. The A-cavity has higher-order-modes (HOM) damped structures.

In HER, RF systems consisted of hybrid system of eight superconducting cavities (SCC, Fig. 1) and 12 ARES cavities, while LER was operated with 20 ARES cavities without SCCs. Table 1 shows operation-related parameters of HER. The total beam power was 5 MW and the total RF voltage was 15 MV. The large beam power and RF voltage were shared with SCC and ARES cavities by giving an appropriate beam phase-offset between them so that each SCC delivered the power of 400 kW to the beam. The HOM load induced by the large beam current was absorbed by a set of ferrite HOM dampers located at the beam pipes of both ends of the cavity, called small beam pipe (SBP) and large beam pipe (LBP). The absorbed power in 1.4 A-operation reached 16 kW without any problems.

Operation statistics and maintenances of SCC in KEKB were summarized in Ref. [3] in detail. Many monitors were set over the ring to identify a cause of each trip. RF trips of the SCC were mainly caused by discharging in the cavity or a high power input coupler. The trip rate in eight cavities was 0.5 times/day at 1.4 A-operation. After adopting the crab crossing, the trip rate decreased to 0.1 times/day because the beam current was lowered to 1.1 A. In order to maintain stable operations, 1) warming up the system to room temperature was performed twice a year, 2) safety inspections due to high pressure safety regulations of cryogenics were carried out once a year, 3) the input coupler conditioning before cooling with bias voltage was performed and 4) regular conditioning every 2 or 3 weeks was carried out. As a result, SRF system of KEKB had been operated safely and stably.

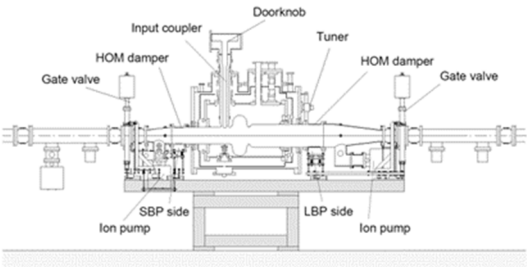


Figure 1: Cross-sectional drawing of the superconducting cavity module of KEKB.

[#]michiru.nishiwaki@kek.jp

Table 2: SCC Parameters

Parameters	KEKB (operation)	SuperKEKB (design)
Number of cavities	8	8
Beam current [A]	1.4	2.6
Bunch length [mm]	6	5
RF voltage [MV/cav.]	1.5	1.5
Beam power [kW/cav.]	400	400
External Q	5×10^4	5×10^4
Unloaded Q at 1.5 MV	1×10^9	1×10^9
HOM power [kW/cav.]	16	37

ISSUES OF SCC FOR UPGRADE TO SUPERKEKB

SuperKEKB is an upgrade machine from KEKB to search for “new physics” beyond the Standard Model. The design luminosity is $8 \times 10^{35} / \text{cm}^2/\text{s}$, which is 40 times higher than that of KEKB [8]. To achieve high luminosity, the design of SuperKEKB is based on a nano-beam scheme. In the scheme, a vertical beam size at an interaction point is designed as 40-50 nm. At the same time, the beam currents will be twice higher than those of KEKB. The first commissioning operation (Phase-1) was performed from Feb. to June 2016 without beam collision. After the installation of Belle-II detector and the positron damping ring commissioning, the second commissioning (Phase-2) was operated successfully from Mar. to July 2018 including the beam collision tuning [9-11].

The design parameters related with RF system of HER are listed in Table 1. The values of KEKB are achieved values [12]. Basically, existing SRF system including cryogenics are to be re-used in order to minimize the modification for SuperKEKB. The main issues are the higher beam current, the shorter bunch length and the large beam power. The beam power will be shared with SCC and ARES as in the case of KEKB. Therefore the beam power delivered by SCC does not change. The SCC-related parameters for KEKB and SuperKEKB are shown in Table 2. The RF voltage is also the same as KEKB. On the other hand, the HOM power becomes large. The expected power reaches 37 kW due to the high beam currents and shorter bunch length. Therefore, the power capacity of existing HOM dampers could be a serious problem.

Additionally, some cavities have been degraded with field emission. Although the degradation is acceptable in SuperKEKB operation, we will need to recover the cavity performance, if the cavities get more degradation. In that case, we have to spend a long time and huge cost to recover the cavity by conventional way. In order to recover efficiently, we need to consider new technique for the performance recovery of the cavities.

We will report a new calculation method to study the SiC damper as countermeasures for the large HOM power and development of new high pressure rinsing system to recover the performances of the degraded cavities.



Figure 2: A KEKB type LBP damper with 4-mm thickness of ferrite, $\phi 300$ mm, length of 150 mm.

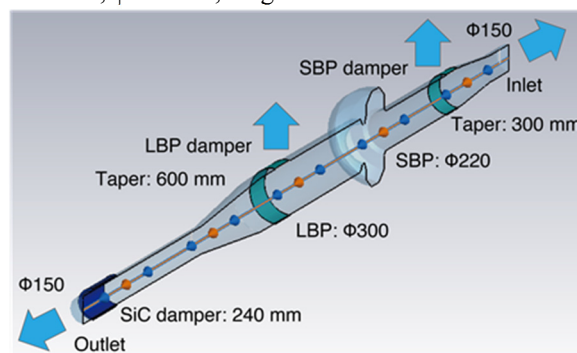


Figure 3: Calculation model of the SCC module. Bunched beam comes from Pin side. Monitors are set at SBP and LBP ferrite dampers and both ends of beam pipes.

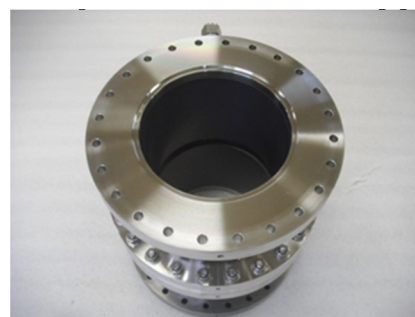


Figure 4: A prototype SiC damper of 240 mm in total length. Two 120-mm SiC dampers are connected together. The thickness of SiC is 10 mm and the inner diameter is 150 mm. The duct length is 220 mm with flanges. The dampers are equipped with a jacket-type water cooling channel.

MEASURES AGAINST HOM POWER

Figure 2 shows a KEKB type ferrite HOM damper. The ferrite was sintered on the copper base pipe by the hot isostatic press (HIP) method. The thickness of the ferrite was chosen as 4 mm for the optimum HOM damping [13]. A pair of the dampers is installed to SBP and LBP. To estimate the HOM load distribution in the module, we developed a new calculation method using CST Particle Studio: wakefield solver [14]. Wake field power flow monitors are set at the surface of dampers and the end of beam pipes as shown in Fig. 3. The time integrals of the power flow signals over the surface give emitted and

absorbed energies through the beam pipe or in the dampers. The total energy including stored energy in the cavity structure is consistent with the energy deposit independently calculated from the loss factor. Using the ratio of the energy, we can get equivalent loss factors and HOM loads of each component as shown in Table 3.

From the calculation results, the existing SBP and LBP ferrite damper loads are not large. However the emitted out power through the outlet beam pipe toward the downstream cavity becomes large. Therefore, the large emission power should be managed.

To reduce the emission power, we studied an additional silicon carbide (SiC) damper using the same calculation method. The SiC damper was located at downstream of outlet beam pipe. From calculation of the loss factor, the length of the damper was optimized to be 240 mm for our SCC modules. The emission power can be 70% reduced by 240-mm SiC damper as shown in Table 3. The loads of ferrite dampers do not change significantly. We will adopt the additional SiC damper as the first measure against the large HOM power [15].

The additional SiC dampers can be installed to the beam pipe outside the gate valve of the module. Therefore, the performance degradation risk due to the air exposure of cavity surface can be avoided.

Table 3: Summary of Equivalent Loss Factors (Eq. LF) and HOM Loads at 2.6-A Beam Operation

Part	Without SiC		With 240-mm SiC	
	Eq.LF [V/pC]	HOM Load [kW]	Eq.LF [V/pC]	HOM Load [kW]
Inlet	0.05	1.3	0.05	1.4
Outlet	0.57	15.4	0.15	4.0
SBP damper	0.32	8.7	0.35	9.5
LBP damper	0.44	11.8	0.47	12.8
Total	1.38	37.2	1.02	27.7
SiC damper	-	-	0.97	26.1

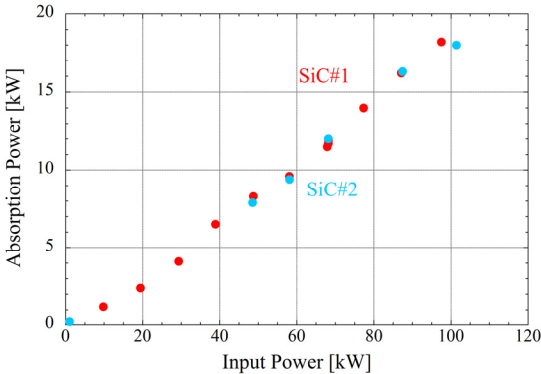


Figure 5: High power RF test results of the prototype of SiC dampers. The absorption powers of 18 kW were achieved by both dampers under the water flow rate of 15 L/min.

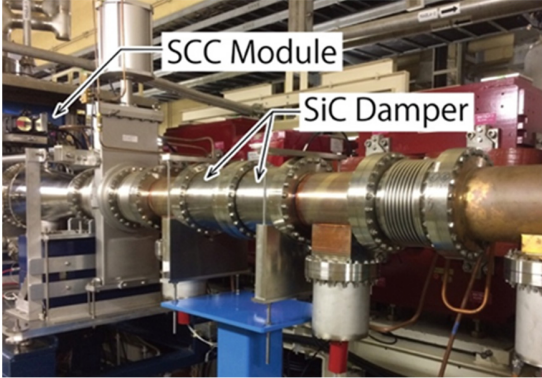


Figure 6: The prototype SiC damper with beam ducts installed downstream of one SCC module. Total SiC length is 240 mm.

A prototype SiC damper consist of two 120-mm SiC dampers (Fig. 4) was fabricated based on the above results. Figure 5 shows the results of the high power absorption tests of the dampers with 15 L/min of the flow late of cooling water. In the tests, the absorption power reached 18 kW for both dampers. The total absorbed power is 1.3 times higher than that of calculation results. The surface temperature of SiC in 18-kW absorption was 80 degrees C and there were no cracks of the surface by the microscope observation after the high power tests.

The prototype SiC damper has been installed before Phase-2 operation (Fig. 6). In Phase-2 operation, the beam test of the SiC damper was performed. Figure 7 shows the absorbed power by the ferrite dampers of the cavities at the beam current of around 760 mA in Phase-1 and Phase-2 operation. The absorbed power of D10B cavity that is downstream of SiC damper decreased remarkably in Phase-2 operation. It was confirmed that the additional SiC damper is effective to reduce the emission power to the downstream cavity.

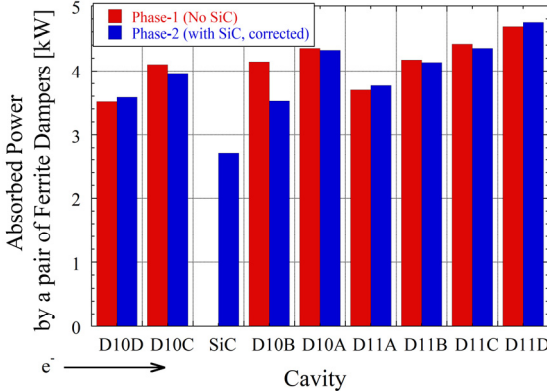


Figure 7: Absorbed HOM power by a pair of ferrite dampers of each cavity. Red: Phase-1 (No SiC damper), Blue: Phase-2 (with SiC damper, with correction factor of 1.05 to correct the systematic error). D10D, D10C and etc on horizontal axis are the cavity name. The beam operation conditions were almost same, the current was around 760 mA. The beam direction is from left to right of the plot. The HOM power of D10B was remarkably decreased by the SiC damper at downstream of D10C in Phase-2 operation.

The SiC dampers will be installed to the other cavities to cope with the large beam current operation.

PERFORMANCE RECOVERY OF DEGRADED CAVITIES

In the long term operation in KEKB, degradation of the SCC performance was observed. The Q values of several cavities degraded significantly at 2 MV with field emission. The degradation of the cavities was caused by the particle contamination during repair work of vacuum

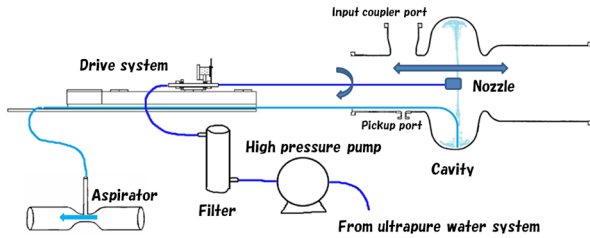


Figure 8: Schematic view of Horizontal HPR system.

leak and change work of coupler gaskets. In the design of SuperKEKB, the present degradations are acceptable because the required RF voltage is 1.5 MV. However further degradation makes the operation difficult. Therefore performance recovery is desirable for stable and long term operation.

Table 4: Horizontal HPR Parameters

Water pressure	7 MPa
Nozzle	Martensitic stainless steel,
Driving speed	$\phi 0.54$ mm in dia., 6 holes
Rotation speed	1 mm/sec.
Rinsing time	6 degrees/sec.
	15 min.

Development of Horizontal High Pressure Rinse

High pressure rinse (HPR) is well known as an effective method to clean up the cavity surface contaminants. If it is possible to apply the HPR to the degraded cavity in the cryomodule, we can omit the re-assembling process, and reduce the risk of contaminations and accidents in the re-assembling process. Furthermore, we can save the time and the cost.

New horizontal HPR (HHPR) system with ultra-pure water ($18.2 \text{ M}\Omega \text{ cm}$) was developed to apply HPR to the degraded cavity [16]. The schematic view of HHPR system is shown in Fig. 8. The system can be set to the cavity without disassembling the cryomodule. Outside accessories such as an inner conductor of input coupler and both end groups including ferrite HOM dampers, bellows chambers, vacuum system and gate valves are dismantled in a clean booth before HHPR. In the system, the water jet nozzle is inserted to the cavity horizontally (Fig. 9). The nozzle is driven automatically in horizontal and rotational movements. Collected water in the cell is pumped up by an aspiration system during rinsing. The

HHPR parameters are summarized in Table 4. The HHPR and vertical tests had been performed to the prototype cavity. In the test, the degraded Q_0 of the cavity was recovered successfully without baking after HHPR [16].

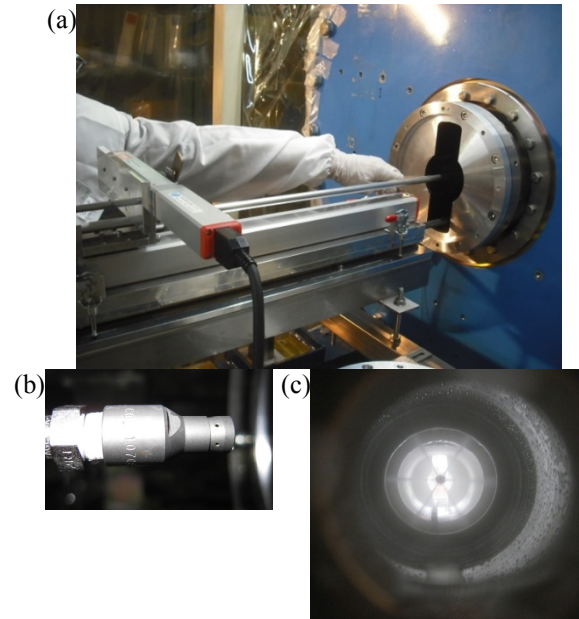


Figure 9: HHPR apparatus. (a) Stainless steel pipe with nozzle inserted from SBP side, (b) nozzle head with 6 holes, (c) water jets during rinsing.

HHPR to Degraded Cavities and Q -Measurements

The HHPR applied to three degraded cavities. The cavities were dried up by evacuation for 4 days before setting the input coupler, the HOM dampers and vacuum system. After setting, the cavities were evacuated by a tarbo-molecular pump and then switched to ion pumps. The baking was not given in the same way as the prototype cavity.

Before cooling down the cavity, the input coupler was conditioned with high RF power up to 300 kW so as to process the electron multipacting discharge on the coupler and outer conductor surfaces. DC bias voltage up to ± 2 kV was applied to the inner conductor [17]. Since the outer conductor surface was exposed to the HHPR water, much water molecules adsorb on the surface even after dried up sufficiently. The minus voltage bias that enhances the multipacting discharge on the outer conductor surface was more effective to condition.

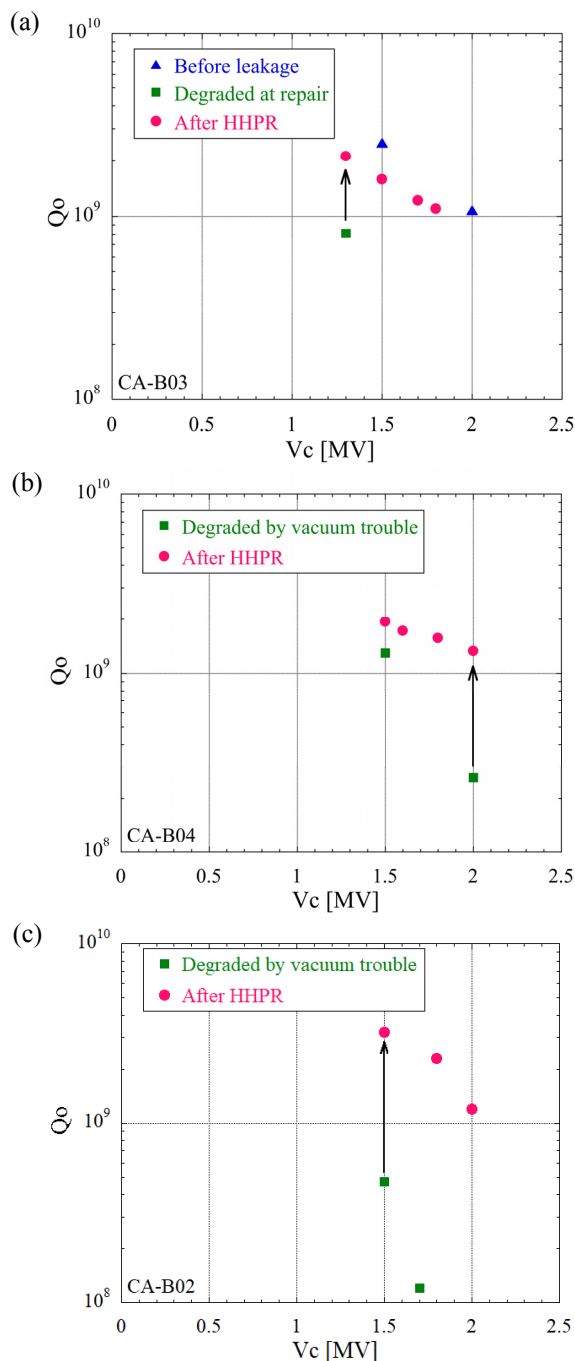


Figure 10: Q_0 measurement results of degraded cavities after HHPR. (a) CA-B03 was degraded at repair work. (b) CA-B04 and CA-B02 were degraded by vacuum trouble. The Q_0 values of all cavities were recovered successfully.

The cavity modules were cooled down to 4.4 K. And then high power conditioning started. Figure 10 shows results of the high power test of two cavities. The Q_0 values at each cavity voltage were obtained from the helium consumption rate of the cryomodule. Degraded cavity “CA-B03” (Fig. 10 (a)) had a leak at indium sealed joint of the beam pipe. The cavity module was disassembled and repaired the leak. But the Q_0 values significantly degraded with strong field emission. In the high power test after HHPR, the field emission of the

cavity was significantly improved. The cavity voltage was finally achieved 2 MV. The field was limited by the radiation safety in the test stand. The Q_0 value is acceptable for SuperKEKB operation. Cavities “CA-B04” and “CA-B02” had vacuum troubles 10 years ago (Fig. 10 (b)) and before Phase-1 operation (Fig. 10 (c)), respectively. Some amount of air dust was accidentally introduced to the cavities and Q_0 values degraded with strong field emission. After this HHPR, the Q_0 values at 2 MV of the cavities increased above 1×10^9 with less field emission. Three cavity performances were successfully recovered by the HHPR. Two of these modules were installed to the ring for SuperKEKB operation. Another one is reserved as a spare cavity module.

RF CONTROL ISSUES FOR SUPERKEKB

Low Level RF Control System

Accuracy and flexibility in accelerating field control are very essential for high-current storage and high-quality beam without instability. Therefore, new low-level RF (LLRF) control system, which is based on recent digital architecture, was developed for the SuperKEKB upgrade [18]. Figure 11 shows a picture of a mass-

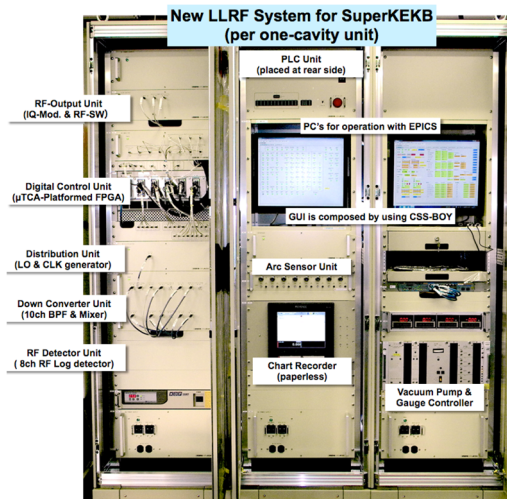


Figure 11: New LLRF control system for SuperKEKB.

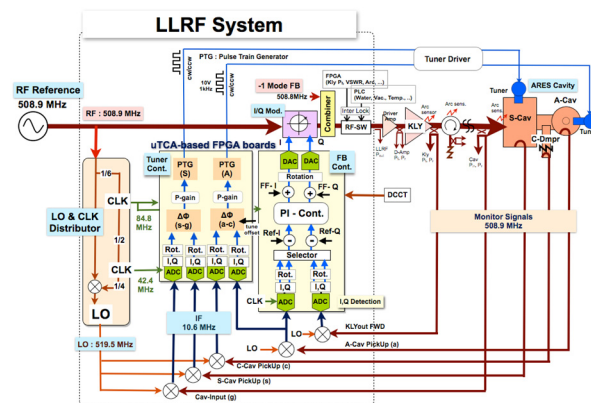


Figure 12: Block diagram of the new LLRF control system for the ARES cavity station.

production model of the new LLRF system for the SuperKEKB. A block diagram of an ARES cavity driving system is shown Fig. 12. The principal functions of this system are performed by five FPGA boards which work on MicroTCA platform as advanced mezzanine cards [19]: Vc-FB controller (FBCNT), cavity-tuner controller (TNRCNT), inter-lock handler (INTLCNT), RF-level detector for the interlock and arc-discharge photo-signal detector. As shown in Fig.12, the new LLRF control system handles I/Q components of controlling signals in the FPGAs. For slow interlocks (e.g. vacuum, cooling water) and sequence control, a PLC is utilized. EPICS-I/O on Linux -OS is embedded in each of the FPGA boards and the PLC [20].

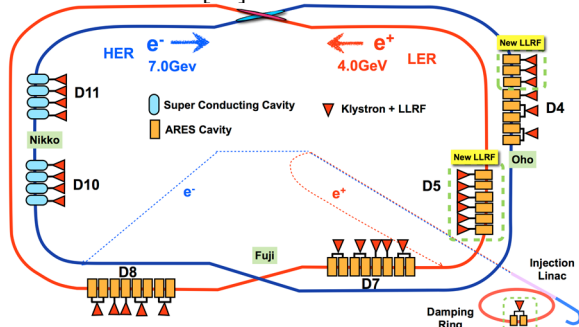


Figure 13: RF system layout for SuperKEKB Phase-1 and Phase-2. Nine LLRF stations were replaced with the new LLRF control system. The new LLRF control system for the damping ring was also newly installed.

In the present state, as shown in Fig. 13, the new digital LLRF control system is applied to 9 stations of ARES at Oho D4 and D5 in the main ring for SuperKEKB Phase-1 operation. Furthermore, the damping ring, which was constructed to reduce emittance of positron beam, is also operated with the new LLRF control system. All of new systems successfully worked well without serious problem in Phase-1 and Phase-2.

On the other hands, the other stations including SCC stations were still operated with existing (old analogue) LLRF control systems, which had been used in the KEKB operation. The digital LLRF control system for SCC will be developed in next year, and then the old ones will be replaced with new ones step by step to achieve the design current.

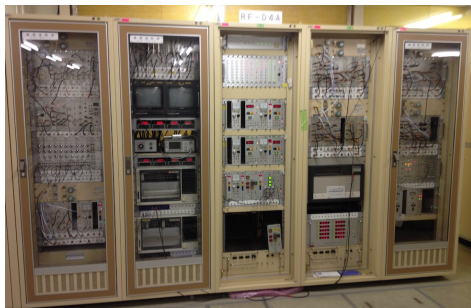
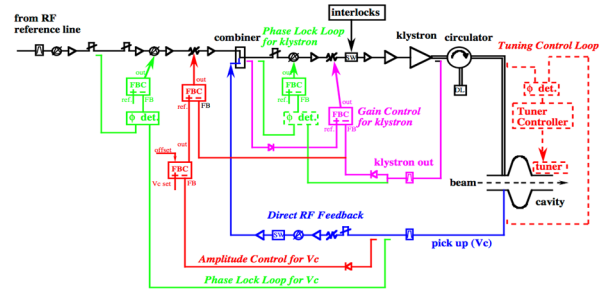


Figure 14: Old LLRF control system, which was used in KEKB operation, continues in use for SuperKEKB.



15: Block diagram of the old LLRF control system for the SCC RF station.

The existing analogue LLRF control systems are composed of combination of NIM standard analogue modules as shown in Fig. 14. Block diagram of the analogue system is shown in Fig. 15. It shows the cavity voltage (Vc amplitude and phase) regulation loop and the cavity tuner control with mechanical tuner and piezo actuator. Direct feedback method is also used in order to suppress coherent beam oscillations. For the detail of the analogue LLRF control system, Ref. [2]. These old systems are controlled remotely via CAMAC system. In the Phase-1 and Phase-2 operation, all systems also soundly worked as well as operated in the KEKB operation, although many old defective modules were replaced with spares in maintenance works.

Coupled Bunch Instabilities due to Acc. Mode

Excitation of longitudinal coupled bunch instabilities (LCBI) caused by an accelerating mode is one of the serious problems for high-current beam storage. In the KEKB operation, so called $\mu=-1$ mode of LCBI had been excited by accelerating cavities. Accordingly, as shown in Fig. 16, a feedback system of LCBI damper had been applied for suppression of the $\mu=-1$ mode in KEKB operation [21].

Block diagram of the -1 Mode Damping System

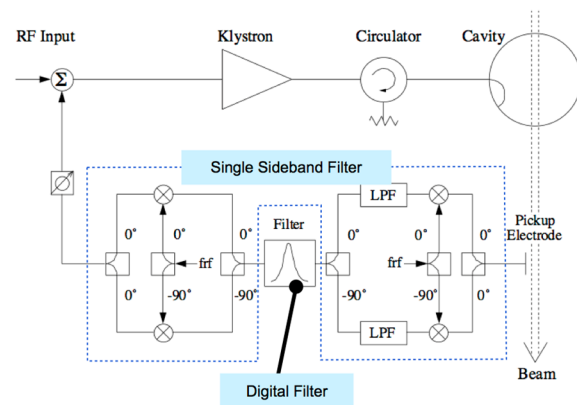


Figure 16: Block diagram of the $\mu=-1$ mode damping system, which had been used in KEKB operation. The $\mu=-1$ mode digital feedback selectively reduces impedance at the driving frequency.

For SuperKEKB upgrade which is aiming at 40-times higher luminosity than that of KEKB, LCBI will become more serious problem. Figure 17 shows estimation of the

growth rates of LCBI due to the accelerating mode plotted as function of the stored beam current for SuperKEKB HER (upper side) and LER (lower side). The black horizontal line shows the radiation-damping rate, which corresponds to threshold for the instabilities. At the design current, optimum (de-)tuning Δf for SC cavity will be approximately -44 kHz to compensate reactive component due to heavy beam loading, while the revolution frequency is about 100 kHz.

The dashed line in the Fig. 17 indicates the grow rate for case that one cavity is parked with -150-kHz detuning due to some troubles.

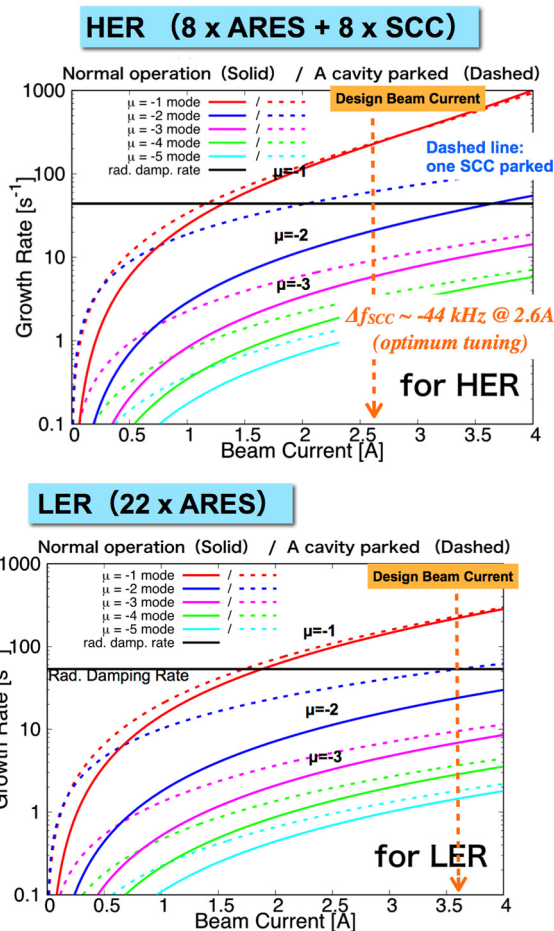


Figure 17: Estimation of the growth rates of LCBI due to the accelerating mode plotted as function of the stored beam current for SuperKEKB HER (upper side) and LER (lower side). Dashed line indicates the case of one cavity parked.

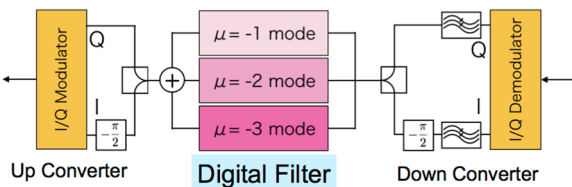


Figure 18: The new LCBI damper with new digital band-pass filters. The three LCBI modes can be treated in parallel, and the feedback parameters can be fine-tuned via EPICS, independently for each mode.

From the estimation of Fig. 17, it is predicted that $\mu = -2$

and -3 modes, in addition of $\mu = -1$ mode, will be excited for achievement of the design currents of SuperKEKB. Therefore, a new LCBI damper system, which can suppress these modes, was developed for SuperKEKB [22]. The digital band-pass filter of the new damper can filter the LCBI modes in parallel for feedback to damp LCBI as shown in Fig. 18, and its feedback parameters (phase, gain, mode frequency and etc.) can be fine-tuned via EPICS, independently for each mode. Independent phase tuning for the respective mode is very essential in our RF system, since the klystron bandwidth is not enough broad (~130 kHz) in comparison to the revolution frequency.

The performance of the new LCBI damper was demonstrated at 620-mA beam current in the Phase-2 operation. The result is shown in Fig. 19. We excite the $\mu = -2$ mode instability on purpose by detuning a SC cavity manually in HER (upper side of Fig. 19), and then the $\mu = -2$ mode could be successfully suppressed by applying the new LCBI damper to the LLRF feedback control for ARES cavity station (lower side of Fig. 19).

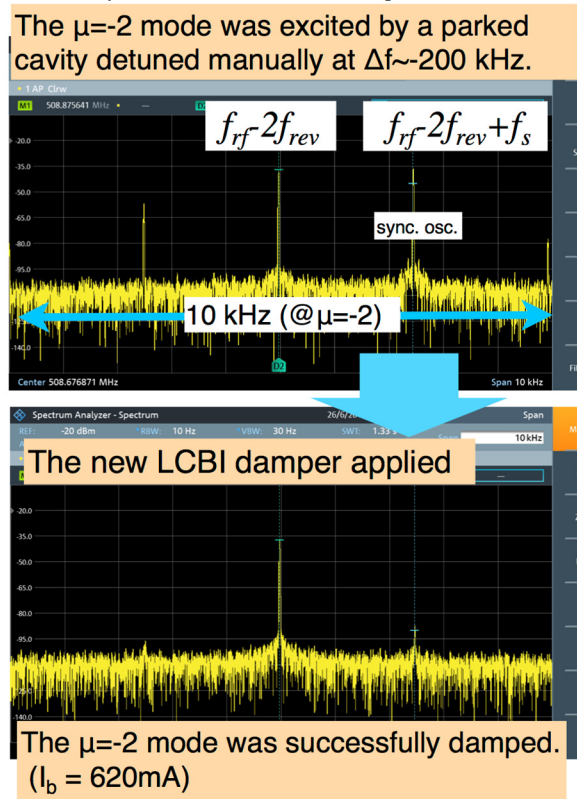


Figure 19: Demonstration of the new LCBI damper at 620-mA beam current in the Phase-2 operation. The $\mu = -2$ mode was excited by a parked SC cavity with manual detuning (upper side). Applying the new damper feedback suppressed the LCBI mode successfully (lower side).

SUMMARY

Against Large HOM Load

By development of a new calculation method with CST particle studio, the distribution of HOM load in the cavity module can be estimated. Calculated results showed the

loads of SBP and LBP ferrite dampers are not large. However the large HOM power is emitted out toward the next cavity. To reduce the emission power, additional SiC damper was studied. The simulation showed that the SiC damper can absorb enough emission power and the SiC of 240 mm length is suitable for our SCC module. The prototype SiC damper has been installed and successfully reduced the emission power to the downstream cavity.

Recovering Degraded Cavity

We have developed a horizontal HPR system with ultra-pure water. This system allows us to apply HPR to the cavity without disassembling the cryomodule. It means that many risks of re-assemble can be avoided. The HHPR was applied to three degraded cavities. The Qo values were successfully recovered in all cavities. Two cavity modules have been installed to the SuperKEKB ring. Another one is reserved as a spare cavity module. The technique of HHPR to recover the cavity performance has been established. We will apply HHPR to other cavities when they significantly degrade during the SuperKEKB operation.

LLRF Control Issues

A new low-level RF (LLRF) control system, which is based on recent digital architecture, was developed for the SuperKEKB upgrade in order to make highly accurate and flexible Vc contro. It was applied to nine klystron stations among about 30 stations for the normal conducting cavity called ARES in the main ring of SuperKEKB, and it worked successfully in the Phase-1 and Phase-2 operation. The digital LLRF control system for SC cavities will be developed in next year, and then old LLRF systems will be replaced with new ones step by step for achievement the design currents of SuperKEKB.

A flexible and fine-tuneable LCBI damper was newly developed for SuperKEKB. The new LBCI damper can suppress the $\mu=-1, 2$ and 3 modes cased by the accelerating mode in parallel, and the feedback parameters (phase, gain and mode frequency) can be controlled remotely in high resolution, independently for respective mode. The performance of the new LCBI damper was demonstrated in the Phase-2 operation. It also worked as expected, and it could suppress LCBIs successfully.

REFERENCES

- [1] T. Abe *et al.*, Prog. Theor. Exp. Phys. (2013) 03A001.
- [2] K. Akai *et al.*, "RF systems for the KEK B-Factor," *Nucl. Instrum. Meth. A* 499, 45–65 (2003)
- [3] T. Abe, *et al.*, "Performance and operation results of the RF systems at the KEK B-Factor," *Prog. Theor. Exp. Phys.* 2013, 03A006 (2013)
- [4] T. Furuya, *et al.*, "Superconducting Accelerating Cavity for KEK B-factory," *Proceedings of SRF1995*, CEA-Saclay, France, 1995, p. 729 (1995).
- [5] S. Mitsunobu, *et al.*, "High Power Test of the Input Coupler for KEKB SC Cavity," *Proceedings of SRF1995*, CEA-Saclay, France, 1995, p. 735 (1995).
- [6] Y. Yamazaki and T. Kageyama, "A Three-Cavity System which Suppresses the Coupled-Bunch Instability Associated with the Accelerating Mode," *Part. Accel.*, 44, 107 (1994)
- [7] T. Kageyama *et al.*, "The ARES cavity for KEKB," *Conf. Proc. of APAC98*, pp. 773-775 (1998)
- [8] K. Akai *et al.*, "Design Progress and Construction Status of SuperKEKB," *IPAC2012*, New Orleans, May 2012, TUPPR006, p. 1822 (2012); <http://accelconf.web.cern.ch/accelconf/IPAC2012/papers/tuppr006.pdf>
- [9] Y. Ohnishi, "Report on SuperKEKB Phase 2 Commissioning", *Proceedings of IPAC2018*, Vancouver, BC, Canada, 2018, MOXGB1, pp. 1-5.
- [10] A. Morita, "Status of SuperKEKB phase-2 commissioning", *ICHEP2018*, 877; <https://indico.cern.ch/event/686555/contributions/2962552/>
- [11] K. Akai, "SuperKEKB/Belle II Status", *ICHEP2018*, 1072; <https://indico.cern.ch/event/686555/contributions/3028068/>
- [12] Y. Morita *et al.*, "KEKB Superconducting Accelerating Cavities and Beam Studies for Super-KEKB", *Proc. of IPAC'10*, Kyoto, Japan, 2010, p.1536-1538.
- [13] T. Tajima, "Development of Higher-Order-Mode (HOM) Absorbers for KEKB Superconducting Cavities," *KEK Report 2000-10* (2000).
- [14] M. Nishiwaki *et al.*, "Developments of HOM Dampers for SuperKEKB Superconducting Cavity," *SRF2013*, Paris, Sept. 2013, TUP061, p. 1052 (2013); <http://ipnweb.in2p3.fr/srf2013/papers/thp061.pdf>
- [15] M. Nishiwaki *et al.*, "Developments of SiC Damper for SuperKEKB Superconducting Cavity", *Proc. of SRF2015*, Whistler, BC, Canada, 2015, p.1289-1292.
- [16] Y. Morita *et al.*, "Horizontal High Pressure Water Rinsing for Performance Recovery," *SRF2013*, Paris, Sept. 2013, TUP051, p. 521 (2013); <http://ipnweb.in2p3.fr/srf2013/papers/tup051.pdf>
- [17] Y. Kijima, *et al.*, "Conditioning of Input Couplers for KEKB Superconducting Cavities," *Proc. of the 10th Workshop on RF Superconductivity, KEK/JAERI*, Tsukuba, 6–11 September 2001, pp. 565-569 (2001).
- [18] T. Kobayashi *et al.*, "Development and Construction Status of New LLRF Control System for SuperKEKB", in *Proc. of IPAC'14*, paper WEPME071, pp. 2444-2446.
- [19] M. Ryoshi *et al.*, "LLRF Board in Micro-TCA Platform," *Proc. of the 7th Annual Meeting of Particle Acc. Society of Japan*, p. 668 (2010).
- [20] J. Odagiri *et al.*, "Fully Embedded EPICS-Based Control of Low Level RF System for SuperKEKB," *Proc. of IPAC'10*, p. 2686 (2010).
- [21] S. Yoshimoto *et al.*, "The -1 Mode Damping System for KEKB", *Proc. of The 14th Symposium on Accelerator Science and Technology*, 1P072 (2003)
- [22] K. Hirokawa *et al.*, "A New Damper for Coupled-Bunch Instabilities caused by the accelerating mode at SuperKEKB", *Proc. of LLRF2017*, arXiv:1803.10886; <https://arxiv.org/pdf/1803.10886.pdf>

CEPC CIVIL ENGINEERING DESIGN*

Yu Xiao[†], Yellow River Engineering Consulting Co., Ltd., 450003 Zhengzhou, China

Abstract

The CEPC is a circular e^+e^- collider located in a 100 km circumference underground tunnel. Preliminary site selection and the design of the CEPC civil engineering will be introduced in this paper.

INTRODUCTION

CEPC consists of a Collider, the injection system into the Collider whose main components are a Linac, a

Booster, and transport lines, and two large physics detectors. Civil construction houses all of the components of the CEPC and reserve space for SPPC, as illustrated in Fig. 1. The layout and construction of each part is determined by their geometric relationships, environmental conditions and safety considerations. Practicality, adaptability and operating efficiency are criteria to be carefully considered in the design of the civil construction.

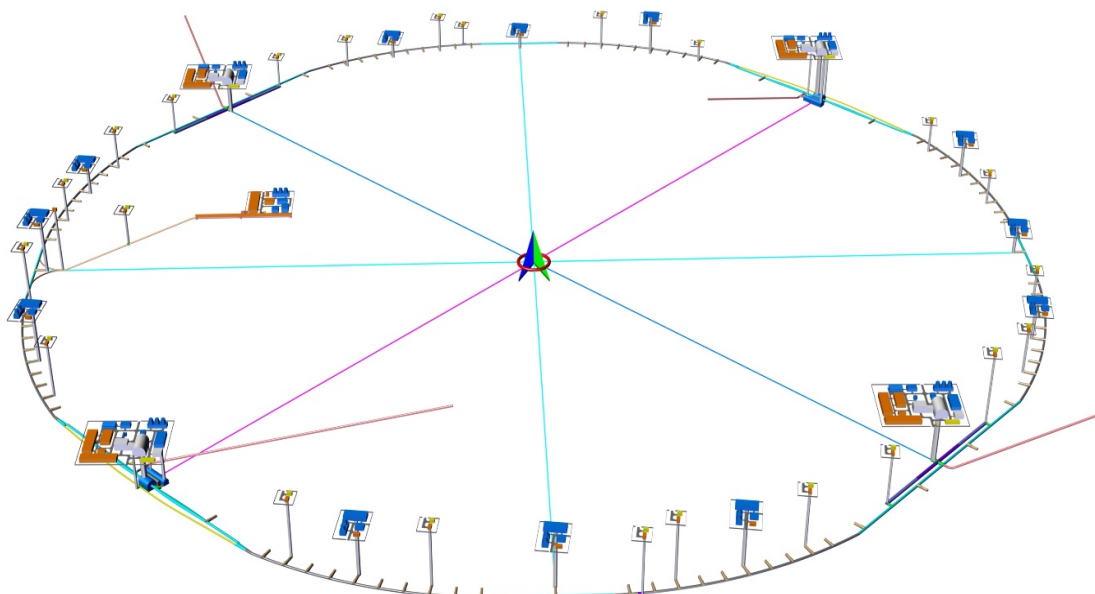


Figure 1: Layout of surface and underground CEPC structures.

The following defines the scope of work and the requirements to be met.

- The main tunnel to house the Collider and Booster synchrotrons, auxiliary tunnels for the Booster bypass and RF equipment, the Linac tunnel and equipment gallery and transport line tunnels. The main tunnel is 100 km in circumference and 100 m below ground.
- The experiment halls are 100 m below ground and span 30~40 m. There are additional chambers such as power source halls, cryogenics halls and spaces for the water cooling system, etc.
- There are accesses to the experiment halls, such as access tunnels, transport shafts, and emergency exits.
- There are ancillary structures at ground level, including structures near the shaft openings, structures to house substations and electric distribution, cryogenics rooms, and ventilation fan rooms.

- Space for staging the construction equipment and materials and dumping sites.
- Included in the project scope are related lifting equipment, conveyance, systems for electric supply, drainage, ventilation and air conditioning, communication, controls and monitoring, safety escape, and firefighting. The firefighting system includes fire alarms, hydrants, gas fire-extinguishing system, and a smoke exhaust system. Maintenance of these systems as well as their potential for future upgrades is fully considered in their design.

PRELIMINARY SITE SELECTION

Basic Principles of Site Selection

In the selection of the CEPC site, besides engineering

* Work supported by Yellow River Engineering Consulting Co., Ltd.
[†] email address: 328565909@qq.com

technology conditions such as topography and geology, the construction conditions that need to be considered include location, local government support, social and cultural environment, regional development and environmental impact. These external construction conditions may sometimes be the decisive factor in site selection.

Following are factors that should be considered in the site selection:

- Geography

The site should be sufficiently large and appropriately located to accommodate the future development of the IHEP. The site should promote the CEPC project and the construction of an international science city.

- Natural conditions

1. The structural stability conditions are good and avoid deep faults, motions and deformations that are recent in geologic time. Seismic peak acceleration is generally less than 0.10g.
2. Good rock conditions. Large area hard rock with stable lithology are suitable for construction of underground caverns.
3. No large height differences, mostly low mountains and hilly areas.
4. The quaternary overburden is not thick.
5. The permeability of rock is relatively low.
6. External dynamic geological phenomena are relatively small.

- Access conditions

In order to minimize capital costs and accelerate the progress in the initial stages of the construction, the site should be located where access is convenient.

- Environmental factors

Few environmental impact problems and no environment sensitive zones should be involved, such as nature preserves, parks, military areas, or other environmental constraints.

- Good construction conditions and related economic factors

Brief Introduction of Each Potential Site

A preliminary study of geological conditions for CEPC's potential site location was carried out in Hebei, Guangdong, Shaanxi, Jiangsu, and Zhejiang provinces. The geological survey of site selection in the conceptual design stage was carried out in the Funing site (Hebei Province), in the site of the Shen-Shan Special Cooperation zone (Guangdong Province), and in the site of Huangling area (Shaanxi province).

The Funing site is located in the Funing District, Qinhuangdao City of Hebei Province, Beidaihe District, Changli and Lulong Counties. This is a hilly area, with elevations of 0 m to 600 m. The main strata are Archaean gneiss, Mesozoic magmatic rocks, volcanism from the Yanshan period, and some Mesozoic sand shale. The rock is mainly hard without thick overburden, and has a basic seismic intensity of degree VII. The site conditions are suitable for construction of large

underground caverns and tunnels. The depths of the underground caverns do not vary a great deal.

The Shen-Shan site is located in the Shen-Shan Special Cooperation zone, Haifeng and Huidong Counties of Guangdong Province. The landform is dominated by low mountain areas with elevations of 20 m to 800 m. The main strata consist of Mesozoic volcano rock and sand-mudstone, granite of the Yanshan period, and a small amount of Cenozoic shaly glutenite. These rocks are mainly hard with fracture structure, no thick overburden, and the basic seismic intensity degree VI~VII. Some of the caverns will be quite deep and require a long shaft. The layout is relatively complex and difficult to construct.

The Huangling area site is located in Huangling County and Luochuan County (Yan'an City, Shanxi Province), Yijun County (Tongchuan City), and Baishui County (Weinan City). The landform belongs to a plateau gully region with elevations of 600 m to 1600 m. The stratum on the horizontal layer and its lithology is Mesozoic Triassic terrestrial clastic rock, with 100 m to 150 m of overlying loess. The rocks are generally of moderate hardness with simple structure, and the basic seismic intensity is mainly of degree VI. The buried depth of underground caverns and the shaft depths vary considerably. The layout for construction is relatively easy, and the construction work of moderate difficulty.

In the conceptual design, Funing was selected as representative site.

PROJECT LAYOUT AND MAIN STRUCTURE

General Layout Principles and Requirements

- The layout, length and buried depth of the tunnel meet the needs of the accelerator and the detectors.
- The operation needs to be secure, with easy management and convenient traffic flow.
- The geologic structure around the circumference of the tunnel is simple and the hydrogeological conditions are suitable for construction.
- Good water and electricity supply conditions.
- Shafts and adits provide entrance to the tunnel. Shafts will avoid densely populated areas. Auxiliary facilities, such as cooling towers and substations are close to the access shafts.
- The layout must meet the requirements for transportation and installation of experimental equipment.
- The number and length of construction adits should be determined by the terrain and geologic conditions, the construction methods and the external transportation situation. It will help to balance and optimize the required person-hours and time requirements among tunnel sections.
- Minimize the impact on the local ecology. The surface facilities should avoid existing buildings.

- Meet the requirements of government regulations and norms.

Layout of the Underground Structures

Figure 2 and 3 show the 100 km circumference tunnel in plan and profile. The tunnel has an inverted U-shape, of 6.00 m width 5.00 m height. Considering the relatively thick overburden of the Yanghe River alluvial plain in the southeast part of the site, point B, through

which the tunnel passes the Yinma River, is designated as the lowest tunnel point, and point A, opposite to point B along the diameter, is designated as the highest tunnel point. The longitudinal slope of the tunnel is 0.3% from topology as well as drainage requirements during construction and operation. Surrounding rocks of the tunnel consist of granite, gneiss, schist and tuff and are mainly of Class II ~ III.

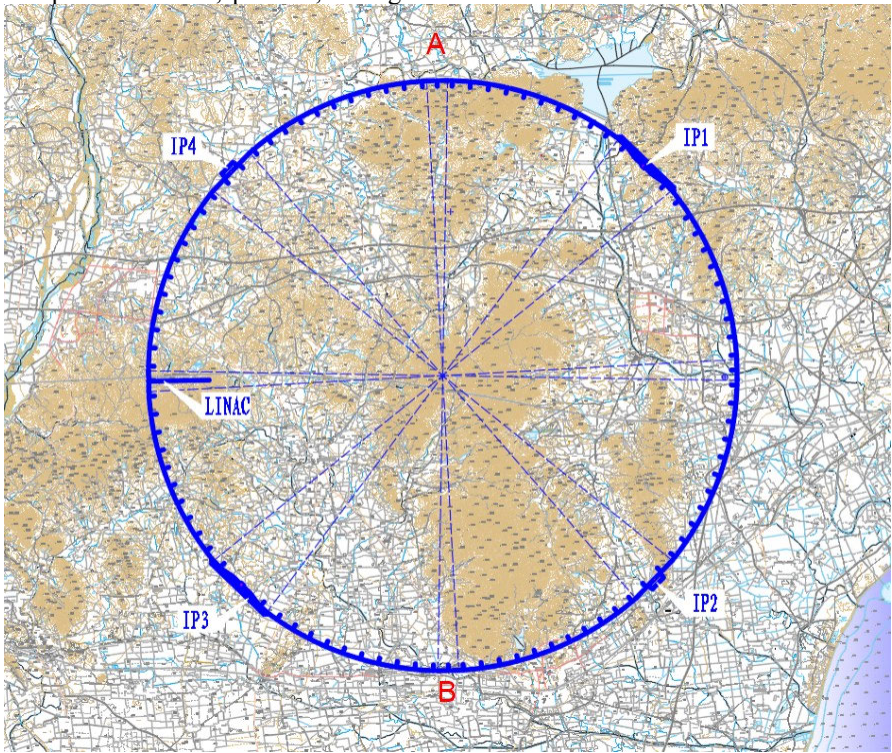


Figure 2: Layout Plan of the CEPC Tunnel.

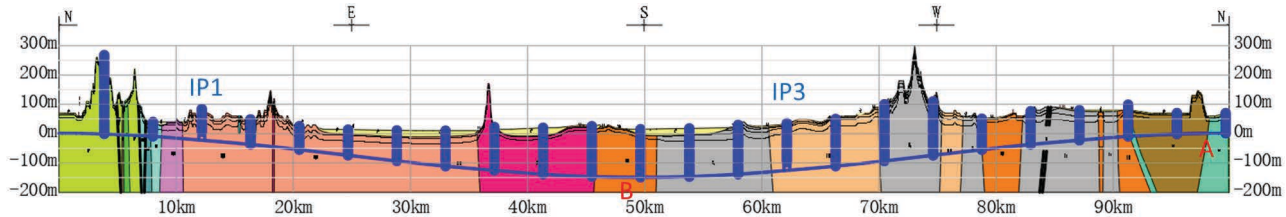


Figure 3: Longitudinal Profile of the CEPC Tunnel.

Underground structures consist of the following as shown in Fig. 4:

- Collider ring tunnel (L=99.67 km);
- Experiment halls (includes main and service caverns): IP1 and IP3 are experiment halls for CEPC, and IP2 and IP4 are future experiment halls for SPPC;
- Linac and BTL tunnels: Linac tunnel, klystron gallery, hall for the damping ring, BTL tunnel and its branch tunnels;
- Auxiliary tunnels: RF auxiliary tunnels, Booster bypass tunnels in the IR and many short auxiliary tunnels;

- Vertical shafts in experiment halls and RF zones and along the ring tunnel for personnel and delivery of equipment to tunnels and halls, and for providing channels for ventilation, refrigeration, cooling and control and monitoring lines.

Layout of the Surface Structures

All surface structures shall be as close to the access shafts as possible. In these buildings are located water cooling facilities, low-temperature facilities, ventilation systems, air compression systems, power transformer substations and electrical transmission and distribution

and DC power supplies. The total area of surface structures is 140450m².

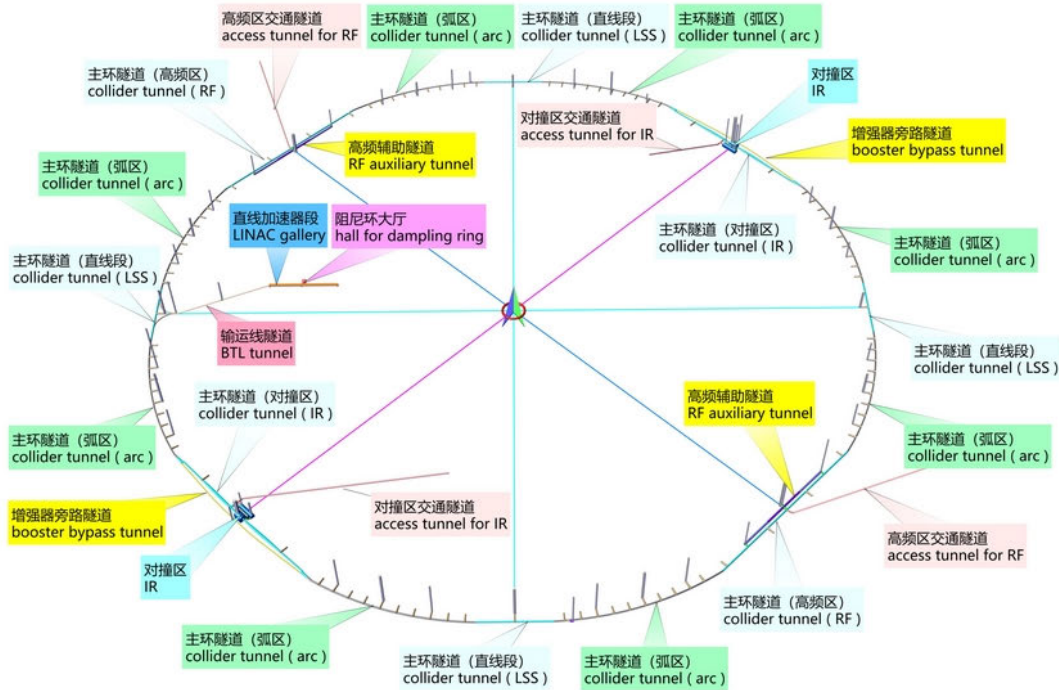


Figure 4: Underground Structure Layouts.

Design of the Underground Structures

- Tunnel shape

Circular, inverted-U, and horseshoe shapes have all been considered for the tunnel cross section. If the TBM method is used, circular will be selected (Fig. 5). If the drill-blast tunnelling method is used, the dimensions will be determined according to construction and

transportation requirements during construction, as well as equipment layout and accessibility requirements during installation and operation. The tunnel shape and construction method will be determined through comprehensive technical and economic comparisons. The inverted U-shape (Fig. 6) is selected at this stage.

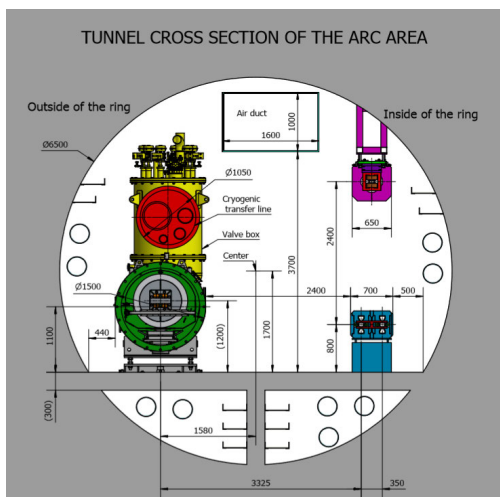


Figure 5: Circular option in the Collider arc section.

- Tunnel lining and waterproofing

Waterproofing of the underground caverns is Grade I. Support and lining structures shall meet structural requirements and waterproof requirements. There are the following types of linings: bolt-shotcrete, reinforced

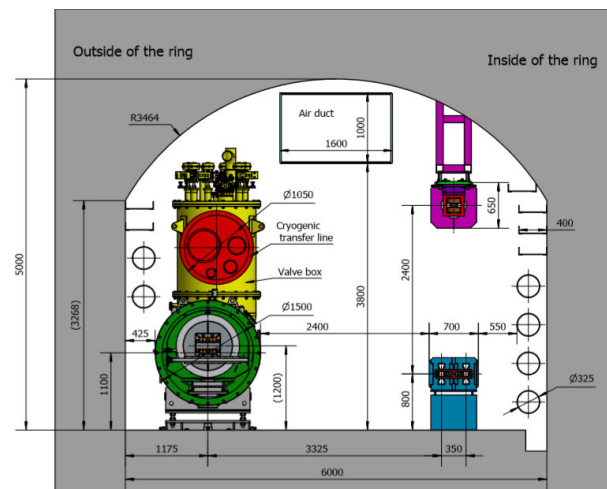


Figure 6: Inverted U-shape option in the Collider arc section.

concrete, steel fiber concrete and steel structure. Waterproof materials includes waterproof membrane, waterproof coating, rigid waterproof material and concrete admixture. Since the lining structure and waterproof material has a significant economic impact,

the types of lining structure and waterproof material will be determined through comprehensive technical and economic comparison according to structural and waterproof requirements. At this stage, the following types are considered: drain holes + profiled steel sheets for the crown in Class II surrounding rocks, drain holes + profiled steel sheets for the crown + damp-proof decorative partitions in Class III surrounding rocks, waterproof membranes / boards / coating + 25~50 cm thick waterproof concrete lining in Class IV~V surrounding rocks.

- Shaft structure

Many shafts are distributed around the tunnels. Their size is determined by their functions. For example, the dimension of the transport shaft is determined by the size of the equipment to be transported, pipeline layout, evacuation passage and thickness required for support. The dimension of the shaft for construction and ventilation purposes is determined by construction ventilation requirements.

Sprayed anchor + reinforced concrete lining is used for shaft support. The thickness of shotcrete and lining concrete is determined by shaft diameter and depth, surrounding rock type, groundwater and other factors.

- Experiment halls

The span is large; class I and II surrounding rocks are selected as much as possible for the cavern locations. The region of large geological tectonic belts, fault fracture zones, joint fissure development zones, high in-situ stress zones, goaf zones (where muck has been removed and the space filled with waste) and copious groundwater shall be avoided. The cavern depths should be determined by comprehensive analysis of the lithology, rock mass completeness, weathering unloading degree, in-situ stress magnitude, groundwater situation, construction conditions and experimental requirements and other factors. In general, the overburden thickness should not be less than twice the excavation width of the cavern.

A combination of flexible support and reinforced concrete lining is used due to the small depth of the experiment halls and the strict waterproof requirement. Flexible support is composed of one or several combinations of shotcrete, rock bolt, and anchor cable.

CONSTRUCTION SCHEDULE

The shafts along the tunnel could be utilized for drill and blast construction with multiple working faces proceeding at the same time. With comprehensive comparison from construction technology, construction period and project cost, the drill and blast method is recommended at present. The total construction period is 54 months, including 8 months for construction preparation, 43 months for construction of main structures and 3 months for completion.

The critical path is as follows: construction preparation (8 months, including land acquisition and resettlement, establishing supplies of water, power and compressed air, road connection and communications and site levelling.) → construction of vertical shafts (5 months) → tunnel excavation (24 months) → tunnel lining and waterproofing (10 months) → installation of ventilation equipment and access equipment of the shaft (4 months) → completion (3 months). The construction of surface structures is carried out as the project progresses, and is carried out concurrently with the underground work, so that will not lengthen the construction time line.

FCC-ee OPERATION MODEL, AVAILABILITY & PERFORMANCE*

Andrea Apollonio, Michael Benedikt, Olivier Brunner, Arto Niemi, Jörg Wenninger, Frank Zimmermann[†], CERN, Geneva, Switzerland; Stephen Myers, ADAM SA, Meyrin, Switzerland; Yoshihiro Funakoshi, Katsunobu Oide, KEK, Tsukuba, Japan; John Seeman, SLAC, Stanford, U.S.A.; Qing Qin, IHEP Beijing, P.R. China; Catia Milardi, INFN Frascati, Italy

Abstract

This document discusses the machine parameters and expected luminosity performance for the proposed future circular lepton collider FCC-ee. Particular emphasis is put on availability, physics run time, and efficiency. Key performance assumptions are compared with the operational experience of several past and present colliders including their injectors — LHC, LEP/LEP-2, PEP-II, KEKB, BEPCII, DAFNE, SLC and the SPS complex.

INTRODUCTION

In the following, we describe the goals and assumptions for the FCC-ee operation plan, and we confront our assumptions with the corresponding statistical information from several similar colliders, especially KEKB and PEP-II.

GOALS, MODES, PARAMETERS

The baseline FCC-ee features four modes of operation: (1) on the Z pole, (2) at the WW threshold, (3) at the HZ production peak, and (4) at the $t\bar{t}$ threshold. Running modes (1)–(3) are combined into a ‘phase 1’. Running mode (4) implies a major reconfiguration and is called ‘phase 2’.

The physics goals of FCC-ee require the following integrated luminosities for the different operation modes [1, 2], summed over two interaction points (IPs): 150 ab^{-1} at and around the Z pole (88, 91, 94 GeV centre-of-mass energy); 10 ab^{-1} at the W^+W^- threshold (~ 161 GeV with a \pm few GeV scan); 5 ab^{-1} at the HZ maximum (~ 240 GeV); 1.5 ab^{-1} at and above the $t\bar{t}$ threshold (a few 100 fb^{-1} with a scan from 340 to 350 GeV, and the remainder at 365 GeV).

FCC-ee machine parameters for all modes of operation are summarized in Table 1.

ESTIMATING ANNUAL PERFORMANCE

The annual luminosity estimates for FCC-ee at each mode of operation are derived from three parameters:

- Nominal luminosity L : taken to be 10–15% lower than the luminosity simulated for the baseline beam parameters. This nominal luminosity is considered from the third year onward in phase 1 (Z pole), and from the second year in phase 2 ($t\bar{t}$ threshold). The luminosity for the first and second year of phase 1 and for the first year of phase 2 are assumed to be smaller, on average, by

another factor or two, in order to account for a learning period during initial operation.

- It is assumed that 185 days per year are scheduled for physics. These 185 days are obtained by subtracting from one year (365 days), 17 weeks of extended winter shutdown (120 days), 30 days of annual commissioning, 20 days for machine development, and 11 days for technical stops.
- Nominal luminosity L and time for physics T are converted into integrated luminosity L_{int} via an ‘efficiency factor’ E , according to

$$L_{\text{int}} = ETL. \quad (1)$$

The efficiency factor E is an empirical factor, whose value can be extrapolated from other similar machines, or by simulations with average failure rate and average downtime. Thanks to the top-up mode of operation, it is expected that E will be about five percent lower than the availability of the collider complex. We assume an availability of at least 80% and, thereby, a corresponding efficiency $E \geq 75\%$.

The assumed 17 weeks of average winter shutdown are longer than the time required for the installation and RF commissioning of new cryomodules (see Table 2 below). Also the 20 days per year allocated for machine development (MD) are higher than the corresponding number for LEP (e.g. in the year 2000 only 5 days of LEP MDs were scheduled [3]).

CONFIGURATIONS AND SHUTDOWNS

The machine operation is expected to start with Z running, similar to LEP-1, as this requires the lowest RF voltage, implying the smallest amount of RF installation and the associated minimum beam impedance.

The changes in the machine configuration required between the Z, W and H running, can be implemented during the successive winter shutdowns.

The length of these FCC-ee winter shutdowns is likely to be dominated by the installation and RF commissioning of new cryomodules in preparing for, or during transition to, the next running modes. Considering only a single cryomodule transport per working day, the minimum total length of the winter shutdown is estimated as

$$n_{\text{working days}} = n_{\text{cryomodule}} + 10 + 10 + 25, \quad (2)$$

where the first 10 days refer to the end of the installation, the second 10 days to the cool down, and the last 25 days to

* This work was supported by the European Commission under the HORIZON 2020 project ARIES no. 730871.

[†] frank.zimmermann@cern.ch

Table 3: Peak luminosity per IP, total luminosity per year (two IPs), luminosity target, and run time for each FCC-ee working point

mode	luminosity [$\text{nb}^{-1}\text{s}^{-1}$]	tot. lumin. [ab^{-1}] / yr	goal [ab^{-1}]	time [yr]
phase 1				
Z two years	1000	24		2
Z other years	2000	48	150	2
W	250	6	10	1–2
H	70	1.7	5	3
phase 2				
RF reconfiguration				1
$t\bar{t}$ 350 GeV	8	0.20	0.2	1
$t\bar{t}$ 365 GeV	14	0.34	1.5	4

shutdown. For this reason, a one-year shutdown is proposed for this final reconfiguration.

The first year of the phase 2 operation is performed at a beam energy of about 175 GeV, requiring somewhat fewer RF cavities than the later operation at 182.5 GeV.

RUN PARAMETERS AND SCHEDULE

Table 3 presents the nominal luminosity, integrated luminosity per year, physics goals and the resulting running time for the different modes of operation, based on the assumptions laid out above. This yields the time line shown in Fig. 1.

Phase 1 comprises two years of running-in and the full Z pole operation, W threshold scans, and Higgs production modes. It can be accomplished within 8 years. After one additional year of shutdown and staging of the RF, operational phase 2, covering the top quark studies, would last for another 5 years. Therefore, with 185 physics days per year, a physics efficiency of 75%, and the baseline peak luminosities (which are 10% lower than the values reached in simulations), the FCC-ee total run time amounts to 15 years.

The aforementioned assumptions were evoked to arrive at the third and fifth columns of Table 3. We will now scrutinize these assumptions, by comparing with the operational performance of several similar machines.

BENCHMARKING

Achieved Luminosity versus Design Luminosity

LEP was a collider similar to FCC-ee, but operating with only a few bunches and no top-up injection, at significantly lower luminosity. In the first year of LEP-1, with 45.6 GeV beam energy, the current per bunch exceeded the design, the design total current was attained in a single beam, but the total design current in 2 beams was NOT achieved. The peak luminosity in the first year of operation was 50% of design. The vertical beam-beam tune shift (V) was less than 50% of design. The two main reasons why not all the design

values could be achieved in the first year were the limitation of the total beam current and the beam-beam tune shift [4]. Looking at the full 12 years of operating LEP [5], the design luminosity was surpassed in 1993 which was the fourth year of operation. LEP-1 achieved 8.4 mA in both beams, higher than the 6 mA design current. It eventually achieved a luminosity of $3.4 \times 10^{31} \text{ cm}^{-2}\text{s}^{-1}$, while the design had been $1.6 \times 10^{31} \text{ cm}^{-2}\text{s}^{-1}$. However this was accomplished with 8 bunches whereas the design had been for 4 bunches. With the design of 4 bunches per beam LEP never reached the design beam-beam tune shift, mostly due to the lower energy (45.6 GeV) and the correspondingly slower transverse damping (confirmed by beam-beam simulations), while the design energy had been 55 GeV [6] (an energy at which LEP never operated since the Z mass was lower than expected during the design). With the faster transverse damping at higher energy for LEP-2, limitations from the beam-beam effect disappeared. LEP-2 exceeded its design luminosity at 95 GeV ($2.7 \times 10^{31} \text{ cm}^{-2}\text{s}^{-1}$) within a few months during the first year of operation. It achieved a total beam current of 6.2 mA, and a luminosity of $1 \times 10^{32} \text{ cm}^{-2}\text{s}^{-1}$, about 4 times higher than the design [6]. It is interesting that LEP-1 and LEP-2 changed the optics almost every year. At highest energy there was little margin in the LEP RF system. A simultaneous trip of more than two klystrons would lose the beam. The cavity gradients were also pushed to their limits. In 1998 LEP operation, the biggest cause of RF trips was “cavity maximum field” interlocks [7]. Via a number of measures the reliability of the LEP RF system was continually improved so that the impact of RF trips on collider operation became almost unnoticeable [7]. The machine availability of LEP exceeded 85%; in several years it was higher than 90% [3, 8–10].

PEP-II was an asymmetric B factory, colliding a 3.1 GeV positron beam and a 9 GeV electron beams. Beam currents reached 3212 mA for the positrons and 2069 mA for the electrons. The PEP-II design luminosity was $3 \times 10^{33} \text{ cm}^{-2}\text{s}^{-1}$, but it ultimately achieved $1.2 \times 10^{34} \text{ cm}^{-2}\text{s}^{-1}$. In 2004 PEP-II switched to a top-up injection mode of operation, which significantly increased its integrated daily luminosity. The design integrated luminosity per day had been 130/pb/day. A much higher value of up to 911/pb/day was actually delivered. The top-up mode greatly improved the efficiency, while it did not seem to negatively affect the availability [11]. PEP-II surpassed its design luminosity after 1.5 years of operation, and ultimately reached 4 times the design value [12].

KEKB equally was an asymmetric B factory. It collided 3.5 GeV positrons and 8.0 GeV electrons. Beam currents of 1637 mA (positrons) and 1188 mA (electrons) were reached. The design luminosity was $1.0 \times 10^{34} \text{ cm}^{-2}\text{s}^{-1}$. A peak luminosity of $2.11 \times 10^{34} \text{ cm}^{-2}\text{s}^{-1}$ was achieved. KEBB delivered up to 1.479/fb/day. KEBB, too, operated with continuous top-up injection from the year 2004 onwards. KEBB reached its design luminosity (which was 3 times higher than the design value of PEP-II) 3.5 years after start

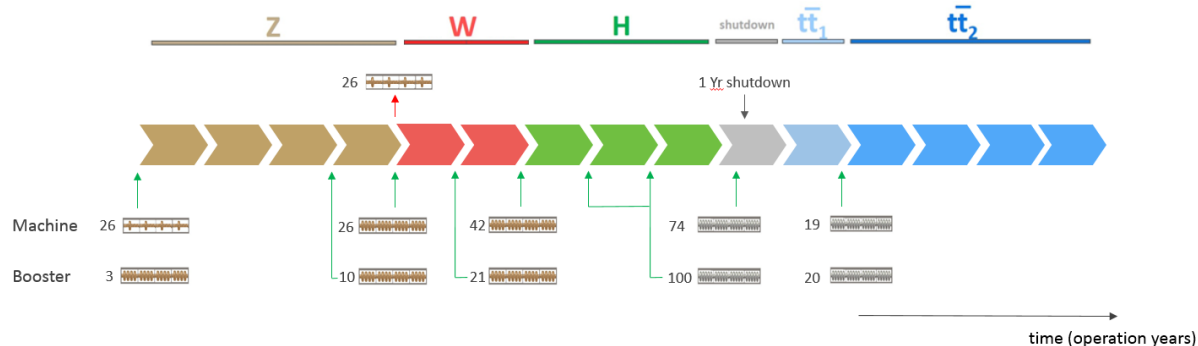


Figure 1: FCC-ee operation time line. The bottom part indicates the number of cryomodules to be installed in the collider and booster, respectively, during the various shutdown periods.

of operation and ultimately exceeded the design luminosity by more than a factor of two [13–15].

Figure 2 shows the daily peak luminosity as a function of day for four consecutive years, 2006–2009. The peak luminosity per day is lower at the start of a run, after longer shut-down periods or hardware interventions, and during periods of beam tuning and machine studies.

From these data we can derive an absolute peak luminosity during a fiscal year, and also an average peak luminosity during a year. These two peak luminosity values are compared in Fig. 3. The difference is of order 30%.

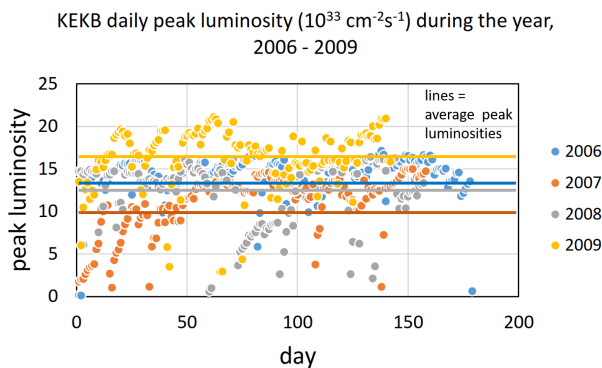


Figure 2: Daily peak luminosity of KEKB as a function of day in the physics run, starting on 1 April, during four consecutive Japanese fiscal years.

BEPCII is a double-ring collider, which runs for high-energy physics (HEP) about 6 months per year, and, in a different configuration, as a light source (BSF) for another two times of 1.5 months, scheduled before and after the HEP run, respectively. The beam energy can be varied from 1.0 to 2.3 GeV. In 2016 BEPCII achieved its design luminosity of $1.0 \times 10^{33} \text{ cm}^{-2} \text{ s}^{-1}$ at 1.89 GeV beam energy, with a current of 850 mA per beam. For the BEPC/BSF synchrotron-radiation operation top up was successfully implemented in November 2015. The availability which on average was already well above 90% increased even further. In 2019 top-up injection will also be implemented for the collider mode of operation.

KEKB annual peak and average daily peak luminosity ($10^{33} \text{ cm}^{-2} \text{ s}^{-1}$) vs JFY

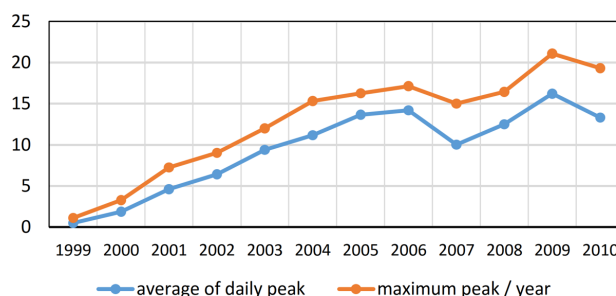


Figure 3: Maximum peak luminosity and average daily peak luminosity of KEKB as a function of Japanese fiscal year.

DAΦNE is an e^+e^- double-ring collider, including injection system, which operates at the c.m. energy of the ϕ -meson resonance (1.02 GeV). DAΦNE often changes the particle detector and corresponding IR magnetic-field configuration. DAΦNE achieved 90% of its design maximum luminosity of $5.3 \times 10^{32} \text{ cm}^{-2} \text{ s}^{-1}$ after about 8 years of operation, and after switching to the crab-waist collision scheme. Typical peak currents are 1500–1700 mA for the electrons and 1200 mA for the positrons, the latter limited by electron-cloud effects.

Run Time

Figure 4 compares the annual days of physics running at the aforementioned lepton-positron colliders, for years where data were easily available. The number of 185 days, assumed for FCC-ee, appears like a good average value. It should be noted that the run lengths of the past colliders were often dictated by the availability of financial budget for operation, and not by any technical or schedule constraints. This is true in particular for PEP-II and KEKB. In addition, for PEP-II the 2005 run length was severely reduced by a SLAC lab-wide investigation, review, and remediation of safety concerns, and re-validation of all systems and procedures.

Every year during the winter shutdown LEP prepared for major changes in the configuration (pretzel schemes, bunch trains, installation of sc cavities etc.). Nevertheless in the

years 1999 and 2000 more than 185 days were scheduled for physics production.

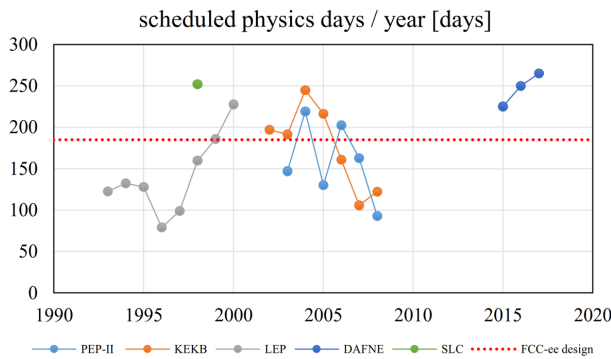


Figure 4: Days of the year dedicated to physics at various past and present e^+e^- colliders.

Availability

Figure 5 shows the availability of the aforementioned lepton-positron colliders, again for the years where data were easily available. All circular e^+e^- colliders operating over the past twenty years (LEP, KEKB, PEP-II, DAFNE, BEPCII) achieved hardware availabilities well above 80%, and some even above 90%. For KEKB, a degraded availability in the year 2005 was due to technical problems at the BELLE detector, unrelated to the KEKB accelerator. In 2007, the KEKB crab cavities were being commissioned.

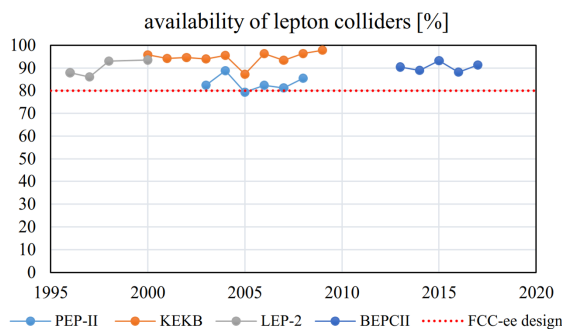


Figure 5: Availability of various past and present e^+e^- colliders.

Through the year 2000, the LEP injector complex (PS and SPS) was operating with proton and ion beams in parallel to LEP e^+e^- operation. Since 1995, the CERN SPS including the entire PS chain delivered beams for physics with an efficiency close to, or above, 80% every year [16], as is illustrated in Fig. 6. The “physics efficiency” of Fig. 6 is a more stringent figure-of-merit than the hardware availability.

The SPS together with the entire PS chain for both proton and ion operation could be argued to be at least of similar complexity as the FCC-ee injector. SPS and PS complex include the proton and ion linacs, the PS booster, LEIR, the PS proper and, of course, the SPS itself, all continually cycled. For comparison, the FCC-ee injector complex comprises a

linac, a positron damping ring, a pre-booster, and a main booster, also all cycled. In 2017 and 2018, even the 27 km LHC, with 1600 independent magnet circuits, together with its entire injector chain, has achieved an availability of about 80%. It may also be worth noting that the peak bending fields in the LHC and SPS are 8 and 2 T, respectively, to be contrasted with a peak field of at most 0.05 T in the FCC-ee and its booster.

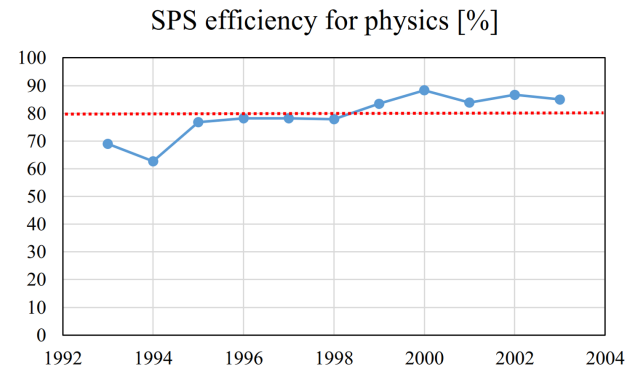


Figure 6: CERN SPS efficiency for physics, including the PS complex [16]. The red dashed line indicates the target availability of FCC-ee.

Efficiency

In the case of FCC-ee, no time is lost for acceleration and the efficiency only reflects the relative downtime due to technical problems and associated re-filling and recovery time. Therefore, the efficiency will be roughly equal to the hardware availability, taken to be at least 80%, minus ~5% reduction for beam recovery after a failure, assuming (for the Z pole operation) the equivalent of three failures leading to complete beam loss per day on average. For example, after a hardware failure in the collider rings proper, on the Z pole it will take close to 20 minutes (or 1.4% of a day) to refill the collider from zero to nominal beam current. For the higher energy modes of operation the refilling time can be up to ten times shorter.

The assumed efficiency value of 75% with respect to the daily peak luminosity is lower than achieved with top-up injection at KEKB and PEP-II. Figure 7 presents example evolutions over 24 h of beam currents and luminosity, during PEP-II operation with on-energy top-up injection in 2004 and in 2008, respectively. Beam currents and luminosity are constant, except for a few short interruptions due to hardware failures. The performance of KEKB looked quite similar, as is illustrated in Fig. 8, with examples from 2005 and 2009.

Comparing this performance model with LEP operation, the main difference lies in the on-energy top-up injection scheme, without any luminosity decay, and in the implied absence of ramp-down and acceleration.

The value of efficiency depends on the choice of the “nominal luminosity”. We can illustrate this with some examples. Several possible choices are plausible. As a first example, in Fig. 9, we present the efficiency of KEKB, PEP-II, LEP

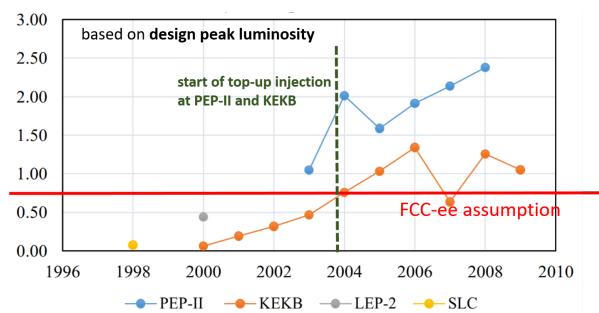


Figure 10: Efficiency calculated from the design luminosity.

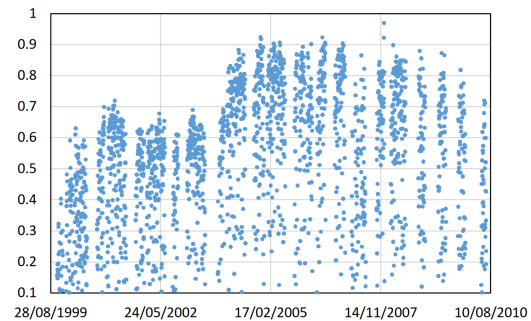


Figure 11: KEKB day-by-day efficiency based on the day-by-day peak and integrated luminosity values.

Interval	Count
≤ 0.1	145
$(0.1, 0.15]$	40
$(0.15, 0.2]$	55
$(0.2, 0.25]$	60
$(0.25, 0.3]$	50
$(0.3, 0.35]$	48
$(0.35, 0.4]$	55
$(0.4, 0.45]$	85
$(0.45, 0.5]$	82
$(0.5, 0.55]$	118
$(0.55, 0.6]$	140
$(0.6, 0.65]$	115
$(0.65, 0.7]$	48
$(0.7, 0.75]$	5
$(0.75, 0.8]$	1

based on "actual" peak luminosity in each year

FCC-ee assumption

PEP-II KEKB LEP-2 SLC

bin	count
<=0.1	200
(0.1, 0.15]	15
(0.15, 0.2]	25
(0.2, 0.25]	38
(0.25, 0.3]	50
(0.3, 0.35]	68
(0.35, 0.4]	35
(0.4, 0.45]	50
(0.45, 0.5]	48
(0.5, 0.55]	68
(0.55, 0.6]	85
(0.6, 0.65]	98
(0.65, 0.7]	135
(0.7, 0.75]	140
(0.75, 0.8]	175
(0.8, 0.85]	140
(0.85, 0.9]	80
(0.9, 0.95]	10
(0.95, 1]	0

Figure 13: Histogram of KEKB day-by-day efficiency values in units of fraction for the time period with top-up injection, from 2004 to 2010; including shutdowns, technical stops, beam commissioning periods, and machine studies.

CONCLUSIONS

In summary, the assumed annual physics run time of 185 days, a hardware availability of at least 80%, a corresponding physics efficiency of 75%, and the projected annual luminosities of FCC-ee appear solid, in view of the experience at several circular lepton colliders over the past 30 years. Even surpassing the baseline values for both peak and integrated luminosity appears a realistic possibility (see appendix).

ACKNOWLEDGEMENT

We thank G. Arduini and M. Giovannozzi for a careful reading of the manuscript.

APPENDIX: BEYOND THE BASELINE

Similar to the experience at LEP/LEP-2, PEP-II, and KEKB, also the FCC-ee could reach luminosity values higher than the design baseline. This could be accomplished as follows:

- The quoted baseline luminosity is conservatively chosen to be 10–15% lower than obtained in simulations.
- Other beam parameter sets, more challenging for the RF system, exist which would allow for higher luminosity.
- The vertical emittance could be pushed down further. The baseline has a small value, but it is far (more than a factor of 10) from the intrinsic limits and features a larger emittance ratio $\varepsilon_y/\varepsilon_x$ than achieved at some of the modern storage-ring light sources.
- The tolerated minimum beam lifetime is longer than what could be supported by the top-up injector complex. Operating with lower lifetime would allow for higher luminosity.
- Assuming two years or one year, respectively, in phase 1 and phase 2 at half the design luminosity could be too pessimistic. LEP-2 and PEP-II reached their design luminosity more quickly.

REFERENCES

- [1] M. Bicer, “First look at the physics case of TLEP,” *Journal of High Energy Physics*, (2014) 164.
- [2] P. Janot, “Perspectives for Future Circular Colliders (1/3)”, CERN Academic Training, Oct 11, CERN, Geneva. Switzerland, 11 October 2017 (2017).

- [3] B. Desforges and A. Lasseur, “2000 SPS & LEP Machine Statistics,” CERN SL-Note-00-060 OP.
- [4] S. Myers, “First Year of LEP Operation,” John Adams Lecture 26 November 1990, Yellow Report CERN 91-08 (1991).
- [5] S. Myers, “The LEP Machine,” *LEP Fest 2000*, October 2000 (2000).
- [6] R. Aßmann, M. Lamont, S. Myers, “A brief history of the LEP collider”, *Nuclear Physics B - Proceedings Supplements*, Vol. 109, 2–3 (2002) pp. 17–31.
- [7] A. Butterworth, “RF Reliability and Operation,” Proc. 9th LEP-SPS Performance Workshop, Chamonix, France, 25–29 January 1999, CERN-OPEN-99-100 (1999) pp. 189–192.
- [8] M. Colin, G. Cultrut, B. Desforges, “1996 SPS & LEP Machine Statistics,” CERN SL-Note 97-01 OP (1997).
- [9] M. Colin, G. Cultrut, B. Desforges, “1997 SPS & LEP Machine Statistics,” CERN SL-Note 97-79 OP (1997).
- [10] M. Colin, G. Cultrut, B. Desforges, D. Picard, “1998 SPS & LEP Machine Statistics,” CERN SL-Note 98-68 OP (1998).
- [11] C.W. Allen, W. Collocho, R. Erickson, M. Stanek, “PEP-II Hardware Reliability,” 2004 IEEE Nuclear Science Symposium and Medical Imaging Conference (NSS/MIC 2004), 16–22 October 2004. Rome, Italy, *IEEE Transactions on Nuclear Science*, Vol. 52, No. 1, February 2005 (2005).
- [12] J.T. Seeman, “Last Year of PEP-II B-factory Operation,” *Proc. EPAC2008*, Genoa (2008).
- [13] S. Fuke, T. Kawasumi, Y. Funakoshi “KEKB Operation Statistics,” *Proc. of the 3rd Annual Meeting of Particle Accelerator Society of Japan and the 31th Linear Accelerator Meeting in Japan*, Sendai, Japan, August 2–4, 2006.
- [14] M. Tanaka, H. Asai, Y. Funakoshi, “Operation Statistics of KEKB in FY2009,” *Proc. Japanese Particle Accelerator Society*.
- [15] T. Abe *et al.*, “KEKB Accelerator — Commissioning of KEKB” *Prog. Theor. Exp. Phys.* (2013) 03A010.
- [16] E. Durieu-Thiry (ed.), “Operation Statistics of the CERN Accelerators Complex for 2003,” CERN AB-Note-2004-027-OP (2004).
- [17] J.T. Seeman *et al.*, “Results and Plans of the PEP-II B-factory,” *Proc. EPAC2004*, Lucerne (2004).
- [18] J.T. Seeman, “KEKB and PEP-II Operational Status,” *Proc. PAC2005*, Knoxville (2005).
- [19] M. Akemoto *et al.*, “KEKB Accelerator – The KEKB Injector Linac,” *Prog. Theor. Exp. Phys.* 03A002 (2013).

KEKB/SUPERKEKB CRYOGENICS OPERATION

K.Nakanishi*, K.Hara, T.Honma, K.Hosoyama, M.Kawai
Y.Kojima, Y.Morita, H.Nakai, N.Ohuchi, H.Shimizu

High Energy Accelerator Research Organization(KEK), 305-0801 Tsukuba, Japan
T.Endo. T,Kanekiyo, Hitachi Plant Mechanics Co.,Ltd., 744-0002 Kudamatsu, Japan

Abstract

At KEK, the operation of the superconducting cavities was started with TRISTAN accelerator in 1988 [1]. The superconducting cavities are continuously operated even after that. In this paper, the operation of the refrigerator for the superconducting cavities of KEBK/SuperKEKB is mainly introduced. In KEBK/SuperKEKB, the superconducting magnets are also used. They have their own refrigerator [2]. The refrigerator for the superconducting cavity for KEBK/SuperKEKB was constructed for the TRISTAN accelerator [3]. The capacity of the refrigeration is 8.1 kW at 4.4 K [4] [5]. Since the number of superconducting cavities used in KEBK / SuperKEKB is smaller than that of TRISTAN, there is a margin for the capacity of the refrigerator. In order to operate this old refrigerator, proper maintenance is necessary, and periodic inspection and equipment updating are carried out.

CRYOGENIC SYSTEM FOR SUPERCONDUCTING CAVITIES

Large-scale Helium Refrigerator

KEKB was built in the tunnel of the TRISTAN accelerator. The TRISTAN accelerator was operated from 1986 to 1995. The superconducting acceleration cavities were installed in 1988 to increase the beam energy. The cryogenic system for superconducting cavities was also established by Hitachi, Ltd. simultaneously. In 1989 superconducting acceleration cavities were added, and cryogenic systems were also enhanced. Its design capacity was increased from 4kW to 6.5kW. Schematic diagram of the refrigerator for superconducting cavities is shown in Fig. 1. By adding expansion turbines (T4 and T5), it became possible to operate the refrigerator without liquid nitrogen. By adopting the supercritical burbine expander (T3), the capacity of refrigerator was increased. And, two compressors (C5 and C6) were added. As a result, the practical refrigeration capacity was reached to 8.1kW at 4.4K.

KEKB took over many facilities from TRISTAN. The cryogenic system for superconducting cavities is one of them. This refrigerator is still used in SuperKEKB.

Superconducting Cavity

In TRISTAN, a cryostat for superconducting acceleration cavities had two of 5cell cavities (See Fig. 2). Finally, 16 cryostats were installed. An estimation of the heat loads are

shown in Table 1. The total heat load for TRISTAN cryogenic system at 4.4K is about 4 kW, which can be sufficiently cooled by the enhanced refrigerator.

KEKB accelerator operated from 1998 to 2010. In KEBK, a cryostat for superconducting acceleration cavities had a single-cell cavity (See Fig. 3). 8 cryostats were installed. The static heat load is about 30W/cryostat [6]. The RF loss is 100W/cavity. As can be seen from Table 1, the main component of the heat load is the RF loss of superconducting cavities. In KEBK, there is enough margin for refrigerating capacity, because the number of superconducting cavities is small. Since the RF loss of the cavity changes according to the acceleration voltage, The sum of the compensation heater power and the RF loss is controlled to be constant. The RF loss of the Table 1 includes the output power of the compensation heaters.

From 2007 to 2010, two superconducting crab cavities were adopted. The crab cavity have a superconducting device called coaxial coupler. To cool the coaxial coupler, a liquid helium of about 5g/s was required (See Fig. 4). As a result, the thermal load appeared to be about 100W larger than the superconducting acceleration cavity.

In SuperKEKB, the crab cavities are not used. They have been removed. The eight superconducting cavities are still in operation.

Transfer Line

A high-performance transfer line is required to supply liquid helium from the helium refrigerator installed on the ground to the underground cryostat. The cross-section of transfer line was shown in Fig. 5 The heat load is about 1W/m as shown in Table 1. In KEBK, an improved transfer line was developed, and the performance was tested. The cross-section of the improved transfer line was shown in Fig. 6. In multi-channel transfer line, the heat load was only 0.05W/m. The multi-channel transfer line was adopted to connect from refrigerator to D10 test stand as shown in Fig. 1. The single-channel transfer line was adopted to connect between the cryostats and existing multi-channel transfer line in KEBK.

Liquid Nitrogen Circulation System

The cryostat of the superconducting cavity and the transfer line have the radiation shield which called 80K shield. To cool the 80K shield, a nitrogen circulation system was adopted. A circulation system is very suitable for cooling the shield by pipe cooling. This is because cooling in a single pass can not sufficiently cool the downstream. In the case of using a circulation system, the refrigerant returns in two-phase flow, so that all passes are completely cooled. As

* kota.nakanishi@kek.jp

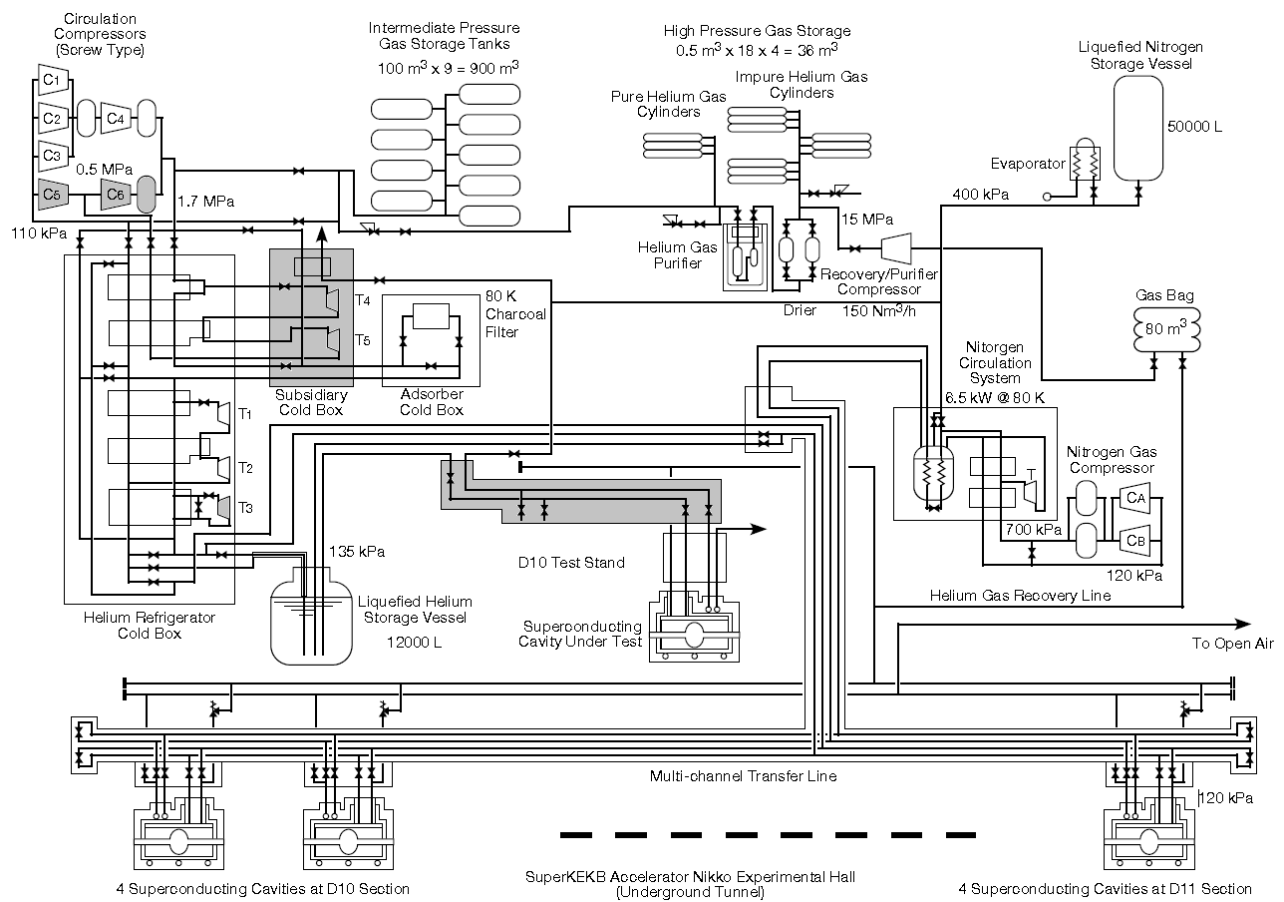


Figure 1: Flow diagram of the refrigerator for superconducting cavities. Shaded areas indicate extended parts.

Table 1: Heat loads of the TRISTAN cryogenic system at 4.4K

Componntns		Heat loads
Cryostats	22.8 W/cryostat × 16	364.8 W
Transfer Lines (380m)		412.4 W
Cold Valves & Joints		147 W
RF Loss	90 W/cavity × 32	2880 W
Total Heat Loads		3804.2 W

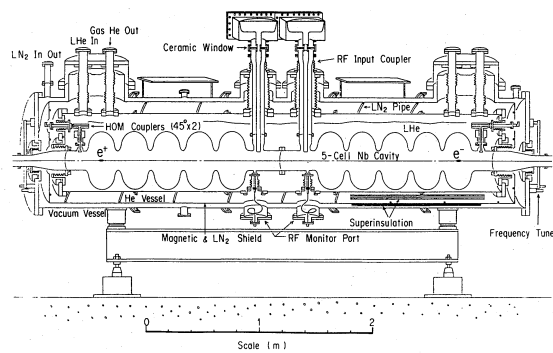


Figure 2: TRISTAN superconducting acceleration cavity cryostat.

shown in Fig. 1, the circulation system for KEKB consists of a compressor, a heat exchanger and a turbine expander. It not only recycles the returned liquid nitrogen, but also liquefies a part of the returning nitrogen gas. By using sensible heat of evaporated gas, consumption of liquid nitrogen was suppressed. The heat load for TRISTAN accelerator at 80K are shown in Table 2. In TRISTAN, the daily consumption of liquid nitrogen decreased from 8000L to 1800L by using the liquid nitrogen circulation system. In KEKB, it is about 1500L. Most of the heat load at 80 K comes from the transfer line, and since this part is not updated, the consumption of liquefied nitrogen has not changed significantly.

Table 2: Heat loads of the TRISTAN cryogenic system at 80K

Componnts	Heat loads	
Cryostats	48.8 W/cryostat × 16	780.8 W
Transfer Lines (380m)		5569 W
Cold Valves & Joints		294 W
Total Heat Loads		6643.8 W

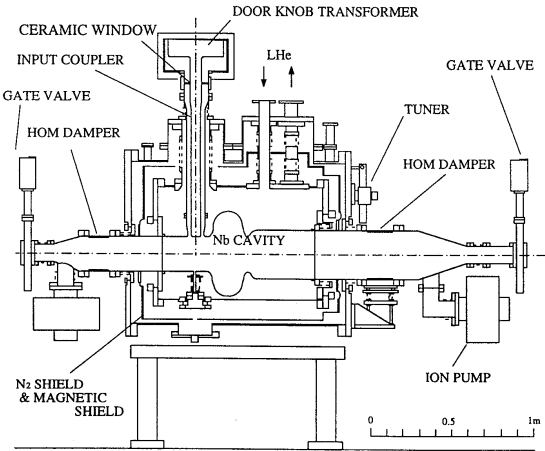


Figure 3: KEKB superconducting acceleration cavity cryostat.

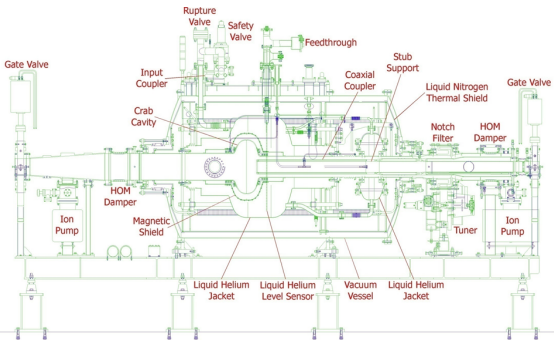


Figure 4: KEKB superconducting crab cavity cryostat.

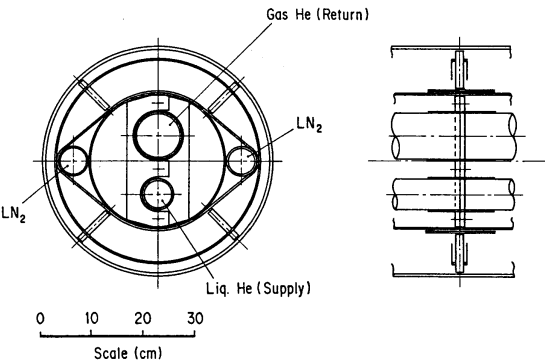


Figure 5: Cross-section of transfer lines for TRISTAN.

Control System

When the cryogenic system was constructed, a distributed process control system Hitachi EX-1000 was adopted. It

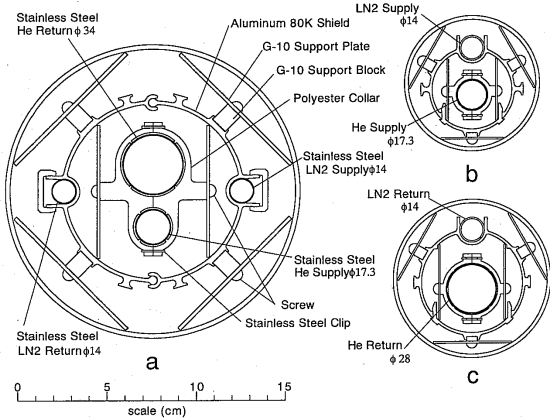


Figure 6: Cross-section of transfer lines for KEKB: a: multi-channel(main), b) single-channel for helium supply, and c) single-channel for helium return [7].

contained 5 Multi-controllers(MLC). The MLC has digital and analog input / output, and it can execute data monitoring, loop control and sequence control. The control period was 1 second. Data logging system is also implemented in the control system. This system is connected to the accelerator control system through the gateway unit and can exchange information necessary for operation. The control system has been updated twice, now EX-8000 is working. A schematic diagram of the control system is shown in Fig. 7.

Currently processed signals are 800 analog inputs, 168 analog outputs, 608 digital inputs and 352 digital outputs. 63 PID loop is working. Currently there are six MLCs, an MLC can handle 768 analog inputs and outputs and 512 digital inputs and outputs. There is sufficient margin for the number of signals that can be handled, and it is possible to respond to the addition of facilities.

Operation Status

In practical operation, it is necessary to cool down the equipment from room temperature. Since the deformation of the equipment due to the temperature difference during cooling down causes misalignment and vacuum leakage, it is required to slowly and uniformly cooling down. In KEKB/SuperKEKB, the cooling rate is required to be 2.5~3K/h. The state of the most recent cooling is shown in the Fig. 8. The cavity was cooled from room temperature to about 40 K at a constant rate. In this example, the cooling rate was targeted at 2.5 K/h. In the initial stage of cooling, the superconducting cavity is cooled by using a helium gas

Content from this work may be used under the terms of the CC BY 3.0 licence (© 2018). Any distribution of this work must maintain attribution to the author(s), title of the work, publisher, and DOI.

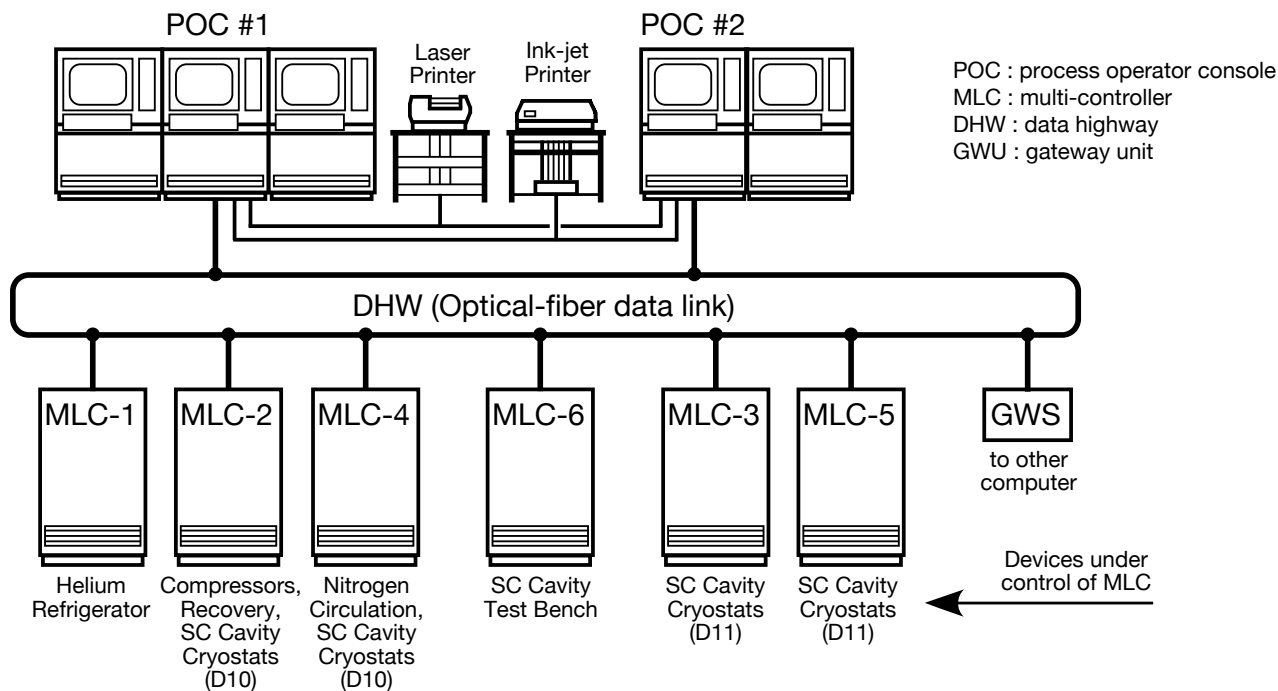


Figure 7: Schematic diagram of the control system for the large-scale helium refrigerator.

cooled by liquid nitrogen in a heat exchanger in the refrigerator. When the cavity temperature reached about 150 K, the expansion turbines (T1 and T2) were started to reduce the temperature of the helium gas to be supplied. The temperature of the supplied helium gas changes, but the cooling rate is controlled through the flow rate of the helium gas. When the cavity temperature reaches about 40 K, liquid helium is supplied from Dewar. After reaching the liquid helium temperature, the helium level in the cryostat is controlled. The refrigerator starts the liquefaction operation and supplies the liquid helium to the dewar.

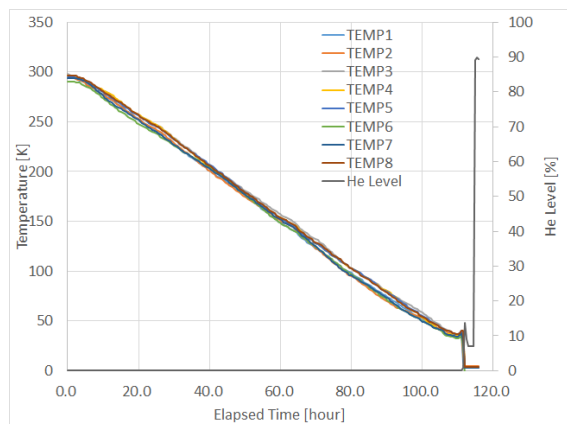


Figure 8: Cool down curves of the SuperKEKB superconducting cavities.

In the steady state, the liquid level in the superconducting cavity cryostat is controlled to be constant. In TRISTAN, the RF loss of superconducting cavity increased from about

30W at beam injection to about 120W at the top energy operation in about two minutes. There was a concern that the state of the refrigerator would not be stabilized due to rapid changes in the temperature and flow rate of the evaporated gas returned to the refrigerator. As already mentioned, this variation was canceled by the compensation heater. In KEKB/SuperKEKB, RF loss is stable, however compensation heaters are still in use.

Maintenance and Updating

In Japan, refrigerators are classified as high-pressure gas equipment. A high-pressure gas equipment should be operated according to the high pressure gas safety act. The maintenance work required for the refrigerator for KEKB/SuperKEKB superconducting cavity is as shown in the Table 3. Maintenance cycle depends on refrigerator specifications.

Electronic devices require periodic maintenance. When the refrigerator was constructed, the control system was EX-1000. It was updated to EX-7000 in 2002 and EX-8000 in 2012. Electronic circuits such as signal converters periodically measure their characteristics and update them as necessary. Inspection and updating are also carried out for actuators for valves and sensors in the same way.

Trouble

The helium refrigerator was operated in the TRISTAN accelerator for seven years from 1988 to 1995, and the operation time was 38000 hours. The cause of the trouble that caused the refrigerator to stop operating during this period was the initial failure such as oil leakage from the mechanical seal of the compressor and mistakes in the set values of

ticle analysis, magnetic field was applied in the Belle. To make the magnetic field, a superconducting solenoid was adopted [2]. This superconducting solenoid is a huge one with an inner diameter of 1.8 m and a length of 3.91 m. A helium refrigerator which was used in TRISTAN was diverted to cool the Belle solenoid. A schematic diagram of the refrigeration system for QCS is shown in the Fig. 11.

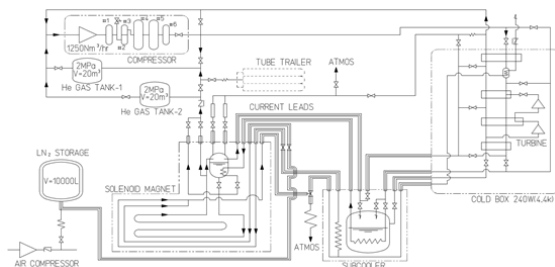


Figure 11: Flow diagram of the Belle solenoid cryogenic system.

The capacity of refrigerator is 250 W at 4.4 K. The heat load and the amount of liquid helium used for current lead cooling of this system were 84W and 26L/h, respectively, with a margin of 102W. Subcooled liquid helium of 10 g / s is supplied through a pipe that is thermally contact with the solenoid, and the magnet is cooled by conduction. The supplied liquid helium becomes a two-phase flow at the pipe exit. It takes 6~7 days to cool this system from room temperature and 4 days to warm it up. Total operating time at KEKB is 75985 hours and will continue to be used in SuperKEKB.

SUMMARY

In SuperKEKB, refrigerators manufactured for TRISTAN are used. These refrigerators have been operated for a long time by undergoing periodic maintenance. Since superconducting cavities of SuperKEKB are fewer than TRISTAN,

the refrigerator for superconducting cavities has sufficient capacity. Hardware development has also been done. The developed a high-performance transfer line and adopted it partly.

In KEKB, superconducting magnets are adopted for QCS and Belle-II. Two of the four refrigerators that had cooled the QCS of TRISTAN were used and cooled QCS and Belle solenoid, respectively.

In SuperKEKB, QCS has been enhanced, so three refrigerators were adopted to cool QCS-L, QCS-R and Belle-II solenoid, respectively.

REFERENCES

- [1] Y.Kojima *et al.*, “Superconducting RF Activities at KEK”, in *Proc of SRF’89*.
- [2] J.Kawai *et al.*, “Cryogenic System in the KEKB Beam Interaction Region and Operation Experience”, *J. Cryo. Super. Soc. Jpn.* Vol.50 No.12 (2015).
- [3] K.Hosoyama *et al.*, “CRYOGENIC SYSTEM FOR TRISTAN SUPERCONDUCTING RF CAVITY”, in *Proc of SRF’89*.
- [4] K.Hosoyama *et al.*, “Cryogenic system for TRISTAN superconducting RF Cavities: upgrading and present status”, *Adv. Cryogen. Engrg*, 37 (1993).
- [5] H.Nakai *et al.*, “Large-scale Helium Refrigeration System for KEKB/TRISTAN Superconducting Cavities -Operation Experience for 27 Years and Next Operation-”, *J. Cryo. Super. Soc. Jpn.* Vol.50 No.12 (2015).
- [6] T.Furuya *et al.*, “BEAM TEST OF A SUPERCONDUCTING DAMPED CAVITY FOR KEKB”, in *Proc of PAC97*, (1997) 3087-3089.
- [7] K.Hosoyama *et al.*, “Development of a high performance transfer line system”, *Adv. Cryogen. Engrg*, 45 (2000) 1395-1402.
- [8] K.Hosoyama *et al.*, “Cryogenic system for TRISTAN superconducting RF cavities: description and operating experience”, in *Proc of ICEC16/ICMC* (1996) 183-186.

CONCEPTIONAL DESIGN OF CEPC CRYOGENIC SYSTEM

Jianqin Zhang[†], Shaopeng Li, Ruixiong Han, IHEP, CAS [100049] Beijing, China

Abstract

The Circular Electron and Positron Collider (CEPC) has two rings, the booster ring and the collider ring. There are 336 superconducting cavities in total, which group into 68 cryomodules. In the booster ring, there are 96 1.3 GHz 9-cell superconducting cavities. In the collider ring, there are 240 650 MHz 2-cell cavities. There are 4 cryo-stations along the 100 km circular collider. Each cryo-station is supplied from a common cryogenic plant, with one refrigerator and one distribution box. The cooling capacity of each refrigerator is 18 kW @ 4.5 K.

INTRODUCTION

The Circumference of CEPC is 100 km with the booster ring and the collider ring. The collider ring is located in the tunnel, with the booster ring on the surface. There are 336 superconducting cavities in total. In the booster ring, there are 96 ILC type 1.3 GHz 9-cell superconducting cavities, eight of them will be packaged in one 12-m-long module. There are 12 such modules. In the collider ring, there are 240 650 MHz 2-cell cavities, six of them will be packaged in one 11-m long module. There are 56 of them.

All the cavities will be cooled in a liquid-helium bath at a temperature of 2 K to achieve a good cavity quality factor. The cooling benefits from helium II thermophysical properties of large effective thermal conductivity and heat capacity as well as low viscosity and is a technically safe and economically reasonable choice. There are 4 cryo-stations along the 100km circular collider, as shown in Fig. 1.

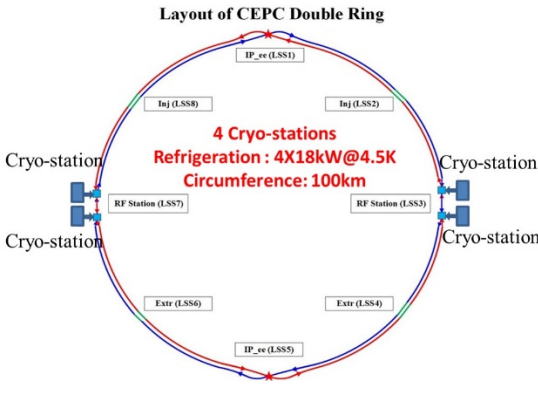


Figure 1: Layout of the CEPC cryogenic system.

CRYOGENIC DISTRIBUTION

General Layout

There are 4 cryo-stations. Each cryo-station includes

[†]jqzhang@ihep.ac.cn.

two strings; one string groups 3 modules from the Booster and the other groups 10 modules from the Collider. The temperature of the RF cavities is 2 K. In order to decrease the high thermodynamic cost of refrigeration at 2 K, the design of the cryogenic components aims at intercepting heat loads at higher temperatures. There are two shields intercept both radiation and conduction at two temperatures: 40 ~80 K and 5~8 K.

During operation, one-phase helium of 2.2 K and 1.2 bar is provided by the refrigerator to all cryomodules. Each cryomodule has one valve box with two valves. The JT-valve is used to expand helium to a liquid helium separator. A two-phase line connects each helium vessel and connects to the major gas return header once per module. A small diameter warm-up/cool-down line connects the bottom of the helium vessels at both ends. The cavities are immersed in baths of saturated superfluid helium, gravity filled from a 2 K two-phase header. Saturated superfluid helium flows along the two-phase header which is connected to the pumping return line and then to the refrigerator. Details of Booster and Collider cryogenic strings are in Figs. 2 and 3.

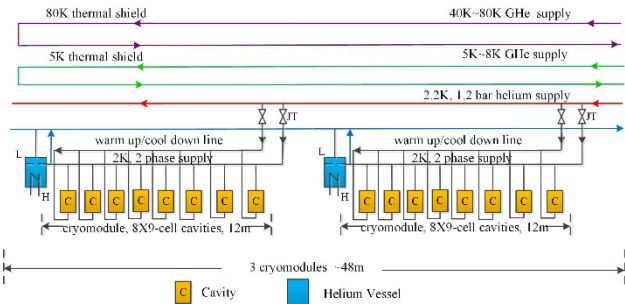


Figure 2: Booster cryogenic string.

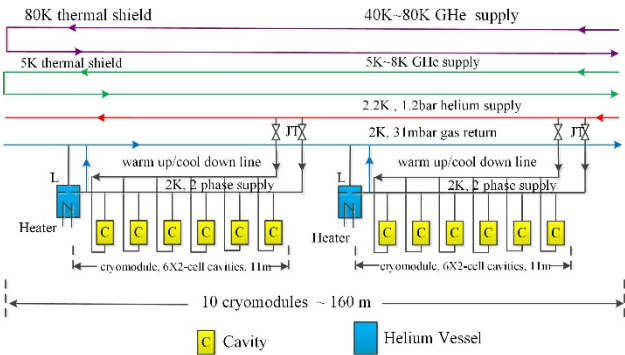


Figure 3: Collider cryogenic string.

Cryomodules

In the booster ring, each eight 1.3 GHz 9-cell superconducting cavities are packaged in one 12-m-long cryomodule. Since many projects have used this type of cryomodule, it is a matured design. In the collider ring, one cryomodule includes six 650 MHz 2-cell cavities, six high power couplers, six mechanical tuners and two HOM absorbers. In order to have a good performance, fast cool-down is introduced, which means 2-3 K/minute below the 9.2 K critical temperature. In the collider cryomodule, the structure design of the collider cryomodule is shown in Fig. 4. The diameter of the vacuum vessel is 1.4 m, and overall length is 9.5 m. The cavity is supported by the post with the material of fiber reinforced plastic (G-10).

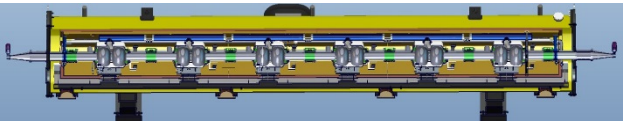


Figure 4: Structural design of the Collider Cryomodule.

Heat Load

The heat load is mainly from the superconducting cavities. The 1.3 GHz 9-cell cavities with quality factor 1×10^{10} @ 19.8 MV/m are for the Booster and the 650 MHz 2-cell cavities with quality factor 1.5×10^{10} @19.7 MV/m are for the Collider. The cavity dynamic heat load of each cryomodule for collider and booster is 153.59 W and 13.98 W.

Table 1 summarizes the static and dynamic heat during Higgs mode at different temperature levels. This amounts to a total equivalent entropic capacity of 47.53 kW at 4.5 K. The corresponding installed power is 10.4 MW. The figures in Table 1 include an “overall net cryogenic capacity multiplier,” a multiplier of the estimated heat loads, and in general use in the cryogenic community. This factor includes a margin for plant regulation, a buffer for transient operating conditions, a buffer for performance decreases during operation and a buffer for general design risks. This multiplier parameter is from the ILC Design report [1]. In the ILC design, the real COP at 40~80 K, 5~8 K and 2 K are 16.4, 197.9 and 700.2 respectively.

Table 1: Heat Load

Higgs Mode	Unit	Collider			Booster		
		40-80K	5-8K	2K	40-80K	5-8K	2K
Predicted static heat load per cryomodule	W	300	60	12	140	20	3
Cavity dynamic heat load per cryomodule	W	0	0	153.59	0	0	13.98
HOM dynamic heat load per cryomodule	W	20	12	2	2	1	1
Input coupler dynamic heat load per cryomodule	W	60	40	6	40	3	0.4
Module dynamic heat load	W	80	52	161.59	42	4	15.38
Connection boxes	W	50	10	10	50	10	10
Cryomodule number			40			12	
Total heat load	kW	17.20	4.88	7.34	2.78	0.41	0.34
Total predicted mass flow	g/s	82.42	152.26	346.58	13.34	12.73	16.07
Overall net cryogenic capacity multiplier		1.54	1.54	1.54	1.54	1.54	1.54
4.5K equiv. heat load with multiplier	kW	1.99	6.80	36.18	0.32	0.57	1.68
Total 4.5K equiv. heat load with multiplier	kW		44.96			2.57	
Total 4.5K equiv. heat load of booster and collider	kW			47.53			
Installed Power	MW		9.84			0.56	
				10.4			

REFRIGERATION

The heat loads shown in Table 1 require the helium refrigerator plants to have a total capacity over 47.53 kW at 4.5 K. Four individual refrigerators will be employed. Including an operating margin, the cryogenic plant capacities are 18 kW at 4.5 K for each cryogenic station. The total cryogenic capacities are equivalent to 72 kW at 4.5 K.

Many aspects must be taken into account during refrigerator design, including cost, reliability, efficiency, maintenance, appearance, flexibility and convenience of use. The initial capital cost of the cryogenic system as well as the high energy costs of its operation over the life of the facility represent a significant fraction of the total project budget, so reducing these costs has been the primary focus of our design. Reliability is also a major concern, as the experimental schedule is intolerant of unscheduled down time.

The refrigerator main components include a compressor station with oil removal system, vacuum pumps and the cold box which is vacuum insulated and houses the aluminum plate-fin heat exchangers and several stages of turbo-expanders.

The fundamental cooling process expanding compressed helium gas to do work against low-temperature expansion engines, then recycling the lower pressure exhaust gas through a series of heat exchangers and subsequent compression is a variant of the Carnot process that has been in use for many decades.

There are five pressure levels in the cryoplant: 20 bara, 4 bara, 1.05 bara, 0.4 bara and 3 kPa. These are obtained with the high pressure screw compressor group, middle pressure screw compressor group, warm compressors and cold compressors. At the 40 K and 5 K temperature levels helium flows are directed to the thermal shields of the cryomodules. The corresponding return flows are fed back to the refrigerator at suitable temperature levels. Inside the refrigerator cold-box the helium is purified of residual air, neon and hydrogen by switchable absorbers at the 80 K and 20 K temperature levels. Figure 5 is the refrigerator flow diagram.

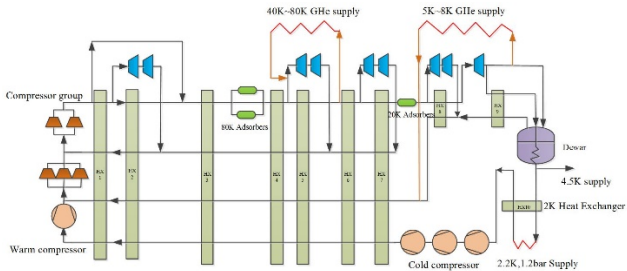


Figure 5: Refrigerator flow diagram.

The cryoplant will supply 4.5 K and 2.2 K helium to the cryomodules. At each cryomodule, the helium goes through a phase separator and a 2K counter flow heat

exchanger to recover the cooling power, then expanded to 31 mbar via a JT-valve, resulting in liquid He II at 2K. The low pressure helium vapor from the 2K saturated baths surrounding the cavities returns to the refrigerator through the gas return pipe. The vapor is pumped away and returned to the cryoplant.

There are two options for such a pumping system. One relies solely on cold compressors; the other employs a set of cold compressors followed by a final stage of warm compression. After superheating in the counter flow heat exchanger, the gas is compressed in the multiple-stage cold compressors to a pressure in the 0.5 to 0.9 bar range. This stream is separately warmed up to ambient in exchangers and goes back to the warm compressors. The choice of a warm vacuum compressor makes it easier to adjust for the heat load variations. This approach, which CERN uses in the LHC [3], also allows for an easier restart of the 2 K system after a system stoppage.

INFRASTRUCTURE

The 2 K cryogenic system consists of oil lubricated screw compressors, a liquefied-helium storage vessel, a 2 K refrigerator cold box, cryomodules, a helium-gas pumping system and high-performance transfer lines. The cryogenic station is located near the RF station. The cooling power required at each RF station will be produced by a refrigerator with a capacity of 18 kW at 4.5 K, installed at four cryogenic stations, and distributed to the adjacent superconducting cavities [2, 3].

For reasons of simplicity, reliability and maintenance, the number of active cryogenic components distributed around the ring is minimized and the equipment locations chosen following these principles:

- 1) Equipment is installed as much as possible above ground to avoid excavation. Normal temperature equipment will be installed at ground level.
- 2) To decrease heat loss, low-temperature equipment will be installed nearby the cryomodules [4].

Equipment at ground level includes the electric substation, the warm compressor station, helium storage tanks, cooling towers and helium purification. Underground are the cold-boxes, cold compressor, 2 K cryomodules, cryogenic transfer lines and distribution valve boxes. Figure 6 shows the overall schematic.

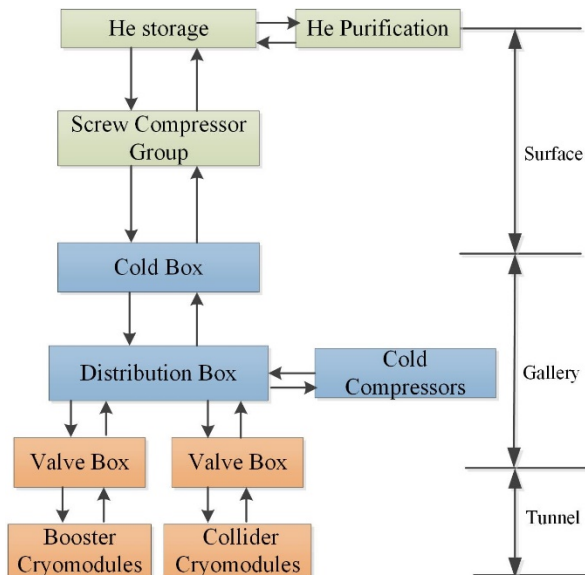


Figure 6: General architecture of the cryogenic system.

Each cryo-station has an underground plant in the gallery, the size is 37 meters long and 8 meters wide, including Cold box, distribution box and cold compressor. The height of the gallery is 5 meters. There are normal temperature magnets between cryomodules. So each cryomodule is equipped with a valve box in the power source tunnel and connected by a transfer line. The cryogenic distribution in the tunnel for booster and collider is shown in Figs. 7 and 8.

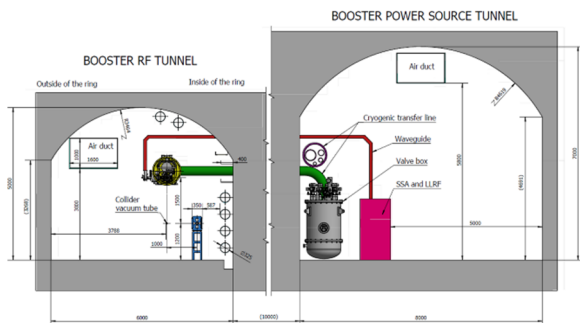


Figure 7: Tunnel for booster.

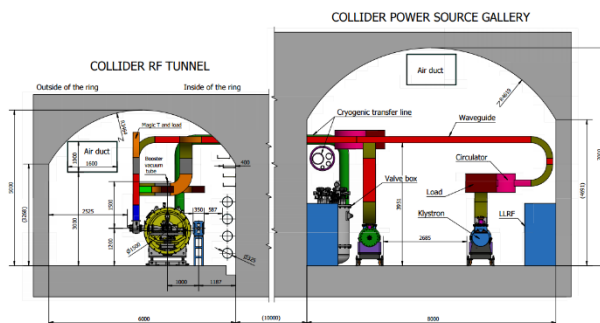


Figure 8: Tunnel for Collider.

HELIUM INVENTORY

Most of the helium inventory is liquid which bathes the RF cavities and is roughly 70% of the whole system. The volumes of one 1.3 GHz module and one 650 MHz module is about 320 liters and 346 liters, respectively. The total liquid helium volume in the system is 17,680 liters.

Accounting for the liquid in the Dewar and in the transfer lines, and using the 70% factor mentioned above, the liquid volume in the system is about 25,257 liters, or about 3,679 kg [5].

Assuming that all the helium is returned to the helium tanks after machine shutdown, the inventory will be $2.3 \times 10^4 \text{ m}^3$. To safely operate the cryogenic system, a factor of 60% is added, so $3.8 \times 10^4 \text{ m}^3$ is required helium inventory system. The total helium inventory of the whole machine is about 6,131 kg.

CONCLUSION

The CEPC cryogenic system were designed with cooling scheme, cryomodules, heat load, refrigeration and architecture. The required total 4.5 K equiv. heat load is 47.53 kW and total installed power is 10.4 MW. There are four cryo-stations and each station has an individual 18 kW@4.5 K refrigerator. Research and discovery about cold compressor and 2 K JT heat exchanger have been carried out. More detailed work will be proceeded later.

REFERENCES

- [1] ILC Technical Design Report: Volume 3, Part II, 54.
- [2] XFEL TDR, 514.
- [3] P. Lebrun, "Cryogenic refrigeration for the LHC (2009)," http://www-fusion-magnetique.cea.fr/matefu/school_2/Tuesday/lebrun-LHCcryogenicrefrigeration.pdf.
- [4] LHC design report, volume 1, chapter 11, cryogenic system.
- [5] P. Lebrun, "Large cryogenic helium refrigeration system for the LHC," in *Proceedings of the 3rd International Conference on Cryogenics & Refrigeration, ICCR2003*, 11-13. 2003.

OPERATION OF SUPERKEKB IN PHASE 2

Y. Funakoshi*, Y. Arimoto, H. Ikeda, T. Ishibashi, N. Ohuchi, S. Terui, X. Wang,
KEK 305-0801 Tsukuba, Japan

Abstract

The Phase 2 commissioning of SuperKEKB was performed from March to July 2018. In this report, the operation statistics and the QCS quench issue which we encountered during Phase 2 are described.

INTRODUCTION

The purpose of SuperKEKB is to search for a new physics beyond the standard model of the particle physics in the B meson regime. SuperKEKB consists of the injector Linac, a damping ring for the positron beam and two main rings; *i.e.* the low energy ring (LER) for positrons and the high energy ring (HER) for electrons and the physics detector named Belle-II. The beam energies of LER and HER are 4 GeV and 7 GeV, respectively. The design beam currents of LER and HER are 3.6 A and 2.6 A, respectively. The design luminosity is $8 \times 10^{35} \text{cm}^{-2}\text{s}^{-1}$. More detailed parameters of SuperKEKB is described elsewhere [1]. The Phase 1 beam commissioning of SuperKEKB was done from Feb. to June 2016 without the Belle-II detector and the IR magnets [2]. The Phase 2 commissioning was performed from March to July 2018. The highlights of the Phase 2 beam commissioning are written elsewhere [3]. In this report, the operation statistics and the QCS quench issue which we encountered during Phase 2 are described.

OPERATION STATISTICS

Figure 1 shows operation statistics of SuperKEKB Phase 2 commissioning from April to July. The Phase 2 main ring commissioning started in the middle of March. But the operation in March is not included in these statistics. During the Phase 2 commissioning, the commissioning of the Belle 2 detector was also done and it collected an integrated luminosity of $\sim 500 \text{pb}^{-1}$. Those are counted as "Luminosity Run". The "Machine Tuning" category includes vacuum scrubbing with beams and other hardware tuning without beams such as tuning of the beam size monitors and RF aging. The "Machine Study" category includes a dedicated machine study on the effects of the electron clouds, a collimator study, a radiation measurement and others. "Beam tuning" includes the optics tuning for squeezing IP (Interaction Point) beta functions, the beam injection or injector tuning, the detector beam background tuning, the beam collision tuning, the beam-based BPM tuning and others. A regular maintenance was done as a general rule every 2 weeks for about 8 hours. The "Troubles" category includes the QCS quench problem shown below. As a comparison, the operation statistics of KEKB for 8 years are also shown in Fig. 2. The beam tuning and machine tuning time are much longer than those in

KEKB, since SuperKEKB is still in an early stage in its life and the first beam collision was done in Phase 2.

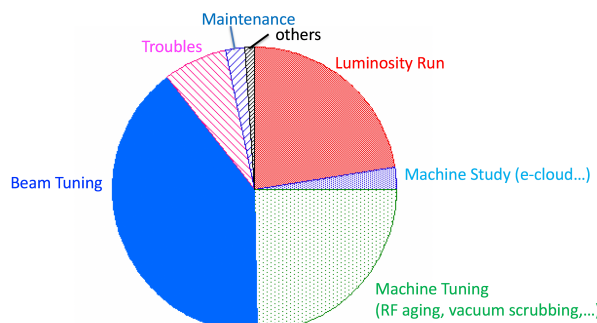


Figure 1: Operation statistics of SuperKEKB Phase 2 (April 2018 ~ July 2018).

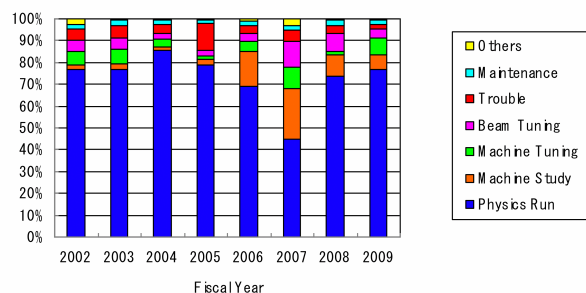


Figure 2: Operation statistics of KEKB for 8 years.

QCS QUENCH ISSUES

QCS is a generic name of the superconducting magnets near the IP at SuperKEKB which includes the final focus doublet named "QC1" and "QC2". The detailed design of the QCS magnets is described elsewhere [1]. Figure 3 shows a schematic view of the QCS magnet system. In addition to the final focus doublet quadrupoles, we need many kinds of corrector coils in order to cancel unwanted leakage fields, to correct effects of fabrication errors or alignment errors of the magnets and to widen dynamic aperture with the extremely small beta functions at the IP.

In the Phase 2 beam commissioning, we recognized that the QCS quench induced by beam hit is a serious issue for beam operation. Table 1 shows a list of the QCS quenches which occurred during the Phase 2 operation [4]. In the table, the injection kicker magnet system for the beam injection consists of two set of pulse magnets, K1 and K2. K1 and K2 make an orbit bump in the horizontal direction around the injection point for the stored beam. The quench on April 1st and 2nd was caused by unbalance of K1 and K2 due to timing errors of the pulse magnets and the orbit

* yoshihiro.funakoshi@kek.jp

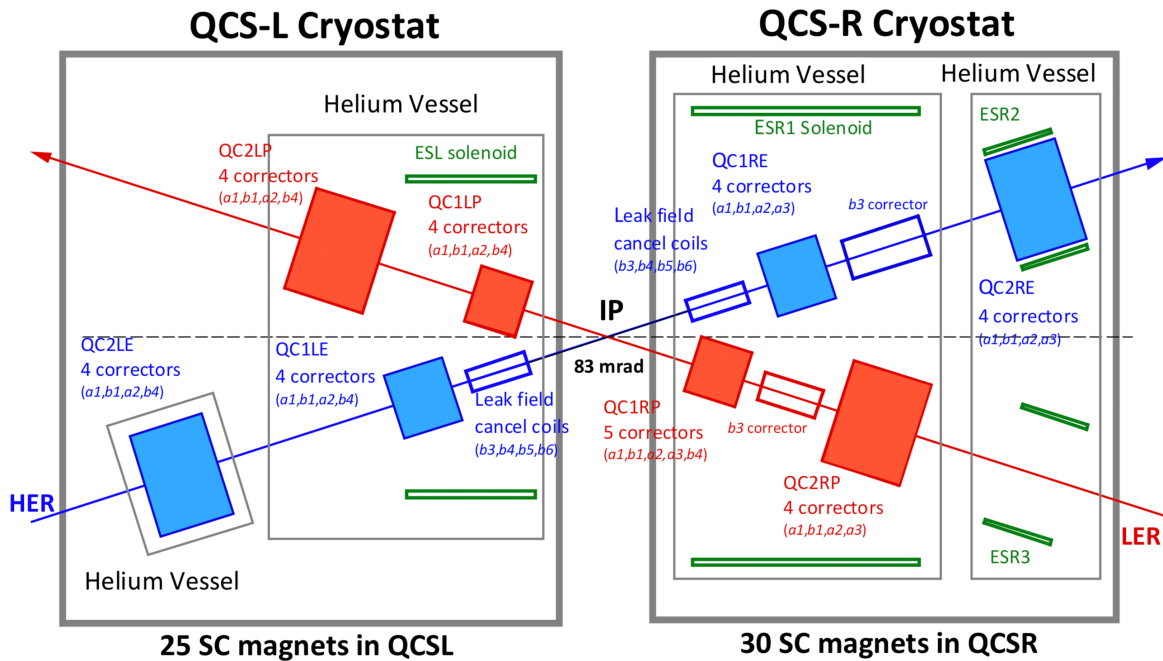


Figure 3: Schematic view of QCS magnet system.

bump was not closed. Each of K1 and K2 consists of 3 magnets. The quench on May 17th was caused by malfunction of one of the K2 magnets (K2-3) of LER. In the table, a1, b1, b3 are corrector coils and denote a skew-dipole (vertical steering), a dipole (horizontal steering) and a sextupole, respectively. On the other hand, QC1LP, QC1RP, QC1LE are main quadrupole coils and denote the final focus defocusing-quadrupole for positron on the left side of the IP, that for positron on the right side and that for electron on the left side, respectively. As is seen in the table, we had no quenches for the focusing-quadrupoles (QC2 magnets) in Phase 2. Figure 4 shows physical aperture and beam envelope around the LER QCS magnets. The blue and red dots show beam pipe aperture in the horizontal and vertical directions, respectively. Except for short sections around QC1 magnets, the beam pipes are circular and have the same aperture in horizontal and vertical directions. The green and orange lines denote horizontal ($80\sigma_x$) and vertical ($105\sigma_y$ for 5% x-y coupling) beam envelop, respectively. The horizontal and vertical beta functions at the IP in this case are 100 mm and 4mm, respectively. The red and blue squares in the figure show the locations of the main quadrupole coils and the other corrector coils of QC1 magnets, respectively. The corrector coils are located on the inner side of the quadrupole coils and are more easily hit by the beam.

During Phase 2, QCS quenches happened 26 times. Once a QCS quench happens, it takes about 1.5 or 2 hours for recovery. Initial quenches in Phase 2 were mainly induced by injecting beams. A simple calculation shows that the QCS quench can be induced by ~ 8000 electrons (7GeV) which lose their entire energy at a small part of a coil [5]. In reality, the electrons lose a small fraction of their energy at the coil

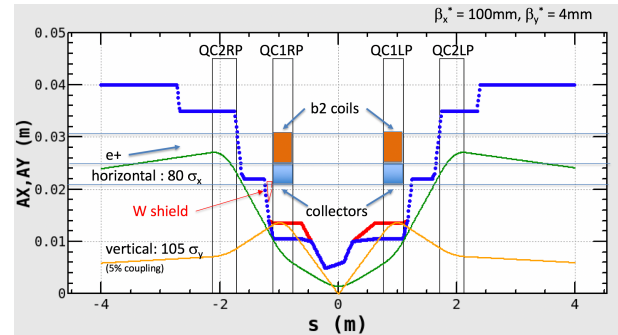


Figure 4: Physical aperture and beam envelop near QCS magnets in LER.

and so more number of electrons are needed for the quench. Even so, it seems that a single pulse of injecting beam from Linac with the charge of ~ 1 nC can anyway induce the QCS quench. The quenches by the injecting beams were almost prevented by setting movable collimators properly on April 11th and introducing the Belle 2 abort using diamond sensors on May 28th [6]. We felt that we had overcome the quenches, since we had no quenches for about a month after the quench on May 24th. However, on June 25th, the quench happened again by a stored LER beam and 4 quenches followed in July. At the end of June, we started to increase the beam currents of LER and HER and also we squeezed the IP vertical beta function β_y^* from 4 mm to 3 mm. One of them was caused by an injecting beam. The quench was induced by a continuously bad injection. The Belle 2 diamond sensors and the beam loss monitors showed relatively high rates. The quench would have been avoided by stopping beam injection

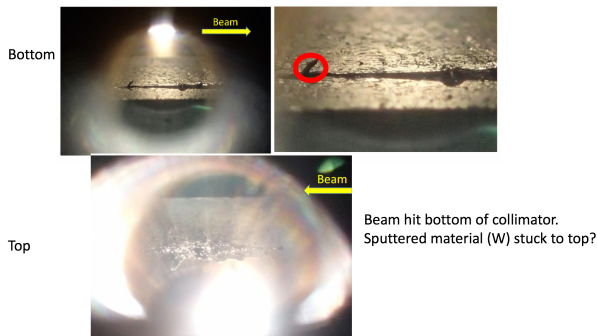


Figure 5: Damaged collimator in LER. The incident happened on June 25th.

with the high rates. Four of them were induced by the stored beam accompanied with a vacuum burst. In 2 cases of the four, a beam hit vertical collimators and gave some damages to the collimators. Figure 5 shows the damaged vertical collimator named “D02V1” hit by the LER beam on June 25th. The collimator is composed of two heads (top and bottom) made of tungsten. It seemed that the beam hit the bottom head and sputtered tungsten material was stuck on the top head. A similar vertical collimator damage was induced in HER named “D01V1” on July 9th. The locations of the collimators in the rings are shown in Fig. 6. The reasons for both collimator damages have not been understood well, since we did not observed any orbit change nor the bunch oscillations in the damage. A hypothesis for the collimator damage is that the beam size was effectively enlarged due to a dust trapping event and some fraction of the beam hit the collimator. If this is the case, not squeezing the IP beta function but increasing the beam currents seems to induce the duct trapping and the QCS quench. We need more study on this issue in Phase 3. The cause of the QCS quench on July 15th was a longitudinal coupled bunch instability in LER whose reason has not been understood well. As a result of the LER QCS quench, the HER beam got unstable and induced the HER QCS quench, since the leakage magnetic field from QC1LP and QC1RP suddenly disappeared.

As measures for the QCS quenches, we will take the following measures. First, we will install more number of collimators before the Phase 3 operation which will start in March 2019. Figure 6 shows the locations of the collimators in both rings [7]. The circles and squares denote the horizontal and vertical collimators, respectively. The collimators in blue color in HER are legacies from KEKB. Since the vacuum chambers in the arc section of HER are reuse from KEKB, we can also reuse the collimators of HER in the arc section. The collimators in red and in orange were prepared for Phase 1 and Phase 2, respectively. The collimators in green will be installed before Phase 3. One more vertical collimator will be installed in LER. Since only one vertical collimator exists in LER so far and the chip scattering at the collimator can be a source of the QCS quench, this additional collimator seems important to reduce the frequency

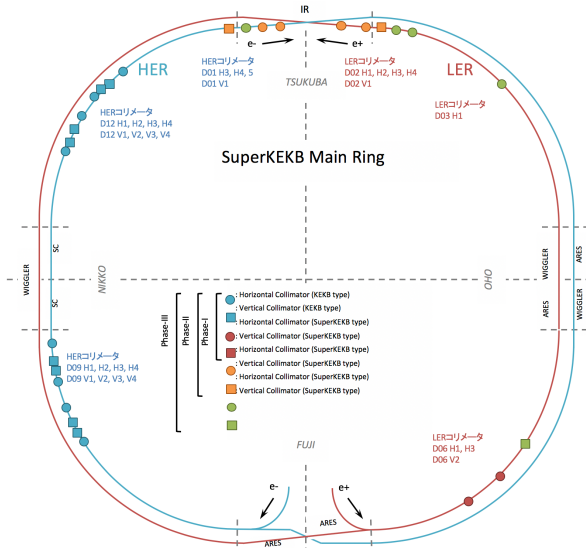


Figure 6: Collimators at SuperKEKB.

of the quenches. Three and one horizontal collimators will also be installed in LER and in HER, respectively. As an additional measure against the QCS quench, the QCS group proposes to install tungsten shields upstream of QC1RP in LER and upstream of QC1LE and Cancel coils on the left side of the IP in HER [8]. The location of the shield in LER is shown in Fig. 4 with a red triangle. Simulations on effectiveness of the W shields are going on. In the earliest case, the shields will be installed in the summer shutdown in 2019. It is also important to understand the mechanism of the QCS quench. Simulations on the dust trapping from the viewpoint of particle hit to the QCS magnets is under planning. It may also be important to do simulations on the effect of continuous particle losses at the QCS magnets due to the Radiative Bhabha scattering or the Touschek effect. In the long term, we may have to consider to remodel the QCS magnets which are more robust against the quenches.

REFERENCES

- [1] T. Abe *et al.*, Technical Design Report of SuperKEKB, in preparation and to be published as a KEK report. An preliminary version is seen in “<https://kds.kek.jp/indico/event/15914/>”.
- [2] Y. Funakoshi *et al.*, paper TUOBA01, *Proc, IPAC2016*, Busan, Korea, May. 9-13, 2016.
- [3] Y. Ohnishi *et al.*, "Highlights from SuperKEKB Phase 2 Commissioning", eeFACT2018, Hong Kong, Sept. 2018, paper MOXAA02, in this conference.
- [4] N. Ohuchi *et al.*, "Operation of Superconducting Final-Focus Magnet System at SuperKEKB", eeFACT2018, Hong Kong, Sept. 2018, paper WEOBB04, in this conference.
- [5] N. Ohuchi, private communications.
- [6] G. Bassi, private communications.
- [7] T. Ishibashi, private communications.
- [8] N. Ohuchi, private communications.

Table 1: Summary of QCS quenches in Phase 2

Date	Time	Quenched Magnets	LER/HER	Causes	Injection/Storage
2018/4/1	20:55	QC1LP	LER	Injection Kicker K1, K2 unbalance	Injection
2018/4/2	19:29	QC1LP	LER	Injection Kicker K1, K2 unbalance	Injection
2018/4/9	17:31	QC1LE-a1	HER	Trial of $\beta_y^*=2.4\text{mm}$	Injection
2018/4/9	20:06	QC1LE-a1	HER	Trial of $\beta_y^*=2.4\text{mm}$	Injection
2018/4/9	20:53	QC1LE-a1	HER	Trial of $\beta_y^*=2.4\text{mm}$	Injection
2018/4/9	21:40	QC1LE-a1	HER	Trial of $\beta_y^*=2.4\text{mm}$	Injection
2018/4/10	17:44	QC1LE-a1	HER	Trial of $\beta_y^*=2.4\text{mm}$	Injection
2018/4/10	21:56	QC1RE-b1	HER	Trial of $\beta_y^*=8\text{mm}$	Injection
2018/4/11	14:21	QC1RE-b1	HER	Trial of $\beta_y^*=8\text{mm}$	Injection
2018/4/11	15:25	Cancel-Mag-b3	HER	Trial of $\beta_y^*=8\text{mm}$	Injection
2018/4/11	18:45	QC1RE-b1	HER	Trial of $\beta_y^*=8\text{mm}$ tune changer	Storage? (10mA)
2018/4/11	20:23	QC1RE-b1	HER	Trial of $\beta_y^*=8\text{mm}$ local bump	Storage (5mA)
2018/4/11	21:15	QC1RE-b1	HER	Trial of $\beta_y^*=8\text{mm}$ local bump	Storage (10mA)
2018/4/20	14:33	QC1RP	LER	RF Phase scan mis-operation	Storage (48mA)
	14:33	QC1LP	LER		
	14:33	QC1RP-b1	LER		
2018/4/21	0:21:49	QC1LP	LER	unknown (after RF phase scan)	Storage (18mA)
	0:21:51	QC1RP	LER		
	0:22:13	QC1RP-b1	LER		
2018/5/6	11:28	QC1LE-b1	HER	Waist knob test	Storage (35mA)
2018/5/13	2:45	QC1RP-b1	LER	Beam injection with large ε_y	Injection
2018/5/17	2:09	QC1RP-b1	LER	$\beta_y^*=6\text{mm}$ K2-3 malfunction	Injection
2018/5/17	4:06	QC1RP-b1	LER	$\beta_y^*=6\text{mm}$ K2-3 malfunction	Injection
2018/5/24	17:17	QCSL-Can-b3	HER	Trial of $\beta_y^*=4\text{mm}$	Injection
2018/6/25	11:20	QC1RP	LER	D02V1 collimator was damaged. Big beam loss was induced. A vacuum burst was observed.	Storage (728mA)
		QC1RP-b1			
		QC1LP			
2018/7/3	5:14	QC1RP-b1	LER	Continuous bad injection	Injection
2018/7/9	11:20	QC1LE	HER	D01V1 collimator was damaged. Big beam loss was induced. Vacuum burst was observed.	Storage(766mA)
		QC1LE-b1			
		QCSL Cancel			
2018/7/15	22:32	QC1RP	LER	Longitudinal instability Induced by LER QCS quench Vacuum burst was observed.	Storage (793mA)
		QC1LE	HER		
		QC1LE-b1			
		QCSL Cancel			
2018/7/16	17:53	QC1LE-b1	HER	Vacuum burst at D02H collimator	Storage (670mA)

SUMMARY ON ACCELERATOR INFRASTRUCTURES AND COMMISSIONING AND OPERATION

Y. Funakoshi*, KEK 305-0801 Tsukuba, Japan

Abstract

In this paper, summary of the working group on “Accelerator Infrastructures and Commissioning & Operation” is described.

LIST OF TALKS

The following talks were given in the working group #12 “Accelerator Infrastructures and Commissioning & Operation”.

- BEPCII Status: given by Qing Qing (IHEP)
- CEPC Civil Engineering design and Infrastructure: given by Yu Xiao (Yellow River Engineering Consulting Co., Ltd)
- Operation Model, Availability and Performance: given by Frank Zimmermann (CERN)
- CEPC Cryogenic System: given by Jianqin Zhang (IHEP)
- LHC Commissioning The good, the bad the ugly: given by Frank Zimmermann (CERN)
- KEKB/SuperKEKB Cryogenics Operation: given by Kota Nakanishi (KEK)
- Operation of SuperKEKB in Phase 2: given by Yoshihiro Funakoshi (KEK)
- A site-specific ILC-CFS design and the Green ILC: given by Masakazu Yoshioka (Iwate University)
- DAΦNE as Open Accelerator Test Facility: given by Catia Milardi (INFN)

The talks are categorized into 3 groups, *i.e.* civil engineering and infrastructure, cryogenic system and beam operation. In the following, a summary of each group is given.

SUMMARY OF CIVIL ENGINEERING AND INFRASTRUCTURE

Two talks were given for this topic. One was on ILC and the other was on CEPC. The talk on ILC covered the site investigation, conceptual designs of a surface access facility, underground facilities and interaction region facilities and reuse of waste heat from the facilities. Of the topics, the site investigation of ILC was very impressive. The unique ILC candidate site is “Kitakami highland”. This site has been decided considering the following aspects, *i.e.* geology, topography, availability of important social infrastructures

and small impact on the natural environment. As for geology, the site consists of a large and uniform granite area without active faults. Due to this feature, the risk for the underground construction is low and the ground motion or vibration is expected to be very small. In the Great East Japan earthquake on March 11th 2011, all fragile equipment and long glass tubes were not damaged at all at “Esashi earth tide observatory underground facility” which locates in the same granite zone as ILC. The reasons for this is that the earthquake ground motion in the granite zone is coherent and that the earthquake ground motion in the deep underground is 20 % of the ground surface. The Japanese government will make an decision on approval or disapproval of ILC within this year (2018).

The other talk is on CEPC. In the talk, the site investigation and the layout of the project, conceptual designs of the civil engineering system. The designs include tunnels, shafts, surface buildings, electrical engineering, the cooling water system, the ventilation and air-conditioning system, the fire protection system and the permanent transportation and lifting equipments. As for the site investigation, 5 candidate sites were investigated. Qinhuangdao site is the best among the five candidate sites based on the terrain and geological conditions. But in general, all the sites are suitable for the underground construction of such a large scale. The main geological problems encountered can be solved by engineering measures. The CDR of the CEPC project was submitted on August 2018.

SUMMARY OF CRYOGENIC SYSTEM

Two talks were given on this subject. One talk was on the KEK cryogenic system. A cryogenic system for the superconducting cavity system was first constructed for TRISTAN in 1988 at KEK. Basically the same system has been used for 30 years also for KEKB and SuperKEKB, since the heat load for KEKB and SuperKEKB was less than that for TRISTAN. Although all of cryogenic system at KEK are very old, they are working very well. Experiences on the maintenance and troubles with the cryogenic system were given in the talk. The experiences should be referred in the future machines.

The other talk was on the cryogenic system for CEPC. Features of the CEPC cryogenic system is a 2K refrigerator using superfluidity He and a high heat load of 47.5 kW (4.5K equivalent heat load). Aggressive R&D works on the 2K JT heat exchanger and the cold compressor are under way. The cryogenic group at IHEP has manufactured 58 1.3GHz 9-cell cryomodules for EXFEL cooperated with domestic companies. This was very impressive. It will be a

* yoshihiro.funakoshi@kek.jp

good foundation for the optimization design for the CEPC cryomodules.

SUMMARY OF BEAM OPERATION

In the session, 5 talks on the beam operation were given. Four of them were on existing machines, *i.e.* DAΦNE, BEPC-II, LHC and SuperKEKB. One of them was a future machine, FCC-ee. As for the 4 existing machines, many experiences were shown in the talks. Among them, several are picked up and listed in Table 1. The experiences are divided into 4 categories, excellent, good, bad and ugly.

DAΦNE came into operation in 2000 and will stop running as a collider in 2020. It is planned to transform it into an accelerator test facility (DAΦNE-TF). The excellent experience at DAΦNE is a beam test of the “crab-waist” scheme. In DAΦNE, it was proved that crab-waist is an effective approach to increase the luminosity in circular colliders even in presence of an experimental solenoid magnet. The crab-waist scheme has become a basic design concept for future new colliders. The longitudinal feedback kicker developed at DAΦNE has been adopted in many machines and become a standard. In DAΦNE, an optics with negative values of the momentum compaction factor was studied. In the study the beam collision was also tried with negative α and a 25 % higher specific luminosity was observed at a low current. However, the beam collision failed at high beam current due to the microwave instability. The similar instability issue with negative α was also observed at KEKB.

BEPCII came into operation in 2006 and is still in operation now. The excellent achievement at BEPCII is that it reached the design luminosity of $1 \times 10^{33} \text{cm}^{-2} \text{s}^{-1}$ on April 5th in 2016. It seems that the lattice evolution such as the low momentum compaction lattice was important to achieve the design luminosity. When they increased the beam currents, they also experienced a lot of hardware failures just like KEKB.

LHC came into beam operation in 2008 and is in the middle of its whole life. The highest peak luminosity of LHC is $2.2 \times 10^{34} \text{cm}^{-2} \text{s}^{-1}$ and broke the world record which KEKB made. The integrated luminosity in Run 2 (2015-2018) with $\sqrt{s} = 13 \text{GeV}$ was 147fb^{-1} and is 50 % higher than the initial target. The famous quench incident happened on Sep. 19th 2008 and the beam operation restarted on Nov. 20th 2009. The machine optics is reproducible and the beta-beating is corrected down to the % level at 6.5 TeV. The IP beta function β^* has been progressively reduced down to 30 cm (design 55 cm). In the beam operation of LHC, they en-

countered peculiar phenomena such as UFOs (Unidentified Falling Objects). UFOs are believed to be dust events and can quench a superconducting magnet. After a two year long shutdown in 2019-2020, the LHC will be back for Run 3 with upgraded injectors. In Run 3, more than a factor of 2 higher peak luminosity is expected and they need the luminosity levelled operation.

SuperKEKB came into operation in 2016. The Phase 1 operation was done from Feb. 2016 to June 2016 without the Belle-II detector and IR magnets. The Phase 2 commissioning was done from March 2018 to July 2018. The excellent achievement in Phase 2 was to verify effectiveness of the “Nano beam scheme” to increase the luminosity. At SuperKEKB, they use a large Piwinski angle collision without the crab-waist scheme. In the talk in this session, only an ugly experience of the QCS quench was discussed. The Phase 3 commissioning will start in March 2019.

The talk on the operation of FCC-ee discussed a study on the operation model, availability of the machine and its performance. The purpose of the study was to validate the operation model of FCC-ee based on achieved values at past machines such as PEP-II and KEKB. The integrated luminosity per year is expressed as the following expression;

$$L_{\text{int}}/\text{year} \approx T \cdot E \cdot L_{\text{nominal}}.$$

Here, T , E and L_{nominal} is a number of days scheduled for physics per year, efficiency and the nominal (design) luminosity, respectively. The efficiency E was estimated based on experiences of past machines. The conclusion of the study is that the assumed annual physics run time of 185 days, hardware availability of at least 80 %, corresponding physics efficiency of 75 %, and projected annual luminosities of FCC-ee look solid, in view of the experience at several circular lepton colliders over the past 30 years.

SUMMARY OF SUMMARY

In the sessions, both old and future machines were reported. Useful lessons from old (or present) machines should be made the most use of in the future machines. Experiences in SuperKEKB may be useful in future machines. Study on the ILC civil engineering investigation is very impressive. Like this, we should learn from machines in other fields such as SR machines. In the next eeFACT workshop at Frascati in 2020, it is expected to hear excellent progress in future machines such as CEPC, FCC-ee, Super t-c factories, DANFE-TF, BEPC-III, SuperKEKB and VEPP-2000.

List of Authors

Bold papercodes indicate primary authors; ~~crossed-out~~ papercodes indicate 'no submission'

— A —

Aiba, M. TUPAB03
Alesini, D. MOYAA02, TUYAA01
Anashin, V.V. MOYBA01
Antoniou, F. TUPAB03
Aoki, K.A. WE0BB04
Apollonio, A. WEPAB03
Arimoto, Y. WE0BB04, WEPBB01
Arinaga, M. TUPBB05
Aumon, S. MOYAA01, TU0AB02

— B —

Bacchetta, N. WEXBA02
Bai, S. MOYAA05, WEXBA05
Bai, Y. TU0BB04
Bambade, P. TUPBB06, WEXBA04
Barryakov, A.M. TUPAB03
Belikov, O.V. MOYBA01
Belli, E. WEXBA02, WE0AB04
Benedikt, M. WEXBA02, WEPAB03
Berkaev, D.E. MOYBA01
Bian, T.J. MOYAA05
Bini, S. MOYAA02
Blanco-García, O.R. MOYAA02, WEXBA02
Blondel, A.P. WEXBA02
Bogomyagkov, A.V. MOYBA02, TU0AB01, WEXAA03, WEXBA02
Bonvicini, G. TUPBB05, TUPBB07
Boscolo, M. MOYAA02, WEXBA02
Brown, D.G. WEXBA04
Brunner, O. WEPAB03
Buonomo, B. MOYAA02
Burkhardt, H. WEXBA02

— C —

Cantarella, S. MOYAA02
Caschera, S. MOYAA02
Castorina, G. MOYAA02
Chaikovska, I. TUPAB03
Charles, T.K. MOYAA01, TUPAB03, TU0AB02
Chavanne, J. MOYAA02
Chehab, R. TUPAB03
Chen, F.S. WE0BB02, WE0BB05
Chi, Y.L. TUPAB04
Collamati, F. WEXBA02
Costa Pinto, P. WE0AB04
Cui, X. MOYAA05, TUPAB05, TUPAB06

— D —

D'Uffizi, A. MOYAA02
Dam, M. WEXBA02

De Santis, A. MOYAA02
Deitrick, K.E. TUYAA03
Delle Monache, G.O. MOYAA02
Di Carlo, S. TUPBB06, WEXBA04
Di Giulio, D.G.C. MOYAA02
Di Pirro, G. MOYAA02
Drago, A. MOYAA02, TUYAA01
Druzhinin, V.P. MOYBA02
Du, C.C. TU0BB04
Duan, Z. TU0BB04

— E —

El Khechen, D. MOYAA01, TUYBA01, TUYBA03, WEXBA02, WEXBA03, WEXBA04
Elsener, K. WEXBA02
Endo, T. WEPAB04
Etisken, O. TUPAB03

— F —

Fisher, A.S. WEXBA04
Flanagan, J.W. TUPBB05
Foggetta, L.G. MOYAA02
Fukuma, H. TUYAA04, TUPBB05
Funakoshi, Y. TU0BB01, TUPAB07, TUPBB06, WEXBA04, WEPAB03, WEPBB01, THXBA01
Furukawa, K. TUPAB01, TUPAB03

— G —

Gallo, A. MOYAA02, TUYAA01
Gao, J. MOYAA05, TUYBA05, TUPAB04, TUPAB06, WEXBA05
Gargana, R. MOYAA02
Geng, H. MOYAA05, WEXBA05
Ghigo, A. MOYAA02, TUYAA01
Giacomelli, P. MOXBA02, TUXAA02
Gil Costa, M. WEXBA02
Glukhov, S.A. TU0AB01
Gong, D.J. MOYAA05
Gorchakov, K. MOYBA01
Guiducci, S. MOYAA02, TUYAA01
Guo, Y.Y. TU0BB04

— H —

Härer, B. TUPAB03
Han, R. WEPAB05
Hara, K. WEPAB04
Hirosawa, K. TU0BB01, TUYBA01, WEYAA03
Hisamatsu, H. WE0AB01
Holzer, B.J. TU0AB02, TUPAB03
Honma, T. WEPAB04

TU0BB03
MOYBA01

— M —

Maestri, M.	MOYAA02
Marhauser, F.	TUYAA03
Martyshkin, P.V.	TUPAB03
Masuzawa, M.	WEXBA04
Meng, C.	MOYAA05, TUPAB04, TUPAB06
Michalski, T.J.	TUYAA03
Michelotti, A.	MOYAA02
Migliorati, M.	WE0AB04
Milardi, C.	MOYAA02, TUYAA01, WEPAB03
Milstein, A.I.	MOYBA02
Mitsuka, G.M.	TUPBB05
Miyahara, F.	TUPAB03, TUPAB07
Mori, K.	TUPBB05
Mori, T.	TUPAB02, TUPAB07
Morita, A.	TU0AB04, TU0BB01, TU0BB02
Morita, Y.	WEPAB04
Motygin, S.V.	MOYBA01
Muchnoi, N.Yu.	TUPBB03
Mulyani, E.	TUPBB05
Myers, S.	WEPAB03

— N —

Nakai, H.	WEPAB04
Nakamura, S.	WEXBA04
Nakanishi, K.	WEYAA03, WEPAB04
Niemi, A.	WEPAB03
Nikiforov, D.A.	TUPAB03
Nikitin, S.A.	WEXAA02
Nikolaev, I.B.	WEXAA01
Nishiwaki, M.	WEYAA03
Novokhatski, A.	WEXBA02

— 0 —

Ogur, S.	TUPAB03
Ohmi, K.	TU0AB04, TU0BB01, TU0BB02, TUYAA04, TUYBA01
Ohnishi, Y.	MOXAA02, TU0AB04, TU0BB01, TU0BB02, TUYBA01, TUPAB07
Ohuchi, N.	WE0BB04, WEPAB04, WEPBB01
Oide, K.	TU0AB02, TU0BB02, TUYBA03, WEXBA03, MOYAA01, WEXBA02, WEPAB03
Oki, T.	WEXBA04
Otboev, A.V.	WEXAA04
Ozcan, E.V.	TUPAB03

— P —

Pagani, C.	WEYAA02
Paladino, A.	WEXBA06
Pang, C.G.	TUPBB06, WEXBA04
Papaphilippou, Y.	TUPAB03

Parker, B. **WE0BB03**
Pei, G. **TUPAB04**
Pei, S. **TUPAB04**
Peinaud, Y. **TUPBB06**
Pellegrino, L. **MOYAA02**
Peng, Y.M. **TU0BB04**
Perevedentsev, E. **MOYBA01**
Perez, E. **WEXBA02**
Polozov, S.M. **TUPAB03**
Prosvetov, V.P. **MOYBA01**

— Q —

Qin, Q. **MOYAA05, TU0BB04, WEPAB03**

— R —

Rabusov, D.V. **MOYBA01**
Raimondi, P. **MOYAA02, TUYAA01**
Ricci, R. **MOYAA02**
Rinolfi, L. **TUPAB03**
Rogovsky, Yu. A. **MOYBA01**
Rotundo, U. **MOYAA02**
Rumolo, G. **WE0AB04**

— S —

Sabbatini, L. **MOYAA02**
Sanelli, C. **MOYAA02**
Sapountzis, A. **WE0AB04**
Seeman, J.T. **WEPAB03**
Seimiya, Y. **TUPAB02, TUPAB07**
Semenov, A.M. **MOYBA01**
Senchenko, A.I. **MOYBA01**
Sensolini, G. **MOYAA02**
Serio, M. **TUYAA01**
Shatilov, D.N. **MOYAA01, MOYBA01, TUYBA02**
Shatunov, P.Yu. **MOYBA01**
Shatunov, Y.M. **MOYBA01**
Shatunov, Yu.M. **WEXAA04**
Shibata, K. **TUYAA04, WE0AB01**
Shimizu, H. **WEPAB04**
Shirai, M. **WE0AB01**
Shubina, O.S. **MOYBA01**
Shwartz, D.B. **MOYBA01**
Sinkovits, T.F. **WE0AB04**
Sinyatkin, S.V. **MOYBA02, TU0AB01, WEXBA02**
Stecchi, A. **MOYAA02**
Stella, A. **MOYAA02, TUYAA01**
Suetsugu, Y. **TUYAA04, WE0AB01**
Sugimoto, H. **TU0AB04, TU0BB02, TUPAB07**
Sugimura, H. **TUPAB07**
Sullivan, M.K. **WEXBA01, WEXBA02, WEXBA04**
Sun, X.J. **WE0BB05**
Sun, Y.S. **TU0BB04**

— T —

Taborelli, M. **WE0AB04**

Tehrani, N.A. **WEXBA02**
Tejima, M. **TUPBB05**
Ten Kate, H.H.J. **WEXBA02**
Terui, S. **WE0AB01, WEPBB01**
Tian, S.K. **TU0BB04**
Timoshenko, M.V. **MOYBA01**
Tobiyama, M. **TUYAA04, TUPBB05, WEXBA04**
Tsuchiya, K. **WE0BB04**
Tydecks, T. **MOYAA01, TU0AB02, TUPAB03**

— U —

Uehara, S. **TUPBB06, WEXBA04**
Ueki, R. **TUPAB07, WEXBA04, WE0BB04**

— V —

Vannozzi, A. **MOYAA02**
Varner, G.S. **TUPBB05**
Viazlo, O. **WEXBA02**
Voutsinas, G.G. **WEXBA02**

— W —

Wang, D. **MOYAA05, TUYBA04, TUPAB04, TUPAB06, WEXBA05**
Wang, J.Q. **TU0BB04**
Wang, N. **MOYAA05, TU0BB04, TUYBA04, TUPAB06**
Wang, X. **WE0BB04, WEPBB01**
Wang, X. **TU0BB04**
Wang, Y. **MOYAA05, TUYBA04, WEXBA05**
Wei, Y. **MOYAA05, TU0BB04**
Wen, Wen. **TU0BB04**
Wenninger, J. **WEPAB03**
Wienands, U. **WEXBA04**
Wu, J. **TU0BB04, TUYBA04**

— X —

Xiao, Y. **WEPAB02**
Xing, Xing. **TU0BB04**
Xu, Xu. **TU0BB04**

— Y —

Yamaoka, H. **WE0BB04**
Yang, M. **WE0BB02, WE0BB05**
Yang, X.C. **WE0BB02**
Yano, Y. **TUPAB07**
Yu, C.H. **MOYAA05, TU0BB04, TUYBA04, TUPAB04, TUPAB05, TUPAB06, WEXBA05**

— Z —

Zanetti, M. **MOYBA04**
Zemlyansky, I.M. **MOYBA01**
Zhai, J.Y. **MOYAA05, TUPAB05, TUPAB06**
Zhang, C. **TU0BB04**

Content from this work may be used under the terms of the CC BY 3.0 licence (© 2018). Any distribution of this work must maintain attribution to the author(s), title of the work, publisher, and DOI.

Zhang, J.Q.	WEPAB05	Zhu, Y.S.	MOYAA05, WEXBA05, WE0BB02, WE0BB05
Zhang, J.R.	TUPAB04		
Zhang, Y.	MOYAA05, TU0BB04, TUYBA04, TUPAB05, TUPAB06, WEXBA05	Zimmermann, F.	MOXBA01, MOYBA04, TU0AB02, TUYBA03, TUPAB03, WEXBA02, WEPAB03
Zharinov, Yu.M.	MOYBA01		
Zheng, H.J.	MOYAA05	Zobov, M.	MOYAA02, TUYAA01, WE0AB04
Zheng, Y.H.	MOYBA05	Zong, Z.G.	WE0BB04
Zhou, D.	TU0AB04, TU0BB01, TUPAB07		
Zhou, Z.S.	WEYBA02		

Institutes List

Ankara University, Faculty of Sciences

Ankara, Turkey

- Etisken, O.

ANL

Argonne, Illinois, USA

- Wienands, U.

BINP SB RAS

Novosibirsk, Russia

- Anashin, V.V.
- Barnyakov, A.M.
- Belikov, O.V.
- Berkaev, D.E.
- Bogomyagkov, A.V.
- Druzhinin, V.P.
- Glukhov, S.A.
- Gorchakov, K.
- Kasaev, A.S.
- Kirpotin, A.N.
- Koop, I.
- Krasnov, A.A.
- Kurkin, G.Y.
- Levichev, A.E.
- Levichev, E.B.
- Lysenko, A.P.
- Martyshkin, P.V.
- Milstein, A.I.
- Motygin, S.V.
- Muchnoi, N.Yu.
- Nikiforov, D.A.
- Nikitin, S.A.
- Nikolaev, I.B.
- Otboev, A.V.
- Perevedentsev, E.
- Prosvetov, V.P.
- Rabusov, D.V.
- Rogovsky, Yu. A.
- Semenov, A.M.
- Senchenko, A.I.
- Shatilov, D.N.
- Shatunov, P.Yu.
- Shatunov, Y.M.
- Shubina, O.S.
- Shwartz, D.B.
- Sinyatkin, S.V.
- Timoshenko, M.V.
- Zemlyansky, I.M.
- Zharinov, Yu.M.

BNL

Upton, Long Island, New York, USA

- Parker, B.

Bogazici University

Bebek / Istanbul, Turkey

- Ozcan, E.V.

Budker INP & NSU

Novosibirsk, Russia

- Shatunov, Yu.M.

CERN

Meyrin, Switzerland

- Antoniou, F.
- Apollonio, A.
- Aumon, S.
- Benedikt, M.
- Brunner, O.
- Burkhardt, H.
- Charles, T.K.
- Costa Pinto, P.
- El Khechen, D.
- Elsener, K.
- Gil Costa, M.
- Härer, B.
- Holzer, B.J.
- Janot, P.
- Kersevan, R.
- Kolano, A.M.
- Leogrande, E.
- Lueckof, M.
- Myers, S.
- Ogur, S.
- Oide, K.
- Papaphilippou, Y.
- Perez, E.
- Rinolfi, L.
- Rumolo, G.
- Sapountzis, A.
- Sinkovits, T.F.
- Taborelli, M.
- Tehrani, N.A.
- Ten Kate, H.H.J.
- Tydecks, T.
- Viazlo, O.
- Voutsinas, G.G.
- Wenninger, J.
- Zimmermann, F.

Cornell University (CLASSE), Cornell Laboratory for Accelerator-Based Sciences and Education

Ithaca, New York, USA

- Deitrick, K.E.

DPNC

Genève, Switzerland

- Blondel, A.P.
- Koratzinos, M.

ESRF

Grenoble, France

- Zhu, Y.S.

INFN- Sez. di Padova

Padova, Italy

- Bacchetta, N.
- Zanetti, M.

INFN-Bologna

Bologna, Italy

- Giacomelli, P.

Roma, Italy

- Belli, E.

Rome, Italy

- Castorina, G.
- Collamati, F.
- Migliorati, M.

Frascati (Roma), Italy

- Alesini, D.
- Bini, S.
- Blanco-García, O.R.
- Boscolo, M.
- Buonomo, B.
- Cantarella, S.
- Caschera, S.
- D'Uffizi, A.
- De Santis, A.
- Delle Monache, G.O.
- Di Giulio, D.G.C.
- Di Pirro, G.
- Drago, A.
- Foggetta, L.G.
- Gallo, A.
- Gargana, R.
- Ghigo, A.
- Guiducci, S.
- Incremona, S.
- Iungo, F.
- Ligi, C.
- Maestri, M.
- Michelotti, A.
- Milardi, C.
- Pellegrino, L.
- Ricci, R.
- Rotundo, U.
- Sabbatini, L.
- Sanelli, C.
- Sensolini, G.
- Serio, M.
- Stecchi, A.
- Stella, A.
- Vannozzi, A.
- Zbov, M.

JLab

Newport News, Virginia, USA

- Li, R.
- Marhauser, F.
- Michalski, T.J.

KEK

Ibaraki, Japan

- Aoki, K.A.
- Arimoto, Y.
- Arinaga, M.
- Flanagan, J.W.
- Fukuma, H.
- Funakoshi, Y.
- Furukawa, K.
- Hara, K.
- Hisamatsu, H.
- Honma, T.
- Hosoyama, K.
- Iida, N.
- Ikeda, H.
- Ishibashi, T.
- Ishii, H.
- Iwabuchi, S.H.
- Kaji, H.
- Kamitani, T.
- Kanazawa, K.
- Kawai, M.K.
- Kawamoto, T.
- Kikuchi, M.
- Kobayashi, T.
- Koiso, H.
- Kojima, Y.
- Kondo, Y.
- Masuzawa, M.
- Mitsuka, G.M.
- Miyahara, F.
- Mori, K.
- Mori, T.
- Morita, A.
- Morita, Y.
- Mulyani, E.
- Nakai, H.
- Nakamura, S.
- Nakanishi, K.
- Nishiwaki, M.
- Ohmi, K.
- Ohnishi, Y.
- Ohuchi, N.
- Oide, K.
- Oki, T.
- Paladino, A.
- Seimiya, Y.
- Shibata, K.
- Shimizu, H.
- Shirai, M.
- Suetsugu, Y.
- Sugimoto, H.
- Sugimura, H.
- Tejima, M.
- Terui, S.

- Tobiyama, M.
- Tsuchiya, K.
- Uehara, S.
- Ueki, R.
- Wang, X.
- Yamaoka, H.
- Yano, Y.
- Zhou, D.
- Zong, Z.G.

LAL

Orsay, France

- Bambade, P.
- Chaikovska, I.
- Chehab, R.
- Di Carlo, S.
- Jehanno, D.
- Kubytskyi, V.
- Pang, C.G.
- Peinaud, Y.

MEPhi

Moscow, Russia

- Polozov, S.M.

NBI

København, Denmark

- Dam, M.

NSU

Novosibirsk, Russia

- Koop, I.
- Perevedentsev, E.
- Rogovsky, Yu. A.
- Senchenko, A.I.
- Shatunov, Y.M.
- Schwartz, D.B.

PSI

Villigen PSI, Switzerland

- Aiba, M.

Sapienza University of Rome

Rome, Italy

- Belli, E.

SLAC

Menlo Park, California, USA

- Brown, D.G.
- Fisher, A.S.
- Novokhatski, A.
- Seeman, J.T.
- Sullivan, M.K.



Sokendai

Ibaraki, Japan

- [Hirosawa, K.](#)
- [Mulyani, E.](#)

Tampere University of Technology

Tampere, Finland

- [Niemi, A.](#)

The University of Melbourne

Melbourne, Victoria, Australia

- [Charles, T.K.](#)

University of Chinese Academy of Sciences

Beijing, People's Republic of China

- [Zheng, Y.H.](#)

University of Hawaii

Honolulu,, USA

- [Varner, G.S.](#)

Università degli Studi di Milano & INFN

Segrate, Italy

- [Pagani, C.](#)

USTC/NSRL

Hefei, Anhui, People's Republic of China

- [Luo, Q.](#)

Wayne State University

Detroit, Michigan, USA

- [Bonvicini, G.](#)

YREC

Zhengzhou, People's Republic of China

- [Xiao, Y.](#)